

Pertanika Journal of
**SCIENCE &
TECHNOLOGY**

JST

VOL. 31 (2) MAR. 2023



A scientific journal published by Universiti Putra Malaysia Press

Pertanika Journal of Science & Technology

About the Journal

Overview

Pertanika Journal of Science & Technology (JST) is the official journal of Universiti Putra Malaysia published by UPM Press. It is an open-access online scientific journal which is free of charge. It publishes the scientific outputs. It neither accepts nor commissions third party content.

Recognized internationally as the leading peer-reviewed interdisciplinary journal devoted to the publication of original papers, it serves as a forum for practical approaches to improving quality in issues pertaining to science and engineering and its related fields.

JST is currently published 6 issues a year, periodically in January, March, April, July, August, and October. It is considered for publication of original articles according to its scope. The journal publishes in **English** and it is open to authors around the world regardless of the nationality.

The Journal is available world-wide.

Aims and scope

Pertanika Journal of Science and Technology aims to provide a forum for high quality research related to science and engineering research. Areas relevant to the scope of the journal include: bioinformatics, bioscience, biotechnology and bio-molecular sciences, chemistry, computer science, ecology, engineering, engineering design, environmental control and management, mathematics and statistics, medicine and health sciences, nanotechnology, physics, safety and emergency management, and related fields of study.

History

Pertanika was founded in 1978. A decision was made in 1992 to streamline *Pertanika* into three journals as Pertanika Journal of Tropical Agricultural Science, Pertanika Journal of Science & Technology, and Pertanika Journal of Social Sciences & Humanities to meet the need for specialised journals in areas of study aligned with the interdisciplinary strengths of the university.

After almost 28 years, as an interdisciplinary Journal of Science & Technology, the journal now focuses on research in science and engineering and its related fields.

Goal of *Pertanika*

Our goal is to bring the highest quality research to the widest possible audience.

Quality

We aim for excellence, sustained by a responsible and professional approach to journal publishing. Submissions are guaranteed to receive a decision within 14 weeks. The elapsed time from submission to publication for the articles averages 5-6 months.

Abstracting and indexing of *Pertanika*

The journal is indexed in SCOPUS (Elsevier), Clarivate-Emerging Sources Citation Index [ESCI (Web of Science)], BIOSIS, National Agricultural Science (NAL), Google Scholar, MyCite and ISC.

Future vision

We are continuously improving access to our journal archives, content, and research services. We have the drive to realise exciting new horizons that will benefit not only the academic community, but society itself.

Citing journal articles

The abbreviation for Pertanika Journal of Science & Technology is *Pertanika J. Sci. Technol.*

Publication policy

Pertanika policy prohibits an author from submitting the same manuscript for concurrent consideration by two or more publications. It prohibits as well publication of any manuscript that has already been published either in whole or substantial part elsewhere. It also does not permit publication of manuscript that has been published in full in Proceedings.

Code of Ethics

The *Pertanika* Journals and Universiti Putra Malaysia takes seriously the responsibility of all of its journal publications to reflect the highest in publication ethics. Thus all journals and journal editors are expected to abide by the Journal's codes of ethics. Refer to *Pertanika's Code of Ethics* for full details, or visit the Journal's web link at http://www.pertanika.upm.edu.my/code_of_ethics.php

International Standard Serial Number (ISSN)

An ISSN is an 8-digit code used to identify periodicals such as journals of all kinds and on all media—print and electronic. All *Pertanika* journals have ISSN as well as an e-ISSN.

Pertanika Journal of Science & Technology: ISSN 0128-7680 (*Print*); ISSN 2231-8526 (*Online*).

Lag time

A decision on acceptance or rejection of a manuscript is reached in 3 to 4 months (average 14 weeks). The elapsed time from submission to publication for the articles averages 5-6 months.

Authorship

Authors are not permitted to add or remove any names from the authorship provided at the time of initial submission without the consent of the Journal's Chief Executive Editor.

Manuscript preparation

Refer to *Pertanika's INSTRUCTIONS TO AUTHORS* through the official website.

Editorial process

Authors are notified with an acknowledgement containing a *Manuscript ID* on receipt of a manuscript, and upon the editorial decision regarding publication.

Pertanika follows a **double-blind peer-review** process. Manuscripts deemed suitable for publication are usually sent to reviewers. Authors are encouraged to suggest names of at least three potential reviewers at the time of submission of their manuscript to *Pertanika*, but the editors will make the final choice. The editors are not, however, bound by these suggestions.

Notification of the editorial decision is usually provided within ten to fourteen weeks from the receipt of manuscript. Publication of solicited manuscripts is not guaranteed. In most cases, manuscripts are accepted conditionally, pending an author's revision of the material.

The Journal's peer-review

In the peer-review process, three referees independently evaluate the scientific quality of the submitted manuscripts.

Peer reviewers are experts chosen by journal editors to provide written assessment of the **strengths** and **weaknesses** of written research, with the aim of improving the reporting of research and identifying the most appropriate and highest quality material for the journal.

Operating and review process

What happens to a manuscript once it is submitted to *Pertanika*? Typically, there are seven steps to the editorial review process:

1. The Journal's Chief Executive Editor (CEE) and the Editorial Board Members (EBMs) examine the paper to determine whether it is appropriate for the journal and should be reviewed. If not appropriate, the manuscript is rejected outright and the author is informed.
2. The CEE sends the article-identifying information having been removed, to 2 or 3 reviewers who are specialists in the subject matter represented by the article. The CEE requests them to complete the review within 3 weeks.

Comments to authors are about the appropriateness and adequacy of the theoretical or conceptual framework, literature review, method, results and discussion, and conclusions. Reviewers often include suggestions for strengthening of the manuscript. Comments to the editor are in the nature of the significance of the work and its potential contribution to the research field.

3. The Editor-in-Chief (EiC) examines the review reports and decides whether to accept or reject the manuscript, invites the author(s) to revise and resubmit the manuscript, or seek additional review reports. Final acceptance or rejection rests with the CEE and EiC, who reserve the right to refuse any material for publication. In rare instances, the manuscript is accepted with almost no revision. Almost without exception, reviewers' comments (to the author) are forwarded to the author. If a revision is indicated, the editor provides guidelines to the authors for attending to the reviewers' suggestions and perhaps additional advice about revising the manuscript.
4. The authors decide whether and how to address the reviewers' comments and criticisms and the editor's concerns. The authors return a revised version of the paper to the CEE along with specific information describing how they have answered the concerns of the reviewers and the editor, usually in a tabular form. The author(s) may also submit a rebuttal if there is a need especially when the authors disagree with certain comments provided by reviewer(s).
5. The CEE sends the revised paper out for re-review. Typically, at least 1 of the original reviewers will be asked to examine the article.
6. When the reviewers have completed their work, the EiC examines their comments and decides whether the paper is ready to be published, needs another round of revisions, or should be rejected. If the decision is to accept, the CEE is notified.
7. The CEE reserves the final right to accept or reject any material for publication, if the processing of a particular manuscript is deemed not to be in compliance with the S.O.P. of *Pertanika*. An acceptance letter is sent to all authors.

The editorial office ensures that the manuscript adheres to the correct style (in-text citations, the reference list, and tables are typical areas of concern, clarity, and grammar). The authors are asked to respond to any minor queries by the editorial office. Following these corrections, page proofs are mailed to the corresponding authors for their final approval. At this point, **only essential changes are accepted**. Finally, the manuscript appears in the pages of the journal and is posted online.

Pertanika Journal of

**SCIENCE
& TECHNOLOGY**

Vol. 31 (2) Mar. 2023



A scientific journal published by Universiti Putra Malaysia Press



EDITOR-IN-CHIEF

Luqman Chuah Abdullah
Chemical Engineering

CHIEF EXECUTIVE EDITOR

Mohd Sapuan Salit

UNIVERSITY PUBLICATIONS COMMITTEE

CHAIRMAN
Nazamid Saari

EDITORIAL STAFF

Journal Officers:

Ellyyanur Puteri Zainal
Kanagamalar Silvarajoo
Muhammad Shafique Ardi Abdul Rahman
Siti Zuhaila Abd Wahid
Tee Syin Ying

Editorial Assistants:

Ku Ida Mastura Ku Baharom
Siti Juridah Mat Arip
Zulinaardawati Kamarudin

English Editor:

Norhanizah Ismail

PRODUCTION STAFF

Pre-press Officers:

Nur Farrah Dila Ismail
Wong Lih Jiun

WEBMASTER

IT Officer:

Illi Najwa Mohamad Sakri

EDITORIAL OFFICE

JOURNAL DIVISION
Putra Science Park
1st Floor, IDEA Tower II
UPM-MTDC Technology Centre
Universiti Putra Malaysia
43400 Serdang, Selangor Malaysia.

Gen Enquiry
Tel. No: +603 9769 1622 | 1616
E-mail:
executive_editor.pertanika@upm.edu.my
URL: www.journals-jd.upm.edu.my

PUBLISHER

UPM Press
Universiti Putra Malaysia
43400 UPM, Serdang, Selangor, Malaysia.
Tel: +603 9769 8851
E-mail: penerbit@putra.upm.edu.my



ASSOCIATE EDITOR

2021-2023

Adem Kilicman
Mathematical Sciences
Universiti Putra Malaysia, Malaysia

Miss Laiha Mat Kiah
Security Services Sn: Digital Forensic, Steganography, Network Security, Information Security, Communication Protocols, Security Protocols
Universiti Malaya, Malaysia

Saidur Rahman
Renewable Energy, Nanofluids, Energy Efficiency, Heat Transfer, Energy Policy
Sunway University, Malaysia

EDITORIAL BOARD

2022-2024

Abdul Latif Ahmad
Chemical Engineering
Universiti Sains Malaysia, Malaysia

Ho Yuh-Shan
Water research, Chemical Engineering and Environmental Studies
Asia University, Taiwan

Mohd Zulkifly Abdullah
Fluid Mechanics, Heat Transfer, Computational Fluid Dynamics (CFD)
Universiti Sains Malaysia, Malaysia

Ahmad Zaharin Aris
Hydrochemistry, Environmental Chemistry, Environmental Forensics, Heavy Metals
Universiti Putra Malaysia, Malaysia

Hsiu-Po Kuo
Chemical Engineering
National Taiwan University, Taiwan

Mohd. Ali Hassan
Bioprocess Engineering, Environmental Biotechnology
Universiti Putra Malaysia, Malaysia

Azlina Harun@Kamaruddin

Enzyme Technology, Fermentation Technology
Universiti Sains Malaysia, Malaysia

Ivan D. Rukhlenko
Nonlinear Optics, Silicon Photonics, Plasmonics and Nanotechnology
The University of Sydney, Australia

Nor Azah Yusof
Biosensors, Chemical Sensor, Functional Material
Universiti Putra Malaysia, Malaysia

Bassim H. Hameed

Chemical Engineering: Reaction Engineering, Environmental Catalysis & Adsorption
Qatar University, Qatar

Lee Keat Teong
Energy Environment, Reaction Engineering, Waste Utilization, Renewable Energy
Universiti Sains Malaysia, Malaysia

Norbahiah Misran
Communication Engineering
Universiti Kebangsaan Malaysia, Malaysia

Biswajeet Pradhan

Digital image processing, Geographical Information System (GIS), Remote Sensing
University of Technology Sydney, Australia

Mohamed Othman
Communication Technology and Network, Scientific Computing
Universiti Putra Malaysia, Malaysia

Roslan Abd-Shukur
Physics & Materials Physics, Superconducting Materials
Universiti Kebangsaan Malaysia, Malaysia

Daud Ahmad Israf Ali

Cell Biology, Biochemical, Pharmacology
Universiti Putra Malaysia, Malaysia

Mohd Shukry Abdul Majid

Polymer Composites, Composite Pipes, Natural Fibre Composites, Biodegradable Composites, Bio-Composites
Universiti Malaysia Perlis, Malaysia

Wing Keong Ng
Aquaculture, Aquatic Animal Nutrition, Aqua Feed Technology
Universiti Sains Malaysia, Malaysia

INTERNATIONAL ADVISORY BOARD

2021-2024

CHUNG, Neal Tai-Shung

Polymer Science, Composite and Materials Science
National University of Singapore, Singapore

Mohamed Pourkashanian

Mechanical Engineering, Energy, CFD and Combustion Processes
Sheffield University, United Kingdom

Yulong Ding

Particle Science & Thermal Engineering
University of Birmingham, United Kingdom

Hiroshi Uyama

Polymer Chemistry, Organic Compounds, Coating, Chemical Engineering
Osaka University, Japan

Mohini Sain

Material Science, Biocomposites, Biomaterials
University of Toronto, Canada

ABSTRACTING AND INDEXING OF PERTANIKA JOURNALS

The journal is indexed in SCOPUS (Elsevier), Clarivate-Emerging Sources Citation Index (ESCI), BIOSIS, National Agricultural Science (NAL), Google Scholar, MyCite, ISC. In addition, Pertanika JSSH is recipient of "CREAM" Award conferred by Ministry of Higher Education (MoHE), Malaysia.

The publisher of Pertanika will not be responsible for the statements made by the authors in any articles published in the journal. Under no circumstances will the publisher of this publication be liable for any loss or damage caused by your reliance on the advice, opinion or information obtained either explicitly or implied through the contents of this publication. All rights of reproduction are reserved in respect of all papers, articles, illustrations, etc., published in Pertanika. Pertanika provides free access to the full text of research articles for anyone, web-wide. It does not charge either its authors or author-institution for refereeing/publishing outgoing articles or user-institution for accessing incoming articles. No material published in Pertanika may be reproduced or stored on microfilm or in electronic, optical or magnetic form without the written authorization of the Publisher.
Copyright ©2021 Universiti Putra Malaysia Press. All Rights Reserved.



Pertanika Journal of Science & Technology
Vol. 31 (2) Mar. 2023

Contents

Foreword <i>Mohd Sapuan Salit</i>	i
<i>Review Article</i>	
The Impact of Integrating Multi-Microgrid System with FACTS Devices for Voltage Profile Enhancement and Real Power Loss Reduction in Power System: A Review <i>Ainna Nadirah Zubidi, Bazilah Ismail, Ibrahim Mohamed Ali Al Hamrounni, Nadia Hanis Abd Rahman and Mohd Helmy Hakimie Mohd Rozlan</i>	633
Modified K-Means Clustering for Demand-Weighted Locations: A Thailand's Convenience Store Franchise - Case Study <i>Chartchai Leenawong and Thanrada Chaikajonwat</i>	655
Visible-Near-Infrared Spectroscopy and Chemometrics for Authentication Detection of Organic Soybean Flour <i>Rudiati Evi Masithoh, Muhammad Fahri Reza Pahlawan, Devi Alicia Surya Saputri and Farid Rakhmat Abadi</i>	671
Optimum Temperature and Salinity Conditions for Growth, Lipid Contents, and Fatty Acids Composition of Centric Diatoms <i>Chaetoceros Calcitrans</i> and <i>Thalassiosira Weissflogii</i> <i>Ahmed Awadh Ahmed Sas, Aziz Arshad, Simon Kumar Das, Suriyanti Su Nyun Pau and Zaidi Che Cob</i>	689
Production of Biosurfactant Using <i>Bacillus subtilis</i> Natto Fermentation <i>Yew Seng Leow, Norhafizah Abdullah, Dayang Radiah Awang Biak, Nur Syakina Jamali, Rozita Rosli and Huey Fang Teh</i>	709
Aquaculture Wastewater Quality Improvement by Floating Raft of Native Aquatic Plants in An Giang Province, Vietnam <i>Khanh Tran Thien Nguyen, Chi Thi Dao Vo, An Thuy Ngo, Nghi Thanh Doan, Luyen Phuc Huynh and Dung Huynh Thuy Tran</i>	729
Characterising Colour Feature Descriptors for <i>Ficus carica</i> L. Ripeness Classification Based on Artificial Neural Network (ANN) <i>Ilyia Adhwa Mazni I, Samsul Setumin, Mohamed Syazwan Osman, Muhammad Khusairi Osman and Mohd Subri Tahir</i>	759

Potential of Fatty Acid Methyl Ester as Diesel Blends Produced from Free Fatty Acid in Waste Cooking Oil Catalyzed by Montmorillonite-Sulfonated Carbon	781
<i>Hasanudin Hasanudin, Wan Ryan Asri, Firda Rahmania Putri, Fahma Riyanti, Zainal Fanani, Addy Rachmat, Novia Novia and Tuty Emilia Agustina</i>	
Transfer Learning VGG16 Model for Classification of Tomato Plant Leaf Diseases: A Novel Approach for Multi-Level Dimensional Reduction	813
<i>Premkumar Borugadda, Ramasami Lakshmi and Satyasangram Sahoo</i>	
Efficient Frequency-Dependent Coefficients of Explicit Improved Two-Derivative Runge-Kutta Type Methods for Solving Third-Order IVPs	843
<i>Lee Khai Chien, Norazak Senu, Ali Ahmadian and Siti Nur Iqmal Ibrahim</i>	
An Optimum Classifier Model with Fuzzy C-Means for Fire Detection Technology	875
<i>Elaiyaraja Gandhi and Kumaratharan Narayanaswamy</i>	
Conceptual Design of a Combined Brake-Accelerator Pedal for Limbs Disabled Driver Using a Hybrid Approach	895
<i>Salami Bahariah Suliano, Siti Azfanizam Ahmad, Azizan As'arry and Faeza Abdul Aziz</i>	
The Photophysiology of Benthic Diatoms in the Intertidal Flats of Pulau Pinang (Malaysia)	911
<i>Sazlina Salleh, Elaine Ee Ling Cheng, Md. Solaiman Hossain, Shakila Samad, Nur Ain Amani Abdul Mubin, Nur Aqilah Muhamad Darif, Michelle Glory G Jonik and Mahadi Mohammad</i>	
<i>Review Article</i>	
The Impact of Calcium Chloride in Cementation Solution on Microbial Induced Calcite Precipitation: A Systematic Review	933
<i>Aljohani Waad Awdah Saad, Siti Norathirah Mohd Anas, Nor Safiqah Seminin, Putri Nur Suhaina Naim, Dardau Abdulaziz, Rusea Go, Nor Azwady Abdul Aziz, Mona Fatin Syazwaneer Mohamed Ghazali and Muskhazli Mustafa</i>	
Lung Function Analysis of Marble Home Industry Workers in Tulungagung Regency	947
<i>Noeroel Widajati, Tri Martiana, Tri Niswati Utami, Juliana Jalaludin and Titi Rahmawati Hamedon</i>	

Heat Stress and Noise Exposure Levels in a Manufacturing Plant <i>Qi Jie Kwong, Nursyifaasahirah Terbizi, Normaisarah Nordin, Emma Marinie Ahmad Zawawi, Azli Abd Razak and Jamalunlaili Abdullah</i>	961
TOPSIS for Analyzing the Risk Factors of Suicidal Ideation Among University Students in Malaysia <i>Sin Yin Chan and Chee Keong Ch'ng</i>	977
Influencing Physical Characteristics of Landslides in Kuala Lumpur, Malaysia <i>Syaidatul Azwani Zulkaflī, Nuriah Abd Majid, Sharifah Zarina Syed Zakaria, Muhammad Rizal Razman and Minhaz Farid Ahmed</i>	995
<i>Review Article</i> Subcritical Water Pretreatment for Anaerobic Digestion Enhancement: A Review <i>Adila Fazliyana Aili Hamzah, Muhammad Hazwan Hamzah, Hasfalina Che Man, Nur Syakina Jamali, Shamsul Izhar Siajam and Pau Loke Show</i>	1011
Distribution of Six Urban Bird Species in Urban Agglomeration of Central Region of Peninsular Malaysia Using Ebird Database <i>Aminah Madi, Fatihah Najihah Arazmi, Shukor Md. Nor and Mohammad Saiful Mansor</i>	1035
A Single Objective Crow Search for Modelling of Horizontal Flexible Plate Structure <i>Aida Nur Syafiqah Shaari, Muhamad Sukri Hadi and Abdul Malek Abdul Wahab</i>	1047
Physical and Electrical Breakdown Characteristics of Oil-Impregnated Kenaf Paper with the Introduction of External PVA for Transformer Application <i>Muhammad Umair, Norhafiz Azis, Rasmina Halis and Jasronita Jasni</i>	1069
The Predictive Ability of Total Genotype Score and Serum Metabolite Markers in Power-Based Sports Performance Following Different Strength Training Intensities — A Pilot Study <i>Elin Elisa Khairul, Wan Atiyyah Ab Wahab, Lay Kek Teh, Mohd Zaki Salleh, Mohd Salleh Rofiee, Raja Mohammed Firhad Raja Azidin and Sarina Md. Yusof</i>	1087

- Investigation of Acoustic and Vibrational Properties Using Laser Doppler Vibrometry (LDV) and Electronic Speckle Pattern Interferometry (ESPI) of the Kulintangan Instruments 1105
Sinin Hamdan, Ahmad Faudzi Musib, Khairul Anwar Mohamad Said, Saiful Hairi Othman and Marini Sawawi
- The Breeding Ecology of the Painted Stork *Mycteria leucocephala* in Central Peninsular Malaysia 1121
Mohd Amir Zakaria, Ummi Nur Syafiqah Daud, Mohammad Saiful Mansor and Shukor Md. Nor

Foreword

Welcome to the second issue of 2023 for the *Pertanika Journal of Science and Technology (PJST)*!

PJST is an open-access journal for studies in Science and Technology published by Universiti Putra Malaysia Press. It is independently owned and managed by the university for the benefit of the world-wide science community.

This issue contains 25 articles; three review articles and the rest are regular articles. The authors of these articles come from different countries namely Bangladesh, China, India, Indonesia, Malaysia, Nigeria, Thailand, Vietnam and Yemen.

A regular article titled “Conceptual Design of a Combined Brake-Accelerator Pedal for Limbs Disabled Driver using a Hybrid Approach” was presented by Salami Bahariah Suliano and her colleagues from Universiti Putra Malaysia, Malaysia. Their study aims to generate and select the best concept design for a combined brake-accelerator pedal with special attention based on the needs of the disabled’s ergonomics. Developing these improved ergonomics combined brake-accelerator pedals avoids braking and accelerating interference. Therefore, it is advantageous over conventional pedals and previously combined pedals. A TRIZ, morphological chart, and Pugh matrix hybrid introduce systematic generation, development, and selection of the concept design. Detailed information on this study is available on page 895.

The next article discussed the influencing physical characteristics of landslides in Kuala Lumpur, Malaysia. In this study, a 100 landslides historical data set and eight landslide factors were obtained from proper field validation and maps provided by those concerned in the government, such as distance to roads, distance to streams, elevation, slope angle, curvature, slope aspect, land use, and lithology. This study found that 18.0% of landslides occurred along the Northwest of Kuala Lumpur, where most of these areas are surrounded by altered slopes. It indicates that the authorities are responsible for constructing an advanced prevention and mitigation procedure as the landslide-prone areas require critical planning and monitoring. In the meantime, a higher slope inclination can contribute to a higher gravity force in pulling materials down the slope, thereby increasing the risk of landslides. Details of this study are available on page 995.

Another article we wish to highlight is on “The Predictive Ability of Total Genotype Score and Serum Metabolite Markers in Power-Based Sports Performance Following Different Strength Training Intensities” by Elin Elisa Khairul et al. from Universiti Teknologi MARA, Malaysia. This study explored the predictive ability of total genotype score (TGS) and serum metabolite markers in power-based sports performance following different strength training (ST) intensities. The researchers recruited 15 novice male field hockey

players (age = 16.27 ± 12 years old, body mass index = 22.57 ± 2.21 kg/m²) and allocated them to; high-intensity strength training (HIST, n=5), moderate intensity strength (MIST, n=5), and control group (C, n=5). Both training groups completed an eight-week ST intervention. Pre- and post-training muscular power (vertical jump) was measured. TGS was calculated to annotate for strength-power (STP) and endurance (END) qualities. It is concluded that STP TGS may influence muscular power changes following MIST in novice field hockey players. Further details of the investigation can be found on page 1087.

We anticipate that you will find the evidence presented in this issue to be intriguing, thought-provoking and useful in reaching new milestones in your own research. Please recommend the journal to your colleagues and students to make this endeavour meaningful.

All the papers published in this edition underwent Pertanika's stringent peer-review process involving a minimum of two reviewers comprising internal as well as external referees. This was to ensure that the quality of the papers justified the high ranking of the journal, which is renowned as a heavily-cited journal not only by authors and researchers in Malaysia but by those in other countries around the world as well.

We would also like to express our gratitude to all the contributors, namely the authors, reviewers, Editor-in-Chief and Editorial Board Members of PJST, who have made this issue possible.

PJST is currently accepting manuscripts for upcoming issues based on original qualitative or quantitative research that opens new areas of inquiry and investigation.

Chief Executive Editor

executive_editor.pertanika@upm.edu.my

Review Article

The Impact of Integrating Multi-Microgrid System with FACTS Devices for Voltage Profile Enhancement and Real Power Loss Reduction in Power System: A Review

Ainna Nadirah Zubidi, Bazilah Ismail*, Ibrahim Mohamed Ali Al Hamrounni, Nadia Hanis Abd Rahman and Mohd Helmy Hakimie Mohd Rozlan

Electrical Engineering Section, Universiti Kuala Lumpur British Malaysian Institute, 53100, Gombak, Selangor, Malaysia

ABSTRACT

Renewable energy is crucial for reducing emissions and meeting future energy demands. However, due to concerns regarding intermittent supply, integrating RE into a multi-microgrid system might pose various power system problems, for instance, unstable electrical power output. As a result, increased load reactive power demands result in voltage losses during peak load demand. Therefore, it can be minimized by utilizing Flexible Alternating Current Transmission System (FACTS) devices in electrical networks, which are designed to strengthen the stability and control of power transfer and act as a controller for the AC transmission specification, which also provides speed and flexibility for certain applications. By identifying the need to implement solutions that can sustain the electric power quality of a microgrid, this paper presents a review of various method approaches which could be used to evaluate the impact of integrating the multi-microgrid

systems with FACTS devices for voltage profile improvement and real power loss reduction in power system. In this paper, a comprehensive study is carried out for optimum multi-microgrid placement, considering the minimization of power losses, enhancement of voltage stability, and improvement of the voltage profile. An attempt has been made to summarize the existing approaches and present a detailed discussion that can help the energy planners

ARTICLE INFO

Article history:

Received: 25 September 2021

Accepted: 02 March 2022

Published: 06 March 2023

DOI: <https://doi.org/10.47836/pjst.31.2.01>

E-mail addresses:

ainna.zubidi01@s.unikl.edu.my (Ainna Nadirah Zubidi)

bazilahismail@unikl.edu.my (Bazilah Ismail)

ibrahim.mohamed@unikl.edu.my (Ibrahim Mohamed Ali Al Hamrounni)

nadiahanis@unikl.edu.my (Nadia Hanis Abd Rahman)

mhelmy@unikl.edu.my (Mohd Helmy Hakimie Mohd Rozlan)

*Corresponding author

decide which objective and planning factors need more attention for optimum locations and capacity for multi-microgrid and FACTS devices.

Keywords: Flexible alternating current transmission system, multi-microgrid, power loss, renewable energy, voltage profile

INTRODUCTION

Decades ago, Malaysia had many natural resources used to generate electricity, despite being heavily dependent on imported coal and oil until impacts were seen on carbon emissions, thus leading to the greenhouse effect. In response to these environmental concerns, the government announced in 2015 to implement renewable sources to create a cleaner and more sustainable environment. Thus, Tenaga Nasional Berhad (TNB) is a well-known Malaysian utility company that runs smart grid projects involving large-scale distributed resources generations (DRGs) in Negeri Sembilan and Kedah (Zahurul et al., 2016). A smart grid (SG) system is an intelligent electrical network that operates inventively in coordinating and controlling all users' actions. This system ensures that power supply and demands are reliable, cost-effective, and stable.

With Malaysia's efforts in moving towards a smart grid system, the Energy Commission has initiated several programs in support of the National Green Technology Master Plan by introducing a 2000 MW Large Scale Solar Photovoltaic coupled with Net Energy Metering (NEM), which is capable of contributing a substantial amount of energy (Malaysia Energy Commission, 2018). Furthermore, in 2019, the government introduced the 10-year Generation Development Plans for Malaysia for the period 2020–2030, where the preferred RE is solar power (Peninsular Malaysia) and hydro (Sabah) to achieve 20% RE by 2025 and a 35% reduction in carbon emission intensity by 2030. Therefore, five companies have been awarded under the LSS scheme in balancing energy security and sustainability while encouraging and strengthening renewable energy in a 21st-century global challenge.

Over these last years, microgrids have gained growing significance and set a new economic model in electricity systems. The increased number of distributed generators is due to increasing load demand growth in the power system (Ackermann et al., 2001). Therefore, microgrid systems have already been introduced in other developed countries such as the USA, China, European Union, and Japan, where they can cope with an increase in electricity demands and saves non-renewable energy consumption, as well as help to prevent major blackouts, or during a power failure. However, the integration of renewable energy resources in microgrid systems can cause several power system problems due to intermittent supply issues. RE technologies in a microgrid, such as solar and wind energy, can cause unstable electrical power output, and the increased load reactive power demands result in voltage losses during peak load demand (Urquizo et al., 2018). These

can be minimized by utilizing FACTS devices in electrical networks. FACTS devices are designed to strengthen the stability and control of power transfer and a controller in AC transmission that provides speed and flexibility for certain applications. However, a few barriers have been identified, including the formation of voltage unbalance, voltage sag and swell, power loss, and poor voltage regulation of the system due to the intermittent nature of the high penetration of renewable energy resources. By identifying the need to implement solutions that can sustain the electric power quality of microgrids, this paper presents a review of various improvement approaches that could enhance the stability and performance of multi-microgrid (MMG) systems with FACTS devices.

SMART GRID SYSTEM

A smart grid is a combination of digital and advanced technologies that allows bi-directional connection between utility and end-users in the same transmission lines and works to monitor, communicate and control the power generation in meeting the electric demands. They also can manage the needs of all generators, grid operators, energy market stakeholders, and end-users to maximize reliability, resilience, and stability while reducing costs and environmental implications. In addition, smart grids incorporate distributed and active resources into power networks and energy markets, such as generating, electric demands, storage, and electric vehicles. These general features of the smart grid system include renewable energy resources, plug-in electric vehicles, electric demand, and a control system, as shown in Figure 1.

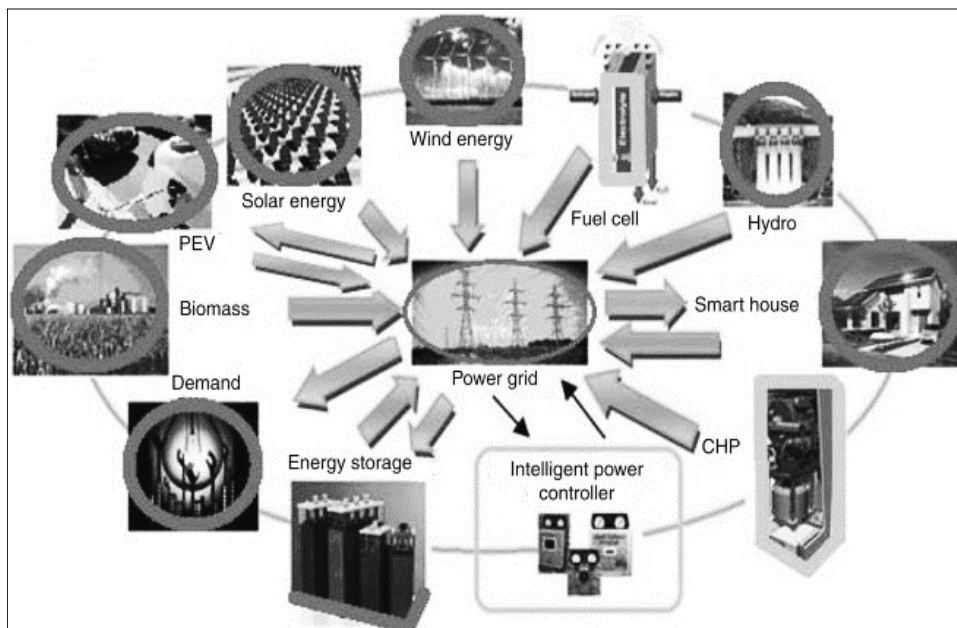


Figure 1. Smart grid system architecture (Funabashi, 2016)

MULTI-MICROGRID COMPONENT

In recent years, microgrid research has expanded dramatically due to the growing interest in microgrid deployment. Later, the idea of multi-microgrids (MMGs) was introduced, which connected several distributed generations (DGs) and loads that could enhance the system's performance and controllability (Haddadian & Noroozian, 2017). Multi-microgrid system comprises several adjacent microgrids with multiple types of distributed generations and loads, which have better performance and reliability in connected and islanded operations modes than a microgrid. The idea of the MMG was developed through the EU's "More Microgrid" program that was proposed in 2006 (Xu et al., 2018). It can be built at the medium-voltage (MV) level by connecting a few low-voltage (LV) microgrids and DG units directly to nearby MV-controlled loads (Vasiljevska et al., 2012). Multi-microgrid systems can be categorized into: alternating current (AC) multi-microgrids, direct current (DC) multi-microgrids, and AC-DC hybrid multi-microgrids. The AC multi-microgrids are conventional multi-microgrids consisting of distributed generations, energy storage systems, and loads connected to AC buses through converters without changing the original structure of the power grid, as shown in Figure 2 (Xu et al., 2018).

There are significant elements for microgrid operation, such as distributed generation, distributed storage, interconnection switches, and control systems. Distributed energy resources are small-scale energy resources that can be implemented at utility plants or house residences to provide local electricity supplies. Distributed generations include microturbines, fuel cells, wind, photovoltaic (PV), and reciprocating internal combustion engines with generators. Some DG needs power electronics to form one form to another by converting power. Distributed storage (DS) also connects the power and energy required in the microgrid. Several kinds of energy storage were used in the microgrid, including flywheels and batteries. A switch that connects the microgrid to the rest of the distribution system is interconnected. The microgrid control system is constructed to operate in grid-parallel and stand-alone modes. The MG control system focuses on the voltage and frequency when the grid is disconnected and provides the real-time power differences between generation and load, differentiating between the reactive power produced and the true power used by the load and protecting the inner of the microgrid (Kroposki et al., 2008). The main advantages of the microgrid are the reduced transmission losses by increasing stability and reliability and powering local loads to avoid any disturbance in the primary grid. Finally, it can enhance renewable energy resources integration such as solar, wind, and biomass.

Multi-Microgrid Controls

Figure 2 shows a multi-microgrid control architecture controlled by the remote terminal unit, with the central autonomous management controller (CAMC) placed at the MV level.

In this way, the system's complexity will be distributed among smaller individual control agents that act as a small distribution management system (DMS) capable of scheduling distributed generation and other control agents deployed under normal and critical events in the system. Apart from that, DMS is in charge of monitoring, controlling, and managing the distribution system. There are two management levels of central DMS where the central autonomous management controller will be installed, and which will accommodate a set of local capabilities assigned to the DMS at the HV/MV substation stage and liable to connect the DMS to lower agents. Furthermore, the microgrid central controller is assigned at the microgrid level for each MV/LV substation to administer the MG, which uses the MG communication infrastructure to control sources and responsive loads in each LV grid voltage monitoring (Lopes et al., 2013). The standard operating mode occurs when the multi-microgrid system is interconnected to the primary distribution grid. Meanwhile, the emergency operating mode is operated when the MMG is in an autonomous or islanded mode or following a power outage. When a black start procedure is triggered, the MMG system will be in restoration service.

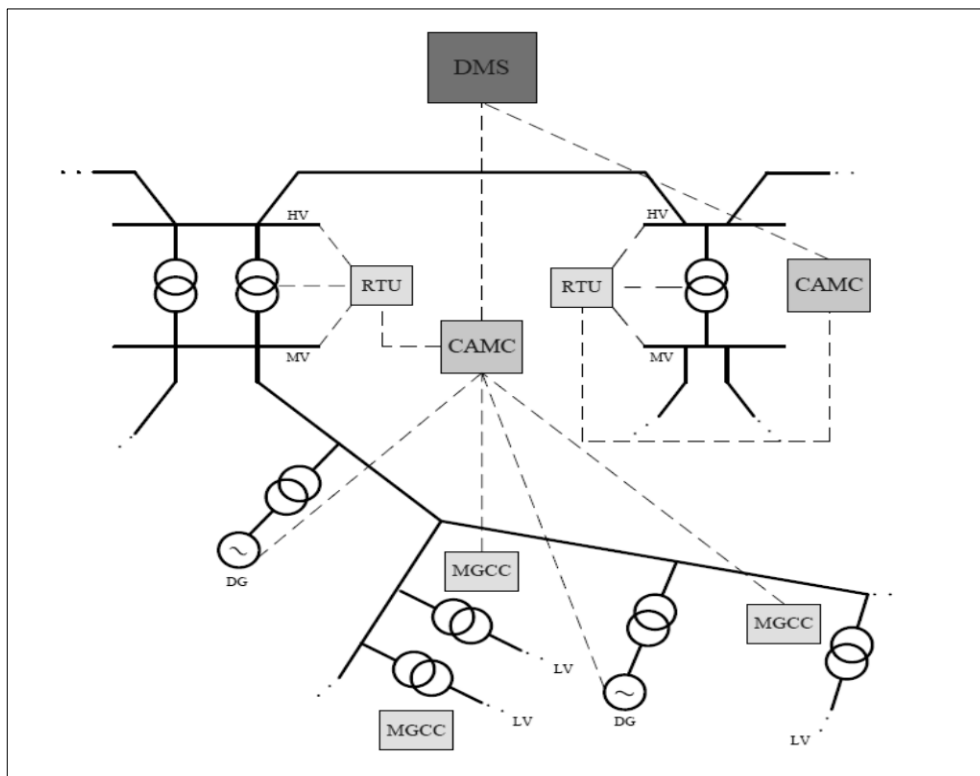


Figure 2. Multi-microgrid control architecture (Lopes et al., 2013)

FLEXIBLE AC TRANSMISSION SYSTEM DEVICES

FACTS technology is a power electronic controller containing some controllers. Researchers have proven the FACTS devices (Jordehi, 2015) to be a very efficient and viable way to deal with transmission systems. Meanwhile, a distribution flexible alternating current transmission system refers to a group of power electronic devices used in distribution networks and has the same benefits as FACTS technology. Hingorani introduced D-FACTS technology in 1985, strengthening and controlling the power system's stability. At the same time, the FACTS controller can improvise the characteristics of the power system and can also control the essential parameters in the transmission network, such as the transmission line power flow, voltage control, transient stability improvement, and oscillation damping (Urquizo et al., 2018). Research is done by Wang et al. (2012) also pointed out that advanced and flexible power electronics are one of the keys to providing a high-quality electricity supply to both customers and utilities, which are divided into three categories (series, shunt, and a combination of series and shunt) as shown in Table 1.

Table 1

Classification of the FACTS devices (Al Ahmad & Sirjani, 2019)

Configuration of FACTS devices	Flexible alternating current transmission system (FACTS devices)	
Shunt connection	SVC	Static var compensator
	TCR	Thyristor controlled reactor
	TSC	Thyristor switched capacitor
	TSR	Thyristor switched reactance
	STATCOM	Static synchronous compensator
Series connection	TCSC	Thyristor-controlled series compensator
	IPC	Interphase power controller
	TSSC	Thyristor switched series capacitor
	TCSR	Thyristor-controlled series reactor
	TCSC	Thyristor-controlled series capacitor
	TSSR	Thyristor switched series reactor
	TCVR	Thyristor-controlled voltage regulator
SSSC	Static synchronous series compensator	
Combination of series and shunt connections	TCPST	Thyristor-controlled phase shift transformer
	UPFC	Unified power flow controller
	IPFC	Interlink power flow controller
	GUPFC	Generalized unified power flow controller

Moreover, voltage stability in the electrical network may be affected by the loss of reactive power demand. Therefore, the characteristics of FACTS controllers can absorb or inject real power into the network and sustain voltage stability. Since the distribution system is usually exposed to power losses, it will produce other issues, such as excessive energy losses and transient and dynamic instabilities. Implementing FACTS devices leads to dynamic and transient stability improvement, increased power transfer capability in the transmission line, enhancement of voltage stability, voltage regulation, power factor correction, and power loss reduction (Chirantan et al., 2018).

IMPACT OF INTEGRATING MULTI-MICROGRID SYSTEM IN CURRENT DISTRIBUTION AND TRANSMISSION SYSTEM

Renewable energy (RE) is critical in reducing emissions and meeting future energy demands. Hence, configuration from the existing electricity networks with the integration of renewable resources has formed an intelligent grid system where the DGs play a significant part in the smart grid system. Since the traditional approach to energy management systems has steadily evolved, some of the networks' DGs have increased. Therefore, high penetration of RE sources in the network will increase the active load, such as storage and loads. Incorporating active power sources in DGs leads to a complex power network. Furthermore, as the generation of renewable sources is weather-dependent, it will indirectly impact power fluctuation, causing voltage instability, frequency deviation, and voltage flicker inside the network.

Furthermore, this problem has been overcome by utilizing energy storage devices, which can cost money to install and maintain. As the power fluctuation of MMG rises, the energy storage capacity of devices will increase. MMGs are usually placed near the demand side to avoid traveling long distances will be costly and inefficient transmission power due to transmission loss. Thus, integrating the MMGs into the transmission and distribution system will enhance the power system efficiency. In addition, MMG produces jobs in the local community while creating clean power generation. Similarly, MMG supplies power to remote and inaccessible areas to help remote populations build their economies. On the other hand, the impact of integrating MMGs is gaining greater attention in the smart home, where the house can send electricity to the grid if it generates greater than the demands. As a result, the homeowner can benefit from the profit generated by selling excess power to a utility provider like TNB. Furthermore, MMG has a shorter installation time and faster reaction than a centralized power plant, which takes longer to set up and provide electricity for additional demand. In extreme weather circumstances like natural disasters, human error, or terrorism, integrating MMG increases energy security over centralized power plants.

Subsequently, the centralized power plants will probably collapse, resulting in a massive power cut affecting residential areas and commercial industries. As a result, all developed

nations have improved their supply reliability and power management, with grid systems operated by independent utilities that allow for effortless power, frequency, and voltage maintenance. Furthermore, it also includes utilizing power storage and control systems to reduce obstruction. Besides, the smart grid may accommodate a high RE capacity, decreasing global dependence on fossil fuels and minimizing greenhouse gas emissions. In the meantime, engineers have faced challenges integrating MMGs into an existing power system. Therefore, MMGs are an essential element of a smart grid, an initiative to move toward an intelligent grid system. Albeit issues and challenges, such as an intermittent supply due to high penetration of RE, can be reduced by determining the best location and capacity of FACTS controller proposed in previous literature. Therefore, introducing FACTS devices into a power system might help solve problems such as increasing power transfer capability in the transmission line, enhancing voltage stability, and reducing power losses caused by integrating a multi-microgrid system.

TECHNIQUES FOR OPTIMAL FACTS DEVICE'S LOCATION AND SIZING IN OPTIMIZING MULTI-MICROGRID PERFORMANCE

Researchers are working on various ways to improve performance in multi-microgrids. Optimization problems in electrical systems are popular for power researchers, especially with microgrid integration. Various optimization methods have been proposed in previous studies to highlight the success rate of the proposed approach in recent years. However, the most optimized methods require extremely high computing resources for large problems relevant to power systems. All existing methods used in the previous study to determine the optimal location and sizing of FACTS devices can be categorized into four groups: (1) analytical approaches, (2) conventional approaches, (3) meta-heuristic approaches, and (4) hybrid approaches (Ismail et al., 2020).

Analytical approaches or sensitive-based approaches utilize mathematical formulation. Conventional approaches are also known as traditional methods that generally start with randomly determining an initial solution and achieving the optimal solution in every solution such as Newton-Raphson (NR), linear programming, nonlinear programming, sequential quadratic programming, dynamic programming, and many more (Ismail et al., 2020). Numerous metaheuristic optimization algorithms have been developed and used in power systems. These techniques are categorized based on the source of inspiration, including evolutionary phenomena, collective animal behavior (swarm techniques), physical rules, or human-related concepts. Furthermore, hybrid-based approaches are combined with existing techniques such as analytical-metaheuristic approaches, traditional-metaheuristic approaches, and metaheuristic-metaheuristic approaches to create hybrid-based approaches. This approach is also known as the two-stage approach, which helps reduce the proposed methods' search space and shows the simpler structure of algorithms that requires less

computation time to solve the optimization problems (Ismail et al., 2020). Table 2 lists the summary of the previous research. Based on Table 2 was assessed through the type of optimization, aims, methods, and indices used for DG and FACTS device integration, benchmark test systems, and case studies.

Yenealem et al. (2019) presented the MG integration, including FACTS devices, using the Newton Raphson (N-R) method to obtain the candidate bus for the MG, STATCOM, and UPFC integration to increase the voltage profile and reduce power losses. However, the MG integrations with STATCOM and UPFC were tested on the IEEE 30 bus system. Furthermore, this study case was compared based on the MG and FACTS device integrations. Based on the findings, the MG system was placed on the weakest bus, Bus 30, and it was observed that voltage fluctuation and high-power losses were further improved. It is observed that in MG integration, the real power loss is further increased. Hence, UPFC was introduced to reduce the real power loss. In Rao and Rao (2017), the author used a two-stage algorithm where in the first stage of the algorithm, the loss sensitivity analysis was adopted to determine the optimum placement for the STATCOM. Next, in the second stage, the parameter setup of STATCOM, the voltage magnitude, and the phase angle have been considered using the N-R power flow technique to reduce power loss and improve the voltage profile. The study was done in IEEE 14 bus test system, and the results were obtained by comparing the power losses before and after STATCOM was integrated.

According to the study presented (Sirjani, 2018), the optimal location and sizing of PV-STATCOM were determined using adaptive particle swarm optimization and power loss index to minimize cost and voltage profile improvement and reduced power loss by considering the real power loss, voltage deviation investment cost, where the constraints for solving the optimization problem are power flow balance, size limit, and bus voltage limits. The case study was tested in the Northern Cyprus electrical transmission system, and the results were obtained by comparing it with three algorithms: lightning search algorithm (LSA), bee colony optimization (BCO), and adaptive particle swarm optimization (APSO). The results show that APSO offers a further reduction in real power loss with the fastest computational time compared to other algorithms. Next, the mixed-integer nonlinear programming (MINLP) was used to find the best placement and sizing of the PV and microturbine with STATCOM, as presented in Luo et al. (2018), in order to reduce annual cost, enhance voltage profile, and reduce power loss considering the power flow equation, voltage limit, branch current limit, DG size constraints, and PV power factor. It was tested in the IEEE 33-bus system and was analyzed using DG and FACTS integration. The results prove that integrated PV solar farms with STATCOM can reduce voltage recovery time and voltage sag depth during an emergency. Also, PV-STATCOM has a high economic value, an improved voltage profile, and reduced power losses. The idea of improving multi-MGs' performance by incorporating IPFC was proposed as a

Table 2
 Taxonomy of studies on optimal placement and sizing of DG and FACTS devices

Reference	Optimization Type	Objectives	Method/Techniques	Index	Type of DG	Type of FACTS	IEEE test system	Case study
Yenealem et al. (2019)	Location	Voltage Profile, Power Losses	Analytical approach	PLF	PV, Wind	UPFC, STATCOM	30-bus	DG and FACTS integration
Gerbex et al. (2001)	Location	System Loadability, Power Losses, Voltage Profile	GA	PLF	PV	TCSC, TCPST, TCVR, SVC	118-bus	Comparative studies using FACTS integration.
Rao and Rao (2017)	Location	Power Losses, Voltage Profile, Power Flow	Analytical Approach	LSF	PV	STATCOM	14-bus	FACTS integration
Sirjani (2018)	Location, Sizing	Power Losses, Voltage Profile, Cost Minimization	APSO	PLI	PV	STATCOM	30-bus 57-bus	DG and FACTS integration
Luo et al. (2018)	Location, Sizing	Total Annual Cost, Voltage Profile, Power Losses	Mixed integer nonlinear programming (MINLP)	WVSAI	PV Micro-Turbine	STATCOM	33-bus	Comparative studies using DG integration.
Kargarian et al. (2012)	Location, Sizing	Power Losses, Voltage Profile, MMG Operating Cost	MOPF	SI	PV	IPFC	33-bus 69-bus	FACTS integration
Yenealem et al. (2020)	Location	Power Losses, Voltage Profile, Power Flow	Fuzzy Logic	CPF	PV, WT	STATCOM	33-bus 69-bus	FACTS integration
Selim et al. (2019)	Location, Sizing	Total Losses, Voltage Profile	Hybrid analytical-metahuristic (sine-cosine algorithm)	VSI	PV, WT BESS	DSTATCOM	12-bus 69-bus	Comparative studies using other analytical and metaheuristic methods.
Iqbal et al. (2018)	Location	Power Losses	Analytical Approach	PLF, LSF, VD	PV, WT Biomass	DSTATCOM	33-bus	Comparative studies using DG and DSTATCOM integration.
Relic et al. (2020)	Location	Real Power Losses, Voltage Profile, and ROI	Conventional approach	NR	PV, WT Micro-hydroelectric	SVC	20 kV rural DN	Comparative studies using SVC integration.

Table 2 (Continue)

Reference	Optimization Type	Objectives	Method/Techniques	Index	Type of DG	Type of FACTS	IEEE test system	Case study
Sannigrahi et al. (2019)	Location	Total Losses, Voltage Profile	Analytical approach	VSI, VPII	PV, WT	DSTATCOM	33-bus 69-bus	DG and FACTS integration
Magham et al. (2012)	Location	Transmission Losses, Voltage Profile	GA	PLF	PV	SVC	2500 kVA DN	Comparative using different times of a day
Ghatak et al. (2018)	Location	Voltage Profile, Benefit Cost Ratio, and Emission Cost Benefit	Particle swarm optimization (PSO)	VSI, VPEI	PV	DSTATCOM	33-bus 69-bus	Comparative studies using the evolutionary method.
Devi and Geethanjali (2014)	Location, Sizing	Power Losses, Voltage Profile	Particle swarm optimization (PSO)	LSF	PV	DSTATCOM	12-bus 34-bus 69-bus	DG and FACTS integration
El-Arini and Ahmed (2012)	Location	System Stability, Power Losses, Voltage Profile	NGSA-II	PLF	PV	SVC, TCSC, UPFC	14-bus	Comparative studies using FACTS integration.
Ćalasan et al. (2020)	Location	Power Losses, Power Flow	Metaheuristic (CONOPT)	OPF	WT	SVC	9-bus 30-bus	DG and FACTS integration, comparative studies using metaheuristic method.
de Koster et al. (2020)	Location, Sizing	MG Performance, Voltage Profile,	Tabu Search	L-index	BESS	Multi-type FACTS	8-bus	FACTS integration
Taher and Afsari (2012)	Location, Sizing	Power Losses, Voltage and Current Profile, Investment Cost	DE	PL	DFIG	UPQC	33-bus 69-bus	Comparative studies using evolutionary method.
Muthubalaji et al. (2018)	Location	Power Losses, Total Cost, Voltage Profile.	MACO- BFOA	SAIDI, SAIFI	PV BESS	DSTATCOM	30-bus 69-bus	Comparative studies with others MOA.
Anbarasan and Kumar (2019)	Location	Real Power Losses, Voltage Profile	Analytical approach	PLF, FVSI	DFIG	STATCOM	9-bus	Comparative with power flow result, DG and STATCOM integration

Table 2 (Continue)

Reference	Optimization Typ	Objectives	Method/Techniques	Index	Type of DG	Type of FACTS	IEEE test system	Case study
Kanwar et al. (2015)	Location	Power loss, voltage profile	Improved cat swarm optimization (ICSO)	-	DG	DSTATCOM with DG	69-bus	Load growth, an optimal solution for DSTATCOM and DG allocation
Weqar et al. (2018)	Location	Active power losses, voltage profiles	Hybrid analytical approaches	VSI LSF	PV	DSTATCOM with DG	33-bus	Optimum location of DG and DSTATCOM. Comparative before and after the installation of the DG and DSTATCOM
Arouna et al. (2019)	Location	Total Losses, installation costs, and voltage deviation	NGSA-II	-	PV	SVC with DG	138 node Calavi HTA	Identify the optimum location and cost installation for PV and SVC
Zellagui et al. (2021)	Location	Active power loss, voltage deviation, techno-economic, and environmental benefits	Hybrid Firefly algorithms-PSO	-	PV	DSTATCOM With DG	33-bus 69-bus	Comparative studies with other hybrid approaches with and without installation of DG and DSTATCOM.
Isha and Jagatheeswari (2021)	Location	Voltage profile, voltage stability, power losses	Hybrid Fuzzy-lightning search algorithm (FLSA)	-	PV	DSTATCOM with DG	30-bus	Optimum location of PV and DSTATCOM. Comparative before and after the installation of the PV and DSTATCOM

multi-objective optimal power flow (MOPF) algorithm that can reduce overall losses and enhance voltage profiles simultaneously (Kargarian et al., 2012). In this study, two different cases have been done: in the first case, only multi-MGs were integrated, and in the second case, both multi-MGs and IPFC were introduced. In each case, there were four strategies, where the first strategy was to reduce operating costs only; the second strategy was to decrease total power loss; the third strategy was to minimize the voltage profile deviation; and the last strategy was to identify the operating point of the system by using proposed multi-objective optimization. The results show that the proposed MOPF with IPFC provides a high-quality MMG system operating point, reduces overall losses, and simultaneously enhances voltage profiles.

Yenealem et al. (2020) proposed using a hybrid approach to solve the optimal location and capacity of PV and wind turbine-based MG integration with STATCOM using fuzzy logic. It was tested in an IEEE 33-bus system connected to the main distribution network. The optimal placement of the MG system and STATCOM was determined using the N-R method as the candidate bus and placed at the weakest bus, bus 30. Meanwhile, the capacity of the MG system and STATCOM has been solved by using fuzzy logic. These case studies compared studies without MG and FACTS integration, with MG, and with both MG and STATCOM integrations. From the findings, it is observed that when both MG and STATCOM are integrated into the benchmark test system, the overall system performance is further enhanced, where the real power is reduced, and the voltage profile is increased compared to the two cases. Selim et al. (2019) conducted a study to obtain the optimal location and sizing of the MG with DSTATCOM using a hybrid approach and tested it on 12-bus and 69-bus radial distribution networks. This study also covered minimizing the total power loss, increasing the voltage profile, and using the voltage stability index (VSI) to determine the candidate location for MG systems and DSTATCOM. The proposed sine-cosine algorithm (SCA) was used to obtain the optimal sizing of the MG systems and DSTATCOM. The results of VSI in IEEE 12-bus obtained clearly show that the optimal location of DG at bud 9 and the appropriate DG sizing, the real power loss, was further reduced. After adding DSTATCOM and incorporating DG into the system, the total active power loss was further reduced.

In addition, the studies by Iqbal et al. (2018) and Sannigrahi et al. (2019) have suggested the same approach, which is the analytical method to find the placement of multiple distributed generations, including DSTATCOM integration to reduce system losses and improve voltage profile. The proposed method by Sannigrahi et al. (2019) for determining the optimal location of DG with DSTATCOM used VSI to determine the weakest bus locations. It was tested on the IEEE 33-bus and IEEE 69-bus distribution networks. The results showed that the optimum placements for DSTATCOM and DG in the 33-bus system

are bus 30 and 31, respectively, whereas the optimal placement for both devices in the 69-bus system is bus 61. The integration of DG, as compared to DSTATCOM, yields better results in terms of voltage profile improvement and line loss reduction. Besides, Magham et al. (2012) introduced the genetic algorithm (GA) to find the suitable location for PV and SVC to reduce transmission losses and improve voltage profile. It was tested on a 2500 kVA distribution network. The results showed that the effectiveness of the proposed algorithm had been proven after being applied to the distribution system as the voltage profile improved. In this paper, the improved particle swarm optimization algorithm (IPSO) was presented to determine the optimal location of DG and DSTATCOM, and security limits were considered (Ghatak et al., 2018). The study was tested in the IEEE 33-bus and IEEE 69-bus systems and has been compared with differential evolution (DE), real-coded genetic algorithms, and PSO. The proposed technique results show that the proposed approach achieved the best performance, including computational efficiency and solution quality.

Since the PSO algorithm is easy to implement and highly relevant for practical application, considering nonlinear constraints and different objectives, Devi and Geethanjali (2014) proposed PSO to estimate the capacity for the DG and DSTATCOM. Meanwhile, the optimum allocation of DG and DSTATCOM was determined using the loss sensitivity factor (LSF). The study was simulated in the 12, 34, and 69 bus radial distribution systems, where the objectives were to reduce the total power loss and improve the voltage profile. Taher and Afsari (2012) proposed a DE algorithm to determine the optimal location and sizing of the Doubly Feed Inductor Generator (DFIG) and UPFC to reduce power losses and improve voltage and current profiles. The efficiency of the proposed algorithm was compared to other evolutionary algorithms like GA and immune algorithms (IA) in terms of minimizing the continuous space functions. The results show that integrating the UPQC reduces power loss by 18.2% and 21.42% in 33-bus and 69-bus distribution systems, respectively. Kanwar et al. (2015) introduced improved cat swarm optimization (ICSO) to reduce power loss and increase voltage profiles. The proposed method was implemented on a 69-bus test distribution network. After optimally placing the DSTATCOM and DG, the results show that a net annual energy loss was decreased by about 94% from the base case and the voltage profile increased to 96%. Finally, the proposed method has also been compared by CSO and PSO and based on the findings, ICSO has a better solution than CSO and PSO in terms of computational time and fast convergence.

Weqar et al. (2018) used analytical approaches to find the optimal location for DG and DSTATCOM to minimize the power losses and enhance the voltage profile. This study uses a voltage stability index and loss sensitivity factor to find the weakest and critical lines, resulting in the optimal allocation for DG and DSTATCOM. This technique was tested on the 33-bus radial distribution system. The results show that the optimum placement of

DG is obtained on buses 9, 13, and 28, while the candidate location for DSTATCOM is on bus 30. The results were analyzed, and there has been an improvement in the voltage profile and reduced total real power loss. In Arouna et al. (2019), SVC and PV placement were done using NGS-II. The multi-objectives had been set to reduce the installation cost of SVC and PV and minimize the power loss. The proposed method has been tested on a real network of 138 nodes. The results show that the optimally placed FACTS and DG contribute to efficiently improving the distribution network's performance while minimizing the installation cost.

Isha and Jagatheeswari (2021) have proposed a hybrid fuzzy-lightning search algorithm to identify the optimum placement of PV with DSTATCOM to minimize power loss and improve voltage profiles. This proposed method was tested on the IEEE 30-bus system. The results show that the power losses were decreased, and voltage profiles improved after the PV with DSTATCOM installation. A few studies validate the proposed optimization approaches' efficiency in terms of computation time and rate of convergence. Based on previous studies, PSO is the most popular optimization method because of its simplicity, small computational load, and fast convergence. Moreover, PSO is very efficient in solving complex problems. However, PSO has a lack of premature convergence upon solving complex problems. The second most popular optimization that has been used is the genetic algorithm (GA). The GA optimization technique is one of the first metaheuristic techniques to solve optimal MMG and FACTS locations. However, it has drawbacks, such as divergence and local minimum problems. In conclusion, most previous researchers have used the common heuristic algorithm such as PSO and GA optimization techniques in the power system to identify the optimal sizing and location.

KEY FINDINGS AND RECOMMENDATIONS

Table 2 summarizes 36 recent research articles from 2012 to 2021 that were reviewed based on the type of optimization involved, the objectives set in the study, the method or techniques adopted, the index involved, the type of FACTS utilized, the adopted benchmark test system and lastly, case studies involved. From the 36 articles reviewed, the most preferred optimization techniques for solving optimal location and sizing are metaheuristic-based approaches (Figure 3). Besides, most previous works have used the common heuristic algorithm such as PSO and GA optimization techniques in the power system to identify the optimal sizing and location.

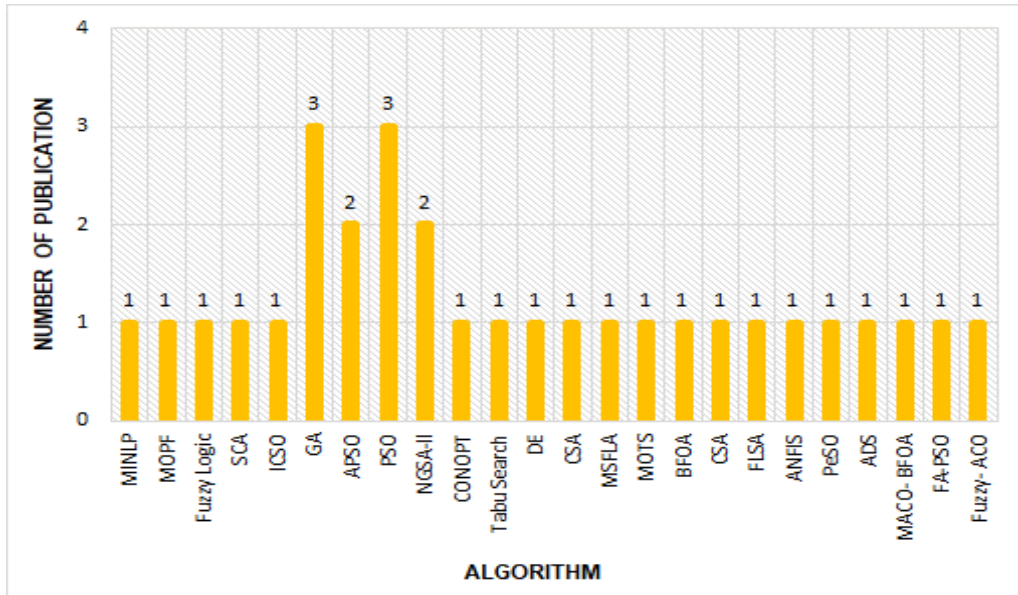


Figure 3. The applied algorithms for solving optimal location and sizing of MMG and FACTS devices

From the reviewed work, a few recommendations for future works in finding the optimal location and sizing of MMG incorporating FACTS devices are proposed below:

Most of the literature reviews were done using metaheuristic approaches that have been used to determine the allocation and sizing of MG and FACTS devices (Figure 3). Hence, there is a limited research technique that uses hybrid approaches. However, no comparative studies have been conducted between the existing hybrid approaches to examine their effectiveness and efficiency, which could be considered for future research.

In addition, most studies were conducted to identify the optimal placement of DG and FACTS devices instead of finding the optimum location and capacity for both DG and FACTS devices to reduce power loss and improve the voltage profile, as shown in Figure 5. Still, finding the proper placement and capacity for MMG and FACTS devices is quite low. Therefore, it must be considered in the future so that the results can be more practical to implement in the existing power system.

Much of the literature usually focuses on the implications of integrating single and multiple DGs to provide high efficacy and achieve better power system reliability, as in Figure 4. However, the consideration of integrating MMG with FACTS technology is still relatively low, and it could be a recommendation for the future to reduce real power losses and improve the voltage profile. Besides that, the potential impact of the high penetration of MMG systems that consist of a variety of renewable energies should also be considered to achieve better performance in the power systems.

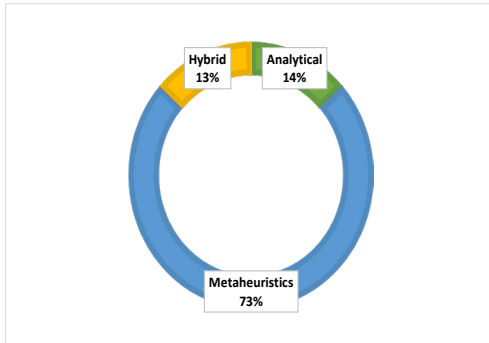


Figure 4. The percentage of the applied techniques for solving optimal location and sizing of MMG and FACTS devices

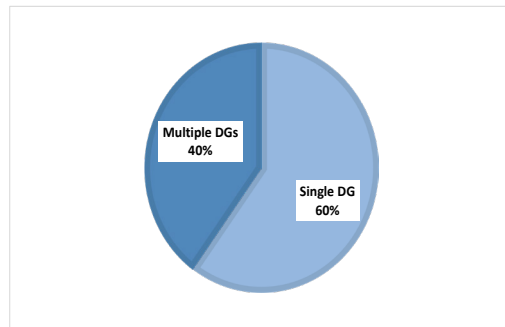


Figure 5. The percentage of the applied number unit of DGs in the power system

CONCLUSION

In conclusion, the best evaluation and optimization techniques in determining the appropriate size and placement of the MMG system and the FACTS controller will improve the MMG system. An attempt has been made to summarize the existing approaches and present a detailed discussion that can help the energy planners decide which objective and planning factors need more attention for optimum locations and capacity for multi-microgrid and FACTS devices. Therefore, a comprehensive study is carried out for optimum multi-microgrid placement considering the minimization of power losses, enhancement of voltage stability, and improvement of the voltage profile.

ACKNOWLEDGEMENT

The Ministry of Higher Education of Malaysia funded this research, grant number FGRS/1/2017/TK04/UNIKL/03/3. The authors sincerely acknowledged Universiti Kuala Lumpur and the Ministry of Higher Education of Malaysia for providing the financial support and necessary facilities to support this work.

REFERENCES

- Ackermann, T., Andersson, G., & Söder, L. (2001). Distributed generation: A definition. *Electric Power Systems Research*, 57(3), 195-204. [https://doi.org/10.1016/S0378-7796\(01\)00101-8](https://doi.org/10.1016/S0378-7796(01)00101-8)
- Al Ahmad, A., & Sirjani, R. (2019). Optimal placement and sizing of multi-type FACTS devices in power systems using metaheuristic optimisation techniques: An updated review. *Ain Shams Engineering Journal*, 11(3), 611-628. <https://doi.org/10.1016/j.asej.2019.10.013>
- Anbarasan, A., & Kumar, C. (2019). Effect of distributed generation and statcom in multi-machine system for real power loss minimization. *International Journal of Scientific and Technology Research*, 8(7), 579-582.

- Arouna, O., Adolphe, M. I., Robert, A. O., Kenneth, A. Z., Antoine, V., Ramanou, B., Herman, T., & Celestin, D. (2019). Technico-economic optimization of distributed generation (DG) and static var compensator (SVC) positioning in a real radial distribution network using the NSGA-II genetic algorithm. *IEEE PES/IAS PowerAfrica Conference: Power Economics and Energy Innovation in Africa, PowerAfrica 2019*, 42-47. <https://doi.org/10.1109/PowerAfrica.2019.8928631>
- Ćalasan, M., Konjić, T., Kecojević, K., & Nikitović, L. (2020). Optimal allocation of static var compensators in electric power systems. *Energies*, 13(12), Article 3219. <https://doi.org/10.3390/en13123219>
- Chirantan, S., Swain, S. C., Panda, P., & Jena, R. (2018). Enhancement of power profiles by various FACTS devices in power system. In *Proceedings of the 2nd International Conference on Communication and Electronics Systems* (pp. 896-901). IEEE Publishing. <https://doi.org/10.1109/CESYS.2017.8321212>
- de Koster, O. A. C., Artal-Sevil, J. S., & Dominguez-Navarro, J. A. (2020). Multi-type FACTS location in a microgrid. In *2020 Fifteenth International Conference on Ecological Vehicles and Renewable Energies (EVER)* (pp. 1-5). IEEE Publishing. <https://doi.org/10.1109/EVER48776.2020.9243070>
- de Koster, O. A. C., & Dominguez-Navarro, J. A. (2020). Multi-objective tabu search for the location and sizing of multiple types of FACTS and DG in electrical networks. *Energies*, 13(11), Article 2722. <https://doi.org/10.3390/en13112722>
- Devalalaji, K. R., & Ravi, K. (2016). Optimal size and siting of multiple DG and DSTATCOM in radial distribution system using bacterial foraging optimization algorithm. *Ain Shams Engineering Journal*, 7(3), 959-971. <https://doi.org/10.1016/j.asej.2015.07.002>
- Devi, S., & Geethanjali, M. (2014). Optimal location and sizing determination of distributed generation and DSTATCOM using Particle Swarm Optimization algorithm. *International Journal of Electrical Power and Energy Systems*, 62, 562-570. <https://doi.org/10.1016/j.ijepes.2014.05.015>
- El-Arini, M. M. M., & Ahmed, R. S. S. (2012). Optimal location of facts devices to improve power systems performance. *Journal of Electrical Engineering*, 12(3), 73-80.
- Funabashi, T. (2016). Chapter 1 - Introduction. In *Integration of Distributed Energy Resources in Power Systems: Implementation, Operation and Control* (pp. 1-14). Elsevier Inc. <https://doi.org/10.1016/B978-0-12-803212-1.00001-5>
- Gandhar, S., Ohri, J., & Singh, M. (2020). Improvement of voltage stability of renewable energy sources-based microgrid using ANFIS-Tuned UPFC. In G. Zhang, N. D. Kaushika, S. C. Kaushik & R. K. Tomar (Eds.), *Advances in Energy and Built Environment* (pp. 133-143). Springer. https://doi.org/10.1007/978-981-13-7557-6_11
- Gerbex, S., Cherkaoui, R., & Germond, A. J. (2001). Optimal location of multi-type FACTS devices in a power system by means of genetic algorithms. *IEEE Transactions on Power Systems*, 16(3), 537-544. <https://doi.org/10.1109/59.932292>
- Ghatak, S. R., Sannigrahi, S., & Acharjee, P. (2018). Comparative performance analysis of DG and DSTATCOM using improved pso based on success rate for deregulated environment. *IEEE Systems Journal*, 12(3), 2791-2802. <https://doi.org/10.1109/JSYST.2017.2691759>

- Haddadian, H., & Noroozian, R. (2017). Multi-microgrids approach for design and operation of future distribution networks based on novel technical indices. *Applied Energy*, 185, 650-663. <https://doi.org/10.1016/j.apenergy.2016.10.120>
- Iqbal, F., Khan, M. T., & Siddiqui, A. S. (2018). Optimal placement of DG and DSTATCOM for loss reduction and voltage profile improvement. *Alexandria Engineering Journal*, 57(2), 755-765. <https://doi.org/10.1016/j.aej.2017.03.002>
- Isha, G., & Jagatheeswari, P. (2021). Optimal allocation of DSTATCOM and PV array in distribution system employing fuzzy-lightning search algorithm. *Automatika*, 62(3), 339-352. <https://doi.org/10.1080/00051144.2021.1963080>
- Ismail, B., Wahab, N. I. A., Othman, M. L., Radzi, M. A. M., Vijyakumar, K. N., & Naain, M. N. M. (2020). A comprehensive review on optimal location and sizing of reactive power compensation using hybrid-based approaches for power loss reduction, voltage stability improvement, voltage profile enhancement and loadability enhancement. *IEEE Access*, 8, 222733-222765. <https://doi.org/10.1109/ACCESS.2020.3043297>
- Jordehi, A. R. (2015). Particle swarm optimisation (PSO) for allocation of FACTS devices in electric transmission systems: A review. *Renewable and Sustainable Energy Reviews*, 52, 1260-1267. <https://doi.org/10.1016/j.rser.2015.08.007>
- Kanwar, N., Gupta, N., Niazi, K. R., & Swarnkar, A. (2015). Improved cat swarm optimization for simultaneous allocation of DSTATCOM and DGs in distribution systems. *Journal of Renewable Energy*, 2015, 1-10. <https://doi.org/10.1155/2015/189080>
- Kargarian, A., Falahati, B., Fu, Y., & Baradar, M. (2012). Multiobjective optimal power flow algorithm to enhance multi-microgrids performance incorporating IPFC. In *IEEE Power and Energy Society General Meeting* (pp. 1-6). IEEE Publishing. <https://doi.org/10.1109/PESGM.2012.6345605>
- Kljajic, R., Maric, P., Relic, F., & Glavas, H. (2020). Battery energy storage systems and FACTS devices influence on microgrid voltage stability. In *Proceedings of 2020 International Conference on Smart Systems and Technologies, SST 2020* (pp. 141-146). IEEE Publishing. <https://doi.org/10.1109/SST49455.2020.9264080>
- Kroposki, B., Basso, T., & DeBlasio, R. (2008). Microgrid standards and technologies. In *2008 IEEE Power and Energy Society General Meeting-Conversion and Delivery of Electrical Energy in the 21st Century* (pp. 1-4). IEEE Publishing. <https://doi.org/10.1109/PES.2008.4596703>
- Lopes, J. A. P., Madureira, A., Gil, N., & Resende, F. (2013). Operation of multi-microgrids. In N. Hatziargyriou (Ed.), *Microgrids* (pp. 165-205). John Wiley and Sons Ltd. <https://doi.org/10.1002/9781118720677.ch05>
- Luo, L., Gu, W., Zhang, X. P., Cao, G., Wang, W., Zhu, G., You, D., & Wu, Z. (2018). Optimal siting and sizing of distributed generation in distribution systems with PV solar farm utilized as STATCOM (PV-STATCOM). *Applied Energy*, 210, 1092-1100. <https://doi.org/10.1016/j.apenergy.2017.08.165>
- Mahdad, B., & Srairi, K. (2016). Adaptive differential search algorithm for optimal location of distributed generation in the presence of SVC for power loss reduction in distribution system. *Engineering Science and Technology, an International Journal*, 19(3), 1266-1282. <https://doi.org/10.1016/j.jestech.2016.03.002>

- Malaysia Energy Commission. (2018). *Energy Malaysia: Strengthening the Future of Energy in Malaysia*. Malaysia Energy Commission. https://www.st.gov.my/en/contents/files/download/112/Energy_Malaysia_Volume_14_20185.pdf
- Moazzami, M., Gharehpetian, G. B., Shahinzadeh, H., & Hosseinian, S. H. (2017). Optimal locating and sizing of DG and D-STATCOM using modified shuffled frog leaping algorithm. In *2017 2nd Conference on Swarm Intelligence and Evolutionary Computation (CSIEC)* (pp. 54-59). IEEE Publishing. <https://doi.org/10.1109/CSIEC.2017.7940157>
- Muthubalaji, S., Anand, R., & Karuppiah, N. (2018). An integrated optimization approach to locate the D-STATCOM in power distribution system to reduce the power loss and total cost. *Periodicals of Engineering and Natural Sciences*, 6(2), 283-294. <https://doi.org/10.21533/pen.v6i2.268>
- Magham, H. R., Sanjari, M. J., Zaker, B., & Gharehpetian, G. B. (2012). Voltage profile improvement in a microgrid including PV units using genetic algorithm. In *Iranian Conference on Smart Grids* (pp. 1-5). IEEE Publishing.
- Prabu, J., & Muthuveerapan, S. (2016). Optimum placement and sizing determination of distributed generation and DSTATCOM using penguins search. *International Journal of Innovative Research in Science, Engineering and Technology*, 3297, 6675-6680.
- Rao, V. S., & Rao, R. S. (2017). Optimal placement of STATCOM using two stage algorithm for enhancing power system static security. *Energy Procedia*, 117, 575-582. <https://doi.org/10.1016/j.egypro.2017.05.151>
- Relic, F., Maric, P., Glavas, H., & Petrovic, I. (2020). Influence of FACTS device implementation on performance of distribution network with integrated renewable energy sources. *Energies*, 13(20), 1-15. <https://doi.org/10.3390/en13205516>
- Sannigrahi, S., Ghatak, S. R., Basu, D., & Acharjee, P. (2019). Optimal placement of DSTATCOM, DG and their performance analysis in deregulated power system. *International Journal of Power and Energy Conversion*, 10(1), 105-128. <https://doi.org/10.1504/IJPEC.2019.096725>
- Selim, A., Kamel, S., & Jurado, F. (2019). Hybrid optimization technique for optimal placement of DG and D-STATCOM in distribution networks. In *2018 Twentieth International Middle East Power Systems Conference (MEPCON)* (pp. 689-693). IEEE Publishing. <https://doi.org/10.1109/MEPCON.2018.8635253>
- Sirjani, R. (2018). Optimal placement and sizing of PV-STATCOM in power systems using empirical data and adaptive particle swarm optimization. *Sustainability*, 10(3), Article 727. <https://doi.org/10.3390/su10030727>
- Taher, S. A., & Afsari, S. A. (2012). Optimal location and sizing of UPQC in distribution networks using differential evolution algorithm. *Mathematical Problems in Engineering*, 2012, Article 838629. <https://doi.org/10.1155/2012/838629>
- Tolabi, H. B., Ali, M. H., & Rizwan, M. (2015). Simultaneous reconfiguration, optimal placement of DSTATCOM, and photovoltaic array in a distribution system based on fuzzy-aco approach. *IEEE Transactions on Sustainable Energy*, 6(1), 210-218. <https://doi.org/10.1109/TSTE.2014.2364230>
- Urquizo, J., Singh, P., Kondrath, N., Hidalgo-Leon, R., & Soriano, G. (2018). Using D-FACTS in microgrids for power quality improvement: A review. In *2017 IEEE Second Ecuador Technical Chapters Meeting (ETCM)* (pp. 1-6). IEEE Publishing. <https://doi.org/10.1109/ETCM.2017.8247546>

- Vasiljevska, J., Lopes, J. A. P., & Matos, M. A. (2012). Evaluating the impacts of the multi-microgrid concept using multicriteria decision aid. *Electric Power Systems Research, 91*, 44-51. <https://doi.org/10.1016/j.epsr.2012.04.013>
- Wang, J., Wang, Z., Xu, L., & Wang, Z. (2012). A summary of applications of D-FACTS on microgrid. In *2012 Asia-Pacific Power and Energy Engineering Conference* (pp. 1-6). IEEE Publishing. <https://doi.org/10.1109/APPEEC.2012.6307225>
- Weqar, B., Khan, M. T., & Siddiqui, A. S. (2018). Optimal placement of distributed generation and D-STATCOM in radial distribution network. *Smart Science, 6*(2), 125-133. <https://doi.org/10.1080/23080477.2017.1405625>
- Xu, Z., Yang, P., Zheng, C., Zhang, Y., Peng, J., & Zeng, Z. (2018). Analysis on the organization and development of multi-microgrids. *Renewable and Sustainable Energy Reviews, 81*, 2204-2216. <https://doi.org/10.1016/j.rser.2017.06.032>
- Yenealem, M. G., Ngoo, L. M. H., Shiferaw, D., & Hinga, P. (2019). Integration of Microgrid including FACTS Controllers to the Distribution Network for Loss Reduction and Power Quality Improvement. *Journal of Electrical and Power System Engineering, 5*(3), 47-68.
- Yenealem, M. G., Ngoo, L. M. H., Shiferaw, D., & Hinga, P. (2020). Management of voltage profile and power loss minimization in a grid-connected microgrid system using fuzzy-based STATCOM controller. *Journal of Electrical and Computer Engineering, 2020*, Article 2040139. <https://doi.org/10.1155/2020/2040139>
- Yuvaraj, T., & Ravi, K. (2018). Multi-objective simultaneous DG and DSTATCOM allocation in radial distribution networks using cuckoo searching algorithm. *Alexandria Engineering Journal, 57*(4), 2729-2742. <https://doi.org/10.1016/j.aej.2018.01.001>
- Yuvaraj, T., Ravi, K., & Devalalaji, K. R. (2017). Optimal allocation of DG and DSTATCOM in radial distribution system using cuckoo search optimization algorithm. *Modelling and Simulation in Engineering, 2017*, Article 2857926. <https://doi.org/10.1155/2017/2857926>
- Zahurul, S., Mariun, N., Grozescu, I. V., Tsuyoshi, H., Mitani, Y., Othman, M. L., Hizam, H., & Abidin, I. Z. (2016). Future strategic plan analysis for integrating distributed renewable generation to smart grid through wireless sensor network: Malaysia prospect. *Renewable and Sustainable Energy Reviews, 53*, 978-992. <https://doi.org/10.1016/j.rser.2015.09.020>
- Zellagui, M., Lasmari, A., Settoul, S., El-Schiemy, R. A., El-Bayeh, C. Z., & Chenni, R. (2021). Simultaneous allocation of photovoltaic DG and DSTATCOM for techno-economic and environmental benefits in electrical distribution systems at different loading conditions using novel hybrid optimization algorithms. *International Transactions on Electrical Energy Systems, 31*(8), 1-35. <https://doi.org/10.1002/2050-7038.12992>



Modified K-Means Clustering for Demand-Weighted Locations: A Thailand's Convenience Store Franchise - Case Study

Chartchai Leenawong* and Thanrada Chaikajonwat

*Department of Mathematics, School of Science, King Mongkut's Institute of Technology Ladkrabang,
Chalongkrung Road, Lat Krabang, Bangkok, Thailand*

ABSTRACT

This research applies and modifies K-means clustering analysis from Data Mining to solving the location problem. First, a case study of Thailand's convenience store franchise in locating distribution centers (DCs) is conducted. Then, the final centroids are served at suggested DC locations. Besides the typical distance, Euclidean, used in K-means, Manhattan, and Chebyshev, is also experimented with. Moreover, due to the stores' different demands, a modification of the centroid calculation is needed to reflect the center-of-gravity effects. For the proposed centroid calculation, the above three distance metrics incorporating the demands as weights give rise to another three approaches and are thus named Weighted Euclidean, Weighted Manhattan, and Weighted Chebyshev, respectively. Besides the optimal locations, the effectiveness of these six clustering approaches is measured by the expected total distribution cost from DCs to their served stores and the expected Davies–Bouldin index (DBI). Concurrently, the efficiency is measured by the expected number of iterations to the final clusters. All these six clustering approaches are then implemented in the case study of locating eight DCs to distribute to 260 convenience stores in Eastern Thailand. The results show that though all approaches yield locations in close proximity, the Weighted Chebyshev is the most effective one having both the lowest expected distribution cost and lowest expected DBI. In contrast, Euclidean is the most efficient approach, with

the lowest expected number of iterations to the final clusters, followed by Weighted Chebyshev. Therefore, the DC locations from Weighted Chebyshev could, ultimately, be chosen for this Thailand's convenience store franchise.

Keywords: Centroid calculation, clustering, Davies–Bouldin index, demand-based, distance metrics, distribution center, K-means, location problem

ARTICLE INFO

Article history:

Received: 03 February 2022

Accepted: 18 July 2022

Published: 06 March 2023

DOI: <https://doi.org/10.47836/pjst.31.2.02>

E-mail addresses:

chartchai.le@kmitl.ac.th (Chartchai Leenawong)

63605011@kmitl.ac.th (Thanrada Chaikajonwat)

*Corresponding author

INTRODUCTION

In Thailand, convenience stores are available on almost every corner (Wang, 2018). New franchises and new stores are emerging regularly, especially in tourist and populated areas. The Eastern part of Thailand is one of the well-known tourist attractions among local and foreign tourists, thanks partly to its terrific location next to the Gulf of Thailand (Ministry of Foreign Affairs, 2017; Surawattananon et al., 2021). Among those popular destinations are Pattaya, Koh Samet, and Koh Kut. Therefore, it is natural for those convenience store franchises to open more branches. Logistics management plays a crucial role in both short-run and long-run plans for franchises to stay competitive. One long-run logistical decision is determining where to locate distribution centers (DCs) (Langley et al., 2020).

This study investigates a case of locating DCs to distribute products to 260 franchised convenience stores in Eastern Thailand. Since Eastern Thailand is comprised of seven provinces: Chachoengsao, Chonburi, Rayong, Chanthaburi, Trat, Prachinburi, and Sa-Kaeo, plus one special governed city, Pattaya, the convenience store franchise of interest chooses to have eight DCs to be located. The objective is to minimize transportation or distribution costs from and to those eight DCs. Figure 1 shows the map of Thailand and the 260 locations of the convenience stores for this study respectively.

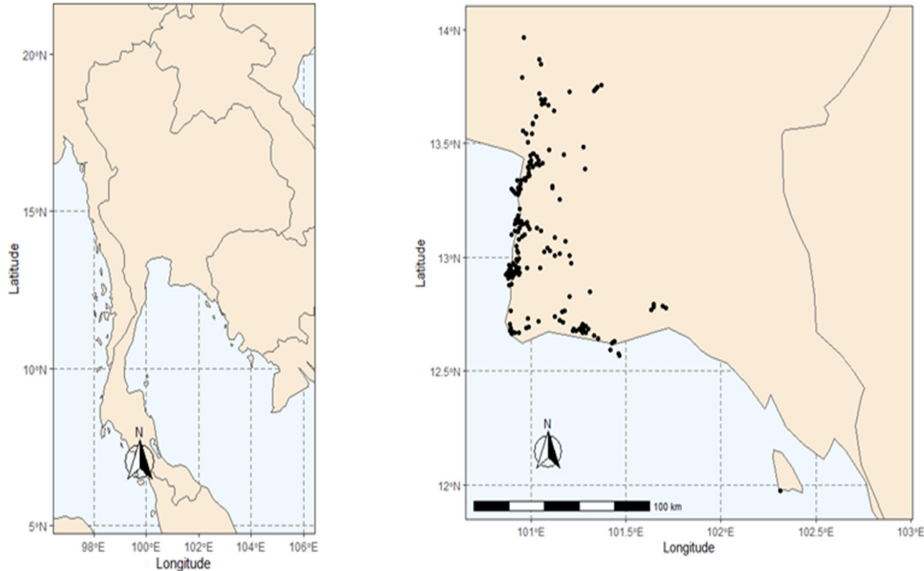


Figure 1. Thailand map and the convenience store locations in Eastern Thailand

There are numerous ways to solve the location problem, for instance, optimization models, the p-center/p-median algorithm, and the grid technique. However, in this research,

as the first contribution of this work, K-means clustering analysis from Data Mining is adapted to find the appropriate locations. The centroid of each final cluster serves as each DC's location. Also, as the second contribution, the typical distance metric, i.e., Euclidean, used in the K-means clustering, is replaced with other distance metrics, namely, Manhattan and Chebyshev. These three-distance metrics constitute the first three clustering approaches to the experiment.

As for the third contribution of this work, due to the nature of the location problem application, the clustering algorithm needs to be modified to fit this problem better. Accordingly, the centroid calculation during each clustering iteration is adjusted to incorporate the center of gravity's impact. That is done by taking the unequal demands required at the served stores as different weights. As a result, three additional clustering approaches with demand-weighted centroid calculation are proposed and named Weighted Euclidean, Weighted Manhattan, and Weighted Chebyshev, respectively.

Altogether, all these six clustering approaches experiment with, and their results are compared, considered both effectiveness and efficiency. The effectiveness is measured by the expected total distribution cost and the expected Davies–Bouldin index (DBI). In contrast, the efficiency is measured by the expected number of iterations to the final clusters.

LITERATURE REVIEW

The facility location problem, or the location problem, refers to how and where to place facilities in a logistics network to minimize total transportation costs from and to those facilities. Four underlying assumptions of the problem are the following: customers assumed to already be at points or on routes, facilities to be located, a space in which customers and facilities are located, and a standard metric that specifies distances or times between customers and facilities. Facilities in the location problem are small relative to the space in which they are located, and interactions between facilities may occur (Farahani & Hekmatfar, 2009).

Facility location decisions are critical to strategic planning for private sectors such as industrial estates, banks, retail facilities, distribution centers (DCs), and public sectors such as hospitals, post offices, and government headquarters. Determining facility locations is one of the broad and long-term decisions influencing numerous operational and logistical decisions. Locating or relocating facilities usually involves huge investments, as it may need to pay enormously for land acquisition and facility construction. Therefore, decision-makers must consider not only every current perspective of the facility but also unforeseen future events that may affect the facility, such as demographics, climate change, and market trend evolution during its lifetime (Farahani & Hekmatfar, 2009).

The location problem was first introduced in 1909 when Alfred Weber considered how to place a single warehouse in such a way as to minimize the total distance between the warehouse and several customers. After that, the location problem was advanced by several other applications. For example, Hakimi (1964) wanted to locate switching centers in a communication network, while Farahani and Hekmatfar (2009) tried to locate police posts along a highway system.

Drezner et al. (2003) studied the best location of a central warehouse to determine the number and the locations of local warehouses. They built simple models that considered inventory and service costs and compared them with those from the traditional model, minimizing the total transportation cost. The models were demonstrated on an example problem with up to 10,000 demand points. Excel Solver solves each model in less than half a second. However, it turned out that the location solutions for all the models were quite different from one another. The conclusion of this research showed that different models led to different locations. Therefore, the decision-maker needed to decide which model was the most appropriate for the situation. In addition, numerical results showed that ignoring inventory costs made the models less accurate.

Yang et al. (2007) investigated the location problem regarding selecting distribution centers from a potential set so that the total relevant cost was minimized under a fuzzy environment. More specifically, the setup cost, turnover cost, and demands of the customers were assumed fuzzy variables. Consequently, a probabilistic-constrained programming model for the problem was designed, and some properties of the model were examined. Tabu search, genetic and fuzzy simulation algorithms were integrated to search for the approximate best solution while satisfying the transportation and assignment constraints of the DCs. The effectiveness and robustness of the hybrid algorithm were tested through a numerical example. As a result, fuzzy chance-constrained programming was constructed as a decision model for the problem. For the convenience of model solving, some mathematical properties of the model were also obtained.

Dantrakul et al. (2014) applied greedy, p-median, and p-center algorithms to the facility location problem to minimize the sum of the setup and transportation costs. Those two costs were considered a function of the number of opened facilities. The network in this work represented the road transportation system of six provinces in Northern Thailand. The facility location model with bounds for the number of the opened facility was constructed in this work. The performances of the constructed methods were tested using 100 random data sets. Simulation results showed that the method developed from the greedy algorithm was suitable for solving the problem when the setup cost was higher than the transportation cost. In contrast, the p-median-based methods were more efficient for the opposite case when the setup cost was lower.

Sharma and Jalal (2017) developed a new clustering and mixed-integer linear programming-based hybrid approach for solving the facility location problem. The main objective was to utilize the facility by maximizing the number of possible customers to maximize profit. The numerical results showed that the profit started to decrease as the number of clusters increased. If the profit kept decreasing, it indicated that the solution procedure would stop.

Chen (2019) studied the location problem of DCs based on the Baumer Walvar model using Jiaji Logistics as a case study. This research aimed to optimize the total DC costs, consisting of four cost components, namely, the transportation cost from the factories to DCs, and from DCs to the customers, the DCs' fixed costs, and the DCs' change fee. The whole cargo of Jiaji logistics was transported from five factories (Chongqing, Chengdu, Xi'an, Zhengzhou, and Lanzhou) to four customers (Guangzhou, Shanghai, Hangzhou, and Tianjin). The company wanted to select the optimal five DCs out of the predetermined eight DCs (Wuhan, Nanchang, Guiyang, Changsha, Shijiazhuang, Beijing, and Nanjing). The economies of scale were also taken into account. The results showed that the minimum cost was 7,301,620 yuan, and the optimal locations of DCs were Nanchang, Nanjing, Guiyang, Changsha, and Shijiazhuang.

As for previous work on the K-means clustering, algorithms, distance metrics, and performance measurement are of our interest and are presented as follows.

Singh et al. (2013) compared the K-means clustering using three different distance metrics: Euclidean, Manhattan, and Minkowski. All the experiments were performed on dummy data. The result showed that Euclidean distance gave the best performance while Manhattan distance yielded the worst.

Sinwar and Kaushik (2014) studied two popular distance metrics, Euclidean and Manhattan, on the simple K-means clustering. They used two real and one synthetic data set, namely, Iris, Diabetes, and BIRCH. The development tool for clustering data items was WEKA, and the numbers of clusters used in this research were 2, 3, 4, 5, 6, and 7. The results showed that the Euclidean method was more efficient than the Manhattan method in terms of the number of iterations performed during centroid calculation.

Gultom et al. (2018) analyzed and compared object clustering from real big data using K-means and K-medoid methods. In both methods, combination testing used three distance metrics: Euclidean, Canberra, and Chebyshev. The sample dataset contained six variables collected from three college classes having 147,679 students at Medan State University. Performance measurement was the Davies-Bouldin index. The results showed that the Chebyshev distance in K-means yielded better results than that in K-medoid in terms of accuracy and quality. On the other hand, the results suggested not to use the Canberra distance in K-means nor K-medoid because the Davies-Bouldin index was undefined.

In the next section, the K-means clustering using three different distance metrics and the proposed demand-weighted approaches is explained.

THE TYPICAL AND PROPOSED CLUSTERING APPROACHES

This section describes the typical K-means clustering along with the proposed modified one in detail. K-means clustering is the most commonly used clustering algorithm and one of the most efficient partitional clustering algorithms. The K-means clustering algorithm's general steps are explained step by step as follows (Gultom et al., 2018; Aggarwal & Reddy, 2014).

Step 1: Determine the number of clusters formed in the dataset, K .

Step 2: Randomly choose K representative points as initial "centroids" of the K clusters.

Step 3: For each point, calculate the distance to each centroid and identify the closest centroid.

Then, assign that point to the cluster.

Step 4: Once all the points are assigned to clusters, update the centroids of all clusters.

Step 5: Repeat step 3 to step 4 until all the points in each cluster do not change. The algorithm stops. The last set of centroids is used as the desired locations.

However, in our application of locating the DCs for a convenience store franchise where the points to be clustered represent the convenience stores and the centroids represent the locations of the DCs serving the stores in the same clusters, it is natural to also take into consideration the different demands at the served stores. Therefore, in our case, the demands are used as weights in computing the updated centroids after the clusters are formed at each iteration.

In the following, the modified K-means clustering algorithm that incorporates the stores' different demands is applied to and explained in our application context. Simultaneously, three distance metrics, namely, Euclidean, Manhattan, and Chebyshev, are experimented with in the algorithm as well. Finally, together with the typical and demand-weighted centroid calculations, six combinations are tried to compete for the best algorithm. The notations used in this article are defined as follows.

K = the number of clusters/centroids/DCs; in our case here, $K = 8$.

N = the total number of convenience stores. Here, $N = 260$.

T_i = the number of convenience stores in cluster i ; $i = 1, 2, \dots, K$.

$X_i = (x_i, y_i)$ refers to the location of centroid i representing DC i , where x_i and y_i are the latitude and longitude of centroid i , $i = 1, 2, \dots, K$, respectively.

$S_j = (r_j, s_j)$ refers to the location of convenience store j , where r_j and s_j are the latitude and longitude of store j , $j = 1, 2, \dots, N$, respectively.

$S_j^i = (r_j^i, s_j^i)$ refers to the location of store j that is assigned to cluster i .
 w_j = the demand at convenience store j

Then, the K-means using each of these three-distance metrics, Euclidean, Manhattan, and Chebyshev, and the modified demand-weighted K-means using each of the above metrics proceed in detail as follows.

Step 1: Random eight initial centroids $X_i; i = 1, 2, \dots, 8$, representing eight initial DCs.

Step 2: For a fixed convenience store S_j , calculate the distance between the store and each centroid

X_i uses one of the three metrics, i.e., Euclidean, Manhattan, and Chebyshev, according to Equations 1, 2, and 3 (Singh et al., 2013).

$$D_{\text{Euclidean}}(S_j, X_i) = \sqrt{(r_j - x_i)^2 + (s_j - y_i)^2} \quad i = 1, 2, \dots, 8 \tag{1}$$

$$\text{or } D_{\text{Manhattan}}(S_j, X_i) = |r_j - x_i| + |s_j - y_i| \quad i = 1, 2, \dots, 8 \tag{2}$$

$$\text{or } D_{\text{Chebyshev}}(S_j, X_i) = \max(|r_j - x_i|, |s_j - y_i|) \quad i = 1, 2, \dots, 8 \tag{3}$$

Then, select the centroid i that minimizes the distance from store j . Assign this store S_j to cluster X_i accordingly. Now, S_j becomes S_j^i ; that is, store j is grouped in cluster i ; in other words, served by centroid or DC i . Repeat this step for all other stores.

Step 3: Calculate the new location of each centroid i , using the typical average of all store locations j in cluster i , as Equation 4.

$$X_i = \left(\frac{\sum_{j=1}^{T_i} r_j^i}{T_i}, \frac{\sum_{j=1}^{T_i} s_j^i}{T_i} \right) \quad \text{for } i = 1, 2, \dots, 8 \tag{4}$$

On the other hand, the effect of each store’s different demand results in the proposed demand-weighted average for computing the new location of each centroid i as Equation 5.

$$X_i = \left(\frac{\sum_{j=1}^{T_i} w_j r_j^i}{\sum_{j=1}^{T_i} w_j}, \frac{\sum_{j=1}^{T_i} w_j s_j^i}{\sum_{j=1}^{T_i} w_j} \right) \quad \text{for } i = 1, 2, \dots, 8 \tag{5}$$

Step 4: Repeat Steps 2 to 3 until all convenience stores in the final clustering are the same as in the immediate previous clustering.

Step 5: The total distribution cost from DCs to their served stores is calculated, and the Davies–Bouldin index (DBI) is computed to measure the effectiveness. As for the efficiency measurement, the number of iterations to the final clusters is determined.

The details of these measures are given in the next section.

Step 6: Repeat Steps 1 through 5 for 10,000 instances to obtain the expected distribution cost, the expected DBI, and the expected number of iterations to the final clusters, accordingly.

Now that all the algorithm steps have been stated, the effectiveness and efficiency of the six clustering approaches will be measured and compared. These issues will be explained in more detail next.

THE EFFECTIVENESS AND EFFICIENCY MEASUREMENT

The modified demand-weighted K-means algorithm described above employs three different distance metrics and two centroid location calculations. As a result, six different approaches are carried out for each problem instance. The first three approaches are named after the three-distance metrics: Euclidean, Manhattan, and Chebyshev. The other three approaches incorporating the demands as the weights in updating the centroid location calculation are Weighted Euclidean, Weighted Manhattan, and Weighted Chebyshev. After the experiments are performed, these six approaches are compared by their effectiveness and efficiency. In terms of effectiveness, the expected total distribution cost and the expected Davies–Bouldin index (DBI) are measured. In contrast, in terms of efficiency, the expected number of iterations to the final clusters is determined for each of the six clustering approaches.

Measurement of Effectiveness: Distribution Cost

For our application, we are most concerned with the overall distribution cost of locating the DCs. Typically, the distribution cost depends on the transportation rate, the shipment weight, and the traveling distance. Let us assume that the transportation rate is \$1 per kilometer per one shipment weight unit. Assume further that the shipment load is the demand at each store S_j served by DC X_i , denoted by l_{ij} . Finally, for the traveling distance between the store and its relevant DC, the Euclidean metric is used in the calculation. Therefore, the distribution cost from DC X_i to store S_j is as in Equation 6.

$$\text{Distribution cost} = \$1 \times l_{ij} \times D_{\text{Euclidean}}(S_j, X_i) \quad (6)$$

Measurement of Effectiveness: Davies–Bouldin Index (DBI)

The Davies-Bouldin Index (DBI), introduced by David L. Davies and Donald W. Bouldin in 1979, is a metric for evaluating clustering algorithms. It is an internal evaluation scheme in which the evaluation of how well the clustering is performed is based on variables and features that are intrinsic to the dataset. The process of calculating DBI is as follows (Davies & Bouldin, 1979):

Step 1: For each cluster i , calculate the average distance between all stores S_j in the cluster and DC X_i , denoted by A_i , by Equation 7.

$$A_i = \frac{1}{T_i} \sum_{j=1}^{T_i} \|S_j^i - X_i\| = \frac{1}{T_i} \sum_{j=1}^{T_i} \sqrt{(r_j^i - x_i)^2 + (s_j^i - y_i)^2}; i=1,2,\dots,8. \quad (7)$$

Step 2: Calculate the distance between DCs X_h and X_i , denoted by M_{hi} , according to Equation 8.

$$M_{hi} = \|X_h - X_i\| = \sqrt{(x_h - x_i)^2 + (y_h - y_i)^2} \quad (8)$$

Step 3: For each pair of DCs X_h and X_i , can calculate using Equation 9

$$R_{h,i} = \frac{A_h + A_i}{M_{h,i}} \quad (9)$$

Then, identify using Equation 10

$$D_i = \max_{h \neq i} R_{h,i} \quad (10)$$

Step 4: Finally, calculate DBI using the following Equation 11.

$$DBI = \frac{1}{K} \sum_{i=1}^K D_i \quad (11)$$

Measurement of Efficiency: Number of Iterations to the Final Clusters

To measure efficiency, for each instance, the number of iterations to the final clusters, where all the stores served by the DCs remain unchanged from the previous iteration, is counted. Once the experiment is repeated for 10,000 instances, an average is obtained for each of the six clustering approaches.

THE EXPERIMENTS, THE RESULTS, AND THE DISCUSSION

This section presents the experiments, their results, and the discussion. First, all the previously mentioned six different clustering approaches, resulting from a combination of three different distance metrics and two calculation methods for centroid locations, are experimented with for our location problem. More precisely, Euclidean, Manhattan, and Chebyshev, together with the other three demand-weighted approaches, are Weighted Euclidean, Weighted Manhattan, and Weighted Chebyshev, are applied to find the optimal eight DC locations for distributing goods to 260 convenience stores in Eastern Thailand.

The experiments conducted in this study use a total of 10,000 different instances. For comparison purposes, each instance randomizes new initial centroids, and these same initial centroids are then used in all six approaches. After the 10,000 instances are carried out for each approach, the effectiveness and efficiency measurement expectations are calculated over these 10,000 instances.

The optimal solutions obtained from these six clustering approaches are first tabulated, followed by their efficiency and effectiveness results reported in tabular and graphical presentation. In addition, a discussion of all the results is provided.

Also, note that all the experiments in this research are run on Intel® Core™ i5-1035G4 with 8 GB of DDR4 memory. The programs are coded in R-programming on RStudio version 1.3.1093.

Optimal Solution Results: The Locations of Eight Centroids or DCs

All eight optimal centroids or DC locations are obtained after implementing all six clustering approaches (Table 1). They all yield the optimal locations nearby, which are not easy to differentiate. Therefore, measurement of the effectiveness and efficiency of the six clustering approaches is needed for comparison purposes.

Table 1
Optimal eight centroids from six different clustering approaches

Clustering Approach	Centroid 1	Centroid 2	Centroid 3	Centroid 4
Euclidean	(13.358,100.988)	(13.017,101.132)	(13.867,101.004)	(12.700,101.341)
Weighted Euclidean	(13.365,100.989)	(13.018, 101.135)	(13.876,101.009)	(12.697,101.337)
Manhattan	(12.380,101.933)	(12.794,101.164)	(13.797,101.208)	(13.152,101.045)
Weighted Manhattan	(12.487,101.842)	(12.786,101.171)	(13.799,101.208)	(13.156,101.042)
Chebyshev	(13.357,100.991)	(13.024,101.126)	(13.867,101.004)	(12.699,101.347)
Weighted Chebyshev	(13.355,100.990)	(13.024,101.130)	(13.876,101.009)	(12.697,101.337)
Clustering Approach	Centroid 5	Centroid 6	Centroid 7	Centroid 8
Euclidean	(12.879,100.912)	(13.624,101.131)	(11.972,102.312)	(13.131,100.950)
Weighted Euclidean	(12.875,100.912)	(13.642,101.151)	(11.972,102.312)	(13.129,100.949)
Manhattan	(13.030,101.060)	(13.507,101.108)	(12.692,100.929)	(12.906,100.928)
Weighted Manhattan	(13.019,101.068)	(13.604,101.075)	(12.691,100.931)	(12.906,100.930)
Chebyshev	(12.876,100.916)	(13.625,101.126)	(11.972,102.312)	(13.131,100.947)
Weighted Chebyshev	(12.875,100.912)	(13.631,101.132)	(11.972,102.312)	(13.130,100.946)

Effectiveness Results: The Expected Distribution Cost

For the effectiveness measurement, the first indicator, the distribution cost from each approach, is calculated (Equation 6) in the previous section and then reported and visualized (Figure 2). The expectation is averaged over 10,000 instances for each clustering approach.

Weighted Chebyshev and Chebyshev produce the first two lowest expected distribution costs of \$1,559.66 and \$1,564.61, respectively. On the contrary, Weighted Manhattan and Manhattan generate the worst two expected distribution costs of \$6,805.71 and \$6,650.62,

respectively. Note that the expected distribution costs of these worst two are also far from those of the remaining approaches.

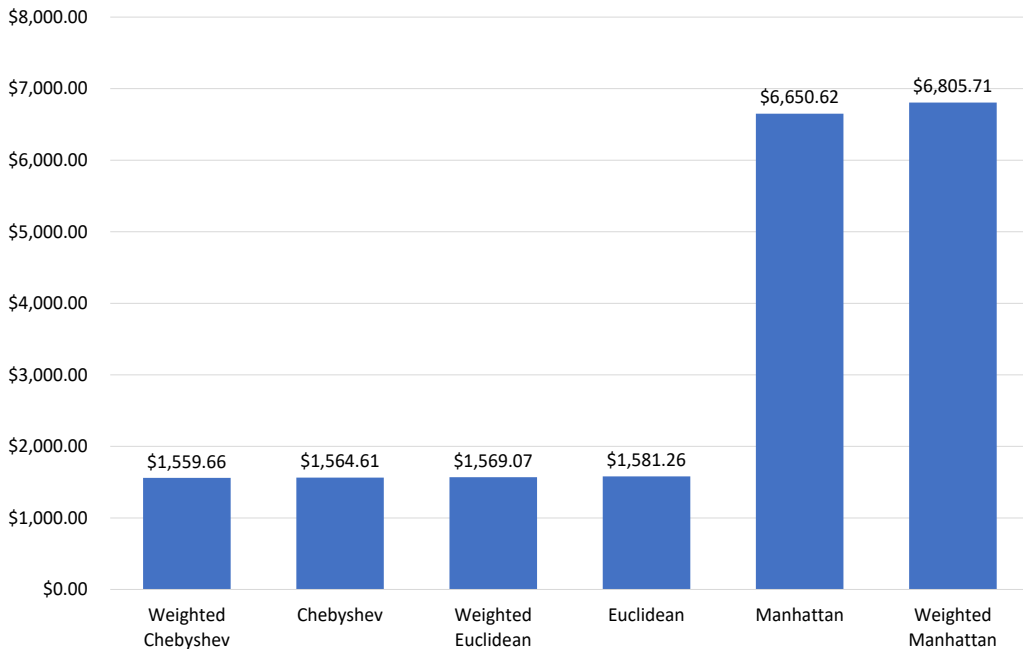


Figure 2. Bar chart of the expected distribution costs over 10,000 instances from each different clustering approach

Effectiveness Results: The Expected DBI

The other indicator of effectiveness is the expected Davies-Bouldin Index (DBI) from the six approaches. They are calculated according to the steps in the previous section and then reported and visualized by bar charts in Figure 3.

The results show that Weighted Chebyshev and Chebyshev yield the best two expected DBIs of 0.6779 and 0.6793, respectively. In contrast, Manhattan and Weighted Manhattan yield the worst two DBIs of 2.1905 and 2.0939, respectively. Similar to the above effectiveness results by the expected distribution costs, the two DBIs of these two worst approaches are far away from those of the remaining approaches even though the worst here, Manhattan, and the second worst, Weighted Manhattan, are interchanged from before.

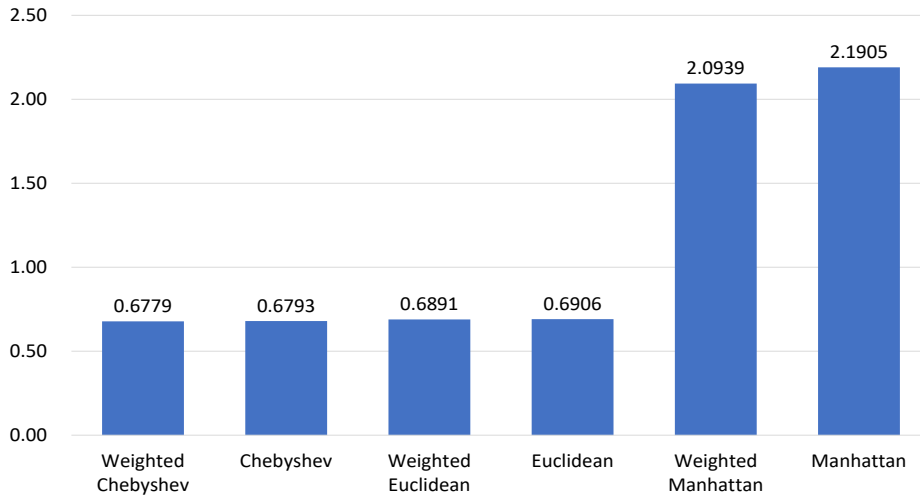


Figure 3. Bar chart of the expected DBI over 10,000 instances from each different clustering approach

Efficiency Results: The Expected Number of Iterations to the Final Clusters

For the efficiency measurement of all six approaches, the expected numbers of iterations to the final clusters are determined and compared. They averaged over 10,000 instances for each clustering approach. Euclidean yields the lowest expected number of iterations at 8.65 (Figure 4). Slightly in the second and third bests are Weighted Chebyshev at 8.88 and Chebyshev at 8.97, while Weighted Manhattan and Manhattan are the worst two with the numbers far away from the rest, that is, 16.01 and 14.84, respectively. Thus, in terms of efficiency, it is fair to say Euclidean, Weighted Chebyshev, and Chebyshev are among the most efficient approaches.

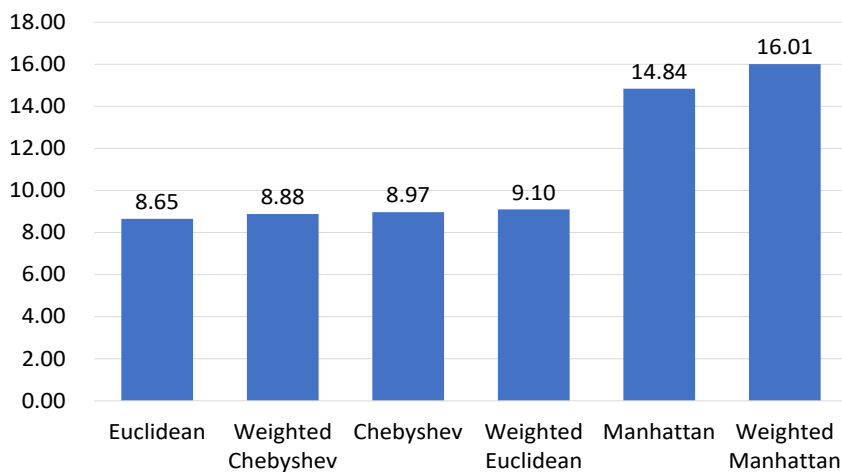


Figure 4. Bar chart of the expected number of iterations to the final clusters over 10,000 instances from each different clustering approach

The Discussion of the Results

The optimal locations obtained from the six clustering approaches are not significantly different (Table 1). Thus, the effectiveness and efficiency measurement can be good indicators for differentiating the six approaches as reported in the previous subsections. Nevertheless, a discussion on the combined results across every approach is needed and hence given here.

Starting with a summary of the effectiveness and efficiency results (Table 2) and obviously, Weighted Chebyshev is most effective either judged by the expected distribution cost or the expected DBI (Figure 5). Moreover, even though Euclidean is the most efficient among the six approaches, the second most efficient, Weighted Chebyshev, is just slightly behind. Hence, Weighted Chebyshev could be the clustering approach that best fits our case study of locating the DCs to serve their convenience stores with different demands.

Table 2
Summary of the effectiveness and efficiency of all six different clustering approaches

Clustering Approach	Effectiveness		Efficiency
	Expected distribution cost	Expected DBI	Expected number of iterations
Weighted Chebyshev	\$1,559.66	0.6779	8.88
Chebyshev	\$1,564.61	0.6793	8.97
Weighted Euclidean	\$1,569.07	0.6891	9.10
Euclidean	\$1,581.26	0.6906	8.65
Manhattan	\$6,650.62	2.1905	14.84
Weighted Manhattan	\$6,805.71	2.0939	16.01

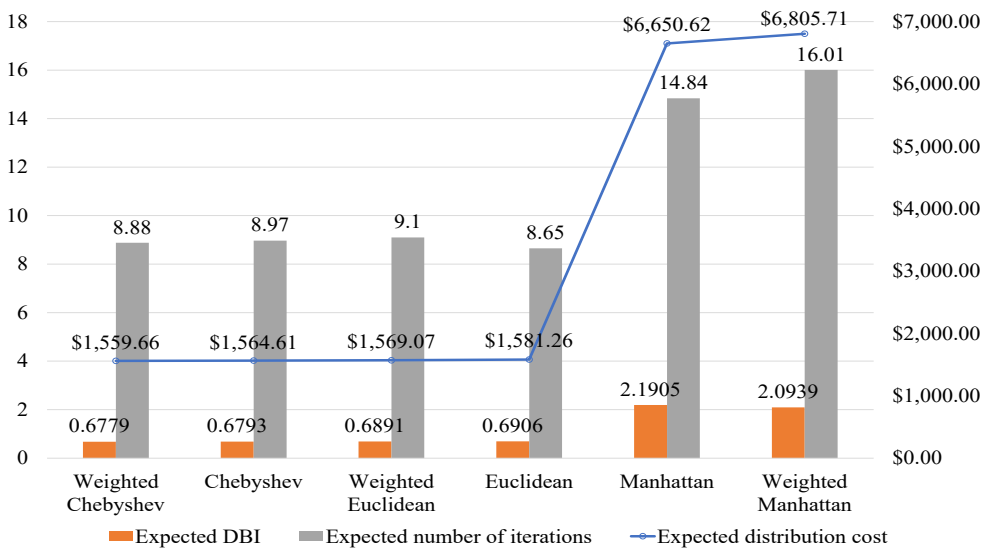


Figure 5. Graphical summary of the effectiveness and efficiency results from all six different clustering approaches

In this section, the results from the six experiments using the three types and three proposed clustering approaches have been reported and discussed combined results. In the next section, a conclusion of this work is first given. Then, suggestions for future research improvement are provided in the end.

CONCLUSION AND SUGGESTIONS

This research examines the location problem with a case study of locating DCs for Thailand's convenience store franchise. The K-means clustering algorithm is adapted so that the centroids in the final iteration can be used as the appropriate locations. In addition to the Euclidian distance typically used in the K-means clustering, two other distance metrics, Manhattan and Chebyshev, are also used.

Furthermore, due to this particular location problem's characteristics of having different demands at the stores and thus different shipment sizes, the locations should be pulled by the center-of-gravity rule. Therefore, modifications to the algorithm are necessary to suit this application better. This research proposes one way of doing so by adjusting the centroid calculation. As a result, the centroid calculation at each iteration is weighted by the stores' different demands. Besides the first three distance metrics, namely, Euclidean, Manhattan, and Chebyshev, another three modified distance metrics are proposed and named Weighted Euclidean, Weighted Manhattan, and Weighted Chebyshev, respectively.

After these, six clustering approaches are experimented on in the case study of locating eight DCs to service 260 convenience stores in Eastern Thailand. The resulting eight DCs' locations show insignificantly different, and thus the effectiveness and efficiency of these approaches play a significant role. In conclusion, the clustering approach best fits this certain problem is the proposed demand-weighted Chebyshev.

Apart from this, several possible ideas for future research are suggested. First, the cost of constructing a DC at each location is usually different, so it should somehow be reflected in the algorithms. The same logic can also be applied to the different transportation rates at different locations.

Also, another way to incorporate the center-of-gravity impact of the stores' different demands is by introducing another attribute into the distance metric Equation. In addition to the latitude and longitude attributes, the store's demand can be treated as another attribute.

Furthermore, other than the three-distance metrics employed here, the distances between the convenience stores and their distribution centers may be figured from the real world based primarily on existing land routes.

Finally, as in the traditional K-means clustering, the complexity of the initialization steps can be viewed as a trade-off to the number of iterations to the final clusters. It is suggested to explore further into this issue to obtain higher algorithm efficiency.

ACKNOWLEDGEMENT

The authors want to thank the anonymous reviewers whose valuable comments and thoughtful suggestions helped enhance the quality of this manuscript. The authors would also like to express sincere thanks to the editors who were always there for us since the very first step of this publication process.

REFERENCES

- Aggarwal, C. C., & Reddy, C. K. (Eds.). (2014). *Data clustering algorithms and applications*. CRC Press.
- Chen, H. (2019). Location problem of distribution center based on Baumer Walvar model: Taking Jiayi logistics as an example. *Open Journal of Business and Management*, 7(2), 1042-1052. <https://doi.org/10.4236/ojbm.2019.72070>
- Dantrakul, S., Likasiri, C., & Pongvuthithum, R. (2014). Applied p-median and p-center algorithms for facility location problems. *Expert Systems with Applications*, 41(8), 3596-3604. <https://doi.org/10.1016/j.eswa.2013.11.046>
- Davies, D. L., & Bouldin, D. W. (1979). A cluster separation measure. *IEEE Transactions on Pattern Analysis and Machine Intelligence*, 1(2), 224-227. <https://doi.org/10.1109/TPAMI.1979.4766909>
- Drezner, Z., Scott, C., & Song, J. S. (2003). The central warehouse location problem revisited. *IMA Journal of Management Mathematics*, 14(4), 321-336. <https://doi.org/10.1093/imaman/14.4.321>
- Farahani, R. Z., & Hekmatfar, M. (Eds.). (2009). *Facility location: Concepts, models, algorithms and case studies*. Springer Science & Business Media.
- Gultom, S., Sriadhi, S., Martiano, M., & Simarmata, J. (2018). Comparison analysis of K-means and K-medoid with Euclidean distance algorithm, distance, and Chebyshev distance for big data clustering. In *IOP Conference Series: Materials Science and Engineering* (Vol. 420, No. 1, p. 012092). IOP Publishing. <https://doi.org/10.1088/1757-899X/420/1/012092>
- Hakimi, S. L. (1964). Optimum locations of switching centers and the absolute centers and medians of a graph. *Operations Research*, 12(3), 450-459. <https://doi.org/10.1287/opre.12.3.450>
- Langley, C. J., Novack, R. A., Gibson, B., & Coyle, J. J. (2020). *Supply chain management: A logistics perspective*. Cengage Learning.
- Ministry of Foreign Affairs. (2017). *Tourism industry in Thailand*. Netherlands embassy in Bangkok. <https://www.rvo.nl/sites/default/files/2017/06/factsheet-toerisme-in-thailand.pdf>
- Sharma, A., & Jalal, A. S. (2017). Clustering based hybrid approach for facility location problem. *Management Science Letters*, 7(12), 577-584. <https://doi.org/10.5267/j.msl.2017.8.007>
- Singh, A., Yadav, A., & Rana, A. (2013). K-means with three different distance metrics. *International Journal of Computer Applications*, 67(10), 13-17. <https://doi.org/10.5120/11430-6785>
- Sinwar, D., & Kaushik, R. (2014). Study of Euclidean and Manhattan distance metrics using simple K-means clustering. *International Journal for Research in Applied Science and Engineering Technology (IJRASET)*, 2(5), 270-274.

- Surawattananon, N., Reanchaoren, T., Prajongkarn, W., Chunanantatham, S., Simakorn, Y., & Gultawatvichai, P. (2021). *Revitalising Thailand's tourism sector*. Bank of Thailand. https://www.bot.or.th/Thai/MonetaryPolicy/EconomicConditions/AAA/250624_WhitepaperVISA.pdf
- Wang, M. (2018). *The research of strategy for the 7-eleven convenience store in Thailand* (Masters dissertation). Siam University, Thailand. https://e-research.siam.edu/wp-content/uploads/2019/08/IMBA-2018-IS-The-Research-of-Strategy-for-the-7-Eleven-Convenience-Store_compressed.pdf
- Yang, L., Ji, X., Gao, Z., & Li, K. (2007). Logistics distribution centers location problem and algorithm under fuzzy environment. *Journal of Computational and Applied Mathematics*, 208(2), 303-315. <https://doi.org/10.1016/j.cam.2006.09.015>

Visible-Near-Infrared Spectroscopy and Chemometrics for Authentication Detection of Organic Soybean Flour

Rudiati Evi Masithoh*, Muhammad Fahri Reza Pahlawan, Devi Alicia Surya Saputri and Farid Rakhmat Abadi

Department of Agricultural and Biosystems Engineering, Faculty of Agricultural Technology, Universitas Gadjah Mada, Yogyakarta, Indonesia

ABSTRACT

Organic and non-organic soybean flours, although visually indifferent, have a significant difference in price and nutrition content. Therefore, the accurate authentication detection of organic soybean flour is necessary. Visible-near-infrared (Vis-NIR) spectroscopy coupled with chemometric methods is a non-destructive technique applied to detect authentic or adulterated organic soybean flour. The spectra of organic, adulterated organic, and non-organic soybean flours were captured using a Vis-NIR spectrometer at 350–1000 nm. The spectra were analyzed using partial least squares (PLS), principal component analysis (PCA), and the combination of these two with discriminant analysis (DA). The results showed that PCA using PC1 and PC2 could differentiate organic and non-organic soybean flours, whereas PC1 and PC4 can detect pure and adulterated organic soybean flours. The PCA–linear DA models showed 98.5% accuracy (Acc) for predicting pure organic and adulterated soybean flours and 100% Acc for predicting organic and non-organic flours. Moreover, PLS regression models resulted in a high R^2 of >95% for predicting organic and non-organic flours and pure and adulterated soybean flours. In addition, the PLS-DA models can differentiate organic from non-organic soybean flour and distinguish pure and adulterated soybean flours with 100% Acc and reliability.

ARTICLE INFO

Article history:

Received: 12 March 2022

Accepted: 28 July 2022

Published: 06 March 2023

DOI: <https://doi.org/10.47836/pjst.31.2.03>

E-mail addresses:

evi@ugm.ac.id (Rudiati Evi Masithoh)

freza836@gmail.com (Muhammad Fahri Reza Pahlawan)

devialicia01@mail.ugm.ac.id (Devi Alicia Surya Saputri)

faridra1998@gmail.com (Farid Rakhmat Abadi)

*Corresponding author

Keywords: Authentication, PCA, PCA-LDA, PLS-DA, PLSR, soybean flour, Vis-NIR

INTRODUCTION

Soybean (*Glycine max* (L.) Merr.) is a protein-rich commodity popularly used as a staple food in some Asian countries (Hartman et al., 2016). Soybean is usually processed into various foods, such as tofu, tempeh, soy sauce, soy milk, miso, and beverages, or consumed as soy grain or flour. Soybean is labeled “organic” if produced from organic farming, where cultivation is performed without synthetic fertilizers and pesticides (Gomiero, 2018). The organic soybean market has grown rapidly along with increased public awareness of the environment, human health, and food safety.

The high demand for organic soybean-based products can lead to potential fraudulent practices such as adulteration. Food adulteration is the intentional addition or substitution of inferior substances into the main food ingredients. Food adulteration can be dangerous to consumers’ health; it affects food safety and quality and reduces consumer trust (Meerza & Gustafson, 2019).

Although organic and non-organic soy flours have similar nutritional contents, they differ in nutritional composition. Organic soybeans contain more sugars, total proteins, and zinc but less fiber, saturated fat, and omega-6 fatty acids than non-organic soybeans (Bøhn et al., 2014). However, organic and non-organic soybean flours have no visible difference, thus causing difficulty in distinguishing them visually if both products are mixed. Given the higher cost of organic soybeans, the addition of non-organic soybeans into organic ones is inevitable. Several methods, ranging from analytical (Martins et al., 2019), chromatographic (Esteki, Simal-gandara, et al., 2018) to spectroscopic ones (Esteki, Shahsavari, et al., 2018), have been used to detect food additives or adulteration.

The infrared (IR) spectroscopy method has been used to detect adulteration (Sørensen et al., 2016) or food fraud (Nobari-Moghaddam et al., 2021). IR spectroscopy studies have been carried out to detect adulteration in commodities that have similar visual appearances, such as adulteration in brown sugar (using Fourier transform (FT)-NIR and FT-IR spectroscopy) (Masithoh, Roosmayanti, et al., 2021; Rismiwandira et al., 2020; Roosmayanti et al., 2021), dairy milk (Jawaid et al., 2013), or sugar (Masithoh, Rondonuwu, et al., 2020). On the other hand, limited studies have been conducted to detect adulteration using visible–near-IR (Vis-NIR) spectroscopy. Some focused on adulterating desiccated coconut powder with coconut milk residue (Pandiselvam et al., 2022) or green banana flour with wheat (Ndlovu et al., 2021). Nonetheless, studies for detecting adulteration of non-organic to organic soybean flours using Vis-NIR spectra have not been studied.

Therefore, this study aimed to investigate the feasibility of Vis-NIR spectroscopy to detect the authentication of organic soybean flour using supervised and unsupervised pattern recognition methods. In this study, the discrimination methods applied were principal component analysis (PCA), which is an unsupervised and often used for dimension reduction and data visualization (Masithoh, Lohumi, et al., 2020) and PCA combined

with linear DA (PCA-LDA), which is a supervised method used to classify data with a predetermined class (Khuwijitjaru et al., 2020). Partial least square regression (PLSR) is the most used quantitative multivariate analysis method for predicting numerical parameters in spectroscopy. For classification with qualitative parameters, PLSR is combined with discriminant analysis (PLS-DA). Therefore, four multivariate analyses were used in the present work: PCA, PCA-LDA, PLSR, and PLS-DA. This research is the first study of the quantitative assessment of authentication and adulteration in organic soybean flour based on Vis-NIR spectroscopy using various pattern recognition methods.

MATERIALS AND METHODS

Sample Preparation

Organic and non-organic soybean flours were obtained from local markets in Indonesia from respected online shops after studying the sellers from the reviews provided by the previous buyers. The sample price for organic soybean was significantly higher compared to non-organic ones. PCA analysis was performed to confirm organic and non-organic samples, which resulted in the clear separation of both samples. Four brands of organic flour and two brands of non-organic flour were used in this study. Soybean flours from different brands were mixed to prepare pure and pure non-organic flours. Pure flours were sieved manually using a 50-mesh sieve (0.29 mm, American Society for Testing and Materials standard) to obtain uniform-size samples. Samples that did not pass the 50-mesh sieve were re-grinded and re-sieved.

Five concentrations (5, 10, 15, 20 and 25%) of non-organic soybean flour as adulterant materials were added to organic soybean flour. Ten samples were prepared for each adulterant concentration. Each sample consisted of 80 g flour mixed manually in a closed bottle for 5 min. Another 20 samples of pure organic and pure non-organic soybean flours were prepared. In total, 70 samples were dried using a food dehydrator at 60°C for 12 h to remove excess water before spectrum acquisition.

Spectrum Acquisition

A soybean flour sample was placed in an aluminum cup with 1 cm height and 4 cm diameter for spectrum acquisition. All samples were scanned using a Vis-NIR miniature spectrometer (Flame-T-VIS-NIR Ocean Optics, 350–1000 nm) with tungsten halogen light (360–2400 nm, HL-2000-HP-FHSA Ocean Optics) and a reflection probe (QR400-7-VIS-NIR Ocean Optics). A probe holder was purposely built to hold the probe and minimize the external light. The distance between the probe and the sample was 5 mm. Figure 1 shows the spectrum measurement setup.

Reflectance spectra were collected using OceanView 1.6.7 software with an integration time of 150 ms, scanning average of 50, and boxcar width of 1. The white and black reference spectra were measured to calibrate the spectrometer instrument. Instrument calibration was repeated every 10 scanings. Ten spectra were obtained for each sample of pure and adulterated soybean flour at room temperature (28°C), resulting in a total of 600 spectra.

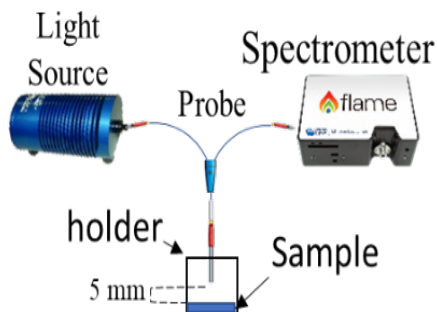


Figure 1. Schematic of the spectrum measurement set-up

Multivariate Analysis

A total of 600 spectra were obtained from pure non-organic, purely organic, and adulterated organic soybean flours (5, 10, 15, 20 and 25% of adulterant). The obtained spectra were compiled in MS Excel® and imported to Unscrambler®X software (CAMO, Oslo, Norway) for multivariate analysis. This research used PCA, PCA-LDA, PLSR, and PLS-DA to differentiate organic and non-organic soybean flours and determine the adulteration concentration of non-organic in organic soybean.

Unsupervised techniques, such as PCA, were used for dimension reduction, pattern recognition, and outlier identification (Berrueta et al., 2007). PCA was applied to discriminate pure organic and non-organic soybean flours using 200 spectra. Moreover, PCA was used to discriminate pure and adulterated organic soybean flours using 600 spectra by omitting the spectra of pure non-organic soybean flour. Outlier identifications were performed by analyzing residuals and T^2 . The supervised analysis used in this study was PCA-LDA, PLSR, and PLS-DA. For supervised analysis, the samples were randomly divided into calibration and prediction data sets. The calibration sets for organic and non-organic analysis consisted of 133 data, whereas pure and adulterated organic analysis consisted of 400 data. The prediction set for organic and non-organic analysis and pure and adulterated organic analysis consisted of 67 and 200 data, respectively.

PCA-LDA was conducted using a linear method with seven components. PCA-LDA uses PCA to reduce the spectral dimension and LDA to maximize the separation of a given class (Berrueta et al., 2007). PCA-LDA was performed using spectra as the predictor and sample types, such as organic, non-organic, and adulterated flours, as classification category variables. The classification category variables used were labeled “Pure” for pure organic soybean flour and “5, 10, 15, 20 and 25%” for adulteration concentrations of non-organic soybean flour. The classification category variables used in the organic and non-organic analysis were the “Organic and “Non-organic” label.

PLSR is a supervised quantitative analysis used to analyze the correlation between spectra and quantitative variables. PLSR analysis was performed using spectrum data as predictors and quantitative variables as responses. The PLSR method was applied to distinguish organic, and non-organic soybean flours using quantitative Y-variables, namely, purely organic and various adulteration concentrations (5, 10, 15, 20 and 25%). Moreover, PLSR analysis was used to predict the adulteration of non-organic to organic soybean flour, using Y-variables based on the binary label “0” for organic soybean flour and “1” for non-organic soybean flour.

PLS-DA is a classification analysis technique that can analyze the correlation between spectra and non-numerical variables in binary label form. Similar to PLSR, PLS-DA is performed using spectrum data as predictors and quantitative variables as responses (Vieira et al., 2021). For the determination of organic and non-organic soybean flour, the binary label was determined as “0” for organic soybean flour and “1” for non-organic soybean flour. For the determination of pure and adulterated organic soybean flour, the binary label “0” was used for the pure organic sample, and the value of “1” was used for adulterated samples in all concentrations. To obtain a clear class prediction, we classified the predicted values <0.5 as “0” and >0.5 as “1.” The predicted binary values were then classified into DA parameters (Table 1). The DA classes from each class were used to calculate the model accuracy (Acc) and reliability (Rel) using Equations 1 and 2, respectively.

$$Acc = \frac{TP + TN}{TP + TN + FP + FN} \times 100\% \quad (1)$$

$$Rel = \left\{ \left(\frac{TP}{TP + TN} + \frac{TN}{TN + FP} \right) - 1 \right\} \times 100\% \quad (2)$$

Table 1

PLS-DA binary predicted value classification

Case	True Class	Predicted Value	Predicted Class	DA Parameter
1	1	0.55	1	True Positive (TP)
2	0	0.37	0	True Negative (TN)
3	0	0.67	1	False Positive (FP)
4	1	0.49	0	False Negative (FN)

RESULTS AND DISCUSSION

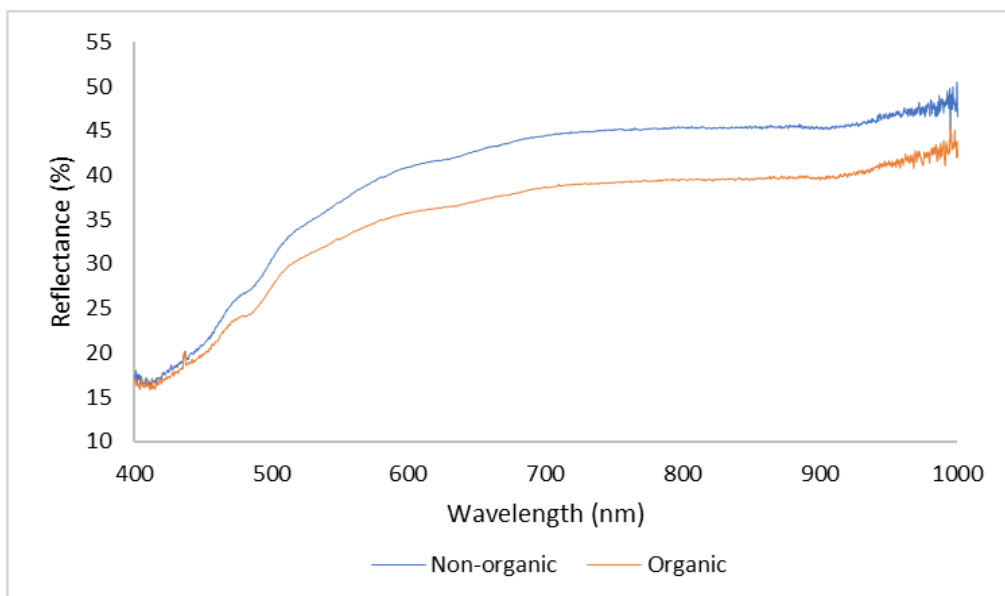
Vis-NIR Spectra of Soybean Flour

Figure 2a shows the Vis-NIR spectra of pure organic and non-organic soybean flour. The Vis-NIR spectra showed information regarding pigments and molecular vibration (Guo et al., 2016). In reflectance spectra, a low reflectance indicates the absorption of photon energy

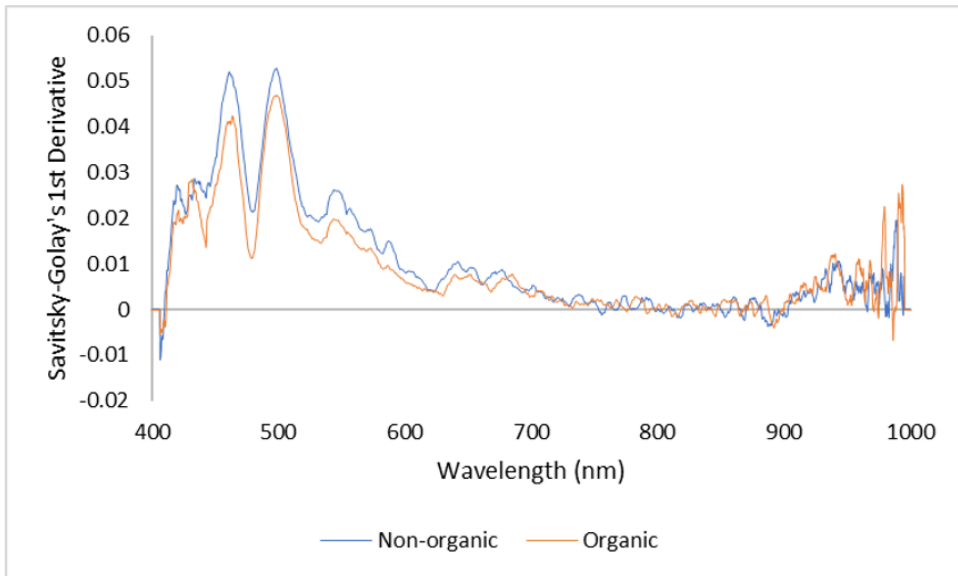
by a certain component. In general, as illustrated in Figure 2a, the absorption of organic flour to visible and NIR light is higher than that of non-organic flour but determining at which wavelength the absorption occurs is difficult. Figure 2b shows the organic and non-organic soybean flours after pre-processing via the Savitzky–Golay 1st derivative method. Unlike the original spectra shown in Figure 2a, in Figure 2b, the absorption peaks or valleys were more distinct at 430–443, 460, 480, 500, 534, 550, and 950–1000 nm.

Figure 3a shows the original Vis-NIR spectra of pure and adulterated organic soybean flours. In general, the higher the concentration of adulterant concentration, the higher the reflectance value. However, similar to Figure 2a, given the original spectra, no distinct peaks revealed the absorption of molecules. After processing the original spectra using the Savitzky–Golay 1st-derivative method, the peaks and valleys became visible (Figure 3b). The peaks and valleys appeared at the wavelengths of 420–443, 460, 480, 500, 533, 550, and 970–1000 nm.

The wavelengths between 400 and 500 nm contained information related to the absorption of carotenoid pigments (Monma et al., 1994). High absorptions at 500–600 nm due to anthocyanin (Merzlyak et al., 2003) were also found in green and yellow soybean flours (Pahlawan et al., 2022). Low values at 600–700 nm denote the weak absorptions of chlorophylls (Lichtenthaler & Buschmann, 2001). The weak water absorption at 700–1000 nm was due to the low detection of water molecules using the Vis/NIR spectrometer (Zhang et al., 2012). However, several troughs around 950–1000 nm reflected the absorption information of O-H, C-H, and N-H bonds, which build the functional components of soybean (Dixit et al., 2011).

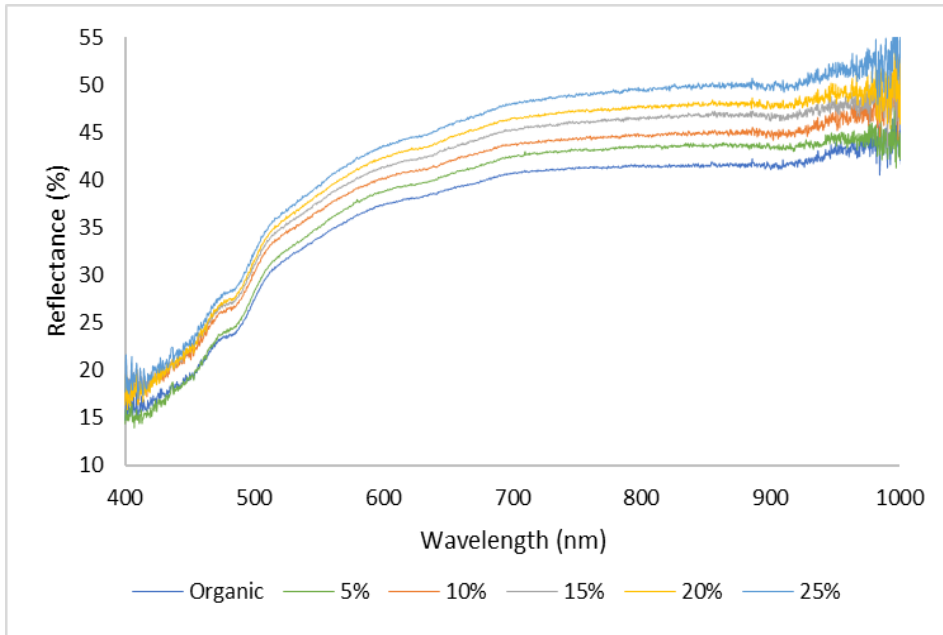


(a)

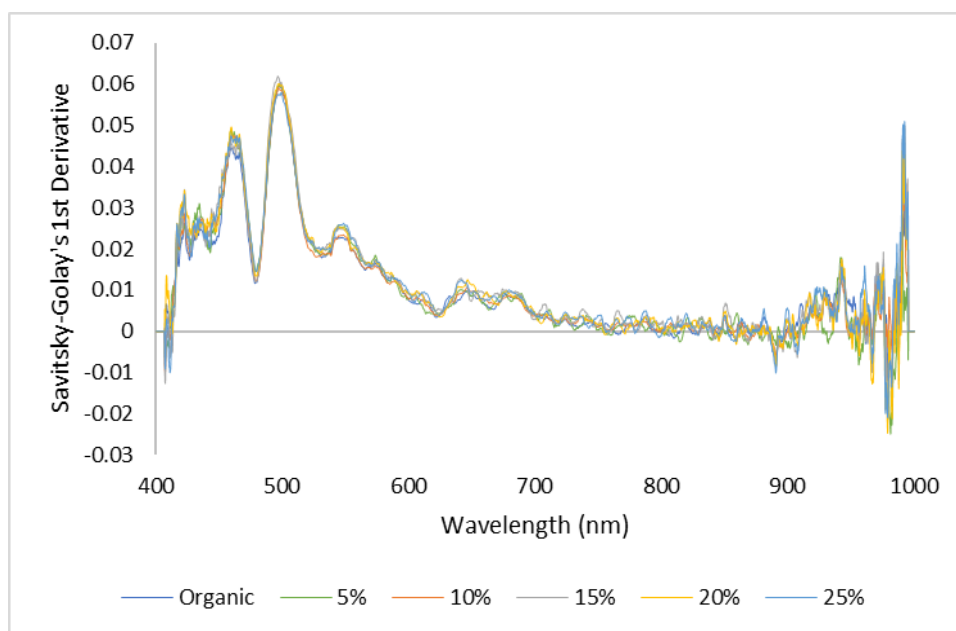


(b)

Figure 2. (a) Original and (b) Savitzky–Golay 1st-derivative spectra of organic and non-organic soybean flour observed with Vis-NIR spectroscopy



(a)



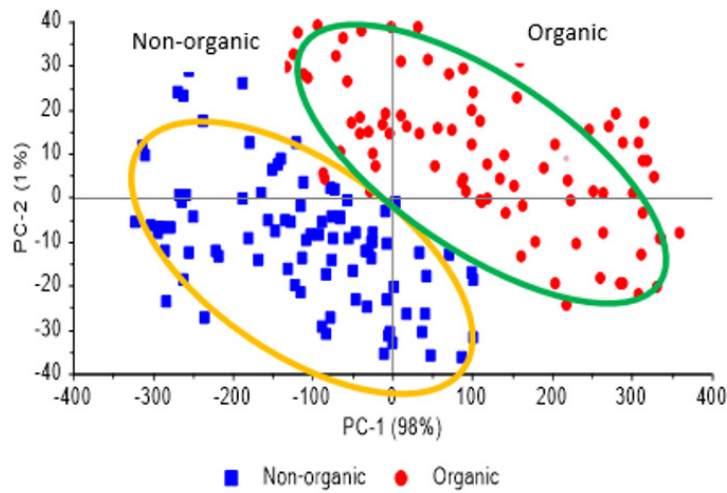
(b)

Figure 3. (a) Original and (b) Savitzky–Golay 1st derivative of the Vis-NIR spectra of pure and adulterated organic soybean flours in various concentrations

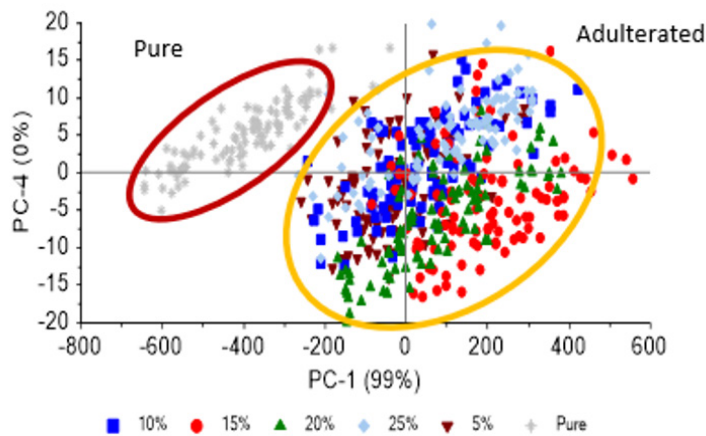
PCA-LDA

Figure 4a shows the PCA score plot of pure organic and pure non-organic soybean flours. The principal component (PC1) and PC2 explained 98% and 1% of the variance, respectively. These PCs classified organic and non-organic flours, in which non-organic flour had a negative PC1, whereas organic flour was PC1 positive. As illustrated in Figure 4b, purely organic and adulterated organic soybean flours were distinctively separated. The clear separation of pure and adulterated organic soybean flours was expressed by PC1 and PC4, which explained 99% of their variance. Pure organic flour was located at the PC1 negative axis, whereas adulterated organic samples were spread from the negative to positive axes of PC1. Samples with 5–20% adulteration concentrations can be differentiated; the higher the adulteration concentration, the higher the PC1 positive score values.

Given that PCA models explained 99% of the total variance, they were considered good. The explained variance showed the percentages of variances represented by the new variable (PC). Therefore, maximizing the explained variance will result in an ideal model to avoid overfitting.



(a)



(b)

Figure 4. PCA score plot of (a) organic and non-organic soybean flours; and (b) pure and adulterated organic soybean flours in various concentrations

Figure 5a displays the loading plot showing the wavelengths that contributed to separating organic and non-organic flours. Loadings of PC1 and PC2 at wavelengths of 400–500 nm, which correspond to carotenoid molecules, were responsible for classifying organic and non-organic flours. The result corresponded to the finding by Lakshmisha et al. (2012), who showed the different carotenoid contents of organic and non-organic soybean leaves and oils.

Based on the loading plot in Figure 5b, the classification of pure and organic adulterated organic soybeans was determined mostly from PC1, whereas the loadings of PC4 were

relatively flat. Using only two axes (PC1 and PC4), the higher the concentration of adulteration of non-organic flour, the higher the values of PC1. However, this trend only applied to 5–15% adulteration. For 20–25% adulteration concentrations, the samples overlapped with other data with different concentrations, implying that another axis or PC is required to describe data for 20–25% adulteration concentrations.

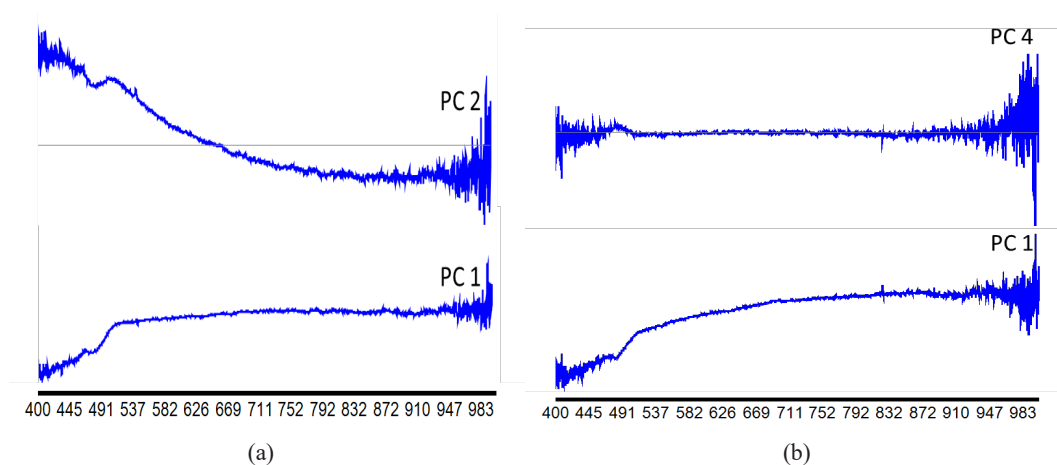


Figure 5. PCA loading plot of (a) organic and non-organic soybean flours; and (b) pure and adulterated organic soybean flours in various concentrations

Figure 6 shows the LDA classification of two organic and non-organic sample categories using a linear model and seven PCs. With the calibration data set, the LDA model can classify with 100% Acc with more distinct separation compared with the classification using PCA (Figure 4a). Table 2 shows that the classification also perfectly works using the prediction data set.

Figure 7 shows the LDA classification of pure and adulterated samples. Although not as good as the organic and non-organic (O versus N) LDA model shown in Figure 6a, the pure organic and adulterated (P versus A) LDA model exhibited a very good Acc (98.5%). The classification capability of the P versus A model was considered good, with only 4 out of 200 samples being misclassified using the prediction data set (Table 3).

The results of PCA-LDA in this research are comparable to those of studies on the classification of soybean oils based on NIR spectra (de Almeida et al., 2021) and LDA for authentication of babassu oil using Mid-IR spectra (Pereira et al., 2022). The results were also better than those of LDA in the authentication of dark-brown sugar using UV-Vis, fluorescence spectroscopy, and mass spectrometry (Chen et al., 2021). Therefore, the PCA-LDA model can classify organic and non-organic soybean flour or detect pure and adulterated organic soybean flour.

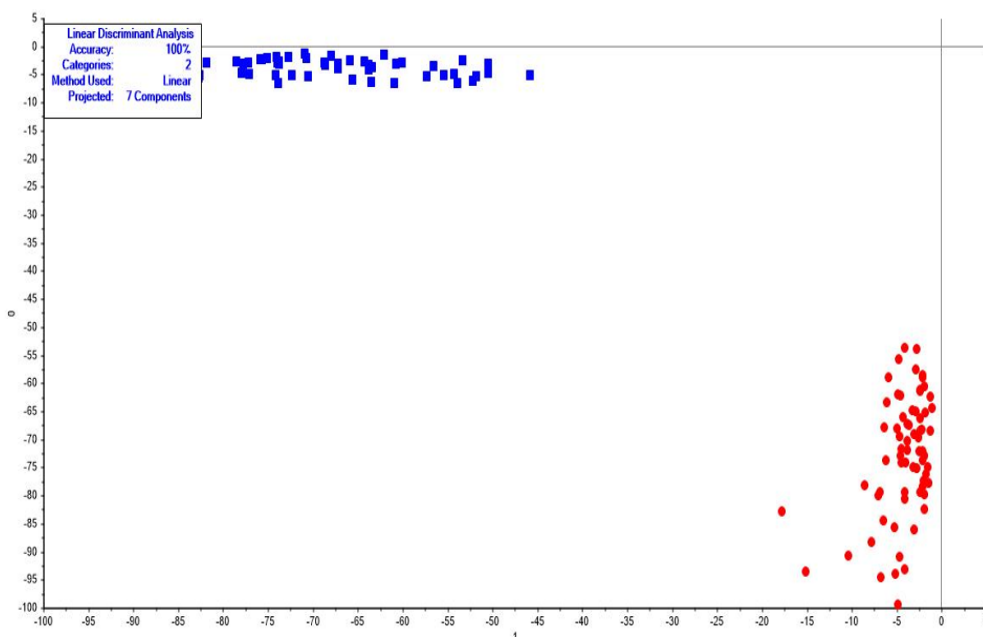


Figure 6. Classification of organic and non-organic soybean flours using PCA-LDA

Table 2

PCA-LDA model of organic and non-organic flours using the prediction data set

True class	N	Predicted Class		Classification Accuracy (%)
		Organic	Non-Organic	
Organic	35	35	0	100
Non-Organic	32	0	32	100

Table 3

PCA-LDA model of pure organic and adulterated flours using the prediction data set

True class	N	Predicted class						Classification Accuracy (%)
		Pure	5%	10%	15%	20%	25%	
Pure	32	32	0	0	0	0	0	100
5%	40	0	37	3	0	0	0	93
10%	38	0	0	38	0	0	0	100
15%	32	0	0	1	31	0	0	97
20%	33	0	0	0	0	33	0	100
25%	25	0	0	0	0	0	25	100

N = number of samples

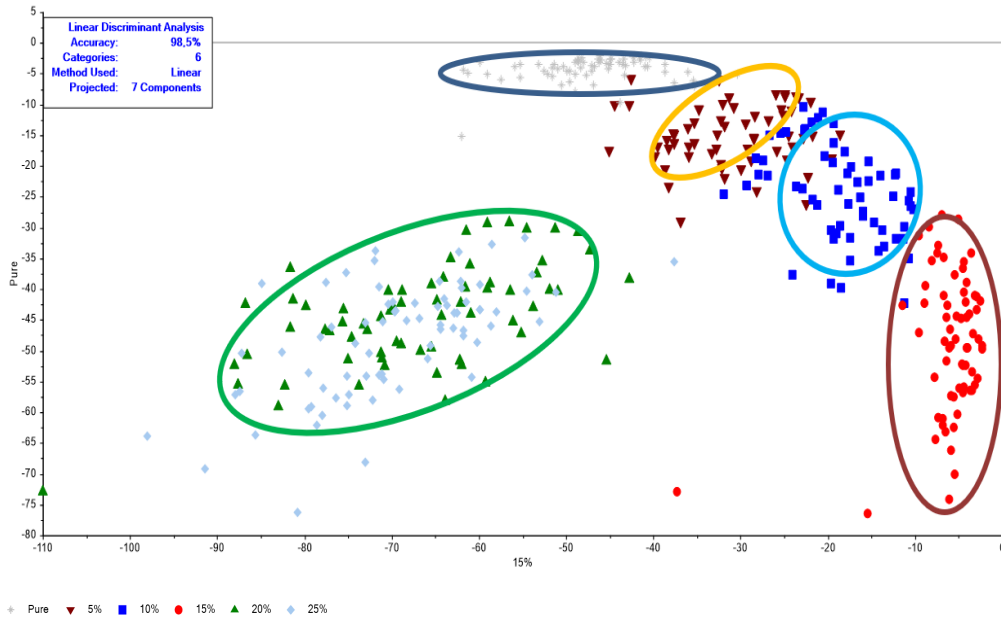


Figure 7. Classification of pure and adulterated soybean flours using PCA-LDA

PLSR and PLS-DA

The PLSR model was used to distinguish organic and non-organic soybean flours. In the PLSR analysis, quantitative variables were based on binary labels “0” for organic and “1” for non-organic flour. Table 4 shows the PLSR results for determining organic and non-organic flour samples. Given the original and several pre-processed spectra (Table 4), the PLSR models had a high determination coefficient (R^2) > 0.97 and low root mean square error (RMSE) < 0.06 for calibration. The results indicated that applying the pre-processing method to the original Vis-NIR spectra did not significantly affect the PLSR results. All the findings showed that the R^2 and RMSE values of all calibration and validation data sets were very close, implying that the calibration PLSR models were robust. When applied to prediction data sets, the obtained PLSR models also yielded a high performance, as indicated by the high value of R^2 (>0.97) and low RMSE (<0.07) of the prediction.

Figure 8a shows the PLSR plot of organic and non-organic soybean flours. The model plot was developed using reflectance spectra as X-variables and binary numbers “0” for pure organic flour and “1” for non-organic flour as Y-variables. By using Savitzky–Golay 1st derivative pre-processed spectra, the PLSR model can predict the class of organic and non-organic soybean flours with R^2 of 0.98 and RMSE of 0.07.

Table 4

PLSR results for distinguishing organic and non-organic soybean flour

Pre-processing	Calibration		Cross Validation		Prediction	
	R ²	RMSE	R ²	RMSE	R ²	RMSE
Raw	0.97	0.07	0.97	0.08	0.98	0.07
SGD1	0.99	0.06	0.97	0.09	0.98	0.07
SGD2	0.98	0.07	0.97	0.08	0.97	0.08
SNV	0.99	0.06	0.98	0.07	0.98	0.08
MSC	0.99	0.06	0.98	0.07	0.98	0.07
Norm	0.99	0.05	0.98	0.06	0.98	0.06

SGD1 = Savitzky–Golay's 1st derivative, SGD2 = Savitzky–Golay's 2nd derivative, SNV = standard normal variate, MSC = multiple scatter correction, Norm = normalization, R² = determination coefficient, and RMSE = root mean square error.

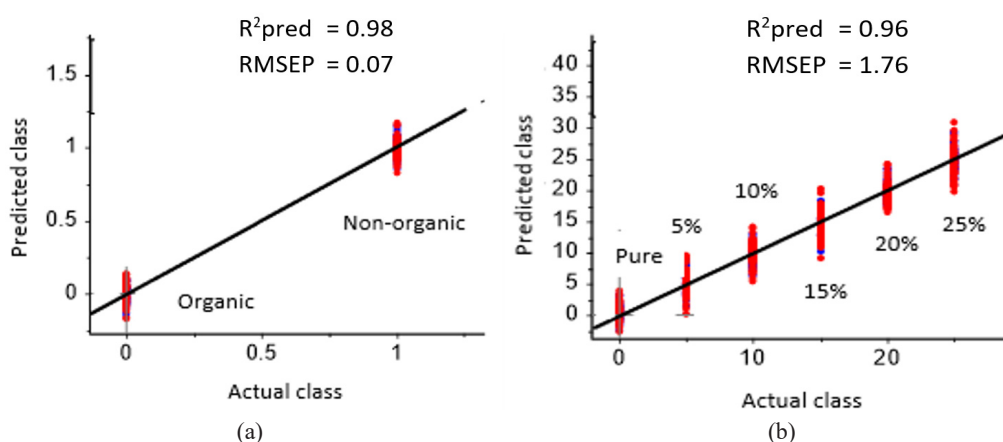


Figure 8. PLSR plots of (a) organic and non-organic soybean flour; and (b) pure and adulterated organic soybean flour

For the differentiation of pure and adulterated organic soybean flours using PLSR, quantitative variables were used as Y-variables and Vis-NIR reflectance spectra as X-variables. Non-organic soybean flour in various concentrations of 0, 5, 10, 15, 20 and 25% was added to the organic soybean flour. Table 5 shows the PLSR results of the prediction for non-organic adulteration in organic soybean flour using various original and pre-processed spectra. For calibration and validation models, all obtained R² were significantly high (>0.95), and the RMSEs were very low (<2%). Similar to the findings shown in Table 4, the effect of pre-processed spectra on PLSR was not significantly different from that without pre-processing and the original spectra. These phenomena

were characteristics of the Vis-NIR spectra; that is, the pre-processing method did not significantly improve the PLSR results, as also reported by (Masithoh, Pahlawan, et al., 2021; Pahlawan et al., 2021) when predicting solid soluble content and the pH of banana.

Figure 8b shows the PLSR plot of pure and adulterated organic soybean flours. Using Savitzky–Golay 1st derivative pre-processing of spectra, the PLSR model can predict the class of organic and non-organic soybean flours with R² of 0.96 and RMSE of 1.76. The PLSR result confirmed the capability of Vis-NIR spectroscopy in detecting low concentrations of non-organic soybean flour adulteration in organic samples.

Table 5

PLSR results for the prediction of adulteration in non-organic to organic soybean flour

Pre-processing	Calibration		Cross Validation		Prediction	
	R ²	RMSE	R ²	RMSE	R ²	RMSE
Original	0.96	1.74	0.95	1.97	0.95	1.99
SGD1	0.97	1.49	0.95	1.89	0.96	1.76
SGD2	0.96	1.75	0.95	1.99	0.95	1.98
SNV	0.95	1.84	0.94	2.06	0.95	0.19
MSC	0.95	1.84	0.94	2.07	0.95	1.96
Norm	0.96	1.77	0.95	1.98	0.95	1.99

SGD1 = Savitzky–Golay’s 1st derivative, SGD2 = Savitzky–Golay’s 2nd derivative, SNV = standard normal variate, MSC = multiple scatter correction, Norm = normalization, R² = determination coefficient, and RMSE = root mean square error

In this research, the determination of organic, non-organic, pure, and adulterated soybean flours was performed using PLS-DA. PLSR and PLS-DA have the same mathematical operations. However, the difference is in the response variables, in which PLS-DA uses categorical responses, whereas PLSR uses continuous sample responses. In PLS-DA, reflectance spectra were used as X-variables, and binary numbers 0 or 1 as Y-variables. The values of 0 and 1 were assigned to organic and non-organic soybean flours, respectively. The values of 0 and 1 were assigned to pure and adulterated organic soybean flours. Table 6 shows the PLS-DA performances of organic and non-organic models and pure and adulterated organic models.

The PLS-DA performances were determined based on the Acc, which showed the percentage of correct classification compared with the number of samples, and Rel, which revealed the model’s capability to predict each class correctly (Vieira et al., 2021). Table 6 shows the Acc and Rel of the PLS-DA model. The Acc and Rel showed that the model could classify samples perfectly. For organic and non-organic models, Acc and Rel of 100%

mean that the model can differentiate organic from non-organic soybean flour. For pure and adulterated organic models, Acc and Rel of 100% mean that PLS-DA can differentiate pure samples (0% of adulterant) from those containing adulterant in various concentrations. In this research, PLS-DA performance was better compared with the authentication of turmeric (Khodabakhshian et al., 2021) or *Ginkgo biloba* extract (Walkowiak et al., 2019).

Table 6

PLS-DA performances using Vis-NIR original spectra

Model	Calibration		Prediction	
	Acc	Rel	Acc	Rel
Organic and non-organic	100%	100%	100%	100%
Pure and adulterated organic	100%	100%	100%	100%

Acc = accuracy; Rel = reliability

CONCLUSION

The authentication of organic soybean flour is important to guarantee product quality. Using Vis-NIR spectroscopy combined with supervised and unsupervised multivariate analysis, namely, PCA, LDA, PLSR, and PLS-DA, organic and non-organic soybean flours can be distinguished perfectly. Moreover, these multivariate analyses determine pure and adulterated organic soybean flours. With the relatively low price of Vis-NIR fiber optic spectra, the resulting models can be used for small-scale soybean industries to assure the quality of their products, especially in food authentication.

ACKNOWLEDGEMENT

Great appreciation is delivered to Universitas Gadjah Mada for financial support under Hibah Rekognisi Tugas Akhir 2021 No: 3190/UN1/DITLIT/DIT-LIT/PT/2021.

REFERENCES

- Berrueta, L. A., Alonso-Salces, R. M., & Héberger, K. (2007). Supervised pattern recognition in food analysis. *Journal of Chromatography A*, 1158(1-2), 196-214. <https://doi.org/10.1016/j.chroma.2007.05.024>
- Bøhn, T., Cuhra, M., Traavik, T., Sanden, M., Fagan, J., & Primicerio, R. (2014). Compositional differences in soybeans on the market: Glyphosate accumulates in Roundup Ready GM soybeans. *Food Chemistry*, 153, 207-215. <https://doi.org/10.1016/j.foodchem.2013.12.054>
- Chen, J. Y., Chen, X. W., Lin, Y. Y., Yen, G. C., & Lin, J. A. (2021). Authentication of dark brown sugars from different processing using three-dimensional fluorescence spectroscopy. *LWT*, 150, Article 111959. <https://doi.org/10.1016/j.lwt.2021.111959>

- de Almeida, V. E., de Sousa Fernandes, D. D., Diniz, P. H. G. D., de Araújo Gomes, A., Vêras, G., Galvão, R. K. H., & Araújo, M. C. U. (2021). Scores selection via Fisher's discriminant power in PCA-LDA to improve the classification of food data. *Food Chemistry*, 363, Article 130296. <https://doi.org/10.1016/j.foodchem.2021.130296>
- Dixit, A., Antony, J. I., Sharma, N. K., & Tiwari, R. K. (2011). Soybean constituents and their functional benefits. *Research Signpost*, 661(2), 367-383.
- Esteki, M., Shahsavari, Z., & Simal-Gandara, J. (2018). Use of spectroscopic methods in combination with linear discriminant analysis for authentication of food products. *Food Control*, 91, 100-112. <https://doi.org/10.1016/j.foodcont.2018.03.031>
- Esteki, M., Simal-gandara, J., Shahsavari, Z., Zandbaaf, S., & Dashtaki, E. (2018). A review on the application of chromatographic methods, coupled to chemometrics, for food authentication. *Food Control*, 93(April), 165-182. <https://doi.org/10.1016/j.foodcont.2018.06.015>
- Gomiero, T. (2018). Food quality assessment in organic vs. conventional agricultural produce: Findings and issues. *Applied Soil Ecology*, 123(February), 714-728. <https://doi.org/10.1016/j.apsoil.2017.10.014>
- Guo, Z., Huang, W., Peng, Y., Chen, Q., Ouyang, Q., & Zhao, J. (2016). Color compensation and comparison of shortwave near infrared and long wave near infrared spectroscopy for determination of soluble solids content of "Fuji" apple. *Postharvest Biology and Technology*, 115, 81-90. <https://doi.org/10.1016/j.postharvbio.2015.12.027>
- Hartman, G. L., Pawlowski, M. L., Herman, T. K., & Eastburn, D. (2016). Organically grown soybean production in the USA: Constraints and management of pathogens and insect pests. *Agronomy*, 6(1), Article 16. <https://doi.org/10.3390/agronomy6010016>
- Jawaid, S., Talpur, F. N., Sherazi, S. T. H., Nizamani, S. M., & Khaskheli, A. A. (2013). Rapid detection of melamine adulteration in dairy milk by SB-ATR-Fourier transform infrared spectroscopy. *Food Chemistry*, 141(3), 3066-3071. <https://doi.org/10.1016/j.foodchem.2013.05.106>
- Khodabakhshian, R., Bayati, M. R., & Emadi, B. (2021). An evaluation of IR spectroscopy for authentication of adulterated turmeric powder using pattern recognition. *Food Chemistry*, 364, Article 130406. <https://doi.org/10.1016/j.foodchem.2021.130406>
- Khuwijitjaru, P., Boonyapisompan, K., & Huck, C. W. (2020). Near-infrared spectroscopy with linear discriminant analysis for green "Robusta" coffee bean sorting. *International Food Research Journal*, 27(2), 287-294.
- Lakshmisha, G., Singh, V. P., Shivakumar, B. G., & Arora, A. (2012). Effect of organic and inorganic nutrients on physiological traits of soybean (*Glycine max* (L.) Merr). *Indian Journal of Plant Physiology*, 17(1), 52-56.
- Lichtenthaler, H. K., & Buschmann, C. (2001). Chlorophylls and carotenoids: Measurement and characterization by UV-VIS spectroscopy. *Current Protocols in Food Analytical Chemistry*, 1, F4.3.1-F4.3.8. <https://doi.org/https://doi.org/10.1002/0471142913.faf0403s01>
- Martins, F. C. O. L., Sentanin, M. A., & De Souza, D. (2019). Analytical methods in food additives determination: Compounds with functional applications. *Food Chemistry*, 272(April 2018), 732-750. <https://doi.org/10.1016/j.foodchem.2018.08.060>

- Masithoh, R. E., Lohumi, S., Amanah, H. Z., Yoon, W. S., & Cho, B. K. (2020). Development of multi-product calibration models of various root and tuber powders by Fourier Transform Near Infra-red (FT-NIR) spectroscopy for the quantification of polysaccharide contents. *Heliyon*, *6*(10), Article e05099. <https://doi.org/10.1016/j.heliyon.2020.e05099>
- Masithoh, R. E., Pahlawan, M. F. R., & Wati, R. K. (2021). Non-destructive determination of SSC and pH of banana using a modular Vis/NIR spectroscopy: comparison of partial least square (PLS) and principle component regression (PCR). In *IOP Conference Series: Earth and Environmental Science* (Vol. 752, No. 1, p. 012047). IOP Publishing. <https://doi.org/10.1088/1755-1315/752/1/012047>
- Masithoh, R. E., Rondonuwu, F., Setyabudi, F. M. C. S., & Cho, B. K. (2020). Development of calibration model for determination of sweeteners additives in Indonesia rice flour-based food by FT-NIR spectroscopy. In *IOP Conference Series: Earth and Environmental Science* (Vol. 542, No. 1, p. 012017). IOP Publishing. <https://doi.org/10.1088/1755-1315/542/1/012017>
- Masithoh, R. E., Roosmayanti, F., Rismiwandira, K., & Pahlawan, M. F. R. (2021). Detection of palm sugar adulteration by fourier transform near-infrared (FT-NIR) and fourier transform infrared (FT-IR) spectroscopy. *Sugar Tech*, *24*(3), 920-929. <https://doi.org/10.1007/s12355-021-01058-3>
- Meerza, S. I. A., & Gustafson, C. R. (2019). Does prior knowledge of food fraud affect consumer behavior? Evidence from an incentivized economic experiment. *PLoS ONE*, *14*(12), 1-14. <https://doi.org/10.1371/journal.pone.0225113>
- Merzlyak, M. N., Solovchenko, A. E., & Gitelson, A. A. (2003). Reflectance spectral features and non-destructive estimation of chlorophyll, carotenoid and anthocyanin content in apple fruit. *Postharvest Biology and Technology*, *27*(2), 197-211. [https://doi.org/10.1016/S0925-5214\(02\)00066-2](https://doi.org/10.1016/S0925-5214(02)00066-2)
- Monma, M., Terao, J., Lto, M., Saito, M., & Chikuni, K. (1994). Carotenoid components in soybean seeds varying with seed color and maturation stage. *Bioscience, Biotechnology, and Biochemistry*, *58*(5), 926-930. <https://doi.org/10.1271/bbb.58.926>
- Ndlovu, P. F., Magwaza, L. S., Tesfay, S. Z., & Mphahlele, R. R. (2021). Vis-NIR spectroscopic and chemometric models for detecting contamination of premium green banana flour with wheat by quantifying resistant starch content. *Journal of Food Composition and Analysis*, *102*, Article 104035. <https://doi.org/10.1016/j.jfca.2021.104035>
- Nobari-Moghaddam, H., Tamiji, Z., Akbari-Lakeh, M., Khoshayand, M. R., & Haji-Mahmoodi, M. (2021). Multivariate analysis of food fraud: A review of NIR based instruments in tandem with chemometrics. *Journal of Food Composition and Analysis*, *107*, Article 104343. <https://doi.org/10.1016/j.jfca.2021.104343>
- Pahlawan, M. F. R., Murti, B. M. A., & Masithoh, R. E. (2022). The potency of Vis/NIR spectroscopy for classification of soybean based of colour. In *IOP Conference Series: Earth and Environmental Science* (Vol. 1018, No. 1, p. 012015). IOP Publishing.
- Pahlawan, M. F. R., Wati, R. K., & Masithoh, R. E. (2021). Development of a low-cost modular VIS / NIR spectroscopy for predicting soluble solid content of banana. In *IOP Conference Series: Earth and Environmental Science* (Vol. 644, No. 1, p. 012047). IOP Publishing. <https://doi.org/10.1088/1755-1315/644/1/012047>

- Pandiselvam, R., Mahanti, N. K., Manikantan, M. R., Kothakota, A., Chakraborty, S. K., Ramesh, S. V., & Beegum, P. P. S. (2022). Rapid detection of adulteration in desiccated coconut powder: vis-NIR spectroscopy and chemometric approach. *Food Control*, 133, Article 108588. <https://doi.org/10.1016/j.foodcont.2021.108588>
- Pereira, S. N. G., De Lima, A. B. S., Oliveira, T. D. F., Batista, A. S., Jesus, J. C. De, Ferrão, S. P. B., & Santos, L. S. (2022). Non-destructive detection of soybean oil addition in babassu oil by MIR spectroscopy and chemometrics. *LWT*, 154, Article 112857. <https://doi.org/10.1016/j.lwt.2021.112857>
- Rismiwandira, K., Roosmayanti, F., Pahlawan, M. F. R., & Masithoh, R. E. (2020). Application of fourier transform near-infrared (FT-NIR) spectroscopy for detection of adulteration in palm sugar. In *IOP Conference Series: Earth and Environmental Science* (Vol. 653, No. 1, p. 012122). IOP Publishing. <https://doi.org/10.1088/1755-1315/653/1/012122>
- Roosmayanti, F., Rismiwandira, K., & Masithoh, R. E. (2021). Detection of coconut (*Cocos nucifera*) sugar adulteration in palm (*Arenga pinnata* Merrill) sugar by fourier transform infrared (FT-IR) spectroscopy. *Food Research*, 5, 31-36.
- Sørensen, K. M., Khakimov, B., & Engelsen, S. B. (2016). The use of rapid spectroscopic screening methods to detect adulteration of food raw materials and ingredients. *Current Opinion in Food Science*, 10, 45-51. <https://doi.org/10.1016/j.cofs.2016.08.001>
- Vieira, L. S., Assis, C., de Queiroz, M. E. L. R., Neves, A. A., & de Oliveira, A. F. (2021). Building robust models for identification of adulteration in olive oil using FT-NIR, PLS-DA and variable selection. *Food Chemistry*, 345, Article 128866. <https://doi.org/10.1016/j.foodchem.2020.128866>
- Walkowiak, A., Ledziński, Ł., Zapadka, M., & Kupcewicz, B. (2019). Detection of adulterants in dietary supplements with Ginkgo biloba extract by attenuated total reflectance Fourier transform infrared spectroscopy and multivariate methods PLS-DA and PCA. *Spectrochimica Acta - Part A: Molecular and Biomolecular Spectroscopy*, 208, 222-228. <https://doi.org/10.1016/j.saa.2018.10.008>
- Zhang, Q., Li, Q., & Zhang, G. (2012). Rapid determination of leaf water content using VIS/NIR spectroscopy analysis with wavelength selection. *Spectroscopy*, 27(2), 93-105. <https://doi.org/10.1155/2012/276795>

Optimum Temperature and Salinity Conditions for Growth, Lipid Contents, and Fatty Acids Composition of Centric Diatoms *Chaetoceros Calcitrans* and *Thalassiosira Weissflogii*

Ahmed Awadh Ahmed Sas^{1,2}, Aziz Arshad³, Simon Kumar Das^{1,4}, Suriyanti Su Nyun Pau^{1,4} and Zaidi Che Cob^{1,4*}

¹Department of Earth Sciences and Environment, Faculty of Science and Technology, Universiti Kebangsaan Malaysia, 43600 UKM, Bangi, Selangor, Malaysia

²Department of Marine Biology, Faculty of Environmental Science and Marine Biology, Hadhramout University, Hadhramout, Yemen

³Department of Aquaculture, Faculty of Agriculture, Universiti Putra Malaysia, 43400 UPM, Serdang, Selangor, Malaysia

⁴Marine Ecosystem Research Centre (EKOMAR), Faculty of Science and Technology, Universiti Kebangsaan Malaysia, 43600 UKM, Bangi, Selangor, Malaysia

ABSTRACT

Microalgae are very important organisms as primary producers and have a wide range of applications in areas such as aquaculture, pharmaceuticals, medicine, biofuels, and others. In this study, the effect of temperature and salinity on growth, biomass, proximate composition, and lipid production of *Chaetoceros calcitrans* (Paulsen) and *Thalassiosira weissflogii* (Grunow) were investigated. The best growth rate (SGR) and highest biomass production were observed at 30°C and 30 ppt for *C. calcitrans* and at 30°C and 25 ppt for *T. weissflogii*. At these optimum temperature and salinity combinations, the maximum cell density was accomplished

by day 12 for *C. calcitrans* (6.74×10^6 cells ml⁻¹) and by day 10 for *T. weissflogii* (3.45×10^6 cells ml⁻¹). The proximate composition during this period was $38.25 \pm 0.99\%$ protein, $16.96 \pm 0.90\%$ lipid, and $9.39 \pm 0.59\%$ carbohydrate in *C. calcitrans*, compared to $13.49 \pm 0.28\%$ protein, $10.43\% \pm 0.25\%$ lipid and $16.49 \pm 0.47\%$ carbohydrate in *T. weissflogii*. Furthermore, over 35% of lipids in *C. calcitrans* were palmitic acid (C16), while in *T. weissflogii*, over 24% of lipids were myristic acid (C14). Although *C.*

ARTICLE INFO

Article history:

Received: 14 March 2022

Accepted: 21 July 2022

Published: 06 March 2023

DOI: <https://doi.org/10.47836/pjst.31.2.04>

E-mail addresses:

p93365@siswa.ukm.edu.my (Ahmed Awadh Ahmed Sas)

azizarshad@putra.upm.edu.my (Aziz Arshad)

simon@ukm.edu.my (Simon Kumar Das)

suriyanti@ukm.edu.my (Suriyanti Su Nyun Pau)

zdcc@ukm.edu.my (Zaidi Che Cob)

*Corresponding author

calcitrans exhibited higher lipid content than *T. weissflogii*, both species displayed higher levels of saturated (SFA) and monounsaturated (MUFAs) fatty acids and low levels of polyunsaturated fatty acids (PUFAs). The findings illustrated that under their optimum temperature and salinity combinations, both species might produce significant sources of lipids, which can be utilised in various activities such as aquaculture, pharmaceuticals, medicine, biofuels and others.

Keywords: Algal biomass, cell density, microalgae, MUFA, myristic acid, palmitic acid, PUFA

INTRODUCTION

Microalgae are very important organisms in the natural environment as primary producers that support the stability and functioning of an ecosystem. Apart from serving as the base of the food pyramids, they also contain various chemicals that have a wide range of current and potential applications, such as in aquacultures, pharmaceuticals, medicine, biofuel industries and others (Becker, 2013; Mandal & Mallick, 2014; Koyande et al., 2019; Sathasivam et al., 2019). The high diversity of microalgae species that contain various types of compounds such as fatty acids, steroids, carotenoids, polysaccharides, amino acids, antioxidants, and others, making them highly significant and most important for such diverse applications (Sathasivam et al., 2019; Barkia et al., 2019; Levasseur et al., 2020). As compared to crops, microalgae can produce 10 to 20 times more lipids per unit area (Chaisutyakorn et al., 2018), apart from their ability to capture solar energy and fixed carbon dioxide 10 to 50 times higher than that of terrestrial plants (Li et al., 2008; Batista et al., 2015).

Diatoms emerged on our planet about 150 million years ago and are responsible for approximately 40% of marine primary productivity (Sims et al., 2006; Kooistra et al., 2007; Falkowski et al., 1998; Field et al., 1998). Diatoms contain many fatty acids and other related organic molecules (Ramachandran et al., 2009; Mandal & Mallick, 2014; Sathasivam et al., 2019). They are very promising in producing high quantities of lipids and polyunsaturated fatty acids, including eicosapentaenoic acid (EPA) and docosahexaenoic acid (DHA) (Vazhappilly & Chen, 1998; Harwood & Guschina, 2009). For better utilisations, optimum culture conditions that allow for maximum cultivations of the diatoms are very important. One successful approach is increasing growth rates and biomass by manipulating environmental standards (Mata et al., 2010). In their natural environment, the growth, biomass, and metabolisms can be highly influenced by temperature (Renaud et al., 2002; Wei et al., 2015) and salinity (Raghavan et al., 2008; Hemaiswarya et al., 2011; Garcia et al., 2012). Both temperature and salinity may affect the nutritional constituent of the microalgae (Renaud et al., 2002; Raghavan et al., 2008; Hemaiswarya et al., 2011). Most microalgae regulate their lipid production

as a physiological response to salinity stress, which, however, depends on the species' capacity to tolerate salinity (Sajjadi et al., 2018).

In aquaculture, two important characteristics to evaluate the potential of microalgae species as feeds are their biochemical composition and the rate of biomass increase (De Castro Araújo & Garcia, 2005). The main biochemical constituents of diatoms are lipids, proteins, and carbohydrates, which are stored in their cells and are directly based on their biomass production (Kwan et al., 2021). Apart from the application as live feeds, a recent study showed the high potential of diatoms as aquaculture feed ingredients as an alternative to traditional fish meal ingredients (Nagappan et al., 2021). Since demand for fish meals has increased by 300% in the last ten years (Nagappan et al., 2021), alternatives are, therefore, highly critical for aquaculture industries. It requires rapid mass production of the algae, which needs a great understanding of their basic cultural requirements. Overall, *Chaetoceros* spp and *Thalassiosira* spp possess the largest distribution areas amongst the marine algae and thus are high potential for mass production and development into aquaculture feeds (Aydýn et al., 2009). However, there is still a scarcity of data on their development characteristics in different environments. Currently, there are limited studies on the influence of temperature and salinity on these marine-centric diatoms. This research aimed to determine the optimal conditions for the best growth and biomass production of *C. calcitrans* and *T. weissflogii* under different temperature and salinity combinations. Apart from that, the protein, carbohydrate, and lipid contents and the fatty acid profiles of both species were also analysed to clarify further the effect of temperature and salinity on the species.

MATERIALS AND METHOD

Microalgal Culture Conditions

Chaetoceros calcitrans, and *Thalassiosira weissflogii* were obtained from the microalgae culture facility of the International Institute of Aquaculture and Aquatic Sciences (I-AQUAS), Universiti Putra Malaysia, Malaysia. Stock cultures of the microalgae strain were regularly maintained in liquid cultures and agar plates. *Chaetoceros calcitrans*, and *T. weissflogii* were grown under controlled conditions in Conway medium solution with the addition of metasilicate (Bennett, 2020). The chemical composition of the Conway medium used in the culture medium is presented in Table 1. About 1 ml of stock solution A, 0.1 ml of stock solution C, 1 ml of stock solution D, and 1 ml of stock solution E were transferred into a volumetric flask and brought to volume. The laboratory glass wares, seawater, and other apparatus were sterilised by autoclave at 121°C for 15 min (LABSTAC vertical autoclave AV223 85L, United Kingdom).

Table 1

Chemical composition of Conway Medium used for the culture of microalgae Chaetoceros calcitrans and Thalassiosira weissflogii

Stock solution	Chemicals	Quantity (gL ⁻¹)
A	Main mineral solution	
1	NaNO ₃	100.00
2	Disodium EDTA C ₁₀ H ₁₆ N ₂ O ₈	45.00
3	H ₃ BO ₃	33.00
4	NaH ₂ PO ₄ . 4H ₂ O	20.00
5	FeCl ₃ .6H ₂ O	1.30
6	MnCl ₂ .4H ₂ O	0.36
7	Trace metal solution (Sol. B)	1.0 ml
8	distilled water	1000 ml
B	Trace metal solution	
1	ZnCl ₂	2.10
2	COCl ₂ .6H ₂ O	2.00
3	(NH ₄) ₆ MO ₇ O ₂₄ .4H ₂ O	0.90
4	CuSO ₄ .5H ₂ O	2.00
5	distilled water	1000 ml
C	Vitamin solution	
1	Thiamine B1	0.20
2	Cyanocobalamin B12	0.01
3	distilled water	100 ml
D	Silicate solution	
1	Na ₂ SiO ₃	20.00
2	distilled water	1000 ml
E	Nitrate solution	
1	KNO ₃	100.00
2	distilled water	1000 ml

Experimental Design

Batch cultures of *C. calcitrans* and *T. weissflogii* were incubated for four days under similar culture room conditions where the temperature was maintained at $27 \pm 3^\circ\text{C}$ and pH 8 ± 0.2 , with continuous aeration. Experiments were carried out simultaneously in 20 L cylindrical containers for 16 days under 12:12 light-dark conditions to evaluate the effect of different temperatures and salinities by using cool white light lamps (fluorescent

lamps 150 $\mu\text{mol photons m}^{-2}\text{s}^{-1}$). A factorial experimental design was conducted with two temperature settings (20°C and 30°C) and four salinities (20 ppt, 25 ppt, 30 ppt, and 35 ppt). The temperature range was selected by considering the wide geographical distribution of the diatom species and the average temperature of tropical waters of around 30°C (Krichnavaruk et al., 2005).

Specific Growth Rate and Biomass

A 5 ml aliquot was collected from each culture container every two days and fixed with Lugol's Iodine solution, from which 1 ml aliquot was taken for cell counting, using a Sedgwick-Rafter counting chamber under a compound microscope (Leica DM1000 LED, Germany) (Liang et al., 2013). Another 30 ml aliquot was collected from each culture container to estimate microalgae biomass. It was done using the previous method described by Ebrahimi and Salarzadeh (2016), with some modifications. After the filtration of culture through GF/F Whatman filter paper. The pre-weighed filter paper with algal biomass was oven-dried at 55°C and then re-weighed. A pre-weighed filter paper soaked in distilled water and dried was used as a blank. The dry weight (DW) of algae biomass was determined gravimetrically, and the growths were expressed in terms of dry weight (g DW L^{-1}). The specific growth rate (SGR) was defined as the increase in biomass per unit of time and calculated using Equation 1:

$$\mu \text{ (day}^{-1}\text{)} = \ln (N_1 / N_0) / t_1 - t_0 \quad [1]$$

where N_0 is the initial microalgae biomass at time (t_0), and N_1 is the biomass at the time of harvest (t_1) (Adenan et al., 2013).

Analysis of Protein and Carbohydrate Content

The algal biomass was harvested by centrifugation at 4000 rpm for 15 min (ALC Multispeed, PK 121R, Korea). Harvested biomasses were freeze-dried (BAXIT BXT-FD-10N, China), recorded dry weights, and microalgal cells were stored at -70°C before analysis. The protein and carbohydrate contents were determined following the methods of the Association of Official Analysis Chemists (AOAC, 2016; Renaud et al., 2002).

Lipid Extraction, Esterification, and Fatty Acids Analysis

The *C. calcitrans* and *T. weissflogii* from the best growth condition amongst the different temperatures and salinity combinations were selected to analyse total lipid and fatty acid composition. The samples were harvested by centrifugation (ALC Multispeed,

PK 121R, Korea) at 7000 rpm for 5 min (Japar et al., 2017) and preserved in an -80°C freezer and finally freeze-dried into powder form (Mini Lyotrap, LTE Scientific, UK). The total lipid and fatty acid composition were then analysed in triplicates, following the Soxhlet method described by Prartono et al. (2013).

The fatty acid composition was determined using the method outlined by Miller et al. (2012) and Nalder (2014). Fatty acids were identified and quantified using Gas Chromatography with Flame Ionization Detection (GC-FID) with an external 38-Component Fatty Acid Methyl Esters (FAME) standard (Supelco 37 Component FAME Mix, St Louis, Missouri, USA). About 15 mg of lipid samples were added to 0.5 ml, 0.5M sodium methoxide (CH_3NaO) solution and were heated at 65°C for 5 min. After that, 1.5 ml of methylating agent ($\text{NH}_4\text{Cl}/\text{MeOH}/\text{H}_2\text{SO}_4$; 2/60/3 w/v/v) was added and allowed to react for another 3 min at the same temperature (65°C). A Hewlett Packard Series II GC equipped with an FID and a DB- 225 capillary column (15 m x 0.25 mm, film thickness 0.25 μm) was used to determine the fatty acid methyl esters (FAMEs) produced. The FAMEs were extracted using hexane (Miller et al., 2012; Nalder, 2014).

Statistical Analysis

All experiments were conducted in triplicates, and the results were expressed as the mean values \pm standard deviation. Data were analysed at a significant level of $P < 0.05$. Two-way analysis of variance (ANOVA), followed by Turkey's tests, was obtained from SPSS version 23 (SPSS Inc., Chicago, IL, USA).

RESULTS

Growth and Biomass

The specific growth rate of *C. calcitrans* and *T. weissflogii* varied greatly under various temperature and salinity conditions, as shown in Table 2. The best growth for *C. calcitrans* was observed in 30°C temperature and 30 ppt salinity, with the SGR value of $0.262 \pm 0.001 \text{ day}^{-1}$. The lowest growth rate was observed at 20°C and 25 ppt ($0.246 \pm 0.002 \text{ day}^{-1}$) ($P < 0.05$). For *T. weissflogii*, the best growth was recorded at 30°C temperature and 25 ppt salinity, with an SGR value of $0.245 \pm 0.081 \text{ day}^{-1}$. At all temperatures and salinity levels, the SGR of *T. weissflogii* was generally lower as compared to *C. calcitrans*. However, there was no significant difference in SGR at all salinity concentrations and temperatures between the two species 168 ($P > 0.05$).

Table 2

Specific growth rates (SGR, day⁻¹) of Chaetoceros calcitrans and Thalassiosira weissflogii cultured under two temperatures and four different salinity concentrations

	Temp.	Salinity			
		20 ppt	25 ppt	30 ppt	35 ppt
<i>Chaetoceros calcitrans</i>	20°C	0.250 ± 0.004	0.246 ± 0.004	0.254 ± 0.002	0.257 ± 0.004
	30°C	0.257 ± 0.002	0.248 ± 0.002	0.262 ± 0.001	0.257 ± 0.0002
<i>Thalassiosira weissflogii</i>	20°C	0.221 ± 0.007	0.226 ± 0.007	0.222 ± 0.007	0.222 ± 0.008
	30°C	0.241 ± 0.075	0.245 ± 0.081	0.239 ± 0.002	0.225 ± 0.002

The biomass of *C. calcitrans* throughout the culture period is presented in Figure 1. Generally, the biomass showed increasing trends and reached maximum biomass at day 12 for most treatments, except for 20°C/25 ppt and 30°C/35 ppt temperature/salinity combinations, with maximum biomass at day 10. Afterwards, the biomass decreased, and the experiment was terminated on day 16. Overall, the highest biomass was recorded in 30°C and 30 ppt treatment (0.657 ± 0.014 g DW L⁻¹), which was significantly higher than all other treatments ($P < 0.05$). The result also indicated that the culture temperature of 20°C showed a low biomass increment during the earlier days of the culture experiment ($P < 0.05$).

The biomass of *T. weissflogii* throughout the culture period is presented in Figure 2. The biomass also showed increasing trends in general and reached maximum output at different times throughout the experiment. For the 20°C treatment, the maximum biomass was recorded on day 10 for the 35 ppt salinity treatment, while the others reached maximum output on day 12. For the 30°C culture temperature, the maximum biomass was recorded as early as day 8 for the 35 ppt treatment, day 10 for the 20 ppt and 25 ppt treatments, and day 12 for the 30 ppt treatment. *Thalassiosira weissflogii* also showed a low biomass increment during the earlier phase of the 20°C temperature treatment. Overall, the highest biomass was recorded at 30°C and 25 ppt treatment with a biomass value of 0.503 ± 0.035 g DW L⁻¹, which was significantly higher compared to 30 ppt and 35 ppt treatments at similar temperatures ($P < 0.05$).

The cell density of *C. calcitrans* throughout the experimental culture period is presented in Figure 3. The growth was significantly higher in the 30°C treatment than in the 20°C treatment, particularly after day 6 ($P < 0.05$). Nevertheless, at both temperatures, the cell density peaked at day 10 and then decreased, except for treatment at 30°C and 30 ppt. The maximum cell density was recorded in the 30°C and 30 ppt treatments on day 12, with a cell density of 6.74×10^6 cells ml⁻¹. It was therefore considered as the optimum temperature and salinity for *C. calcitrans*. The cell density of *T. weissflogii* is presented in Figure 4. Likewise, the growth was significantly higher in the 30°C temperature than in the 20°C treatment, particularly after day 6 of culture ($p < 0.05$). In the 20°C treatment, the cell

density decreased after day 10, while in the 30°C, the cell density decreased after day 12, except for the 30°C and 25 ppt treatments. The maximum cell density was recorded at 30°C and 25ppt on day 10, with a cell density of 3.45×10^6 cells ml⁻¹.

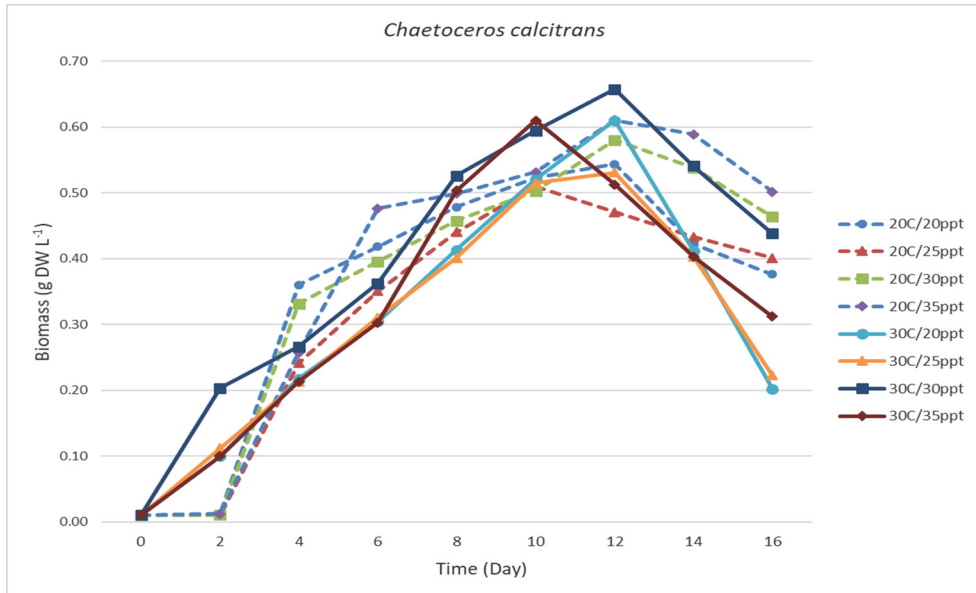


Figure 1. Biomass (g DW L⁻¹) of *Chaetoceros calcitrans* at different temperatures and salinities throughout the culture period

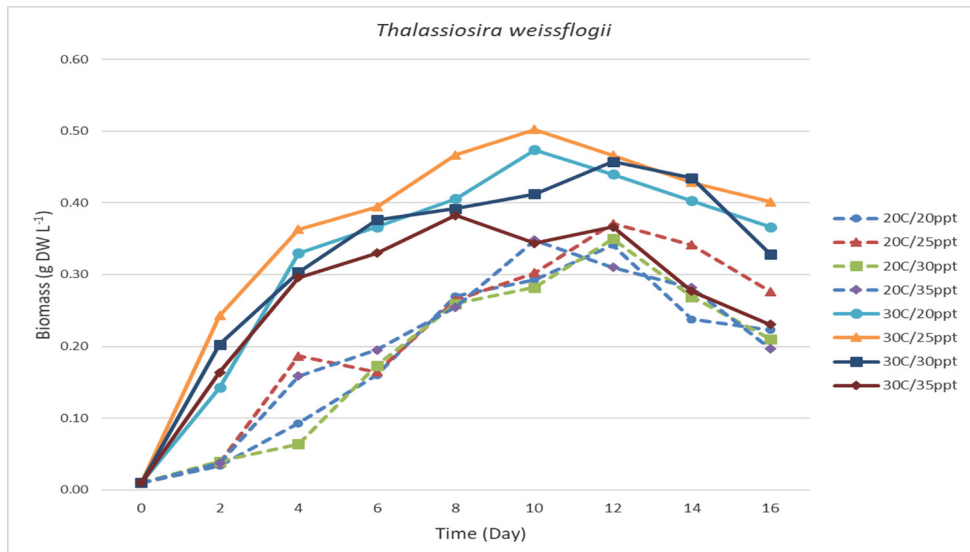


Figure 2. Biomass (g DW L⁻¹) of *Thalassiosira weissflogii* at different temperatures and salinities throughout the culture period

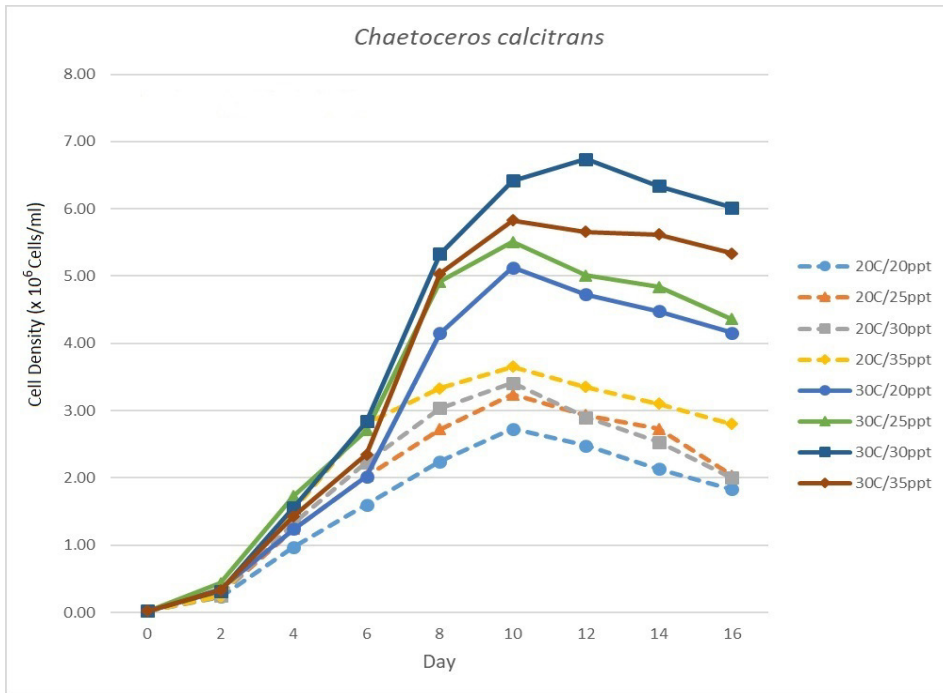


Figure 3. The cell density (cells ml⁻¹) of *Chaetoceros calcitrans* at different temperatures and salinities throughout the culture period

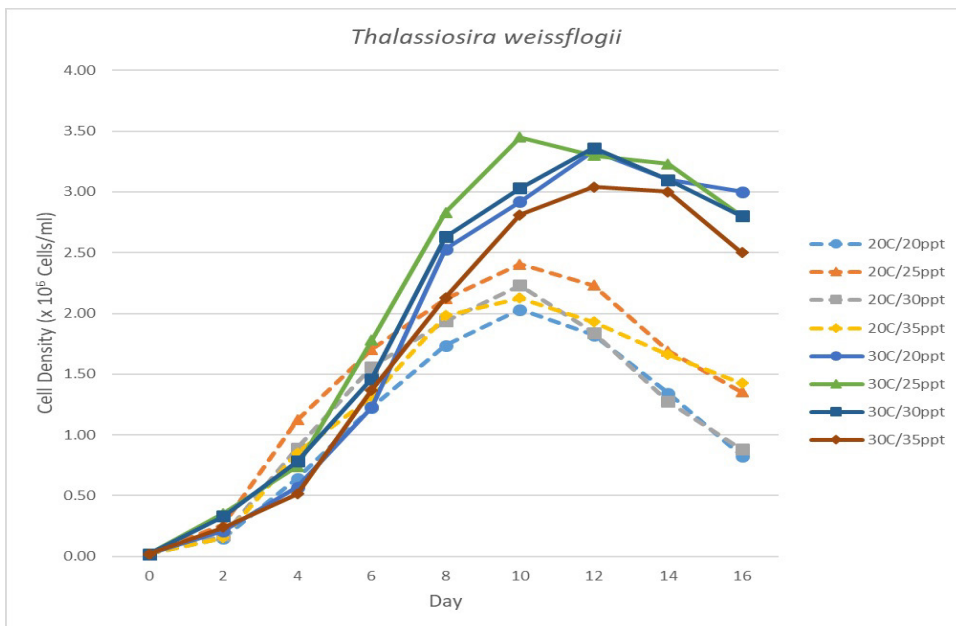


Figure 4. The cell density (cells ml⁻¹) of *Thalassiosira weissflogii* at different temperatures and salinities throughout the culture period

Protein and Carbohydrate Composition

Under the optimal temperature and salinity conditions, *C. calcitrans* recorded $38.25 \pm 0.99\%$ of protein and $9.39 \pm 0.59\%$ of carbohydrates, whilst *T. weissflogii* recorded $13.49 \pm 0.28\%$ of protein and $16.49 \pm 0.47\%$ of carbohydrates. The protein content was significantly higher in *C. calcitrans* compared with *T. weissflogii* ($P < 0.05$). On the other hand, the carbohydrate contents were significantly higher in *T. weissflogii* compared with *C. calcitrans* ($P < 0.05$).

Lipid and Fatty Acid Composition

Table 3 demonstrates the total lipid content, and fatty acid compositions of *C. calcitrans* and *T. weissflogii* recorded from their optimal temperature and salinity conditions. The lipid content of *C. calcitrans* was significantly higher than *T. weissflogii*, with total percentages of $16.96 \pm 0.90\%$ and $10.43 \pm 0.25\%$, respectively ($P < 0.05$). Both species recorded higher composition of saturated fatty acids (SFA) and monounsaturated fatty acids (MUFA) as compared to polyunsaturated fatty acids (PUFA). In *T. weissflogii*, the total SFA was about 76.10%, the highest fatty acid component, followed by MUFA at 13.79% and PUFA at 10.11%. *Chaetoceros calcitrans* showed a similar trend with an SFA content of 52.32%, followed by MUFA at 27.45% and PUFA at 20.23%. The most abundant fatty acids methyl esters detected from *C. calcitrans* were Palmitic (C 16) 35.63%, Palmitoleic (C 16:1) 22.0%, EPA (C 20:5n3) 13.58%, Myristic (C 14) 7.10%, and Pentadecanoic (C15) 5.08%. On the other hand, *T. weissflogii* mainly contained Myristic (C14) 24.3%, Palmitic (C16) 23.10%, Lauric (C 12:0) 20.21%, Palmitoleic (C 16:1) 7.32%, EPA (C 20:5n3) 6.75%, and Oleic (C 18:1n9c) 5.44%.

Table 3

Lipid content and fatty acid composition (n = 3) of Chaetoceros calcitrans and Thalassiosira weissflogii during their optimal growth at 30°C / 30 ppt and 30°C / 25 ppt, respectively

N. D.* = not detected		<i>C. calcitrans</i>	<i>T. weissflogii</i>
Lipid Contents (LC)		$16.96 \pm 0.90\%$	$10.43\% \pm 0.25\%$
C 4	Butyric	0.06 ± 0.03	0.24 ± 0.08
C 6	Caproic	0.04 ± 0.05	0.23 ± 0.02
C 8	Caprylic	0.12 ± 0.01	2.40 ± 0.13
C 10	Capric	0.12 ± 0.01	2.13 ± 0.03
C 11	Undecanoic	N.D.	N.D.
C 12	Lauric	1.20 ± 0.22	20.10 ± 1.61
C 13	Tridecanoic	0.10 ± 0.01	N.D.
C 14	Myristic	7.10 ± 0.30	24.3 ± 3.93

Table 3 (Continue)

C 15	Pentadecanoic	5.08 ± 0.67	0.43 ± 0.11
C 16	Palmitic	35.63 ± 1.13	23.10 ± 3.60
C 17	Heptadecanoic	0.64 ± 0.03	N.D.
C 18	Stearic	1.38 ± 0.09	3.17 ± 31
C 20	Arachidic	0.32 ± 0.05	N.D.
C 21	Henicosanoic	N.D.	N.D.
C 22	Behenic	0.53 ± 0.16	N.D.
C 23	Tricosanoic	N.D.	N.D.
C 24	Lignoceric	N.D.	N.D.
Σ Saturated Fatty Acid (SFA %)		52.32 ± 2.59	76.10 ± 2.00
C14:1	Myristoleic	0.10 ± 0.04	0.19 ± 0.08
C 15:1	Cis-10- Pentadecenoic	0.34 ± 0.002	0.84 ± 0.30
C 16:1	Palmitoleic	22.0 ± 0.83	7.32 ± 2.84
C 17:1	Cis-10- Heptadecanoic	0.90 ± 0.01	N.D.
C 18:1n9t	Elaidic (Trans)	1.62 ± 0.07	N.D.
C 18:1n9c	Oleic	1.77 ± 0.11	5.44 ± 2.21
C 20:1n9	Cis-11-Eicosenoic	N.D.	N.D.
C 22:1n9	Erucic	0.72 ± 0.04	N.D.
C 24:1	Nervonic	N.D.	N.D.
Σ Monounsaturated Fatty Acid (MUFAs %)		27.45 ± 0.67	13.79 ± 0.72
C 18:2n6	Linolelaidic (Trans)	N.D.	N.D.
C 18:2n6c	Linoleic (Cis)	0.90 ± 0.08	N.D.
C 18:3n6	g-Linolenic	0.52 ± 0.33	0.20 ± 0.31
C 18:3n3	a-Linolenic	0.54 ± 0.04	N.D.
C 20:2	Cis-11,14- Eicosadienoic	N.D.	N.D.
C 20:3n6	Cis-8,11,14- Eicosatrienoic	N.D.	N.D.
C 20:3n3	Cis-11,14,17- Eicosatrienoic	1.52 ± 0.52	N.D.
C 20:4n6	Arachidonic	N.D.	N.D.
C 20:5n3	Cis-5,8,11,14,17- eicosapentaenoic (EPA)	13.58 ± 0.95	6.75 ± 0.67

Table 3 (Continue)

C 22:2	Cis-13, 16-Docosadienoic	N.D.	0.67 ± 0.01
C 22:6n3	Cis-4,7,10,13,16,19- Docosahexaenoic (DHA)	3.17 ± 0.77	2.49 ± 0.03
Σ Polyunsaturated Fatty Acid (PUFAs %)		20.23 ± 1.36	10.11 ± 1.36

DISCUSSIONS

Diatoms such as *C. calcitrans* and *T. weissflogii* have widely been used as feed for live food organisms such as *Artemia* and rotifers. They were also used directly as feeds for the early larval stages of fish, molluscs, and crustaceans. The temperature and salinity of cultivation are two important environmental factors affecting microalgae growth and performance, particularly in tropical areas. However, many microalgae grew across a wide range of temperature and salinity values, demonstrating high adaptability to these two important parameters (Cho et al., 2007). This study showed that both microalgae species increased in growth rates with increasing temperature, with the highest SGR of 0.262 ± 0.001 and $0.245 \pm 0.081 \text{ day}^{-1}$, respectively, in their optimum culture conditions. These findings agreed with the study by Yusoff et al. (2013), who reported higher growths of diatoms and green algae when cultured at higher temperatures. Other studies reported that *C. calcitrans* could tolerate high ambient temperatures of more than 30°C (Banerjee et al., 2011; Lai et al., 2012). Microalgae growth is influenced by temperature partly due to variations in cell metabolic processes and the activity of essential enzymes (Chaisutyakorn et al., 2018). However, their growth rate may drop to some extent due to increased respirations at higher temperatures (Fogg & Thake, 1987).

Furthermore, this study showed that the highest growth rates were achieved at different salinity levels. The *C. calcitrans* recorded the highest SGR at 30 ppt, while *T. weissflogii* showed the highest SGR at 25 ppt, considered intermediate salinity relative to the range of salinities tested. These results were also in accordance with the previous report by Adenan et al. (2013) on *C. calcitrans*, whereby the optimum salinity for the best growth was about 30 ppt. Salinity is considered a major factor in the life cycle of plants, as it can slow down important metabolic activities such as photosynthesis (Liska et al., 2004). Based on the ability to regulate and tolerate salinity variations, microalgae can be categorised as halophilic or halotolerant (Rao et al., 2007). For instance, *Thalassiosira pseudonana* and *T. curviseriata* have been described as euryhaline and eurythermal in local Korean aquatic ecosystems (Popovich & Gayoso, 1999; Baek et al., 2011).

In terms of cell density and biomass, both species showed a similar pattern where the best values were recorded at higher temperatures (30°C) and again at 30 ppt for *C. calcitrans* and 25 ppt for *T. weissflogii*. These results were in accordance with the previous report on *C. calcitrans*, where the optimum salinity for growth was about 30 ppt (Adenan et al., 2013), and the report on *T. weissflogii* at optimum salinity of 25 ppt (García et al., 2012). In addition, Baek et al. (2011) reported that the density of *T. pseudonana* was higher with increasing temperatures from 10 to 30°C. According to Sheehan (1998), increasing temperatures may induce cell multiplication, most likely as a result of changes in cell metabolic activity in reaction to environmental stress. In this study, the abundance and biomass of both species were increased gradually, with a sharp increase around day 6 to day 8 and reached maximum values around day 10 to day 12. Adenan et al. (2013) reported that active duplication in microalgae usually begins on day 5 or day 7 of the development phase, and cultivation generally can last from 2 to 3 weeks, depending on the species.

Several studies have linked the variations of microalgal chemical composition in response to changes in temperatures and salinity among microalgae species (Renaud et al., 2002; Ebrahimi & Salarzadeh, 2016). Banerjee et al. (2011) cultured *C. calcitrans* at an average temperature of 30°C and recorded a much higher protein of $41.60 \pm 4.20\%$ compared with this study of only around 13%. The lipid and carbohydrates were similar in this study (26.80 ± 5.20 lipid and $8.70 \pm 1.20\%$ carbohydrate). They also reported that protein and carbohydrate were not significantly different when cultured at a different temperature, but there was significantly higher lipid production at 30°C compared with the 20°C average culture temperature (Banerjee et al., 2011). The *T. weissflogii* in this study showed higher carbohydrate content but lower lipid and protein content. Unfortunately, no previous study was conducted on temperatures and the proximate composition of this algae species. However, a study on the effect of salinity showed maximum protein and carbohydrate production at lower salinities (García et al., 2012). This study also recorded that the lipid content of *C. calcitrans* was significantly higher than *T. weissflogii*. It agreed with Lin et al. (2018), who also reported that *Chaetoceros muelleri* showed higher lipid production than *T. weissflogii*. Indeed, the percentage of lipids obtained from this study was quite similar to the reported lipid content for *Chaetoceros* by Renaud et al. (2002) and Bhattacharjya et al. (2020). For *Thalassiosira* sp., Bhattacharjya et al. (2020) and Ohse et al. (2015) reported a much higher percentage of lipids than the value reported for *T. weissflogii* recorded in this study. The analysis of the FAMES for *C. calcitrans* and *T. weissflogii* showed higher SFA and MUFA content than PUFA at the optimal culture temperature (30°C).

According to Renaud et al. (2002), higher temperatures tend to favour SFA synthesis due to changes in the fluidity of cell membrane phospholipid layers in many marine microalgae species. Ohse et al. (2015) also reported a higher proportion of MUFAs to PUFAs

in *Thalassiosira pseudonana* cultured at 25°C. Previous studies indicated that above the optimal temperature, the lipid content of microalgae tends to decrease due to stress in photosystem II activity (Sheng et al., 2011; Mathur et al., 2014). It has also been reported that environmental stress affects lipid composition, lipid content, and, ultimately, species biomass and growth (Sajjadi et al., 2018). In terms of fatty acid compositions in membrane lipids, microalgal cells adapt to exist at various temperatures by modifying membrane fluidity (Olofsson et al., 2012). This study indeed showed that the lipid content of microalgae was inversely proportional to growth rate, similar to the study by Prartono et al. (2013). It has been proven that when the growth rate is slow, the energy required for growth is diverted to lipid production as food storage (Sajjadi et al., 2018).

Miller et al. (2012) reported higher total production of the PUFA in *C. calcitrans* cultivated at 20°C culture temperature. Despite the lower production of PUFAs recorded in this study, *C. calcitrans* is considered one of the microalgae with high nutritional value for aquatic culture systems (Raghavan et al., 2008; Nalder, 2014). As shown in this study, the predominant fatty acids in *C. calcitrans* were palmitic and palmitoleic and myristic. On the other hand, myristic, palmitic and lauric contributed the highest percentages of fatty acids in *T. weissflogii*. These results were consistent with other studies whereby the myristic (C14:0), palmitic (C16:0), palmitoleic (C16:1n-7), DHA (C22:6n3), and EPA (C20:5n3) were the most frequent fatty acids found in diatoms (Volkman et al., 1989; Nalder, 2014; Yi et al., 2017), which are important for the manufacturing of animal feed additives. The relative content of MUFAs was remarkably high in palmitoleic acid (C16:1) and oleic acid (C18:1n9c) in both species. This finding supports previous research that confirmed an increase in the relative proportion of palmitic acid and oleic acid of *Desmodesmus abundans* under high salinity (Xia et al., 2014). This study suggested that temperature and salinity may affect lipid production in the species studied. According to Sajjadi et al. (2018), high salinity stress affects lipids primarily on the membrane fluidity and permeability, but optimal salinity stress can boost lipid synthesis. Nevertheless, apart from temperature and salinity, there are other factors affecting the lipid content and fatty acids, such as life cycle, growth phase, culture medium composition, carbon content, nitrogen and phosphorus deprivation, pH, light intensity and others (Zhukova & Aizdaicher, 2001; Chaisutyakorn et al., 2018; Sajjadi et al., 2018). More studies are therefore needed for these two important microalgae species in tropical waters.

CONCLUSION

The highest growth of both *C. calcitrans* and *T. weissflogii* occurred at a similar temperature of 30°C but in different salinity regimes of 30 ppt and 25 ppt, respectively. These are therefore suggested as optimum temperature and salinity for the cultivation of the two species, particularly in tropical areas. In terms of quality, *C. calcitrans* exhibited

higher lipid content than *T. weissflogii*. However, both species displayed high levels of saturated and monounsaturated fatty acids and low levels of polyunsaturated fatty acids. Lipid analysis of *C. calcitrans* indicated that over 35% of lipids were (C16) palmitic acid, while in *T. weissflogii*, over 24% of lipids were (C14) myristic acid.

ACKNOWLEDGMENT

The authors want to thank the International Institute of Aquaculture and Aquatic Sciences (I-AQUAS), Universiti Putra Malaysia (UPM), for providing the laboratory facilities and technical staff for the experiment. This research was funded by the UKM research fund (GUP- 2021-049).

REFERENCES

- Adenan, N. S., Yusoff, F. M., & Shariff, M. (2013). Effect of salinity and temperature on the growth of diatoms and green algae. *Journal of Fisheries and Aquatic Science*, 8(2), 397-404. <https://doi.org/10.3923/jfas.2013.397.404>
- AOAC. (2016). *Official methods of analysis* (20th ed.). AOAC International.
- Aydýn, G. S., Kocata, A., & Büyüki, B. (2009). Effects of light and temperature on the growth rate of potentially harmful marine diatom: *Thalassiosira allenii* Takano (Bacillariophyceae). *African Journal of Biotechnology*, 8(19), 4983-4990.
- Baek, S. H., Jung, S. W., & Shin, K. (2011). Effects of temperature and salinity on growth of *Thalassiosira pseudonana* (Bacillariophyceae) isolated from ballast water. *Journal of Freshwater Ecology*, 26(4), 547-552.
- Banerjee, S., Hew, W. E., Khatoon, H., Shariff, M., & Yusoff, F. M. (2011). Growth and proximate composition of tropical marine *Chaetoceros calcitrans* and *Nannochloropsis oculata* cultured outdoors and under laboratory conditions. *African Journal of Biotechnology*, 10(8), 1375-1383.
- Barkia, I., Saari, N., & Manning, S. R. (2019). Microalgae for high-value products towards human health and nutrition. *Marine Drugs*, 17(5), Article 304. <https://doi.org/10.3390/md17050304>
- Batista, A. P., Ambrosano, L., Graça, S., Sousa, C., Marques, P. A., Ribeiro, B., Botrel, E. P., Neto, P. C., & Gouveia, L. (2015). Combining urban wastewater treatment with biohydrogen production - An integrated microalgae-based approach. *Bioresource Technology*, 184, 230-235. <https://doi.org/10.1016/j.biortech.2014.10.064>
- Becker, E. W., (2013). Microalgae for aquaculture: Nutritional aspects. In: A. Richmond & Q. Hu (Eds.), *Handbook of Microalgal Culture: Applied Phycology and Biotechnology* (pp 671-691). Wiley-Blackwell.
- Bennett, L. A. M. (2020). *Developing a protocol for the sustainable culture of microalgae for mangrove oyster (Crassostrea rhizophorae) under hatchery conditions in Jamaica* (Final Year Project). UNESCO GRÓ-Fisheries Training Programme. <https://www.grocentre.is/static/gro/publication/701/document/Leanne19prf.pdf>

- Bhattacharjya, R., Marella, T. K., Tiwari, A., Saxena, A., Singh, P. K., & Mishra B. (2020). Bioprospecting of marine diatoms *Thalassiosira*, *Skeletonema* and *Chaetoceros* for lipids and other value-added products. *Bioresource Technology*, 318, Article 124073. <https://doi.org/10.1016/j.biortech.2020.124073>
- Chaisutyakorn, P., Praiboon, J., & Kaewsuralikhit, C. (2018). The effect of temperature on growth and lipid and fatty acid composition on marine microalgae used for biodiesel production. *Journal of Applied Phycology*, 30(1), 37-45.
- Cho, S. H., Ji, S. C., Hur, S. B., Bae, J., Park, I. S., & Song, Y. C. (2007). Optimum temperature and salinity conditions for growth of green algae *Chlorella ellipsoidea* and *Nannochloris oculata*. *Fisheries Science*, 73(5), 1050-1056. <https://doi.org/10.1111/j.1444-2906.2007.01435.x>
- De Castro Araújo, S., & Garcia, V. M. T. (2005). Growth and biochemical composition of the diatom *Chaetoceros* cf. *wighamii* brightwell under different temperature, salinity and carbon dioxide levels. I. Protein, carbohydrates and lipids. *Aquaculture*, 246(1-4), 405-412.
- Ebrahimi, E., & Salarzadeh, A. (2016). The effect of temperature and salinity on the growth of *Skeletonema costatum* and *Chlorella capsulata* in vitro. *International Journal of Life Sciences*, 10(1), 40-44. <https://doi.org/10.3126/ijls.v10i1.14508>
- Falkowski, P. G., Barber, R. T., & Smetacek, V. (1998). Biogeochemical controls and feedbacks on ocean primary production. *Science*, 281(5374), 200-206. <https://doi.org/10.1126/science.281.5374.200>
- Field, C. B., Behrenfeld, M. J., Randerson, J. T., & Falkowski, P. (1998). Primary production of the biosphere: Integrating terrestrial and oceanic components. *Science*, 281(5374), 237-240. <https://doi.org/10.1126/science.281.5374.237>
- Fogg, G. E., & Thake, B. (1987). *Algae Cultures and Phytoplankton Ecology* (3rd Ed.). University of Wisconsin Press.
- García, N., Elias, J. A. L., Miranda, A., Porchas, M. M., Huerta, N., & Garcia, A. (2012). Effect of salinity on growth and chemical composition of the diatom *Thalassiosira weissflogii* at three culture phases. *Latin American Journal of Aquatic Research*, 40(2), 435-440.
- Harwood, J. L., & Guschina, I. A. (2009). The versatility of algae and their lipid metabolism. *Biochimie*, 91(6), 679-684. <https://doi.org/10.1016/j.biochi.2008.11.004>
- Hemaiswarya, S., Raja, R., Kumar, R. R., Ganesan, V., & Anbazhagan, C. (2011). Microalgae: A sustainable feed source for aquaculture. *World Journal of Microbiology and Biotechnology*, 27, 1737-1746.
- Japar, A. S., Azis, N. M., Takriff, M. S., & Yasin, N. H. M. (2017). Application of different techniques to harvest microalgae. *Transactions on Science and Technology*, 4(2), 98-108.
- Kooistra, W. H. C. F., Gersonde, R., Medina, M., & Mann, D. G. (2007). The origin and evolution of the diatoms: Their adaptation to a planktonic existence. In P. Falkowski & Knoll, A. H. (Eds.), *Evolution of Primary Producers in the Sea* (pp 207-249). Elsevier Academic Press.
- Koyande, A. P., Chew, K. W., Rambabu, K., Tao, Y., Chou, D. T., & Show, P. L. (2019). Microalgae: A potential alternative to health supplementation for humans. *Food Science and Human Wellness*, 8(1), 16-24. <https://doi.org/10.1016/j.fshw.2019.03.001>

- Krichnavaruk, S., Loataweesup, W., Powtongsook, S., & Pavasant, P. (2005). Optimal growth conditions and the cultivation of *Chaetoceros calcitrans* in airlift photobioreactor. *Chemical Engineering Journal*, *105*(3), 91-98.
- Kwan, P. P., Banerjee, S., Shariff, M., & Yusoff, F. M. (2021). Influence of light on biomass and lipid production in microalgae cultivation. *Aquaculture Research*, *52*(4), 1337-1802. <https://doi.org/10.1111/are.15023>
- Lai, J. I., Yusoff, F. M., & Shariff, M. (2012). Large-scale culture of a tropical marine microalga *Chaetoceros calcitrans* (Paulsen) Takano 1968 at different temperatures using annular photobioreactors. *Pakistan Journal of Biological Sciences*, *15*(13), 635-640.
- Levasseur, W., Perré, P., & Pozzobon, V. (2020). A review of high value-added molecules production by microalgae in light of the classification. *Biotechnology Advances*, *41*, Article 107545. <https://doi.org/10.1016/j.biotechadv.2020.107545>
- Li, Y., Horsman, M., Wu, N., Lan, C. Q., & Dubois-Calero, N. (2008). Biofuels from microalgae. *Biotechnology Progress*, *24*(4), 815-820. <https://doi.org/10.1021/bp070371k>
- Liang, J. R., Ai, X. X., Gao, Y. H., & Chen, C. P. (2013). MALDI-TOF MS analysis of the extracellular polysaccharides released by the diatom *Thalassiosira pseudonana*. *Journal of Applied Phycology*, *25*(2), 477-484.
- Lin, Q., Zhuo, W. H., Wang, W. W., Chen, C. P., Gao, Y. H., & Liang, J. R. (2018). Effects of fundamental nutrient stresses on the lipid accumulation profiles in two diatom species *Thalassiosira weissflogii* and *Chaetoceros muelleri*. *Bioprocess and Biosystems Engineering*, *41*(3), 1-12. <https://doi.org/10.1007/s00449-018-1950-z>
- Liska, A. J., Shevchenko, A., Pick, U., & Katz, A. (2004). Enhanced photosynthesis and redox energy production contribute to salinity tolerance in *Dunaliella* as revealed by homology-based proteomics. *Plant Physiology*, *136*(1), 2806-2817.
- Mandal, S., & Mallick, N. (2014). Microalgae: The tiny microbes with a big impact. In V. K. Gupta, M. G. Tuohy, C. P. Kubicek, J. Saddler & F. Xu (Eds.), *Bioenergy Research: Advances and Applications* (pp. 171-184). Elsevier. <https://doi.org/10.1016/B978-0-444-59561-4.00011-5>
- Mata, M. T., Martins, A. A., & Caetano, N. S. (2010). Microalgae for biodiesel production and other applications: A review. *Renewable Sustainable Energy Review*, *14*, 217-232.
- Mathur, S., Agrawal, D., & Jajoo, A. (2014). Photosynthesis: Response to high temperature stress. *Journal of Photochemistry and Photobiology B: Biology*, *137*, 116-126. <https://doi.org/10.1016/j.jphotobiol.2014.01.010>
- Miller, M. R., Quek, S. Y., Staehler, K., Nalder, T., & Packer, M. A. (2012). Changes in oil content, lipid class and fatty acid composition of the microalga *Chaetoceros calcitrans* over different phases of batch culture. *Aquaculture Research*, *45*(10), 1634-1647.
- Nagappan, S., Das, P., Quadir, M. A., Thaher, M., Khan, S., Mahata, C., Al-Jabri, H., Vatland, A. K., & Kumar, G. (2021). Potential of microalgae as a sustainable feed ingredient for aquaculture. *Journal of Biotechnology*, *341*, 1-20. <https://doi.org/10.1016/j.jbiotec.2021.09.003>

- Nalder, T. D. (2014). *Microalgal Lipids, Lipases and Lipase Screening Methods* [Unpublished Doctoral dissertation]. Deakin University, Victoria, Australia.
- Ohse, S., Derner, R. B., Ozório, R. Á., Corrêa, R. G., Furlong, E. B., & Cunha, P. C. R. (2015). Lipid content and fatty acid profiles in ten species of microalgae. *Idesia*, 33(1), 93-101.
- Olofsson, M., Lamela, T., Nilsson, E., Bergé, J. P., Del Pino, V., Uronen, P., & Legrand, C. (2012). Seasonal variation of lipids and fatty acids of the microalgae *Nannochloropsis oculata* grown in outdoor large-scale photobioreactors. *Energies*, 5(5), 1577-1592. <https://doi.org/10.3390/en5051577>
- Popovich, C. A., & Gayoso, A. M. (1999). Effect of irradiance and temperature on the growth rate of *Thalassiosira curviseriata* Takano (Bacillariophyceae), a bloom diatom in Bahía Blanca estuary (Argentina). *Journal of Plankton Research*, 21(6), 1101-1110.
- Prariono, T., Kawaroe, M., & Katili, V. (2013). Fatty acid composition of three diatom species *Skeletonema costatum*, *Thalassiosira* sp. and *Chaetoceros gracilis*. *International Journal of Environment and Bioenergy*, 6(1), 28-43.
- Raghavan, G., Haridevi, C. K., & Gopinathan C. P. (2008). Growth and proximate composition of the *Chaetoceros calcitrans* f. *pumilus* under different temperature, salinity and carbon dioxide levels. *Aquaculture Research*, 39, 1053-1058. <https://doi.org/10.1111/j.1365-2109.2008.01964.x>
- Ramachandra, T. V., Mahapatra, D. M., Karthick, B., & Gordon, R. (2009). Milking diatoms for sustainable energy: Biochemical engineering versus gasoline-secreting diatom solar panels. *Industrial and Engineering Chemistry Research*, 48(19), 8769-8788. <https://doi.org/10.1021/ie900044j>
- Rao, A. R., Dayananda, C., Sarada, R., Shamala, T. R., & Ravishankar, G. A. (2007). Effect of salinity on growth of green alga *Botryococcus braunii* and its constituents. *Bioresource Technology*, 98(3), 560-564.
- Renaud, S. M., Thinh, L. V., Lambrinidis, G., & Parry, D. L. (2002). Effect of temperature on growth, chemical composition and fatty acid composition of tropical Australian microalgae grown in batch cultures. *Aquaculture*, 211(1-4), 195-214. [https://doi.org/10.1016/S0044-8486\(01\)00875-4](https://doi.org/10.1016/S0044-8486(01)00875-4)
- Sajjadi, B., Chen, W. Y., Raman, A. A. A., & Ibrahim, S. (2018). Microalgae lipid and biomass for biofuel production: A comprehensive review on lipid enhancement strategies and their effects on fatty acid composition. *Renewable and Sustainable Energy Reviews*, 97, 200-232.
- Sathasivam, R., Radhakrishnan, R., Hashem, A., & Allah, E. F. A. (2019). Microalgae metabolites: A rich source for food and medicine. *Saudi Journal of Biological Sciences*, 26(4), 709-722.
- Sheehan, J. (1998). *A look back at the U.S. Department of Energy's Aquatic Species Program: Biodiesel from algae*. National Renewable Energy Laboratory.
- Sheng, J., Kim, H. W., Badalamenti, J. P., Zhou, C., Sridharakrishnan, S., Krajmalnik-Brown, R., Rittmann, B. E., & Vannela, R. (2011). Effects of temperature shifts on growth rate and lipid characteristics of *Synechocystis* sp. PCC6803 in a bench-top photobioreactor. *Bioresource Technology*, 102(24), 11218-11225.
- Sims, P. A., Mann, D. G., & Medlin, L. K. (2006). Evolution of the diatoms: Insights from fossil, biological and molecular data. *Phycologia*, 4, 361-402.

- Vazhappilly, R., & Chen, F. (1998). Eicosapentaenoic acid and docosahexaenoic acid production potential of microalgae and their heterotrophic growth. *Journal of the American Oil Chemists' Society*, 75(3), 393-397. <https://doi.org/10.1007/s11746-998-0057-0>
- Volkman, J. K., Jeffrey, S. W., Nichols, P. D., Rogers, G. I., & Garland, C. D. (1989). Fatty acid and lipid composition of 10 species of microalgae used in mariculture. *Journal of Experimental Marine Biology and Ecology*, 128(3), 219-240. [https://doi.org/10.1016/0022-0981\(89\)90029-4](https://doi.org/10.1016/0022-0981(89)90029-4)
- Wei, L., Huang, X., & Huang, Z. (2015). Temperature effects on lipid properties of microalgae *Tetraselmis subcordiformis* and *Nannochloropsis oculata* as biofuel resources. *Chinese Journal of Oceanology and Limnology*, 33(1), 99-106.
- Xia, L., Rong, J., Yang, H., He, Q., Zhang, D., & Hu, C. (2014). NaCl as an effective inducer for lipid accumulation in freshwater microalgae *Desmodesmus abundans*. *Bioresource Technology*, 161, 402-409.
- Yi, Z., Xu, M., Di, X., Brynjolfsson, S., & Fu, W. (2017). Exploring valuable lipids in diatoms. *Frontiers in Marine Science*, 4, Article 17. <https://doi.org/10.3389/fmars.2017.00017>
- Yusoff, F. M., Adenan, N. S., & Shariff, M. (2013). Effect of salinity and temperature on the growth of diatoms and green algae. *Journal of Fisheries and Aquatic Science*, 8(2), 397-404.
- Zhukova, N. V., & Aizdaicher, N. A. (2001). Lipid and fatty acid composition during vegetative and resting stages of the marine diatom *Chaetoceros salsugineus*. *Botanica Marina*, 44(3), 287-293.



Production of Biosurfactant Using *Bacillus subtilis* Natto Fermentation

Yew Seng Leow¹, Norhafizah Abdullah^{1*}, Dayang Radiah Awang Biak¹, Nur Syakina Jamali¹, Rozita Rosli² and Huey Fang Teh³

¹Chemical and Environmental Engineering Department, Faculty of Engineering, Universiti Putra Malaysia, 43400 UPM, Serdang, Selangor, Malaysia

²Faculty of Medicine and Health Sciences, Universiti Putra Malaysia, 43400 UPM, Serdang, Selangor, Malaysia

³Sime Darby Technology Centre, 43400 Serdang, Selangor, Malaysia

ABSTRACT

Biosurfactants are microbial amphiphiles produced as primary metabolites by varieties of microorganisms. They are preferred over chemically derived surfactants owing to their intrinsic properties, such as superior environmental compatibility, biodegradability, anti-inflammatory and antimicrobial activity, and higher tolerance towards extreme environmental conditions such as temperature, salinity, and pH levels. However, commercial production of biosurfactants is still lacking. The main reason for this is the low yields obtained from fermentation processes, which causes them to be unable to compete compared to chemical surfactants. The present study conducted a one-factor-at-a-time (OFAT) analysis on fermentation conditions to enhance biosurfactant yield from a probiotic strain, *Bacillus subtilis* Natto. The fermentation was conducted by varying parameters such as nitrogen source, vegetable oils, inoculum size, amino acids, and pH of the fermentation medium.

Results showed a significant improvement of 45% in biosurfactant production from *B. subtilis* Natto when the initial pH of the fermentation medium was adjusted to pH 6.8, urea as the nitrogen source, inoculum size of 6% v/v and the addition of palm olein at a concentration of 2% v/v as a substrate in the fermentation medium.

Keywords: *B. subtilis* Natto, biosurfactant production, fermentation, OFAT analysis

ARTICLE INFO

Article history:

Received: 21 May 2022

Accepted: 16 August 2022

Published: 06 March 2023

DOI: <https://doi.org/10.47836/pjst.31.2.05>

E-mail addresses:

gs52837@student.upm.edu.my (Yew Seng Leow)

nhafizah@upm.edu.my (Norhafizah Abdullah)

dradiah@upm.edu.my (Dayang Radiah Awang Biak)

syakina@upm.edu.my (Nur Syakina Jamali)

rozita@upm.edu.my (Rozita Rosli)

teh.huey.fang@simedarbyplantation.com (Huey Fang Teh)

*Corresponding author

INTRODUCTION

The development of a new sustainable blueprint in microbial technologies to transform biomass into environmental-friendly carriers is needed for the sustainability of energy and the environment (Liu, 2020). Biosurfactants synthesized by microorganisms are amphipathic molecules consisting of hydrophilic heads and hydrophobic tails, normally hydrocarbon chains of lipids or fatty acids (Banat et al., 2014). They are categorized into three different types such as glycolipids (glucose and lipid), lipopeptides (protein and lipid), and phospholipids (phosphate and lipid) (Singh et al., 2018). These surface-active molecules can reduce surface or interfacial tension in liquids, exhibiting high emulsifying properties, and are stable at extreme pH, salinity, and temperature (Sharma et al., 2018). Compared to synthetic surfactants, they are less toxic, highly biodegradable, lower critical micellar concentration value, and are highly tolerant of extreme temperatures and pH (Varvaresou & Iakovou, 2015). Due to their intrinsic properties, they are particularly preferred in pharmaceutical, food, and cosmetic industries and environmental bioremediation (Bhattacharya et al., 2017; Felix et al., 2019).

A group of biosurfactants known as lipopeptides is commonly produced by *the Bacillus* genus due to their noteworthy efficiency and wide commercial applications (Hentati et al., 2019). There are three different families of lipopeptides: surfactins, iturins, and fengycins. These can be identified based on their multiple homologous and isoforms with different amino acid sequences and varied fatty acid chains (Ibrar & Zhang, 2020). In the biosynthesis of surfactin, the synthetase consists of four enzymatic subunits (SrfA, SrfB, SrfC, and SrfD). They are the catalysts in the nonribosomal mechanism, which incorporates specific amino acids into peptides and modules (Jahan et al., 2020). These bioactive lipopeptides can be applied in various biotechnological and biopharmaceutical fields owing to their ability to act as antibiotics, antiviral, antitumor agents, bioremediation and oil recovery agent for polluted crude-oil sites, disinfectant, and harmless to normal cells (PBMC and PC12) (Balan et al., 2017; Fanaei & Emtiazi, 2018; Yuliani et al., 2018).

Current fermentation processes to produce lipopeptides cannot fulfill industrial demand due to low production yield. Many efforts to improve lipopeptide production are reported, such as using other cheaper and more effective substrates from agro-industrial waste (bagasse), but the yield is still unsatisfactory (Das & Kumar, 2019; Liu et al., 2020). This issue motivated the application of vegetable oil derived from palm and coconut in biosurfactant production from *Bacillus subtilis* natto, as the exploration of these substrates is yet to be reported for this strain. These vegetable oils have been reported to increase biosurfactant yield for other strains, such as *Starmerella bombicola* and *Pseudomonas aeruginosa* (Hirata et al., 2021).

This study aims to conduct OFAT analysis of fermentation parameters in the small-scale production of biosurfactants from *B. subtilis* Natto culture. *B. subtilis* Natto is a food-grade

strain and has been traditionally used as a probiotic food supplement. It would be a novel finding to explore the ability of this strain not only as a probiotic but also as a biosurfactant producer. A recent study in 2019 reported on the use of this strain to produce surfactin, one type of biosurfactant. They reported a high yield of surfactin using enriched media (Landy medium) with the incorporation of attapulgit powder (Sun et al., 2019). This paper aims to assess the potential of vegetable oils, such as palm-based oils, which are widely available in Malaysia, and to investigate their effect on biosurfactant production from *B. subtilis* Natto. The production is expected to improve when the fermentation parameters from OFAT analysis are identified.

MATERIALS AND METHODS

Materials

Bacillus subtilis Natto spp. was procured in the form of food-grade powder from Isetan Japanese supermarket (Kuala Lumpur, Malaysia). Nutrient broth and agar powder were purchased from Sigma Aldrich (New Jersey). Meanwhile, to produce biosurfactants from *Bacillus subtilis* Natto, only analytical grades of chemicals and solutions were used. The compositions of growth media are 0.5% w/v sucrose (R&M Chemicals, U.K.), modified mineral salts medium comprised of 0.4% w/v mono-potassium hydrogen phosphate (Bio Basic, Canada), 1.4% w/v disodium hydrogen phosphate dodecahydrate, 0.02% w/v magnesium sulfate heptahydrate, 0.0002% w/v manganese sulfate monohydrate, 0.0001% w/v ferrous sulfate heptahydrate (R&M Chemicals, U.K.), 2% w/v bacteriological peptone (Oxoid, U.K.) and 0.05% w/v yeast extract (Fischer BioReagents, U.S.A.). Different types of vegetable oils, a substrate for biosurfactant production used were palm kernel oil, palm-based olein (donated by Sime Darby Technology Centre, Malaysia) and coconut oil (purchased from Ayam Brand, Malaysia). Leucine and glutamic acid precursors were donated by Sime Darby Technology Centre, Malaysia.

Hydrochloric acid, sodium hydroxide (Sigma-Aldrich, New Jersey), and ethyl acetate (R&M Chemicals, U.K) were used for biosurfactant extraction. HPLC grade of methanol and acetic acid (R&M Chemicals, U.K) were used for biosurfactant quantification analysis.

Microbial Growth for Inoculum Preparation and Biosurfactant Production

B. subtilis Natto strain was stored at -80°C in 20% v/v glycerol stock solution after growing in a nutrient broth (NB) medium at a 1% w/v for 24 hours. For seed culture preparation, 1% v/v of stock solution was placed into NB medium in an Erlenmeyer flask (250 mL) with 100 mL of working solution. It was incubated at 37°C under orbital stirring at 150 rpm for 16 hours.

The strain was cultivated in a modified Cooper's basic mineral salts medium with the following composition: sucrose (20 g/L), yeast extract (0.5 g/L), MgSO₄.7H₂O (0.8 mM),

$\text{Na}_2\text{HPO}_4 \cdot 12\text{H}_2\text{O}$ (40 mM), KH_2PO_4 (30 mM), $\text{MnSO}_4 \cdot \text{H}_2\text{O}$ (10 μM) and $\text{FeSO}_4 \cdot 7\text{H}_2\text{O}$ (4 μM) plus different nitrogen sources such as peptone, urea, ammonium chloride and sodium nitrate at variable concentrations to produce the biosurfactant (Kim et al., 1997). The initial pH of the medium was then adjusted to pH 6.8 before autoclaving at 121°C for 15 minutes. For small-scale operations, inoculum placed into the medium was 2% w/v in the Erlenmeyer flask with a working volume of 100 mL. Tests were carried out on a very small scale as oxygen access to the medium was ensured. Incubation was carried out at conditions as shown in Table 1.

Table 1

Fermentation conditions of medium for the production of biosurfactant from B. subtilis Natto as control

Parameter	Description
Temperature	37°C
Duration	24 hours
Agitation speed	150 rpm
Working volume	100 mL
Nitrogen source	Peptone
Inoculum size	2% v/v
Concentration of vegetable oil	0% v/v
Initial pH	pH 6.8

Selection of Nitrogen Sources, Vegetable Oils, and Amino Acids

Nitrogen sources: peptone, NH_4Cl , urea, and NaNO_3 were screened for medium formulation. The addition of NH_4Cl , urea, and NaNO_3 into the fermentation medium at the concentration (g/L) of 2.67, 3.00, and 4.25, respectively, except peptone, which was added at 20 g/L (Cao et al., 2009). Nitrogen sources are autoclaved together with other nutrients in a fermentation medium at 121°C for 15 minutes. The high peptone concentration in the media formulation could increase biosurfactant production (Bertrand et al., 2018).

Meanwhile, vegetable oils such as palm oil, palm kernel oil, and coconut oil were tested at a concentration of 2.0% (w/v) as substrates for biosurfactant production. The best-performance vegetable oil was tested at different concentrations (4.0, 6.0, and 8.0 % v/v).

Next, amino acids, such as leucine and glutamic acid, were added to the medium at a concentration of 0.1 mM (Liu et al., 2012).

Effect of Culture Conditions on Biosurfactant Production

OFAT analysis on biosurfactant production in the culture medium was further investigated using different inoculum sizes (4.0, 6.0, and 8.0% v/v) and different initial pH of the fermentation medium (pH 5.5, 6.0, 6.5, and 7.5).

Extraction of Biosurfactant

After 24-hour fermentation, the culture broth was centrifuged using a centrifuge model 5810 R (Eppendorf, Hamburg) at 10000 x g for 10 min at 4°C. Cell-free supernatant was then acidified to pH 2.0 with 3.0 M HCl solution to precipitate biosurfactant and left overnight in a chiller at 4°C. Then, it was centrifuged at 10000 x g for 10 min at 4°C. The precipitate was freeze-dried using CoolSafe Freeze Dryer (Scanvac, Denmark), followed by liquid-liquid extraction. In this extraction, the precipitate was dissolved in 0.1M NaOH solution and the pH was adjusted to pH 8.0 using 1.0 M HCl. An equal volume of ethyl acetate was then added to the solution. The mixture was shaken at 210 rpm for 24 hours at 30°C. The organic phase was removed and evaporated in a rotary evaporator (Eyela, Japan). This liquid-liquid extraction was repeated three times to ensure the complete removal of biosurfactants (Chen & Juang, 2008).

Analytical Determinations

In order to obtain dry cell mass, 100 mL samples were centrifuged using a centrifuge model 5810 R (Eppendorf, Hamburg) at 10000 x g for 10 min at 4°C. After centrifugation at 10000 x g for 10 minutes, the pellet (biomass) was further subjected to rinsing with distilled water and then re-centrifuged at 3000 x g for 10 minutes. These rinsing and centrifugation steps are repeated three times. It was then dried in an oven at 100°C for 48 hours, followed by a desiccator filled with silica gel at room temperature. It was then reported using gravimetric analysis as cell dry weight. The obtained biosurfactant was also reported using gravimetric analysis. Biosurfactant yield was calculated as biosurfactant mass obtained in a given sample volume. In gravimetric analysis, the cell and biosurfactant mass were weighed using an analytical balance (Sartorius, Germany). Cell dry weight and biosurfactant yield were calculated based on the formula used by previous researchers displayed in Equations 1 and 2, respectively (Li & De Orduña, 2010; Santos et al., 2018).

$$\text{Cell dry weight (g/L)} = \frac{\text{Dry cell mass (g)}}{\text{Volume of sample taken (L)}} \quad (1)$$

$$\text{Biosurfactant yield (mg/L)} = \frac{\text{Biosurfactant mass (mg)}}{\text{Volume of sample taken (L)}} \quad (2)$$

Characterization of Biosurfactant

After acidic precipitation and biosurfactant extraction, samples were analyzed for oil displacement assay and emulsification activity of biosurfactant against palm-based olein. For the oil displacement assay, 5 ml of distilled water was placed inside the petri dish. 100 µL of vegetable oil was spread onto the surface, and a biosurfactant solution of 10 µL was placed onto the oil surface. The diameter of the oil displaced was then measured (Morikawa et al., 1993). Next, emulsification activity was performed by adding 2.0 ml of

palm-based olein into 2.0 ml of biosurfactant solution, followed by vortexing at high speed for 2 minutes. The emulsification index, E24, was later calculated as a ratio of the height of the emulsion layer to the total height of the mixture and expressed as a percentage in Equation 3 (Cooper & Goldenberg, 1987)

$$E24 (\%) = \frac{\text{height of emulsified layer}}{\text{height of liquid layer}} \times 100\% \quad (3)$$

Statistical Analyses

All measurements of dry cell mass, biosurfactant mass, oil displacement assay and emulsification index were performed in triplicate. The triplicate refers to the repetition of the assay in one test. Means and standard deviation were calculated with Microsoft Office Excel 2016. SPSS analysis software was computed for ANOVA analysis to determine the significance of data with α set at 0.05.

RESULTS AND DISCUSSION

OFAT Analysis on Fermentation Conditions to Produce Biosurfactant

This study aimed to find suitable conditions based on significant operating parameters affecting biosurfactant production using OFAT analysis. These parameters are carbon source, nitrogen source, vegetable oils, inoculum size and pH of the culture.

Effect of Nitrogen Source. Four nitrogen sources tested were peptone, ammonium chloride, urea, and sodium nitrite. From Figure 1, peptone yielded the highest cell mass (1.48 ± 0.08 g/L) but the lowest biosurfactant yield relative to nitrogen content (4.03 ± 0.11 mg/g nitrogen content). In contrast, ammonium chloride and sodium nitrate resulted in a similar cell mass and biosurfactant yield relative to the nitrogen content of around 1 g/L and 16 mg/g nitrogen content, respectively. Meanwhile, a medium with urea as a nitrogen source for biosurfactant production from *B. subtilis* Natto contributed to the lowest cell mass (0.69 ± 0.02 g/L). However, its biosurfactant yield relative to nitrogen content (21.11 ± 1.50 mg/g nitrogen content) was the highest. It showed that urea was the most suitable nitrogen source for *B. subtilis* Natto to produce biosurfactants.

Urea will be selected as a nitrogen source based on the OFAT analysis. It was because the biosurfactant yield from urea was the highest, and urea is the cheapest alternative nitrogen source compared to peptone, ammonium chloride and sodium nitrate (Zhang et al., 2016). There was an indication that all inorganic nitrogen sources (ammonium chloride, sodium nitrate and urea) and organic nitrogen sources (peptone) with yeast extract can induce the production of surface-active compounds by microbes and regulation of biosurfactant synthesis (Eswari et al., 2016). According to Purwasena et al. (2020), nitrate

needs to be broken into ammonium to be absorbed by the cells, while ammonium is ready to be consumed by the cells, which suggests that sodium nitrate and ammonium chloride are used by *B. natto* for cell maintenance. Meanwhile, Ibrar and Zhang (2020) revealed the amino acid sequence in biosurfactant produced from *the Bacillus* genus, which hypothesized that urea helped in the biosurfactant production as urea is a carbamide with two amide group joined by a carbonyl functional group. So, selecting urea as a nitrogen source would be an economical approach for biosurfactant production from *B. subtilis* Natto.

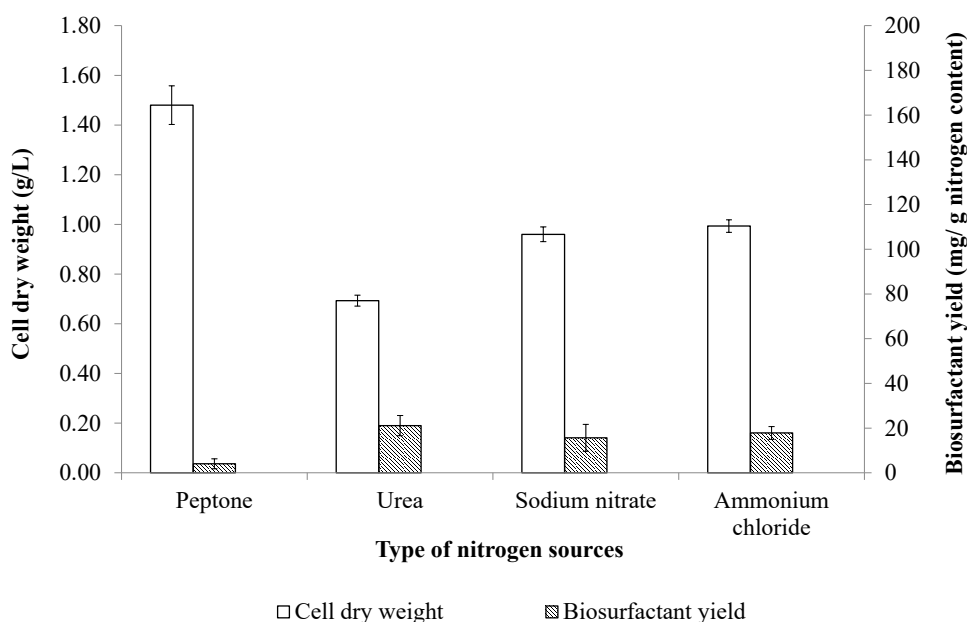


Figure 1. Effect of different nitrogen sources on biosurfactant production from *B. subtilis* Natto with sucrose as carbon source, inoculum size of 2% v/v and culture pH of 6.8

Effect of Vegetable Oils. The addition of vegetable oils (palm oil, palm kernel oil and coconut oil) at a concentration of 2% v/v into the medium increased the biosurfactant production from *B. subtilis* Natto by approximately two-fold. In Figure 2, the highest biosurfactant production (at 198.00 ± 9.90 mg/L) from *B. subtilis* Natto was obtained with palm kernel oil as substrate compared to palm oil and coconut oil, which yielded 167.33 ± 14.01 mg/L and 187.67 ± 10.66 mg/L, respectively. The medium supplemented with palm oil enabled cell mass production of 1.66 ± 0.01 g/L, while cell mass in culture with palm kernel oil and coconut oil was 1.53 ± 0.02 g/L and 1.53 ± 0.01 g/L of cell mass, respectively. Thus, palm kernel oil will be chosen as substrate added in the medium for biosurfactant production. This vegetable is also relatively cheap since it is abundantly available in Malaysia.

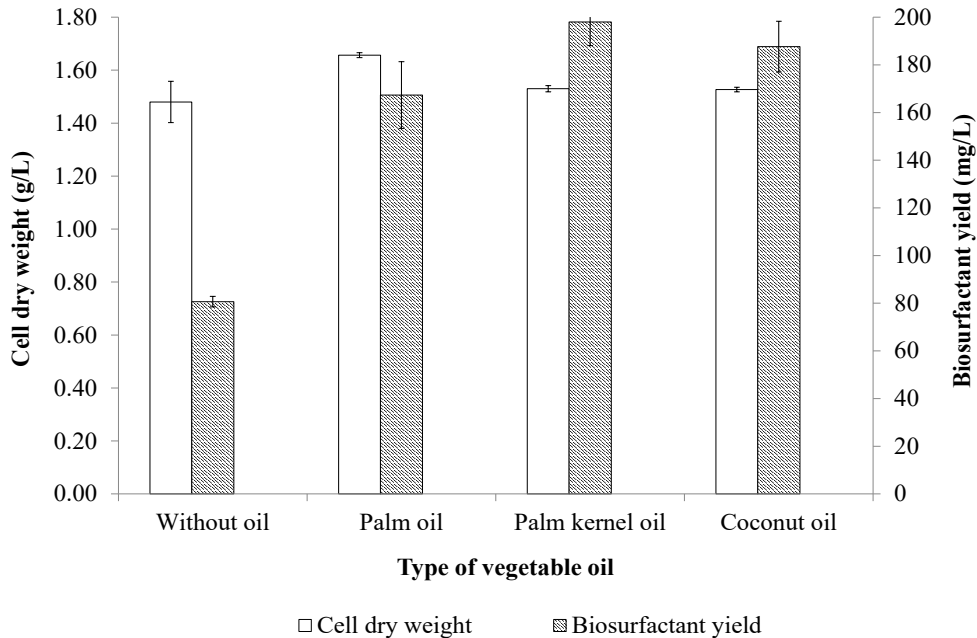


Figure 2. Effect of addition of different vegetable oil on biosurfactant production from *B. subtilis* Natto with sucrose as carbon source, peptone as nitrogen source, inoculum size of 2% v/v and culture pH of 6.8

Microbes fed on vegetable oils during the growth phase exhibited lipase activity to degrade vegetable oils into free fatty acid, mono and diacylglycerols. These compounds can reduce surface tension because they have surfactant properties (Ferraz et al., 2002). It also proved that biosurfactant produced by *B. subtilis* Natto was stimulated by adding the short-chain and long-chain fatty acids such as palmitic acid and lauric acid present in the fermentation medium. In agreement with past researchers who stated that nutrient uptake by the bacterial cell could be enhanced during the emulsification of these vegetable oils, leading to biosurfactant synthesis (Janek et al., 2010). These hydrophobic substrates also improved the yield of sophorolipids produced from *C. floricola* ZM1502 when incorporated into the medium (Konishi et al., 2018).

Effect of Different Concentrations of Vegetable Oils. In this part of the study, five different concentration of palm kernel oil was used to determine their effect on biosurfactant production from *B. subtilis* Natto. Figure 3 showed that increasing concentration from 0% to 2% v/v of palm kernel oil gave the highest cell and biosurfactant mass at 1.53 ± 0.02 g/L and 198.00 ± 9.90 mg/L, respectively. It showed that palm kernel oil was an inducer for biosurfactant production. Increasing palm kernel oil concentration from 2% v/v to 8% v/v resulted in a significant reduction in both cell mass and biosurfactant from 1.53 ± 0.02 g/L to 0.72 ± 0.03 g/L and from 198.00 ± 9.90 mg/L to 45.00 ± 2.83 mg/L, respectively. A

higher concentration of vegetable oil was found to inhibit the growth of *B. subtilis* Natto to produce biosurfactant because it caused a decrease in cell mass and biosurfactant. It suggested that an optimal concentration of vegetable oil is required as higher oils will most likely interfere with oxygen uptake by bacterial cells. The addition of vegetable oils at 2% v/v was chosen because it gave high biomass and biosurfactant yield and resulted in a low amount of residual oil at the end of fermentation. The lower the oil content on the fermentation harvest, the less likely it is to complicate subsequent downstream processes.

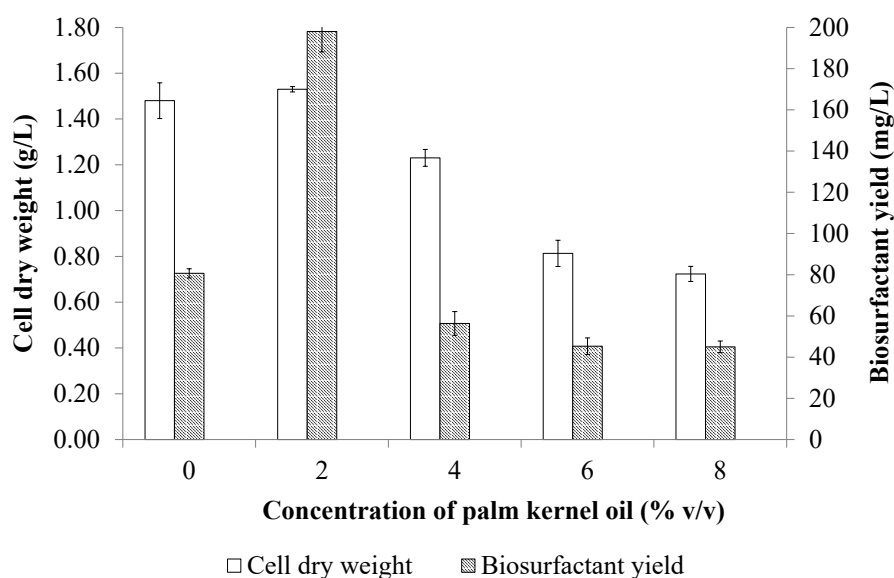


Figure 3. Effect of different concentrations of palm kernel oil on biosurfactant from *B. subtilis* Natto with sucrose as carbon source, peptone as nitrogen source, palm kernel oil as substrate, inoculum size of 2% v/v and culture pH of 6.8

By increasing palm kernel oil concentration above 2%, v/v inhibited the growth and production of biosurfactants from *B. subtilis* Natto. It indicated that substrates need to be supplied in optimal concentration for cell mass production and biosurfactant production. Khondee et al. (2015) and Thavasi et al. (2008) also reported using a low concentration of hydrophobic substrates (vegetable and crude oils) to enhance production from *Bacillus megaterium* and *Bacillus* sp. GY19. In this work, the amount of oil added to the reaction mixture had to be optimized to minimize the amount of oil left after fermentation for easier downstream processing.

Effect of Amino Acids. Two different amino acids (leucine and glutamic acid) were added into the medium to determine their effect on biosurfactant production from *B. subtilis* Natto. From Figure 4, the Addition of leucine to the culture medium caused a lower cell mass production (0.77 ± 0.01 g/L), but a slight increase of biosurfactant mass at 84.00 ± 4.55 mg/L was obtained. For a medium with glutamic acid, lower cell mass (1.14 ± 0.07 g/L) and decreased biosurfactant mass (76.33 ± 6.02 mg/L) were obtained. Although leucine improved the biosurfactant production (84.00 mg/L) compared to the medium without adding amino acids (80.67 ± 4.99 mg/L), the enhancement effect was insignificant. In other words, adding amino acid in the medium did not significantly enhance *B. subtilis* Natto to produce biosurfactants and help its growth. So, both amino acids would not be added to the medium for biosurfactant production from *B. subtilis* Natto.

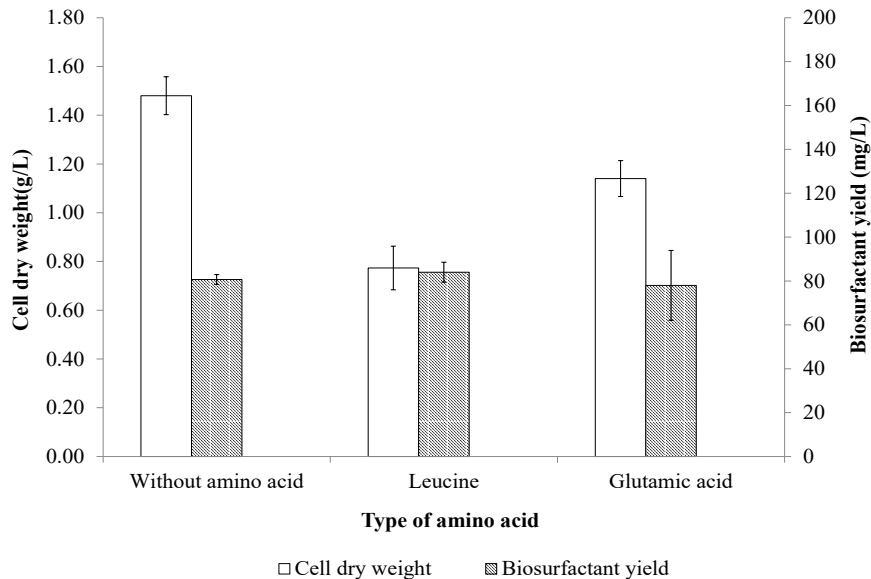


Figure 4. Effect of addition of leucine and glutamic acid on biosurfactant production from *B. subtilis* Natto with sucrose as carbon source, peptone as nitrogen source, inoculum size of 2% v/v and culture pH of 6.8

Another researcher reported that adding different amino acids did not improve surfactin production from *Bacillus subtilis* CS5 (Abdel-Mawgoud et al., 2008). However, there were other findings suggested that amino acids were suitable substrates for biosurfactant production by *S. ruminantium* and *Pseudomonas fluorescens*, which indicated that these two strains were able to yield more biosurfactant when grown in a medium supplied with amino acids (Saimmai et al., 2013; Biniarz et al., 2018). Therefore, from this finding, *B. subtilis* Natto did not require additional amino acid in the fermentation medium to produce

biosurfactant even though the biosurfactant produced by *B. subtilis* strains contains amino acids moiety consisting of leucine, valine, glutamic acid and aspartic acid (Pecci et al., 2010).

Effect of Inoculum Size. In Figure 5, *B. subtilis* Natto, with an inoculum size of 6% v/v, yielded the highest biosurfactant mass of 105.67 ± 11.15 mg/L and cell mass of 1.28 ± 0.07 g/L. Although an inoculum size of 2% v/v gave the highest cell mass of 1.48 ± 0.08 g/L, it yielded the lowest biosurfactant mass of 80.67 ± 2.25 mg/L. Figure 5 shows a decreasing trend of cell mass when inoculum size is increased from 2% to 4% v/v. When the inoculum size was further increased from 4 to 6% v/v, a gradual increase in cell mass from 1.15 ± 0.03 g/L to 1.28 ± 0.07 g/L was recorded. Nevertheless, when the inoculum was raised higher to 8% v/v, it caused a reduction in cell mass production at 1.19 ± 0.06 g/L. As for the yield of biosurfactant, increasing inoculum size from 2% to 6% v/v led to the increment in yield from 80.67 ± 2.25 mg/L to 105.67 ± 11.15 mg/L. Nevertheless, it dropped to 96.00 ± 6.98 mg/L in a higher % of inoculum size (8% v/v) culture. From this finding, 6% v/v is the most suitable inoculum size for use in the medium for biosurfactant production from *B. subtilis* Natto culture.

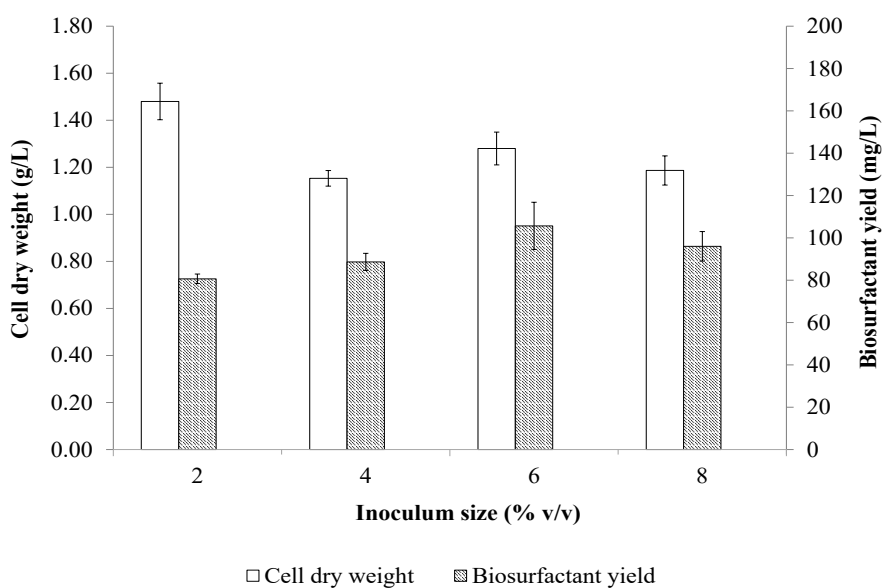


Figure 5. Effect of different inoculum sizes on biosurfactant production from *B. subtilis* Natto with sucrose as carbon source, peptone as nitrogen source and culture pH of 6.8

The maximum biosurfactant mass was recorded when *B. subtilis* Natto was inoculated into the medium at 6% v/v because inoculum size above 6% v/v decreased the mass of

biosurfactant produced. It showed the limitation of increasing inoculum size in improving microorganisms' growth and growth-related activities. When a lower inoculum size was used, the number of cells present in the production medium was low, which required a longer time to reach the exponential phase to utilize the substrate in the formation of the desired product (Nalini & Parthasarathi, 2018). So, selecting a suitable inoculum size in the production medium was important to maintain the balance between inoculum size and the media volume. As reported by previous work, increasing inoculum size would decrease microbial activity due to the limited availability of nutrients in the medium used by microorganisms (Korai et al., 2014).

Effect of Initial pH of Fermentation Medium. Five initial pH of fermentation medium (pH 5.5, 6.0, 6.5, 6.8 and 7.5) were tested for their effects on biosurfactant production. From Figure 6, as the initial pH of the fermentation medium increased from pH 5.5 to pH 6.8, cell mass increased from 1.38 ± 0.06 g/L to 1.48 ± 0.06 g/L while biosurfactant mass increased from 32.00 ± 2.16 mg/L to 80.67 ± 4.99 mg/L. When *B. subtilis* Natto was grown in a fermentation medium with an initial pH of 7.5, cell mass remained constant at 1.48 ± 0.02 g/L. However, biosurfactant production decreased to 60.33 ± 0.47 mg/L compared to the initial pH of 6.8 (80.67 ± 4.99 mg/L). So, a fermentation medium with an initial pH of 6.8 was selected for *B. subtilis* Natto in biosurfactant production. This initial pH of 6.8 provided a suitable environment for *B. subtilis* Natto to produce biosurfactant, as proven by its highest cell and biosurfactant mass.

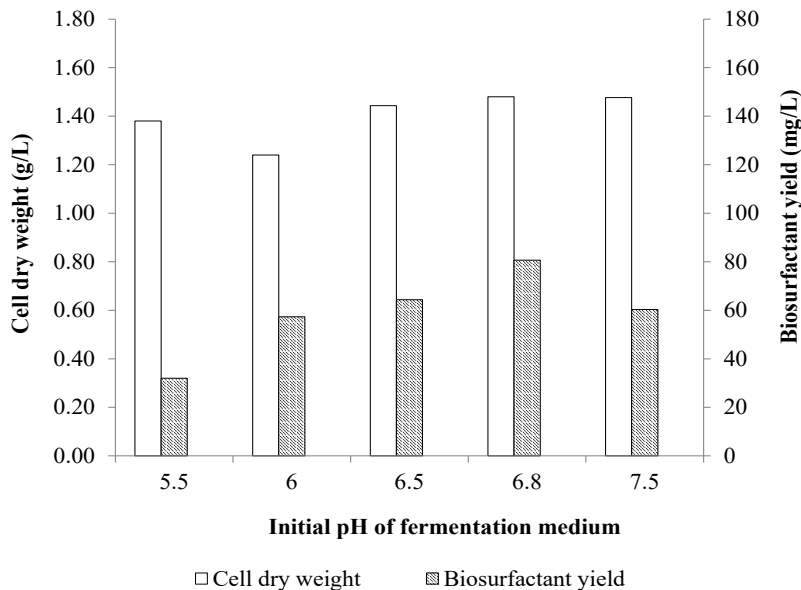


Figure 6. Effect of different initial pH of fermentation medium on production from *B. subtilis* Natto with sucrose as carbon source, peptone as nitrogen source, inoculum size of 2% v/v and culture pH of 6.8

There was a drastic decline in biosurfactant production at lower pH of 5.5 compared to higher pH of 7.5, which illustrated that acidic and alkaline medium provided an unsuitable environment for *B. subtilis* Natto to produce biosurfactants. However, biosurfactant mass was the highest at pH 6.8, indicating that a medium of nearly neutral pH was preferred for biosurfactant production from *B. subtilis* Natto. This result was in agreement with Kiran et al. (2010) and Vigneshwaran et al. (2018), who reported medium of neutral pH was suitable for biosurfactant production from *Brevibacillus* sp. and *Brevibacterium aureum*. So, the pH of the fermentation medium was important for bacterial growth because it can affect the absorption of nutrients, reproduction and activity of the enzyme of microorganisms (Zhang et al., 2015).

Fermentation Conditions from OFAT Analysis. Using ANOVA Analysis Tools, all the parameters were significant except for adding amino acid into the fermentation medium. It was because the p-value calculated for Figure 4 was 0.40, which was greater than the value of α set at 0.05. For the nitrogen source, urea was chosen over peptone and sodium nitrate for economic reasons, and the p-value shows that the biosurfactant yield was significant. Urea is the cheapest nitrogen source used for fermentation. When *B. subtilis* Natto was grown in the fermentation medium with the combination of the selected parameters, which are urea as nitrogen source, initial pH of 6.8 in the fermentation medium, inoculum size of 6% v/v, and addition of palm kernel oil at a concentration of 2% v/v, the yield for biomass and biosurfactant obtained were 1.56 ± 0.02 g/L and 362.33 ± 19.48 mg/L. The biosurfactant yield improved by 45.00% from 80.67 ± 4.99 mg/L to 362.33 ± 19.48 mg/L.

In Table 2, de Sousa et al. (2014) and Youssef et al. (2013) also reported low biosurfactant yield of 158.14 mg/L and 28.00 mg/L from *Bacillus subtilis* ATCC 6633 and *Bacillus subtilis* subsp. *subtilis* spizizenii NRRL B-23049, respectively. However, one researcher reported a higher biosurfactant yield of 657.23 mg/L from *Bacillus subtilis* subsp. *natto* NT-6 (Sun et al., 2019). There was a disparity in the yield because the strain was grown in a Landy medium at 28°C for 36 hours. Another researcher reported a higher biosurfactant yield of 657 mg/L when they incorporated brewery waste into a nutrient salt medium (Moshtagh et al., 2018). So, this research provided a new insight that vegetable oil such as palm kernel oil which is abundant in Malaysia, exhibits the ability as a substrate for biosurfactant production from *B. subtilis* Natto. Food-grade *B. subtilis* Natto can act as a probiotic strain and biosurfactant producer.

Table 2

Comparison of biosurfactant yield from other researchers

Types of strain	Biosurfactant yield (mg/L)	Reference
<i>Bacillus subtilis</i> ATCC 6633	158.14	de Sousa et al. (2014)
<i>Bacillus licheniformis</i> RS-1	20	
<i>Bacillus subtilis</i> subsp. <i>subtilis spizizenii</i> NRRL B-23049	28	Youssef et al. (2013)
<i>Bacillus subtilis</i> subsp. <i>natto</i> NT-6	657.23	Sun et al. (2019)
<i>Bacillus subtilis</i> N3-1P	657	Moshtagh et al. (2018)

Characterization of Biosurfactant

The product obtained from *B. subtilis* Natto fermentation was subjected to qualitative characterization to confirm that it is a biosurfactant. Two of the characteristics of biosurfactants are oil displacement and emulsification ability. Figure 7 showed the product recovered from *B. subtilis* Natto was able to displace palm oil, with a clear zone measured 5.50 ± 0.08 cm. Meanwhile, Figure 8 shows the formation of an emulsion layer when *B. subtilis* Natto product was added to the water-oil mixture after vortexing. The emulsification index was calculated at 45.67 ± 2.49 %.

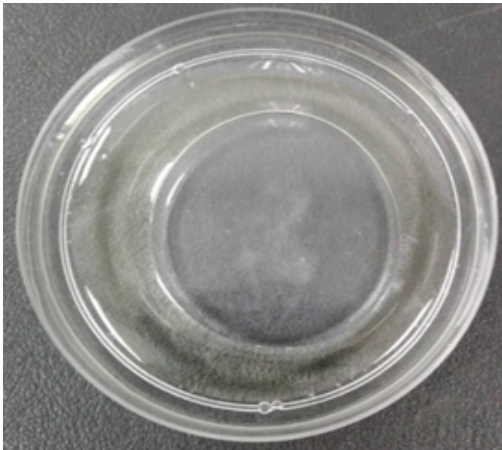


Figure 7. Oil displacement assay for biosurfactant produced from *B. subtilis* Natto



Figure 8. Emulsification assay for biosurfactant produced from *B. subtilis* Natto

The clear zone and emulsion formation indicated biosurfactant-producing capability by *B. subtilis* Natto. Besides, many researchers have used the oil displacement method to determine biosurfactant production efficiency because it depends on the decrease in water-oil interfacial tension regardless of biosurfactant structure (Parthipan et al., 2017). In this field, Anjum et al. (2016) reported the highest emulsification index for biosurfactant produced from *Bacillus sp.* MTCC 5877 was $76 \pm 0.57\%$, while E24 of biosurfactant from *Bacillus cereus* and *Bacillus subtilis* were reported by Jaysree et al. (2011) with values ranging between 15 and 30% for diesel and engine oil, respectively. Emulsification index obtained from this research was $45.67 \pm 2.49\%$. It also suggested that biosurfactants produced exhibited a low ability to emulsify vegetable oil which can be used as an antimicrobial agent in nanoemulsion against food-borne pathogens (Joe et al., 2012).

CONCLUSION

OFAT analysis of biosurfactant production from *B. subtilis* Natto showed an improvement of 45% in biosurfactant yield when *B. subtilis* Natto was grown in fermentation medium using urea as nitrogen source, initial pH 6.8 of fermentation medium, with inoculum size of 6% v/v and addition of palm kernel oil at a concentration of 2% v/v into the fermentation medium. From the endpoint of fermentation results, the important parameters in enhancing the production are types of nitrogen source, inoculum size, types and concentrations of vegetable oils, and initial pH of the fermentation medium. Using ANOVA analysis tools, the most significant parameters to enhance production are vegetable oils. *B. subtilis* Natto can act as a probiotic strain and biosurfactant producer.

ACKNOWLEDGMENTS

We thank Sime Darby Technology Centre for their support in donating lab chemicals and permission to use their equipment in their facilities. In addition, Yew Seng Leow appreciates Yayasan Sime Darby for providing the YSD-UPM scholarship for his M. Sc. study, which part of his study is presented in this paper.

REFERENCES

- Abdel-Mawgoud, A. M., Aboulwafa, M. M., & Hassouna, N. A. H. (2008). Optimization of surfactin production by *Bacillus subtilis* isolate BS5. *Applied Biochemistry and Biotechnology*, 150(3), 305-325. <https://doi.org/10.1007/s12010-008-8155-x>
- Anjum, F., Gautam, G., Edgard, G., & Negi, S. (2016). Biosurfactant production through *Bacillus sp.* MTCC 5877 and its multifarious applications in food industry. *Bioresource Technology*, 213, 262-269. <https://doi.org/10.1016/j.biortech.2016.02.091>

- Balan, S. S., Kumar, C. G., & Jayalakshmi, S. (2017). Aneurinifactin, a new lipopeptide biosurfactant produced by a marine *Aneurinibacillus aneurinilyticus* SBP-11 isolated from Gulf of Mannar: Purification, characterization and its biological evaluation. *Microbiological Research*, *194*, 1-9. <https://doi.org/10.1016/j.micres.2016.10.005>
- Banat, I. M., De Rienzo, M. A. D., & Quinn, G. A. (2014). Microbial biofilms: Biosurfactants as antibiofilm agents. *Applied Microbiology and Biotechnology*, *98*(24), 9915-9929. <https://doi.org/10.1007/s00253-014-6169-6>
- Bertrand, B., Martínez-Morales, F., Rosas-Galván, N. S., Morales-Guzmán, D., & Trejo-Hernández, M. R. (2018). Statistical design, a powerful tool for optimizing biosurfactant production: A review. *Colloids and Interfaces*, *2*(3), Article 36. <https://doi.org/10.3390/colloids2030036>
- Bhattacharya, B., Ghosh, T. K., & Das, N. (2017). Application of bio-surfactants in cosmetics and pharmaceutical industry. *Scholars Academic Journal of Pharmacy (SAJP)*, *6*(7), 320-329. <https://doi.org/10.21276/sajp>
- Biniarz, P., Coutte, F., Gancel, F., & Łukaszewicz, M. (2018). High-throughput optimization of medium components and culture conditions for the efficient production of a lipopeptide pseudofactin by *Pseudomonas fluorescens* BD5. *Microbial Cell Factories*, *17*(1), 1-18. <https://doi.org/10.1186/s12934-018-0968-x>
- Cao, X. H., Liao, Z. Y., Wang, C. L., Yang, W. Y., & Lu, M. F. (2009). Evaluation of a lipopeptide biosurfactant from *Bacillus natto* TK-1 as a potential source of anti-adhesive, antimicrobial and antitumor activities. *Brazilian Journal of Microbiology*, *40*(2), 373-379. <https://doi.org/10.1590/s1517-83822009000200030>
- Chen, H. L., & Juang, R. S. (2008). Recovery and separation of surfactin from pretreated fermentation broths by physical and chemical extraction. *Biochemical Engineering Journal*, *38*(1), 39-46. <https://doi.org/10.1016/j.bej.2007.06.003>
- Chen, W. C., Juang, R. S., & Wei, Y. H. (2015). Applications of a lipopeptide biosurfactant, surfactin, produced by microorganisms. *Biochemical Engineering Journal*, *103*, 158-169. <https://doi.org/10.1016/j.bej.2015.07.009>
- Cooper, D. G., & Goldenberg, B. G. (1987). Surface-active agents from two *Bacillus* species. *Applied and Environmental Microbiology*, *53*(2), 224-229. <https://doi.org/10.1128/aem.53.2.224-229.1987>
- Das, A. J., & Kumar, R. (2019). Production of biosurfactant from agro-industrial waste by *Bacillus safensis* J2 and exploring its oil recovery efficiency and role in restoration of diesel contaminated soil. *Environmental Technology and Innovation*, *16*, Article 100450. <https://doi.org/10.1016/j.eti.2019.100450>
- de Sousa, M., Dantas, I. T., Felix, A. K. N., de Sant'ana, H. B., Melo, V. M. M., & Gonçalves, L. R. B. (2014). Crude glycerol from biodiesel industry as substrate for biosurfactant production by *Bacillus subtilis* ATCC 6633. *Brazilian Archives of Biology and Technology*, *57*(2), 295-301. <https://doi.org/10.1590/S1516-89132014000200019>
- Dobler, L., Vilela, L. F., Almeida, R. V., & Neves, B. C. (2016). Rhamnolipids in perspective: Gene regulatory pathways, metabolic engineering, production and technological forecasting. *New Biotechnology*, *33*(1), 123-135. <https://doi.org/10.1016/j.nbt.2015.09.005>
- Donio, M. B. S., Ronica, S. F. A., Viji, V. T., Velmurugan, S., Jenifer, J. A., Michaelbabu, M., & Citarasu, T. (2013). Isolation and characterization of halophilic *Bacillus sp.* BS3 able to produce pharmacologically important biosurfactants. *Asian Pacific Journal of Tropical Medicine*, *6*(11), 876-883. [https://doi.org/10.1016/S1995-7645\(13\)60156-X](https://doi.org/10.1016/S1995-7645(13)60156-X)

- Eswari, J. S., Anand, M., & Venkateswarlu, C. (2016). Optimum culture medium composition for lipopeptide production by *Bacillus subtilis* using response surface model-based ant colony optimization. *Sadhana*, 41(1), 55-65. <https://doi.org/10.1007/s12046-015-0451-x>
- Fanaei, M., & Emtiazi, G. (2018). Microbial assisted (*Bacillus mojavensis*) production of bio-surfactant lipopeptide with potential pharmaceutical applications and its characterization by MALDI-TOF-MS analysis. *Journal of Molecular Liquids*, 268, 707-714. <https://doi.org/10.1016/j.molliq.2018.07.103>
- Felix, A. K. N., Martins, J. J. L., Lima Almeida, J. G., Giro, M. E. A., Cavalcante, K. F., Maciel Melo, V. M., Loiola Pessoa, O. D., Ponte Rocha, M. V., Rocha Barros Gonçalves, L., & Saraiva de Santiago Aguiar, R. (2019). Purification and characterization of a biosurfactant produced by *Bacillus subtilis* in cashew apple juice and its application in the remediation of oil-contaminated soil. *Colloids and Surfaces B: Biointerfaces*, 175(July 2018), 256-263. <https://doi.org/10.1016/j.colsurfb.2018.11.062>
- Ferraz, C., De Araújo, Á. A., & Pastore, G. M. (2002). The influence of vegetable oils on biosurfactant production by *Serratia marcescens*. *Applied Biochemistry and Biotechnology*, 98(1), 841-847. <https://doi.org/10.1385/abab:98-100:1-9:841>
- Hentati, D., Chebbi, A., Hadrich, F., Frikha, I., Rabanal, F., Sayadi, S., Manresa, A., & Chamkha, M. (2019). Production and characterization of lipopeptide biosurfactants from a novel marine *Bacillus stratosphericus* strain FLU5. *Ecotoxicology and Environmental Safety*, 167, 441-449. <https://doi.org/10.1016/j.ecoenv.2018.10.036>
- Hirata, Y., Igarashi, K., Ueda, A., & Quan, G. L. (2021). Enhanced sophorolipid production and effective conversion of waste frying oil using dual lipophilic substrates. *Bioscience, Biotechnology and Biochemistry*, 85(7), 1763-1771. <https://doi.org/10.1093/bbb/zbab075>
- Ibrar, M., & Zhang, H. (2020). Construction of a hydrocarbon-degrading consortium and characterization of two new lipopeptides biosurfactants. *Science of the Total Environment*, 714, Article 136400. <https://doi.org/10.1016/j.scitotenv.2019.136400>
- Jahan, R., Bodratti, A. M., Tsianou, M., & Alexandridis, P. (2020). Biosurfactants, natural alternatives to synthetic surfactants: Physicochemical properties and applications. *Advances in Colloid and Interface Science*, 275, Article 102061. <https://doi.org/10.1016/j.cis.2019.102061>
- Janek, T., Łukaszewicz, M., Rezanka, T., & Krasowska, A. (2010). Isolation and characterization of two new lipopeptide biosurfactants produced by *Pseudomonas fluorescens* BD5 isolated from water from the Arctic Archipelago of Svalbard. *Bioresource Technology*, 101(15), 6118-6123. <https://doi.org/10.1016/j.biortech.2010.02.109>
- Jaysree, R. C., Basu, S., Singh, P. P., Ghosal, T., Patra, P. A., Keerthi, Y., & Rajendran, N. (2011). Isolation of biosurfactant producing bacteria from environmental samples. *Pharmacologyonline*, 3, 1427-1433. <https://doi.org/10.1002/abio.370110405>
- Joe, M. M., Bradeeba, K., Parthasarathi, R., Sivakumaar, P. K., Chauhan, P. S., Tipayno, S., Benson, A., & Sa, T. (2012). Development of surfactin based nanoemulsion formulation from selected cooking oils: Evaluation for antimicrobial activity against selected food associated microorganisms. *Journal of the Taiwan Institute of Chemical Engineers*, 43(2), 172-180. <https://doi.org/10.1016/j.jtice.2011.08.008>

- Khondee, N., Tathong, S., Pinyakong, O., Müller, R., Soonglerdsongpha, S., Ruangchainikom, C., Tongcumpou, C., & Luepromchai, E. (2015). Lipopeptide biosurfactant production by chitosan-immobilized *Bacillus sp.* GY19 and their recovery by foam fractionation. *Biochemical Engineering Journal*, *93*, 47-54. <https://doi.org/10.1016/j.bej.2014.09.001>
- Kim, H. S., Yoon, B. D., Lee, C. H., Suh, H. H., Oh, H. M., Katsuragi, T., & Tani, Y. (1997). Production and properties of a lipopeptide biosurfactant from *Bacillus subtilis* C9. *Journal of Fermentation and Bioengineering*, *84*(1), 41-46. [https://doi.org/10.1016/S0922-338X\(97\)82784-5](https://doi.org/10.1016/S0922-338X(97)82784-5)
- Kiran, G. S., Thomas, T. A., Selvin, J., Sabarathnam, B., & Lipton, A. P. (2010). Optimization and characterization of a new lipopeptide biosurfactant produced by marine *Brevibacterium aureum* MSA13 in solid state culture. *Bioresource Technology*, *101*(7), 2389-2396. <https://doi.org/10.1016/j.biortech.2009.11.023>
- Konishi, M., Morita, T., Fukuoka, T., Imura, T., Uemura, S., Iwabuchi, H., & Kitamoto, D. (2018). Efficient production of acid-form sophorolipids from waste glycerol and fatty acid methyl esters by *Candida floricola*. *Journal of Oleo Science*, *67*(4), 489-496. <https://doi.org/10.5650/jos.ess17219>
- Korai, A. G., Ameer, Y., Asif, S., Habib, H., Abbasi, M. H., Akhtar, R. M., Rasheed, M. A., Salahuddin, Tariq, A., & Awais, H. (2014). Biosurfactant production by *Pseudomonas aeruginosa* strains on 4 ml of inoculum size. *Pakistan Journal of Medical and Health Sciences*, *8*(1), 21-24.
- Li, E., & De Orduña, R. M. (2010). A rapid method for the determination of microbial biomass by dry weight using a moisture analyser with an infrared heating source and an analytical balance. *Letters in Applied Microbiology*, *50*(3), 283-288. <https://doi.org/10.1111/j.1472-765X.2009.02789.x>
- Liu, J. F., Yang, J., Yang, S. Z., Ye, R. Q., & Mu, B. Z. (2012). Effects of different amino acids in culture media on surfactin variants produced by *Bacillus subtilis* TD7. *Applied Biochemistry and Biotechnology*, *166*(8), 2091-2100. <https://doi.org/10.1007/s12010-012-9636-5>
- Liu, K., Sun, Y., Cao, M., Wang, J., Lu, J. R., & Xu, H. (2020). Rational design, properties, and applications of biosurfactants: A short review of recent advances. *Current Opinion in Colloid and Interface Science*, *45*, 57-67. <https://doi.org/10.1016/j.cocis.2019.12.005>
- Liu, X. (2020). Microbial technology for the sustainable development of energy and environment. *Biotechnology Reports*, *27*, Article e00486. <https://doi.org/10.1016/j.btre.2020.e00486>
- Morikawa, M., Daido, H., Takao, T., Murata, S., Shimonishi, Y., & Imanaka, T. (1993). A new lipopeptide biosurfactant produced by *Arthrobacter sp.* strain MIS38. *Journal of Bacteriology*, *175*(20), 6459-6466. <https://doi.org/10.1128/jb.175.20.6459-6466.1993>
- Moshtagh, B., Hawboldt, K., & Zhang, B. (2018). Optimization of biosurfactant production by *Bacillus subtilis* N3-1P using the brewery waste as the carbon source. *Environmental Technology*, *40*(25), 3371-3380. <https://doi.org/10.1080/09593330.2018.1473502>
- Nalini, S., & Parthasarathi, R. (2018). Optimization of rhamnolipid biosurfactant production from *Serratia rubidua* SNAU02 under solid-state fermentation and its biocontrol efficacy against Fusarium wilt of eggplant. *Annals of Agrarian Science*, *16*(2), 108-115. <https://doi.org/10.1016/j.aasci.2017.11.002>
- Parthipan, P., Preetham, E., Machuca, L. L., Rahman, P. K. S. M., Murugan, K., & Rajasekar, A. (2017). Biosurfactant and degradative enzymes mediated crude oil degradation by bacterium *Bacillus subtilis* A1. *Frontiers in Microbiology*, *8*, 1-14. <https://doi.org/10.3389/fmicb.2017.00193>

- Pecci, Y., Rivardo, F., Martinotti, M. G., & Allegrone, G. (2010). LC/ESI-MS/MS characterisation of lipopeptide biosurfactants produced by the *Bacillus licheniformis* V9T14 strain. *Journal of Mass Spectrometry*, 45(7), 772-778. <https://doi.org/10.1002/jms.1767>
- Purwasena, I. A., Astuti, D. I., & Utami, S. G. (2020). Nitrogen optimization on rhamnolipid biosurfactant production from *Pseudoxanthomonas* sp. G3 and its preservation techniques. *Sains Malaysiana*, 49(9), 2119-2127. <https://doi.org/10.17576/jsm-2020-4909-10>
- Saimmai, A., Onlamool, T., Sobhon, V., & Maneerat, S. (2013). An efficient biosurfactant-producing bacterium *Selenomonas ruminantium* CT2, isolated from mangrove sediment in south of Thailand. *World Journal of Microbiology and Biotechnology*, 29(1), 87-102. <https://doi.org/10.1007/s11274-012-1161-8>
- Santos, A. P. P., Silva, M. D. S., Costa, E. V. L., Rufino, R. D., Santos, V. A., Ramos, C. S., Sarubbo, L. A., & Porto, A. L. F. (2018). Production and characterization of a biosurfactant produced by *Streptomyces* sp. DPUA 1559 isolated from lichens of the Amazon region. *Brazilian Journal of Medical and Biological Research*, 51(2), 1-10. <https://doi.org/10.1590/1414-431x20176657>
- Sharma, R., Singh, J., & Verma, N. (2018). Production, characterization and environmental applications of biosurfactants from *Bacillus amyloliquefaciens* and *Bacillus subtilis*. *Biocatalysis and Agricultural Biotechnology*, 16, 132-139. <https://doi.org/10.1016/j.bcab.2018.07.028>
- Singh, R., Glick, B. R., & Rathore, D. (2018). Biosurfactants as a biological tool to increase micronutrient availability in soil: A review. *Pedosphere*, 28(2), 170-189. [https://doi.org/10.1016/S1002-0160\(18\)60018-9](https://doi.org/10.1016/S1002-0160(18)60018-9)
- Sun, D., Liao, J., Sun, L., Wang, Y., Liu, Y., Deng, Q., Zhang, N., Xu, D., Fang, Z., Wang, W., & Gooneratne, R. (2019). Effect of media and fermentation conditions on surfactin and iturin homologues produced by *Bacillus natto* NT-6: LC-MS analysis. *AMB Express*, 9(1), Article 120. <https://doi.org/10.1186/s13568-019-0845-y>
- Thavasi, R., Jayalakshmi, S., Balasubramanian, T., & Banat, I. M. (2008). Production and characterization of a glycolipid biosurfactant from *Bacillus megaterium* using economically cheaper sources. *World Journal of Microbiology and Biotechnology*, 24(7), 917-925. <https://doi.org/10.1007/s11274-007-9609-y>
- Varvaresou, A., & Iakovou, K. (2015). Biosurfactants in cosmetics and biopharmaceuticals. *Letters in Applied Microbiology*, 61(3), 214-223. <https://doi.org/10.1111/lam.12440>
- Vigneshwaran, C., Sivasubramanian, V., Vasantharaj, K., Krishnanand, N., & Jerold, M. (2018). Potential of *Brevibacillus* sp. AVN 13 isolated from crude oil contaminated soil for biosurfactant production and its optimization studies. *Journal of Environmental Chemical Engineering*, 6(4), 4347-4356. <https://doi.org/10.1016/j.jece.2018.06.036>
- Youssef, N., Simpson, D. R., McInerney, M. J., & Duncan, K. E. (2013). *In-situ* lipopeptide biosurfactant production by *Bacillus* strains correlates with improved oil recovery in two oil wells approaching their economic limit of production. *International Biodeterioration and Biodegradation*, 81, 127-132. <https://doi.org/10.1016/j.ibiod.2012.05.010>
- Yuliani, H., Perdani, M. S., Savitri, I., Manurung, M., Sahlan, M., Wijanarko, A., & Hermansyah, H. (2018). Antimicrobial activity of biosurfactant derived from *Bacillus subtilis* C19. *Energy Procedia*, 153, 274-278. <https://doi.org/10.1016/j.egypro.2018.10.043>

- Zhang, J., Xue, Q., Gao, H., Lai, H., & Wang, P. (2016). Production of lipopeptide biosurfactants by *Bacillus atrophaeus* 5-2a and their potential use in microbial enhanced oil recovery. *Microbial Cell Factories*, 15(1), 1-11. <https://doi.org/10.1186/s12934-016-0574-8>
- Zhang, W., Zhang, X., & Cui, H. (2015). Isolation, fermentation optimization and performance studies of a novel biosurfactant producing strain *Bacillus amyloliquefaciens*. *Chemical and Biochemical Engineering Quarterly*, 29(3), 447-456. <https://doi.org/10.15255/CABEQ.2014.2037>

Aquaculture Wastewater Quality Improvement by Floating Raft of Native Aquatic Plants in An Giang Province, Vietnam

Khanh Tran Thien Nguyen^{1,2*}, Chi Thi Dao Vo^{1,2}, An Thuy Ngo^{1,2}, Nghi Thanh Doan^{1,2}, Luyen Phuc Huynh³ and Dung Huynh Thuy Tran³

¹An Giang University, 18 Ung Van Khiem, Long Xuyen, An Giang, Vietnam

²Vietnam National University, Ho Chi Minh City, Vietnam

³An Giang Center for Environmental Monitoring and Techniques, Resources, 822 Tran Hung Dao, Long Xuyen, An Giang, Vietnam

ABSTRACT

The development of aquaculture in An Giang province posed a risk of lowering the surface water quality of the Mekong River. This study assessed the pollution level of surface water affected by aquaculture areas in the province and the efficiency of the floating raft of native aquatic plants on aquaculture wastewater quality improvement. Water samples were analyzed for SS, COD, BOD₅, N-NH₄⁺, Total N, and Total P. The Water Quality Index was calculated according to the Vietnamese technical guidelines (VN_WQI). The quadrat method was applied to determine the density of aquatic plants. The result showed that surface water quality affected by aquaculture areas in An Giang province did not meet national standards, and the WQI ranged from heavy to good pollution. Experimental results showed that when using the treatment tank, including floating rafts of Water hyacinth (*Eichhornia crassipes*), Morning glory plants (*Ipomoea aquatica*), and Climbing dayflower (*Commelina diffusa*),

the removal percentages of SS, COD, BOD₅, N-NH₄⁺, Total N, and Total P were 92.6%, 89.6%, 93.9%, 93.4%, 64.3%, and 94.6%, respectively, in the first three months of the farming season. The removal percentages of SS, COD, BOD₅, N-NH₄⁺, Total N, and Total P were 92.7%, 89.9%, 91.5%, 93.6%, 67.8%, and 94%, respectively, in the fourth month until fish harvest in the treatment tank. Therefore, floating rafts of native aquatic plants could absorb nutrients and

ARTICLE INFO

Article history:

Received: 17 May 2022

Accepted: 05 October 2022

Published: 06 March 2023

DOI: <https://doi.org/10.47836/pjst.31.2.06>

E-mail addresses:

nttkhanh@agu.edu.vn (Khanh Tran Thien Nguyen)

vtchi@agu.edu.vn (Chi Thi Dao Vo)

ntan@agu.edu.vn (An Thuy Ngo)

dtngghi@agu.edu.vn (Nghi Thanh Doan)

pl.huynh.mt280594@gmail.com (Luyen Phuc Huynh)

thuy_dung1592002@yahoo.com (Dung Huynh Thuy Tran)

*Corresponding author

quickly remove pollutants. The quality of aquaculture wastewater after treatment was significantly improved.

Keywords: Aquaculture wastewater, *Commelina diffusa*, *Eichhornia crassipes*, floating raft, *Ipomoea aquatica*, wastewater treatment, water quality

INTRODUCTION

An Giang is a province in the Mekong Delta located in southwest Vietnam. The dense system of rivers, canals, and channels and abundant surface water all year round brings many advantages in varieties and food for aquaculture (An Giang Center for Environmental Monitoring and Techniques, Resources, 2019). The province's aquaculture has experienced remarkable growth in quantity and quality, making a significant contribution to the socio-economic development of the province. However, the strong development of aquaculture caused many increasing environmental impacts on a large and alarming scale, especially the impacts on water bodies receiving aquaculture wastewater. Currently, most aquaculture wastewater from farming fish farms in An Giang province is discharged directly into the natural environment without treatment. Only a few farming areas of enterprises have the investment in wastewater treatment systems (accounting for approximately 10% of farming areas) (Shipin et al., 2005; Khanh et al., 2013; Khanh et al., 2015; An Giang Department of Natural Resources and Environment, 2020). It is necessary to assess the pollution level of aquaculture wastewater in the province and provide solutions.

The Vietnam Water Quality Index (VN_WQI) is suggested by Vietnam Environment Administration and is commonly used in Vietnam. There is much research using VN_WQI. Giao et al. (2021) conducted a study to evaluate and classify surface water quality in Dong Thap, Vietnam, using set pair analysis (SPA) and the VN_WQI method. The findings present that water quality in Dong Thap was ranked at level III (medium) based on the SPA; this water quality rank was at level IV (poor) using the VN_WQI, which was suitable for irrigation and other equivalent purposes. Ha et al. (2021) studied integrating the remote sensing technology with in-situ ground observation to assess the water quality status in Ca Mau city through VN_WQI. The results also illustrated the low quality of surface water and heavy pollution. Lan and Long (2011) assessed surface water quality by VN_WQI at the Cai Sao canal, An Giang. The water quality index (VN_WQI) was in the range of 39-29, indicating mild pollution at the two sites close to the joining of the canal with the river, increasing severe pollution along the rest of the canal. The equations used to calculate the VN_WQI are easy to use; thus, it is a valuable tool for observing the water environment and monitoring pollution.

Many studies show that using plants to treat wastewater is an effective method. The study of Minh et al. (2012) evaluated the ability of Water hyacinth and Vetiver to treat

dissolved organic nitrogen (N) and phosphorus (P) pollution in ponds used for intensive catfish cultivation in the Mekong River Delta. They found that after one month, Water hyacinth could reduce 88% organic N and 100% organic P compared to their initial concentrations. Similarly, the concentrations of organic N and P reduced by 85% and 99%, respectively, when Vetiver was grown in the culture. Nhien and Trang (2013) researched the role of *Typha orientalis* L. in constructed wetlands to treat close-recirculated intensive catfish culture. The result showed that *T. orientalis* helped remove about 17% N and 34% P from wastewater via vegetative uptake. Kieu et al. (2015) studied the evolution of nitrogen forms in wastewater of intensive catfish pond growing Hymenachne grass (*Hymenachne acutigluma*). The result showed that *Hymenachne* grass reduced $\text{NH}_4^+\text{-N}$, $\text{NO}_2^-\text{-N}$, $\text{NO}_3^-\text{-N}$, and TKN in wastewater at 69.7–96.9; 96.6–97.3; 99.3–99.9; 48.5–73.5%, respectively. In addition, *Hymenachne* grass reduced TP and $\text{PO}_4^{3-}\text{-P}$ with respective deduction percentages of 84.8–95.6 and 85.7–92.5% compared to the initial phosphorus level. In the study of Snow and Ghaly (2008), Water hyacinth, Water lettuce, and Parrot's feather plants were examined for their ability to remove nutrients from aquaculture wastewater at two retention times. The TSS, COD, $\text{NH}_4^+\text{-N}$, $\text{NO}_2^-\text{-N}$, $\text{NO}_3^-\text{-N}$, and $\text{PO}_4^{3-}\text{-P}$ reductions ranged from 21.4 to 48.0%, from 71.1 to 89.5%, from 55.9 to 76.0%, from 49.6 to 90.6%, from 34.5 to 54.4% and from 64.5 to 76.8%, respectively. Li and Li (2009) investigated nutrient removal and water quality by planting aquatic vegetables on artificial beds in 36 m² concrete fishponds. After treatment of 120 days, 30.6% of TN and 18.2% of TP were removed from the total input nutrients by 6 m² aquatic vegetable *Ipomoea aquatica*.

The TN, TP, COD, and Chlorophyll concentrations in planted ponds were significantly lower than those in non-planted ponds. No significant differences in the concentration of (TAN), $\text{NO}_2^-\text{-N}$, and $\text{NO}_3^-\text{-N}$ were found between planted and non-planted ponds. Zhang et al. (2014) used a water spinach floating bed to improve the aquaculture wastewater quality. The results showed significant improvement in the aquaculture water quality at the experimental site, with removal percentages of TN, $\text{NH}_4^+\text{-N}$, $\text{NO}_2^-\text{-N}$, and TP being 11.2%, 60.0%, 60.2%, and 27.3%, respectively. De Vasconcelos et al. (2021) evaluated the efficiency of using the floating aquatic macrophytes *Eichhornia crassipes*, *Pistia stratiotes*, and *Salvinia molesta* for the treatment of aquaculture effluents. They found that with floating aquatic macrophytes, the concentrations of all evaluated limnology parameters included TN, $\text{NO}_2^-\text{-N}$, $\text{NO}_3^-\text{-N}$, $\text{NH}_4^+\text{-N}$, TP, turbidity, dissolved oxygen, electrical conductivity, total alkalinity, BOD, and COD, improved significantly. There was also an improvement in the physical aspect of the effluent (transparency and turbidity).

This study assessed the pollution level of aquaculture wastewater in An Giang province and the efficiency of using native aquatic species, including Water hyacinth (*Eichhornia crassipes*), Morning glory plants (*Ipomoea aquatica*), and Climbing dayflower (*Commelina diffusa*) on aquaculture wastewater improvement. The role of the combination of these three

native aquatic plants in the treatment of aquaculture wastewater has been investigated for the first time by the model of a floating raft through an experimental method. The study has proposed a biological solution using aquatic plants to remove pollutants in aquaculture wastewater in An Giang province.

MATERIALS AND METHODS

Location of Water Sampling

Surface water samples were collected at 18 sampling locations affected by aquaculture areas. The sample collection schedule was in March and June 2021. Figure 1 shows the location map of surface water sampling. Table 1 shows the code, coordinates, and characteristics of sampling locations.

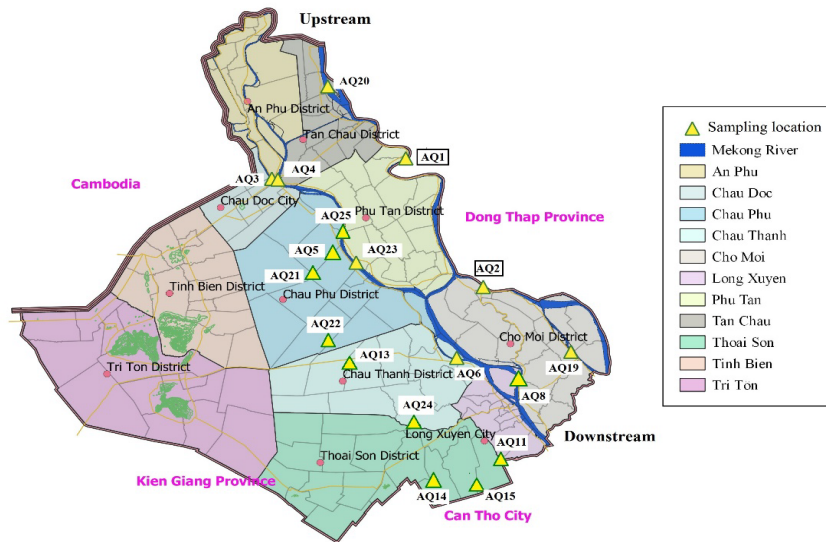


Figure 1. The location map of surface water sampling

Table 1

Location of surface water sampling

No.	Code	Coordinate	Location	Feature
1	AQ1	559.880 1.188.560	Long Hoa commune, Phu Tan district	The end of wastewater source of the Long Hoa raft floating fish farming
2	AQ2	570.753 1.168.426	Kien An commune, Cho Moi district	The end of wastewater source of pen culture and pond fish farming area in Kien An

Table 1 (Continue)

No.	Code	Coordinate	Location	Feature
3	AQ3	540.104 1.184.937	Chau Phu A ward, Chau Doc city	The end of wastewater source of the Vinh Nguon raft floating fish farming
4	AQ4	540.708 1.184.988	Da Phuoc commune, An Phu district	The end of wastewater source of the Da Phuoc raft floating fish farming
5	AQ5	548.722 1.172.710	Vinh Thanh Trung commune, Chau Phu district	Impact of wastewater from fish farming ponds on Xang Vinh Tre canal
6	AQ6	567.496 1.156.042	Binh Thanh commune, Chau Thanh district	The end of wastewater source of pond fish farming area in Binh Thanh
7	AQ8	576.289 1.151.944	My Hoa Hung commune, Long Xuyen city	The end of wastewater source of pen culture and pond fish farming area in My Hoa Hung
8	AQ11	574.103 1.139.929	My Thoi ward, Long Xuyen city	Impact of wastewater from fish farming ponds
9	AQ13	552.267 1.153.651	Vinh Thanh commune, Chau Thanh district	Impact of wastewater from a rice-shrimp farming area
10	AQ14	572.673 1.139.250	Phu Thuan commune, Thoai Son district	The beginning of the Don Dong canal, adjacent to the Moi canal
11	AQ15	565.734 1.136.318	Vinh Khanh commune, Thoai Son district	The beginning of the Don Dong channel, adjacent to the Ong Co canal
12	AQ19	584.521 1.157.065	My An commune, Cho Moi district	Impact of wastewater from a raft floating fish farming
13	AQ20	548.134 1.201.285	Vinh Hoa commune, Tan Chau town	Impact of wastewater from pond fish farming area
14	AQ21	546.162 1.169.627	Phu My commune, Chau Phu district	Impact of wastewater from Loc Kim Chi fish farming area, the confluence between Hao De Lon canal and Xang Vinh Tre canal
15	AQ22	548.706 1.158.636	Binh Phu commune, Chau Phu district	Impact from wastewater from Nam Viet Binh Phu fish farming area, the confluence between 13 canals and Xang Cay Duong canal

Table 1 (Continue)

No.	Code	Coordinate	Location	Feature
16	AQ23	552.578 1.171.504	Phu Binh commune, Phu Tan district	Impact of wastewater from Pangasius farming area in Phu Binh commune
17	AQ24	561.948 1.145.178	Vinh Trach commune, Thoai Son district	Impacts from aquatic discharge source
18	AQ25	550.885 1.177.362	Hoa Lac commune, Phu Tan district	Impact of wastewater from pond fish farming area of Hoa Lac

Methods of Sampling, Preserving, and Analyzing Water Samples

The parameters for the assessment of 18 water samples included: Temperature, pH, Dissolved Oxygen (DO), Chemical oxygen demand (COD), Biological oxygen demand (BOD₅), Total Suspended Solids (TSS), Ammonium (N-NH₄⁺), Nitrate (N-NO₃⁻), Phosphate (P-PO₄³⁻), Total Nitrogen (TN), Total Phosphorus (TP) and Coliform.

The order and methods of environmental monitoring were implemented in accordance with Circular 24/2017/TT-BTNMT on promulgating technical regulations on environmental monitoring and Vietnamese standards and regulations (Vietnam Ministry of Natural Resources and Environment, 2017). Surface water and wastewater were sampled and preserved according to the methods in TCVN 6663-1:2011 and TCVN 6663:3:2016 (Vietnam Ministry of Science and Technology, 2011; Vietnam Ministry of Science and Technology, 2016).

Methods of analyzing samples were in accordance with Standard Methods (Lipps et al., 2018a, 2018b, 2018c, 2018d, 2018e, 2018f) and Vietnam National standard on water quality (Vietnam Ministry of Science and Technology, 1995, 1996, 2000, 2011, 2016) (Tables 2 and 3). Measuring probe used to measure temperature, DO, and pH was PCD 650/pH 600 Eutech.

Table 2

Method of analyzing/measuring water samples

No.	Parameter	Method of analyzing / measuring
1	Chemical oxygen demand (COD)	SMEWW 5220C:2017
2	Biological oxygen demand (BOD ₅)	SMEWW 5210B:2017
3	Total Suspended Solids (TSS)	SMEWW 2540D:2017
4	Ammonium (N-NH ₄ ⁺)	TCVN 5988:1995
5	Total Nitrogen (TN)	TCVN 6638:2000
6	Total Phosphorus (TP)	SMEWW 4500.P.B&E:2017

Table 2 (Continue)

No.	Parameter	Method of analyzing / measuring
7	Nitrate (N-NO ₃ ⁻)	SMEWW 4500-NO ₃ -E:2017
8	Phosphate (P-PO ₄ ³⁻),	SMEWW 4500-P.E:2017
9	Coliform	TCVN 6187-2:1996

Water Quality Assessment

The analytical results of water samples were compared with surface water quality parameters according to QCVN:08-MT:2015/BTNMT-National technical regulation on the surface water quality of Vietnam (Vietnam Ministry of Natural Resources and Environment, 2015).

The Water Quality Index (WQI) was calculated based on Decision 1460/QD-TCMT on promulgating technical guidelines for calculation and the Vietnam water quality index (VN_WQI) (Vietnam Environment Administration, 2019). This study's parameters used to calculate WQI include temperature, pH, DO, BOD₅, COD, N-NO₃⁻, N-NH₄⁺, P-PO₄³⁻, and Coliform.

The calculation equations are as follows:

For parameters of BOD₅, COD, N-NO₃⁻, N-NH₄⁺, P-PO₄³⁻, Coliform, and WQI are calculated according to the following Equation 1:

$$WQI_{SI} = \frac{q_i - q_{i+1}}{BP_{i+1} - BP_i} (BP_{i+1} - C_p) + q_{i+1} \quad [1]$$

In particular:

WQI_{SI} (SI: sub-index): is the water quality index calculated for each parameter

BP_i: lower limit concentration of monitoring parameters corresponding to level i

BP_{i+1}: upper limit concentration of monitoring parameters corresponding to level i+1

q_i: WQI at level i given corresponds to BP_i

q_{i+1}: WQI at level i+1 corresponds to BP_{i+1}

C_p: Monitoring parameters are taken into account

Calculating WQI_{DO} using Equation 2:

$$WQI_{SI} = \frac{q_{i+1} - q_i}{BP_{i+1} - BP_i} (C_p - BP_i) + q_i \quad [2]$$

In particular:

WQI_{SI} (SI: sub-index): is the water quality index calculated for each parameter

C_p: Saturated DO%

BP_i, BP_{i+1}, q_i, q_{i+1} are the values corresponding to the level i, i+1

Calculating WQI_{pH} :

If $pH < 5.5$ or $pH > 9$, $WQI_{pH} = 10$.

If $5.5 < pH < 6$, using Equation 2 to calculate WQI_{pH}

If $6 \leq pH \leq 8.5$, $WQI_{pH} = 100$

If $8.5 < pH < 9$, using Equation 1 to calculate WQI_{pH}







After calculating WQI for each of the above parameters, the WQI calculation is applied according to the following Equation 3:

$$WQI = \frac{WQI_{pH}}{100} \left[\frac{1}{6} (\sum_{i=1}^6 WQI_a)^2 \times WQI_b \right]^{\frac{1}{3}} \quad [3]$$

where WQI_a : The value of WQI has been calculated for six parameters: DO, BOD₅, COD, N-NO₃⁻, N-NH₄⁺, P-PO₄³⁻; WQI_b : WQI value calculated for Total Coliform; WQI_{pH} : WQI has calculated for pH coefficient.

Table 3 displays the water quality rating based on Water Quality Index ranges and recommendations for surface water usage.

Table 3
Water quality rating and recommendation of usage

Water quality Index Range	Water Quality Rating	Color	Intended use
91-100	Excellent		Good for water supply
76-90	Good		For water supply but requires appropriate treatment measures
51-75	Medium		For irrigation and other similar purposes
26-50	Poor		For water transport and other similar purposes
10-25	Polluted		Water is heavily polluted and requires future treatment
<10	Serious polluted		Water is poisoned and requires treatment

Note. From “Decision 1460/QD-TCMT on promulgating technical guidelines for calculation and Vietnam water quality index (VN_WQI)” by Vietnam Environment Administration, 2019

Assessment of Wastewater Quality of Pangasius Catfish Ponds

Two fish farms raising pangasius catfish were selected in Chau Phu district, An Giang province. Aquaculture wastewater was sampled in the pangasius catfish ponds of these two fish farms and analyzed parameters of SS, COD, BOD₅, N-NH₄⁺, Total N, and Total P.

There are two growth stages of the pangasius catfish. In the first three months of the farming season, food must be ensured to have a protein content of 25–28%. In the fourth month until harvest, the protein content of the feed is reduced to 18–22%. Therefore, the study collected wastewater samples in two stages in two fish farms:

Stage 1: Wastewater was sampled in pangasius catfish ponds of Fish Farm 1 in the first three months of the farming season. Fish Farm 1 has a pond water surface area of 12,500 m² 2 m deep water level. Farmers used homemade food combined with industrial feed with a 25–28% protein content. Wastewater was changed periodically every three days and discharged 10% of the water in the pond with a flow of 2,500 m³/day and night.

Stage 2: Wastewater was sampled in pangasius catfish ponds of Fish Farm 2 in the fourth month until the harvest: Fish Farm 2 has a pond water surface area of 8,000 m², 2 m deep of water level. Farmers fully used industrial pellets with a protein content of 18–22%. Wastewater was changed every three days and discharged 30% of the water in the pond with a flow of 4,800 m³/day and night.

Selection of Native Aquatic Plants

In the areas affected by wastewater from two selected fish farms in Chau Phu district, a survey was conducted to identify native aquatic plant species and determine the density of aquatic plants. Identification of plant species was based on An Illustrated Flora of Vietnam parts I, II, II (Ho, 1999a, 1999b, 1999c) and Common weeds in Vietnam (Koo et al., 2000). Floating aquatic plants were collected from the wastewater discharge area of the fishponds. The Quadrat method (Dan et al., 2012; Rastogi, 1999) was applied to determine the density of aquatic plants in the study site. The area of each quadrat was 1 m² (1 m x 1m). Five transects were laid in the study site. In each transect, four quadrats were laid from the riverbank to determine the frequency of species occurrence (%). All aquatic plants presented in the quadrant were recorded. The frequency of occurrence and density was defined by Equations 4 and 5.

Frequency of occurrence (%):

$$F_i = \frac{a}{b} \times 100 \quad [4]$$

Where: F_i : Frequency of occurrence of species i (%); a : Number quadrats with the species i ; b : Total number of quadrats studied

Density (plants/m²):

$$D_i = \frac{n_i}{N} \quad [5]$$

Where: D_i : Density of species i ; n_i : Total number of plants of species i ; N : Total number of quadrats studied

Design of Experiment

The study was carried out at two selected fish farms in Chau Phu district, An Giang province. The experiment had three main parts: wastewater tank, wastewater, and floating aquatic plants. The wastewater tank was surrounded by bamboo poles and had a waterproof rubber lining with dimensions of 1.5 m x 1.5 m x 1 m. The depth of water level for planting plants was 0.8 m. So, the total water storage volume is 1.8 m³ (1.5 m x 1.5 m x 0.8 m). Floating aquatic plants were collected at the wastewater discharge area according to the survey density. Water hyacinth plants in the experiment had a length of 20 cm and 4–5 leaves. Their roots were cut, and their damaged stems and leaves were removed. Water hyacinth plants were put in clean water for seven days before the experiment (Loc, 2015).

Morning glory plants and climbing dayflowers in the experiment were young, immature, healthy, and uniform in color with a height of 20 cm and were washed with distilled water before the experiment (Khoi et al., 2012). The frame of the aquatic floating raft was made of D90mm PVC pipe, the length and width of the raft were 1 m x 1 m, and the net supporting the aquatic plants in groups was a polyethylene net with meshes of 2 cm. Wastewater was collected at the wastewater discharge pipe of two fishponds in the selected fish farms above for each stage. Aquatic plants were arranged in floating rafts with a distance between plants of 30 cm and a distance between rows of 30 cm across the wastewater tank. According to the test in practice, this distance was the appropriate distance for arrangement and suitable for the size of the plants. In each floating raft, there were three types of plants, including nine groups of plants with 2–3 types of plants per group. The density of plants was arranged in the rafts according to the actual density investigated in the survey area. Then the rafts were fixed with ropes in the wastewater tank.

Figure 2 displays the wastewater tank and floating raft, and Figure 3 displays the design of the experiment.

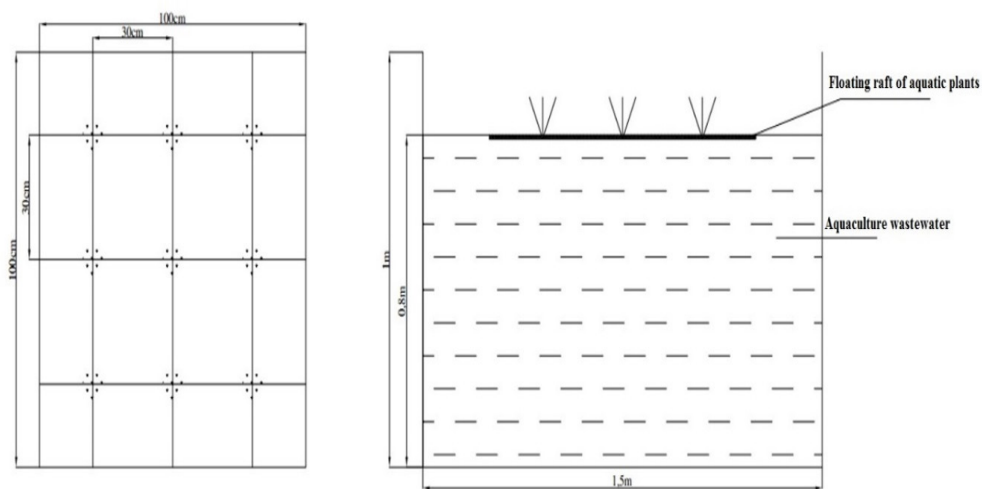


Figure 2. The wastewater tank and the floating raft of aquatic plants

The experiment was arranged in batch form, loaded with water once, with the following treatments:

Treatment 1 (T1): Wastewater in the first three months of the farming season + aquatic flora with actual density investigated in the natural area

Treatment 2 (T2): Wastewater in the first three months of the farming season (control)

Treatment 3 (T3): Wastewater in the fourth month until harvest + aquatic flora with actual density investigated in the natural area

Treatment 4 (T4): Wastewater in the fourth month until harvest (control)

Each treatment was repeated thrice with a maximum retention time of 28 days. Wastewater was sampled after seven days, 14 days, 21 days, and 28 days with one sample per treatment in the morning. Water quality was evaluated through parameters such as SS, COD, BOD₅, N-NH₄⁺, Total N, and Total P. The analytical results of water samples were compared with surface water quality parameters according to QCVN 40:2011/ BTNMT–National Technical Regulations on industrial wastewater, column A (Vietnam Ministry of Natural Resources and Environment, 2011). The plant growth ability in the wastewater treatment tank was evaluated by counting the number of branches of each plant at each experimental stage and measuring the length of the plant’s stem before and after the experiment of 28 days.

Wastewater samples were collected with a volume of 2 L in the middle of the tank with a depth of about 20 cm according to Vietnamese standards—TCVN 6663-1:2011. Wastewater samples after collection were analyzed immediately for physico-chemical criteria or acidified and refrigerated at 4°C if not analyzed immediately, according to Vietnamese standards—TCVN 6663:3:2016.



Wastewater tank

Floating raft with aquatic plants

Figure 3. Design of experiment

Microsoft Excel 2010 was used to synthesize data, and Statgraphics software to analyze and process data on treatment efficiency as well as statistics on the difference in treatment efficiency at different pollutant loads and hydraulic retention time. In this study, the removal percentages (%) of SS, COD, BOD₅, N-NH₄⁺, Total N, and Total P were calculated by the following Equation 6 (de Vasconcelos et al., 2021):

$$\%R = 100 - \left(100 \times \frac{CE_t}{CE_b} \right) \quad [6]$$

Where: %R is the removal percentage, CE_t is the nutrient concentration in the treated effluent, and CE_b is the nutrient concentration in the raw effluent.

RESULTS AND DISCUSSION

Surface Water Quality Assessment of Areas Affected by Aquaculture Wastewater in An Giang Province

The results of surface water monitoring affected by aquaculture areas in An Giang province in the first six months of 2021 (Tables 4 and 5) showed that 7/10 parameters at sampling locations, including DO, TSS, COD, BOD₅, P-PO₄³⁻, N-NH₄⁺ and Coliform that exceeded allowable limits in the National technical regulation on surface water quality of Vietnam—QCVN 08-MT:2015/BTNMT (column A1); pH and N-NO₃⁻ were within the allowable limits. DO of surface water at the aquaculture areas ranged from 2.12–5.26 mg/L, which was 1.14–2.83 times lower than the allowable limits in National technical regulations at 18/18 sampling locations. TSS of surface water at the aquaculture areas ranged from 45–112 mg/L, which was 2.25–5.60 times higher than the allowable limits in National technical regulations at 18/18 sampling locations.

COD of surface water at the aquaculture areas ranged from 14–79 mg/L, 1.40–7.90 times higher than the allowable limits in National technical regulations at 18/18 sampling locations. BOD₅ of surface water at the aquaculture areas ranged from 8–50 mg/L, 2–12.5 times higher than the allowable limits in National technical regulation at 18/18 sampling locations. P-PO₄³⁻ of surface water at the aquaculture areas ranged from 0–0.996 mg/L that were 1.21–9.96 times higher than the allowable limits in National technical regulation at 11/18 sampling locations. N-NH₄⁺ of surface water at the aquaculture areas ranged from 0.126–6.98 mg/L, which was 1.04–23.27 times higher than the allowable limits in National technical regulation at 18/18 sampling locations. Coliform of surface water at the aquaculture areas ranged from 1.5–110 MPN/100 mL, which was 1.72–44 times higher than the allowable limits in National technical regulations at 17/18 sampling locations. The pH of surface water in the aquaculture areas ranged from 6.63–7.51, all within the allowable limits according to the National Technical Regulation. N-NO₃⁻ of surface water

at the aquaculture areas ranged from 0.032–0.327, all within the allowable limits according to the National Technical Regulation. The results of monitoring surface water affected by aquaculture areas in the first six months of 2021 (Tables 4 and 5) show that pond fish farming had higher pollution than cage and raft floating fish farming. The main reason is that the ponds are often more stagnant than cage and raft floating fish, and their exchange and water self-cleaning capacities are also more limited. Therefore, the wastewater needs to be treated before being discharged into the receiving source.

In An Giang, pond fish farming is the main form with high economic efficiency. It refers to the commercial cultivation and the rearing of fish in the enclosures as ponds for food production. The main cultured species of pond fish farming are pangasius conchophilus, tinfoil barb, mozambique tilapia, snakehead fish, and red tilapia. Most aquaculture wastewater from fishponds is discharged directly into rivers and canals (accounting for approximately 90% of farming areas) (An Giang Department of Natural Resources and Environment, 2020). Cage culture is an aquaculture production system with fish in floating net pens. The cage culture of fish utilizes existing water resources but encloses the fish in a cage or basket, which allows water to pass freely between the fish and the pond, permitting water exchange and waste removal into the surrounding water (Soltan, 2016). The main cultured species of cage culture are pangasius, snakehead fish, giant freshwater prawns, mozambique tilapia, catfish, and flounder.

Several aquatic species are commercially produced in the Mekong delta, of which striped catfish (*Pangasius*) is the most important. There are two kinds of feed used in catfish farming in Viet Nam—manufactured pelleted feeds (MPF) and farm-made feeds (FMF). The most used ingredients in MPF are fishmeal, soybean meal, rice bran, blood meal, and meat and bone meal. The FMF is formulated from inexpensive, locally available feed ingredients, including rice bran, broken rice, fresh trash fish and/or dried trash fish, soybean meal, and fishmeal (Nguyen, 2013). Catfish absorb only 27–30% nitrogen, 16–30% phosphorus, and 25% organic matter from the feed; the rest was retained in the aquatic environment. This excess food affected the quality of the pond water environment and the growth and normal development of aquatic species, especially the rate of fish parasite infection (Gross, 1989). Before treatment, pond waters are tainted by fish feces, uneaten feed, dead fish, and related chemicals, including toxic substances and pathogens (Nguyen et al., 2014).

Table 4
 Analytical results of surface water affected by raft floating fish farming areas

Code	Month	Temperature		pH	DO	TSS	COD	BOD ₅	N-NO ₃ ⁻	P-PO ₄ ³⁻	N-NH ₄ ⁺	Coliform
		°C	mg/L									
AQ1	Mar	30.8	51	7.13	5.08	51	17	11	0.036	ND	0.413	15,000
	Jun	30.9	64	7.38	3.87	64	29	18	0.180	0.121	0.978	110,000
AQ3	Mar	27.4	47	7.23	5.05	47	16	10	0.122	0.045	0.314	9,300
	Jun	30.8	48	7.20	3.33	48	14	9	0.236	0.056	0.438	75,000
AQ4	Mar	27.2	45	7.21	4.95	45	18	12	0.063	0.063	0.484	7,500
	Jun	32.0	49	7.04	3.50	49	17	11	0.085	0.064	0.666	24,000
AQ19	Mar	30.8	46	7.22	5.12	46	15	10	0.061	0.065	0.189	24,000
	Jun	31.8	51	7.16	4.99	51	19	12	0.047	0.052	0.654	9,300
National technical regulation			20	6-8.5	≥6	20	10	4	2	0.1	0.3	2,500

Notes: "Underline": The value does not meet the standard according to QCVN 08-MT:2015/BTNMT: National technical regulation on surface water quality, column A1 ; ND = Not detected

Table 5
Analytical results of surface water affected by pond fish farming areas

Code	Month	Temperature		DO	TSS	COD	BOD ₅	N-NO ₃ ⁻	P-PO ₄ ³⁻	N-NH ₄ ⁺	Coliform
		°C	pH								
AQ2	Mar	29.5	7.27	4.75	56	24	16	0.087	0.041	1.21	15,000
	Jun	29.8	7.20	5.13	57	31	20	0.117	0.285	2.94	15,000
AQ5	Mar	28.4	6.72	2.99	68	67	43	0.06	0.904	4.5	24,000
	Jun	32.8	6.63	2.59	73	79	50	0.12	0.996	6.98	15,000
AQ6	Mar	27.9	6.85	5.26	46	19	12	0.131	0.077	0.47	4,300
	Jun	31.5	7.12	2.36	48	16	10	0.18	0.042	0.385	93,000
AQ8	Mar	28.3	7.19	5.11	50	20	13	0.077	ND	0.934	9,300
	Jun	31.6	7.3	4.98	46	24	15	0.106	0.08	0.673	2,300
AQ11	Mar	28.7	6.89	3.91	89	32	21	0.093	0.057	2.46	24,000
	Jun	32.8	7.35	4.31	60	32	21	0.122	0.277	3.01	46,000
AQ13	Mar	31.6	7.51	3.82	112	21	13	0.094	0.187	2.72	4,300
	Jun	33.7	7.45	2.67	58	26	16	0.221	0.049	1.06	9,300
AQ14	Mar	28.9	6.91	4.03	52	24	15	0.096	0.089	3.03	9,300
	Jun	33.1	7.28	4.69	55	28	17	0.203	0.202	1.94	24,000

Table 5 (Continue)

Code	Month	Temperature		DO	TSS	COD	BOD ₅	N-NO ₃ ⁻	P-PO ₄ ³⁻	N-NH ₄ ⁺	Coliform
		°C	pH								
AQ15	Mar	28.7	6.91	4.07	55	30	20	0.08	0.039	1.75	9,300
	Jun	33.3	7.29	4.71	50	29	18	0.117	0.189	2.35	9,300
AQ20	Mar	31.6	7.18	4.54	46	20	13	0.032	ND	0.311	9,300
	Jun	29.6	7.18	4.86	48	14	8	0.208	0.042	0.391	15,000
AQ21	Mar	29.1	6.89	3.13	98	39	25	0.11	0.172	1.74	46,000
	Jun	32.6	7.23	2.12	60	32	21	0.068	0.201	2.72	21,000
AQ22	Mar	30.1	7.19	3.51	48	32	21	0.132	0.516	2.81	15,000
	Jun	32.3	6.97	2.23	56	34	22	0.185	0.279	2.56	7,500
AQ23	Mar	31.2	7.15	4.26	48	21	14	0.192	0.845	3.41	4,300
	Jun	28.9	7.18	5.08	54	15	10	0.327	0.031	0.199	2,300
AQ24	Mar	29.8	7.16	4.18	53	14	9	0.124	0.042	0.459	9,300
	Jun	33.6	7.31	4.81	64	22	14	0.188	0.089	1.25	110,000
AQ25	Mar	29.4	7.36	4.69	45	15	10	0.088	0.041	0.126	2,300
	Jun	31.4	7.18	4.81	59	31	19	0.281	0.243	4.29	1,500
National technical regulation			6-8.5	≥6	20	10	4	2	0.1	0.3	2,500

Notes: "Underline": The value does not meet the standard according to QCVN 08-MT:2015/BTNMT: National technical regulation on surface water quality, column A1; ND = Not detected

Figure 4 displays that the quality of surface water affected by aquaculture areas according to the Water Quality Index in the first six months of 2021 ranged from the level of pollution (water is heavily polluted, needing future treatment) to the good level (water could be used for domestic water supply but requires appropriate treatment measures). Surface water quality was suitable for water transport purposes for the monitoring period. Farmers need to have measures and technology to treat wastewater to meet national standards before discharging it to surface water sources.

Figure 4 shows that AQ5 was the most polluted site. The reason was that this was the site with the largest area of fishpond farming, with a large amount of wastewater discharged to the watercourse. Besides, water samples were collected in the Xang Vinh Tre canal, which has poor circulation, and low self-cleaning ability, leading to the most polluted water quality. The water quality at AQ6, AQ8, AQ23, and AQ25 was much better. Because these sites had a small area of fishpond farming compared to other sites, and the amount of wastewater discharged was small. Water samples were collected in the river with good circulation and self-cleaning ability, so the water quality was less polluted.

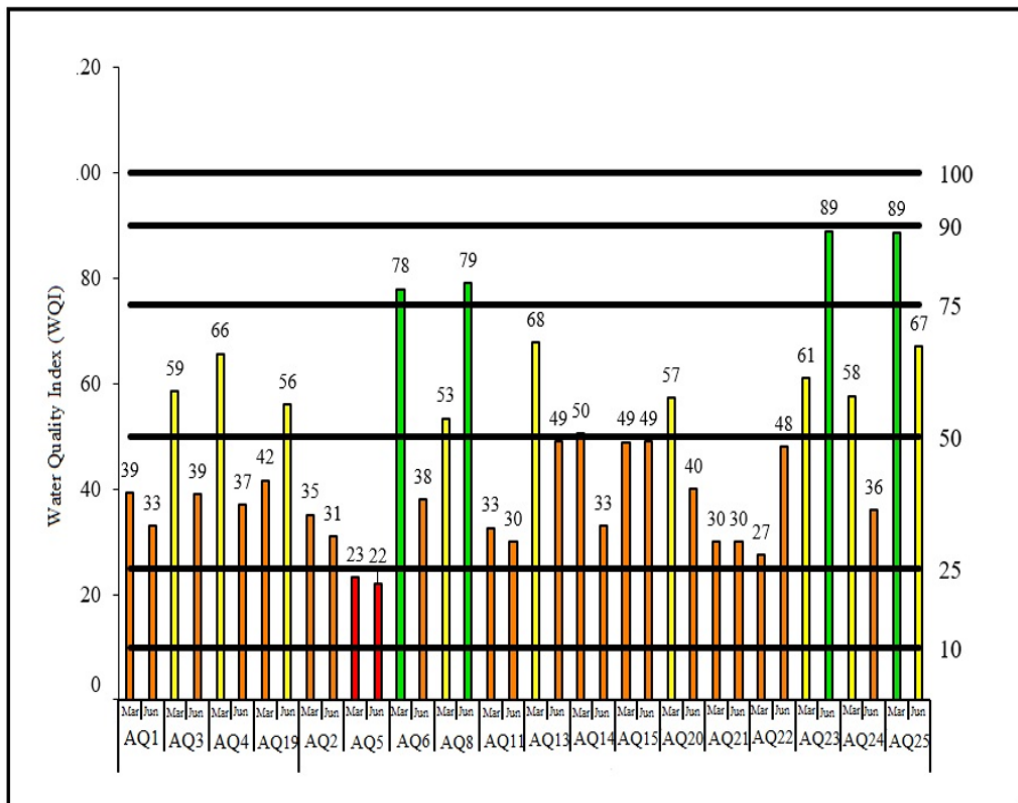


Figure 4. Water Quality Index of surface water

Analytical Results of Wastewater Samples from Pangasius Catfish Fishponds

The results of the wastewater sample analysis of the two catfish ponds are shown in Table 6. The results showed that all parameters have values exceeding the allowable standards according to QCVN 40:2011/BTNMT—National Technical Regulations on industrial wastewater, column A. That means the aquaculture wastewater of these two fish farms needs to be treated before being discharged into the receiving watercourse.

Table 6

Analytical results of two fishponds at two fish farms in Chau Phu district

Location	SS	COD	BOD ₅	N-NH ₄ ⁺	Total N	Total P
	mg/L	mg/L	mg/L	mg/L	mg/L	mg/L
Treatment 1 (Fish farm 1)	118	106	68	14.80	<u>22.14</u>	2.38
Treatment 2 (Fish farm 2)	76	60	39	<u>8.93</u>	10.23	4.20
National Technical Regulations	50	75	30	5	20	4

The Density of Aquatic Plants

Through the field survey at two wastewater discharge areas of two fish farms in Chau Phu district, An Giang province, three native species of floating aquatic plants have been found. They were Water hyacinth (*Eichhornia crassipes*), Morning Glory (*Ipomoea aquatica*) and Climbing Dayflower (*Commelina diffusa*). Figure 5 shows three native aquatic plants used in the study. Although there was not a great diversity of species in the two survey areas, all three species are valuable species in the treatment of pollutants in water, which has been proven through many studies (Viet & Hoang, 2004; Nguyen et al., 2020).



Figure 5. Native aquatic plants used in the study

Climbing Dayflower (*Commelina Diffusa*) has the characteristics of Herbaceous creeping, with roots at the nodes, almost hairless, with a soft stem 0.5–1.5 m long. Leaves are slender or oval, 2–6 cm long, 1–2 cm wide, pointed apex, and sheath with hairy margins. The flowers are small, blue, and 1 cm wide. Morning Glory (*Ipomoea aquatica*) is a semi-aquatic tropical plant, a leafy vegetable with a crawling stem on land or in water. Stems are hollow, thick, eye-rooted, usually hairless in the hot season, and hairy in the cold. Leaves are triangular, pointed, sometimes narrow, and long. Flowers are large, white, or purple-pink, light purple flower tubes, and 1–2 flowers on a stalk. Water hyacinth (*Eichhornia crassipes*) is an aquatic herbaceous floating in the water, growing about 30 cm high with round, green, smooth, and smooth leaves and long and narrow arched veins. Leaves entwined like petals. The petiole expands like a porous bubble to help the plant float on the water. The three sepals are like three petals. Water hyacinth roots look like black feathers falling into the water, up to 1 m long. Water hyacinth reproduces very quickly, so it is easy to clog ponds, lakes, and canals (Ho, 1999a, 1999b, 1999c).

The Quadrat method is applied to determine the density of aquatic plants in the survey areas (Dan et al., 2012; Rastogi, 1999). According to the calculation Equations 4 and 5, the frequency of occurrence and density of aquatic plants at each survey area are shown in Table 7.

Table 7
Frequency of occurrence of aquatic plants in the survey areas

Area	Aquatic plants	Frequency of occurrence (%)	Density (plants/m ²)
Area of fish farm 1	Water Hyacinth (<i>Eichhornia crassipes</i>)	90	13
	Morning Glory Plants (<i>Ipomoea aquatica</i>)	85	10
	Climbing dayflower (<i>Commelina diffusa</i>)	80	8
Area of fish farm 2	Water Hyacinth (<i>Eichhornia crassipes</i>)	100	15
	Morning Glory Plants (<i>Ipomoea aquatica</i>)	30	1
	Climbing dayflower (<i>Commelina diffusa</i>)	45	8

The growth ability of water hyacinth, morning glory, and climbing dayflower was shown by the increased number of plants and the stem length during the experiment. From Table 8, the length of the stem and the number of water hyacinths in T1 change from 20 cm to 32 cm and from 13 to 62, respectively. The stem length and the number of morning glory plants in T1 change from 20 cm to 28 cm and from 10 to 43, respectively. The stem length and the number of climbing dayflowers in T1 change from 20 cm to 36 cm and 15 to 71, respectively. The length of the stem and the number of water hyacinths in T2 change from 20 cm to 36 cm and from 15 to 71, respectively. The length of the stem and

the number of morning glory Plants in T2 change from 20 cm to 32 cm and from 1 to 5, respectively. The length of the stem and the number of climbing dayflowers in T2 change from 20 cm to 28 cm and from 8 to 49, respectively. The results showed that, in general, the aquatic plants, including water hyacinth (*Eichhornia crassipes*), morning glory plants (*Ipomoea aquatica*), and climbing dayflower (*Commelina diffusa*), grow and develop well in the aquaculture wastewater. The optimum growth rate of water hyacinth greatly affects wastewater purification efficiency in a continuous system, and nutrient removal was successfully achieved (Rezania et al., 2016). Regarding removal mechanisms, the removal of nitrogen and phosphorus by water hyacinth primarily depended on plant adsorption (Bin et al., 2018).

Table 8
Length of aquatic plants before and after the experiment

Treatment	Aquatic plant	Plant morphology	Before the experiment	End of experiment
T1	Water hyacinth (<i>Eichhornia crassipes</i>)	Length of the stem (cm)	20	32
		The number of plants	13	62
		Number of dead plants		13
	Morning Plory plants (<i>Ipomoea aquatica</i>)	Length of the stem (cm)	20	28
		The number of plants	10	43
		Number of dead plants		3
	Climbing dayflower (<i>Commelina diffusa</i>)	Length of the stem (cm)	20	30
		The number of plants	8	27
		Number of dead plants		4
T3	Water hyacinth (<i>Eichhornia crassipes</i>)	Length of stem (cm)	20	36
		The number of plants	15	71
		Number of dead plants		15
	Morning Glory plants (<i>Ipomoea aquatica</i>)	Length of the stem (cm)	20	32
		The number of plants	1	5
		Number of dead plants		0
	Climbing dayflower (<i>Commelina diffusa</i>)	Length of the stem (cm)	20	28
		The number of plants	8	49
		Number of dead plants		0

The experimental results in Table 8 show that after 28 days of the experiment, there were 13 dead plants of water hyacinth, three dead plants of morning glory, and four dead plants of climbing dayflower in tank T1. There were only 15 plants of water hyacinth, no dead plants of morning glory, and a climbing dayflower in tank T3. Some plants of water hyacinths died in tank T1 and tank T3, possibly due to the competition for nutrients between species at the end of the experiment and the growth cycle of the plants. There were dead plants of morning glory and climbing glory in tank T1 in the first phase of the experiment, possibly because the plants had not yet adapted to the new environment.

The Efficiency of Floating Raft of Native Aquatic Plants on Aquaculture Wastewater Improvement

Variation of Suspended Solids (SS). Figure 6 shows that the concentration of SS in the wastewater in the experimental tanks decreased sharply during the first three months of farming and in the fourth month until harvest. The concentration of SS in the treatment T1 and treatment T2 met the standards for seven days when compared with the National technical regulation on industrial wastewater of Vietnam. During the first three months of the farming, SS removal efficiency was 92.6% in the tanks treated by plants and 83% in the control tanks until the day of 28. In the fourth month until harvest, SS removal efficiency reached 92.7% in the tank-treated plants and 82.8% in the control tank until day 28.

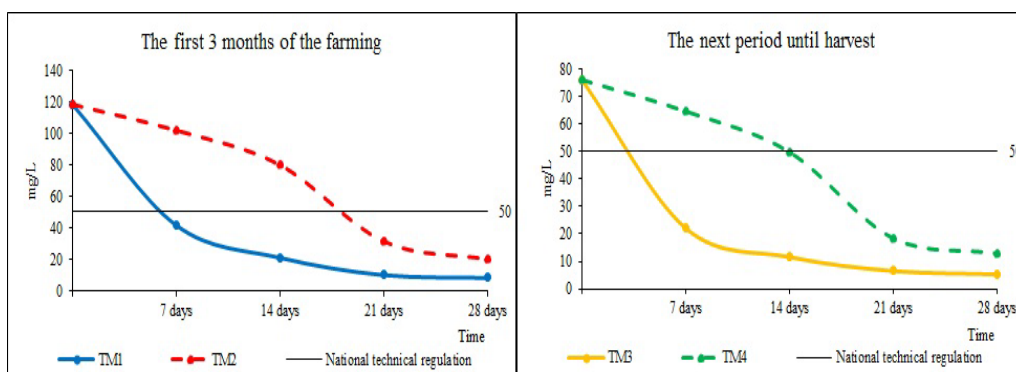


Figure 6. Variation of suspended solids (SS)

Variation of Chemical Oxygen Demand (COD). Figure 7 shows that the concentration of COD in the wastewater in the experimental tanks decreased sharply during the first three months of farming and in the fourth month until harvest. The concentration of SS in the treatment T1 and treatment T2 met the standards for seven days when compared with National technical regulations. During the first 3three months of the farming, COD removal efficiency was 89.6% in the tanks treated by plants and 78.7% in the control tanks until

the day of 28. In the fourth month until harvest, COD removal efficiency reached 89.9% in the tank-treated plants and 78.3% in the control tank until day 28.

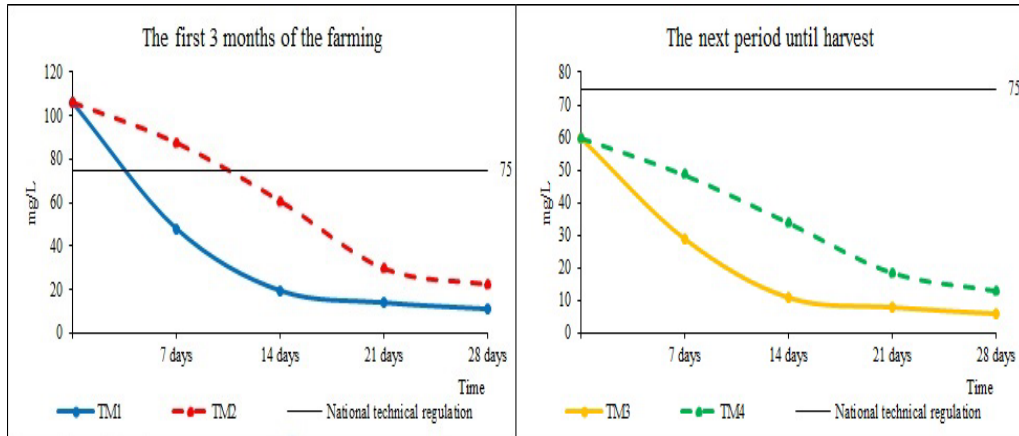


Figure 7. Variation of chemical oxygen demand (COD)

Variation of Biological Oxygen Demand (BOD₅). Figure 8 shows that the concentration of BOD₅ in the wastewater in the experimental tanks decreased sharply during the first three months of the farming and in the fourth month until harvest. The BOD₅ in the treatment T1 and treatment T2 met the standards for seven days compared to National technical regulations. During the first three months of the farming, the BOD₅ removal efficiency was 93.9% in the tanks treated by plants and 82.5% in the control tanks until the day of 28. In the fourth month until harvest, SS removal efficiency reached 91.5% in the tank-treated plants and 79.7% in the control tank until day 28.

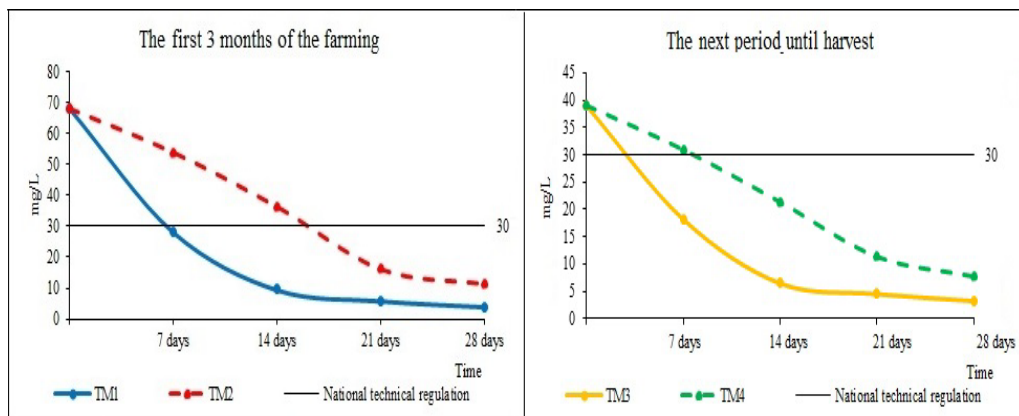


Figure 8. Variation of Biological oxygen demand (BOD₅)

Variation of Ammonium (N-NH₄⁺). Figure 9 shows that the concentration of N-NH₄⁺ in the wastewater in the experimental tanks decreased sharply during the first three months of the farming and in the fourth month until harvest. The concentration of N-NH₄⁺ in the treatment T1 and treatment T2 met the standards for seven days compared with National technical. During the first three months of the farming, the N-NH₄⁺ removal efficiency was 93.4% in the tanks treated by plants and 69.4% in the control tanks until the day of 28. In the fourth month until harvest, N-NH₄⁺ removal efficiency reached 93.6% in the tank-treated plants and 69.5%; in the control tank until day 28.

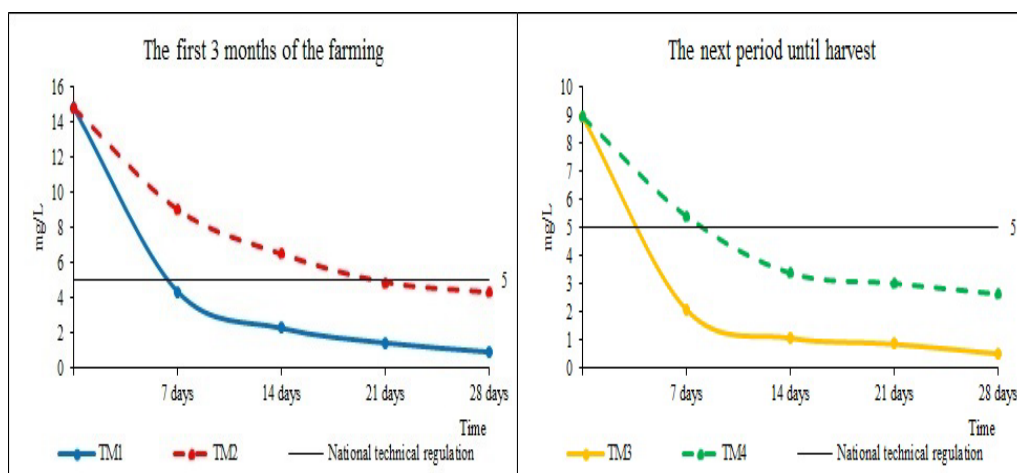


Figure 9. Variation of Ammonium (N-NH₄⁺)

Variation of Total Nitrogen. Figure 10 shows that the concentration of Total Nitrogen in the wastewater in the experimental tanks decreased sharply during the first three months of farming and in the fourth month until harvest. The concentration of SS in the treatment T1 and treatment T2 met the standards for seven days when compared with National technical regulations. During the first three months of the farming, Total Nitrogen removal efficiency was 64.3% in the tanks treated by plants and 34.8% in the control tanks until the day of 28. In the fourth month until harvest, TN removal efficiency reached 67.8% in the tank-treated plants and 32.8% in the control tank until day 28.

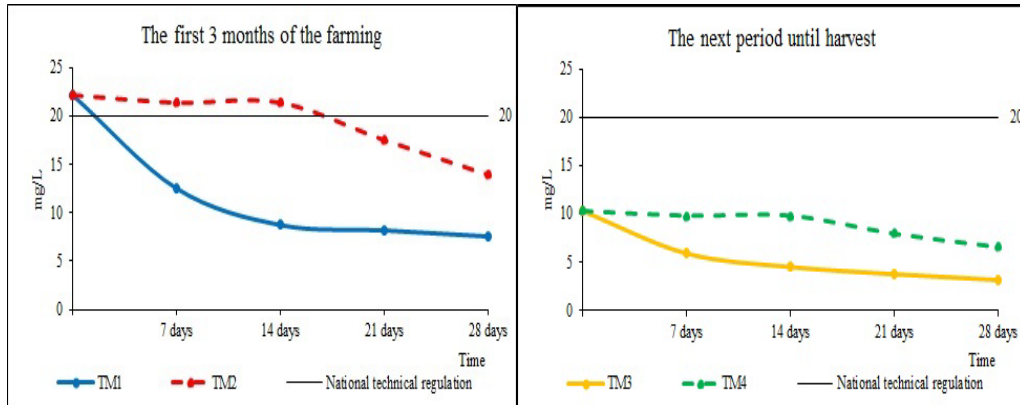


Figure 10. Variation of Total Nitrogen (TN)

Variation of Total Phosphorus. Figure 11 shows that the concentration of TP in the wastewater in the experimental tanks decreased sharply during the first three months of farming and in the fourth month until harvest. The concentration of SS in the treatment T1 and treatment T2 met the standards for seven days when compared with National technical regulations. During the first three months of the farming, TP removal efficiency was 94.6% in the tanks treated by plants and 33.5% in the control tanks until the day of 28. In the fourth month until harvest, TP removal efficiency reached 94% in the tank-treated plants and 35.3% in the control tank until day 28.

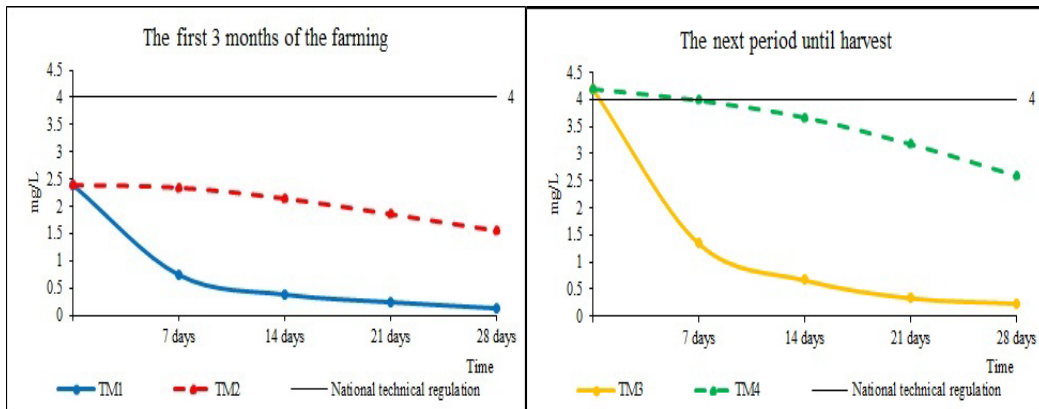


Figure 11. Variation of Total Phosphorus (TP)

In general, using a floating raft of native aquatic plants in the wastewater discharged area to treat aquaculture wastewater is effective. Water Hyacinth (*Eichhornia crassipes*), Morning Glory Plants (*Ipomoea aquatica*), and Climbing dayflower (*Commelina diffusa*)

have strong absorption capacity for nutrients and quickly remove pollutant components in aquaculture wastewater. The quality of wastewater after treatment was significantly improved.

After 28 days of the experiment, the treatment efficiency of SS was 92.6%, COD was 89.6%, BOD₅ was 93.9%, N-NH₄⁺ was 93.4%, TN was 64.3%, TP reached 94.6% in the T1, and the treatment efficiency of SS was 92.7%, COD was 89.9%, BOD₅ was 91.5%, N-NH₄⁺ was 93.6%, TN was 67.8%, TP was 94% in the T3. In order to ensure that aquaculture wastewater meets the standards of National Technical Regulation on industrial wastewater before being discharged to the receiving source with the most optimal time for fish farms, the hydraulic retention time in the wastewater treatment tank must be seven days in both stages.

Water hyacinth, morning glory plants, and climbing dayflowers used in the study are common plants in the Mekong Delta, with diverse uses. Utilizing biomass of these plants after wastewater treatment brings economic value and can increase income for farmers. Morning glory plants and climbing dayflowers can be used as human food in Vietnam. The current price of morning glory plants in Vietnam is about 30,000–40,000 VND/kg. Climbing dayflower is also a medicinal herb that is used in the treatment of many different diseases in humans. All plants can be used as animal feed for poultry and livestock. Water hyacinth is used to make handicraft products. The price of dried water hyacinth on the Vietnamese market currently ranges from 20,000–30,000 VND/kg. In addition, much previous research showed that aquatic plants can be used for bioenergy production and organic fertilizer. By integrating the growth of aquatic plants in a water recycling system to produce biomass, power can be produced from that biomass (Fedler et al., 2007). Water hyacinth is a more promising aquatic plant biomass for bioenergy production (Fedler & Duan, 2011). Farmers in the Mekong Delta can apply water hyacinth and rice straw as additional feeding material for biogas digester in case of pig manure shortage (Ngan et al., 2012; Nam et al., 2017). Silaging and composting water hyacinth plants generated from ponds treating pig farm wastewater were technically and economically feasible to implement at farm scale levels (Polprasert et al., 1994). The study by Vidya and Girish (2014) signified using Water Hyacinth (*Eichhornia crassipes*) as the organic manure. Water Hyacinth can be brought to make compost, mulch, and clean the sewage. The study by Trang et al. (2018) showed that the water hyacinth was suitable for testing the production of microbial organic fertilizers.

Wastewater treatment using aquatic plants does not require much initial construction cost compared to conventional treatment systems, does not require complicated and expensive machinery and equipment, has low operating and maintenance costs, and is easy to manage. Aquatic plants are widely distributed throughout the Mekong Delta. They are easy to collect in many places of the natural environment as riversides, canals, and ponds, which do not cost much for starting materials. After treatment, the biomass of aquatic

plants can be used for many different purposes, bringing economic value. Wastewater treatment by aquatic plants is suitable in rural conditions. The development of vegetation has contributed to bringing landscape value.

CONCLUSION

Surface water quality affected by aquaculture areas in An Giang province did not meet the standards according to QCVN 08-MT: 2015/BTNMT - National technical regulation on surface water quality. The DO content was lower than the allowable standards, and surface water was polluted mainly by suspended solids, organic matter (COD, BOD), nutrients (N, P), and micro-organisms. Using a floating raft of native aquatic plants, including Water hyacinth (*Eichhornia crassipes*), Morning glory plants (*Ipomoea aquatica*), and Climbing dayflower (*Commelina diffusa*) for aquaculture wastewater treatment can improve the wastewater quality. These three species grow and develop well in aquaculture wastewater. After the experiment of 28 days, the removal percentages of SS, COD, BOD₅, N-NH₄⁺, Total N, and Total P were 92.6%, 89.6%, 93.9%, 93.4%, 64.3%, 94.6%, respectively, in the first three months of the farming season. The removal percentages after 28 days of SS, COD, BOD₅, N-NH₄⁺, Total N, and Total P were 92.7%, 89.9%, 91.5%, 93.6%, 67.8%, 94%, respectively, in the fourth month until fish harvest. In order to ensure that the outlet wastewater meets the national standards on industrial wastewater before being discharged into the receiving water source, the most optimal retention time in the wastewater treatment tank is seven days for two stages.

ACKNOWLEDGEMENT

This research is funded by Vietnam National University Ho Chi Minh City (VNU-HCM) under grant number “B2021-16-03.”

REFERENCES

- An Giang Center for Environmental Monitoring and Techniques, Resources. (2019). *Report on results of environmental monitoring in An Giang province November, 2019*. People’s Committee of An Giang province. https://media.angiang.gov.vn/pictures/2021/01/31/58_dinh%20kem_cong%20bo%20hien%20trang%20moi%20truong%20ag%202016-2020.pdf
- An Giang Department of Natural Resources and Environment. (2020). *Report on environmental status of An Giang province in the period 2016-2020*. People’s Committee of An Giang province. https://media.angiang.gov.vn/quan%20trac%20moi%20truong/2019/12/BC%20Ket%20qua%20quan%20trac%20dot%20T11_2019.pdf
- Bin, L., Zhongshuo, X., Jianguo, L., & Xiaoli, C. (2018). Removal of water nutrients by different aquatic plant species: An alternative way to remediate polluted rural rivers. *Ecological Engineering*, 110, 18-26. <https://doi.org/10.1016/j.ecoleng.2017.09.016>

- Dan, T. H., Duy, N. P., & Tho, B. T. (2012). The distribution of aquatic plants in the organic polluted canals in Can Tho City, Vietnam in rainy season. *Can Tho University Journal of Science*, 23a, 283-293.
- de Vasconcelos, V. M., de Morais, E. R. C., Faustino, S. J. B., Hernandez, M. C. R., Gaudêncio, H. R. D. S. C., de Melo, R. R., & Junior, A. P. B. (2021). Floating aquatic macrophytes for the treatment of aquaculture effluents. *Environmental Science and Pollution Research*, 28(3), 2600-2607. <https://doi.org/10.1007/s11356-020-11308-8>
- Fedler, C. B., & Duan, R. (2011). Biomass production for bioenergy using recycled wastewater in a natural waste treatment system. *Resources, Conservation and Recycling*, 55(8), 793-800. <https://doi.org/10.1016/j.resconrec.2011.04.001>
- Fedler, C. B., Hammond, R., Chennupati, P., & Ranjan, R. (2007). *Biomass Energy Potential from Recycled Wastewater*. Texas Tech University. <https://doi.org/10.13140/RG.2.1.3061.8009>
- Giao, N. T., Nhien, H. T. H., Anh, P. K., & Van Ni, D. (2021). Classification of water quality in low-lying area in Vietnamese Mekong delta using set pair analysis method and Vietnamese water quality index. *Environmental Monitoring and Assessment*, 193(6), 1-16. <https://doi.org/10.1007/s10661-021-09102-1>
- Grosse, W. (1989). Thermoosmotic air transport in aquatic plants affecting growth activities and oxygen diffusion to wetland soils. In D. A. Hammer (Ed.), *Constructed Wetlands for Wastewater Treatment* (1st ed., pp. 416-469). Lewis Publishers. <https://doi.org/10.1201/9781003069850>
- Ha, N. N., Huong, T. T. T., & Van, T. T. (2021). Surface water pollution risk from Vietnam Water Quality Index (VN-WQI) in the Ca Mau City, Mekong Delta. *Nature Environment & Pollution Technology*, 20(4), 1449-1464. <https://doi.org/10.46488/NEPT.2021.v20i04.007>
- Ho, P. H. (1999a). *An illustrated flora of Vietnam (Part 1)*. Tre Publishing House.
- Ho, P. H. (1999b). *An illustrated flora of Vietnam (Part 2)*. Tre Publishing House.
- Ho, P. H. (1999c). *An illustrated flora of Vietnam (Part 3)*. Tre Publishing House.
- Khanh, N., Kitaya, Y., Xiao, L., Endo, R., & Shibuya, T. (2013). Selection of microalgae suitable for culturing with digestate from methane fermentation. *Environmental Technology*, 34(13-14), 2039-2045. <https://doi.org/10.1080/09593330.2013.828093>
- Khanh, N., Kitaya, Y., Xiao, L., Endo, R., & Shibuya, T. (2015). Microalgae culture with digestate from methane fermentation - Effects of pH and concentrations of digestate on growth of *Euglena gracilis*. *Eco-Engineering*, 27(1), 7-11. <https://doi.org/10.11450/seitaikogaku.27.7>
- Khoi, C. M., Dung, N. V. C., & Nhien, C. T. (2012). Khả năng xử lý ô nhiễm đạm, lân hữu cơ hòa tan trong nước thải ao nuôi cá tra của lục bình (*Eichhorina crassipes*) và cỏ vetiver (*Vetiver zizanioides*) [Amelioration of organic nitrogen and phosphorus dissolved in catfish ponds by using water hyacinth (*Eichhornia crassipes*) and vetiver (*Vetiver zizanioides*)]. *Can Tho University Journal of Science*, 21b, 151-160.
- Kieu, C. L. D., Quoc, N. P., Huynh, N. T. T., & Diễm, T. N. T. (2015). Diễn biến thành phần đạm của nước thải ao nuôi thâm canh cá tra (*Pangasianodon hypophthalmus*) trong điều kiện thủy canh cỏ mồm mỡ (*Hymenachne acutigluma*) [The changes of nitrogen in wastewater from intensive catfish (*Pangasianodon hypophthalmus*) in hydraphic conditions of *Hymenachne*grass (*Hymenachne acutigluma*)]. *Can Tho University Journal of Science*, 2015, 80-87.

- Koo, S. J., Kwon, Y. W., Chin, D. V., & Chung, H. A. (2000). *Common Weeds in Vietnam*. Ho Chi Minh City Agricultural Publishing House.
- Lan, T. T., & Long, N. P. (2011). Assessment of surface water quality by Water Quality Index (WQI) at the Cai Sao canal, An Giang province, Vietnam. *Livestock Research for Rural Development*, 23(7), Article 151.
- Li, W., & Li, Z. (2009). *In situ* nutrient removal from aquaculture wastewater by aquatic vegetable *Ipomoea aquatica* on floating beds. *Water Science & Technology*, 59(10), 1937-1943. <https://doi.org/10.2166/wst.2009.191>
- Lipps, W. C., Baxter, T. E., & Braun-Howland, E. (Eds.). (2018a). 2540 Solids. In: *Standard methods for the examination of water and wastewater*: APHA Press.
- Lipps, W.C., Baxter, T. E., & Braun-Howland, E. (Eds.). (2018b). 2550 temperature. APHA Press.
- Lipps, W.C., Baxter, T. E., & Braun-Howland, E. (Eds.). (2018c). 4500 - P Phosphorus. APHA Press.
- Lipps, W.C., Baxter, T. E., & Braun-Howland, E. (Eds.). (2018d). 4500-NO₃ Nitrogen (Nitrate). APHA Press.
- Lipps, W.C., Baxter, T. E., & Braun-Howland, E. (Eds.). (2018e). 5220 Chemical Oxygen Demand (COD). APHA Press.
- Lipps, W.C., Baxter, T. E., & Braun-Howland, E. (Eds.). (2018f). 5210 Biochemical Oxygen Demand (BOD). APHA Press.
- Loc, N. T., Thu, V. T. C., Thinh, D. C., & Hang, P. T. (2015). Evaluation of treatment efficiency of domestic wastewater by aquatic plants. *Can Tho University Journal of Science*, 2015, 119-128.
- Minh, K. C., Chi, D. N. V., & Thi, Nhen, C. (2012). Khả năng xử lý ô nhiễm đạm, lân hữu cơ hòa tan trong nước thải ao nuôi cá tra của lục bình (*Eichhorina crassipes*) và cỏ vetiver (*Vetiver zizanioides*) [The ability to treat organic nitrogen and phosphorus of water hyacinth (*Eichhornia crassipes*) and vetiver (*Vetiver zizanioides*) in ponds used for intensive catfish (*Pangasianodon hypophthalmus*) cultivation]. *Can Tho University Journal of Science*, 21b, 151-160.
- Nam, T. S., Ingvorsen, K., Khanh, H. V., Kha, L. T. M., Thao, H. V., Viet, L. H., Chiem, N. H., & Ngan, N. V. C. (2017). Khả năng sinh khí biogas của rơm và lục bình theo phương pháp ủ yếm khí theo mẻ với hàm lượng chất rắn khác nhau [The possibility of producing biogas from rice straw and water hyacinth at different VS's concentration in batch anaerobic experiment]. *Can Tho University Journal of Science*, 1, 93-99. <https://doi.org/10.22144/ctu.jsi.2017.035>
- Ngan, N. V. C., Thanh, N. T., & Loc, N. H. (2012). Potential use of water hyacinth and rice straw as additional loading materials for biogas digester. *Can Tho University Journal of Science*, 2012(22a), 213-221.
- Nguyen, P. Q., Le, H. Y., Cong, N. V., & Phu, T. Q. (2014). Diễn biến một số chỉ tiêu chất lượng nước trong ao nuôi cá tra (*Pangasianodon hypophthalmus*) thâm canh [Variation of some water quality parameters in intensive catfish (*Pangasianodon hypophthalmus*) ponds]. *Can Tho University Journal of Science*, 34, 128-136.
- Nguyen, T. H. A., Hieu, T. T., Van Tung, T., Thang, N. V., Nguyen, H. K., Quoc Vi, L., Thao, N. T. P., & Thanh Hai, L. (2020). Study on the proposal of a community of freshwater aquaculture and vegetable farming in An Giang. *Science & Technology Development Journal - Science of The Earth & Environment*, 4(1), 115-127. <https://doi.org/https://doi.org/10.32508/stdjsee.v4i1.505>

- Nguyen, T. P. (2013). On-farm feed management practices for striped catfish (*Pangasianodon hypophthalmus*) in Mekong River Delta, Viet Nam. *FAO Fisheries and Aquaculture Technical Paper*, 583, 241-267.
- Nhien, L. T. M., & Trang, N. T. D. (2013). Vai trò của bèo bồng trong hệ thống đất ngập nước kiến tạo xử lý nước thải ao nuôi cá tra thâm canh tuần hoàn kín [The role of *Typha orientalis* in constructed wetlands for treatment close-recirculated intensive catfish culture]. *Can Tho University Journal of Science*, 29, 31-36.
- Polprasert, C., Kongsricharoern, N., & Kanjanaprapin, W. (1994). Production of feed and fertilizer from water Hyacinth plants in the tropics. *Waste Management & Research*, 12(1), 3-11. [https://doi.org/10.1016/s0734-242x\(94\)90016-7](https://doi.org/10.1016/s0734-242x(94)90016-7)
- Rastogi, A. (1999). Methods in applied ethnobotany: Lesson from the field. In *Discussion paper series - Mountain Natural Resources, International Centre for Integrated Mountain Development* (p.72). International Center for Integrated Mountain Development.
- Rezania, S., Din, M. F. M., Taib, S. M., Dahalan, F. A., Songip, A. R., Singh, L., & Kamyab, H. (2016). The efficient role of aquatic plant (water hyacinth) in treating domestic wastewater in continuous system. *International Journal of Phytoremediation*, 18(7), 679-685. <https://doi.org/10.1080/15226514.2015.1130018>
- Shipin O., Koottatep T., Khanh, N. T. T., & Polprasert, C. (2005). Integrated natural systems for developing communities: Low-tech N-removal through fluctuating microbial pathways. *Water Science and Technology*, 51(12), 299-306. <https://doi.org/10.2166/wst.2005.0488>
- Snow, A. M., & Ghaly, A. E. (2008). A Comparative study of the purification of aquaculture wastewater using water Hyacinth, water lettuce and parrot's feather. *American Journal of Applied Sciences*, 5(4), 440-453. <https://doi.org/10.3844/ajassp.2008.440.453>
- Soltan, M. (2016). *Cage culture of freshwater fish*. ResearchGate. <https://doi.org/10.13140/RG.2.1.4802.2803>
- Trang, T., V., Hung, N., T., Q., & Kỳ, N., M. (2018). Nghiên cứu ảnh hưởng của cây lục bình (*eichhornia crassipes*) đến môi trường nước mặt kênh trần văn đồng và đề xuất thu gom sản xuất phân hữu cơ vi sinh [The study of the effects of water hyacinth (*eichhornia crassipes*) on surface water resources in tran van dong canal and proposing solutions to make microbial organic fertilizer]. *Journal of Environmental and Hydraulic Science Technology*, 61, 37-61.
- Vidya, S., & Girish, L. (2014). Water hyacinth as a green manure for organic farming. *International Journal of Research in Applied, Natural and Social Sciences*, 2(6), 65-72.
- Viet, L. H., & Hoang, N. X. (2004). Wastewater treatment by water Hyacinth. *Can Tho University Journal of Science*, 21b, 151-160.
- Vietnam Environment Administration. (2019). *Decision No.1460/QĐ-TCMT on Promulgating Technical Guidelines for Calculation and Publication of Vietnam Water Quality Index (VN_WQI)*. https://cem.gov.vn/storage/news_file_attach/QĐ%201460%20TCMT%20ngày%202012.11.2019%20WQI.pdf
- Vietnam Ministry of Natural Resources and Environment. (2011). *QCVN 40:2011/BTNMT – National Technical Regulations on Industrial Wastewater*. <https://emas.tdtu.edu.vn/sites/emas/files/EMAS/V%C4%83n%20b%E1%BA%A3n%20ph%C3%A1p%20lu%E1%BA%ADt/qc-vn-40-n%C6%B0%E1%BB%9Bc-th%E1%BA%A3i-cn.pdf>

- Vietnam Ministry of Natural Resources and Environment. (2015). *QCVN 08-MT:2015/BTNMT-National Technical Regulation on Surface Water Quality Of Vietnam*. <http://cem.gov.vn/storage/documents/5d6f3ecb26484qcvn-08-mt2015btnmt.pdf>
- Vietnam Ministry of Natural Resources and Environment. (2017). *Circular 24/2017/TT-BTNMT on Promulgating Technical Regulations on Environmental Monitoring and Vietnamese Standards and Regulations*. http://vanban.chinhphu.vn/portal/page/portal/chinhphu/hethongvanban?class_id=1&mode=detail&document_id=191603&category_id=0
- Vietnam Ministry of Science and Technology. (1995). *TCVN 5988:1995 -Vietnam National Standard on Water Quality- Determination of Aminoium - Distillation and Titration Method*. <https://tieuchuan.vsqi.gov.vn/tieuchuan/view?sohieu=TCVN+5988%3A1995>
- Vietnam Ministry of Science and Technology. (1996). *TCVN 6187-2:1996 - Vietnam National Standard on Water Quality-Detection and Enumeration of Organisms Thermotolerant Coliform Organisms and Presumptive Escherichia Coli. Part 2: Multiple Tube (most probable number) method*. <https://tieuchuan.vsqi.gov.vn/tieuchuan/view?sohieu=TCVN%206187-2:2020>
- Vietnam Ministry of Science and Technology. (2000). *TCVN 6638:2000 -Vietnam National Standard on Water Quality - Determination of Nitrogen - Catalytic Digestion after Reduction with Devarda's Alloy* <https://tieuchuan.vsqi.gov.vn/tieuchuan/view?sohieu=TCVN+6638%3A2000>
- Vietnam Ministry of Science and Technology. (2011). *TCVN 6663-1:2011-Vietnam National standard on water quality-Sampling-Part 1: Guidance on the design of sampling*. <https://circabc.europa.eu/sd/a/97d7bd92-e92e-4b42-a2b3-6a1d8d00d81d/National%20Technical%20Regulation%20on%20Industrial%20Wastewater.pdf>
- Vietnam Ministry of Science and Technology. (2016). *TCVN 6663-6:2008-Vietnam National standard on water quality-Sampling-Part 3: Preservation and handling of water samples*. <https://tieuchuan.vsqi.gov.vn/tieuchuan/view?sohieu=TCVN%206663-3:2016>
- Zhang, Q., Achal, V., Xu, Y., & Xiang, W. N. (2014). Aquaculture wastewater quality improvement by water spinach (*Ipomoea aquatica* Forsskal) floating bed and ecological benefit assessment in ecological agriculture district. *Aquacultural Engineering*, 60, 48-55. <https://doi.org/10.1016/j.aquaeng.2014.04.002>

Characterising Colour Feature Descriptors for *Ficus carica* L. Ripeness Classification Based on Artificial Neural Network (ANN)

Iylia Adhwa Mazni¹, Samsul Setumin^{1*}, Mohamed Syazwan Osman², Muhammad Khusairi Osman¹ and Mohd Subri Tahir³

¹Faculty of Electrical Engineering, Universiti Teknologi MARA, Cawangan Pulau Pinang, Permatang Pauh, 13500 UiTM, Pulau Pinang, Malaysia

²EMZI-UiTM Nanoparticles Colloids & Interface Industrial Research Laboratory (NANO-CORE), School of Chemical Engineering, College of Engineering, Universiti Teknologi MARA, Cawangan Pulau Pinang, Permatang Pauh, 13500 UiTM, Pulau Pinang, Malaysia

³Department of Business Management, Universiti Teknologi MARA, Cawangan Pulau Pinang, Permatang Pauh, 13500 UiTM, Pulau Pinang, Malaysia

ABSTRACT

Excessive feature dimensions impact the effectiveness of machine learning, computationally expensive and the analysis of feature correlations in the engineering area. This paper uses the colour descriptor to get the most optimal feature to improve time consumption and efficiency. This study investigated *Ficus carica* L. (figs) with three classification stages. The ripening classification of fig was examined using colour features descriptor with two different colour models, RGB and HSV. In addition, the machine learning classification model based on Artificial Neural Network (ANN) that utilised the Feed-Forward Neural Network (FFNN) model to classify the ripeness of fig is considered in this characterisation. Five different numbers of binning were characterised for RGB and HSV. Both colour

feature descriptors were compared in terms of accuracy, sensitivity, precision, and time consumption to identify the dimension of the optimal feature. Based on the result, reducing the size of images will improve the time consumption with comparable accuracy. Moreover, the reduction of features dimension cannot be too small or too big due to inequitable enough to differentiate the ripeness stages and lead to

ARTICLE INFO

Article history:

Received: 17 May 2022

Accepted: 16 August 2022

Published: 06 March 2023

DOI: <https://doi.org/10.47836/pjst.31.2.07>

E-mail addresses:

iyliaadhwa@gmail.com (Iylia Adhwa Mazni)

samsuls@uitm.edu.my (Samsul Setumin)

syazwan.osman@uitm.edu.my (Mohamed Syazwan Osman)

khusairi@uitm.edu.my (Muhammad Khusairi Osman)

mohdsubri@uitm.edu.my (Mohd Subri Tahir)

*Corresponding author

a false error state. The optimal features dimension in binning for RGB was 8 (R/G/B) bins with 96.7% accuracy. Meanwhile, 96.7% accuracy for HSV at 15, 5, and 5 (H, S, V) bins as optimal colour features.

Keywords: ANN, colour descriptor, colour features, FFNN, fig, histogram, HSV, RGB, ripening

INTRODUCTION

Ficus carica L. (fig) is a fruit from the family of Moraceae, native to western Asia and the Mediterranean. Fig is also well-known for its benefit that cannot be denied. This fruit contains a high source of minerals, vitamins and fibre that are always used as dietary fibre as they are free from cholesterol and fat and contain many amino acids (Baigvand et al., 2015). Figs have a variety of families, such as Brown Turkey, Super Red Hybrid (SRH), Chicago Hardy, and Celeste. This kind of fig family will change its colour from green to brown or purple as the fruits ripen. In the other case, figs like Kadota, LSU Gold and Champagne have a green or yellow colour even though the figs are already mature.

Similar to other fruits, figs also undergo a ripening stage that could be categorised as climacteric fruit (Marei & Crane, 1971). It shows increased acidity level, ethylene production and respiratory response after harvesting (Marei & Crane, 1971). Furthermore, the significant changes during fruit ripening are becoming soft and the colour changes to less green (Skolik et al., 2019). Normally, a fig undergoes three ripening stages (Figure 1). In stage 1, fruits rapidly grow. While in stage 2, the figs will remain almost the same size, firmness, and colour. The last stage is stage 3, where the size of figs will grow to its maximum size while colour and texture change into an edible state (Freiman et al., 2015). According to Hssaini et al. (2019), the colour parameter exhibits an important variable in classification. More than 95% of their sample shows figs varying from green or yellow to purple.

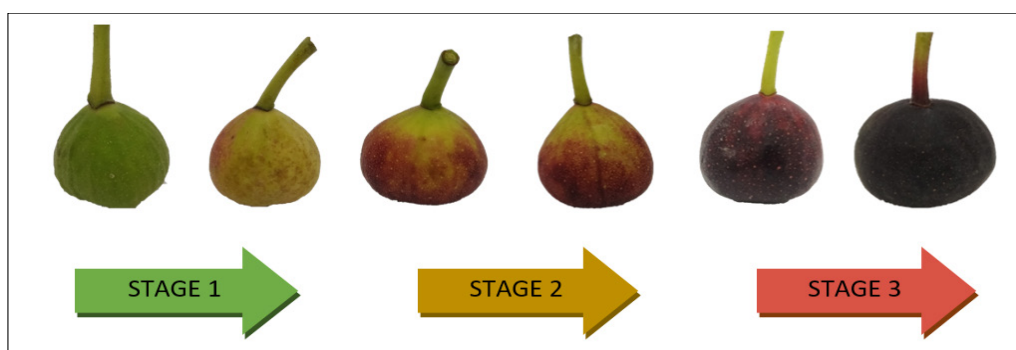


Figure 1. Ripening stage for figs based on colour changes

This study introduces a classification ripening stage of figs using image processing where the colour histogram approach is a colour descriptor based on RGB and HSV colour space. Images are the most basic way of physical prediction of the quality of fruits representing the conception of the human brain and are considered one of the fundamental steps for image improvement. Outside appearance can easily affect physical factors, including an inconsistent evaluation result. For example, the fruit's price was determined by the internal and external quality of the fruits or depending on the tag "best-if-used-before date." It could be why quality assessment of the fruits is a continuous task. Therefore, colour features have the potential to replace the conventional method of accessing quality parameters such as the ripeness of the fruits, as theoretically, the colour was obvious between the stages of ripeness (unripe, ripe, and overripe). Fast processing and low cost could be the main advantage of colour in the future (Taghizadeh et al., 2011).

RGB stand for red (R), green (G) and blue (B) channels in colour space, as shown in Figure 2. Combining these three channels will produce a resultant colour of the fruit (El Abbadi & San, 2013). The colour of the image can be obtained by adjusting the range between 0 to 255 (Pérez-rodríguez & Gómez-garcía, 2019). If all the channels demonstrated a pixel value at 0, the pure black colour would be shown, while the pixel value at 255 would represent all-white. HSV will provide a hue (colour depth or pure colour), saturation (amount of grey or purity colour) and value (colour brightness) in a colour space (Bargshady et al., 2020), as shown in Figure 2. Hue has a range of 0 to 360, and specific colours can be obtained by simply adjusting the Hue range. On the other hand, saturation shows a value from 0 to 100%, which refers to the purity of the colour. Value also takes the range from 0 to 100%, which refers to the brightness of the colour, where 0 is completely black, and 100 is the brightest and reveals the most colour (Hamuda et al., 2017). By combining these three parameters, a more specific colour can be obtained, for example, human skin tone or fruit skin colour (Hamuda et al., 2017).

RGB and HSV colour space can be classified using the histogram approach into specific bins that organise a group of data into a particular range (Hamdani et al., 2021) and be interpreted into a graph. For example, RGB colour space has a 256-intensity value and was binned into 4, 8, 16 and 32 according to a suitable value for the studies. For HSV, each channel for hue, saturation and value also can be grouped into a specific number of bins, such as 15 x 5 x 5 (Hue x Saturation x Value) or other binning values depending on the cases. This method helps a better resolution without losing any information and increases the number of accuracies (Bargshady et al., 2020; Hamdani et al., 2021). This study reported the ideal number of feature dimensions in bins colour histograms using a machine learning (ML) approach and handcrafted features based on RGB and HSV colour space.

Nowadays, image processing and machine learning (ML) are extensively used in agriculture as an essential approach corresponding to human vision in safely classifying

the ripeness of fruits without destroying the shape and appearance of the fruits (Ortac et al., 2016). That could be why image processing and ML have picked the curiosity among research and become a trend nowadays. There is a variety of ML models that have been used widely in fruit classification, such as Artificial Neural Networks (ANN), Convolutional Neural Networks (CNN), k-Nearest Neighbour (k-NN), and Support Vector Machine (SVM) (Behera et al., 2020). All these methods depend on the characteristics and specifications of the researcher according to their studies. This type of algorithm data chosen depends on the data the researcher wants to classify.

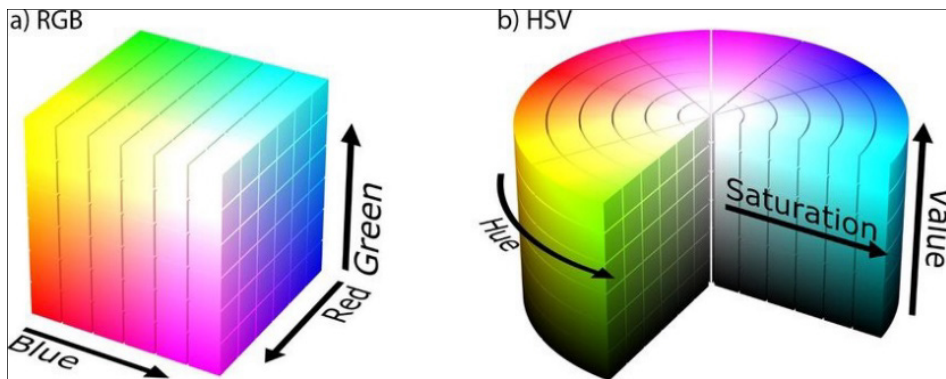


Figure 2. a) RGB and b) HSV colour feature descriptor model (Popov et al., 2018)

For the past few years, colour features and ML have been widely used in the agricultural industry to determine the ripening stage of fruits. Various fruits are used to evaluate the ripeness stage, such as apples, bananas, figs, grapes, lime, mango, oil palm, orange, papaya, peach, pineapple, strawberry, and sweet potatoes. According to previous researchers, the apple is one of the most popular fruits (Bratu et al., 2021; Tang et al., 2018; Song et al., 2020) and followed by of banana (Nguyen-Do-Trong et al., 2018; Zulkifli et al., 2019; Pu et al., 2019), orange (Li et al., 2016; Fermo et al., 2021; Bhosale, 2017) and peach (Yang et al., 2020; Minas et al., 2021). The least fruit was figs (Yijing et al., 2021; Bahar & Lichter, 2018), grapes (Cavallo et al., 2019), limes (Teerachaichayut & Ho, 2017), mango (Khalid et al., 2018), oil palm (Ali et al., 2020) and watermelon (Mohd et al., 2017). It would be the reason to discuss figs' ripeness classification; to the author's knowledge, only a few papers have discussed image processing on figs. Hssaini et al. (2019) are one of the researchers that investigated and considered taking figs as a study sample.

They used pomological and colourimetric traits derived from CIE measurement to characterise the type of figs based on qualitative and quantitative methods. As a result, ANN was used to classify the ripeness of fig fruit by using colour descriptors in this paper at three stages (unripe, ripe, and overripe). Besides, the research has only been done on

colour features such as RGB. Considering different colour spaces using the colour histogram method could give an advantage in the figs gap of study. According to (Ikmal et al., 2021), no comprehensive work has been performed to utilise image analysis of figs to classify the various ripening stages using ANN. Therefore, the ideal colour features descriptor has been investigated in this paper using a similar suggested architecture of the ANN model to classify the ripening stage of figs.

RELATED WORK

Nowadays, the ripeness classification of fruits using image processing and ML is currently being developed continuously in agriculture. Effective data for image perception, interpretation, and object classification are extracted as a feature. Colour, texture, shape and morphological features are widely utilised to evaluate fruit defects and ripeness (Bhargava & Bansal, 2021). In a previous study, more than one feature extraction had been used. The most used were colour (Song et al., 2020; Nguyen-Do-Trong et al., 2018; Bahar & Lichter, 2018; Cavallo et al., 2019; Khalid et al., 2018; Nugroho et al., 2021; Sanchez et al., 2020; Munera et al., 2018; Manthou et al., 2020) texture (Nguyen-Do-Trong et al., 2018; Nugroho et al., 2021; Sanchez et al., 2020; Munera et al., 2018; Manthou et al., 2020), and size (Nugroho et al., 2021). Colour and texture were frequently and normally combined to get a better accuracy result (Septiarini et al., 2021). For example, Kangune et al. (2019) extract colour and texture to estimate grape ripeness using several neural networks models such as ANN, SVM and k-NN that give an excellent accuracy result. According to Fatima & Seshashayee (2022), the combination of features provides a better accuracy result where a multiple feature extraction method and extraction method at different ML model has been investigated in their study. Colour features can be extracted using RGB and HSV with the histogram binning method, as suggested by Hamdani et al. (2021). Both colour models have been tested and discussed in this paper.

Lately, several studies in ripeness classification have applied machine learning by Rady et al. (2017), which uses colour as a feature descriptor to detect the ripeness stages of the fruits. The Colour histogram approach (Hamdani et al., 2021) is based on RGB (Pérez-rodíguez & Gómez-garcía, 2019) and HSV (Bargshady et al., 2020; Hamuda et al., 2017) colour model had widely been used as image features to characterise and classify the fruits according to ripeness stages. Several studies would convert the RGB descriptor to another colour descriptor (i.e., HSV, HSL, and HSI). The combination of RGB and HSV also was often used in several studies to reach a better performance with higher frequency, as proposed by El Abbadi & San (2013). Therefore, the histogram binning approach used for both RGB and HSV descriptors has been discussed in this paper.

Several researchers used neural networks and machine learning to predict and classify fruits and vegetables. A study by Cho and Koseki (2021) proposed a deep learning method

using the ANN model to determine the quality of bananas using image processing during the ripening stages. Prediction of the internal qualities of the banana was determined using different colour features such as HSV, luminance and chrominance extracted from RGB using the ANN model. Septiarini et al. (2021) developed a neural network model to classify oil palms based on colour and texture features using the ANN model to specify the maturity level. ANN with a back-propagation algorithm was applied in the classification process to obtain the prediction class. Worasawate et al. (2022) used ANN based on an ML classifier of feed-forward artificial neural network (FFNN) with a mean accuracy of 89.6% for classifying the ripeness stages of mangoes into three stages: unripe, ripe, and overripe. They used only colour features by evaluating different classifiers. Besides, a study from Magabilin et al. (2022) assesses multiple existing CNN models (MobileNetV2, VGG19 and Inception V3) to get the ideal model for classifying the Philippine Guyabano fruits based on colour features. After all, most researchers used colour features to assess the quality of fruits, especially in ripeness classification at different types of neural networks. It could be the reason that corresponds to this study's specific objective to find the ideal colour histogram binning either in RGB or HSV colour.

This paper compared and discussed the relationship between colour features and neural networks to classify the ripeness of figs according to the prediction class with a suitable number of feature dimensions in bins. The performance for each bin will be evaluated in terms of accuracy and classification performance. The procedure of this investigation will be explained more in methodology.

METHODOLOGY

In this paper, colour features have been investigated and discussed to classify the ripeness of the figs. The general procedure of this study is shown in Figure 3, where the raw image of 30 figs was taken from six different angles (Ikmal et al., 2021). Then, each image undergoes a pre-processing stage where the resizing happens. It is based on the trade-off between processing time and the size of images at the initial classification stage in machine learning (ML).

Subsequently, the colour feature of the image will be extracted by using RGB and HSV colour space as colour descriptor characterisation. Each RGB and HSV descriptor will employ the colour histogram method for each channel into a dedicated number of bins. The features dimension will be reduced to five different numbers in a set of bins for both RGB and HSV to conclude the best colour descriptor to be used in this study, and the performance will be discussed in this paper. Artificial Neural Network (ANN) was used as a handcrafted feature in these studies to predict the ripening stage. The number of features dimension was investigated to achieve a better computational time with a great classification performance. Lastly, extracted features will undergo classification performance evaluation, such as accuracy, sensitivity, and precision.

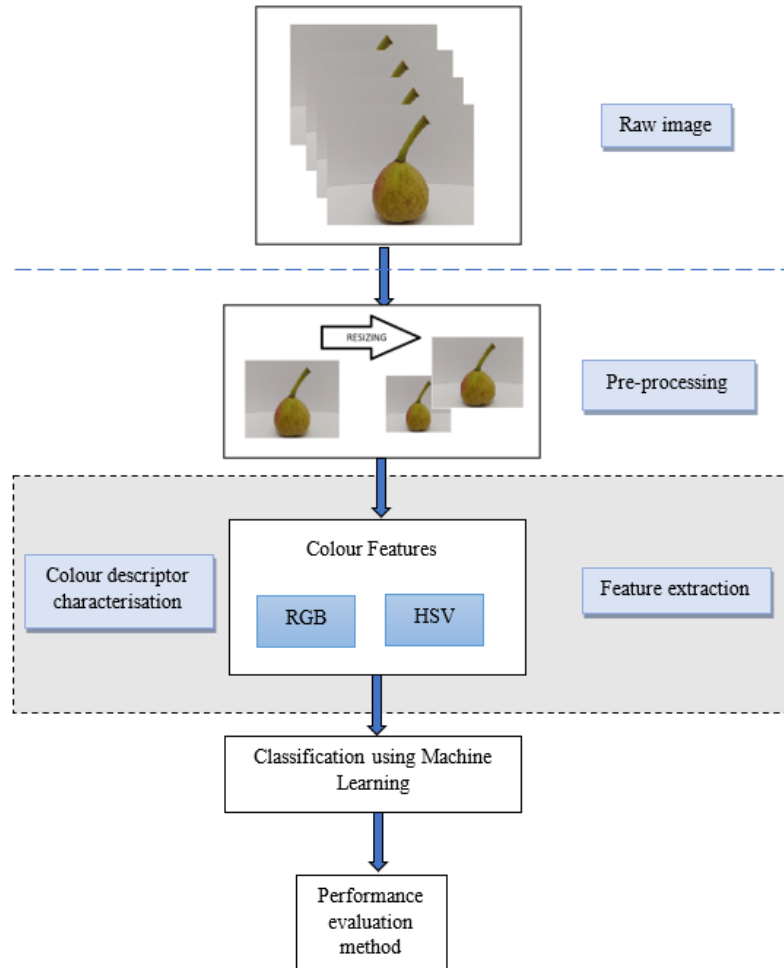


Figure 3. The process of ripeness classification using colour features for figs

Experimental Data Preparation

The dataset of this study was derived from the figs' skin colour to classify the ripeness. The image acquisition techniques for figs images were taken in a small studio setup by Ikmal et al. (2021), using a smart mobile phone stand to maintain the same distance as the fruits. The backgrounds are white with bright light to perform a better-quality image to prevent any unforeseen occurrence or wall texture from disturbing the images. Initially, 30 sets of figs with the same type of fig family, which is Super Red Hybrid (SRH), were collected from a fig farm and classified according to three-stage (10 for stage 1, 10 for stage 2 and 10 for stage 3) of figs ripeness (unripe, ripe, and overripe) by the expert. Then, each fig was photographed at six different angles (left, right, top, bottom, back and front) (Figure 4). As a result, 180 (30 x 6) images with 4000 x 3000 pixels are acquired to extract colour features.

Next, each of the images has been resized into five different sizes, which are default size 4000 x 3000), reducing to 50% (1500 x 2000), 80% (600 x 800), 90% (300 x 400) and 98% (60 x 80) size for RGB and HSV colour descriptor. The biggest size will be 4000 x 3000 or default, while the smallest one will be 60 x 80. These different sizes will be used to investigate the time consumed even though, and theoretically, the bigger image size will consume more time. This result will help for further investigation of colour descriptor performance. Lastly, two different sizes (default and smallest) will be evaluated in terms of accuracy, sensitivity, and precision.

Feature Extraction

The main objective of this paper is to classify the ripeness of the figs using colour features that act as a good descriptor (Hamdani et al., 2021). The image of each fig has been extracted using RGB and HSV colour descriptors using the colour histogram method. Five different numbers of bins were tested for each colour model (RGB and HSV).

RGB

RGB colour model involves three channels: Red, Green and Blue. RGB consists of 256 levels, and each colour channel will be histogrammed into several bins (4, 8, 16, 32 and 64) (Figure 4). For example, if the number of bins is 8, then about 32 levels of intensity will be grouped into one bin. Then, the number of features will be binned according to a specific range to become one dimension (1D) feature vector that concatenates six features from each fruit angle (Figure 4). The total features vector (γ) for eight bins will be 144 dimensions have been extracted as this number can be obtained from Equation 1:

$$\gamma = a \times b \times c \quad , b=3 \quad (1)$$

where γ is the total feature vector, 'a' is the number of bins, 'b' is the number of channels is three represents each red, green and blue channel. Every fig fruit undergoes six angle images that had been taken, which represent 'c.' The value of α is the total dimension from each angle of fruits which is the total of (a x b) (Figure 4).

HSV

Similar to RGB, different numbers of histogram bins will also be tested in the HSV colour model. HSV consist of three channels: hue (H), saturation (S), and value (V). These channels can be converted from RGB (Hamdani et al., 2021) by using Equations 2 to 5:

$$H = \begin{cases} \theta, & B \leq G \\ 360 - \theta, & B > G \end{cases} \quad (2)$$

$$\theta = \cos^{-1} \left\{ \frac{\frac{1}{2} (R - G) + (R - B)}{[x(R - G)^2 + (R - B)(G - B)]^{1/2}} \right\} \quad (3)$$

$$S = \begin{cases} 0, & \max(R, G, B) = 0 \\ 1 - \frac{\min(R, G, B)}{\max(R, G, B)}, & \text{otherwise} \end{cases} \quad (4)$$

$$V = \max f_0 (R, G, B) \quad (5)$$

Some five different combinations of bins for each channel had been tested for HSV. The combinations are (13, 3 and 3), (14, 3 and 3), (15, 5 and 5), (16, 4 and 4) and (17, 6 and 6). Then, these features were reshaped into 1D with a total value (H x S x V). For example, if the value of the bin is 16, 4 and 4 for the H, S and V, respectively. Then the total value (α) becomes 256. Since the total image angle for each fig fruit is 6, the features vector was concatenated as shown in Figure 4, similar to RGB.

The total dataset of the feature vector is $30 \times \gamma$, and every value of the features vector will be labelled according to ripeness level (phases 1, 2 or 3).

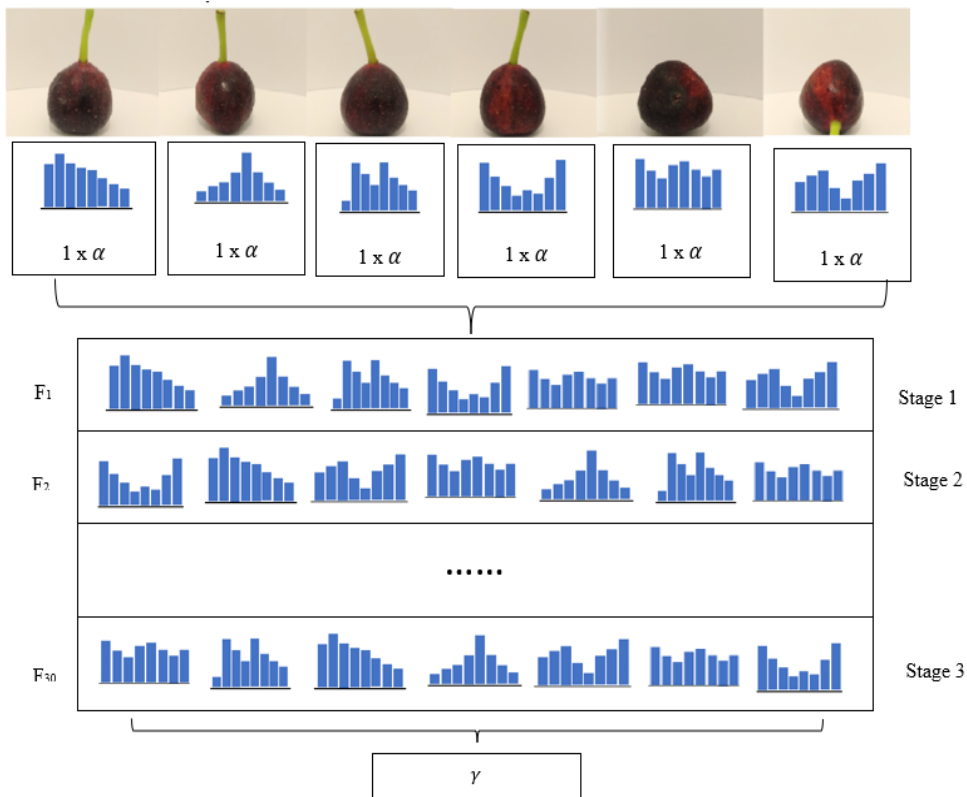


Figure 4. Example of 30 sets of figs extracted using colour features

Artificial Neural Network (ANN)

ANN classification model was used in this paper to predict and classify the ripeness stage based on colour features extracted from the fig fruit images. Based on the classification or pattern recognition technique, identifying in the context of ripening fruit stages was implemented by using Feed-Forward Neural Network (FFNN) model. RGB and HSV descriptors were trained to extract the feature from fig images.

The structural framework of FFNN was divided into three layers: an input layer, a hidden layer and an output layer (Figure 5). This model's training algorithm helps minimise the layer's error, highly responsive data, fast and less complex (Rady et al., 2017).

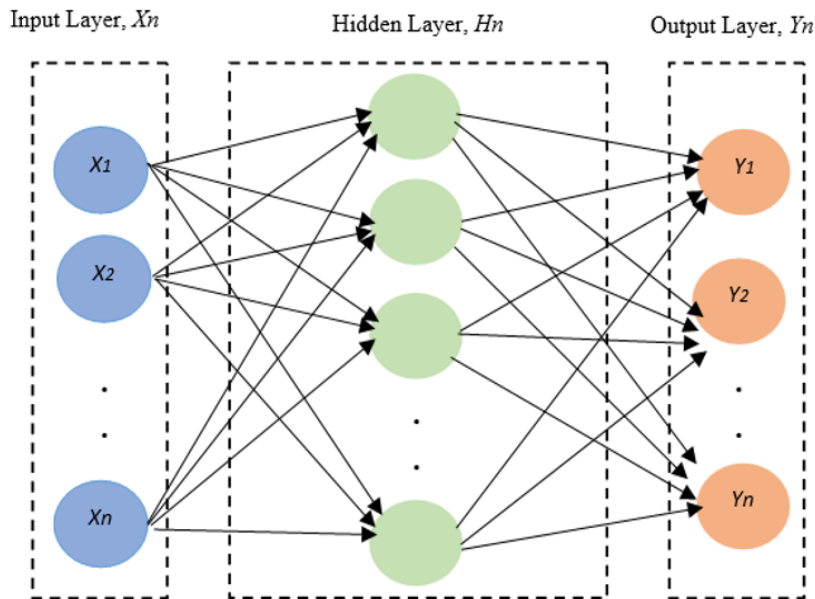


Figure 5. Typical model of Feed-Forward Neural Network (Ikmal et al., 2021)

The number of neurons or hidden nodes used in the hidden layer was set to default 10. The higher number of neurons, the highest the learning improvement of FFNN to classify the ripeness stages was computationally expensive. The input layer was the number of total dimensions at the extracted features containing spectral data, and the output layer contained the assigned stage (stage 1, stage 2 and stage 3). The transfer function for hidden and output layers undergoes log-sigmoid and scale gradient back-propagation respectively (Rady et al., 2017). The process of training a neural network that assigns the correct target classes or stages with input patterns is known as pattern recognition. Once trained, the network can classify the pattern it has not seen before.

Training Methodology

The sample of figs had been divided into three learning stages: Training, Validation and Testing. Training configuration had been set accordingly (Table 1). During the training stage, 70% of the sample is submitted to the network, which is changed based on inaccuracy. Then 15% of the samples are selected for validation and testing. Validation samples track the network generalisation and cease training when the generalisation plateaus. Hence, a testing sample will measure the network performance independently after the training phase. The number of hidden nodes was set up to 10 neurons (Ikmal et al., 2021) in this configuration for each RGB and HSV colour feature.

The number of 10 neurons was chosen according to the investigation by Ikmal et al. (2021) with a different number of neurons.

Table 1

ANN training configuration setup

CPU	AMD Ryzen 5 4600U
GPU	Radeon 2.10GHz
RAM	8.00 GB
Operating system	64 bits
Processor	X64-based processor
OS	Windows 10
Software	MATLAB R2021a
Machine learning	Neural Network Pattern Recognition
Features	RGB and HSV colour model
Hidden nodes	10 neurons (Ikmal et al., 2021)

Performance Evaluation Method

The descriptor of the colour features to classify the ripeness of figs was evaluated using sensitivity, precision and accuracy. Each number of bins used for both RGB and HSV colour descriptor were reported in this paper. The Machine Learning (ML) classification problem can be concluded using a confusion matrix. Each row and column correspond to a predicted and actual class that reports true positive (TP), false positive (FP), false negative (FN) and true negative (TN). Then, the count of the correct or incorrect data sample (training, validation or testing) filled up Table 2. The confusion matrix result shows the value of sensitivity, precision, and accuracy, as shown in Equations 6 to 11.

$$\text{Sensitivity } (S) = \frac{TP}{TP + FN} \quad (6)$$

$$\text{Average sensitivity} = \frac{S_1 + S_2 + \dots + S_n}{n} \quad (7)$$

$$\text{Precision } (P) = \frac{TP}{TP + FP} \quad (8)$$

$$\text{Average precision} = \frac{P_1 + P_2 + \dots + P_n}{n} \quad (9)$$

$$\text{Accuracy } (A) = \frac{TP + TN}{TP + FP + FN + TN} \quad (10)$$

$$\text{Average accuracy} = \frac{A_1 + A_2 + \dots + A_n}{n} \quad (11)$$

Table 2

Example of the confusion matrix table

	Actual positive (1)	Actual negative (0)
Predicted Positive (1)	True Positive (TP)	False Positive (FP)
Predicted Negative (0)	False Negative (FN)	True Negative (TN)

The sensitivity, known as recall, where the positive class mattered the most compared to the negative, is similar to precision. Accuracy is used to evaluate the ratio of a correctly predicted data sample to the total data sample.

RESULT AND DISCUSSION

The proposed method using a colour descriptor was examined to study the relationship of colour features with classification performance using the ANN model. The classification performance of sensitivity, precision and accuracy in a percentage has been evaluated in this paper.

This study starts by investigating the time consumption with different sizes of images. The image size was resized or reshaped from a default size (3000 x 4000) to four other different sizes by reducing it to 50% (1500 x 2000), 80% (600 x 800), 90% (300 x 400) and 98% (60 x 80) size for both RGB and HSV colour descriptor that had been evaluated as shown in Figure 6 and Figure 7. The result of time consumed demonstrated as the bigger size of the image, the more time consumed will be increased. It is a fact that reducing the size will also reduce time consumption. Nevertheless, we are interested in investigating colour descriptors' accuracy and performance while the size is reducing. The other performance classification method was examined to align with this result.

Two sizes of RGB and HSV were selected, the default and the smallest, to see whether the performance was affected in terms of accuracy and classification performance. Surprising, that the size did not necessarily impact the performance, as shown in Figure 8. The average accuracy for RGB and HSV between the two sizes has a narrow gap of accuracy value in a percentage ranging from 93.3 to 97.6%. In addition, the HSV colour model has a slightly higher accuracy value, which is more accurate at 97.6%, while RGB is 95.6%. It proved what had been mentioned by Wu et al. (2020), where HSV is better suited in colour recognition as it is very similar to human perception of distinct colour features if compared to RGB.

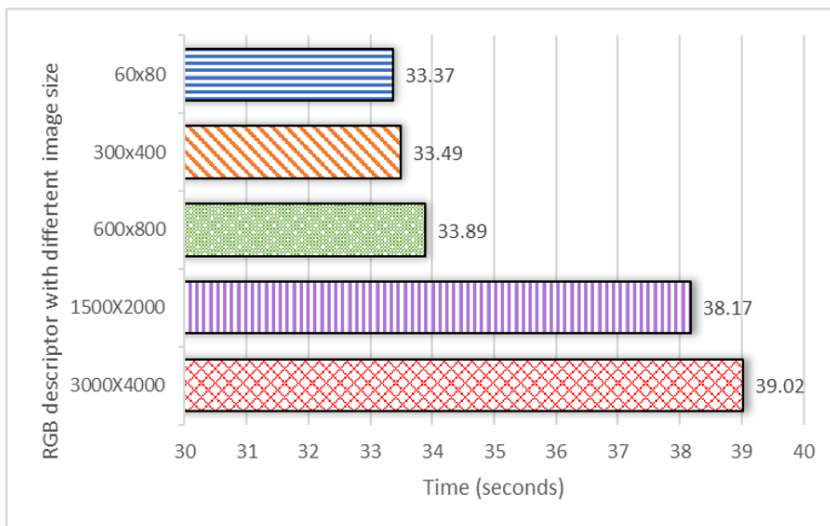


Figure 6. Time consumed for different RGB image sizes

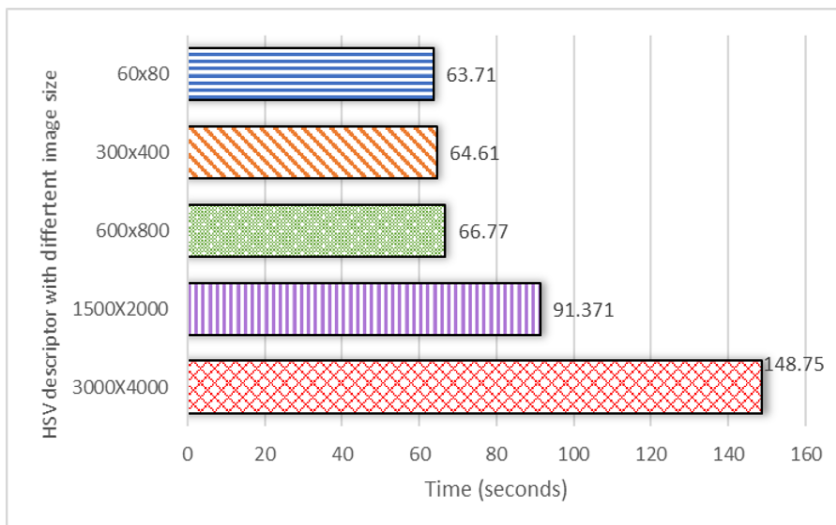


Figure 7. Time consume for different HSV image sizes

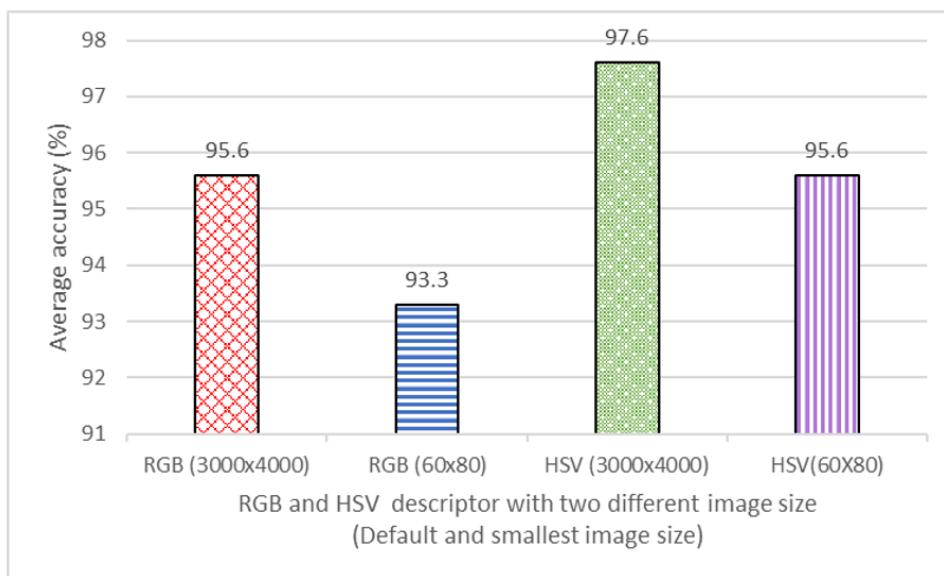


Figure 8. RGB and HSV average accuracy with two different image sizes

The performance classification method for the RGB colour model with two different sizes (default size and smallest size) was evaluated (Tables 3 and 4). The evaluation method was examined using several features extracted set at bins 4, 8, 16, 32 and 64, which were then classified using a neural network.

Table 3

RGB sensitivity, precision and accuracy value at 3000 x 4000 image size

No. of bins. (R/G/B)	Sensitivity (%)			Precision (%)			Accuracy (%)
	Stage 1	Stage 2	Stage 3	Stage 1	Stage 2	Stage 3	
4	83.3	100	90.9	100	70.0	100	90.0
8	100	90.9	100	90.0	100	100	96.7
16	90.9	100	100	100	90.0	100	96.7
32	83.3	100	100	100	80.0	100	93.3
64	71.4	100	71.4	100	20.0	100	86.7

Table 4

RGB sensitivity, precision and accuracy value at 60 x 80 image size

No. of bins. (R/G/B)	Sensitivity (%)			Precision (%)			Accuracy (%)
	Stage 1	Stage 2	Stage 3	Stage 1	Stage 2	Stage 3	
4	90.0	80.0	90.0	90.0	80.0	90.0	73.3
8	90.9	100	90.9	100	80.0	100	93.3
16	90.0	90.0	100	90.0	90.0	100	93.3
32	81.8	88.9	100	90.0	80.0	100	90.0
64	90.9	100	76.9	100	60.0	100	73.3

Sensitivity and precision were evaluated in each stage (1, 2 and 3). The value of sensitivity and precision is low, especially in stages 1 and 2. It is because, as mentioned before, the colour of stage 1 and stage 2 has a colour that is nearly the same. Nevertheless, the average value was quite good (Figure 9). The sensitivity, known as recall, reflects the ability to recognise a positive sample. The highest average sensitivity value was 97% for the default image size and 93.3% for the smallest image size. Meanwhile, the lowest average sensitivity was 80.9% for the default image size and 86.7% for the smallest image size. The average precision used to evaluate the classification accuracy of positive samples with the highest value is 96.7% for the default image size and 93.3% for the smallest size. The lowest value was 73.3% and 86.7% for both sizes, accordingly. The highest percentage obtained for sensitivity and precision was highest when the image size was 3000 x 4000 (default size) compared to the smaller image size. Five different numbers of bins were investigated, and for performance evaluation, the lowest accuracy value was 86.7% at bins 64, while 73.3% at bins 4 and 64 when the size was reduced (Tables 3 and 4). It proves bin 4 is inequitable enough to differentiate the ripeness stages for figs, and bin 64 is too big that tends to have a false rate. Meanwhile, the highest accuracy values were 96.7% and 93.3% which were used in bins 8 and 16. The result shows that bins 8 and 16 are ideal for colour feature descriptors in the RGB colour model.

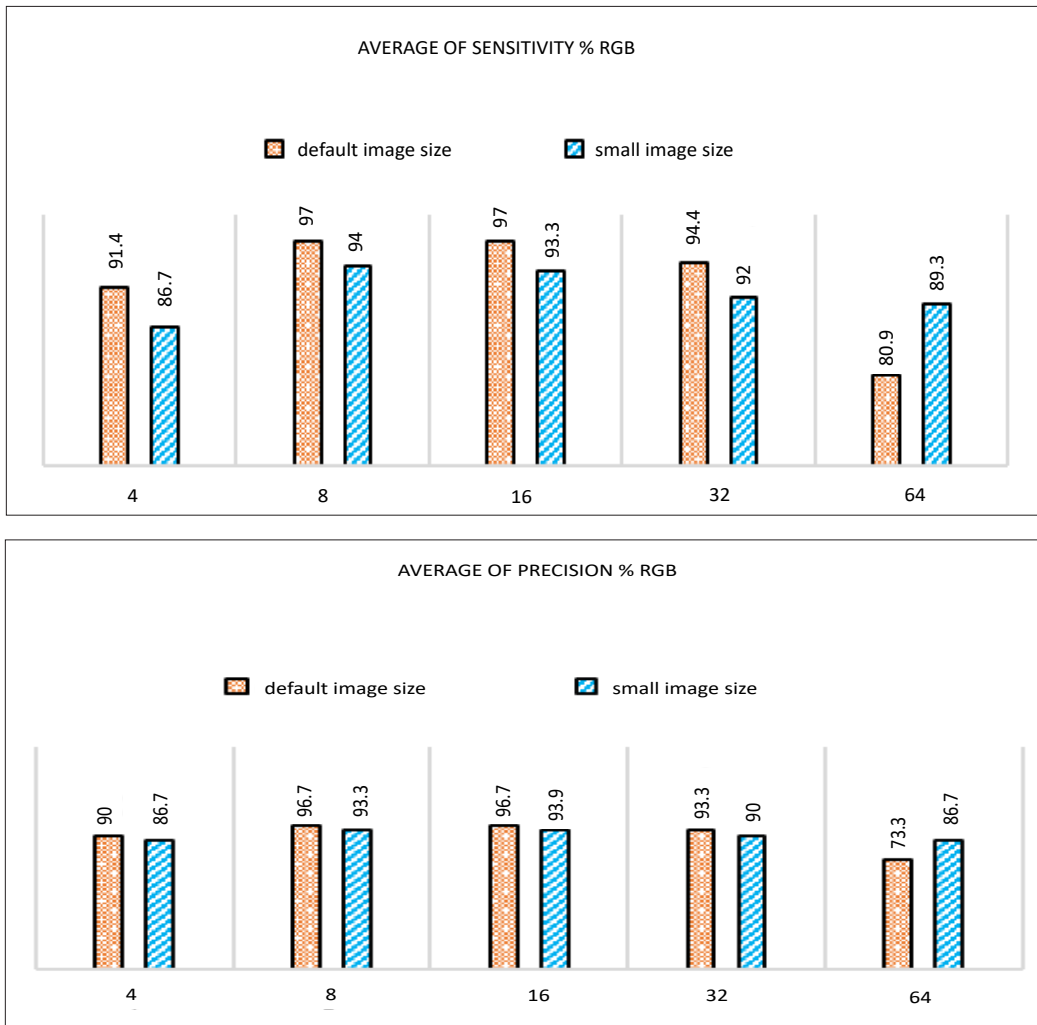


Figure 9. Average of sensitivity and precision in percentage for RGB colour model

The performance classification method for the HSV colour model with two different sizes was also evaluated (Tables 5 and 6). Similar to RGB, the value of sensitivity and precision in the HSV colour model was examined for each ripeness stage at two different sizes (default size and smallest size). Several features were extracted using five different sets of bins: (13, 3, 3), (14, 3, 3), (15, 5, 5), (16, 4, 4) and (17, 6, 6) also were examined. The average result for each stage in sensitivity and precision is illustrated in Figure 10.

Table 5

HSV sensitivity, precision and accuracy value at 3000 x 4000 image size

No of bins (H, S, V)	Sensitivity (%)			Precision (%)			Accuracy (%)
	Stage 1	Stage 2	Stage 3	Stage 1	Stage 2	Stage 3	
13, 3, 3	88.9	75.0	100	80.0	90.0	90.0	86.7
14, 3, 3	100.0	83.3	100	80.0	100	100	93.3
15, 5, 5	90.9	100	100	100	90.0	100	96.7
16, 4, 4	100	76.9	100	90.0	100	80.0	90.0
17, 6, 6	100	76.9	100	70.0	100	100	90.0

Table 6

HSV sensitivity, precision and accuracy value at 60 x 80 image size

No of bins (H, S, V)	Sensitivity (%)			Precision (%)			Accuracy (%)
	Stage 1	Stage 2	Stage 3	Stage 1	Stage 2	Stage 3	
13, 3, 3	72.7	81.8	100	80.0	90.0	80.0	83.3
14, 3, 3	90.0	90.0	100	90.0	90.0	100	93.3
15, 5, 5	100	90.9	100	90.0	100	100	96.7
16, 4, 4	90.0	81.8	100	90.0	90.0	90.0	90.0
17, 6, 6	87.5	75.0	100	70.0	90.0	100	86.7

The average sensitivity values were 97% (default size) and 93.3% (smallest size). Meanwhile, the lowest sensitivity was 88% (default size) and 84.8% (smallest size). Similar to RGB, the default image size shows a better average sensitivity and precision result than small image sizes. It can conclude that the default image was better without resizing as the number of pixels and intensity could be changed and lead to the lowest result. The lowest accuracy was 86.7% (default size) and 83.3% (smaller size), which were obtained from a set of bins (13, 3, 3) and (17, 6, 6). Having too many numbers and too small of features extracted would be difficult for the model to classify the differences in ripeness stage based upon their characteristic. The highest accuracy values were 96.75% and 93.3% for the bins (14, 3, 3) and (15, 5, 5). For the HSV colour model, the features extracted bins (14, 3, 3) and (15, 5, 5) were concluded to have a good performance.

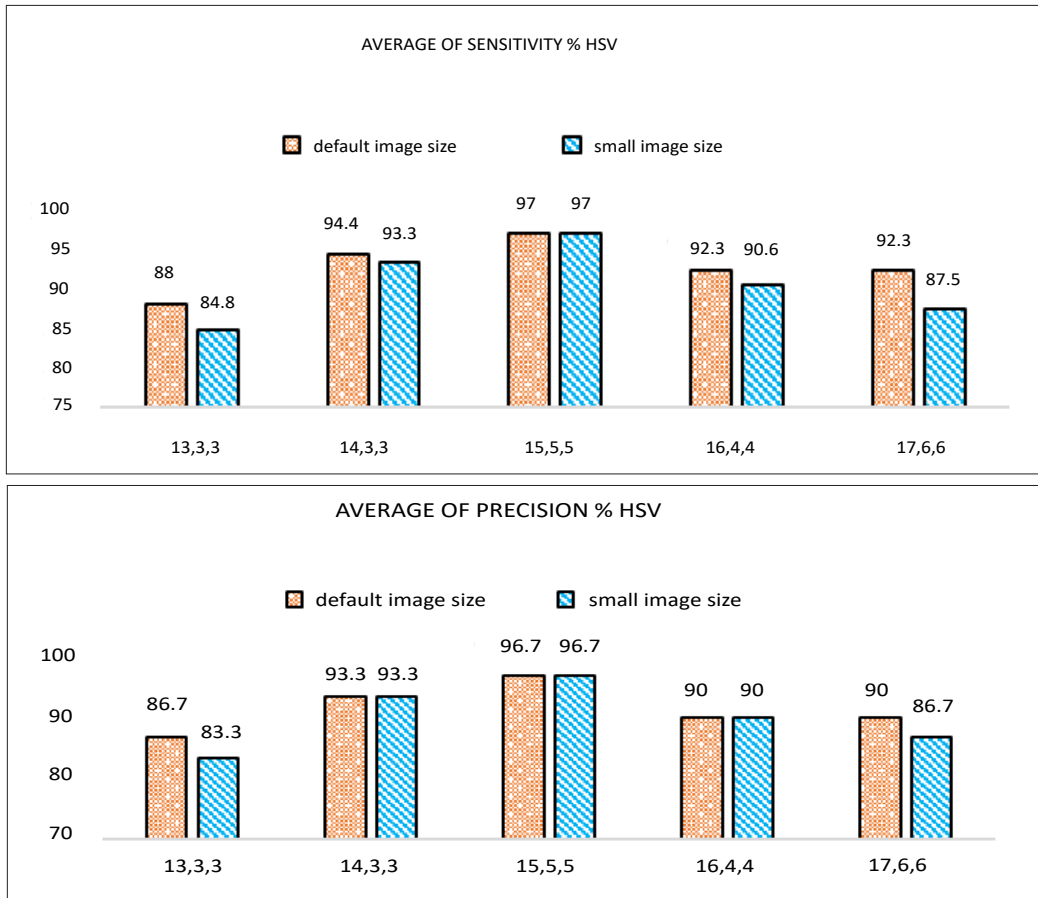


Figure 10. Average of sensitivity and precision in percentage for HSV colour model

The difference between RGB and HSV can be concluded by considering the overall performance evaluation method, where HSV has the highest average accuracy, sensitivity and precision as the colour features descriptor of figs ripeness classification.

CONCLUSION

In conclusion, the classification of figs' ripeness was examined using colour features descriptor for both RGB and HSV colour models. About 30 figs with six different angles were trained using ANN with a base of the FFNN model as a pattern recognition and classification model to determine the ripeness stages of figs. The reduction of features dimension was investigated using histogram binning with five different numbers of bins for both colour models. The ideal number of bins for dimension features for RGB was 8 and 16, with an average accuracy of 96.7% and 93.3%. Meanwhile HSV colour model has 96.7% for HSV at the 15, 5, 5 (H, S, V) bin set. The value of sensitivity and precision also

had been examined throughout this study. The highest value for sensitivity was 97%, and precision was 96.7% for RGB (8 and 16) and HSV (15, 5, 5) bins, respectively. In addition, reducing the image size and feature dimension did not degrade the performance as the accuracy was above 90%, which also helped to reduce the time consumption. However, the result shows HSV has a better average accuracy result due to the sensitivity of hue, saturation and value in colour space. For future work, texture and colour as combination features would be envisaged to increase the performance of ripeness classification. Besides, we suggest using a different machine learning approach, such as Convolutional Neural Network (CNN), to distinguish the appearance in terms of ripeness stages to correspond colour descriptors with image features of figs. It is due to image features correlating with a colour descriptor, especially for figs, which are seldom discussed.

ACKNOWLEDGEMENT

The authors thank Universiti Teknologi MARA (UiTM) Cawangan Pulau Pinang for supporting the research, especially the Faculty of Electrical Engineering.

REFERENCES

- Ali, M. M., Hashim, N., & Hamid, A. S. A. (2020). Combination of laser-light backscattering imaging and computer vision for rapid determination of oil palm fresh fruit bunches maturity. *Computers and Electronics in Agriculture*, *169*, Article 105235. <https://doi.org/10.1016/j.compag.2020.105235>
- Bahar, A., & Lichter, A. (2018). Effect of controlled atmosphere on the storage potential of Ottomanit fig fruit. *Scientia Horticulturae*, *227*, 196-201. <https://doi.org/10.1016/j.scienta.2017.09.036>
- Baigvand, M., Banakar, A., Minaei, S., Khodaei, J., & Behroozi-khazaei, N. (2015). Machine vision system for grading of dried figs. *Computers and Electronics in Agriculture*, *119*, 158-165. <https://doi.org/10.1016/j.compag.2015.10.019>
- Bargshady, G., Zhou, X., Deo, R. C., Soar, J., & Whittaker, F. (2020). The modeling of human facial pain intensity based on Temporal Convolutional Networks trained with video frames in HSV color space. *Applied Soft Computing*, *97*, Article 106805. <https://doi.org/10.1016/j.asoc.2020.106805>
- Behera, S. K., Rath, A. K., & Sethy, P. K. (2020). Maturity status classification of papaya fruits based on machine learning and transfer learning approach. *Information Processing in Agriculture*, *8*(2), 244-250. <https://doi.org/10.1016/j.inpa.2020.05.003>
- Bhargava, A., & Bansal, A. (2021). Fruits and vegetables quality evaluation using computer vision: A review. *Journal of King Saud University - Computer and Information Sciences*, *33*(3), 243-257. <https://doi.org/10.1016/j.jksuci.2018.06.002>
- Bhosale, A. A. (2017). Detection of sugar content in citrus fruits by capacitance method. *Procedia Engineering*, *181*, 466-471. <https://doi.org/10.1016/j.proeng.2017.02.417>
- Bratu, A. M., Popa, C., Bojan, M., Logofatu, P. C., & Petrus, M. (2021). Non-destructive methods for fruit quality evaluation. *Scientific Reports*, *11*(1), 1-15. <https://doi.org/10.1038/s41598-021-87530-2>

- Cavallo, D. P., Cefola, M., Pace, B., Logrieco, A. F., & Attolico, G. (2019). Non-destructive and contactless quality evaluation of table grapes by a computer vision system. *Computers and Electronics in Agriculture*, 156, 558-564. <https://doi.org/10.1016/j.compag.2018.12.019>
- Cho, B. H., & Koseki, S. (2021). Determination of banana quality indices during the ripening process at different temperatures using smartphone images and an artificial neural network. *Scientia Horticulturae*, 288, Article 110382. <https://doi.org/10.1016/j.scienta.2021.110382>
- El Abbadi, N., & San, K. M. (2013). Face detection using a hybrid approach that combines HSV and RGB Face detection using a hybrid approach that combines HSV and RGB. *International Journal of Computer Science and Mobile Computing*, 2(3), 127-136.
- Fatima, S., & Seshashayee, M. (2022). Feature fusion of fruit image categorization using machine learning. *International Journal of Nonlinear Analysis and Applications*, 13, 2008-6822. <http://dx.doi.org/10.22075/ijnaa.2022.6332>
- Fermo, I. R., Cavali, T. S., Bonfim-Rocha, L., Srutkoske, C. L., Flores, F. C., & Andrade, C. M. G. (2021). Development of a low-cost digital image processing system for oranges selection using hopfield networks. *Food and Bioprocess Processing*, 125, 181-192. <https://doi.org/10.1016/j.fbp.2020.11.012>
- Freiman, Z. E., Rosianskey, Y., Dasmohapatra, R., Kamara, I., & Flaishman, M. A. (2015). The ambiguous ripening nature of the fig (*Ficus carica* L.) fruit: A gene-expression study of potential ripening regulators and ethylene-related genes. *Journal of Experimental Botany*, 66(11), 3309-3324. <https://doi.org/10.1093/jxb/erv140>
- Hamdani, H., Septiarini, A., Sunyoto, A., & Suyanto, S. (2021). Detection of oil palm leaf disease based on color histogram and supervised classifier. *Optik*, 245, Article 167753. <https://doi.org/10.1016/j.ijleo.2021.167753>
- Hamuda, E., Ginley, B. M., Glavin, M., & Jones, E. (2017). Automatic crop detection under field conditions using the HSV colour space and morphological operations. *Computers and electronics in agriculture*, 133, 97-107. <https://doi.org/10.1016/j.compag.2016.11.021>
- Hssaini, L., Hanine, H., Razouk, R., Ennahli, S., Mekaoui, A., & Charafi, J. (2019). Characterization of local fig clones (*Ficus carica* L.) collected in Northern Morocco. *Fruits, The International Journal of Tropical and Subtropical Horticulture*, 74(2), 55-64. <https://doi.org/10.17660/th2019/74.2.1>
- Ikmal, M., Maruzuki, F., Shahrin, A. S., Setumin, S., Ramli, R. A., & Fithry, S. (2021). A Multilayer perceptron approach for *Ficus carica* (fig) ripening classification. *ESTEEM Academic Journal*, 17, 56-66.
- Kangune, K., VKulkarni, V., & Kosamkar, P. (2019). Automated estimation of grape ripeness. *Asian Journal of Convergence in Technology*, 5(1), 1-6.
- Khalid, N. S., Abdullah, A. H., Shukor, S. A. A., Syahir, A. S. F., Mansor, H., & Dalila, N. D. N. (2018). Non-destructive technique based on specific gravity for post-harvest *Mangifera Indica* L. cultivar maturity. In *Asia Modelling Symposium 2017 and 11th International Conference on Mathematical Modelling and Computer Simulation* (pp. 113-117). IEEE Publishing. <https://doi.org/10.1109/AMS.2017.26>
- Li, J., Huang, W., Tian, X., Wang, C., Fan, S., & Zhao, C. (2016). Fast detection and visualization of early decay in citrus using Vis-NIR hyperspectral imaging. *Computers and Electronics in Agriculture*, 127, 582-592. <https://doi.org/10.1016/j.compag.2016.07.016>

- Magabilin, M. C. V., Fajardo, A. C., & Medina, R. P. (2022). Optimal Ripeness Classification of the Philippine Guyabano Fruit using Deep Learning. In *2022 Second International Conference on Power, Control and Computing Technologies (ICPC2T)* (pp. 1-5). IEEE Publishing. <https://doi.org/10.1109/ICPC2T53885.2022.9777014>
- Manthou, E., Lago, S. L., Dagres, E., Lianou, A., Tsakanikas, P., Panagou, E. Z., Anastasiadi, M., Mohareb, F., & Nychas, G. J. E. (2020). Application of spectroscopic and multispectral imaging technologies on the assessment of ready-to-eat pineapple quality: A performance evaluation study of machine learning models generated from two commercial data analytics tools. *Computers and Electronics in Agriculture*, *175*, Article 105529. <https://doi.org/10.1016/j.compag.2020.105529>
- Marei, N., & Crane, J. C. (1971). Growth and respiratory response of fig (*Ficus carica* L. cv. Mission) fruits to ethylene. *Plant Physiology*, *48*(3), 249-254. <https://doi.org/10.1104/pp.48.3.249>
- Minas, I. S., Blanco-Cipollone, F., & Sterle, D. (2021). Accurate non-destructive prediction of peach fruit internal quality and physiological maturity with a single scan using near infrared spectroscopy. *Food Chemistry*, *335*, Article 127626. <https://doi.org/10.1016/j.foodchem.2020.127626>
- Mohd, M., Hashim, N., Khairunniza, S., & Shamsudin, R. (2017). Postharvest biology and technology quality evaluation of watermelon using laser-induced backscattering imaging during storage. *Postharvest Biology and Technology*, *123*, 51-59. <https://doi.org/10.1016/j.postharvbio.2016.08.010>
- Munera, S., Amigo, J. M., Aleixos, N., Talens, P., Cubero, S., & Blasco, J. (2018). Potential of VIS-NIR hyperspectral imaging and chemometric methods to identify similar cultivars of nectarine. *Food Control*, *86*, 1-10. <https://doi.org/10.1016/j.foodcont.2017.10.037>
- Nguyen-Do-Trong, N., Dusabumuremyi, J. C., & Saeys, W. (2018). Cross-polarized VNIR hyperspectral reflectance imaging for non-destructive quality evaluation of dried banana slices, drying process monitoring and control. *Journal of Food Engineering*, *238*, 85-94. <https://doi.org/10.1016/j.jfoodeng.2018.06.013>
- Nugroho, C. S., Ainuri, M., & Falah, M. A. F. (2021). Physical quality determination of fresh strawberry (*Fragaria x ananassa* var. Osogrande) fruit in tropical environment using image processing approach. *IOP Conference Series: Earth and Environmental Science*, *759*, 1-6. <https://doi.org/10.1088/1755-1315/759/1/012020>
- Ortac, G., Bilgi, A. S., Gorgulu, Y. E., Gunes, A., Kalkan, H., & Tasdemir, K. (2016). Classification of black mold contaminated figs by hyperspectral imaging. In *2015 IEEE International Symposium on Signal Processing and Information Technology, ISSPIT 2015* (pp. 227-230). IEEE Publishing. <https://doi.org/10.1109/ISSPIT.2015.7394332>
- Pérez-Rodríguez, F., & Gómez-García, E. (2019). Codelplant: Regression-based processing of RGB images for colour models in plant image segmentation. *Computers and Electronics in Agriculture*, *163*, Article 104880. <https://doi.org/10.1016/j.compag.2019.104880>
- Popov, V., Ostarek, M., & Tenison, C. (2018). Practices and pitfalls in inferring neural representations. *NeuroImage*, *174*, 340-351. <https://doi.org/10.1016/j.neuroimage.2018.03.041>
- Pu, Y. Y., Sun, D. W., Buccheri, M., Grassi, M., Cattaneo, T. M. P., & Gowen, A. (2019). Ripeness classification of bananito fruit (*Musa acuminata*, AA): A comparison study of visible spectroscopy and hyperspectral imaging. *Food Analytical Methods*, *12*(8), 1693-1704. <https://doi.org/10.1007/s12161-019-01506-7>

- Rady, A., Ekramirad, N., Adedeji, A. A., Li, M., & Alimardani, R. (2017). Hyperspectral imaging for detection of codling moth infestation in GoldRush apples. *Postharvest Biology and Technology*, *129*, 37-44. <https://doi.org/10.1016/j.postharvbio.2017.03.007>
- Sanchez, P. D. C., Hashim, N., Shamsudin, R., & Nor, M. Z. M. (2020). Quality evaluation of sweet potatoes (*Ipomoea batatas* L.) of different varieties using laser light backscattering imaging technique. *Scientia Horticulturae*, *260*, Article 108861. <https://doi.org/10.1016/j.scienta.2019.108861>
- Septiarini, A., Sunyoto, A., Hamdani, H., Kasim, A. A., Utaminigrum, F., & Hatta, H. R. (2021). Machine vision for the maturity classification of oil palm fresh fruit bunches based on color and texture features. *Scientia Horticulturae*, *286*, Article 110245. <https://doi.org/10.1016/j.scienta.2021.110245>
- Skolik, P., Morais, C. L. M., Martin, F. L., & McAinsh, M. R. (2019). Determination of developmental and ripening stages of whole tomato fruit using portable infrared spectroscopy and Chemometrics. *BMC Plant Biology*, *19*(1), 1-15. <https://doi.org/10.1186/s12870-019-1852-5>
- Song, W., Jiang, N., Wang, H., & Guo, G. (2020). Evaluation of machine learning methods for organic apple authentication based on diffraction grating and image processing. *Journal of Food Composition and Analysis*, *88*, Article 103437. <https://doi.org/10.1016/j.jfca.2020.103437>
- Taghizadeh, M., Gowen, A. A., & O'Donnell, C. P. (2011). Comparison of hyperspectral imaging with conventional RGB imaging for quality evaluation of *Agaricus bisporus* mushrooms. *Biosystems Engineering*, *108*(2), 191-194. <https://doi.org/10.1016/j.biosystemseng.2010.10.005>
- Tang, C., He, H., Li, E., & Li, H. (2018). Multispectral imaging for predicting sugar content of 'Fuji' apples. *Optics and Laser Technology*, *106*, 280-285. <https://doi.org/10.1016/j.optlastec.2018.04.017>
- Teerachaichayut, S., & Ho, H. T. (2017). Postharvest biology and technology non-destructive prediction of total soluble solids, titratable acidity and maturity index of limes by near infrared hyperspectral imaging. *Postharvest Biology and Technology*, *133*, 20-25. <https://doi.org/10.1016/j.postharvbio.2017.07.005>
- Worasawate, D., Sakunasinha, P., & Chiangga, S. (2022). Automatic classification of the ripeness stage of mango fruit using a machine learning approach. *AgriEngineering*, *4*(1), 32-47. <https://doi.org/10.3390/agriengineering4010003>
- Wu, G., Li, B., Zhu, Q., Huang, M., & Guo, Y. (2020). Using color and 3D geometry features to segment fruit point cloud and improve fruit recognition accuracy. *Computers and Electronics in Agriculture*, *174*, Article 105475. <https://doi.org/10.1016/j.compag.2020.105475>
- Yang, B., Gao, Y., Yan, Q., Qi, L., Zhu, Y., & Wang, B. (2020). Estimation Method of Soluble Solid Content in Peach Based on Deep Features of Hyperspectral Imagery. *Sensors*, *20*(18), Article 5021. <https://doi.org/10.3390/s20185021>
- Yijing, W., Yi, Y., Xue-fen, W., Jian, C., & Xinyun, L. (2021). Fig fruit recognition method based on YOLO v4 deep learning. In *2021 18th International Conference on Electrical Engineering/Electronics, Computer, Telecommunications and Information Technology (ECTI-CON)* (pp. 303-306). IEEE Publishing. <https://doi.org/10.1109/ECTI-CON51831.2021.9454904>
- Zulkifli, N., Hashim, N., Abdan, K., & Hanafi, M. (2019). Application of laser-induced backscattering imaging for predicting and classifying ripening stages of "Berangan" bananas. *Computers and Electronics in Agriculture*, *160*, 100-107. <https://doi.org/10.1016/j.compag.2019.02.031>

Potential of Fatty Acid Methyl Ester as Diesel Blends Produced from Free Fatty Acid in Waste Cooking Oil Catalyzed by Montmorillonite-Sulfonated Carbon

Hasanudin Hasanudin^{1,2*}, Wan Ryan Asri^{1,2}, Firda Rahmania Putri^{1,2}, Fahma Riyanti^{1,2}, Zainal Fanani^{1,2}, Addy Rachmat^{1,2}, Novia Novia³ and Tuty Emilia Agustina³

¹Department of Chemistry, Faculty of Mathematics and Natural Science, Universitas Sriwijaya, Indralaya 30662, Indonesia

²Biofuel Research Group, Laboratory of Physical Chemistry, Faculty of Mathematics and Natural Science, Universitas Sriwijaya, Indralaya 30662, Indonesia

³Department of Chemical Engineering, Department of Engineering, Universitas Sriwijaya, Indralaya 30662, Indonesia

ABSTRACT

This research, biodiesel production from waste cooking oil (WCO), was conducted using a montmorillonite-sulfonated carbon catalyst from molasses. The biodiesel product would be blended with diesel fuel with various volume variations to see its fuel properties. The catalyst was assessed by Fourier-transform infrared spectroscopy (FTIR), scanning electron microscope (SEM), N₂ adsorption-desorption isotherm, and acidity analysis using the titration method. The effect of the weight ratio of montmorillonite to sulfonated carbon was also evaluated. The process of esterification reaction was optimized using

the response surface methodology with a central composite design (RSM-CCD). The study showed that the weight ratio of montmorillonite to sulfonated carbon of 1:3 generated the highest acidity of 9.79 mmol/g with a prominent enhanced surface area and was further employed to optimize the esterification reaction. The optimum condition was obtained at a reaction temperature of 78.12°C, catalyst weight of 2.98 g, and reaction time of 118.27 with an FFA conversion of 74.101%. The optimum condition for the mixture of

ARTICLE INFO

Article history:

Received: 19 May 2022

Accepted: 22 July 2022

Published: 06 March 2023

DOI: <https://doi.org/10.47836/pjst.31.2.08>

E-mail addresses:

hasanudin@mipa.unsri.ac.id (Hasanudin Hasanudin)

wanryanryan@gmail.com (Wan Ryan Asri)

08031281722023@student.unsri.ac.id (Firda Rahmania Putri)

fatechafj@unsri.ac.id (Fahma Riyanti)

zainalf313@unsri.ac.id (Zainal Fanani)

addy.tea@gmail.com (Addy Rachmat)

novia@ft.unsri.ac.id (Novia Novia)

tuty_agustina@unsri.ac.id (Tuty Emilia Agustina)

*Corresponding author

FAME and diesel fuel was achieved at the composition of the B20 blend, which met the FAME standard. The reusability study revealed that the catalyst had adequate stability at three consecutive runs, with a reduced performance was 18.60%. The reduction of FFA conversion was due to the leaching of the catalyst's active site. This study disclosed that the FAME generated from the esterification of FFA on WCO-catalyzed montmorillonite-sulfonated carbon had a promising option as biodiesel blends for increasing the quality of commercial diesel.

Keywords: Biodiesel blends, free fatty acid conversion, montmorillonite, optimization, sulfonated carbon, waste cooking oil

INTRODUCTION

The demand for petroleum is rising in tandem with the economic and population expansion rate. Petroleum reserves are depleted due to increased oil usage in transportation and industry. Renewable and ecologically acceptable alternative energy is required to solve the energy sector's growing issues (Sari et al., 2021; Yuliana et al., 2020). It has known that solar, wind, and bioenergy considerably contribute to the resources of global energy production and pollution reductions. Waste resources, for example, have been employed to make biofuels, which can play an essential part in the energy sector and greatly enhance the world's socioeconomic structure (Jamil et al., 2020). Biodiesel is the potential choice among biofuels due to its low toxicity, biodegradable, carbon-neutral emissions with less sulfur, hydrocarbons, and carbon monoxide content. Biodiesel has the primary prospective to replace conventional diesel as a favorable alternative fuel in diesel engines (Chen et al., 2019).

Various raw materials for biodiesel production have been widely developed due to they are directly related to production costs. Generally, raw materials sourced from non-edible oil are much preferable to vegetable oil (Ali et al., 2018). Non-edible oil such as jatropha or castor oil can be used as raw material for biodiesel production. Even though those materials can produce biodiesel, it does not compete directly with food-grade oil and still requires a large plantation area, so their utilization becomes ineffective (Mazubert et al., 2014). In the recent development of biodiesel feedstocks, the uses of oil wastes have been massively studied due to their numerous advantages (Chen et al., 2021). Waste cooking oil (WCO), palm oil waste, animal fat, and grease, as low-cost raw materials, have been utilized for biodiesel production (Boffito et al., 2013). Currently, a large amount of waste oil is specifically generated by the food processing industry, which, unfortunately, is mostly discharged into municipal sewer systems. This condition contributes to the pollution of various areas and potentially poses a hazard to ecosystems and humans (Soegiantoro et al., 2019). This situation indicates implications for broad opportunities to use WCO as biodiesel feedstock.

WCO has high free fatty acid (FFA) content which can be used as a precursor for biodiesel (Sree et al., 2021). In the study of biodiesel production from WCO, the use of catalysts is critical and dramatically affects the effectiveness and efficiency of biodiesel production. Various types of catalysts have been employed to produce biodiesel from WCO. A homogeneous catalyst such as sulfuric acid has a high FFA conversion capability and exhibits a high biodiesel yield (Ding et al., 2012). Nonetheless, the homogeneous catalyst is corrosive and challenging to separate, generates much water due to purification, and takes up high costs (Suwannasom et al., 2016). The heterogeneous catalyst as a prominent component clearly could resolve those problems as indicated it can be separated and reused, which inherently decreases the cost of production and increases the production efficiency (Zik et al., 2020).

Currently, along with the development of science, the types of catalysts are increasingly diverse in the context of biodiesel production from WCO. The heterogeneous catalyst such as eggshells (Gupta & Rathod, 2018; Kamaranzaman et al., 2020b), bimetallic-CaO derived from eggshells (Mansir et al., 2018), bone-based catalysts (Ali et al., 2018; Suwannasom et al., 2016), sulfonated resin/PVA composite (Zhang et al., 2016), solid acid resins (Boffito et al., 2013), tailored magnetic nano-alumina (Bayat et al., 2018), Fe-montmorillonite K10 (Yahya et al., 2020), Mg/Al hydrotalcite (Ma et al., 2016), and sulfonated carbon (Kumar et al., 2020; Nata et al., 2017), have been extensively used and studied in the biodiesel production from WCO. The use of sulfonated carbon catalysts has attracted interest in biodiesel production because highly active sites result in high catalytic activity in FFA conversion (Bastos et al., 2020).

Interestingly, low-cost carbon sources are abundantly available and can be easily functionalized with sulfonate functional groups. Numerous low-cost precursors derived from biomasses have been employed as carbon precursors (Bastos et al., 2020; Farabi et al., 2019; Lathiya et al., 2018; Ngaosuwan et al., 2016; Niu et al., 2018; Rocha et al., 2019). As waste from sugar factories, Molasse has a good prospective as a source of carbon material because they have a fairly high sugar content (Palmonari et al., 2020). Carbon derived from molasses shows good physical, chemical, and absorptive properties (Kumar et al., 2020).

Hence, the carbonization of molasse potentially generated high carbon content, effectively promoting the functionalization of the sulfonated group. In order to increase the sulfonated carbon catalytic activity, it is necessary to combine with layered or porous supported materials (Munir et al., 2021). It has been reported that clay material such as montmorillonite has Bronsted and Lewis acid, which could promote high conversion and catalytic activity (Hasanudin, Asri, Tampubolon, et al., 2022; Yahya et al., 2020). Therefore, combining montmorillonite with sulfonated carbon derived from molasses potentially exhibits a synergetic effect on the FFA conversion from WCO.

Optimization of FFA conversion from WCO is crucial to getting the desired product along with improving the process feasibility and profitability (Al-Sakkari et al., 2020; Helmi et al., 2020; Sahani et al., 2020; Sharma et al., 2019; Tan et al., 2017; Sree et al., 2021). Furthermore, the simultaneous interaction of each process variable also greatly affects the magnitude of the FFA conversion (Tan et al., 2017). Response surface methodology (RSM) with central composite design (CCD) is a statistical tool that can optimize as well as evaluate the interaction of variables (Singh et al., 2018). The RSM-CCD is highly efficient for demonstrating the second-order model of experimental data and provides adequate estimation (Dhawane et al., 2015; Karmakar & Halder, 2021).

According to the literature review, there are neither studies nor explorations regarding the optimization of FFA conversion from WCO using montmorillonite-sulfonated carbon catalyst by RSM-CCD, as well as the potential of FAME produced as diesel blends. In this study, RSM-CCD was employed to determine the optimum FFA conversion derived from WCO as a response variable using a montmorillonite-sulfonated carbon catalyst. The process variables were assessed: reaction time, catalyst weight, and reaction temperature. The effect of the montmorillonite to sulfonated carbon ratio on the acidity catalyst was evaluated. The catalyst was characterized using FTIR, SEM, and N₂ adsorption-desorption isotherm. The reusability of the catalyst was investigated in three consecutive cycles. Moreover, to see the potential of fatty acid methyl ester (FAME) derived from WCO as diesel blends, the FAME product would be blended with diesel fuel with various volume variations to see its physicochemical properties such as water content, density, volume distillate, kinematic viscosity, and pour point, color, and cetane index.

MATERIALS AND METHODS

Preparation of Catalyst

Briefly, 200-mesh of natural montmorillonite was washed using demineralized water and dried at 120°C for 24 hours in the oven. Next, various weight ratios of montmorillonite to molasses were dissolved in 500 ml of demineralized water, namely 3:1, 2:1, 1:1, 1:2, 1:3, 1:4 (% w/w), and stirred for 1 hour at 80°C. The mixture was later dried in the oven at 120°C. According to Suganuma et al. (2012), the carbonization was conducted with some modifications by employing a temperature of 400°C for 15 hours in the N₂ atmosphere. The powder was referred to as montmorillonite-carbon composites. The sulfonation was conducted using 20 g of the montmorillonite-carbon composite and mixed with 100 ml of concentrated H₂SO₄ in the reflux system at 175°C for 15 hours. After that, the powder was washed with hot water until the pH was close to neutral, followed by centrifugation, and dried for one day at 120°C. The powder was referred to as montmorillonite-sulfonated carbon composite. The acidity of the catalyst was determined using the titration method. The catalyst morphology and its elemental content were assessed using SEM (JEOL), whereas

the functional group catalyst was characterized using FT-IR (Shimadzu). The textural properties were characterized using N₂ adsorption-desorption isotherm (Quantachrome NOVA)

Esterification of FFA from WCO

The esterification was conducted under a reflux system. 25 g of WCO was mixed with 79 ml of methanol, followed by the montmorillonite-sulfonated carbon composite catalyst from molasses. The esterification product was separated from the catalyst. Subsequently, 50 mL of distilled water was added and allowed to stand until two layers, such as FAME and glycerol, were formed. The FAME was later distilled to remove the alcohol and water. The product was characterized using FTIR. The FFA content was analyzed using the titration method with NaOH. The FFA conversion (X) was calculated according to Equation 1:

$$X \text{ (wt\%)} = \frac{F_0 - F}{F_0} \tag{1}$$

Where F₀ and F are the FFA content of feedstock and the esterification product, respectively.

Experimental Design

This study consisted of 17 run experiments to investigate the optimum interaction and conditions in the conversion of FFA from WCO. The design of the experiment using CCD is shown in Table 1. The quadratic model is shown in Equation 2:

$$Y = \alpha_0 + \sum_{i=1}^n \alpha_i X_i + \sum_{i=1}^n \alpha_{ii} X_i^2 + \sum_{i=1}^{n-1} \sum_{j=i+1}^n \alpha_{ij} X_i X_j \tag{2}$$

Where Y is the response (FFA conversion), α₀ is the constant coefficient, whereas α_i, α_{ii}, and b_{ij} are the coefficients for linear, quadratic, and interaction effects, respectively; X_i and X_j are the process variables (Anguebes-Franceschi et al., 2018). The model’s fit was evaluated using analysis of variance (ANOVA).

Table 1
The levels of process variables using CCD

Process variable	Unit	Levels				
		-1.628	-1	0	+1	+1.628
Reaction temperature (A)	°C	63.18	70	80	90	96.82
Catalyst weight (B)	g	0.31	1	2	3	3.68
Reaction time (C)	min	69.55	90	120	150	170.45

Catalyst Reusability

Regarding the catalyst reusability study, the spent catalyst after the esterification reaction was vacuum filtered and washed with alcohol four times. The catalyst was later dried and stored for employment in the next cycle of esterification at optimum conditions.

FAME and Diesel Blend Composition

The FAME produced from the highest FFA conversion was blended with diesel fuel with various compositions (Table 2). The sample was shaken for 10 minutes and then allowed to stand for one hour at room temperature.

Table 2

Blend composition of FAME and diesel fuel

Product	FAME		Diesel fuel	
	%	mL	%	mL
B5	5	20	95	380
B10	10	20	90	360
B15	15	60	85	340
B20	20	80	80	320

FAME Characterization

The FAME, diesel, and blended water content were analyzed according to ASTM D6304 using the Karl Fischer method. The density was analyzed according to ASTM D1298 using a hydrometer. ASTM D86 was used to evaluate the distillation volume of fuel. The kinematic viscosity was determined according to ASTM D445. The color of the fuel was analyzed using ASTM D1500. Furthermore, the standard of ASTM D97 and ASTM D4737 was used to evaluate the fuel's pour point and cetane index, respectively. The FAME product was compared to the European FAME standard (EN 14214:2012). The functional groups of FAME were also assessed using FTIR.

RESULTS AND DISCUSSION

Catalyst Characterization

The montmorillonite-sulfonated carbon catalyst was characterized using FT-IR, SEM, and acidity. Figure 1 shows the FT-IR spectra of the catalyst with a variation ratio of montmorillonite to sulfonated carbon of 1:3, 1:1, and 3:1 (% w/w). The absorption peaks at 1087.05 cm^{-1} and 779.23 cm^{-1} were attributed to the interaction of Si-O-Si

and Si-O-Al bonds from montmorillonite (Munir et al., 2021). The absorption band at 3424.2 cm^{-1} indicated stretching vibrations of the hydroxyl groups. Subsequently, the functional groups of C=C and C-H aromatic were observed at 1628.28 cm^{-1} and 665.26 cm^{-1} due to the carbonization of molasses, which formed a polycyclic aromatic carbon compound, respectively (Flores et al., 2019). All peaks appeared in all catalyst variations. The absorption band at 1082 cm^{-1} corresponded to the $-\text{SO}_3\text{H}$ functional group due to the sulfonation process (Fadhil et al., 2016), whereas the absorption band at 452 cm^{-1} indicated the C-S-C bond (Fauziyah et al., 2020). Furthermore, Figure 1 shows that the sulfonated group intensity gradually increased as the carbon ratio increased. The more molasses composition, thus the more molasses is converted into carbon. This carbon framework could support the catalyst's active site (Tang et al., 2020). Hence, more SO_3H group was functionalized in the polycyclic aromatic carbon.

The effect of the montmorillonite to sulfonated carbon (% w/w) ratio on the acidity of the catalyst is shown in Figure 2. The acidity increased along with the increase in carbon composition. The highly volatile components of molasses are released during the carbonization process, leaving catalyst support with a high carbon content that provides the functionalization of the $-\text{SO}_3\text{H}$ active site during the sulfonation process (Endut et al., 2017). As molasses weight composition increased, the carbon formation also increased; consequently, a more sulfonated group was effectively attached to the carbon structure. The highest acidity of the catalyst (9.79 mmol/g) was obtained at the montmorillonite to sulfonated carbon 1:3 ratio. This finding was consistent with the FTIR analysis. The H^+ provided by the heterogeneous acid catalyst, the $-\text{SO}_3\text{H}$ group, was considered the active site, wherein the acidity was positively correlated to the catalytic activity (Xincheng et al., 2019). The sulfonated groups act as a Bronsted acid which could catalyze the esterification of FFA (Bastos et al., 2020). However, a prolonged high-weight ratio of montmorillonite to sulfonated carbon generated a relatively constant catalyst acidity (9.75 mmol/g) because the sulfonation process had already saturated, whereby the hydroxyl groups present in the carbon framework had been sulfonated and reached a maximum so that the acidity of the catalyst tends to remain constant.

The morphology surfaces of montmorillonite and montmorillonite-carbon sulfonated carbon catalyst is shown in Figure 3. Platy particles consisting of stacks of the layered thin structure were observed in Figure 3a. Alshabanat et al. (2013) reported that the typical montmorillonite structure was irregularly shaped and had many sides. Other studies reported similar findings (Munir et al., 2021). The composite of montmorillonite-sulfonated carbon revealed a significant morphological surface change with porous structure due to carbonization followed by sulfonation (Figure 3a). The carbonization process of molasses into carbon increases the number of cavities and pores. This condition increases the contact area over the sulfonated group, enhances the diffusion of alcohol, and promotes efficient interaction of FFA towards the active site (Fonseca et al., 2020).

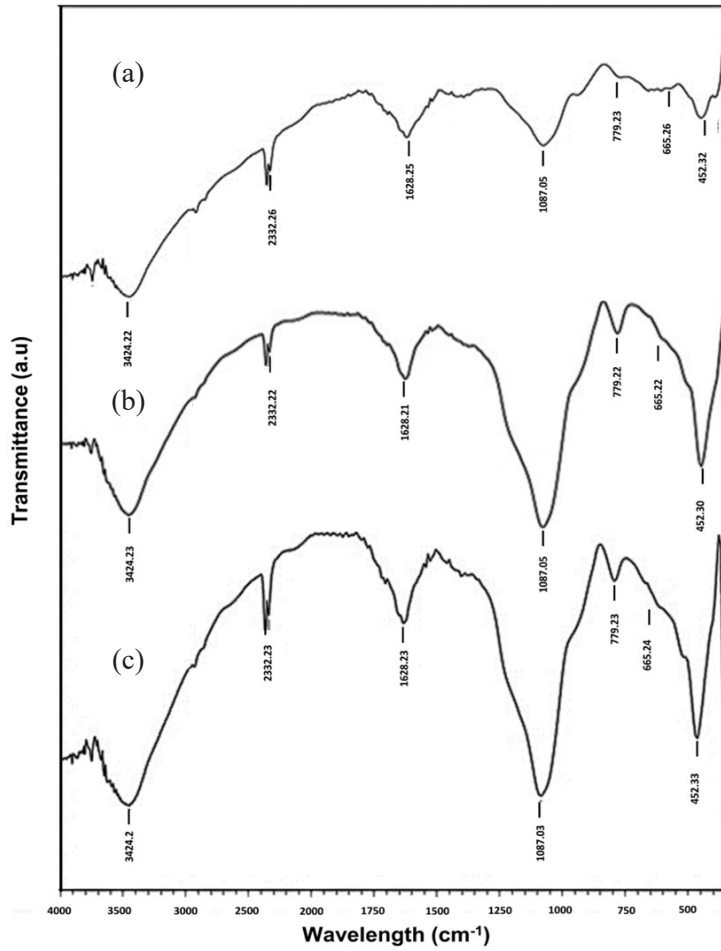


Figure 1. FTIR spectra of montmorillonite-sulfonated carbon of (a) 3:1 (b) 1:1 and (c) 1:3 catalyst

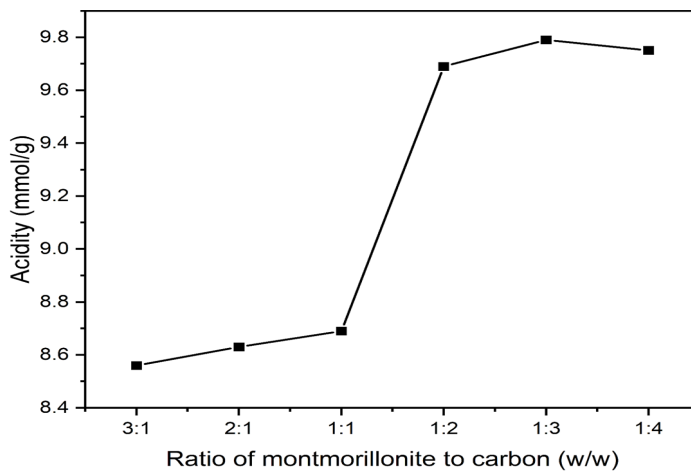


Figure 2. Effect of ratio of montmorillonite to carbon (% w/w) on catalyst acidity

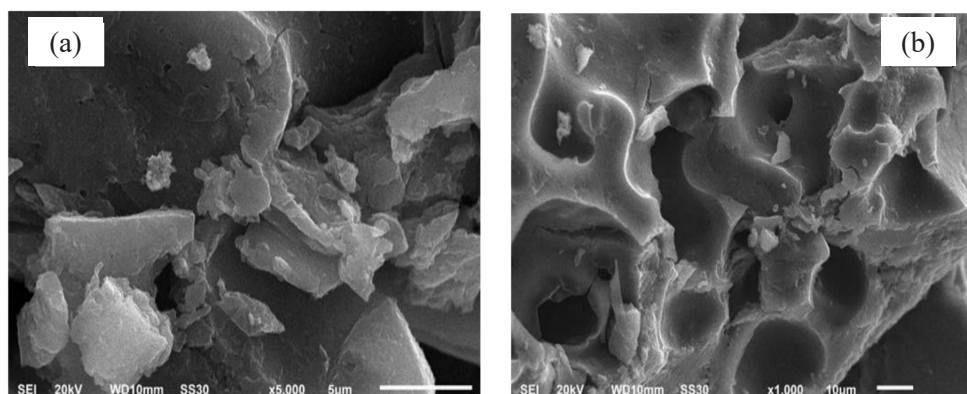


Figure 3. SEM images of (a) montmorillonite and (b) montmorillonite-sulfonated carbon catalyst

Figure 4 shows the N_2 adsorption-desorption of montmorillonite and montmorillonite-sulfonated carbon catalysts. Montmorillonite and montmorillonite-sulfonated carbon revealed type IV isotherm, which had a wide pore distribution (Rabie et al., 2018). Another study reported a similar finding (Lin et al., 2018). It also can be noticed that all catalysts had an H4 hysteresis that corresponded to the aggregates of laminar, which was nearly associated with the layer structure of bentonite (Amaya et al., 2020). Moreover, The typical adsorption-desorption curve at a relative pressure (~ 0.45) was attributed to the existence of small mesopores on the catalyst (de Oliveira et al., 2019). This small mesopore could promote the high accessibility of the active site. N_2 adsorption-desorption isotherm in Figure 4b revealed a distinctive curve at high relative pressure compared with montmorillonite, and this condition occurred presumably due to the sulfonated carbon effect. This curve was consistent with Lathiya et al. (2018), which utilized the sulfonated carbon catalyst derived from the waste orange peel for esterifying corn acid oil.

Table 3 represents the textural properties of montmorillonite and montmorillonite-sulfonated carbon. The montmorillonite-sulfonated carbon catalyst exhibited high surface area than montmorillonite. The montmorillonite was introduced to the sulfonated carbon, thereby increasing the surface area. A High surface area promoted the extent of the functional group ($-SO_3H$) to occupy the catalyst surface (Farabi et al., 2019). Furthermore, the increase in surface area was might presumably due to the repulsion force between SO_3H and other groups induced on the catalyst surface (Rahimzadeh et al., 2018).

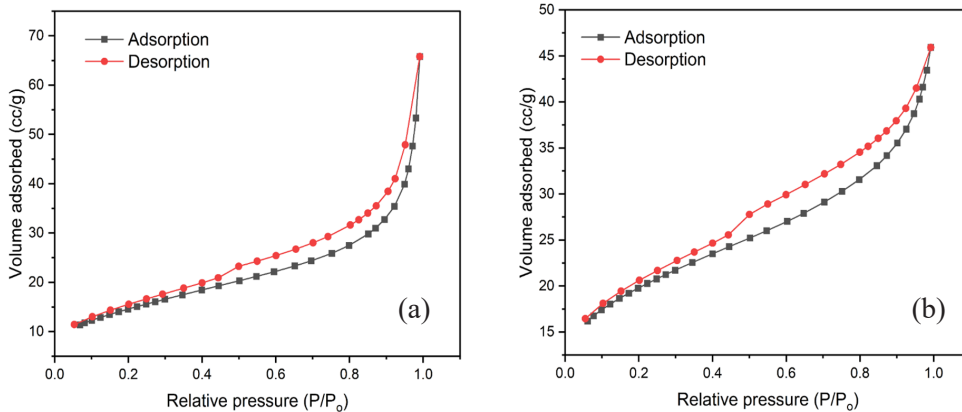


Figure 4. N₂ adsorption-desorption of (a) montmorillonite and (b) montmorillonite-sulfonated carbon catalyst

Table 3

Surface area, total pore volume, and average pore radius of catalysts

Catalyst	Surface area (m ² /g)	Total pore volume (cc/g)	Average pore radius (Å)
Montmorillonite	52.06	0.11	39.09
Montmorillonite-sulfonated carbon	67.12	0.071	21.16

Model Development and ANOVA

In this study, the montmorillonite-sulfonated carbon with a ratio variation of 1:3 was used for optimization because it showed the highest acidity catalyst. The relationship between the response, namely the conversion of FFA, and the process variables, namely reaction temperature, catalyst, and reaction time, were investigated. The experimental design results for 17 runs based on CCD are shown in Table 4. Substantial results were observed in the conversion of FFA under different mild conditions. FFA conversions obtained ranged from 45 to 74.29 %.

Table 4

Experimental result of FFA conversion using CCD

Run	Reaction temperature (°C)	Catalyst weight (g)	Reaction time (min)	FFA conversion (%)
1	70	1	90	45
2	90	1	90	49.821
3	70	3	90	54.214
4	90	3	90	64.286

Table 4 (Continue)

Run	Reaction temperature (°C)	Catalyst weight (g)	Reaction time (min)	FFA conversion (%)
5	70	1	150	47.321
6	90	1	150	56.25
7	70	3	150	73.214
8	90	3	150	74.286
9	63.18	2	120	44.286
10	96.82	2	120	50.179
11	80	0.31	120	47.679
12	80	3.68	120	73.75
13	80	2	69.55	52.679
14	80	2	170.45	55.464
15	80	2	120	65.964
16	80	2	120	65.321
17	80	2	120	65.179

The quadratic model for the conversion of FFA in the coded form is shown in Equation 3:

$$Y = 65.18 + 2.55A + 8.16B + 3.11C - 0.32AB - 0.61AC + 2.53BC - 5.40A^2 - 0.63B^2 - 2.98C^2 \quad (3)$$

The terms A, B, and C represented the single effect regarding the reaction temperature, catalyst, and reaction time, respectively (Equation 3). AB, AC, and BC represented the interaction effect for each variable, whereas the terms A^2 , B^2 , and C^2 were the quadratic effects. The positive and negative signs correspond to the synergistic and antagonistic effects on the FFA conversion, respectively (Almadani et al., 2018). The ANOVA of the model (95% confidence level) derived from Equation 3 is shown in Table 5.

The P-value of the model was 0.0060, which indicates that the model was statistical significance (Table 5). Likewise, the model's F-value correlated to the FFA conversion was 8.01. This F-value explained that the model was significant, and there was only a 0.60% chance that this high F-value could occur owing to noise (Balajii & Niju, 2021). Subsequently, the terms B, C, and A^2 showed a P-value of <0.05, which indicated that the terms were statistically significant. Furthermore, a sufficient adequate precision value was observed to be more than 4, which was 9.3020. This condition indicated that the model generated an adequate signal and could navigate the quadratic model design (Boey et al., 2013). The statistical diagnostic was conducted to understand the development of the model

(Figure 5). The normal plot (Figure 5a) revealed a straight line that expressed a decent direct agreement between normal probability (%) and externally studentized residuals (Hasanudin, Asri, Said et al., 2022). It appeared that the response transformation was not required and that there were no major problems with the data's normality (Chandane et al., 2020).

The residual plot (Figure 5b) showed that the data were randomly scattered, indicating that the proposed model accurately described the process (Helmi et al., 2020). Figure 5c shows the plot of the predicted value obtained from the quadratic model with respect experimental value. The predicted value based on the model calculation was close to the experimental data, with the coefficient of determination (R^2) value found to be 0.9115. This R^2 value indicated that the prediction model was sufficiently accurate to identify the optimal process parameters with a response variability of 91% (Balajii & Niju, 2021). Figure 5d shows the externally studentized residual respect with a run number plot. The outliers from the run experiments showed that all residual points were in the +3.8 and -3.8 intervals, indicating a good distribution for the CCD design (Noshadi et al., 2012). The leverage respect with a run number plot is shown in Figure 5e. According to the plot, all points are less than one, which was associated with no significant error that could affect the model. Furthermore, the parameter of Cook's distance in Figure 5f revealed that all the points were under the expected, which attributed that there was no significant error in observation (Kusumaningtyas et al., 2021). All statistical diagnostics indicated that the proposed quadratic model was proficient in optimizing the FFA conversion using montmorillonite-sulfonated carbon from a molasses catalyst.

Table 5
ANOVA for the quadratic model

Source	Sum of square	df	Mean	F-value	P-value	
Model	1559.27	9	173.25	8.01	0.0060	significant
A-Reaction temperature	88.70	1	88.70	4.10	0.0825	
B-Catalyst weight	909.58	1	909.58	42.07	0.0003	
C-Reaction time	131.85	1	131.85	6.10	0.0429	
AB	0.8489	1	0.8489	0.0393	0.8486	
AC	2.99	1	2.99	0.1384	0.7209	
BC	51.26	1	51.26	2.37	0.1675	
A ²	328.99	1	328.99	15.22	0.0059	
B ²	4.55	1	4.55	0.2106	0.6602	
C ²	100.39	1	100.39	4.64	0.0681	
Residual	151.34	7	21.62			
Lack of Fit	150.99	5	30.20	172.5821	0.0058	
Pure Error	0.3499	2	0.1750			
Cor Total	1710.61	16				

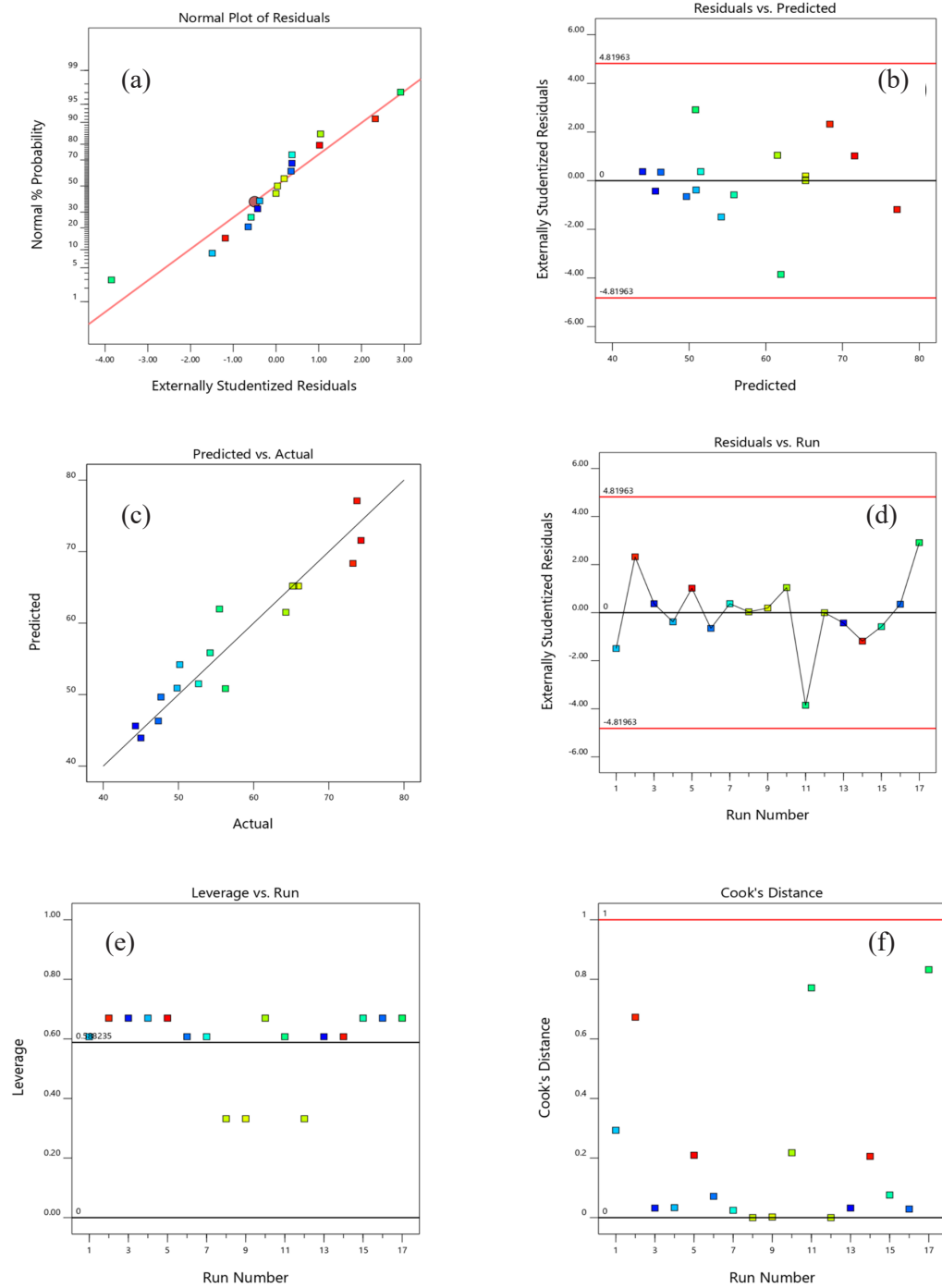


Figure 5. The statistical diagnostic of the development model

Optimization Study

Graphical and numerical optimization procedures were used to predict the optimum conditions of three factors, including reaction temperature, catalyst weight, and reaction time, which resulted in the desired goal of the response variable, namely FFA conversion. The response surface and contour plots were assessed to see the interaction of variables (Figure 6). The interaction effect of a catalyst weight and a reaction temperature at a constant reaction time of 120 min is shown in Figure 6a. The highest FFA conversion was achieved up to 70% when the catalyst weight was higher than 3 g, and the reaction temperature ranged from 70–90°C. Under these conditions, a high catalyst weight presumably increased the number of active catalyst sites, promoting the high FFA conversion (Anguebes-Franceschi et al., 2018). As the temperature increased to 90°C, the collisions between reactants also increased, sufficiently leading to high FFA conversion. Furthermore, these conditions also tended to reduce the mixture's viscosity, thereby increasing diffusion through the pores (Mulay & Rathod, 2021). Gan et al. (2012) reported that the highest conversion of FFA in WCO was achieved up to 60.2% at a temperature of 65°C and a concentration catalyst of 4 wt.% using Amberlyst-15 catalyst. Özbay et al. (2008) used a series of ion-exchange resins, such as an Amberlyst-based catalyst. They showed that the FFA conversion was achieved up to 45.7% when the temperature was 60°C with 2% wt catalyst concentration. Sulfonated nanomagnetic biochar derived from oil palm empty fruit bunch was employed by Jenie et al. (2020), which revealed that at 2.5%wt catalyst concentration, the oleic acid conversion was exhibited up to 71.2%. The montmorillonite-sulfonated carbon derived from the molasse catalyst was likely promising in catalyzing the FFA esterification in WCO relative to previously reported catalysts.

The interaction effect of reaction time and catalyst weight at a constant reaction temperature of 80°C is presented in Figure 6b. The FFA conversion increased at a high catalyst loading of more than 2 g and reaction time ranged from 90–20 min. The longer reaction time did not result in a substantial increase in the FFA conversion. The reaction would approach equilibrium; therefore, no additional conversion would be generated. Jenie et al. (2020) stated that the considerable drop in conversion at longer reaction periods could be attributed to by-product generation or deactivation of the catalyst's active sites. Suresh et al. (2017) utilized sulfonated polystyrene (PSS) for esterification of FFA in WCO and reported that at a reaction temperature of 75°C and PSS concentration of 2% w/w, the conversion exhibited up to 80.8%. Zhang et al. (2015) used sulfonated mesoporous carbon for the esterification of FFA and showed that a prolonged reaction time of up to three hours would produce high FFA conversion than 80%, whereas Dawodu et al. (2014) generated high FFA conversion derived from sludge palm oil at 4 hours reaction when employing sulfonated carbon from glucose with *C. inophyllum* seed cake.

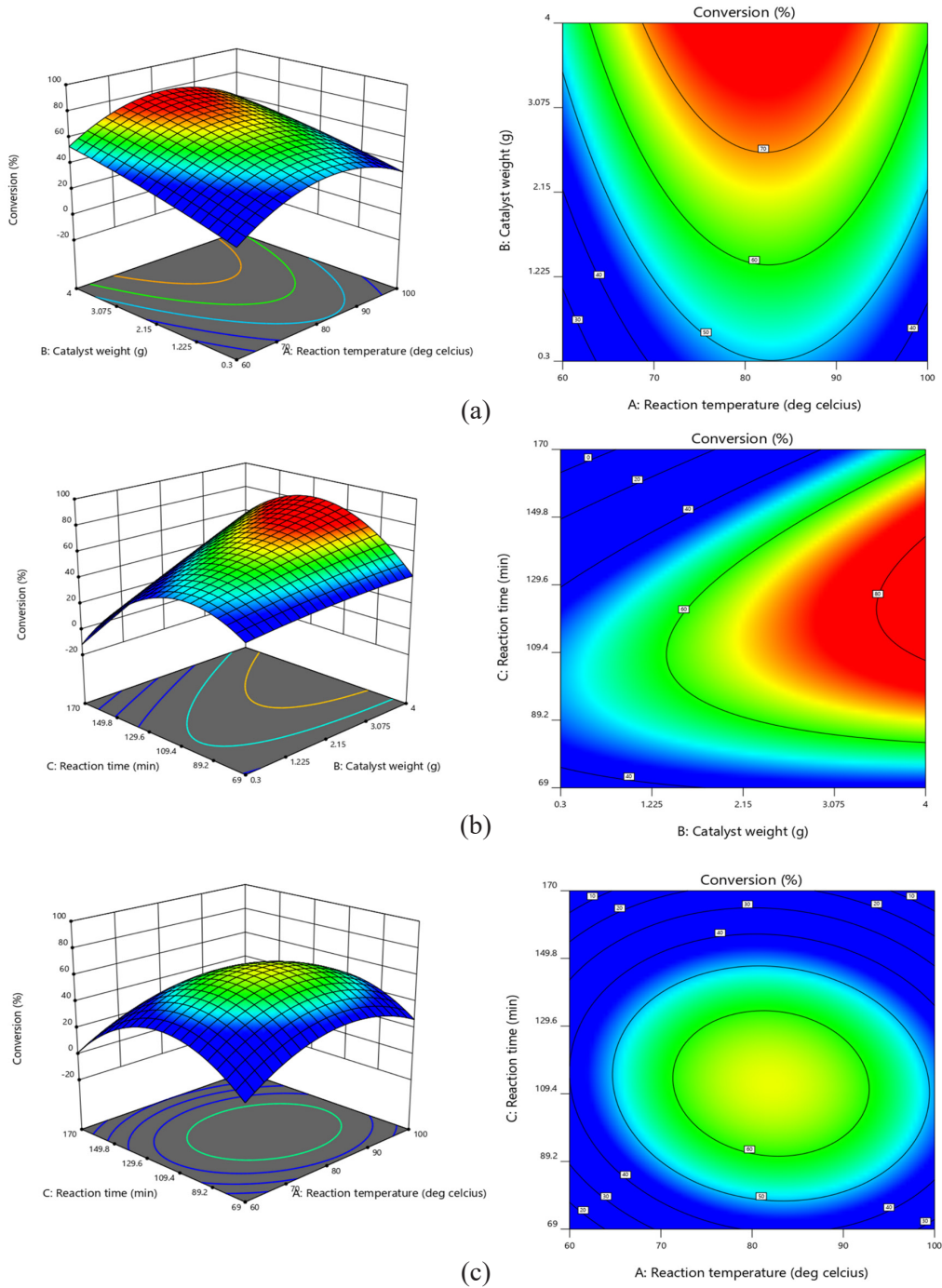


Figure 6. The 3D surface and contour plot of interaction variables on the FFA conversion

The interaction effect of reaction time and reaction temperature at a constant catalyst weight of 2 g is shown in Figure 6c. It was found that the highest FFA conversion was achieved up to 60% at a reaction temperature of 70–90°C and a reaction time of 90–130 min. When the reaction temperature was too high, it would encourage the reverse reaction, decreasing FFA conversion. Simultaneously, the high temperature accelerates the methanol loss rate, potentially reducing catalytic effectiveness (Zhang et al., 2021). As reaction time gradually increased, the FFA conversion also increased due to the availability of sufficient time to complete the reaction (Figure 6c). However, the FFA conversion began to decrease at a long reaction time due to the reverse reaction. These results are also in accordance with the previous report (Narula et al., 2017). Furthermore, a higher reaction time was unfavorable for the esterification reaction since it consumes more energy (Fawaz et al., 2020).

The optimization of FFA conversion by Design-Expert using the numerical method was used to optimize the studied parameters. According to the optimization, the optimum condition was obtained at a reaction temperature of 78.12°C, catalyst weight of 2.98 g, and reaction time of 118.27 with an FFA conversion of 74.101%. In addition, the desirability function was found to be one, which indicated that the developed solution was good. The validation showed that the predicted response was in good accordance with the experimental results.

Catalyst Reusability

The study of catalyst reusability was conducted under the optimized condition obtained from RSM-CCD. Figure 7 represents montmorillonite-sulfonated carbon's reusability performance in FFA conversion at three consecutive runs. It can be noticed that the FFA conversion was slightly decreased in the first cycle. In this first cycle, 70.25% of FFA conversion was achieved, indicating a decrease in the catalyst performance up to 5.07% relative to the fresh catalyst (74% FFA conversion). Moreover, the catalyst's performance was shown significantly reduce up to 9.55% in the second cycle and noticeably decreased in the three consecutive runs, which only generated 60.23% FFA conversion. The decrease in FFA conversion could presumably be due to the active site's leaching, i.e., the sulfonate group (Dhawane et al., 2016). Another study consistently reported a similar finding (Farabi et al., 2019; Tang et al., 2020). This leaching was likely due to insufficient and ineffective regeneration through the alcohol-washing process (Ngaosuwan et al., 2016). In this regard, catalyst regeneration by performing a sulfonation process on the spent catalyst was necessary to return the catalytic activity.

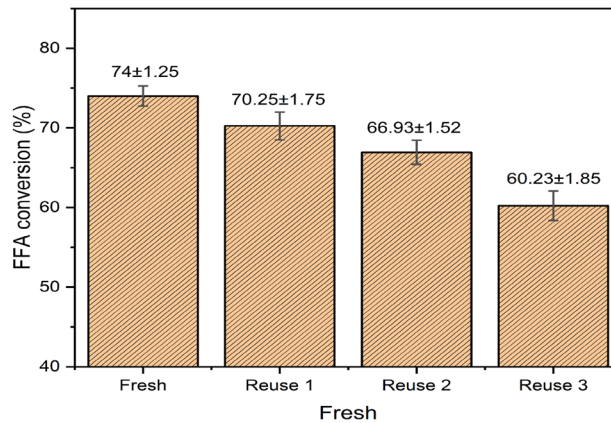


Figure 7. Reusability of catalyst

FAME Physicochemical Properties

The FAME product generated from the optimized esterification reaction and the feedstock, namely WCO, were analyzed using GC and FTIR. GC analysis showed that WCO contained the highest fatty acid composition, namely oleic acid at 43.51% and palmitic acid at 39.75%. This finding was similar to Azman et al. (2021), which reported that WCO consisted of oleic acid (48.1%) as the primary fatty acid, followed by palmitic acid (22%). In contrast, Kumar et al. (2020) found that the WCO consisted of 46.32 wt% palmitic acid and 41.65% oleic acid. These different results are due to the diversity of waste cooking oil sources. The analysis results of FFA content in WCO using the titration method were 36.94%. The FFA content on WCO decreased to 5.938% after esterification using montmorillonite-sulfonated carbon catalyst with a conversion of 83.925%, which indicated that FFA from WCO was potential as a FAME feedstock. In this reaction, the sulfonated groups on the montmorillonite framework act as an active site of Bronsted acid, which could catalyze the esterification of FFA from WCO (Hasanudin, Putri, et al., 2022). The FTIR of WCO and the product of esterification are presented in Figure 8. It can be seen that due to the main structural change was the substitution of methanol in the hydrocarbon chain, the FTIR spectrum of FAME was mainly similar to the WCO, as consistent with previous reports (Kamaranzaman et al., 2020a; Rafati et al., 2019).

The absorption bands from Figure 8a at 2924.02 cm^{-1} and 2854 cm^{-1} were attributed to C-H symmetrical and asymmetrical alkane groups (Banerjee et al., 2019). Subsequently, absorption bands at 1743.65 cm^{-1} corresponded to the ester groups from triglyceride. Furthermore, the region bands at 1458.16 cm^{-1} and 1373.23 cm^{-1} indicated the C-H bending vibration (Mahesh et al., 2015), also revealed in Figure 8b. FAME provided a strong absorption band due to the vibrations of the C=O and C-O bonds. The absorption band at

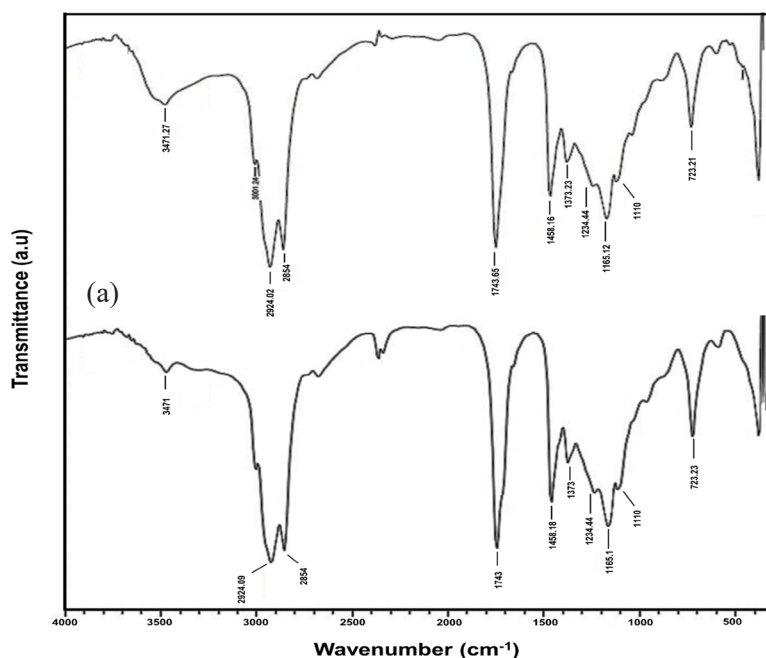


Figure 8. FTIR spectra of (a) WCO and (b) Esterification product

1743.65 cm^{-1} was commonly from the C=O carbonyl group in saturated aliphatic esters (Helmi et al., 2020). The aryl and α,β -unsaturated structures could generate a minor shift in these bands to lower wavenumber (Omidvarborna et al., 2016).

Subsequently, the C-O stretching vibrations appeared at a broader range at 1110 cm^{-1} and were also observed in the FAME spectrum. Long-chain fatty acids in FAME often exhibited an increment to maximum absorption approximately at the absorption band at 1234.44 cm^{-1} , 1165 cm^{-1} , and 723.23 cm^{-1} , respectively (Bahú et al., 2017; Wu et al., 2015). The absorption band at 3471 cm^{-1} indicated the hydroxyl group vibration absorbed by the catalyst (Akram et al., 2019).

The results of the FAME properties analysis from WCO and its standard are shown in Table 6. It shows that the FAME from WCO had a water content of 344 ppm, presumably appearing from palm oil's endocarp component. Besides that, the WCO had been in contact with other components during frying, which caused water's presence. Viscosity and density are the main factors for diesel fuel injection and efficient combustion (Ibeto et al., 2012). The higher the water content in the FAME, led the density (0.8711 Kg/L) and viscosity (4.872 cSt) were also higher. A heavy fraction in the methyl ester accompanies a higher distillation temperature and less distillate (92 mL) that is directly related to the relatively high carbon residue. This condition might inhibit the performance of the diesel engine. The FAME from WCO had the same color characteristics (1.5) as the pure diesel

fuel, which indicated that the FAME had similar good quality. In addition, the cetane index shows a reasonably good value (53.5) above the minimum standard of biodiesel (51). The higher the cetane index of fuel, the better the quality of the fuel as well as provided lower the delay period in the engines (Abdelhady et al., 2020). These results indicated that the FAME derived from WCO has the potential to be used as a blend to improve the quality of diesel fuel.

Table 6

Physicochemical properties of FAME from WCO

Properties	Units	Results	FAME standard (EN 14214:2012)
Water content	ppm	344	Max. 500
Density	Kg/L	0.8711	0.860-0.900
Volume distillate	mL	92	Min. 90
Kinematic viscosity, 40°C	mm ² /s (cSt)	4.872	3.5-5.0
Pour point	°C	6	-
Color	-	1.5	-
Cetane index	-	53.5	Min. 51

Effect of the FAME and Diesel Composition Blend

In this study, the FAME product derived from the WCO esterification was blended with diesel with various blends, namely B5, B10, B15, and B20, as previously mentioned. The B0 was referred to as the diesel without adding FAME, whereas the B100 was vice versa. The effect of FAME and diesel composition blend on water content and density are shown in Figure 9.

Analysis of water content using the ASTM D-6304 method showed that the FAME from WCO had a water content of 344 ppm (Figure 9). This value encounters the maximum limit of the biodiesel standard (500 ppm). The water content in methyl esters was quite high since biodiesel's density was close to water; thus, biodiesel was more easily bound to water. When the volume added of FAME to diesel fuel increased, the water content also increased (Figure 9). The lowest water content (314 ppm) was achieved by B5, whereas the highest water content (339 ppm) was achieved by B20. In this study, all blend compositions obtained a water content below 500 ppm, which met the criteria of the biodiesel standard. Most diesel engines are composed of metal, which is corrosive in the combustion chamber. High water content in the fuel could cause the hydrolysis of FAME and provoke the growth of microorganisms, which could block the flow in the combustion engine (Fregolente et al., 2012; Lin & Ma, 2020).

The density of diesel blended increased with the increasing volume of methyl ester added to diesel fuel (Figure 9). FAME contained oleic acid ($C_{18}H_{34}O_2$), almost similar to diesel oil ($C_{15}-C_{20}$). When the methyl ester of oleic acid was mixed with diesel oil, it increased the length of the bond chain; thereby, the fraction in the blend increased. The density was directly proportional to the molecular weight. Thus, when the molecule's chain length increased, the blend's density also increased (Hajilar & Shafei, 2019). The density of the diesel composition blend ranged from 0.8507 to 0.8615 Kg/L, which indicated that the results follow the density of diesel fuel standards.

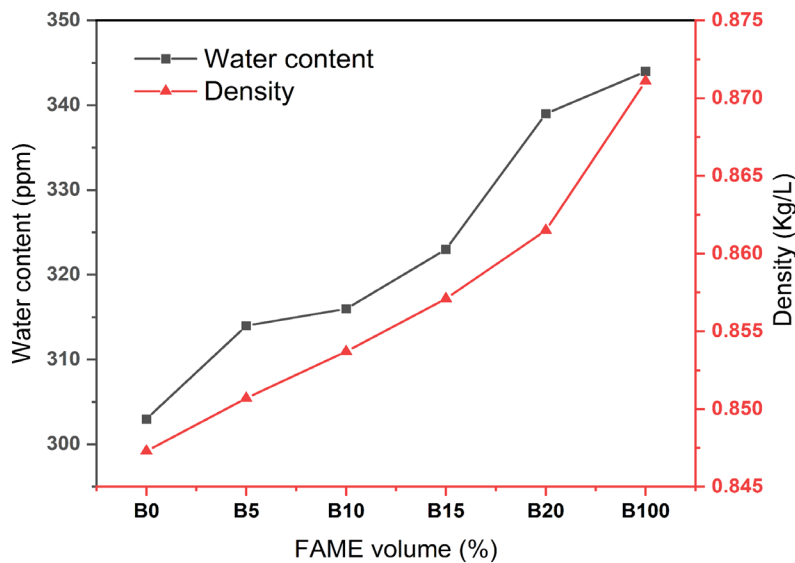


Figure 9. Effect of FAME and diesel composition blend on water content and density

The effect of FAME and diesel composition blend on distillate volume and viscosity are presented in Figure 10. The volume of distillate from the blend of FAME with diesel was lower than the FAME itself, which indicated that the weight fraction in FAME from WCO was relatively high. Similarly, the distillate volume decreased as the amount of FAME added to the diesel blend increased.

Viscosity reveals the lubricating properties of the fuel. Kinematic viscosity measurements using the ASTM D-445 method are conducted to determine the viscosity of fuel or the amount of internal resistance of a liquid to flow related to the supply of fuel consumption in the diesel engine combustion chamber. Kinematic viscosity was directly proportional to the length of the carbon chain and density. Subsequently, it can be seen from Figure 10 that the viscosity increased along with the increase of FAME volume to the diesel fuel. As viscosity is directly proportional to molecular weight, adding FAME to diesel would increase the carbon length chain, thereby increasing the viscosity. The higher

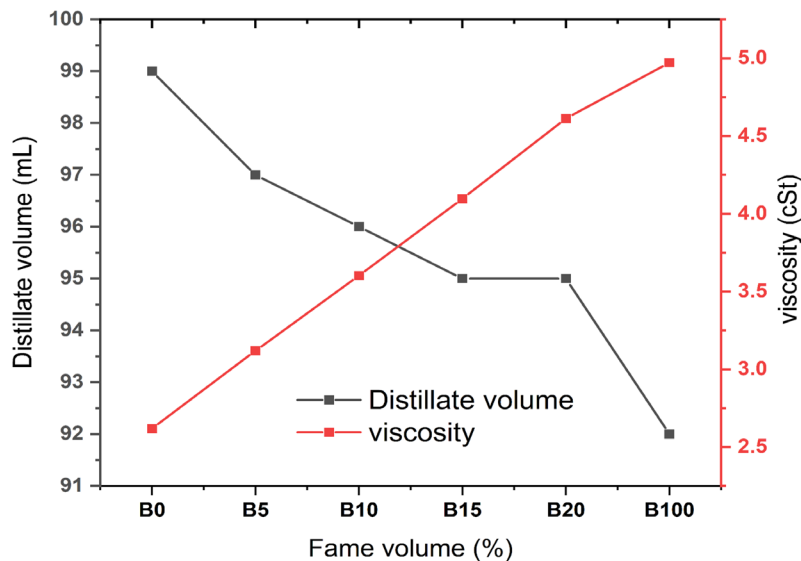


Figure 10. Effect of FAME and diesel composition blend on distillate volume and viscosity

the viscosity, the more difficult the combustion and the slower the piston work. All the blends were in accordance with diesel fuel standards, which corresponded to the engine's good atomization and complete combustion of biodiesel (Karmakar et al., 2018).

Kinematic viscosity measurements using the ASTM D-445 method are conducted to determine the viscosity of fuel or the amount of internal resistance of a liquid to flow related to the supply of fuel consumption in the diesel engine combustion chamber. Kinematic viscosity was directly proportional to the length of the carbon chain and density. Subsequently, it can be seen from Figure 10 that the viscosity increased along with the increase of FAME volume to the diesel fuel. As viscosity is directly proportional to molecular weight, adding FAME to diesel would increase the carbon length chain, thereby increasing the viscosity. The higher the viscosity, the more difficult the combustion and the slower the piston work. All the blends were in accordance with diesel fuel standards, which corresponded to the engine's good atomization and complete combustion of biodiesel (Karmakar et al., 2018).

The effect of FAME and diesel composition blend on color and pour point are shown in Figure 11. Color is a parameter that prevents the possibility of contamination by heavier fuels or water and other substances. This contamination affects the oil quality, resulting in operating failure and engine damage. The color observations results show a linear line on a scale of 1.5 (max. standard diesel = 3), which indicated that the FAME derived from WCO and their blends had a fairly good quality because they had an observation scale that was relatively close to diesel color (Figure 11).

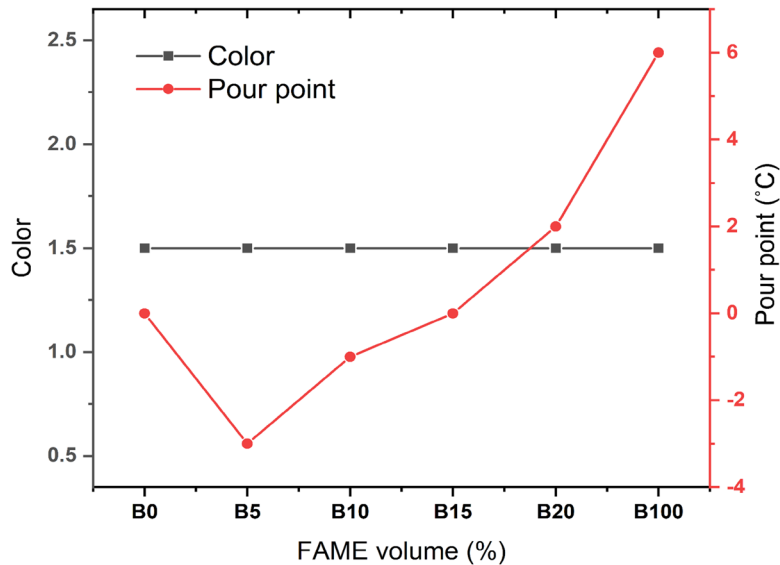


Figure 11. Effect of FAME and diesel composition blend on color and pour point

The pour point of FAME was quite high, at a temperature of 6°C, whereas diesel fuel was achieved at a temperature of 0°C (Figure 11). The pour points of B5 and B10 reached low temperatures of -3°C and -1°C, respectively, exceeding the pour point of pure diesel, whereas, in a blend of B15, the pour point was the same as the pure diesel, which was 0°C. Furthermore, the pour point of the B20 blend increased closer to FAME. The lower the pour point of the fuel, the better the engine's combustion quality because the fuel could still work to lubricate the engine at the lowest temperature. If the fuel is difficult to flow into the combustion chamber, it signifies that converting heat into motion energy by the piston is increasingly difficult. The type of oil and the content or components present in the oil influences the pour point quantity. In addition, the density, viscosity, and solubility of a gas in oil were also influenced.

The cetane index measurement was conducted to determine the ignition quality of diesel fuel. Diesel engines required a cetane number of roughly 50. The fuel cetane number was a volume percentage of cetane and alpha-methyl naphthalene, wherein cetane has better ignition qualities than alpha-methyl naphthalene. The cetane index was needed to prevent engine knocking. The higher the cetane index of diesel fuel, the better the combustion properties (Giakoumis & Sarakatsanis, 2018). The effect of FAME and diesel composition blend on the cetane index is presented in Figure 12.

The index increases along with the amount of FAME added to the diesel blend (Figure 12). The cetane index of pure diesel was 48.5, whereas, after the addition of FAME (B20), the cetane index of the blend increased up to 51.2%. Furthermore, the blend of B10 and

B15 showed no significant difference in cetane index between the two blends. Generally, biodiesel has a higher cetane number than diesel, ranging from 46 to 70. The length of the hydrocarbon chain contained in the FAME caused the cetane number of biodiesel to be higher than diesel (Mishra et al., 2016). The increase of the cetane number from 48.5 to 51.2 would reduce carbon monoxide emissions by 5.27%. In terms of fuel consumption, increasing the cetane number would reduce both fuel engine consumption and engine noise (Rodríguez-Fernández et al., 2019). The results showed that the cetane index of all blends was in accordance with the standard for diesel, with a minimum cetane number of 48. The higher cetane number of biodiesel than diesel leads to better combustion properties of the engine.

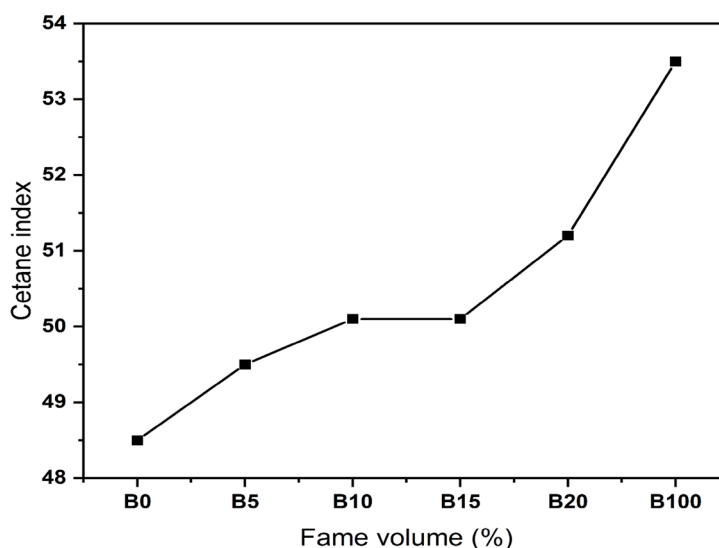


Figure 12. Effect of FAME and diesel composition blend on cetane index

CONCLUSION

In this research, the free fatty acid (FFA) conversion from waste cooking oil (WCO) using montmorillonite-sulfonated carbon catalyst was conducted using response surface methodology (RSM) with a central composite design (CCD). The highest acidity of the catalyst was achieved up to 9.79 mmol/g by montmorillonite to sulfonated carbon 1:3 weight ratio catalyst. The montmorillonite-sulfonated carbon exhibited a higher surface area compared with montmorillonite. The optimum condition was obtained at a reaction temperature of 78.12°C, catalyst weight of 2.98 g, and reaction time of 118.27 with an FFA conversion of 74.101%. A sufficient statistical diagnostic revealed that the RSM-CCD quadratic model could accurately predict the FFA conversion from WCO using a montmorillonite-sulfonated carbon catalyst. The optimum condition for the blend of FAME

and diesel fuel was achieved at the composition of the blend of B20 and in good accordance with the FAME standard. The reusability of the catalyst at three consecutive runs showed that the catalyst had adequate stability but tended to decrease due to the leaching of the active site catalyst.

ACKNOWLEDGEMENTS

The authors thank the Physical Chemistry laboratory and all members of the Biofuel Research Group, Faculty of Mathematics and Natural Science, Universitas Sriwijaya, for supporting research facilities.

REFERENCES

- Abdelhady, H. H., Elazab, H. A., Ewais, E. M., Saber, M., & El-Deab, M. S. (2020). Efficient catalytic production of biodiesel using nano-sized sugar beet agro-industrial waste. *Fuel*, *261*, Article 116481. <https://doi.org/10.1016/j.fuel.2019.116481>
- Akram, S., Mumtaz, M. W., Danish, M., Mukhtar, H., Irfan, A., Raza, S. A., Wang, Z., & Arshad, M. (2019). Impact of cerium oxide and cerium composite oxide as nano additives on the gaseous exhaust emission profile of waste cooking oil based biodiesel at full engine load conditions. *Renewable Energy*, *143*, 898-905. <https://doi.org/10.1016/j.renene.2019.05.025>
- Ali, C. H., Asif, A. H., Iqbal, T., Qureshi, A. S., Kazmi, M. A., Yasin, S., Danish, M., & Mu, B. Z. (2018). Improved transesterification of waste cooking oil into biodiesel using calcined goat bone as a catalyst. *Energy Sources, Part A: Recovery, Utilization and Environmental Effects*, *40*(9), 1076-1083. <https://doi.org/10.1080/15567036.2018.1469691>
- Almadani, E. A., Harun, F. W., Radzi, S. M., & Muhamad, S. K. (2018). Cu²⁺ montmorillonite K10 clay catalyst as a green catalyst for production of stearic acid methyl ester: Optimization using response surface methodology (RSM). *Bulletin of Chemical Reaction Engineering & Catalysis*, *13*(1), 187-195. <https://doi.org/10.9767/bcrec.13.1.1397.187-195>
- Al-Sakkari, E. G., Abdeldayem, O. M., El-Sheltawy, S. T., Abadir, M. F., Soliman, A., Rene, E. R., & Ismail, I. (2020). Esterification of high FFA content waste cooking oil through different techniques including the utilization of cement kiln dust as a heterogeneous catalyst: A comparative study. *Fuel*, *279*, Article 118519. <https://doi.org/10.1016/j.fuel.2020.118519>
- Alshabanat, M., Al-Arrash, A., & Mekhamer, W. (2013). Polystyrene/montmorillonite nanocomposites: Study of the morphology and effects of sonication time on thermal stability. *Journal of Nanomaterials*, *2013*, Article 650725. <https://doi.org/10.1155/2013/650725>
- Amaya, J., Suarez, N., Moreno, A., Moreno, S., & Molina, R. (2020). Mo or W catalysts promoted with Ni or Co supported on modified bentonite for decane hydroconversion. *New Journal of Chemistry*, *44*(7), 2966-2979. <https://doi.org/10.1039/c9nj04878b>
- Anguebes-Franseschi, F., Abatal, M., Bassam, A., Soberanis, M. A. E., Tzuc, O. M., Bucio-Galindo, L., Quiroz, A. V. C., Ucan, C. A. A., & Ramirez-Elias, M. A. (2018). Esterification optimization of crude African palm olein using response surface methodology and heterogeneous acid catalysis. *Energies*, *11*(1), Article 157. <https://doi.org/10.3390/en11010157>

- Azman, N. S., Marliza, T. S., Asikin-Mijan, N., Hin, T. Y. Y., & Khairuddin, N. (2021). Production of biodiesel from waste cooking oil via deoxygenation using Ni-Mo/Ac catalyst. *Processes*, 9(5), Article 750. <https://doi.org/10.3390/pr9050750>
- Bahú, J., Hernandez, N., Bonon, A., Bonon, A. D. J., Mart, M., & Gregorio, J. (2017). Epoxy monomers obtained from castor oil using a toxicity-free catalytic system Related papers. *Journal of Molecular Catalysis A: Chemical*, 426, 550-556.
- Balajii, M., & Niju, S. (2021). Esterification optimization of underutilized Ceiba pentandra oil using response surface methodology. *Biofuels*, 12(5), 495-502. <https://doi.org/10.1080/17597269.2018.1496384>
- Banerjee, S., Sahani, S., & Sharma, Y. C. (2019). Process dynamic investigations and emission analyses of biodiesel produced using Sr-Ce mixed metal oxide heterogeneous catalyst. *Journal of Environmental Management*, 248, Article 109218. <https://doi.org/10.1016/j.jenvman.2019.06.119>
- Bastos, R. R. C., da Luz Corrêa, A. P., da Luz, P. T. S., da Rocha Filho, G. N., Zamian, J. R., & da Conceição, L. R. V. (2020). Optimization of biodiesel production using sulfonated carbon-based catalyst from an amazon agro-industrial waste. *Energy Conversion and Management*, 205, Article 112457. <https://doi.org/10.1016/j.enconman.2019.112457>
- Bayat, A., Baghdadi, M., & Bidhendi, G. N. (2018). Tailored magnetic nano-alumina as an efficient catalyst for transesterification of waste cooking oil: Optimization of biodiesel production using response surface methodology. *Energy Conversion and Management*, 177, 395-405. <https://doi.org/10.1016/j.enconman.2018.09.086>
- Boey, P. L., Ganesan, S., Maniam, G. P., Khairuddean, M., & Efendi, J. (2013). A new heterogeneous acid catalyst for esterification: Optimization using response surface methodology. *Energy Conversion and Management*, 65, 392-396. <https://doi.org/10.1016/j.enconman.2012.08.002>
- Boffito, D. C., Pirola, C., Galli, F., Di Michele, A., & Bianchi, C. L. (2013). Free fatty acids esterification of waste cooking oil and its mixtures with rapeseed oil and diesel. *Fuel*, 108, 612-619. <https://doi.org/10.1016/j.fuel.2012.10.069>
- Chandane, V. S., Rathod, A. P., Wasewar, K. L., & Jadhav, P. G. (2020). Response surface methodology and artificial neural networks for optimization of catalytic esterification of lactic acid. *Chemical Engineering and Technology*, 43(11), 2315-2324. <https://doi.org/10.1002/ceat.202000041>
- Chen, C., Chitose, A., Kusadokoro, M., Nie, H., Xu, W., Yang, F., & Yang, S. (2021). Sustainability and challenges in biodiesel production from waste cooking oil: An advanced bibliometric analysis. *Energy Reports*, 7, 4022-4034. <https://doi.org/10.1016/j.egy.2021.06.084>
- Chen, S. Y., Attanatho, L., Chang, A., Laosombut, T., Nishi, M., Mochizuki, T., Takagi, H., Yang, C. M., Abe, Y., Toba, M., Chollacoop, N., & Yoshimura, Y. (2019). Profiling and catalytic upgrading of commercial palm oil-derived biodiesel fuels for high-blend fuels. *Catalysis Today*, 332, 122-131. <https://doi.org/10.1016/j.cattod.2018.05.039>
- Dawodu, F. A., Ayodele, O., Xin, J., Zhang, S., & Yan, D. (2014). Effective conversion of non-edible oil with high free fatty acid into biodiesel by sulphonated carbon catalyst. *Applied Energy*, 114, 819-826.
- de Oliveira, A. de N., de Lima, M. A. B., Pires, L. H. de O., da Silva, M. R., da Luz, P. T. S., Angélica, R. S., Filho, G. N. d. R., da Costa, C. E. F., Luque, R., & do Nascimento, L. A. S. (2019). Bentonites modified

- with phosphomolybdic heteropolyacid (HPMo) for biowaste to biofuel production. *Materials*, *12*(9), Article 1431. <https://doi.org/10.3390/ma12091431>
- Dhawane, S. H., Kumar, T., & Halder, G. (2015). Central composite design approach towards optimization of flamboyant pods derived steam activated carbon for its use as heterogeneous catalyst in transesterification of *Hevea brasiliensis* oil. *Energy Conversion and Management*, *100*, 277-287. <https://doi.org/10.1016/j.enconman.2015.04.083>
- Dhawane, S. H., Kumar, T., & Halder, G. (2016). Biodiesel synthesis from *Hevea brasiliensis* oil employing carbon supported heterogeneous catalyst: Optimization by Taguchi method. *Renewable Energy*, *89*, 506-514. <https://doi.org/10.1016/j.renene.2015.12.027>
- Ding, J., Xia, Z., & Lu, J. (2012). Esterification and deacidification of a waste cooking oil (TAN 68.81 mg KOH/g) for biodiesel production. *Energies*, *5*(8), 2683-2691. <https://doi.org/10.3390/en5082683>
- Endut, A., Abdullah, S. H. Y. S., Hanapi, N. H. M., Hamid, S. H. A., Lananan, F., Kamarudin, M. K. A., Umar, R., Juahir, H., & Khatoun, H. (2017). Optimization of biodiesel production by solid acid catalyst derived from coconut shell via response surface methodology. *International Biodeterioration and Biodegradation*, *124*, 250-257. <https://doi.org/10.1016/j.ibiod.2017.06.008>
- Fadhil, A. B., Aziz, A. M., & Al-Tamer, M. H. (2016). Biodiesel production from *Silybum marianum* L. seed oil with high FFA content using sulfonated carbon catalyst for esterification and base catalyst for transesterification. *Energy Conversion and Management*, *108*, 255-265. <https://doi.org/10.1016/j.enconman.2015.11.013>
- Farabi, M. S. A., Ibrahim, M. L., Rashid, U., & Taufiq-Yap, Y. H. (2019). Esterification of palm fatty acid distillate using sulfonated carbon-based catalyst derived from palm kernel shell and bamboo. *Energy Conversion and Management*, *181*, 562-570. <https://doi.org/10.1016/j.enconman.2018.12.033>
- Fauziyah, M., Widiyastuti, W., & Setyawan, H. (2020). Sulfonated carbon aerogel derived from coir fiber as high performance solid acid catalyst for esterification. *Advanced Powder Technology*, *31*(4), 1412-1419. <https://doi.org/10.1016/j.apt.2020.01.022>
- Fawaz, E. G., Salam, D. A., & Daou, T. J. (2020). Esterification of linoleic acid using HZSM-5 zeolites with different Si/Al ratios. *Microporous and Mesoporous Materials*, *294*, Article 109855. <https://doi.org/10.1016/j.micromeso.2019.109855>
- Flores, K. P., Omega, J. L. O., Cabatingan, L. K., Go, A. W., Agapay, R. C., & Ju, Y. H. (2019). Simultaneously carbonized and sulfonated sugarcane bagasse as solid acid catalyst for the esterification of oleic acid with methanol. *Renewable Energy*, *130*, 510-523. <https://doi.org/10.1016/j.renene.2018.06.093>
- Fonseca, J. M., Spessato, L., Cazetta, A. L., Bedin, K. C., Melo, S. A. R., Souza, F. L., & Almeida, V. C. (2020). Optimization of sulfonation process for the development of carbon-based catalyst from crambe meal via response surface methodology. *Energy Conversion and Management*, *217*, Article 112975. <https://doi.org/10.1016/j.enconman.2020.112975>
- Fregolente, P. B. L., Fregolente, L. V., & Wolf MacIel, M. R. (2012). Water content in biodiesel, diesel, and biodiesel-diesel blends. *Journal of Chemical and Engineering Data*, *57*(6), 1817-1821. <https://doi.org/10.1021/jc300279c>

- Gan, S., Ng, H. K., Chan, P. H., & Leong, F. L. (2012). Heterogeneous free fatty acids esterification in waste cooking oil using ion-exchange resins. *Fuel Processing Technology*, *102*, 67-72. <https://doi.org/10.1016/j.fuproc.2012.04.038>
- Giakoumis, E. G., & Sarakatsanis, C. K. (2018). Estimation of biodiesel cetane number, density, kinematic viscosity and heating values from its fatty acid weight composition. *Fuel*, *222*, 574-585. <https://doi.org/10.1016/j.fuel.2018.02.187>
- Gupta, A. R., & Rathod, V. K. (2018). Waste cooking oil and waste chicken eggshells derived solid base catalyst for the biodiesel production: Optimization and kinetics. *Waste Management*, *79*, 169-178. <https://doi.org/10.1016/j.wasman.2018.07.022>
- Hajilar, S., & Shafei, B. (2019). Thermal transport properties at interface of fatty acid esters enhanced with carbon-based nanoadditives. *International Journal of Heat and Mass Transfer*, *145*, Article 118762. <https://doi.org/10.1016/j.ijheatmasstransfer.2019.118762>
- Hasanudin, H., Asri, W. R., Tampubolon, K., Riyant, F., Purwaningrum, W., & Wijaya, K. (2022). Dehydration isopropyl alcohol to diisopropyl ether over molybdenum phosphide pillared bentonite. *Pertanika Journal of Science & Technology*, *30*(2), 1739-1754. <https://doi.org/10.47836/pjst.30.2.47>
- Hasanudin, H., Asri, W. R., Said, M., Hidayati, P. T., Purwaningrum, W., Novia, N., & Wijaya, K. (2022). Hydrocracking optimization of palm oil to bio-gasoline and bio-aviation fuels using molybdenum nitride-bentonite catalyst. *RSC Advances*, *12*(26), 16431-16443. <https://doi.org/10.1039/D2RA02438A>
- Hasanudin, H., Putri, Q. U., Agustina, T. E., & Hadiyah, F. (2022). Esterification of free fatty acid in palm oil mill effluent using sulfated carbon-zeolite composite catalyst. *Pertanika Journal of Science & Technology*, *30*(1), 377-395. <https://doi.org/10.47836/pjst.30.1.21>
- Helmi, M., Tahvildari, K., Hemmati, A., Aberoomand Azar, P., & Safekordi, A. (2020). Phosphomolybdic acid/graphene oxide as novel green catalyst using for biodiesel production from waste cooking oil via electrolysis method: Optimization using with response surface methodology (RSM). *Fuel*, *287*, Article 119528. <https://doi.org/10.1016/j.fuel.2020.119528>
- Ibeto, C. N., Okoye, C. O. B., & Ofoefule, A. U. (2012). Comparative study of the physicochemical characterization of some oils as potential feedstock for biodiesel production. *ISRN Renewable Energy*, *2012*, 1-5. <https://doi.org/10.5402/2012/621518>
- Jamil, U., Khoja, A. H., Liaquat, R., Naqvi, S. R., Omar, W. N. N. W., & Amin, N. A. S. (2020). Copper and calcium-based metal organic framework (MOF) catalyst for biodiesel production from waste cooking oil: A process optimization study. *Energy Conversion and Management*, *215*, Article 112934. <https://doi.org/10.1016/j.enconman.2020.112934>
- Jenie, S. N. A., Kristiani, A., Sudiaryanto, Khaerudini, D. S., & Takeishi, K. (2020). Sulfonated magnetic nanobiochar as heterogeneous acid catalyst for esterification reaction. *Journal of Environmental Chemical Engineering*, *8*(4), Article 103912. <https://doi.org/10.1016/j.jece.2020.103912>
- Kamaronzaman, M. F. F., Kahar, H., Hassan, N., Hanafi, M. F., & Sapawe, N. (2020a). Analysis of biodiesel product derived from waste cooking oil using fourier transform infrared spectroscopy. *Materials Today: Proceedings*, *31*, 329-332. <https://doi.org/10.1016/j.matpr.2020.06.088>

- Kamaronzaman, M. F. F., Kahar, H., Hassan, N., Hanafi, M. F., & Sapawe, N. (2020b). Optimization of biodiesel production from waste cooking oil using eggshell catalyst. *Materials Today: Proceedings*, 31, 324-328. <https://doi.org/10.1016/j.matpr.2020.06.080>
- Karmakar, B., & Halder, G. (2021). Accelerated conversion of waste cooking oil into biodiesel by injecting 2-propanol and methanol under superheated conditions: A novel approach. *Energy Conversion and Management*, 247, Article 114733. <https://doi.org/10.1016/j.enconman.2021.114733>
- Karmakar, R., Kundu, K., & Rajor, A. (2018). Fuel properties and emission characteristics of biodiesel produced from unused algae grown in India. *Petroleum Science*, 15(2), 385-395. <https://doi.org/10.1007/s12182-017-0209-7>
- Kumar, S., Shamsuddin, M. R., Farabi, M. S. A., Saiman, M. I., Zainal, Z., & Taufiq-Yap, Y. H. (2020). Production of methyl esters from waste cooking oil and chicken fat oil via simultaneous esterification and transesterification using acid catalyst. *Energy Conversion and Management*, 226, Article 113366. <https://doi.org/10.1016/j.enconman.2020.113366>
- Kusumaningtyas, R. D., Prasetiawan, H., Putri, R. D. A., Triwibowo, B., Kurnita, S. C. F., Anggraeni, N. D., Veny, H., Hamzah, F., & Rodhi, M. N. M. (2021). Optimisation of free fatty acid removal in nyamplung seed oil (*Callophyllum inophyllum* l.) using response surface methodology analysis. *Pertanika Journal of Science and Technology*, 29(4), 2605-2623. <https://doi.org/10.47836/PJST.29.4.20>
- Lathiya, D. R., Bhatt, D. V., & Maheria, K. C. (2018). Synthesis of sulfonated carbon catalyst from waste orange peel for cost effective biodiesel production. *Bioresource Technology Reports*, 2, 69-76. <https://doi.org/10.1016/j.biteb.2018.04.007>
- Lin, C. Y., & Ma, L. (2020). Influences of water content in feedstock oil on burning characteristics of fatty acid methyl esters. *Processes*, 8(9), Article 1130. <https://doi.org/10.3390/PR8091130>
- Lin, J., Jiang, B., & Zhan, Y. (2018). Effect of pre-treatment of bentonite with sodium and calcium ions on phosphate adsorption onto zirconium-modified bentonite. *Journal of Environmental Management*, 217, 183-195. <https://doi.org/10.1016/j.jenvman.2018.03.079>
- Ma, Y., Wang, Q., Zheng, L., Gao, Z., Wang, Q., & Ma, Y. (2016). Mixed methanol/ethanol on transesterification of waste cooking oil using Mg/Al hydrotalcite catalyst. *Energy*, 107, 523-531. <https://doi.org/10.1016/j.energy.2016.04.066>
- Mahesh, S. E., Ramanathan, A., Begum, K. M. M. S., & Narayanan, A. (2015). Biodiesel production from waste cooking oil using KBr impregnated CaO as catalyst. *Energy Conversion and Management*, 91, 442-450. <https://doi.org/10.1016/j.enconman.2014.12.031>
- Mansir, N., Teo, S. H., Rabi, I., & Taufiq-Yap, Y. H. (2018). Effective biodiesel synthesis from waste cooking oil and biomass residue solid green catalyst. *Chemical Engineering Journal*, 347, 137-144. <https://doi.org/10.1016/j.cej.2018.04.034>
- Mazubert, A., Aubin, J., Elgue, S., & Poux, M. (2014). Intensification of waste cooking oil transformation by transesterification and esterification reactions in oscillatory baffled and microstructured reactors for biodiesel production. *Green Processing and Synthesis*, 3(6), 419-429. <https://doi.org/10.1515/gps-2014-0057>

- Mishra, S., Anand, K., & Mehta, P. S. (2016). Predicting the cetane number of biodiesel fuels from their fatty acid methyl ester composition. *Energy and Fuels*, 30(12), 10425-10434. <https://doi.org/10.1021/acs.energyfuels.6b01343>
- Mulay, A., & Rathod, V. K. (2021). Microwave-assisted heterogeneous esterification of dibutyl maleate: Optimization using response surface methodology. *Chemical Data Collections*, 34, Article 100740. <https://doi.org/10.1016/j.cdc.2021.100740>
- Munir, M., Ahmad, M., Mubashir, M., Asif, S., Waseem, A., Mukhtar, A., Saqib, S., Munawaroh, H. S. H., Lam, M. K., Shiong Khoo, K., Bokhari, A., & Loke Show, P. (2021). A practical approach for synthesis of biodiesel via non-edible seeds oils using trimetallic based montmorillonite nano-catalyst. *Bioresource Technology*, 328, Article 124859. <https://doi.org/10.1016/j.biortech.2021.124859>
- Narula, V., Khan, M. F., Negi, A., Kalra, S., Thakur, A., & Jain, S. (2017). Low temperature optimization of biodiesel production from algal oil using CaO and CaO/Al₂O₃ as catalyst by the application of response surface methodology. *Energy*, 140, 879-884. <https://doi.org/10.1016/j.energy.2017.09.028>
- Nata, I. F., Putra, M. D., Irawan, C., & Lee, C. K. (2017). Catalytic performance of sulfonated carbon-based solid acid catalyst on esterification of waste cooking oil for biodiesel production. *Journal of Environmental Chemical Engineering*, 5(3), 2171-2175. <https://doi.org/10.1016/j.jece.2017.04.029>
- Ngaosuwan, K., Goodwin, J. G., & Prasertdham, P. (2016). A green sulfonated carbon-based catalyst derived from coffee residue for esterification. *Renewable Energy*, 86, 262-269. <https://doi.org/10.1016/j.renene.2015.08.010>
- Niu, S., Ning, Y., Lu, C., Han, K., Yu, H., & Zhou, Y. (2018). Esterification of oleic acid to produce biodiesel catalyzed by sulfonated activated carbon from bamboo. *Energy Conversion and Management*, 163(17923), 59-65. <https://doi.org/10.1016/j.enconman.2018.02.055>
- Noshadi, I., Amin, N. A. S., & Parnas, R. S. (2012). Continuous production of biodiesel from waste cooking oil in a reactive distillation column catalyzed by solid heteropolyacid: Optimization using response surface methodology (RSM). *Fuel*, 94, 156-164. <https://doi.org/10.1016/j.fuel.2011.10.018>
- Omidvarborna, H., Kumar, A., & Kim, D. (2016). Science of the total environment variation of diesel soot characteristics by different types and blends of biodiesel in a laboratory combustion chamber. *Science of the Total Environment*, 544, 450-459. <https://doi.org/10.1016/j.scitotenv.2015.11.076>
- Özbay, N., Oktar, N., & Tapan, N. A. (2008). Esterification of free fatty acids in waste cooking oils (WCO): Role of ion-exchange resins. *Fuel*, 87(10-11), 1789-1798. <https://doi.org/10.1016/j.fuel.2007.12.010>
- Palmonari, A., Cavallini, D., Sniffen, C. J., Fernandes, L., Holder, P., Fagioli, L., Fusaro, I., Biagi, G., Formigoni, A., & Mammi, L. (2020). Short communication: Characterization of molasses chemical composition. *Journal of Dairy Science*, 103(7), 6244-6249. <https://doi.org/10.3168/jds.2019-17644>
- Rabie, A. M., Mohammed, E. A., & Negm, N. A. (2018). Feasibility of modified bentonite as acidic heterogeneous catalyst in low temperature catalytic cracking process of biofuel production from nonedible vegetable oils. *Journal of Molecular Liquids*, 254(2018), 260-266. <https://doi.org/10.1016/j.molliq.2018.01.110>
- Rafati, A., Tahvildari, K., & Nozari, M. (2019). Production of biodiesel by electrolysis method from waste cooking oil using heterogeneous MgO-NaOH nano catalyst. *Energy Sources, Part A: Recovery, Utilization and Environmental Effects*, 41(9), 1062-1074. <https://doi.org/10.1080/15567036.2018.1539139>

- Rahimzadeh, H., Tabatabaei, M., Aghbashlo, M., Panahi, H. K. S., Rashidi, A., Goli, S. A. H., Mostafaei, M., Ardjmand, M., & Nizami, A. S. (2018). Potential of acid-activated bentonite and SO_3H -functionalized MWCNTs for biodiesel production from residual olive oil under biorefinery scheme. *Frontiers in Energy Research*, 6, 1-10. <https://doi.org/10.3389/fenrg.2018.00137>
- Rocha, P. D., Oliveira, L. S., & Franca, A. S. (2019). Sulfonated activated carbon from corn cobs as heterogeneous catalysts for biodiesel production using microwave-assisted transesterification. *Renewable Energy*, 143, 1710-1716. <https://doi.org/10.1016/j.renene.2019.05.070>
- Rodríguez-Fernández, J., Hernández, J. J., Calle-Asensio, A., Ramos, Á., & Barba, J. (2019). Selection of blends of diesel fuel and advanced biofuels based on their physical and thermochemical properties. *Energies*, 12(11), Article 2034. <https://doi.org/10.3390/en12112034>
- Sahani, S., Roy, T., & Sharma, Y. C. (2020). Smart waste management of waste cooking oil for large scale high quality biodiesel production using Sr-Ti mixed metal oxide as solid catalyst: Optimization and E-metrics studies. *Waste Management*, 108, 189-201. <https://doi.org/10.1016/j.wasman.2020.04.036>
- Sari, E. P., Wijaya, K., Trisunaryanti, W., Syoufian, A., Hasanudin, H., & Saputri, W. D. (2021). The effective combination of zirconia superacid and zirconia-impregnated CaO in biodiesel manufacturing: Utilization of used coconut cooking oil (UCCO). *International Journal of Energy and Environmental Engineering*, 13, 967-978. <https://doi.org/10.1007/s40095-021-00439-4>
- Sharma, A., Kodgire, P., & Kachhwaha, S. S. (2019). Biodiesel production from waste cotton-seed cooking oil using microwave-assisted transesterification: Optimization and kinetic modeling. *Renewable and Sustainable Energy Reviews*, 116, Article 109394. <https://doi.org/10.1016/j.rser.2019.109394>
- Singh, V., Belova, L., Singh, B., & Sharma, Y. C. (2018). Biodiesel production using a novel heterogeneous catalyst, magnesium zirconate ($\text{Mg}_2\text{Zr}_5\text{O}_{12}$): Process optimization through response surface methodology (RSM). *Energy Conversion and Management*, 174, 198-207. <https://doi.org/10.1016/j.enconman.2018.08.029>
- Soegiantoro, G. H., Chang, J., Rahmawati, P., Christiani, M. F., & Mufrodi, Z. (2019). Home-made ECO green biodiesel from chicken fat (CIAT) and waste cooking oil (pail). *Energy Procedia*, 158, 1105-1109. <https://doi.org/10.1016/j.egypro.2019.01.267>
- Sree, J. V., Chowdary, B. A., Kumar, K. S., Anbazhagan, M. P., & Subramanian, S. (2021). Optimization of the biodiesel production from waste cooking oil using homogeneous catalyst and heterogeneous catalysts. *Materials Today: Proceedings*, 46(10), 4900-4908. <https://doi.org/10.1016/j.matpr.2020.10.332>
- Suganuma, S., Nakajima, K., Kitano, M., & Hayashi, S. (2012). sp^3 -linked amorphous carbon with sulfonic acid groups as a heterogeneous acid catalyst. *ChemSusChem*, 5(9), 1841-1846. <https://doi.org/10.1002/cssc.201200010>
- Suresh, R., Antony, J. V., Vengalil, R., Kochimoolayil, G. E., & Joseph, R. (2017). Esterification of free fatty acids in non-edible oils using partially sulfonated polystyrene for biodiesel feedstock. *Industrial Crops and Products*, 95, 66-74. <https://doi.org/10.1016/j.indcrop.2016.09.060>
- Suwannasom, P., Tansupo, P., & Ruangviriyachai, C. (2016). A bone-based catalyst for biodiesel production from waste cooking oil. *Energy Sources, Part A: Recovery, Utilization and Environmental Effects*, 38(21), 3167-3173. <https://doi.org/10.1080/15567036.2015.1137998>

- Tan, Y. H., Abdullah, M. O., Nolasco-Hipolito, C., & Zauzi, N. S. A. (2017). Application of RSM and Taguchi methods for optimizing the transesterification of waste cooking oil catalyzed by solid ostrich and chicken-eggshell derived CaO. *Renewable Energy*, *114*, 437-447. <https://doi.org/10.1016/j.renene.2017.07.024>
- Tang, Z. E., Lim, S., Pang, Y. L., Shuit, S. H., & Ong, H. C. (2020). Utilisation of biomass wastes based activated carbon supported heterogeneous acid catalyst for biodiesel production. *Renewable Energy*, *158*, 91-102. <https://doi.org/10.1016/j.renene.2020.05.119>
- Wu, Z., Li, H., & Tu, D. (2015). Application of fourier transform infrared (FT-IR) spectroscopy combined with chemometrics for analysis of rapeseed oil adulterated with refining and purificating waste cooking oil. *Food Analytical Methods*, *8*(10), 2581-2587. <https://doi.org/10.1007/s12161-015-0149-z>
- Xincheng, T., Niu, S., Zhao, S., Zhang, X., Li, X., Yu, H., Lu, C., & Han, K. (2019). Synthesis of sulfonated catalyst from bituminous coal to catalyze esterification for biodiesel production with promoted mechanism analysis. *Journal of Industrial and Engineering Chemistry*, *77*, 432-440. <https://doi.org/10.1016/j.jiec.2019.05.008>
- Yahya, S., Wahab, S. K. M., & Harun, F. W. (2020). Optimization of biodiesel production from waste cooking oil using Fe-Montmorillonite K10 by response surface methodology. *Renewable Energy*, *157*, 164-172. <https://doi.org/10.1016/j.renene.2020.04.149>
- Yuliana, M., Santoso, S. P., Soetaredjo, F. E., Ismadji, S., Ayucitra, A., Angkawijaya, A. E., Ju, Y. H., & Tran-Nguyen, P. L. (2020). A one-pot synthesis of biodiesel from leather tanning waste using supercritical ethanol: Process optimization. *Biomass and Bioenergy*, *142*, Article 105761. <https://doi.org/10.1016/j.biombioe.2020.105761>
- Zhang, B., Gao, M., Geng, J., Cheng, Y., Wang, X., Wu, C., Wang, Q., Liu, S., & Cheung, S. M. (2021). Catalytic performance and deactivation mechanism of a one-step sulfonated carbon-based solid-acid catalyst in an esterification reaction. *Renewable Energy*, *164*, 824-832. <https://doi.org/10.1016/j.renene.2020.09.076>
- Zhang, H., Gao, J., Zhao, Z., Chen, G. Z., Wu, T., & He, F. (2016). Esterification of fatty acids from waste cooking oil to biodiesel over a sulfonated resin/PVA composite. *Catalysis Science and Technology*, *6*(14), 5590-5598. <https://doi.org/10.1039/c5cy02133b>
- Zhang, M., Sun, A., Meng, Y., Wang, L., Jiang, H., & Li, G. (2015). High activity ordered mesoporous carbon-based solid acid catalyst for the esterification of free fatty acids. *Microporous and Mesoporous Materials*, *204*, 210-217. <https://doi.org/10.1016/j.micromeso.2014.11.027>
- Zik, N. A. F. A., Sulaiman, S., & Jamal, P. (2020). Biodiesel production from waste cooking oil using calcium oxide/nanocrystal cellulose/polyvinyl alcohol catalyst in a packed bed reactor. *Renewable Energy*, *155*, 267-277. <https://doi.org/10.1016/j.renene.2020.03.144>



Transfer Learning VGG16 Model for Classification of Tomato Plant Leaf Diseases: A Novel Approach for Multi-Level Dimensional Reduction

Premkumar Borugadda*, Ramasami Lakshmi and Satyasangram Sahoo

Department of Computer Science, School of Engineering & Technology, Pondicherry University, Karaikal Campus, Puducherry-609605, India

ABSTRACT

Tomato is the most popular and cultivated crop in the world. Nevertheless, the quality and quantity of tomato crops have been declining due to various diseases that afflict tomato crops. Hence, it becomes necessary to detect the disease early to prevent crop damage and increase the yield. The proposed model in this article predicts the infected tomato leaf images (9 classified diseases and also healthy class) obtained from the Plant Village dataset. In this model, Transfer learning was used to extract features from images by VGG16, yielding a high dimension of 25088 features. Overfitting is a commonly anticipated problem because of the higher dimensionality of data. To mitigate this problem, the authors have adopted a novel dimensional reduction-based technique: filter methods, feature extraction techniques like Principal Components Analysis (PCA), and the Boruta feature selection technique of wrapper methods. This adoption enables the proposed model to attain a significantly improved high accuracy of 95.68% and 95.79% in MLP and VGG16, respectively, by reducing its initial dimension on the tomato dataset containing 18160 images across 10 classes.

Keywords: Boruta algorithm, filter methods, plant leaves dataset, principal component analysis, tomato leaf disease classification, VGG16

ARTICLE INFO

Article history:

Received: 21 May 2022

Accepted: 16 August 2022

Published: 06 March 2023

DOI: <https://doi.org/10.47836/pjst.31.2.09>

E-mail addresses:

premkumar.jones@gmail.com (Premkumar Borugadda)

prof.rlakshmi@gmail.com (Ramasami Lakshmi)

smartlincoln@gmail.com (Satyasangram Sahoo)

*Corresponding author

ISSN: 0128-7680
e-ISSN: 2231-8526

INTRODUCTION

Tomato (*Lycopersicon esculentum*) is an extensively farmed agricultural crop. This crop's growing season lasts about 90 to 150 days, with typical daytime average temperatures of 18 to 25°C and nighttime temperatures of 10 to 20°C (Gadekallu et al., 2021). Excess humidity

and reduced sunlight exposure negatively impact crop quality. Generally, excess humidity renders crops vulnerable to pests, diseases, and decay. Hence a dry climate is necessary for producing high-quality tomatoes. Crops ought to be closely monitored for signs of fungi, bacteria, and virus invasion. Necessary preventive actions should be in place to check and control diseases early. It can be achieved by roping in experts and field workers to detect and identify diseases at an early stage, albeit the task might prove to be laborious and economically unviable when there is high acreage involved. It becomes essential to make use of technology that could significantly reduce human intervention for performing real-time monitoring with the highest precision possible. The recent developments in the deep learning (DL) models make it possible to detect and identify diseases in tomato plants at an early stage.

Precision farming may be used to combat diseases and pests that affect crops. Sensor networks, remote sensing, robotics, computer vision, machine learning, and DL are employed in precision farming. Computer vision forms an integral part of precision agriculture. For plant disease recognition and classification in agriculture, computer vision DL-based algorithms have been applied. Various studies have used DL agriculture models to diagnose crop problems (Guo et al., 2003). DL networks contain several layers of complex formation that increase the model's accuracy. Nodes of one layer are interconnected with another node of layers to form classification-based architectures and require additional computational power for training. Convolution neural networks (CNNs) are broadly used in the DL architecture framework. CNN is involved in many applications, such as image classification and object recognition (Tang & Wu, 2016) which significantly improves image classification in several fields, such as agriculture. The present study proposed a multi-level dimension reduction (filter methods, principal component analysis (PCA) and Boruta feature selection) method to obtain optimal features and classify tomato plant leaf diseases using VGG16, multi-layer perceptron (MLP), and machine learning algorithms (MLA). This study might help farmers identify the diseases early and prevent loss so that the crop yield would increase. The tomato leaf dataset for the present study was obtained from the plant village dataset (Mohanty et al., 2016). The framework was used to classify the infected and healthy images of the tomato leaves. The performance of CNN-based models, VGG16, MLP, and MLA, was analyzed based on different evaluation metrics, such as training accuracy, validation accuracy, and weighted average F1 score.

This study primarily focused on the declined dimension in a multi-level model, as extensive data on the number of samples and features from images were collected. Classifying the images with the extracted features from a high-dimensional feature vector is critical. In some cases, the number of features (F) is more compared to the number of samples (S) ($F > S$), which is known as the curse of dimensionality (CoD). Due to the huge dimension, the dimensionality of the image data needs to be reduced using

dimension reduction techniques that help with image classification without losing the most significant information. Hence, this study focused primarily on addressing the high dimensionality of data. The machine learning (ML) or DL models were trained effectively on high dimensionality data; however, the models encounter problems, such as overfitting, requiring more training time, consumption of significant resources, high model complexity, containing trainable parameters, and taking up a large amount of storage space. A multi-level dimension reduction algorithm was proposed in this study to overcome these issues. It consisted of multi-level dimension reduction methods, such as filter methods of feature selection in dimension reduction as level 1, principal components analysis (PCA) of feature transformation as level 2, and Boruta wrapper method as level 3.

REVIEW OF LITERATURE

Computer vision with data science is a trending technology in agriculture for the classification of the disease of plants. In the early days, traditional MLA was used to identify plant leaf diseases in agriculture as machine learning methods were unable to classify the images due to large-scale image datasets.

Durmuş et al. (2017) trained AlexNet (Krizhevsky et al., 2012) and SqueezeNet (Iandola et al., 2016) on the 18160 tomato leaf images taken from the plant village dataset and classified the tomato diseases using the supercomputer Nvidia Jetson Tx1; the training and validation presented an accuracy of 94.3% and 95.65% using SqueezeNet and AlexNet, respectively.

Tm et al. (2018) proposed an approach that includes data acquisition, preprocessing and classification. In the present study, a variation of LeNet was applied to the tomato dataset. It consisted of approximately 18160 images belonging to ten different classes of tomato leaf diseases. Keras, a neural network API (Application Programming Interface) written in Python, has been used for the model implementation. The highest validation accuracy of 94.8% was obtained over 30 epochs of training.

Durmus et al. (2017) proposed deep-CNNs, such as ResNet50, for tomato leaf disease detection using PyTorch. A DL technique with transformation and augmentation was used to overcome the overfitting problem and improve the model's performance. The proposed model yielded 97% accuracy after fine-tuning the weights for the ResNet model.

Gadekallu et al. (2021) proposed a novel PCA-whale optimization algorithm (WOA) hybrid optimization technique for significant features extracted from the 18160 tomato leaf images. The deep neural network was trained on the optimal features with 94% accuracy. The present study used multi-level three dimension reduction techniques (filter method, feature transformation (PCA), and Boruta of wrapper methods) to obtain the optimal features. The final results improved and were compared to the previous results on the same number of tomato leaf images in the tomato dataset.

The objective of this study was to reduce the high-dimension features into optimal features using a multi-level dimension reduction algorithm. With the high dimension of data, problems, such as overfitting, high training time, model complexity, trainable parameters, and large storage space of the model, occurred. Thus, to prevent all these problems and improve accuracy, the study proposes three types of dimension reduction techniques to build an efficient agricultural tomato leaf disease classification model.

METHODOLOGY

The detailed methodology for the tomato leaf disease classification framework is given below as follows:

Figure 1 illustrates the classification framework consisting of six stages: data acquisition, preprocessing data, feature extraction stage, dimensionality reduction stage, classification stage, and selecting the optimal prediction model.

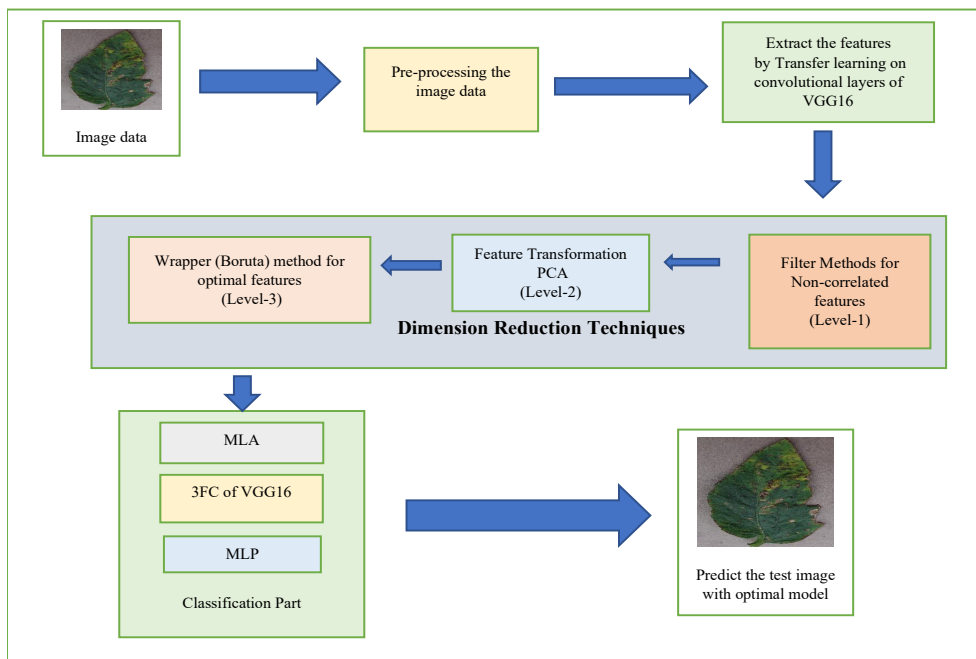


Figure 1. Architecture framework for classification of tomato leaf images

Dataset

In the initial stage, the images of tomato disease were taken from the plant village dataset (Mohanty et al., 2016). A total of 54,345 photos of 14 crops were included in this plant village collection. These crops include various fruits and vegetables, such as apples and blueberries. Images of tomato leaves were utilized in this investigation. Table 1 shows the

number of images for each class of tomato leaves, as illustrated in Figure 2. Ten categories of tomato images, including those considered healthy, were available. In the present study, 18160 images of the tomato dataset were split in the ratio of 90:05:05 for training, validation, and testing, respectively.

Table 1

Dataset

S. No	Name of the class	No. of images
	Tomato_Bacterial spot	2127
	Tomato_Early_blight	1000
	Tomato_Late_blight	1909
	Tomato_Leaf Mold	952
	Tomato_Septoria_leaf_spot	1771
	Tomato_Spider_mites Two-spotted_spider_mite	1676
	Tomato__Target Spot	1404
	Tomato__Tomato_Yellow_Leaf_Curl_Virus	5357
	Tomato__Tomato_mosaic_virus	373
	Tomato__healthy	1591
	Total number of images	18160

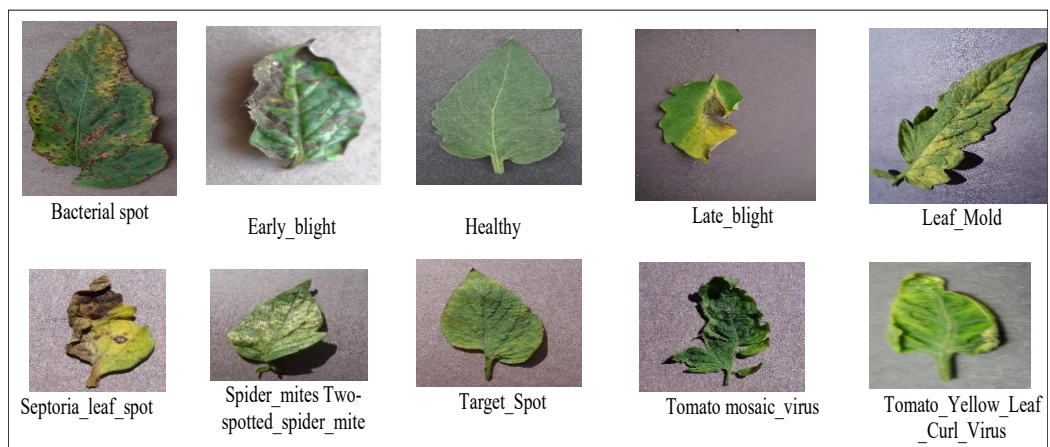


Figure 2. Sample tomato leaf images of different classes of the plant village dataset

Preprocessing

In the preprocessing, the size of the input image was 256×256 pixels, which was resized into 224×224 pixels. The labels of the image dataset were categorical. Thus, label encoding

(Cerde & Varoquaux, 2020) and one-hot encoding (Li et al., 2018) were applied for numerical values. The normalized pixel values of the image were placed between 0 and 1.

Feature Extraction

In the feature extraction stage, the standard VGG16 (Simonyan & Zisserman, 2014) model was applied to extract the features of image data, as shown in Figure 3. The two feature extraction methods were as follows: First, 13 convolutional layers of the VGG16 model were applied, and the high-dimensional features of the images were extracted, as shown in Figure 4. Second, the transfer learning method (Tammina, 2019) was applied to 13 convolutional layers of VGG16 for feature extraction (Figure 5).

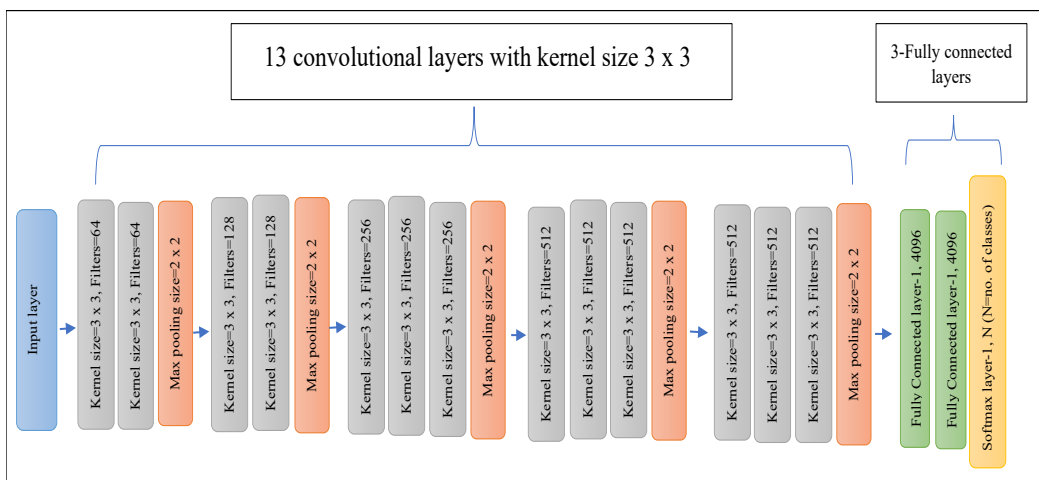


Figure 3. Standard VGG16 model architecture

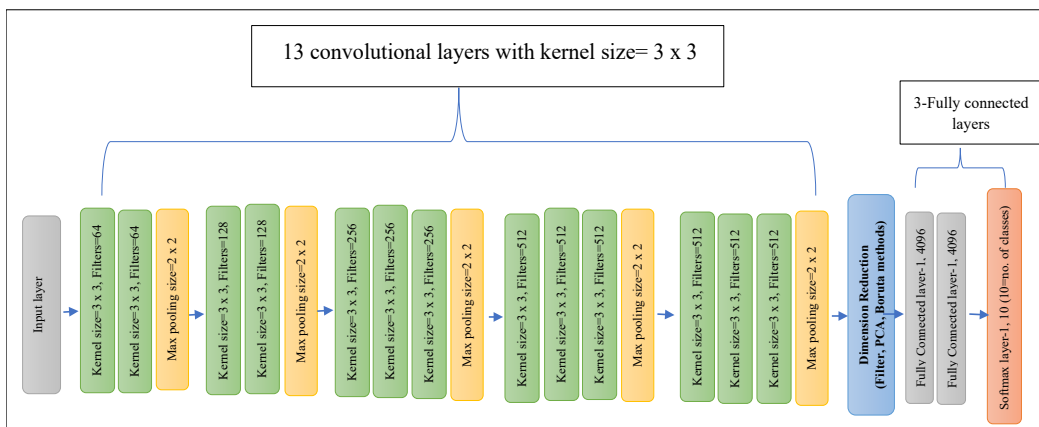


Figure 4. Applying dimension reduction techniques between 13 convolutional layers and 3 fully connected layers of VGG16

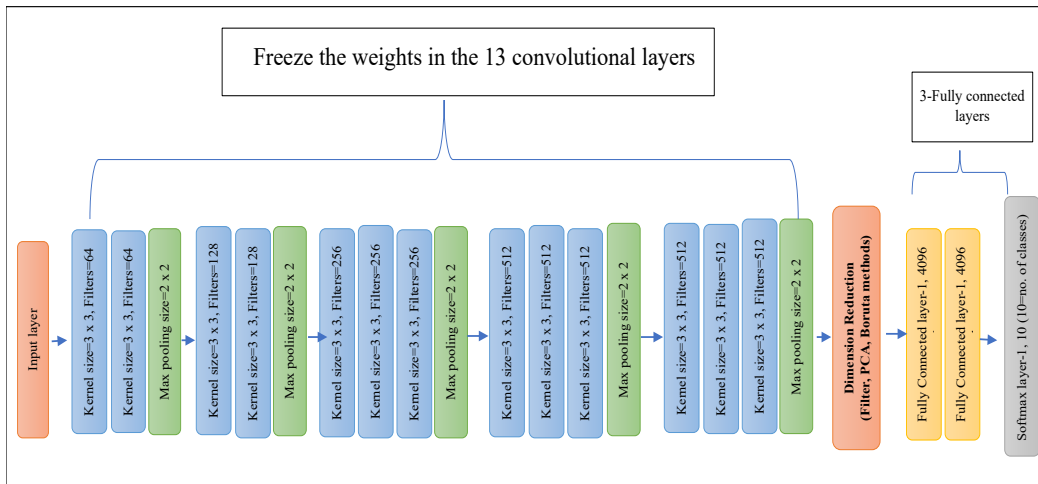


Figure 5. Applying dimension reduction methods between transfer learning on 13 convolutional layers of VGG16 and 3 fully connected layers

Dimension Reduction Technique

In the feature extraction stage, high dimensional features of 25088 were obtained with 13-convolutional layers of the pre-transfer learning stage on VGG16. If the classification models were trained using MLA, MLP, and three fully connected layers of VGG16 with high dimensional features, the models faced the following issues: the possibility that the model is biased towards overfitting, model computation will be high, and the performance of the models may be reduced due to curse of dimensionality. In order to overcome these problems, the model proposed a multi-level dimension reduction technique, such as filter, PCA, and Boruta, so that less significant features were eliminated from the images.

Filter Methods for Non-Correlated Features

Variance and correlation statistical methods were selected to obtain the optimal features.

Removing Constant Features

Constant features contain only one value, and the variance threshold value is 0. Totally of 994 constant features were identified from 25088 high-dimensional features (Doquire & Verleysen, 2013). However, the constant features do not affect the models and are removed, leaving 24094 high-dimensional features.

Removing Quasi-Constant Features

Quasi-constant features are similar to constant features with a variance threshold value of

0.01 (Ma et al., 2018). A total of 13175 quasi-constant features were identified and excluded from 24094 high dimensional features, retaining 10919 features.

Removing Correlated Features

Correlated features create redundancy and should be removed (Chuanlei et al., 2017). Three different threshold values, such as 0.6, 0.7, or 0.8, were typically applied to identify the correlated features. Depending on the dataset requirements, the threshold value of 0.8 was applied, and 136 correlated features were identified and eliminated. Finally, 10783 non-correlated features were identified in filter methods of dimension reduction level 1, as shown in Figure 6.

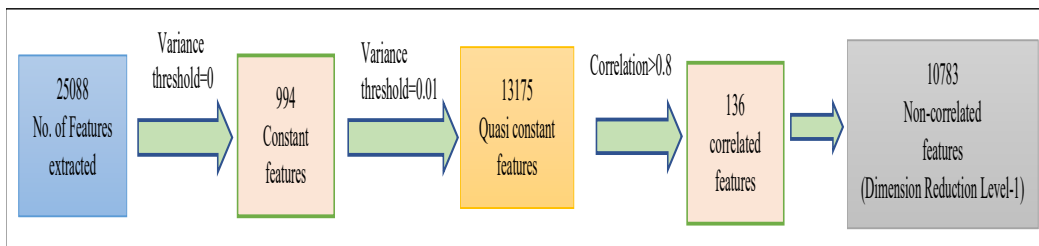


Figure 6. Filter method for non-correlated features at dimension reduction level 1

Application of the Feature Transfer Method-PCA

PCA was used for feature extraction. This method created new features by projecting existing features (Mudrova & Procházka, 2005). PCA is a dimensionality reduction technique to transform into a new lower-dimension dataset without losing critical information.

The dataset consisted of ‘X’ independent variables (dimensions) and one target variable. So, the total dimension size was ‘X+1’.

Step 1: Standardize or scale the input dataset ‘X’ using Z-score.

$$Z = \frac{xi - \bar{x}}{Std(X)} \quad (1)$$

Initially, the mean and standard deviation were calculated for each independent variable ‘X’.

$$\bar{x} = \text{mean of } X = X = \frac{\sum_{i=1}^n X_i}{n} \quad (2)$$

Standardized value of $X_i = (X_i - \text{mean of } X) / \text{Standard deviation of } X$

$$\text{Std}(x) = \text{standard deviation of } X = \sqrt{\frac{\sum_{i=1}^n (X_i - \bar{x})^2}{n-1}} \quad (3)$$

Step 2: Covariance matrix of the scaled data without the target variable was calculated

$$\text{Cov}(x,y) = \frac{\sum_{i=1}^n (X_i - \bar{x})(y_i - \bar{y})}{n-1} \quad (4)$$

Step 3: Eigenvalues were computed

Step 4: Eigenvectors were defined

Step 5: Existing input datasets were projected into new dimensions using eigenvectors.

With 99% of the variance, PCA formed a new set of 5720 components from 10783 non-correlated features (Figure 7).

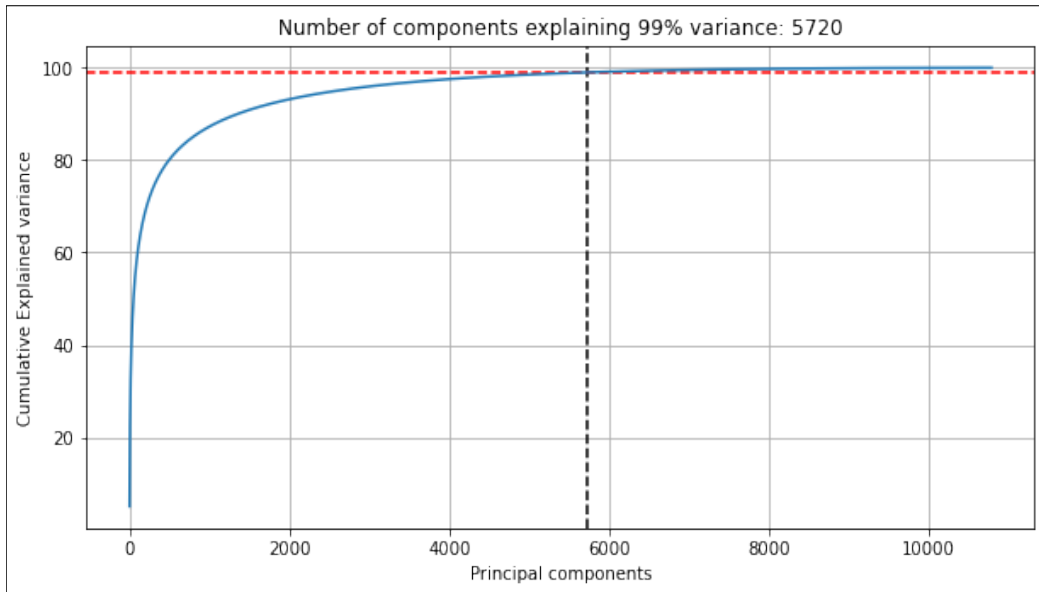


Figure 7. Number of components explained 99% of variance vs. cumulative explained variance

In Figure 7, principal components were represented on the horizontal axis and cumulative experience variance on the vertical axis at 99% of explained variance ratio; subsequently, 5720 principal components were obtained. In Figure 8, 10783 non-correlated features of dimension reduction level 1 were transformed into 5720 principal components.

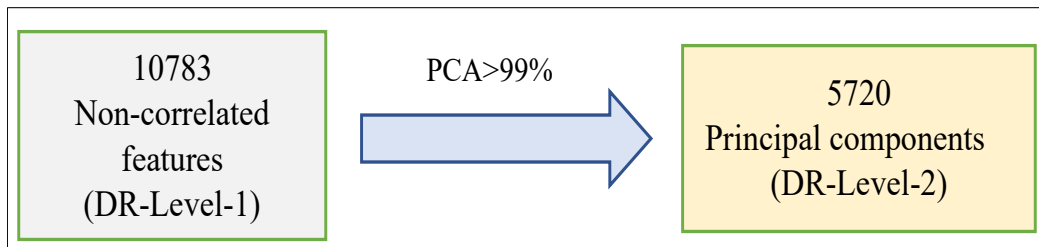


Figure 8. Conversion of non-correlated features at level 1 into principal components at level 2

Application of the Wrapper Methods (Boruta Feature Selection Algorithm)

The wrapper feature selection method identified optimal features using MLA (Chen & Chen, 2015). Herein, the random forest classification algorithm was used as a base model for the

Boruta algorithm (Kursa & Rudnicki, 2010). The algorithm consisted of the following steps:

1. In the first step, Boruta begins by cloning the supplied collection of original features. These were referred to as shadow features to distinguish them from the originals. The values of the shadow features were then rearranged to exclude the correlations.
2. In the second step, the significance features were validated using the mean decrease impurity (MDI), and the shadow features were trained using the random forest (RF) classifier. MDI determined each cloned feature's relevance.
3. The Z score was used to determine whether the original feature provided had a higher Z score than the maximum MDI score of the shadow feature.
4. 'Hits' were assigned to a vector with a high Z value. When the number of iterations was reached, a hit table was generated at the end of the process.
5. A feature with the highest Z score was marked as essential in each algorithm iteration. The final collection of features was derived from the hit vector.

All the procedures from the beginning to this point were repeated until the qualities of all the offered features were identified.

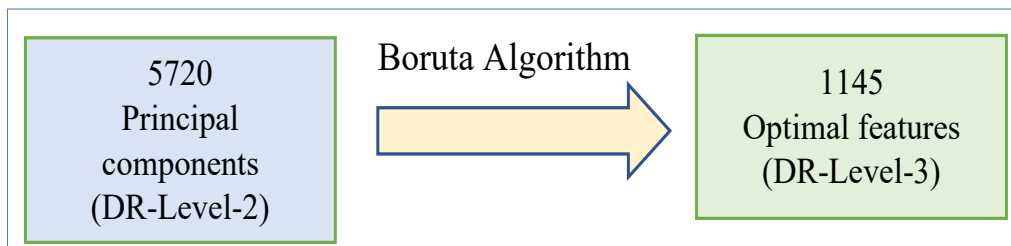


Figure 9. Conversion of principal components at level 2 into optimal features at level 3 with the Boruta algorithm

A total of 5720 principal components were obtained in dimension reduction level 2. Then, the Boruta feature selection algorithm was applied to these principal components, and 1145 optimal features were obtained at dimension reduction level 3 (Figure 9).

The proposed multi-level dimension reduction algorithm is shown in Figure 10. It represented an overview of the multi-level dimension reduction using a raw image as input; subsequently, optimal features were generated. The final feature was considered the reduced dimension available from the multi-level dimension, which was considered a maximum hit in the Boruta-based method.

Classification Algorithms

A total of 1145 optimal features were obtained in the Boruta feature selection algorithm. The classification algorithms were applied to these features.

```

Input: Images
image ← resize.image
dimension ← calculate_Dim(shape.Image)
Initialize Reduced_Dim ← dimension
Initialize Level ← None
If 'Reduced_Dim == dimension' then:
    image.Weight ← image.VGG16(ImageNet)
    Reduced_Dim ← image.Weight
    add(level,1)
    Return(Reduced_Dim)
If 'Reduced_Dim < dimension' & 'level==1' then:
    Remove constant features:
        Set feature_filter.threshold = 0
        Constant_features ← feature_filter (Reduced_Dim.shape)
        subtract (Reduced_Dim, Constant_features)
    Remove Quasi_constant features:
        Set feature_filter.threshold = 0.01
        Quasi_features ← featurefilter(Reduced_Dim.shape)
        subtract(Reduced_Dim, Quasi_features)
    Remove correlated features:
        Set feature_filter.threshold = 0.8
        correlated_features ← features_filter(Reduced_Dim.shape)
        subtract(Reduced_Dim, correlated_features)
    add (level,1)
    Return (Reduced_Dim)
If 'Reduced_dim < dimension' & 'level==2' then:
    Set variance =99
    Components ← PCA(Reduced_dim, variance)
    Reduced_dim ← components
    add (level, 1)
    Return(Reduced_Dim)
If 'Reduced_Dim < dimension' & 'level==3' then:
    Initialize n ← 0
    Max_Iteration ← max (n, 50)
    Repeat upto 'Max_Iteration' or 'Reduced_dim'
        cloned_dim[i] ← Reduced_dim[i]
        suffle.feature(cloned_dim[i])
        merge (Cloned_dim[i], Reduced_dim[i])
        Z_Score [i] = Radom_forest(reduced_dim)
        MDI_Score [i] = Random_forest(cloned_dim)
        Hit_count ← calculate (Z_Score [i] > max (MDI_Score[i]))
        Add (n, 100)
    Final_Features ← max (Hit_Count)
    
```

Figure 10. The Proposed multi-level dimension reduction algorithm

MLA

Classification is the process of organizing a given set of data into classes. Classification algorithms map the input data to classes, and the model predicts the input class. All MLA, such as logistic regression (Dreiseitl & Ohno-Machado, 2002), decision tree classifier (DTC) (Ali et al., 2012), random forest classifier (RFC) (Ali et al., 2012), Ada boost classifier (ABC) (Khammari et al., 2005), K Nearest Neighbor (KNN) (Zhang & Zhou, 2005), support vector classifier (SVC) (Awad & Khanna, 2015) and XG Boost (XGB) (Torlay et al., 2017) are not suitable for high dimension without any reduction techniques. Thus, we proposed a model of the eased task as a classifier. Finally, 1145 optimal features were fed to classification algorithms, the models were trained, and the results were compared with the above algorithms.

MLP

MLP is an example of an artificial neural network. It is applied broadly to solve several problems, such as pattern recognition and interpolation (Noriega, 2005). MLP is a neural network with fully connected multiple dense layers. The MLP network comprises input, hidden, and output layers that perform the computational work.

The neurons of the MLP are prepared to perform backpropagation learning for any classification and forecast job in the network. Several studies have applied different optimization methods for MLP. Ramchoun et al. (2016) presented a different approach for optimizing MLP architecture to instruct the network with a backpropagation algorithm. The inputs to the neuron (x) feature and the amounts in terms of weight (w) were computed for classification. The activation function (f) was included in the sum of the outcome to construct the output in an MLP. MLP network wherein the input layer contains nodes equal to the number of features extracted. The MLP's output layer uses softmax activation for multi-class classification, while the hidden layer uses relu activation functions. If a dataset has 'm' classes, the output layer uses 'm' nodes for model prediction.

Three Fully Connected Layers of VGG16

The VGG16 architecture consisted of 16 layers, of which 13 convolutional layers were explained in the feature extraction phase. The remaining three fully connected layers were used for classification purposes. 2/3 of the fully connected layers consisted of 4096 nodes, and the third fully connected layer had the softmax activation function for classification, which consisted of several labels (classes) (Gao & Pavel, 2017). In the present study dataset, ten classes were available.

RESULTS AND DISCUSSION

The performance measures classification models are described with respect to the experimental setup and hyperparameter tuning. Subsequently, the classification performance of the proposed model was evaluated and compared to the three fully connected layers of VGG16, MLP, and state-of-the-art MLA.

Performance Evolution

The performance of the classification models was evaluated using a confusion matrix, as shown in Figure 11. The evaluation parameters in the confusion matrix are accuracy, precision, recall (sensitivity), F1_Score, true-positive (TP_i), false-positive (FP_i), true-negative (TN_i), false-negative (FN_i), and class C_k. The subscript ‘k’ indicates the number of classes, and ‘i’ values from 0 to ‘K’. PVC₁ means predicted values of class C₁, and AVC₁ means the actual values of class C₁. This study calculated precision, recall, and F1_Score over the validation dataset. The training and validation datasets were imbalanced. Thus, performance measures, such as accuracy, weighted-average-based precision, recall, and F1 score (Sokolov & Lapalme, 2009; Behera et al., 2019), were used to evaluate the performance of the classification models. The performance measurements of accuracy, W.A.P, W.A.R, and W.A.F1, were defined as follows.

$$\text{Accuracy} = \frac{\sum_{i=1}^K \frac{TP_i + TN_i}{2TP_i + FP_i + FN_i + TN_i}}{K} \tag{5}$$

$$\text{Weighted Average Precession (W.A.P)} = \frac{\sum_{i=1}^K |S_i| \frac{TP_i}{TP_i + FP_i}}{\sum_{i=1}^K |S_i|} \tag{6}$$

$$\text{Weighted Average Recall (W.A.R)} = \frac{\sum_{i=1}^K |S_i| \frac{TP_i}{TP_i + FN_i}}{\sum_{i=1}^K |S_i|} \tag{7}$$

$$\text{Weighted Average F1_Score (W.A.F1)} = \frac{\sum_{i=1}^K |S_i| \frac{2TP_i}{2TP_i + FP_i + FN_i}}{\sum_{i=1}^K |S_i|} \tag{8}$$

		PREDICTED CLASSES				
		C ₁	C ₂	...	C _K	
ACTUAL CLASSES	C ₁	TP ₁				AVC ₁
	C ₂		TP ₂			AVC ₁
	
	C _K				TP _K	AVC ₁
		PVC ₁	PVC ₂		PVC _K	

Figure 11. Confusion matrix of multi-class

Experimental setup and hyper-parameter setting

The present experiment was executed on Jupiter notebook support to implement ML and DL algorithms in Python 3.6.7. The hardware configuration is given in Table 2. The experiment used transfer learning on VGG16 for extracting features and multi-layer perception for classification. Table 2 describes the hardware and software configuration used to train a proposed model for tomato disease classification.

Table 2

Machine specifications

S. No	Hardware and software	Characteristics
1	Memory (RAM)	16 GB
2	Processor	Intel(R) Core i7-10875H CPU@ 2.30 GHz
3	Graphics (GPU)	NVIDIA GeForce RTX 2070-8GB
4	Operating system	Windows 10 and 64 bits
5	Integrated development environment (IDE)	Jupiter Notebook

Hyperparameters are values determined during an algorithm learning process that were optimized to improve the model results. The early stopping condition and dropout ratio were applied for activation, and the nodes of the hidden layers were deactivated while model training to address the model overfitting problem. The hyperparameters of VGG16 selected in the classification layer were Relu, softmax activation functions in hidden layers, and the output layer. SGD (Stochastic Gradient Descent) optimizer, along with learning rate, was 0.0001, dropout was 0.5, decay was 1e-6, momentum was 0.9, patience was 30, the minimum delta was 0.0001, batch size was 8 and epochs were 97. The selected hyperparameters of MLA, such as SVC, were C=10, gamma=0.0001 and kernel='rbf'.

VGG16 has three fully connected layers. Among these, two dense layers were fully connected and comprised 4096 nodes. The third layer consisted of 10 neurons corresponding to the number of classes of the dataset. The final layer was the soft-max layer. Hyperparameters, such as activation functions like 'relu' and 'softmax,' dropout, learning rate, decay, momentum, optimizer, batch size, and epochs, are shown in Table 3, and hyperparameters of MLA are shown in Table 4.

Table 3
Hyperparameters of DL

S. No	Hyperparameter	Values
1	Activation functions	Relu, softmax
2	Optimizers	SGD, Adam
3	Learning rate	0.1,0.001,0.0001,0.00001
4	Dropout	0.2,0.3,0.4,0.5
5	Decay	1e-3, 1e-4, 1e-5, 1e-6
6	Momentum	0.8,0.9
7	Patience	15,20,30
8	Minimum delta	0.01, 0.001, 0.0001
9	Batch size	8,16,32,64,128,256
10	Epochs	100, 500, 1000

Table 4
Hyper-parameters of machine learning algorithms

S. No	Machine learning models	Hyperparameter	Values
1	ABC	Learning rate	[0.01, 0.001, 0.001, 0.0001]
		n_estimators	[300, 500, 700, 900]
2	DTC	Criterion	[Gini, entropy]
		max_depth	Range (1, 10)
		min_samples_leaf	Range (1, 5)
		min_samples_split	Range (1, 10)
3	KNN	Metric	['minkowski', 'euclidean', 'manhattan']
		n_neighbors	[5, 7, 9, 11, 13, 15]
		Weights	['uniform', 'distance']
4	LR	C	[100, 10, 1.0, 0.1, 0.01]
		max_iter	[100, 500, 700, 900]
		Penalty	[1, 2]
		solver	['newton-cg', 'lbfgs', 'liblinear']

Table 4 (Continue)

S. No	Machine learning models	Hyperparameter	Values
5	RFC	Criterion	[Gini, entropy]
		Max_depth	[4, 5, 6, 7, 8]
		max_features	['auto', 'log2', 'sqrt', 0.33]
		min_samples_leaf	Range (1,5)
		min_samples_splt	Range (1,10)
		n_estimators	[200, 500,700,900]
6	SVC	C	[0.1, 1, 10, 100, 1000]
		Gamma	[1, 0.1, 0.01, 0.001, 0.0001]
		Kernel	['rbf']
7	XGB	Learning rate	[0.01, 0.05, 0.1]
		Max_depth	[3, 5, 7, 9]
		gamma	[0, 0.1, 0.001]

Analysis of Experimental Results

The experimental results were analyzed in five steps. In the first step, the model trained the three fully connected layers of VGG16, MLP, and MLA on dimension reduction level 1 of 10783 non-correlated features. In the second step, the model trained the three fully connected layers of VGG16, MLP, and MLA on dimension reduction level 2 of 5720 principal components. In the third step, the model trained the three fully connected layers of VGG16, MLP, and MLA on dimension reduction level 3 of 1145 optimal features. In the fourth step, the results among the above three-dimension reduction levels were compared, and the best level was selected. In the fifth step, the proposed work results were compared to the previous study on the same dataset.

From the first multi-level dimension reduction, the results were obtained from three fully connected layers of VGG16, MLP, and MLA of 10783 non-correlated features, 5720 principal components, and 1145 optimal features, respectively.

Results of 10783 Non-Correlated Features

The three fully connected VGG16, MLP, and MLA layers on non-correlated features at dimension reduction level 1 are shown in Tables 5, 6, and 7, respectively.

Table 5

Results of VGG16 on 10783 non-correlated features

T.T (H:M:S)	T.A (%)	T.L	V.A (%)	V.L	V.S (903)	
					CP	WP
0:23:55	99.94	0.006	94.91	0.18	857	46
W.A.P (%)	W.A.R (%)	W.A.F1 (%)	S.S	T.P	Tr.P	N.T.P
95.04	94.91	94.88	465 MB	60,993,546	60,993,546	0

Note. T.T-Training time; T.A-Training accuracy; T.L-Train loss; V.A-Validation accuracy; V.L-Validation loss; V.S-Validation samples; CP-Correct predictions; WP-Wrong predictions; W.A.P-Weighted average precession, W.A.R- Weighted average recall; W.A.F1_score- Weighted average F1_Score; S.S-Storage space; T.P-Total parameters; Tr. P-Trainable parameters; N.T.P- Non-trainable parameters

Table 6

Results of MLP on 10783 optimal features

T.T (H:M:S)	T.A (%)	T.L	V.A (%)	V.L	V.S (903)	
					CP	WP
0:14:49	100.0	0.001	94.80	0.17	856	47
W.A.P (%)	W.A.R (%)	W.A.F1 (%)	S.S	T.P	Tr.P	N.T. P
94.93	94.80	94.80	88.3 MB	11,572,746	11,572,746	0

Note. T.T-Training time; T.A-Training accuracy; T.L-Train loss; V.A-Validation accuracy; V.L-Validation loss; V.S-Validation samples; CP-Correct predictions; WP-Wrong predictions; W.A.P-Weighted average precession, W.A.R- Weighted average recall; W.A.F1_score- Weighted average F1_Score; S.S-Storage space; T.P-Total parameters; Tr. P-Trainable parameters; N.T.P- Non-trainable parameters

Table 7

Results of MLA on 10783 optimal features

Classification model	Training time (H: M:S)	Training accuracy (%)	validation accuracy (%)	Total validation samples (903)		W.A.P (%)	W.A.R (%)	W.A.F1 (%)	Storage space
				CP	WP				
				LR	0:03:43				
RFC	2:20:09	100.0	82.17	742	161	82.38	82.17	80.52	107 MB
DTC	0:03:10	59.77	54.93	496	407	50.62	54.93	51.60	18.1 KB

Table 7 (Continue)

Classification model	Training time (H: M:S)	Training accuracy (%)	validation accuracy (%)	Total validation samples (903)		W.A.P (%)	W.A.R (%)	W.A.F1 (%)	Storage space
				CP	WP				
ABC	0:35:59	40.80	40.53	366	537	42.71	40.53	30.81	173 KB
KNN	0:00:37	100.0	84.50	763	140	85.82	84.50	83.57	2.05 GB
SVC	0:42:40	99.16	95.13	859	44	95.23	95.13	95.12	328 MB
XGB	0:41:58	100.0	92.13	832	71	92.08	92.14	92.03	3.71 MB

Note. T.T-Training time; T.A-Training accuracy; T.L-Train loss; V.A-Validation accuracy; V.L-Validation loss; V.S-Validation samples; CP-Correct predictions; WP-Wrong predictions; W.A.P-Weighted average precession, W.A.R- Weighted average recall; W.A.F1_score- Weighted average F1_Score; S.S-Storage space; T.P-Total parameters; Tr. P-Trainable parameters; N.T.P- Non-trainable parameters

Results of 5720 Principal Components

The three fully connected layers of VGG16, MLP, and MLA were applied on non-correlated features at dimension reduction level 2, and the results are shown in Tables 8, 9, and 10, respectively.

Table 8

Results of VGG16 on 5720 principal components

T.T (H:M:S)	T.A (%)	T.L	V.A (%)	V.L	V.S (903)	
					CP	WP
0:30:04	100.0	0.006	95.13	0.15	859	44
W.A.P (%)	W.A.R (%)	W.A.F1 (%)	S.S	T.P	Tr.P	N.T.P
95.22	95.13	95.11	307 MB	40,255,498	40,255,498	0

Note. T.T-Training time; T.A-Training accuracy; T.L-Train loss; V.A-Validation accuracy; V.L-Validation loss; V.S-Validation samples; CP-Correct predictions; WP-Wrong predictions; W.A.P-Weighted average precession, W.A.R- Weighted average recall; W.A.F1_score- Weighted average F1_Score; S.S-Storage space; T.P-Total parameters; Tr. P-Trainable parameters; N.T.P- Non-trainable parameters

Table 9

Results of MLP on 5720 principal components

T.T (H: M:S)	T.A (%)	T.L	V.A (%)	V.L	V.S (903)	
					CP	WP
0:04:06	99.99	0.002	95.24	0.18	860	43

Table 9 (Continue)

W.A.P (%)	W.A.R (%)	W.A.F1 (%)	S.S	T.P	Tr.P	N.T.P
95.33	95.24	95.22	60.8 MB	7,967,754	7,967,754	0

Note. T.T-Training time; T.A-Training accuracy; T.L-Train loss; V.A-Validation accuracy; V.L-Validation loss; V.S-Validation samples; CP-Correct predictions; WP-Wrong predictions; W.A.P-Weighted average precession, W.A.R- Weighted average recall; W.A.F1_score- Weighted average F1_Score; S.S-Storage space; T.P-Total parameters; Tr. P-Trainable parameters; N.T.P- Non-trainable parameters

Table 10

Results of MLA at 5720 components

Classification Model	Train time (H: M:S)	Training accuracy (%)	Validation accuracy (%)	Total validation samples (903)		W.A.P (%)	W.A.R (%)	W.A.F1 (%)	Storage space
				CP	WP				
LR	0:04:11	98.91	93.24	842	61	93.23	93.24	93.18	447 KB
RFC	2:09:01	99.98	75.19	679	224	75.05	75.19	73.26	119 MB
DTC	0:03:12	59.11	59.03	533	370	54.61	59.03	55.65	18.1 KB
ABC	0:35:12	40.94	41.75	377	526	27.79	41.75	30.67	173 KB
KNN	0:00:15	100.0	84.61	764	139	86.06	84.61	93.73	1.08 GB
SVC	0:26:37	99.07	95.13	859	44	95.23	95.13	95.12	329 MB
XGB	0:44:11	100.0	86.05	777	126	85.94	86.05	85.49	4.63 MB

Note. T.T-Training time; T.A-Training accuracy; T.L-Train loss; V.A-Validation accuracy; V.L-Validation loss; V.S-Validation samples; CP-Correct predictions; WP-Wrong predictions; W.A.P-Weighted average precession, W.A.R- Weighted average recall; W.A.F1_score- Weighted average F1_Score; S.S-Storage space; T.P-Total parameters; Tr. P-Trainable parameters; N.T.P- Non-trainable parameters

Results of 1145 Optimal Features

The three fully connected layers of VGG16, MLP, and MLA were applied on non-correlated features at dimension reduction level 2, and the results are shown in Tables 11, 12, and 13, respectively.

Table 11

Results of VGG16 on 1145 optimal features

T.T (H:M:S)	T.A (%)	T.L	V.A (%)	V.L	V.S (903)	
					CP	WP
0:58:37	100.0	0.0016	95.79	0.15	865	38
W.A.P (%)	W.A.R (%)	W.A.F1 (%)	S.S	T.P	Tr.P	N.T.P
95.88	95.79	95.80	164 MB	21,516,298	21,516,298	0

Note. T.T-Training time; T.A-Training accuracy; T.L-Train loss; V.A-Validation accuracy; V.L-Validation loss; V.S-Validation samples; CP-Correct predictions; WP-Wrong predictions; W.A.P-Weighted average precession, W.A.R- Weighted average recall; W.A.F1_score- Weighted average F1_Score; S.S-Storage space; T.P-Total parameters; Tr. P-Trainable parameters; N.T.P- Non-trainable parameters

Table 12

Results of MLP on 1145 optimal features

T.T (H: M:S)	T.A (%)	T.L	V.A (%)	V.L	V.S (903)	
					CP	WP
0:04:59	99.98	0.0067	95.68	0.16	864	39
W.A.P (%)	W.A.R (%)	W.A.F1 (%)	S.S	T.P	Tr.P	N.T.P
95.71	95.68	95.66	115 MB	15,193,098	15,193,098	0

Note. T.T-Training time; T.A-Training accuracy; T.L-Train loss; V.A-Validation accuracy; V.L-Validation loss; V.S-Validation samples; CP-Correct predictions; WP-Wrong predictions; W.A.P-Weighted average precession, W.A.R- Weighted average recall; W.A.F1_score- Weighted average F1_Score; S.S-Storage space; T.P-Total parameters; Tr. P-Trainable parameters; N.T.P- Non-trainable parameters

Table 13

Results of MLA at 1145 optimal features

Classification model	Training time (H:M:S)	Train accuracy (%)	Validation accuracy (%)	Total validation samples (903)		W.A.P (%)	W.A.R (%)	W.A.F1 (%)	Storage space
				CP	WP				
				LR	0:00:46				
RFC	0:25:29	99.96	77.30	698	205	78.49	77.30	75.45	125 MB

Table 13 (Continue)

Classification model	Training time (H:M:S)	Train accuracy (%)	Validation accuracy (%)	Total validation samples (903)		W.A.P (%)	W.A.R (%)	W.A.F1 (%)	Storage space
				CP	WP				
DTC	0:00:36	59.11	59.02	533	370	54.59	59.03	55.64	18.1 KB
ABC	0:06:38	40.95	41.75	377	526	27.79	41.75	30.67	173 KB
KNN	0:00:02	100.0	85.94	776	127	87.09	85.94	85.19	223 MB
SVC	0:02:51	97.97	94.35	852	51	94.44	94.35	94.35	60.9 MB
XGB	0:08:43	100.0	87.04	786	87	86.80	87.04	86.59	4.74 MB

Note. T.T-Training time; T.A-Training accuracy; T.L-Train loss; V.A-Validation accuracy; V.L-Validation loss; V.S-Validation samples; CP-Correct predictions; WP-Wrong predictions; W.A.P-Weighted average precession, W.A.R- Weighted average recall; W.A.F1_score- Weighted average F1_Score; S.S-Storage space; T.P-Total parameters; Tr. P-Trainable parameters; N.T.P- Non-trainable parameters

Tables 14 and 15 and Figure 12 show the comparison between the without and with dimension reduction results and the optimal results of the highest validation accuracy of 95.79% and weighted average F1_Score of 95.80% obtained at level 3 of dimension reduction by three fully connected (fc) layers of VGG16. Training and validation loss curves of 3fc of VGG16 and MLP without and with dimensional reduction levels are shown in Figures 13(a) to (d). The lowest validation loss was identified at level 3 by 3fc of VGG16 in Figure 13(d). Similarly, the training and validation accuracy curves of 3fc of VGG16 and MLP without and with dimension reduction levers are shown in Figures 14(a) to (d). The highest validation accuracy of 95.79% was identified at level 3 by 3fc of VGG16, as shown in Figure 14(d). The confusion matrix of 3fc of VGG16, SVC, and MLP without and with dimension reduction levels are shown in Figures 15(a) to (e). Of the 906 validation samples of images (0.05%), 865 correct predictions (CP) and 38 wrongly predicted (WP) samples are identified in level 3 by 3fc of VGG16 and shown in Figure 15(e). The classification reports of 3fc of VGG16, SVC, and MLP without and with dimension reduction levels are shown in Figures 16(a) to 16(e). The optimal results of VGG16 are precession, recall, and f1_scores are shown in Figure 16(e).

Table 14

Comparing the performance measure of classification models at three different dimension reduction levels, including without dimension reduction

Dimension reduction level	Features/components	Model	Training accuracy	Training loss	Validation accuracy	Validation loss	Weighted average F1_score
0	25088	VGG16	99.91	0.0125	94.80	0.18	94.82
1	10783	SVC	99.16	-	95.13	-	95.12
2	5720	MLP	99.99	0.002	95.24	0.17	95.22
3	1145	MLP	99.98	0.0067	95.68	0.16	95.66
3	1145	VGG16	100.0	0.0016	95.79	0.15	95.80

Table 15

Comparing the parameters, training time, and storage space of classification models at three different dimension reduction levels, including without dimension reduction

Dimension reduction level	Validation samples-903 (0.05%)		Training time (HH:MM:SS)	Total parameters	Trainable parameters	Non-trainable parameters	Storage Space (MB)
	CP	WP					
0	856	47	23:30:33	134,301,514	119,586,826	14,714,688	968
1	859	44	0:42:40	-	-	-	626
2	860	43	0:04:06	21,967,754	21,967,754	0	260
3	864	39	0:04:59	15,193,098	15,193,098	0	115
3	865	38	0:58:37	21,516,298	21,516,298	0	164

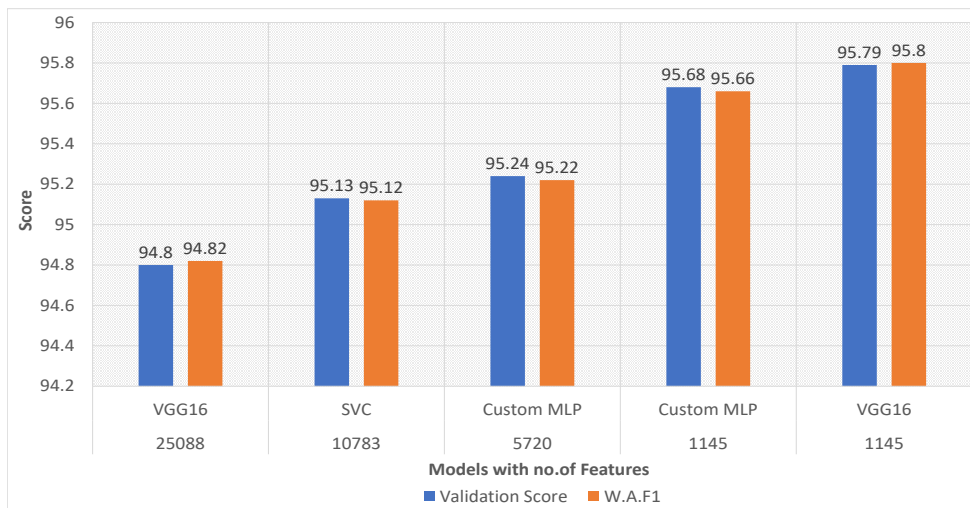


Figure 12. Comparison of results at three different dimension reduction levels

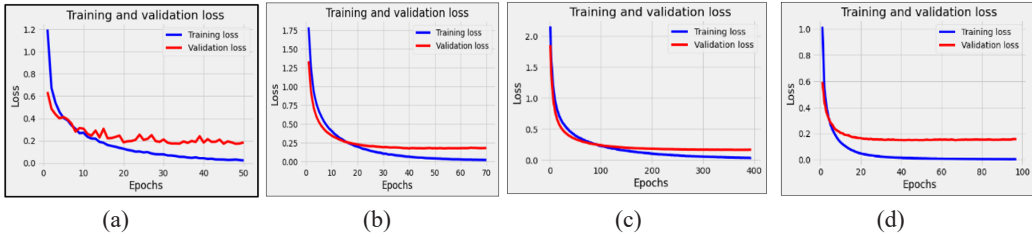


Figure 13. Training and validation loss: (a) without dimensionality reduction; (b) at principal components 5720 by MLP; (c) at optimal features 1145 by MLP; (d) at optimal features 1145 by VGG16

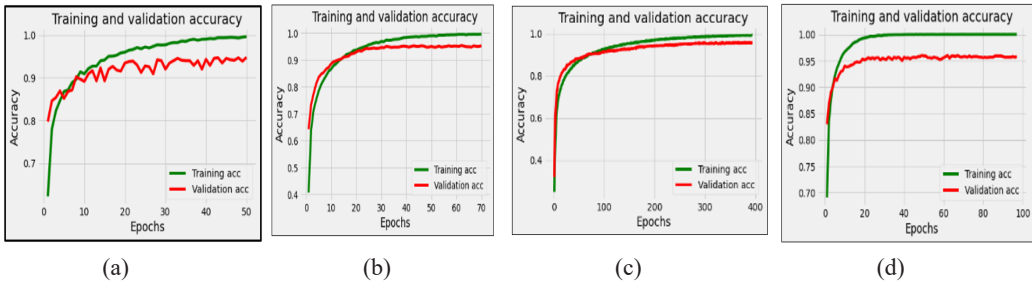


Figure 14. Training and validation accuracy: (a) without dimensionality reduction; (b) at principal components 5720 by MLP; (c) at optimal features 1145 by MLP; (d) at optimal features 1145 by VGG16

Confusion Matrix of VGG16 at extracted features 25088 (Without dimension reduction)											
T.B	414	7	0	0	0	0	4	0	0	0	0
T.E	3	187	2	2	0	4	0	2	0	0	0
T.L	2	187	2	2	0	4	0	2	0	0	0
T.Le	2	123	239	10	0	3	1	2	0	1	0
T.Se	43	106	1	14	178	3	2	2	3	2	0
T.Sp	0	13	0	0	0	318	1	3	0	0	0
T.T	9	77	0	1	0	45	141	3	0	4	0
T.T.Y	6	16	0	0	0	2	0	1047	0	0	0
T.M	0	3	0	9	1	3	0	0	58	0	0
T.H	2	3	0	0	0	3	0	0	0	0	310
	T.B	T.E	T.L	T.Le	T.Se	T.Sp	T.T	T.T.Y	T.M	T.H	

(a)

Confusion Matrix of SVC at Non-correlated feature 10783											
T.B	106	0	0	0	0	0	0	0	0	0	0
T.E	1	38	3	2	0	0	4	2	0	0	0
T.L	0	9	83	3	0	0	0	1	0	0	0
T.Le	0	0	0	46	0	0	0	0	0	0	0
T.Se	0	1	2	4	80	0	0	1	0	0	0
T.Sp	0	1	0	0	0	79	3	0	0	0	0
T.T	0	0	1	0	0	4	64	0	0	0	0
T.T.Y	0	0	0	0	0	1	0	266	0	0	0
T.M	0	0	0	0	0	0	0	0	18	0	0
T.H	0	0	0	0	0	0	0	0	0	0	79
	T.B	T.E	T.L	T.Le	T.Se	T.Sp	T.T	T.T.Y	T.M	T.H	

(b)

Confusion Matrix of MLP at Principal components 5720											
T.B	106	0	0	0	0	0	0	0	0	0	0
T.E	1	38	1	2	0	0	6	2	0	0	0
T.L	0	5	85	2	1	0	1	0	0	1	0
T.Le	0	0	0	46	0	1	0	0	0	0	0
T.Se	0	2	1	3	81	0	0	1	0	0	0
T.Sp	0	1	0	0	0	78	4	0	0	0	0
T.T	0	1	0	0	1	3	63	0	0	2	0
T.T.Y	0	0	0	1	0	0	0	266	0	0	0
T.M	0	0	0	0	0	0	0	0	18	0	0
T.H	0	0	0	0	0	0	0	0	0	0	79
	T.B	T.E	T.L	T.Le	T.Se	T.Sp	T.T	T.T.Y	T.M	T.H	

(c)

Confusion Matrix of MLP at optimal features 1145											
T.B	105	0	0	0	1	0	0	0	0	0	0
T.E	1	42	2	0	1	0	2	1	0	1	0
T.L	0	4	86	3	0	0	1	0	0	0	1
T.Le	0	0	0	45	1	1	0	0	0	0	0
T.Se	0	1	1	3	81	0	0	1	1	0	0
T.Sp	0	1	0	0	0	78	3	0	0	1	0
T.T	0	0	0	0	1	3	63	0	0	3	0
T.T.Y	0	0	0	0	0	0	0	267	0	0	0
T.M	0	0	0	0	0	0	0	0	18	0	0
T.H	0	0	0	0	0	0	0	0	0	0	79
	T.B	T.E	T.L	T.Le	T.Se	T.Sp	T.T	T.T.Y	T.M	T.H	

(d)

Confusion Matrix of VGG16 at optimal features 1145											
TRUE LABELS	T. B	105	0	0	0	1	0	0	0	0	
	T. E	1	44	1	0	0	0	2	1	0	
	T. L	0	7	86	2	0	0	0	0	0	
	T. Le	0	0	0	45	1	1	0	0	0	
	T. Se	0	1	3	3	80	0	0	1	0	
	T. Sp	0	1	0	0	0	79	3	0	0	
	T. T	0	1	0	0	1	4	63	0	0	
	T.T.Y	0	0	0	1	0	0	0	266	0	
	T.M	0	0	0	0	0	0	0	0	18	
	T.H	0	0	0	0	0	0	0	0	0	
		T. B	T. E	T. L	T. Le	T. Se	T. Sp	T. T	T.T.Y	T. M	T. H
PREDICTED LABELS											

(e)

Figure 15. Confusion matrices: (a) VGG16 without dimension reduction; (b) SVC at non correlated feature 10783; (c) MLP at principal components 5720; (d) MLP at optimal features 1145; (e) VGG16 at optimal features 1145.

Note. **T.B**=Tomato Bacterial spot; **T.E**=Tomato Early blight; **T.L**=Tomato Late blight; **T.Le**=Tomato Leaf Mold; **T.Se**=Tomato Septoria leaf spot; **T.Sp**=Tomato Spider mites Two-spotted spider mite; **T.T**=Tomato Target Spot; **T.T.Y**=Tomato Tomato Yellow Leaf Curl Virus; **T.M**=Tomato Tomato mosaic virus; **T.H**=Tomato healthy

Classes	Precision	Recall	F1_Score	Support
T. B	0.9906	0.9906	0.9906	106
T. E	0.7407	0.8000	0.7692	50
T. L	0.9630	0.8211	0.8864	95
T. Le	0.7966	1.0000	0.8868	47
T. Se	0.9643	0.9205	0.9419	88
T. Sp	0.9412	0.9639	0.9524	83
T. T	0.9130	0.9000	0.9065	70
T.T. Y	0.9888	0.9963	0.9925	267
T.M	1.0000	1.0000	1.0000	18
T. H	1.0000	0.9873	0.9936	79
Accuracy			0.9480	903
Macro AVG	0.9298	0.9380	0.9320	903
Weighted AVG	0.9511	0.9480	0.9482	903

(a)

Classes	Precision	Recall	F1_Score	Support
T. B	0.9907	1.0000	0.9953	106
T. E	0.7755	0.7600	0.7677	50
T. L	0.9326	0.8737	0.9022	95
T. Le	0.8364	0.9787	0.9020	47
T. Se	1.0000	0.9091	0.9524	88
T. Sp	0.9405	0.9518	0.9461	83
T. T	0.9014	0.9143	0.9078	70
T.T. Y	0.9815	0.9963	0.9888	267
T.M	1.0000	1.0000	1.0000	18
T. H	1.0000	1.0000	1.0000	79
Accuracy			0.9513	903
Macro AVG	0.9359	0.9384	0.9362	903
Weighted AVG	0.9523	0.9513	0.9512	903

(b)

Classes	Precision	Recall	F1_Score	Support
T. B	0.9907	1.0000	0.9953	106
T. E	0.8085	0.7600	0.7835	50
T. L	0.9770	0.8947	0.9341	95
T. Le	0.8519	0.9787	0.9109	47
T. Se	0.9759	0.9202	0.9474	88
T. Sp	0.9512	0.9398	0.9455	83
T. T	0.8514	0.9000	0.8750	70
T.T. Y	0.9888	0.9963	0.9925	267
T.M	1.0000	1.0000	1.0000	18
T. H	0.9634	1.0000	0.9814	79
Accuracy			0.9524	903
Macro AVG	0.9359	0.9390	0.9365	903
Weighted AVG	0.9533	0.9524	0.9522	903

(c)

Labels	Precision	Recall	F1_Score	Support
T. B	0.9906	0.9906	0.9906	106
T. E	0.8750	0.8400	0.8571	50
T. L	0.9663	0.9053	0.9348	95
T. Le	0.8824	0.9574	0.9184	47
T. Se	0.9529	0.9205	0.9364	88
T. Sp	0.9512	0.9398	0.9455	83
T. T	0.9130	0.9000	0.9065	70
T.T. Y	0.9926	1.0000	0.9963	267
T.M	0.9474	1.0000	0.9730	18
T. H	0.9294	1.0000	0.9634	79
Accuracy			0.9568	903
Macro AVG	0.9401	0.9453	0.9422	903
Weighted AVG	0.9571	0.9568	0.9566	903

(d)

Classes	Precision	Recall	F1_Score	Support
T. B	0.9906	0.9906	0.9906	106
T. E	0.8148	0.8800	0.8462	50
T. L	0.9556	0.9053	0.9297	95
T. Le	0.8824	0.9574	0.9184	47
T. Se	0.9639	0.9091	0.9357	88
T. Sp	0.9405	0.9518	0.9461	83
T. T	0.9265	0.9000	0.9130	70
T.T. Y	0.9925	0.9963	0.9944	267
T.M	1.0000	1.0000	1.0000	18
T. H	0.9753	1.0000	0.9875	79
Accuracy			0.9579	903
Macro AVG	0.9442	0.9490	0.9462	903
Weighted AVG	0.9588	0.9579	0.9580	903

(e)

Figure 16. Classification reports: (a) VGG16 without dimension reduction; (b) SVC at non correlated feature 10783; (c) MLP at principal components 5720; (d) MLP at optimal features 1145; (e) VGG16 at optimal features 1145

Note. **T.B**=Tomato Bacterial spot; **T.E**=Tomato Early blight; **T.L**=Tomato Late blight; **T.Le**=Tomato Leaf Mold; **T.Se**=Tomato Septoria leaf spot; **T.Sp**=Tomato Spider mites Two-spotted spider mite; **T.T**=Tomato Target Spot; **T.T.Y**=Tomato Tomato Yellow Leaf Curl Virus; **T.M**=Tomato Tomato mosaic virus; **T.H**=Tomato healthy

Table 16

Comparison of the performance measures of proposed models with previous models on 18169 images of the tomato dataset

Methods	Training accuracy (%)	Train loss	Validation accuracy (%)	Validation loss	Weighted average F1_score (%)
DNN (Gadekallu et al., 2021)	99	NA	94	NA	NA
Variation of the LeNet (Tm et al., 2018)	99.3	NA	94.8	NA	94.81
Squeeze Net (Durmus et al., 2017)	NA	NA	94.3	NA	NA
AlexNet (Durmus et al., 2017)	NA	NA	95.65	NA	NA
Filter+PCA+Boruta (proposed)+MLP	99.98	0.0067	95.68	0.16	95.66
Filter+PCA+Boruta (proposed)+VGG16	100.0	0.0016	95.79	0.15	95.80

Table 17

Comparison of the parameters, training time, and storage space of proposed models to previous models on 18169 images of the tomato dataset

Methods	Total parameters	Trainable parameters	Non-Trainable parameters	Train Time (HH:MM:SS)	Storage Space (MB)
DNN (Gadekallu et al., 2021)	NA	NA	NA	NA	NA
variation of the LeNet (Tm et al., 2018)	NA	NA	NA	NA	NA
Squeeze Net (Durmus et al., 2017)	NA	NA	NA	NA	2.9
AlexNet (Durmus et al. 2017)	NA	NA	NA	NA	227.6
Filter+PCA+Boruta (proposed)+MLP	15,193,098	15,193,098	0	0:04:59	115
Filter+PCA+Boruta (proposed)+VGG16	21,516,298	21,516,298	0	0:58:37	164

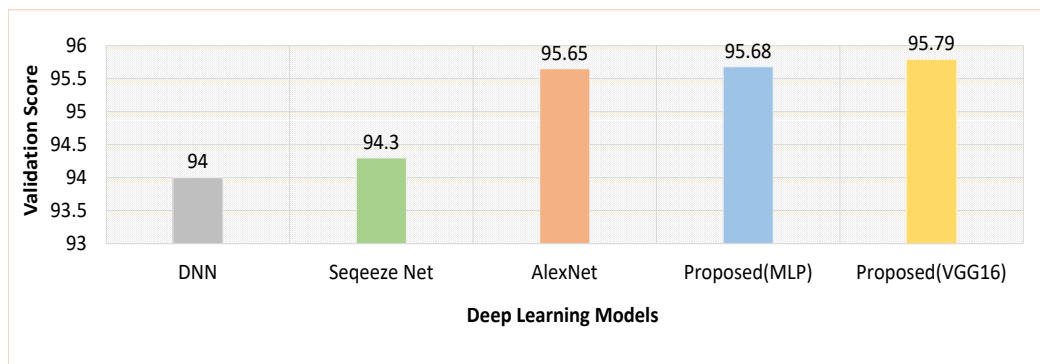


Figure 17. Comparison of the validation accuracy of the proposed models with previous models

Comparison of the Validation Accuracy of the Proposed Model with Previous Models

The performance of the proposed models was compared to the previously proposed DL models: DNN, SequeezeNet, and AlexNet. Figure 17 shows the comparison of the proposed model to previous models on tomato images of the Plant Village dataset. Tables 16 and 17 show the comparison output of proposed models with previously developed models of train accuracy, train loss, validation accuracy, validation loss, weighted average f1_score, trainable parameters, non-trainable parameters, and storage space. The highest validation

accuracy of 95.68% and 95.79% and the highest weighted average F1_score of 95.66% and 95.80% were obtained in the proposed multi-level dimension algorithm by MLP and 3fc of VGG16, respectively. The validation accuracy of the proposed models was improved compared to that of the previous models, such as DNN (94%), SqueezeNet (94.3%), and AlexNet (95.65%).

CONCLUSION

In the present study, multi-level dimensionality reduction-based algorithms, Filter and PCA, and Boruta feature methods were developed to obtain optimal features. The classification performance of VGG16, MLP, and MLA was compared at each level of optimal features. Finally, it was concluded that level 3 of dimension reduction provides 1145 optimal features, recorded as the best among all the previous studies. MLP and VGG16 provided the best validation accuracy of 95.68% and 95.79%, respectively.

FUTURE RESEARCH DIRECTION

The present study examined the prediction of tomato leaf diseases based on the proposed multi-level dimension reduction algorithm. Therefore, in future studies, a robust model may be developed by adding other dimension reduction techniques, such as particle swarm optimization (PSO), linear discernment analysis (LDA), and autoencoders to overcome the overfitting problem and identify the diseases in plants, crops, and vegetables based on the images and prevent crop loss at an early stage in favor of farmers. A minor limitation in the proposed approach is that the Filter method for identifying non-correlated features and the Boruta feature selection algorithm for obtaining the optimal features are time-consuming processes.

ACKNOWLEDGEMENT

Pondicherry University, Puducherry, under the guidelines of research supervisor Dr. Ramasami Lakshmi, supported this research. We (Premkumar Borugadda, Ramasami Lakshmi, and Satyasangram Sahoo), the authors of the research paper titled “Transfer Learning VGG16 Model for Classification of Tomato Plant Leaf Diseases: A Novel Approach for Multi-level Dimensional Reduction,” would like to express our deep sense of gratitude for the entire editorial team of *Pertanika Journal of Science and Technology* for accepting the manuscript.

REFERENCES

- Ali, J., Khan, R., Ahmad, N., & Maqsood, I. (2012). Random forests and decision trees. *International Journal of Computer Science*, 9(5), Article 272.

- Awad, M., & Khanna, R. (2015). Support vector machines for classification. In *Efficient Learning Machines* (pp. 39-66). Apress Berkeley, CA. https://doi.org/10.1007/978-1-4302-5990-9_3
- Behera, B., Kumaravelan, G., & Kumar, P. (2019). Performance evaluation of deep learning algorithms in biomedical document classification. In *2019 11th International Conference on Advanced Computing (ICoAC)* (pp. 220-224). IEEE Publishing. <https://doi.org/10.1109/ICoAC48765.2019.246843>
- Cerda, P., & Varoquaux, G. (2020). Encoding high-cardinality string categorical variables. *IEEE Transactions on Knowledge and Data Engineering*, *34*(3), 1164-1176. <https://doi.org/10.1109/TKDE.2020.2992529>
- Chen, G., & Chen, J. (2015). A novel wrapper method for feature selection and its applications. *Neurocomputing*, *159*, 219-226. <https://dl.acm.org/doi/abs/10.5555/2781902.2782171>
- Chuanlei, Z., Shanwen, Z., Jucheng, Y., Yancui, S., & Jia, C. (2017). Apple leaf disease identification using genetic algorithm and correlation-based feature selection method. *International Journal of Agricultural and Biological Engineering*, *10*(2), 74-83. <https://doi.org/10.3965/j.ijabe.20171002.2166>
- Doquire, G., & Verleysen, M. (2013). A graph Laplacian based approach to semi-supervised feature selection for regression problems. *Neurocomputing*, *121*, 5-13. <https://doi/abs/10.1016/j.neucom.2012.10.028>
- Dreiseitl, S., & Ohno-Machado, L. (2002). Logistic regression and artificial neural network classification models: A methodology review. *Journal of Biomedical Informatics*, *35*(5-6), 352-359. [https://doi.org/10.1016/S1532-0464\(03\)00034-0](https://doi.org/10.1016/S1532-0464(03)00034-0)
- Durmuş, H., Güneş, E. O., & Kırıcı, M. (2017). Disease detection on the leaves of the tomato plants by using deep learning. In *2017 6th International Conference on Agro-Geoinformatics* (pp. 1-5). IEEE Publishing. <https://10.1109/Agro-Geoinformatics.2017.8047016>
- Gadekallu, T. R., Rajput, D. S., Reddy, M., Lakshmana, K., Bhattacharya, S., Singh, S., & Alazab, M. (2021). A novel PCA-whale optimization-based deep neural network model for classification of tomato plant diseases using GPU. *Journal of Real-Time Image Processing*, *18*(4), 1383-1396. <https://doi.org/10.1007/s11554-020-00987-8>
- Gao, B., & Pavel, L. (2017). *On the properties of the softmax function with application in game theory and reinforcement learning*. arXiv Preprint. <https://doi.org/10.48550/arXiv.1704.00805>
- Guo, G., Wang, H., Bell, D., Bi, Y., & Greer, K. (2003). KNN model-based approach in classification. In R. Meersman, Z. Tari & D. C. Schmidt (Eds.), *OTM Confederated International Conferences "On the Move to Meaningful Internet Systems"* (pp. 986-996). Springer. https://doi.org/10.1007/978-3-540-39964-3_62
- Iandola, F. N., Han, S., Moskewicz, M. W., Ashraf, K., Dally, W. J., & Keutzer, K. (2016). *Squeeze Net: AlexNet-level accuracy with 50x fewer parameters and < 0.5 MB model size*. arXiv Preprint. <https://doi.org/10.48550/arXiv.1602.07360>
- Khammari, A., Nashashibi, F., Abramson, Y., & Laugeau, C. (2005). Vehicle detection combining gradient analysis and AdaBoost classification. In *Proceedings. 2005 IEEE Intelligent Transportation Systems* (pp. 66-71). IEEE Publishing. <https://doi.org/10.1109/ITSC.2005.1520202>
- Krizhevsky, A., Sutskever, I., & Hinton, G. E. (2012). ImageNet classification with deep convolutional neural networks. In *Advances in Neural Information Processing Systems 25* (p. 1). Morgan Kaufmann Publishers.

- Kursa, M. B., & Rudnicki, W. R. (2010). Feature selection with the Boruta package. *Journal of Statistical Software*, 36, 1-13. <https://doi.org/10.18637/jss.v036.i11>
- Li, J., Si, Y., Xu, T., & Jiang, S. (2018). Deep convolutional neural network-based ECG classification system using information fusion and one-hot encoding techniques. *Mathematical Problems in Engineering*, 2018, Article 7354081. <https://doi.org/10.1155/2018/7354081>
- Ma, H., Li, Y., Chen, Q., Zhang, L., & Xu, J. (2018). A single-stage integrated boost-LLC AC–DC converter with quasi-constant bus voltage for multichannel LED street-lighting applications. *IEEE Journal of Emerging and Selected Topics in Power Electronics*, 6(3), 1143-1153. <https://doi.org/10.1109/JESTPE.2018.2847327>
- Mohanty, S. P., Hughes, D. P., & Salathé, M. (2016). Using deep learning for image-based plant disease detection. *Frontiers in Plant Science*, 7, Article 1419. <https://doi.org/10.3389/fpls.2016.01419>
- Mudrova, M., & Procházka, A. (2005, November 15). Principal component analysis in image processing. In *Proceedings of the MATLAB Technical Computing Conference* (pp. 1-4). Prague, Czech Republic.
- Noriega, L. (2005). *Multilayer perceptron tutorial*. Staffordshire University. <https://citeseerx.ist.psu.edu/document?repid=rep1&type=pdf&doi=4c8339b893423f1e14e34cc1543faee4e5ee4244>
- Ramchoun, H., Ghanou, Y., Ettaouil, M., & Idrissi, M. A. J. (2016). Multilayer perceptron: Architecture optimization and training. *International Journal of Interactive Multimedia and Artificial Intelligence*, 4(1), 26-30. <http://doi.org/10.9781/ijimai.2016.415>
- Simonyan, K., & Zisserman, A. (2014). *Very deep convolutional networks for large-scale image recognition*. arXiv Preprint. <https://doi.org/10.48550/arXiv.1409.1556>
- Sokolova, M., & Lapalme, G. (2009). A systematic analysis of performance measures for classification tasks. *Information Processing & Management*, 45(4), 427-437. <https://doi.org/10.1016/j.ipm.2009.03.002>
- Tammina, S. (2019). Transfer learning using VGG-16 with deep convolutional neural network for classifying images. *International Journal of Scientific and Research Publications*, 9(10), 143-150. <https://doi.org/10.29322/IJSRP.9.10.2019.p9420>
- Tang, Y., & Wu, X. (2016). Saliency detection via combining region-level and pixel-level predictions with CNNs. In *European Conference on Computer Vision* (pp. 809-825). Springer. <https://doi.org/10.48550/arXiv.1608.05186>
- Tm, P., Pranathi, A., SaiAshritha, K., Chittaragi, N. B., & Koolagudi, S. G. (2018). Tomato leaf disease detection using convolutional neural networks. In *2018 eleventh international conference on contemporary computing (IC3)* (pp. 1-5). IEEE Publishing. <https://doi.org/10.1109/IC3.2018.8530532>
- Torlay, L., Perrone-Bertolotti, M., Thomas, E., & Baciú, M. (2017). Machine learning–XGBoost analysis of language networks to classify patients with epilepsy. *Brain Informatics*, 4(3), 159-169. <https://doi.org/10.1007/s40708-017-0065-7>
- Zhang, M. L., & Zhou, Z. H. (2005). A k-nearest neighbor-based algorithm for multi-label classification. In *2005 IEEE International Conference on Granular Computing* (Vol. 2, pp. 718-721). IEEE Publishing. <https://doi.org/10.1109/GRC.2005.1547385>



Efficient Frequency-Dependent Coefficients of Explicit Improved Two-Derivative Runge-Kutta Type Methods for Solving Third-Order IVPs

Lee Khai Chien^{1*}, Norazak Senu^{1,2}, Ali Ahmadian³ and Siti Nur Iqmal Ibrahim^{1,2}

¹Institute for Mathematical Research, Universiti Putra Malaysia, 43400 UPM, Serdang, Selangor, Malaysia

²Department of Statistics and Mathematics, Universiti Putra Malaysia, 43400 UPM, Serdang, Selangor, Malaysia

³Institute of Industry Revolution 4.0, The National University of Malaysia, 43600 UKM, Bangi, Selangor, Malaysia

ABSTRACT

This study aims to propose sixth-order two-derivative improved Runge-Kutta type methods adopted with exponentially-fitting and trigonometrically-fitting techniques for integrating a special type of third-order ordinary differential equation in the form $u'''(t) = f(t, u(t), u'(t))$. The procedure of constructing order conditions comprised of a few previous steps, k_i for third-order two-derivative Runge-Kutta-type methods, has been outlined. These methods are developed through the idea of integrating initial value problems exactly with a numerical solution in the form of linear composition of the set functions e^{wt} and e^{-wt} for exponentially fitted and e^{iwt} and e^{-iwt} for trigonometrically-fitted with $w \in \mathbb{R}$. Parameters of two-derivative Runge-Kutta type method are adapted into principle frequency of exponential and oscillatory problems to construct the proposed methods. Error analysis of proposed methods is analysed, and the computational efficiency

of proposed methods is demonstrated in numerical experiments compared to other existing numerical methods for integrating third-order ordinary differential equations with an exponential and periodic solution.

ARTICLE INFO

Article history:

Received: 21 May 2022

Accepted: 05 October 2022

Published: 06 March 2023

DOI: <https://doi.org/10.47836/pjst.31.2.10>

E-mail addresses:

kelee_1017@hotmail.com (Lee Khai Chien)

norazak@upm.edu.my (Norazak Senu)

ali.ahmadian@ukm.edu.my (Ali Ahmadian)

iqmal@upm.edu.my (Siti Nur Iqmal Ibrahim)

*Corresponding author

Keywords: Exponentially-fitted, third-order ordinary differential equations, trigonometrically-fitted, two-derivative runge-kutta methods

INTRODUCTION

Third-order ordinary differential equations (ODEs) are widely applied in the fields of engineering and physics, such as thermohaline convection, incompressible Newtonian fluid, turbulent transport of viscoelastic fluids in penetrable channels, jerk mechanical system with jerk curves, thin film flow systems and other disciplines (Herrera, 2019; Allogmany & Ismail, 2020).

This article focuses on developing an improved two-derivative Runge-Kutta type method with exponentially and trigonometrically fitting techniques based on frequency evaluation for integrating third-order ODEs with exponential or oscillatory solution (Equation 1).

$$\begin{aligned}
 u'''(t) &= f(t, u(t), u'(t)) \\
 u(t_0) &= u_0, \quad u'(t_0) = u'_0, \quad u''(t_0) = u''_0.
 \end{aligned}
 \tag{1}$$

In recent, many research are widely studied by researchers regarding the characteristics of solutions with frequency-dependent properties and the development of efficient methods to solve ODEs with exponential and oscillatory solutions to illustrate the model of application problems such as orbital mechanics, molecular dynamics and electronics, Van der Pol's equations, Kepler's problem in a dynamical system, Bessel equations and harmonic oscillator (Franco & Randez, 2018; Ahmad et al., 2020).

Simos and Williams (1999) constructed exponentially and trigonometrically fitted Runge-Kutta methods with order three for solving the Schrödinger equation. The numerical results proved the efficiency of the proposed methods. Then, Zhang et al. (2013) extended Simos and Williams' works by proposing fifth-order trigonometrically fitted two-derivative Runge-Kutta (TDRK) methods for solving the Schrödinger equation. The stability and phase properties of the proposed methods are investigated. Some research concentrate on solving application problems through TDRK methods. Chen et al. (2015) applied newly developed TDRK method oscillatory properties in integrating oscillatory genetic regulatory systems, which is important to illustrate the chemical reaction in living cells. Monovasilis and Kalogiratos (2021) developed amplification-fitted and phase-fitted seventh-order TDRK methods with frequency-reliant coefficients. Proposed methods are built based on minimised dispersion and dissipation error, leading to high efficiency in solving Stiefel and Bettis and harmonic oscillator problems.

Also, some research is on constructing direct methods with exponential and trigonometric fitting techniques for integrating high-order ODEs with exponential and trigonometric solutions. D'Ambrosio et al. (2014) revised the multistage Runge-Kutta-Nyström method with the exponentially-fitting technique for integrating special second-order ODEs with periodic or oscillatory solutions. Demba et al. (2016) applied the Simos

technique in developing the symplectic explicit Runge-Kutta-Nyström method with a trigonometrically-fitting technique. Mei et al. (2017) implemented finite-energy conditions into the traditional Runge-Kutta-Nyström method to solve nonlinear wave equations. Zhai et al. (2018) constructed implicit symplectic and symmetric and exponentially-fitted Runge-Kutta-Nyström with linear combinations of exponential functions to solve second-order oscillatory problems. Two years later, Samat and Ismail (2020) derived a four-stage explicit sixth-order hybrid method with variable steps based on a trigonometrically-fitting technique. Demba et al. (2020) developed 5(3) embedded explicit Runge-Kutta-Nyström methods with an exponentially-fitting technique to reduce the computational cost in error estimation for solving special second-order ODEs with a periodic solution. The variable step-size technique is utilised for the derivation of the methods, and the numerical results proved the efficiency of the methods by generating more accurate results than other existing methods.

Some researchers are interested in developing the Improved Runge-Kutta (IRK) method, which comprises a few previous terms in the formulation to compute the future value. Several previous terms, such as b - i and k - i are inserted in the formulation to improve the method's accuracy in numerical integration. Rabiei (2011) proposed the improved Runge-Kutta methods and attained an order of up to five. Later, the stability of the methods was discussed as well. Rabiei and Ismail (2012) also constructed the improved Runge-Kutta method for solving first and second ODEs by presenting the new terms k - i , which is the previous step of k_i . Another modified, improved Runge-Kutta fifth-order five-stage technique is proposed by Senthilkumar et al. (2013) to solve a second-order robot arm problem. The study illustrates the importance of improved methods of visualising application problems. IRK method is not only used to solve first-order ODEs, but some researchers utilised IRK method to solve high-order ODEs or other types of differential equations. Hussain et al. (2017) emphasised solving high-order ODEs, and they developed a fourth-order improved RK method with a lower number of function evaluations for solving third-order ODEs directly. The stability polynomial of the proposed method was studied, and the great numerical performance of the method was proved by yielding a low maximum absolute error. Tang and Xiao (2020) modified the classical IRK methods into improved Runge-Kutta-Chebyshev methods based on spatial discretisation of partial differential equations (PDEs). The width of the stability domain increased significantly, and the proposed methods are applied to solve several numerical problems, including advection-diffusion-reaction equations with dominating advection.

However, there is no improved two-derivative Runge-Kutta type method with exponentially and trigonometrically fitting techniques developed in the current research field for solving high-order ODEs. Thus, we propose a three-stage sixth-order explicit improved two-derivative Runge-Kutta type method with exponentially and trigonometrically fitting

techniques, denoted as EFIRKT6 and TFIRKT6 methods, to solve third-order ODEs with exponential and oscillatory solutions. Nonoscillatory and oscillatory properties of third-order ODEs are discussed. We developed order conditions for an improved TDRKT method. Then, exponentially-fitted and trigonometrically-fitted improved TDRKT methods are derived by adapting a linear combination of frequency-dependent coefficients and constructed EFIRKT6 and TFIRKT6 methods. Analysis of error for EFIRKT6 and TFIRKT6 methods was discussed. The numerical performance of EFIRKT6 and TFIRKT6 methods and other existing numerical methods are shown. This article ends with a discussion and conclusion.

METHODOLOGY

The explicit three-stage sixth-order two-derivative improved Runge-Kutta type method with exponentially and trigonometrically fitting techniques are proposed. Here we introduce the criteria for achieving nonoscillatory and oscillatory properties of third-order ordinary differential equations.

Oscillatory and Nonoscillatory Standard for Third-Order Linear Differential Equations

The oscillatory and nonoscillatory standards for third-order ordinary differential equations are mentioned as follows (Lee et al., 2020):

$$u'''(t) + \alpha(t)u'(t) + \beta(t)u(t) = 0. \tag{2}$$

Equation 2 consists of an oscillatory solution if both $\alpha(t)$ and $\beta(t)$ are constant, negative and fulfil the following requirement in Equation 3:

$$-\beta(t) - \frac{2}{3\sqrt{3}}(\alpha(t))^{\frac{3}{2}} > 0. \tag{3}$$

then two linear independent oscillatory solutions exist, and zeroes of any oscillatory solutions are split in which the oscillatory solution of Equation 2 is a linear combination of them (Lazer, 1966). The solution of Equation 2 is oscillatory iff it contains an infinite number of zeroes in $(0, +\infty)$ and nonoscillatory iff it contains a finite number of zeroes in $(0, +\infty)$. We focus on $\beta(t) = 0$ as follow:

1. $u'''(t) = \alpha(t)u'(t)$, $\alpha(t) > 0$, the solution of characteristic roots equations contains exponential function if those equations contain two real solutions and one zero.
2. $u'''(t) = -\alpha(t)u'(t)$, $\alpha(t) > 0$, the solution of characteristic roots equations contains an oscillatory function if those equations contain one real solution and two conjugate roots.

Exponentially-Fitted and Trigonometrically-Fitted Two-Derivative Improved Runge-Kutta Type Methods

The criteria for developing an explicit two-derivative improved Runge-Kutta type method with exponentially and trigonometrically fitting techniques denoted as EFIRKT and TFIRKT methods will be proposed. Here we include two parameters, γ_i and $\hat{\gamma}_p$, into U'_i and U''_i to implement oscillatory properties into the formulation of the two-derivative Runge-Kutta-type TDIRKT method as in Equation 4.

$$\begin{aligned}
 u_{n+1} &= u_n + \frac{3}{2}hu'_n - \frac{1}{2}hu'_{n-1} + \frac{5h^2}{12}(u''_n - u''_{n-1}) \\
 &\quad + \frac{h^3}{6}[f(t_n, u_n(t), u'_n(t)) - f(t_{n-1}, u_{n-1}(t), u'_{n-1}(t))] \\
 &\quad + h^4 \sum_{i=2}^s b_i [g(t_n + c_i h, U_i(t), U'_i(t), U''_i(t)) - g(t_{n-1} + c_i h, U_{-i}(t), U'_{-i}(t), U''_{-i}(t))] \\
 u'_{n+1} &= u'_n + \frac{3}{2}hu''_n - \frac{1}{2}hu''_{n-1} + \frac{5h^2}{12}[f(t_n, u_n(t), u'_n(t)) - f(t_{n-1}, u_{n-1}(t), u'_{n-1}(t))] \\
 &\quad + h^3 \sum_{i=2}^s b'_i [g(t_n + c_i h, U_i(t), U'_i(t), U''_i(t)) - g(t_{n-1} + c_i h, U_{-i}(t), U'_{-i}(t), U''_{-i}(t))] \\
 u''_{n+1} &= u''_n + \frac{3}{2}hf(t_n, u_n(t), u'_n(t)) - \frac{1}{2}hf(t_{n-1}, u_{n-1}(t), u'_{n-1}(t)) \\
 &\quad + h^2 \sum_{i=2}^s b''_i [g(t_n + c_i h, U_i(t), U'_i(t), U''_i(t)) - g(t_{n-1} + c_i h, U_{-i}(t), U'_{-i}(t), U''_{-i}(t))]
 \end{aligned}$$

where

$$\begin{aligned}
 U_i &= u_n + c_i hu'_n + \frac{(c_i h)^2}{2}u''_n + \frac{(c_i h)^3}{6}f(t_n, u_n, u'_n) \\
 &\quad + h^4 \sum_{j=1}^s A_{i,j} g(t_n + c_i h, U_j(t), U'_j(t), U''_j(t)) \\
 U_{-i} &= u_{n-1} + c_i hu'_{n-1} + \frac{(c_i h)^2}{2}u''_{n-1} + \frac{(c_i h)^3}{6}f(t_{n-1}, u_{n-1}, u'_{n-1}) \\
 &\quad + h^4 \sum_{j=1}^s A_{i,j} g(t_{n-1} + c_i h, U_{-j}(t), U'_{-j}(t), U''_{-j}(t)) \\
 U'_i &= u'_n \gamma_i + c_i hu''_n + \frac{(c_i h)^2}{2}f(t_n, u_n, u'_n) + h^3 \sum_{j=1}^s \bar{A}_{i,j} g(t_n + c_i h, U_j(t), U'_j(t), U''_j(t))
 \end{aligned}$$

$$\begin{aligned}
 U'_{-i} &= u'_{n-1}\gamma_i + c_i h u''_{n-1} + \frac{(c_i h)^2}{2} f(t_{n-1}, u_{n-1}, u'_{n-1}) \\
 &\quad + h^3 \sum_{j=1}^s \bar{A}_{i,j} g(t_n + c_i h, U_{-j}(t), U'_{-j}(t), U''_{-j}(t)) \\
 U''_i &= u''_n + c_i h f(t_n, u_n, u'_n) \hat{\gamma}_i + h^2 \sum_{j=1}^s \hat{A}_{i,j} g(t_n + c_i h, U_j(t), U'_j(t), U''_j(t)) \\
 U''_{-i} &= u''_{n-1} + c_i h f(t_{n-1}, u_{n-1}, u'_{n-1}) \hat{\gamma}_i \\
 &\quad + h^2 \sum_{j=1}^s \hat{A}_{i,j} g(t_{n-1} + c_i h, U_{-j}(t), U'_{-j}(t), U''_{-j}(t))
 \end{aligned}$$

for $i = 1, 2, \dots, s$. (4)

The parameters for the TDIRKT method are $c_i, A_{i,j}, \bar{A}_{i,j}, \hat{A}_{i,j}, b_i, b'_i, b''_i, \gamma_i$ and $\hat{\gamma}_i$ for $i = 1, 2, \dots, s$. TDIRKT method is explicit if all $A_{i,j}, \bar{A}_{i,j}, \hat{A}_{i,j} = 0$ and $i \leq j$ and elsewhere for implicit TDIRKT method. The general TDIRKT method is modified into the form of Butcher tableau, which is exhibited in Table 1.

Table 1
General formulation for TDIRKT methods in butcher tableau

c	A	$\bar{\mathbf{A}}$	$\hat{\mathbf{A}}$
\mathbf{b}''_{-1}	\mathbf{b}^T	\mathbf{b}'^T	\mathbf{b}''^T

Order Conditions of TDIRKT Method

Order conditions for explicit TDIRKT method up to order 7 are shown in Equations 5 to 17.

The order conditions of u :

Fifth order: (5)

$$\sum_{i=2}^s b_i = \frac{31}{720},$$

Sixth order: (6)

$$\sum_{i=2}^s b_i c_i = \frac{1}{120},$$

Seventh order: (7)

$$\sum_{i=2}^s b_i c_i^2 = \frac{1}{756},$$

The order conditions of u' :

Fourth order: (8)

$$\sum_{i=2}^s b'_i = \frac{31}{720},$$

Fifth order: $\sum_{i=2}^s b'_i c_i = \frac{1}{120},$ (9)

Sixth order: $\sum_{i=2}^s b'_i c_i^2 = \frac{1}{756},$ (10)

Seventh order: $\sum_{i=2}^s b'_i c_i^3 = \frac{1}{252}, \quad \sum_{i=2, j<i}^s b'_i \hat{A}_{i,j} = \frac{1}{1512},$ (11)

The order conditions of u'' :

Second order: $b''_1 - b''_{-1} = 0,$ (12)

Third order: $\sum_{i=2}^s b''_i + b''_{-1} = \frac{5}{12},$ (13)

Fourth order: $\sum_{i=2}^s b''_i c_i = \frac{1}{6},$ (14)

Fifth order: $\sum_{i=2}^s b''_i c_i^2 = \frac{31}{360},$ (15)

Sixth order: $\sum_{i=2}^s b''_i c_i^3 = \frac{1}{20}, \quad \sum_{i=2, j<i}^s b''_i \hat{A}_{i,j} = \frac{1}{120},$ (16)

Seventh order: $\sum_{i=2}^s b''_i c_i^4 = \frac{1}{63}, \quad \sum_{i=2, j<i}^s b''_i \bar{A}_{i,j} = \frac{1}{1512},$
 $\sum_{i=2, j<i}^s b''_i \hat{A}_{i,j} c_j = \frac{1}{1512}, \quad \sum_{i=2, j<i}^s b''_i c_i \hat{A}_{i,j} = \frac{1}{378},$ (17)

The coefficients of the improved TDRKT method with three-stages sixth order are shown in Table 2 in the form of Butcher tableau (Equation 18).

Table 2
 The improved TDRKT method with a three-stage sixth order

0	0	0	0		0		0				
c₂	γ_2	$\hat{\gamma}_2$	$A_{2,1}$	0	$\bar{A}_{2,1}$	0	$\hat{A}_{2,1}$	0			
c₃	γ_3	$\hat{\gamma}_3$	$A_{3,1}$	$A_{3,2}$	0	$\bar{A}_{3,1}$	$\bar{A}_{3,2}$	0	$\hat{A}_{3,1}$	$\hat{A}_{3,2}$	0
b''₋₁			b_1	b_2	b_3	b'_1	b'_2	b'_3	b''_1	b''_2	b''_3

where

$$c_1 = 0, c_2 = \frac{5 - \sqrt{5}}{10}, b_1 = \frac{1}{40}, b_2 = \frac{1}{60}, b'_2 = \frac{1}{12} + \frac{\sqrt{4790}}{1440}, b'_3 = \frac{1}{12} - \frac{\sqrt{4790}}{1440},$$

$$b''_{-1} = -\frac{7}{558}, b''_1 = -\frac{7}{558}, b''_2 = \frac{479}{2232} - \frac{\sqrt{4790}}{59396}, b''_3 = \frac{479}{2232} + \frac{\sqrt{4790}}{59396},$$

$$\hat{A}_{3,2} = -\frac{172440}{3545129} \hat{A}_{2,1} \left(\frac{12}{31} - \frac{\sqrt{4790}}{310} \right) - \frac{107836199}{109898999} \hat{A}_{2,1} - \hat{A}_{3,1} + \frac{688323}{17725645} - \frac{54\sqrt{4790}}{17725645},$$

$$\gamma_2 = 1, \gamma_3 = 1, \hat{\gamma}_2 = 1, \hat{\gamma}_3 = 1. \tag{18}$$

Exponentially-Fitted TDIRKT Method

To develop an exponentially-fitted two-derivative improved Runge-Kutta-type method, we integrate $e^{\omega x}$ and $e^{-\omega x}$ at every stage. The relations $\sinh(v) = (e^v - e^{-v})/2$ and $\cosh(v) = (e^v + e^{-v})/2$, we get the following Equations 19 to 21:

$$e^{\pm c_i v} = 1 \pm c_i v + \frac{1}{2} (c_i v)^2 \pm \frac{1}{6} (c_i v)^3 + v^4 \sum_{i=2}^s A_{i,j} e^{\pm c_j v}, \tag{19}$$

$$e^{\pm c_i v} = \gamma_i \pm c_i v + \frac{1}{2} (c_i v)^2 + v^3 \sum_{j=1}^s \bar{A}_{i,j} e^{\pm c_j v}, \tag{20}$$

$$e^{\pm c_i v} = 1 \pm \hat{\gamma}_i c_i v + v^2 \sum_{j=1}^s \hat{A}_{i,j} e^{\pm c_j v}, \tag{21}$$

Similarly, we integrate $e^{\omega x}$ and $e^{-\omega x}$ corresponding to u, u' and u'' we obtain Equations 22 to 24.

$$e^{\pm v} = 1 \pm \frac{3}{2} v \mp \frac{v}{2} e^{\mp v} + \frac{5}{12} v^2 (1 - e^{\mp v}) \pm \frac{1}{6} v^3 (1 - e^{\mp v}) + v^4 \sum_{i=2}^s b_i [e^{\pm c_i v} - e^{\pm v(c_i-1)}] \tag{22}$$

$$e^{\pm v} = 1 \pm \frac{3}{2} v \mp \frac{v}{2} e^{\mp v} + \frac{5}{12} v^2 (1 - e^{\mp v}) \mp v^3 \sum_{i=2}^s b'_i [e^{\pm c_i v} - e^{\pm v(c_i-1)}] \tag{23}$$

$$e^{\pm v} = 1 \pm \frac{3}{2} v \mp \frac{v}{2} e^{\mp v} + v^2 \sum_{i=2}^s b''_i [e^{\pm c_i v} - e^{\pm v(c_i-1)}] \tag{24}$$

where $v = \omega h, \omega \in \mathbb{R}$. The relation and are substituted in Equations 22 to 24.

Here, we obtain hyperbolic functions of v as in Equation 25.

$$\cosh(v) = 1 + \frac{v}{2} \sinh(v) + \frac{5}{12} v^2 (1 - \cosh(v)) + \frac{1}{6} v^3 \sinh(v)$$

$$+ v^4 \sum_{i=2}^s b_i [\cosh(v c_i) - \cosh(v(c_i - 1))],$$

$$\begin{aligned} \sinh(v) &= \frac{3}{2}v - \frac{v}{2}\cosh(v) + \frac{5}{12}v^2 \sinh(v) + \frac{1}{6}v^3(1 - \cosh(v)) \\ &\quad + v^4 \sum_{i=2}^s b_i [\sinh(v c_i) - \sinh(v(c_i - 1))], \\ \cosh(v) &= 1 + \frac{v}{2}\sinh(v) + \frac{5}{12}v^2(1 - \cosh(v)), \\ &\quad + v^3 \sum_{i=2}^s b'_i [\cosh(v c_i) - \cosh(v(c_i - 1))] \\ \sinh(v) &= \frac{3}{2}v - \frac{v}{2}\cosh(v) + \frac{5}{12}v^2 \sinh(v) + v^3 \sum_{i=2}^s b'_i [\sinh(v c_i) - \sinh(v(c_i - 1)) \\ \cosh(v) &= 1 + \frac{v}{2}\sinh(v) + v^2 \sum_{i=2}^s b''_i [\cosh(v c_i) - \cosh(v(c_i - 1))], \\ \sinh(v) &= \frac{3}{2}v - \frac{v}{2}\cosh(v) + v^2 \sum_{i=2}^s b''_i [\sinh(v c_i) - \sinh(v(c_i - 1))], \end{aligned} \tag{25}$$

Solving Equations 19 to 21, the coefficients $A_{i,j}, \bar{A}_{i,j}, \hat{A}_{i,j}, \gamma_i$ and $\hat{\gamma}_i$ can be determined as Equations 26 to 30:

$$A_{i,i-1} = \frac{\cosh(v c_i) - 1 - \frac{1}{2}(c_i v)^2 - v^4 \sum_{j=1}^{i-2} A_{i,j} \cosh(v c_j)}{v^4 \cosh(v c_{i-1})}, \tag{26}$$

$$\bar{A}_{i,i-1} = \frac{\sinh(v c_i) - v c_i - v^3 \sum_{j=1}^{i-2} \bar{A}_{i,j} \cosh(v c_j)}{v^3 \cosh(v c_{i-1})}, \tag{27}$$

$$\hat{A}_{i,i-1} = \frac{\cosh(v c_i) - 1 - v^2 \sum_{j=1}^{i-2} \hat{A}_{i,j} \cosh(v c_j)}{v^2 \cosh(v c_{i-1})}, \tag{28}$$

$$\gamma_i = \cosh(v c_i) - \frac{1}{2}(c_i v)^2 - v^3 \sum_{j=1}^{i-1} \bar{A}_{i,j} \sinh(v c_j), \tag{29}$$

$$\hat{\gamma}_i = \frac{\sinh(v c_i) - v^2 \sum_{j=1}^{i-1} \hat{A}_{i,j} \sinh(v c_j)}{v c_i}. \tag{30}$$

Then, Equations 26 to 30 are integrated by replacing with Equation 18, and we get the terms as in Equation 31.

$$A_{2,1} = \frac{\cosh(v c_2) - 1 - \frac{1}{2}(c_2 v)^2}{v^4},$$

$$A_{3,2} = \frac{\cosh(v c_3) - 1 - \frac{1}{2}(c_3 v)^2 - v^4 A_{3,1}}{v^4 \cosh(v c_2)},$$

$$\bar{A}_{2,1} = \frac{\sinh(v c_2) - v c_2}{v^3},$$

$$\begin{aligned} \bar{A}_{3,2} &= \frac{\sinh(v c_3) - v c_3 - v^3 \bar{A}_{3,1}}{v^3 \cosh(v c_2)}, \\ \hat{A}_{2,1} &= \frac{\cosh(v c_i) - 1}{v^2}, \\ \hat{A}_{3,2} &= \frac{\sinh(v c_3) - 1 - v^2 \hat{A}_{3,1}}{v^2 \cosh(v c_2)}, \\ \gamma_2 &= \cosh(v c_2) - \frac{1}{2} (c_2 v)^2, \\ \gamma_3 &= \cosh(v c_3) - \frac{1}{2} (c_3 v)^2 - v^3 \bar{A}_{3,2} \sinh(v c_2), \\ \hat{\gamma}_2 &= \frac{\sinh(v c_2)}{v c_2}, \\ \hat{\gamma}_3 &= \frac{\sinh(v c_3) - v^2 \hat{A}_{3,2} \sinh(v c_2)}{v c_3}, \end{aligned} \tag{31}$$

Equation 31 can be further modified through Taylor series expansion, yield Equation 32.

$$\begin{aligned} A_{2,1} &= \frac{6441601}{2216450400} - \frac{1919\sqrt{4790}}{46176050} + \left(\frac{22950627839}{639002650320000} - \frac{4602241\sqrt{4790}}{8875036810000} \right) v^2 \\ &+ \left(\frac{82135555848961}{343885666296211200000} - \frac{12361432319\sqrt{4790}}{3582142357252200000} \right) v^4 \\ &+ \left(\frac{294040876575811199}{29742671277959306688000000} - \frac{35404382065921\sqrt{4790}}{2478555939829942224000000} \right) v^6 \\ &+ \left(\frac{1052674973624775070081}{377291733695169397198617600000000} - \frac{15089188630912457\sqrt{4790}}{374297354856318846427200000000} \right) v^8, \\ A_{3,2} &= \frac{6441601}{2216450400} + \frac{1919\sqrt{4790}}{46176050} + \left(\frac{1816462073}{319501325160000} + \frac{3841\sqrt{4790}}{2218759202500} \right) v^2 \\ &+ \left(\frac{214076712633923}{343885666296211200000} - \frac{12449882867\sqrt{4790}}{3582142357252200000} \right) v^4 \\ &- \left(\frac{710975672934795007}{106223825992711809600000000} - \frac{1142430575083613\sqrt{4790}}{12392779699149711120000000} \right) v^6 \\ &+ \left(\frac{3731786017565356409130181}{377291733695169397198617600000000} - \frac{373072793565778149857\sqrt{4790}}{2620081483994231924990400000000} \right) v^8, \end{aligned}$$

$$\begin{aligned} \bar{A}_{2,1} &= \frac{2877}{148955} - \frac{4799\sqrt{4790}}{17874600} + \left(\frac{2023681}{5725830200} - \frac{17495041\sqrt{4790}}{3435498120000} \right) v^2 \\ &+ \left(\frac{36177468473}{11555297926620000} - \frac{62713990079\sqrt{4790}}{1386635751194400000} \right) v^4 \\ &+ \left(\frac{2055628007863}{126910186371220800000} - \frac{224539256163841\sqrt{4790}}{959441008966429248000000} \right) v^6 \\ &+ \left(\frac{463627866671572789}{8451875754820102983840000000} - \frac{803863978325073599\sqrt{4790}}{1014225090578412358060800000000} \right) v^8, \\ \bar{A}_{3,2} &= \frac{1586517831}{86745135890} - \frac{4799\sqrt{4790}}{17874600} + \left(\frac{111041410223}{833620755902900} - \frac{374850995583\sqrt{4790}}{333448302361160000} \right) v^2 \\ &+ \left(-\frac{1010573345229507}{320443818569074760000} + \frac{912680614276573\sqrt{4790}}{11535977468486691360000} \right) v^4 \\ &+ \left(\frac{24054389059591111633}{36953581157385701323200000} - \frac{378876794375477242093\sqrt{4790}}{39909867649976557429056000000} \right) v^6 - \\ &- \left(\frac{485935333951896962763298489}{4922017460825525533463094720000000} - \frac{140588309086395387940503173\sqrt{4790}}{98440349216510510669261894440000000} \right) v^8, \\ \hat{A}_{2,1} &= \frac{1919}{19220} - \frac{6\sqrt{4790}}{4805} + \left(\frac{6441601}{2216450400} - \frac{1919\sqrt{4790}}{46176050} \right) v^2 \\ &+ \left(\frac{22950627839}{639002650320000} - \frac{4602241\sqrt{4790}}{8875036810000} \right) v^4 \\ &+ \left(\frac{8213555848961}{343885666296211200000} - \frac{12361432319\sqrt{4790}}{3582142357252200000} \right) v^6 \\ &+ \left(\frac{294040876575811199}{29742671277959306880000000} - \frac{35404382065921\sqrt{4790}}{247855939829942224000000} \right) v^8, \\ \hat{A}_{3,2} &= \frac{28631109}{793997420} + \frac{6\sqrt{4790}}{4805} + \left(\frac{24812903941}{3662551298976} - \frac{72658291\sqrt{4790}}{1907578801550} \right) v^2 \\ &- \left(\frac{19126585411486231}{26397838487369520000} - \frac{3904934862021\sqrt{4790}}{366636645657910000} \right) v^4 \\ &+ \left(\frac{314869203983050706341}{2841252152072556176640000} - \frac{236564868394367731\sqrt{4790}}{147981882920445634200000} \right) v^6 \\ &- \left(\frac{205505666501846260968448531}{12286994931637769185879680000000} - \frac{24742878882947640783241\sqrt{4790}}{102391624430314743215664000000} \right) v^8, \end{aligned}$$

$$\begin{aligned}
 \gamma_2 &= 1 + \left(\frac{6441601}{2216450400} - \frac{1919\sqrt{4790}}{46176050} \right) v^4 + \left(\frac{22950627839}{639002650320000} - \frac{4602241\sqrt{4790}}{8875036810000} \right) v^6 \\
 &\quad + \left(-\frac{82135555848961}{343885666296211200000} - \frac{12361432319\sqrt{4790}}{3582142357252200000} \right) v^8 \\
 \gamma_3 &= 1 + \left(-\frac{3231057493}{129076762204320} - \frac{90673209\sqrt{4790}}{26890992125900} \right) v^4 \\
 &\quad + \left(-\frac{55410348606113}{8860197748453680000} + \frac{122935235569\sqrt{4790}}{8875036815168448686597980000000} \right) v^6 \\
 &\quad + \left(-\frac{3351360448784910563}{2043516008703356755200000} - \frac{746512915113451\sqrt{4790}}{29801275126923952680000} \right) v^8 \\
 \hat{\gamma}_2 &= 1 + \left(\frac{4799\sqrt{4790}-345240}{5766(\sqrt{4790}-120)} \right) v^2 + \left(\frac{17495041\sqrt{4790}-1214208600}{11082252000(\sqrt{4790}-120)} \right) v^4 \\
 &\quad + \left(\frac{62713990079\sqrt{4790}-4341296216760}{4473018552240000(\sqrt{4790}-120)} \right) v^6 \\
 &\quad + \left(\frac{224539256163841\sqrt{4790}-15540547739444280}{309497099666590080000(\sqrt{4790}-120)} \right) v^8 \\
 \hat{\gamma}_3 &= 1 + \left(\frac{4(4548889\sqrt{4790}-1137646755)}{59549806(\sqrt{4790}+120)} \right) v^2 + \left(\frac{644664336581\sqrt{4790}-46082914655200}{7630315206200(\sqrt{4790}+120)} \right) v^4 \\
 &\quad + \left(\frac{117946514812127927\sqrt{4790}-8193004367907021360}{9239243470579332000(\sqrt{4790}+120)} \right) v^6 \\
 &\quad + \left(\frac{12326167192820800831583\sqrt{4790}-853303436327430405622080}{63928173421632513974400000(\sqrt{4790}+120)} \right) v^8 \tag{32}
 \end{aligned}$$

Afterwards, the coefficients in Equation 25 are utilised to obtain parameters $b_2, b_3, b'_2, b'_3, b''_2$ and b''_3 through Taylor series expansion, yielding Equation 33.

$$\begin{aligned}
 b_2 &= \frac{31}{1440} + \frac{31\sqrt{4790}}{114960} + \left(\frac{2377\sqrt{4790}}{1496779200} + \frac{2651}{18748800} \right) v^2 + \left(\frac{12453977\sqrt{4790}}{2589128660160000} - \frac{14221}{20591539200} \right) v^4 \\
 &\quad + \left(\frac{152021375417\sqrt{4790}}{1642180743993081600000} + \frac{184288690451}{6856704567820800000} \right) v^6 \\
 &\quad + \left(-\frac{429376762287585683\sqrt{4790}}{172332417891526774801920000000} - \frac{2048157093308653}{2616548383245804134400000} \right) v^8, \\
 b_3 &= \frac{31}{1440} - \frac{31\sqrt{4790}}{114960} + \left(-\frac{2377\sqrt{4790}}{1496779200} + \frac{2651}{18748800} \right) v^2 - \left(\frac{12453977\sqrt{4790}}{2589128660160000} - \frac{14221}{20591539200} \right) v^4 \\
 &\quad + \left(-\frac{152021375417\sqrt{4790}}{1642180743993081600000} + \frac{184288690451}{6856704567820800000} \right) v^6 \\
 &\quad + \left(-\frac{429376762287585683\sqrt{4790}}{172332417891526774801920000000} - \frac{2048157093308653}{2616548383245804134400000} \right) v^8,
 \end{aligned}$$

$$\begin{aligned}
 b'_{2'} &= \frac{1}{12} - \frac{\sqrt{4790}}{1440} + \left(\frac{241\sqrt{4790}}{96566400} \right) v^2 + \left(\frac{518389\sqrt{4790}}{18560062080000} + \frac{1973}{193737600} \right) v^4 \\
 &\quad + \left(-\frac{76233665681\sqrt{4790}}{105947144773747200000} - \frac{10186361}{41890912560000} \right) v^6 \\
 &\quad + \left(-\frac{204301546417014479\sqrt{4790}}{11118220509130759664640000000} + \frac{294637773487}{472350759116544000000} \right) v^8, \\
 b'_{3'} &= \frac{1}{12} - \frac{\sqrt{4790}}{1440} - \left(\frac{241\sqrt{4790}}{96566400} \right) v^2 + \left(-\frac{518389\sqrt{4790}}{18560062080000} + \frac{1973}{193737600} \right) v^4 \\
 &\quad + \left(\frac{76233665681\sqrt{4790}}{105947144773747200000} - \frac{10186361}{41890912560000} \right) v^6 \\
 &\quad + \left(-\frac{204301546417014479\sqrt{4790}}{11118220509130759664640000000} + \frac{294637773487}{472350759116544000000} \right) v^8, \\
 b'_{2''} &= \frac{479}{2232} - \frac{\sqrt{4790}}{59396} + \left(-\frac{351\sqrt{4790}}{1663088000} + \frac{1907}{37497600} \right) v^4 + \left(-\frac{2412191\sqrt{4790}}{647282165040000} - \frac{492499}{386091360000} \right) v^6 \\
 &\quad + \left(-\frac{3273299154193\sqrt{4790}}{32843614879861632000000} + \frac{977694255779}{27426818271283200000} \right) v^8, \\
 b'_{3''} &= \frac{479}{2232} + \frac{\sqrt{4790}}{59396} + \left(\frac{351\sqrt{4790}}{1663088000} + \frac{1907}{37497600} \right) v^4 + \left(-\frac{2412191\sqrt{4790}}{647282165040000} - \frac{492499}{386091360000} \right) v^6 \\
 &\quad + \left(\frac{3273299154193\sqrt{4790}}{32843614879861632000000} + \frac{977694255779}{27426818271283200000} \right) v^8, \tag{33}
 \end{aligned}$$

where $\gamma_i, \hat{\gamma}_i = 1$.

Trigonometrically-Fitted Improved TDRKT Method

Trigonometrically-fitted improved TDRKT method can be derived by substituting $v = wh$ with iwh and solving Equations 19 to 21 to obtain the coefficients.

$$A_{i,i-1} = \frac{\cos(vc_i) - 1 + \frac{1}{2}(c_i v)^2 - v^4 \sum_{j=1}^{i-2} A_{i,j} \cos(vc_j)}{v^4 \cos(vc_{i-1})}, \tag{34}$$

$$\bar{A}_{i,i-1} = \frac{vc_i - \sin(vc_i) - v^3 \sum_{j=1}^{i-2} \bar{A}_{i,j} \cos(vc_j)}{v^3 \cos(vc_{i-1})}, \tag{35}$$

$$\hat{A}_{i,i-1} = \frac{1 - \cosh(vc_i) + v^2 \sum_{j=1}^{i-2} \hat{A}_{i,j} \cos(vc_j)}{v^2 \cos(vc_{i-1})}, \tag{36}$$

$$\gamma_i = \cos(vc_i) + \frac{1}{2}(c_i v)^2 + v^3 \sum_{j=1}^{i-1} \bar{A}_{i,j} \sin(vc_j), \tag{37}$$

$$\hat{\gamma}_i = \frac{\sin(vc_i) + v^2 \sum_{j=1}^{i-1} \hat{A}_{i,j} \sin(vc_j)}{vc_i}. \tag{38}$$

Later, Equations 34 to 38 are solved by substituting Equation 18.

$$\begin{aligned}
 A_{2,1} &= \frac{\cos(vc_2) - 1 + \frac{1}{2}(c_2v)^2}{v^4}, \\
 A_{3,2} &= \frac{\cos(vc_3) - 1 + \frac{1}{2}(c_3v)^2 - v^4 A_{3,1}}{v^4 \cos(vc_2)}, \\
 \bar{A}_{2,1} &= \frac{vc_2 - \sin(vc_2)}{v^3}, \\
 \bar{A}_{3,2} &= \frac{vc_3 - \sin(vc_3) - v^3 \bar{A}_{3,1}}{v^3 \cos(vc_2)}, \\
 \hat{A}_{2,1} &= \frac{1 - \cos(vc_i)}{v^2}, \\
 \hat{A}_{3,2} &= \frac{1 - \sin(vc_3) + v^2 \hat{A}_{3,1}}{v^2 \cos(vc_2)}, \\
 \gamma_2 &= \cos(vc_2) + \frac{1}{2}(c_2v)^2, \\
 \gamma_3 &= \cos(vc_3) + \frac{1}{2}(c_3v)^2 + v^3 \bar{A}_{3,2} \sin(vc_2), \\
 \hat{\gamma}_2 &= \frac{\sin(vc_2)}{vc_2}, \\
 \hat{\gamma}_3 &= \frac{\sinh(vc_3) + v^2 \hat{A}_{3,2} \sin(vc_2)}{vc_3}, \tag{39}
 \end{aligned}$$

Equation 39 is then modified through Taylor series expansion, generating Equation 40:

$$\begin{aligned}
 A_{2,1} &= \frac{6441601}{2216450400} - \frac{1919\sqrt{4790}}{46176050} - \left(\frac{22950627839}{639002650320000} - \frac{4602241\sqrt{4790}}{8875036810000} \right) v^2 \\
 &+ \left(\frac{82135555848961}{343885666296211200000} - \frac{12361432319\sqrt{4790}}{3582142357252200000} \right) v^4 \\
 &- \left(\frac{294040876575811199}{297426712779593066880000000} - \frac{35404382065921\sqrt{4790}}{2478555939829942224000000} \right) v^6 \\
 &+ \left(\frac{1052674973624775070081}{377291733695169397198617600000000} - \frac{15089188630912457\sqrt{4790}}{374297354856318846427200000000} \right) v^8,
 \end{aligned}$$

$$\begin{aligned}
 A_{3,2} &= \frac{6441601}{2216450400} + \frac{1919\sqrt{4790}}{46176050} + \left(\frac{1816462073}{319501325160000} + \frac{3841\sqrt{4790}}{2218759202500} \right) v^2 \\
 &+ \left(\frac{214076712633923}{343885666296211200000} - \frac{12449882867\sqrt{4790}}{3582142357252200000} \right) v^4 \\
 &+ \left(\frac{710975672934795007}{10622382599271180960000000} - \frac{1142430575083613\sqrt{4790}}{1239277969914971112000000} \right) v^6 \\
 &+ \left(\frac{3731786017565356409130181}{377291733695169397198617600000000} - \frac{373072793565778149857\sqrt{4790}}{2620081483994231924990400000000} \right) v^8, \\
 \bar{A}_{2,1} &= \frac{2877}{148955} - \frac{4799\sqrt{4790}}{17874600} - \left(\frac{2023681}{5725830200} - \frac{17495041\sqrt{4790}}{3435498120000} \right) v^2 \\
 &+ \left(\frac{36177468473}{11555297926620000} - \frac{62713990079\sqrt{4790}}{1386635751194400000} \right) v^4 \\
 &- \left(\frac{2055628007863}{126910186371220800000} - \frac{224539256163841\sqrt{4790}}{959441008966429248000000} \right) v^6 \\
 &+ \left(\frac{463627866671572789}{8451875754820102983840000000} - \frac{803863978325073599\sqrt{4790}}{1014225090578412358060800000000} \right) v^8, \\
 \bar{A}_{3,2} &= \frac{1586517831}{86745135890} - \frac{4799\sqrt{4790}}{17874600} - \left(\frac{111041410223}{833620755902900} - \frac{374850995583\sqrt{4790}}{333448302361160000} \right) v^2 \\
 &+ \left(-\frac{1010573345229507}{320443818569074760000} + \frac{912680614276573\sqrt{4790}}{11535977468486691360000} \right) v^4 \\
 &- \left(\frac{24054389059591111633}{36953581157385701323200000} - \frac{378876794375477242093\sqrt{4790}}{39909867649976557429056000000} \right) v^6 \\
 &- \left(\frac{485935333951896962763298489}{4922017460825525533463094720000000} - \frac{140588309086395387940503173\sqrt{4790}}{98440349216510510669261894400000000} \right) v^8,
 \end{aligned}$$

$$\begin{aligned}
 \hat{A}_{2,1} &= \frac{1919}{19220} - \frac{6\sqrt{4790}}{4805} - \left(\frac{6441601}{2216450400} - \frac{1919\sqrt{4790}}{46176050} \right) v^2 \\
 &+ \left(\frac{22950627839}{639002650320000} - \frac{4602241\sqrt{4790}}{8875036810000} \right) v^4 \\
 &- \left(\frac{82135555848961}{343885666296211200000} - \frac{12361432319\sqrt{4790}}{3582142357252200000} \right) v^6 \\
 &+ \left(\frac{294040876575811199}{297426712779593066880000000} - \frac{35404382065921\sqrt{4790}}{2478555939829942224000000} \right) v^8, \\
 \hat{A}_{3,2} &= \frac{28631109}{793997420} + \frac{6\sqrt{4790}}{4805} - \left(\frac{24812903941}{3662551298976} - \frac{72658291\sqrt{4790}}{1907578801550} \right) v^2 \\
 &- \left(\frac{19126585411486231}{26397838487369520000} - \frac{3904934862021\sqrt{4790}}{366636645657910000} \right) v^4 \\
 &- \left(\frac{314869203983050706341}{2841252152072556176640000} - \frac{236564868394367731\sqrt{4790}}{147981882920445634200000} \right) v^6 \\
 &- \left(\frac{205505666501846260968448531}{12286994931637769185879680000000} - \frac{24742878882947640783241\sqrt{4790}}{102391624430314743215664000000} \right) v^8, \\
 \gamma_2 &= 1 + \left(\frac{6441601}{2216450400} - \frac{1919\sqrt{4790}}{46176050} \right) v^4 - \left(\frac{22950627839}{639002650320000} - \frac{4602241\sqrt{4790}}{8875036810000} \right) v^6 \\
 &+ \left(-\frac{82135555848961}{343885666296211200000} - \frac{12361432319\sqrt{4790}}{3582142357252200000} \right) v^8
 \end{aligned}$$

$$\begin{aligned}
 \gamma_3 &= 1 + \left(-\frac{3231057493}{129076762204320} - \frac{90673209\sqrt{4790}}{26890992125900} \right) v^4 \\
 &\quad - \left(-\frac{55410348606113}{8860197748453680000} + \frac{122935235569\sqrt{4790}}{8875036815168448686597980000000} \right) v^6 \\
 &\quad + \left(-\frac{3351360448784910563}{2043516008703356755200000} - \frac{746512915113451\sqrt{4790}}{29801275126923952680000} \right) v^8 \\
 \hat{\gamma}_2 &= 1 - \left(\frac{4799\sqrt{4790} - 345240}{5766(\sqrt{4790} - 120)} \right) v^2 + \left(\frac{17495041\sqrt{4790} - 1214208600}{11082252000(\sqrt{4790} - 120)} \right) v^4 \\
 &\quad - \left(\frac{62713990079\sqrt{4790} - 4341296216760}{4473018552240000(\sqrt{4790} - 120)} \right) v^6 \\
 &\quad + \left(\frac{224539256163841\sqrt{4790} - 15540547739444280}{30949709966590080000(\sqrt{4790} - 120)} \right) v^8 \\
 \hat{\gamma}_3 &= 1 + \left(\frac{4(4548889\sqrt{4790} - 1137646755)}{59549806(\sqrt{4790} + 120)} \right) v^2 + \left(\frac{644664336581\sqrt{4790} - 46082914655200}{7630315206200(\sqrt{4790} + 120)} \right) v^4 \\
 &\quad - \left(\frac{117946514812127927\sqrt{4790} - 8193004367907021360}{9239243470579332000(\sqrt{4790} + 120)} \right) v^6 \\
 &\quad + \left(\frac{12326167192820800831583\sqrt{4790} - 853303436327430405622080}{6392817342163251397440000(\sqrt{4790} + 120)} \right) v^8 \tag{40}
 \end{aligned}$$

Afterwards, the coefficients in Equation 40 are utilised to obtain parameters $b_2, b_3, b'_2, b'_3, b''_2$ and b''_3 through Taylor series expansion, yielding Equation 41.

$$\begin{aligned}
 b_2 &= \frac{31}{1440} + \frac{31\sqrt{4790}}{114960} - \left(\frac{2377\sqrt{4790}}{1496779200} + \frac{2651}{18748800} \right) v^2 + \left(\frac{12453977\sqrt{4790}}{2589128660160000} - \frac{14221}{20591539200} \right) v^4 \\
 &\quad - \left(-\frac{152021375417\sqrt{4790}}{1642180743993081600000} + \frac{184288690451}{6856704567820800000} \right) v^6 \\
 &\quad + \left(-\frac{429376762287585683\sqrt{4790}}{17233241789152677480192000000} - \frac{2048157093308653}{2616548383245804134400000} \right) v^8,
 \end{aligned}$$

$$\begin{aligned}
 b_3 = & -\frac{31}{1440} + \frac{31\sqrt{4790}}{114960} + \left(-\frac{2377\sqrt{4790}}{1496779200} + \frac{2651}{18748800} \right) v^2 \\
 & - \left(\frac{12453977\sqrt{4790}}{2589128660160000} - \frac{14221}{20591539200} \right) v^4 \\
 & - \left(\frac{152021375417\sqrt{4790}}{1642180743993081600000} + \frac{184288690451}{6856704567820800000} \right) v^6 \\
 & + \left(-\frac{429376762287585683\sqrt{4790}}{172332417891526774801920000000} - \frac{2048157093308653}{2616548383245804134400000} \right) v^8, \\
 b'_3 = & \frac{1}{12} - \frac{\sqrt{4790}}{1440} + \left(\frac{241\sqrt{4790}}{96566400} \right) v^2 + \left(-\frac{518389\sqrt{4790}}{18560062080000} + \frac{1973}{193737600} \right) v^4 \\
 & - \left(\frac{76233665681\sqrt{4790}}{105947144773747200000} - \frac{10186361}{41890912560000} \right) v^6 \\
 & + \left(-\frac{204301546417014479\sqrt{4790}}{11118220509130759664640000000} + \frac{294637773487}{47235075911654400000} \right) v^8, \\
 b''_2 = & \frac{479}{2232} - \frac{\sqrt{4790}}{59396} + \left(-\frac{351\sqrt{4790}}{1663088000} + \frac{1907}{37497600} \right) v^4 - \left(\frac{2412191\sqrt{4790}}{647282165040000} - \frac{492499}{386091360000} \right) v^6 \\
 & + \left(-\frac{3273299154193\sqrt{4790}}{32843614879861632000000} + \frac{977694255779}{27426818271283200000} \right) v^8, \\
 b''_3 = & \frac{479}{2232} + \frac{\sqrt{4790}}{59396} + \left(\frac{351\sqrt{4790}}{1663088000} + \frac{1907}{37497600} \right) v^4 - \left(-\frac{2412191\sqrt{4790}}{647282165040000} - \frac{492499}{386091360000} \right) v^6 \\
 & + \left(\frac{3273299154193\sqrt{4790}}{32843614879861632000000} + \frac{977694255779}{27426818271283200000} \right) v^8, \tag{41}
 \end{aligned}$$

where $\gamma_i, \hat{\gamma}_i = 1$.

As $v \rightarrow 0$, the coefficients $b_i, b'_i, b''_i, A_{i,j}, \bar{A}_{i,j}, \hat{A}_{i,j}, \gamma_i$ and $\hat{\gamma}_i$ of the proposed methods will return to the coefficients of the original form. It means that both EFIRKT6 and TFIRKT6 methods have the same error constant as the three-stage, sixth-order improved TDRKT method.

Error Analysis of EFIRKT6 and TFIRKT6 Methods

Local truncation errors (*LTE*) for $u(t), u'(t)$ and $u''(t)$ for EFIRKT6 and TFIRKT6 methods are analysed in this part. Here, Taylor series expansion is applied over the step

size, h , for the exact solution, $u(t_n + h)$ and its derivatives, $u'(t_n + h)$ and $u''(t_n + h)$. Then, we get local truncation errors of u, u' and u'' as Equation 42:

$$\tau_{n+1}^{(m)} = u_{n+1}^{(m)} - u^{(m)}(t_n + h), \quad m = 0, 1, 2. \tag{42}$$

where u_{n+1}, u'_{n+1} and u''_{n+1} are the approximation solutions for u, u' and u'' .

Both EFIRKT6 and TFIRKT6 methods contain algebraic order p if $LTE = u_{n+1} - u(t_n + h) = u'_{n+1} - u'(t_n + h) = u''_{n+1} - u''(t_n + h) = \mathcal{O}(h^{p+1})$ and $\mathcal{O}(h^q) = 0, q = 1, \dots, p$. *LTE* of $u(t), u'(t)$ and $u''(t)$ of proposed methods are shown as in Equations 43 to 45:

$$\begin{aligned}
 LTE(u) = & -\frac{11}{2520}h^7(g_{u,u,u}u'^3 + 3g_{u,u,u'}u'^2u'' + 3g_{u,u}u'u'' + 3g_{u,u'}u'u''^2u' \\
 & + 3g_{u,u'}u'f + 3g_{u,u'}u''^2 + g_{u,f} + g_{u',u',u'}u''^3 + 3g_{u',u'}u''f + g_{u',g}) + \mathcal{O}(h^8)
 \end{aligned} \tag{43}$$

$$\begin{aligned}
 LTE(u') = & \frac{11}{3360}h^7(12g_{u,u',u'}u'u''f + g_{u',u',u',u'}u''^4 + 3g_{u',u'}u''f^2 + g_{u,g} \\
 & + g_{u,u,u,u}u'^4 + 3g_{u,u}u''^2 + 6g_{u,u',u'}u''^2 + g_{u'}(g_uu' + g_{u'}u'') \\
 & + 4u'^3g_{u,u,u,u}u'' + 6u'^2g_{u,u,u}u'' + 6u'^2g_{u,u,u,u'}u''^2 + 6u'^2g_{u,u,u}f \\
 & + 12u'g_{u,u,u'}u''^2 + 4u'g_{u,u,f} + 4u'g_{u,u',u'}u''^3 + 4u'g_{u,u'}g \\
 & + 10u''g_{u,u'}f + 6u''^2g_{u',u',u'}f + 4u''g_{u',u'}g + \mathcal{O}(h^8)
 \end{aligned} \tag{44}$$

$$\begin{aligned}
 LTE(u'') = & \frac{1}{5040}h^7(30u'^2u''g_{u,u,u',u'}f + 30u'u''^2g_{u,u',u',u'}f + 20u'u''g_{u,u',u'}g \\
 & + 50u'u''g_{u,u,u}f + 10g_{u',u'}g + 10u'^3g_{u,u,u,u}f + 10u'^2g_{u,u,u}f \\
 & + 10u'^2g_{u,u,u}g + 15u'g_{u,u',u'}f^2 + 5u'g_{u,u,g} + 10g_{u,u'}f^2 + g_{u,u,u,u,u}u'^5 \\
 & + g_{u',u',u',u'}u''^5 + 15g_{u,u,u}u''^3 + 10g_{u,u',u',u'}u''^4 + 10u'^3g_{u,u,u,u}u'' \\
 & + g_{u'}(g_{u,u}u'^2 + 2u'g_{u,u'}u'' + g_{u,u''} + g_{u',u'}u''^2 + g_{u',f}) \\
 & + g_u(g_uu' + g_{u'}u'') + 10g_{u,u,u,u'}u''^2 + 30u'^2g_{u,u,u,u}u''^2 \\
 & + 10u'^2g_{u,u,u',u'}u''^3 + 15u'g_{u,u,u}u''^2 + 30u'g_{u,u,u',u'}u''^3 \\
 & + 5u'g_{u,u',u',u'}u''^4 + 5u'g_{u,u'}(g_uu' + g_{u'}u'') + 10u''g_{u,u}f \\
 & + 40u''^2g_{u,u',u'}f + 15u''g_{u,u'}g + 10u''^3g_{u',u',u',u'}f + 10u''^2g_{u',u',u'}g \\
 & + 15u''g_{u',u',u'}f^2 + 5u''g_{u',u'}g_{u,u'} + g_{u',u''} + 5u''^4g_{u,u,u,u,u}u'') + \mathcal{O}(h^8)
 \end{aligned} \tag{45}$$

The order for both EFIRKT6 and TFIRKT6 methods is six since the entire coefficients are up to $h^6 = 0$. Thus, $LTE = \mathcal{O}(h^{p+1}) = \mathcal{O}(h^7)$. By comparison, $p = 6$.

RESULT AND DISCUSSION

EFIRKT6 and TFIRKT6 methods solve $u'''(t) = f(t, u(t), u'(t))$ with exponential or oscillatory solutions and application problems. Problems 1 to 4 are third-order exponential problems, while problems 5 to 7 are third-order trigonometrical problems. The proposed method was also used to test the efficiency in solving the application problem, thin-film flow, in problem 8. The proficiency of EFIRKT6 and TFIRKT6 methods are demonstrated as they are contrasted with the classic Runge-Kutta method and Runge-Kutta direct methods with exponentially-fitted and trigonometrically-fitted techniques. The selected comparative methods contain fitting techniques or have similar order to the proposed methods.

The selected methods as below are compared numerically:

- EFIRKT6: Three-stage sixth-order explicit improved TDRKT method with exponentially-fitting technique.
- TFIRKT6: Three-stage sixth-order explicit improved TDRKT method with trigonometrically-fitting technique.
- EFTDRKT6: Exponentially-fitted explicit TDRKT method with three stages sixth-order, the exponential technique is implemented into the method constructed by Lee et al. (2020)
- TFTDRKT6: Trigonometrically fitted explicit TDRKT method with three stages sixth-order, the trigonometrical technique is implemented into the method constructed by Lee et al. (2020)
- RK6S: Explicit RK method with seven-stage sixth order developed by Al-Shimmary (2017)
- EFRKT5: Four-stage fifth-order exponential-fitted explicit Runge-Kutta type method developed by Ghawadri et al. (2018)
- TFRKT5: Trigonometrically-fitted explicit Runge-Kutta-type method with four stages fifth order, developed by Ghawadri et al. (2018)
- ATDRKT6: Trigonometrically-fitted explicit two-derivative Runge-Kutta method with four stages sixth order, developed by Ahmad et al. (2019)

Problem 1 (Exponential problem)

$$u''' = 2u'(t),$$

$$u(0) = 0, u'(0) = 1, u''(0) = 0, \quad t \in [0, 5],$$

whose analytic solution is $u(t) = \frac{\sqrt{2}e^{\sqrt{2}t}}{4} - \frac{\sqrt{2}e^{-\sqrt{2}t}}{4}$.

Problem 2 (Exponential problem)

$$u''' = 5u'(t) + \sinh(t),$$

$$u(0) = -\frac{1}{4}, u'(0) = 0, u''(0) = \frac{1}{4}, \quad t \in [0,5],$$

whose analytic solution is $u(t) = -\frac{e^t}{8} - \frac{e^{-t}}{8}$.

Problem 3 (Exponential problem)

$$u_1''' = 8u_3', u_2''' = 8u_1', u_3''' = u_2',$$

$$u_1(0) = 2, u_1' = 4, u_1'' = 8,$$

$$u_2(0) = 4, u_2' = 8, u_2'' = 16,$$

$$u_3(0) = 1, u_3' = 2, u_3'' = 4,$$

whose analytic solution is $u_1(t) = 2e^{2t}, u_2(t) = 4e^{2t}, u_3(t) = e^{2t}, \quad t \in [0,5]$.

Problem 4 (Exponential problem)

$$u_1''' = u_3' + 1, u_2''' = u_1' + 2, u_3''' = u_2' + 3,$$

$$u_1(0) = 2, u_1' = 3, u_1'' = 5,$$

$$u_2(0) = 1, u_2' = 2, u_2'' = 5,$$

$$u_3(0) = 0, u_3' = 4, u_3'' = 5,$$

whose analytic solution is $u_1(t) = 5e^t - 2t - 3, u_2(t) = 5e^t - 3t - 4, u_3(t) = 5e^t - t - 5, \quad t \in [0,5]$.

Problem 5 (Trigonometrical problem)

$$u''' = -27u'(t),$$

$$u(0) = 1, u'(0) = 3\sqrt{3}, u''(0) = -27, \quad t \in [0,10000],$$

whose analytic solution is $u(t) = \cos(3\sqrt{3}t) + \sin(3\sqrt{3}t)$.

Problem 6 (Trigonometrical problem)

$$u''' = -100 u'(t) + 99 \cos(t),$$

$$u(0) = 1, u'(0) = 11, u''(0) = -100, \quad t \in [0, 10000],$$

whose analytic solution is $u(t) = \cos(10t) + \sin(10t) + \sin(t)$.

Problem 7 (Trigonometrical problem)

$$u_1''' = 2u_1' + 6u_2', \quad u_2''' = -2u_1' - 5u_2',$$

$$u_1(0) = 2, u_1'(0) = 0, u_1''(0) = -2,$$

$$u_2(0) = -1, u_2'(0) = 0, u_2''(0) = 1,$$

whose analytic solution is $u_1(t) = 2 \cos(t), u_2(t) = -\cos(t), t \in [0, 10000]$.

Problem 8 (Application problem)

Application Problem of Third-Order ODEs-Thin Film Flow

We consider the famous fluid dynamic and engineering problem, the thin film flow of fluid transporting over the solid surface. Usually, thin film flow simulates thermal and mass transfer, gravity and centrifugal force (Kumar & Singh, 2012). According to Duffy and Wilson (1997), thin film flow can describe the dynamic balance between surface tension and viscous force in the thin film layer without gravity. Recently, various direct methods have been developed to solve particular problems (Ghawadri et al., 2018; Lee et al., 2020; Jikantoro et al., 2018; Haweel et al., 2018). The thin film flow problem can be represented by Equation 46:

$$u''' = f(u(t)), \tag{46}$$

where

$u(t)$ implies the cartesian coordinate system in flowing fluid, and we express $f(u(t))$ in various terms:

$$f(u) = -1 + u^{-2},$$

$$f(u) = -1 + (1 + \gamma + \gamma^2)u^{-2} - (\gamma + \gamma^2)u^{-3},$$

$$f(u) = u^{-2} - u^{-3},$$

$$f(u) = u^{-2}.$$

Here, we focus on solving the nonlinear thin film flow problem, which is utilised to demonstrate the fluid-depleting problem on a torrid surface as Equation 47.

$$u''' = u^{-2} - u^{-3}, u(0) = 1, u'(0) = 1, u''(0) = 0 \tag{47}$$

The numerical curve of thin film flow is demonstrated in Figure 1 to exhibit the thin film flow model.

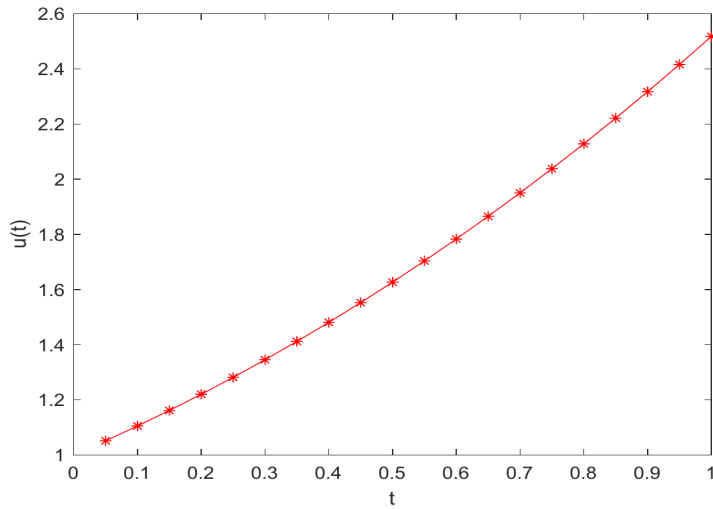


Figure 1. Numerical solution curves for thin film flow

For comparison purposes, the classical order 4 Runge-Kutta method with tremendously low step size, $h = 10^{-6}$ is used to compare the selected methods for obtaining numerical approximation due to the absence of an exact solution in a thin film flow problem. Figure 1 exhibits the numerical results of the Runge-Kutta method with step size $h = 10^{-6}$ in solving problem 8.

Figures 2 to 9 exhibit the performance of selected methods numerically measured through the maximum global truncation error against computational time.

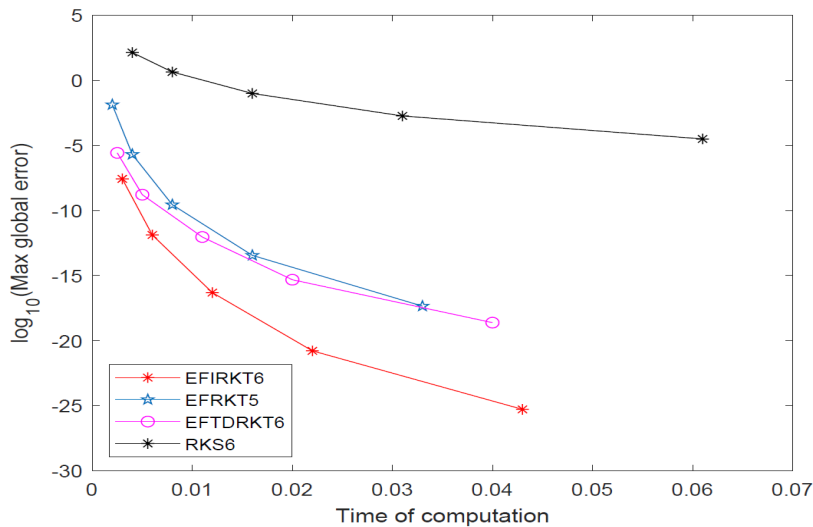


Figure 2. Numerical curves of selected methods of problem 1 with $h = \frac{0.5}{2^i}, i = 0, \dots, 4$.

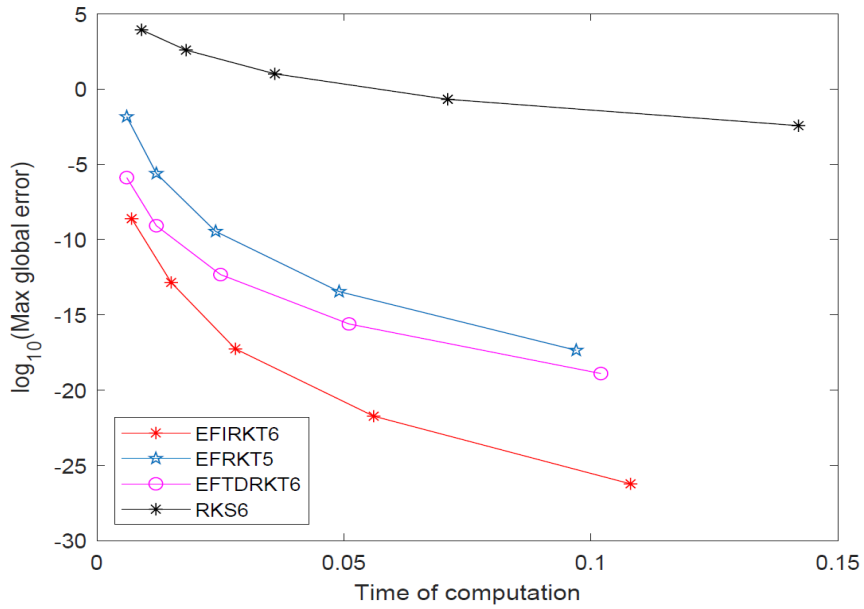


Figure 3. Numerical curves of selected methods of problem 2 with $h = \frac{0.5}{2^i}, i = 0, \dots, 4$.

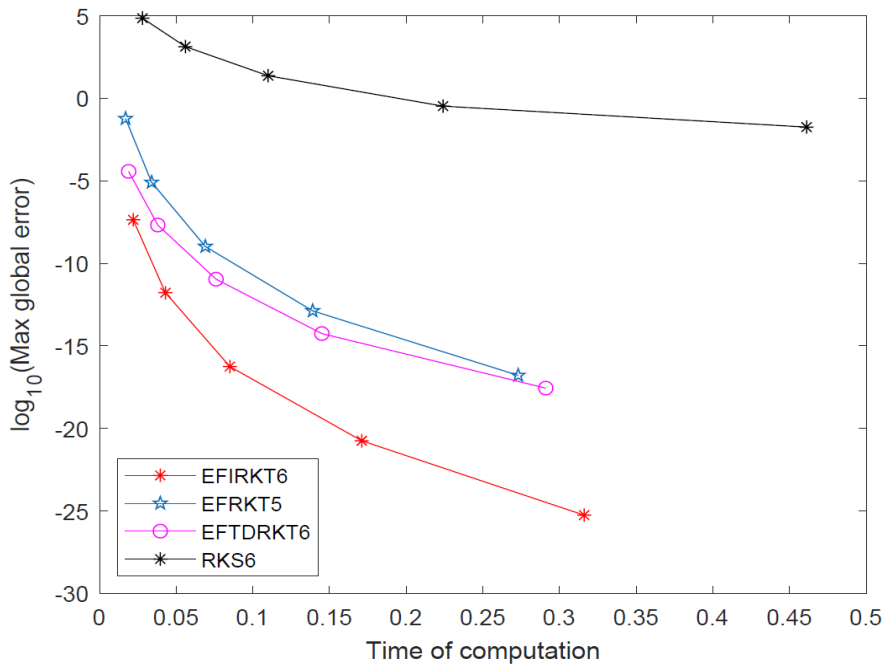


Figure 4. Numerical curves of selected methods of problem 3 with $h = \frac{0.2}{2^i}, i = 0, \dots, 4$.

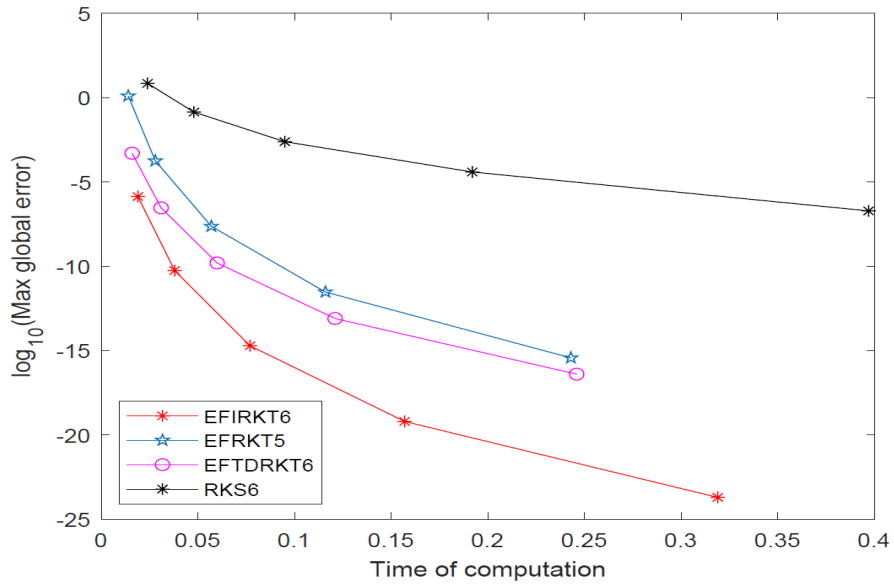


Figure 5. Numerical curves of selected methods of problem 4 with $h = \frac{0.5}{2^i}, i = 0, \dots, 4$.

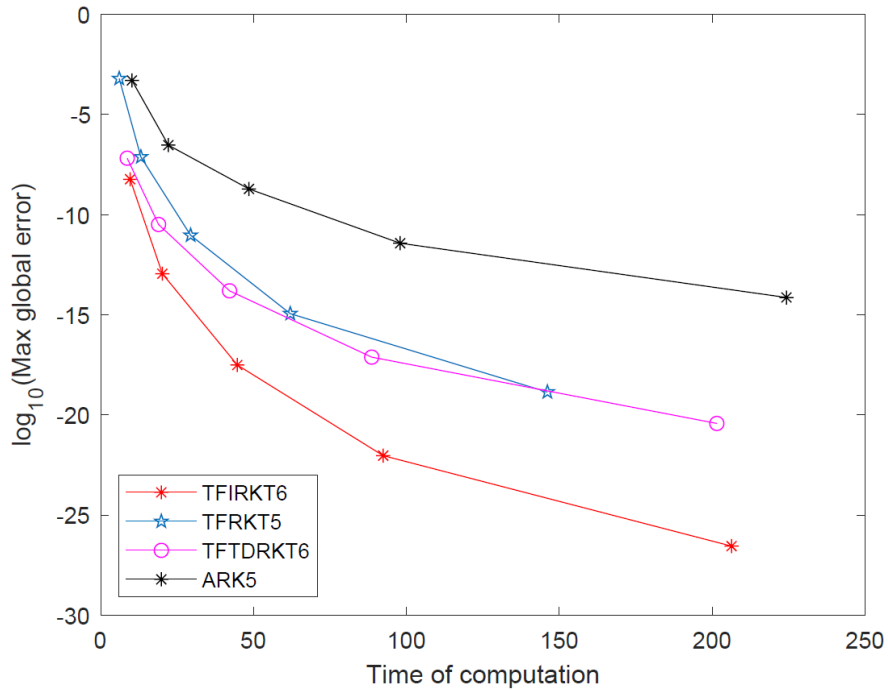


Figure 6. Numerical curves of selected methods of problem 5 with $h = \frac{0.5}{2^i}, i = 0, \dots, 4$.

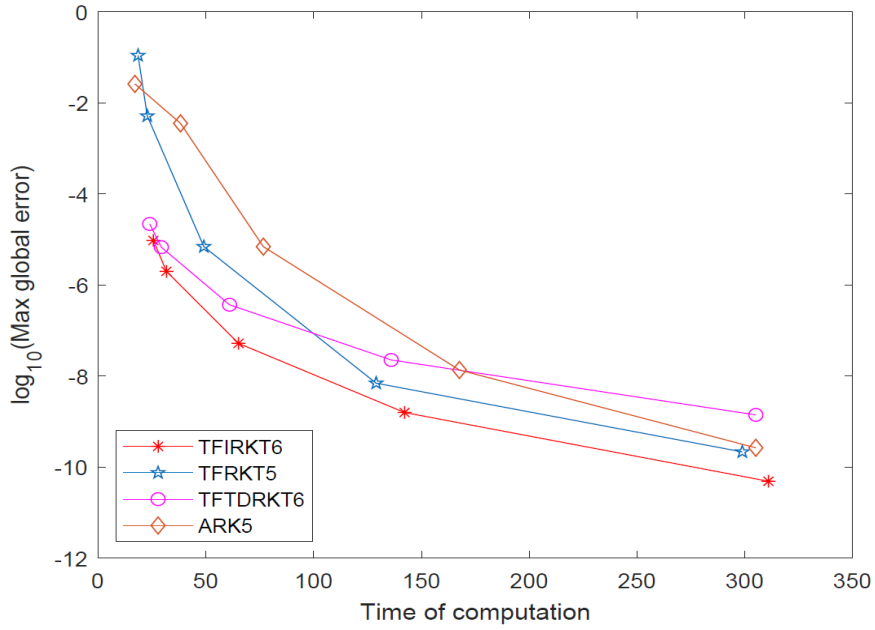


Figure 7. Numerical curves of selected methods of problem 6 with $h = 0.25, 0.2, 0.1, 0.05, 0.025$

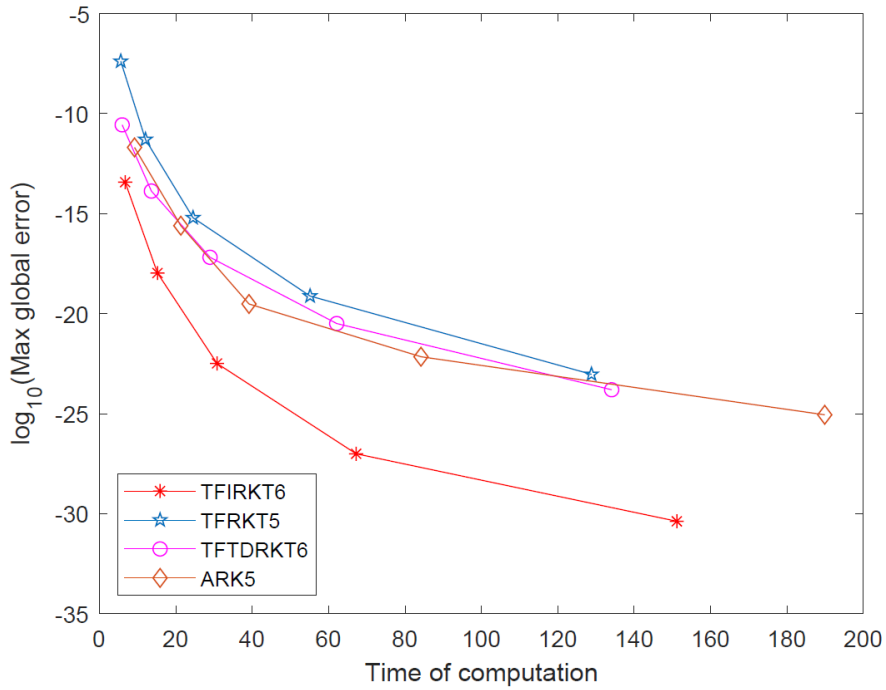


Figure 8. Numerical curves of selected methods of problem 7 with $h = \frac{0.4}{2^i}, i = 0, \dots, 4$.

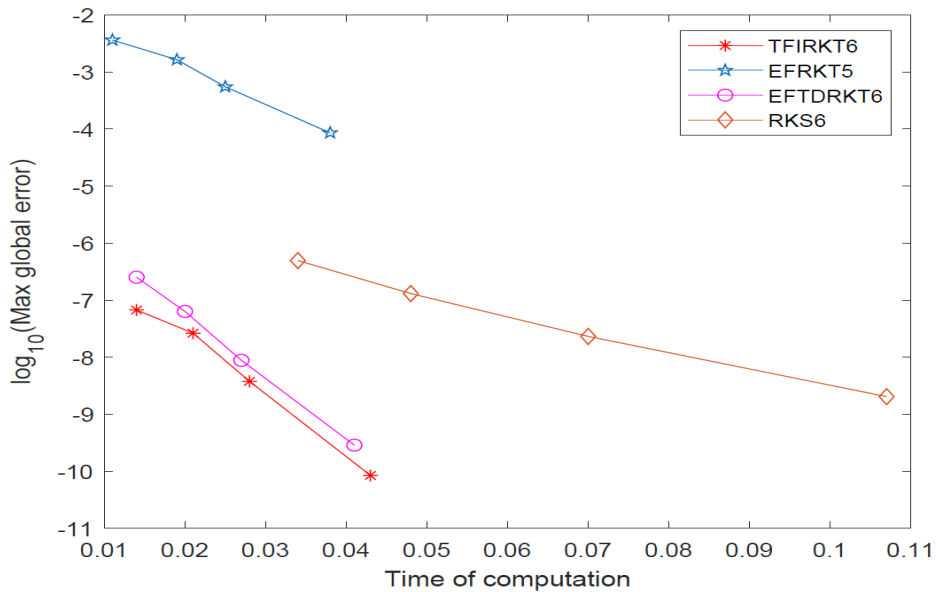


Figure 9. Numerical curves of selected methods of a thin film flow problem

The proposed methods, TDRKT methods fitting techniques are used to contrast with other existing numerical methods in solving third-order ordinary initial value problems with exponential and trigonometrical solutions based on a maximum global error against computation time. The numerical results are plotted in Figures 2 to 9. The numerical approach solves the selected problems by taking step size with smaller values for subsequent approximation and comparing the solutions to illustrate the convergence performance and accuracy curves obtained by all selected methods. Global errors obtained by all methods are getting lesser when the step size becomes smaller. It is because the local truncation error in approximating the numerical problem is reduced when the step size becomes smaller and causes the accuracy for the next approximation to become higher. Improved Runge-Kutta comprises the previous step in the function evaluation, which highly improves the method's accuracy. Hence, the results in Figures 2 to 5 clearly show that the EFIRKT6 method outperforms EFTDRKT6, RKS6 and EFRKT5 methods for solving exponential third-order ODEs by yielding the lowest maximum global error in similar time computation with the same step size. RKS6 acquires a higher number of function evaluations because it requires converting higher-order differential equations into three first-order differential equations and solving them subsequently. Meanwhile, the complexity of function evaluation of the RK6 method is the least compared to the other three selected methods, causing the computation time is not too large comparatively. The complexity of each function evaluation for EFIRKT6 methods is higher than other existing methods because of the inclusion of derivative of f -evaluation; however, due to the advantage of a low number of function

evaluations and the extremely low global error, EFIRKT6 method is the best-performed method among the selected methods by generating the least maximum global error with similar computational time.

In addition, the TFIRKT6 method performs better than TFTDRKT6, ARK6 and TFRKT5 methods by obtaining the least maximum global error in integrating third-order ODEs with the oscillatory solution shown in Figures 6 to 8. The numerical curves are displayed in Figures 6 to 8 as the logarithms of maximum global errors are plotted against the computational time in seconds. Maximum global error obtained by all selected methods reduces readily as the step size becomes lower due to the convergence property acquired by all methods. Even though the complexity of the function for the TFIRKT6 method is higher compared to other methods, the number of function evaluations is one of the lowest in all selected methods, leading to low computation time. Improved Runge-Kutta-type methods collocate with the fitting technique have the largest advantage in accuracy compared to other methods due to the inclusion of a few previous steps in approximating the next term. In dealing with third-order application problems, the EFIRKT6 method is more proficient than the selected existing methods in solving thin film flow problems by generating the least maximum global error for all step sizes compared to existing methods.

CONCLUSION

In this article, we combined two-derivative Runge-Kutta-type methods with exponentially and trigonometrically-fitting techniques by developing exponentially-fitted and trigonometrically-fitted explicit improved two-derivative Runge-Kutta type methods with three-stage sixth-order denoted as EFIRKT6 and TFIRKT6 methods respectively. This article contributes to constructing improved two-derivative Runge-Kutta-type methods. It demonstrates how to adopt exponentially-fitting and trigonometrically-fitting techniques on the proposed methods to solve third-order periodic and exponential third-order ODEs with a much lower time of computation. The formulation comprises the previous step, b_{-i} , which vastly improves the accuracy of the existing two-derivative Runge-Kutta-type methods. Third and multiple fourth derivatives are formulated into the proposed methods to solve third-order ODEs in $u'''(t) = f(t, u(t), u'(t))$ with exponential or oscillatory solutions. The order conditions of generally improved two-derivative Runge-Kutta-type methods are proposed. Then exponential and trigonometrical techniques are implemented to construct frequency-reliant coefficients which integrate exactly suitable exponential and trigonometrical polynomials with exponential and periodic types.

Numerical tests prove the efficacy of EFIRKT6 and TFIRKT6 methods in solving third-order ODEs with exponential and trigonometrical solutions by generating the least maximum global error and low time of computation in similar step sizes when compared with other sixth-order existing methods. Through this research, a few topics can be explored.

EFIRKT6 and TFIRKT6 methods can be modified to solve and delay differential equations in the form of $u'''(t) = f(t, u(t), u(t - \tau), u'(t), u'(t - \tau))$ with the exponential and oscillatory solution. Also, the symmetric and symplectic properties can be adapted into exponentially-fitted and trigonometrically-fitted improved TDRKT methods to form modified methods with zero-dissipative and algebraically stable. Characterisations of symmetric and symplectic can be analysed, and numerical efficiency can be proved by solving oscillatory Hamiltonian systems effectively.

ACKNOWLEDGEMENT

The authors gratefully acknowledge the financial support from Universiti Putra Malaysia (UPM) under the Putra-IPB grant: GP-IPB/2017/9542402.

REFERENCE

- Ahmad, N. A., Senu, N., & Ibrahim, Z. B., Othman, M., & Ismail, Z. (2020). High order three derivative runge-kutta method with phase-fitting and amplification-fitting technique for periodic IVPs. *Malaysian Journal of Mathematical Sciences*, 14(3), 403-418.
- Ahmad, N. A., Senu, N., & Ismail, F. (2019). Trigonometrically-fitted higher order two derivative runge-kutta method for solving orbital and related periodical IVPs. *Hacetatepe Journal of Mathematics and Statistics*, 48(5), 1312-1323. <https://doi.org/10.15672/HJMS.2018.568>
- Allogmany, R., & Ismail, F. (2020). Implicit three-point block numerical algorithm for solving third order initial value problem directly with applications. *Mathematics*, 8(10), Article 1771. <https://doi.org/10.3390/math8101771>
- Al-Shimmary, A. F. A. (2017). Solving initial value problem using runge-kutta 6-th order method. *ARPN Journal of Engineering and Applied Sciences*, 12(13), 3953-3961.
- Chen, Z., Li, J., Zhang, R., & You, X. (2015). Exponentially fitted two-derivative runge-kutta methods for simulation of oscillatory genetic regulatory systems. *Computational and Mathematical Methods in Medicine*, 2015, 1-14. <https://doi.org/10.1155/2015/689137>
- D'Ambrosio, R., Paternoster, B., & Santomauro, G. (2014). Revised exponentially-fitted runge-kutta-nyström methods. *Applied Mathematics Letters*, 30, 56-60. <https://doi.org/10.1016/j.aml.2013.10.013>
- Demba, M. A., Kumam, P., Watthayu, W., & Ismail, F. (2020). Embedded exponentially-fitted explicit runge-kutta-nyström method for solving periodic problems. *Computation*, 8(2), 165-178. <http://www.ijpam.eu> doi: 10.12732/ijpam.v11i12.3
- Demba, M. A., Senu, N., & Ismail, F. (2016). A four-stage third-order symplectic explicit trigonometrically-fitted Runge-Kutta-Nyström method for the numerical integration of oscillatory initial-value problems. *International Journal of Pure and Applied Mathematics*, 111(2), 165-178.
- Duffy, B. R., & Wilson, S. K. (1997). A third-order differential equation arising in thin-film flows and relevant to tanner's law. *Applied Mathematics Letters*, 10(3), 63-68. [https://doi.org/10.1016/S0893-9659\(97\)00036-0](https://doi.org/10.1016/S0893-9659(97)00036-0)

- Franco, J. M., & Randez, L. (2018). An eighth-order exponentially fitted two-step hybrid method of explicit type for solving orbital and oscillatory problems. *Numerical Algorithms*, 78(1), 243-262. <https://doi.org/10.1007/s11075-017-0374-1>
- Ghawadri, N., Senu, S., Ismail, F., & Ibrahim, Z. B. (2018). Exponentially fitted and trigonometrically fitted explicit modified runge-kutta type methods for solving $y''' = f(x, y, y')$. *Journal of Applied Mathematics*, 2018, Article 4029371. <https://doi.org/10.1155/2018/4029371>
- Haweel, M. T, Zahran, O., & El-Samie, F. E. A. (2018). Adaptive polynomial method for solving third-order ODE with application in thin film flow. *IEEE Access*, 9, 67874-67889.
- Herrera, L. (2019). Causal heat conduction contravening the fading memory paradigm. *Entropy*, 21(10), Article 950. <https://doi.org/10.3390/e21100950>
- Hussain, K., Ismail, F., & Senu, N. (2017). Fourth-order improved runge-kutta method for directly solving special third-order ordinary differential equations. *Iranian Journal of Science and Technology, Transaction A: Science*, 41, 429-437. <https://doi.org/10.1007/s40995-017-0258-1>
- Jikantoro, Y. D., Ismail, F., Senu, N., & Ibrahim, Z. B. (2018). A new integrator for special third order differential equations with application to thin film flow problem. *Indian Journal of Pure and Applied Mathematics*, 49, 151-167. <https://doi.org/10.1007/s13226-018-0259-6>
- Kumar, M., & Singh, N. (2012). Phase plane analysis and traveling wave solution of third order nonlinear singular problems arising in thin film evolution. *Computers & Mathematics with Application*, 64(9), 2886-2895. <https://doi.org/10.1016/j.camwa.2012.05.003>
- Lazer, A. C. (1966). The behavior of solutions of the differential equation $y''' + p(x)y' + q(x)y = 0$. *Pacific Journal of Mathematics*, 17(3), 435-466.
- Lee, K. C., Senu, N., Ahmadian, A., & Ibrahim, S. N. I. (2020). Numerical study of third-order ordinary differential equations using a new class of two derivative Runge-Kutta type methods. *Alexandria Engineering Journal*, 59(4), 2449-2467. <https://doi.org/10.1016/j.aej.2020.03.008>
- Mei, L., Liu, C., & Wu, X. (2017). An essential extension of the finite-energy condition for extended runge-kutta-nyström integrators when applied to nonlinear wave equations. *Communications in Computational Physics*, 22(3), 742-764. <https://doi.org/10.4208/cicp.OA-2016-0141>
- Monovasilis, T., & Kalogiratou, Z. (2021). High order two-derivative runge-kutta methods with optimized dispersion and dissipation error. *Mathematics*, 9(3), Article 232. <https://doi.org/10.3390/math9030232>
- Rabiei, F. (2011). Third-order improved runge-kutta method for solving ordinary differential equation. *International Journal of Applied Physics and Mathematics*, 1(3), 191-194. <http://doi.org/10.7763/IJAPM.2011.V1.37>
- Rabiei, F., & Ismail, F. (2012). Fifth-order improved runge-kutta method with reduced number of function evaluations. *Australian Journal of Basic and Applied Sciences*, 6(3), 97-105.
- Samat, F., & Ismail, E. S. (2020). Variable step exponentially fitted explicit sixth-order hybrid method with four stages for spring-mass and other oscillatory problems. *Symmetry*, 12(3), Article 387. <https://doi.org/10.3390/sym12030387>

- Senthilkumar, S., Lee, M., & Jeong, G. (2013). A modified improved runge-kutta fifth stage technique to study industrial robot arm. *International Journal of Pattern Recognition and Artificial Intelligence*, 27(6), 1359004. <https://doi.org/10.1142/S0218001413590040>
- Simos, T. E., & Williams, P. S. (1999). Exponential-fitted runge-kutta third algebraic order methods for the numerical solution of the schrödinger equation and related problems. *International Journal of Modern Physics C*, 10(5), 839-851. <https://doi.org/10.1142/S0129183199000656>
- Tang, X., & Xiao, A. (2020). Improved runge-kutta-chebyshev methods. *Mathematics and Computers in Simulation*, 174, 59-75. <https://doi.org/10.1016/j.matcom.2020.02.021>
- Zhai, H. Y., Zhai, W. J., & Chen, B. Z. (2018). A class of implicit symmetric symplectic and exponentially fitted Runge–Kutta–Nyström methods for solving oscillatory problems. *Journal of Inequalities and Applications*, 2018, Article 321. <https://doi.org/10.1186/s13660-018-1915-4>
- Zhang, Y., Che, H., Fang, Y., & You, X. (2013). A new trigonometrically fitted two-derivative runge-kutta method for the numerical solution of the schrödinger equation and related problems. *Journal of Applied Mathematics*, 2013, Article 937858. <http://dx.doi.org/10.1155/2013/937858>

An Optimum Classifier Model with Fuzzy C-Means for Fire Detection Technology

Elaiyaraja Gandhi^{1*} and Kumaratharan Narayanaswamy²

¹Department of Electronics and Communication Engineering, VEMU Institute of Technology, P. Kothakota, Chittoor, PIN-517112, Andhra Pradesh, India

²Department of Electronics and Communication Engineering, Sri Venkateswara College of Engineering, Sriperumbudur, PIN-602117, Tamilnadu, India

ABSTRACT

Flames recognition methodology is most important for completely diminishing the flame losses in different fired environmental conditions. However, there is delayed detection and lower accuracy in the various common detection methods. Thus, optimum image/video fire detection technology is proposed in this paper based on a support vector machine (SVM) with the fuzzy c-mean, discrete wavelet transform (DWT), and gray level co-occurrence matrices (GLCM) feature extraction for the detection of fires. This algorithm has been tested on various fire and non-fire images for classification accuracy. A performance evaluation of the proposed classifier algorithm and existing algorithms is compared, showing that the accuracy and other metrics of the proposed classifier algorithm are higher than other algorithms. Furthermore, simulation results show that the proposed classifier model is improved the forecast detection accuracy of fires.

Keywords: Discrete wavelet transform, feature extraction, fuzzy c-means algorithm, SVM classifier

ARTICLE INFO

Article history:

Received: 20 February 2022

Accepted: 31 May 2022

Published: 06 March 2023

DOI: <https://doi.org/10.47836/pjst.31.2.11>

E-mail addresses:

elaiyarg@gmail.com (Elaiyaraja Gandhi)

kumaratharan@svce.ac.in (Kumaratharan Narayanaswamy)

*Corresponding author

INTRODUCTION

Fire detection methods are among the most significant components in surveillance systems that observe buildings and the environment. As part of early warning systems, it is preferable that the system can report the earliest stage of a fire/smoke. Almost all fire/smoke detection systems currently use built-in sensors that depend mainly on the consistency and positional

distribution of the sensors. It is necessary that these sensors are distributed densely for a high-precision fire/smoke detection system. In a sensor-based fire/smoke detection system for an outdoor atmosphere, coverage of large areas is not practical due to the requirement of a regular distribution of sensors in closeness. For many years, fire accidents occurred in some locations, including buildings, forests, agriculture, hospitals, aviation, aerospace, and industries. It causes vast losses to all communities and also human life. In order to save production losses and protect against early fire detection, technology is necessary to provide prior information and control the fire in many locations. However, conventional fire detection technologies are unsuitable for large spaces and complex buildings. In preceding fire detection techniques, untrue alarms, missed detections, delays of detection, and other tiny tribulations will arise. To overcome the issues in the previous methods in this paper used optimum deep learning classifier model which is explained in materials and methods section in detail. The objective of proposed model to improve the competency of early fire detection.

Related Works

Many researchers introduced various image fire detection techniques for early effective fire detection to determine the fire hazard from the images/videos. Coppo (2015) proposed an end-to-end fire detection technique by infrared imagers from geostationary satellites for real-time early warning and monitoring. In this method, Metro Second Generation (MSG) SEVIRI and Meteosat Third Generation (MTG) Flexible Combined Imager (FCI) characteristics were simulated. This fire-detection model evaluates the maximum and minimum fire-detectable active region and temperature. This method provides analytical results for MSG-SEVIRI and MTG-FCI characteristics, as a consequence, in agreement with literature statistics information. This model can be helpful for early fire detection compared to existing methods from new satellite infrared imagers. The drawback of this system is inaccurate when the system is unaffordable and complex.

Zhang et al. (2018) proposed a wild-land forest fire smoke detection using a faster RCNN to keep away from the complex manual features extraction method in conventional smoke detection techniques. In this scheme, by adding smoke and simulative smoke, synthetic smoke images are produced into the background of forest images to solve the need for training data and eliminate the work of sample labeling. The two synthetic images are trained and tested in the dataset. The simulation results for simulative smoke are the superior choices in the aspect of a detection rate, and this model is not sensitive to thin-smoke images. Further, this algorithm's performance may be tested on video frames or forest fire smoke images.

Singh et al. (2018) presented an effective image retrieval algorithm and a nonlinear SVM classifier. First, the Color-Histogram (C-H), Color-Difference Histogram (C-DH), and Orthogonal Combination-Local Binary Patterns (OC-LBP) features are combined. Then the

performances of the three descriptors are analyzed, combined, and individually. Detailed simulation results reveal that the C-H+C-DH+OC-LBP combined algorithm achieved the highest flame detection rate. Also, the nonlinear SVM classifier is more effective than linear SVM and RBF kernels. Moreover, this combined algorithm provides good accuracy for all training datasets using pre-computed square-chord kernel values.

Hou et al. (2019) demonstrated an anomaly fire-detection algorithm for Internet-of-Thing (IoT) applications working environment based on deep learning from fire-smoke detection and video/image personnel detection. The results of fire/smoke detection and multi-stream Convolution Neural Network (ms-CNN) based vision monitoring video/image personnel detection algorithms have excellent detection compared to other methods. However, the drawbacks of this system are multiple gestures visible in the detected image due to people's movement and the difficulty of abnormal detection due to the uncertainty of fire-smoke increases (Scholkopf & Smola, 2018; Schölkopf et al., 2001).

Peng et al. (2019) proposed a video/image smoke-detection algorithm with a deep learning model and effective hand-designed features. In this algorithm, the initially suspected smoke area is extracted using a manual design approach, and then images are classified using an optimized SqueezeNet network (Elaiyaraja et al., 2015; Elaiyaraja et al., 2022). This method achieves quick and accurate smoke detection through real-time monitoring of the forest smoke environment.

Li et al. (2020) demonstrated CNN-based object detection algorithms such as R-FCN, Faster-RCNN, YOLO v3, and SSD for image/video fire detection algorithms. A comparison of various objection detection techniques illustrates that object-detection CNNs algorithms achieve higher performance than other fire detection methods. Particularly, the average precision of the YOLO v3 algorithm is higher than the other algorithms; the detection speed reaches 28 frames per second (FPS) and also has the strongest robustness (Cristianini & Shawe-Taylor, 2000; Dunning & Breckon, 2018).

Muhammad et al. (2018) proposed an early image/video fire detection framework with fine CNN for effective disaster management. The dynamic channel selection algorithm is implemented in this method for cameras based on cognitive radio networks (CRNs), ensuring reliable data broadcasting. This fire detection scheme provides higher accuracy (94.39%) than state-of-the-art methods. Moreover, this algorithm improves the accuracy value of fire detection with minimum false alarms Escalera et al., 2009; Esfahlani, 2019; Fan et al., 2005; Filizzola et al., 2016; Fürnkranz, 2002).

Fire-detection methodology based on video frames can avoid many errors in traditional algorithms and detect fires. The Rough Set (RS) theory with an SVM classifier is introduced to detect fires and gives fire alert warnings (Huang et al., 2020). RS is used in this method as the front-end system yields improved performance. In addition, the recognition efficiency is improved, and the recognition time is reduced in this algorithm. The experimental result

reveals that the RS-SVM optimum classifier algorithm yields a fast recognition speed, higher recognition rate, a wide range of applications, and excellent robustness (Garcia-Jimenez et al., 2017; Genovese et al., 2011; Gottuk et al., 2006).

Seydi et al. (2022) proposed Fire-Net (deep-CNN) to detect active forest fires in different area. This method provides higher accuracy and sensitivity compared to other common machine learning algorithms. But due to level of active fires in small region, this algorithm could not detect active fires (Hackner et al., 2016; Hastie et al., 2009; Jia et al., 2016; Kapil et al., 2016; Kecman et al., 2005; Koltunov et al., 2016).

Many authors are proposed several of machine and deep learning-based algorithm along with suitable technique such as feature extraction, segmentation etc. for image/video fire detection. All existing algorithms have less accuracy, low miss detection rate for small regions (Sharma et al., 2017; Ansari & Ghrera, 2017; Ansari & Ghrera, 2018; Ansari et al., 2016; Ansari et al., 2018; Chen et al., 2017). In the need the further improvement for complex situations in this paper optimum SVM based classifier model is proposed for effective and early fire detection (Li, 2009; Lin et al., 2018; López-García et al., 2022; Mallat, 1989).

MATERIALS AND METHODS

The detailed process of the proposed flow diagram of the Optimum SVM Based Classifier Model is shown in Figure 1.

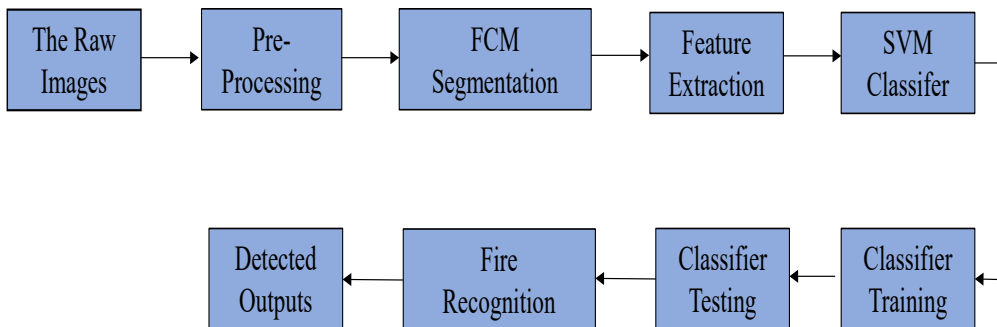


Figure 1. Flow diagram of proposed optimum SVM-based classifier model

The algorithm steps of the proposed optimum classifier model are as follows:

Step 1: Read the raw images, which consist of 150 training images and 50 testing image sets. In the training set, 106 images are fired images, and 44 are non-fired images; in the testing set, 30 are fired images, and 20 are non-fired images.

Step 2: Pre-processing

The image is preliminarily analyzed through the Pre-processing module. This module consists of image resizing, gray conversion, and image enhancement.

The algorithm steps of pre-processing are as follows:

Step 2.1: Image Resize: Here, the input raw images ($M \times N$) are resized to 256×256 .

Step 2.2: Gray Conversion: Converts true color image pixel values to grayscale pixel values by evaluating the optimum scaled sum of the components of Red (R), Green (G), and Blue (B): $0.2989 R + 0.5870 G + 0.1140 B$.

Step 2.3: Image Enhancement: In this step, the quality of the gray converted image is enhanced to the maximum level.

Step 3: Fuzzy C-Mean (FCM) Segmentation

The algorithm steps of the FCM segmentation process are as follows:

Step 3.1: Convert matrix to intensity image

Step 3.2: Computes a global image threshold using Otsu's method.

The global image threshold σ_B^2 is the maximum of between-class variance values and is expressed in Equation 1:

$$\sigma_B^2 = (k_1^*, k_2^*) = \max_{1 \leq k_1 < k_2 < L} \sigma_B^2 = (k_1, k_2) \quad (1)$$

Step 3.3: Convert an intensity image into a binary image using global image threshold value σ_B^2 .

Step 3.4: Using a three-class fuzzy c-means (Fc-M) clustering (Xiong, 2021), outputs the threshold level of an image and binary image. It frequently works again than Otsu's technique, which gives an image a smaller or larger threshold outputs value. For example, in a Switch of cutoff position, one's (1's) indicates a slice between the middle and large class, and zeros (0's) indicate a slice between the small and middle classes.

The Fc-M algorithm divides a finite group of n elements $z = \{z_1, \dots, z_n\}$ into a group of fuzzy clusters with respect to given rules.

Given a finite group of data, the algorithm returns a list of c cluster centers $c = \{c_1, \dots, c_n\}$ and a partition matrix $p = p_{ij} \in [0, 1]$, $i = 1, \dots, n$, $j = 1, \dots, c$, where each element, p_{ij} , tells the degree to which element, z_i , belongs to cluster c_j .

The Fc-M clustering algorithm aims to average and minimize (arg min) an objective function and is expressed in Equation 2:

$$\arg \min_c \sum_{i=1}^n \sum_{j=1}^c p_{ij}^m \|z_i - c_j\|^2$$

Where

$$p_{ij} = \frac{1}{\sum_{k=1}^c \left(\frac{\|z_i - c_j\|}{\|z_i - c_k\|} \right)^{\frac{2}{m-1}}} \tag{2}$$

Step 4: Feature Extraction

In the proposed framework, 11 features are extracted from the segmented image of the dataset using DWT and GLCM to provide high-detail image components with higher resolution (Cohen, 1994; Meyer, 1995; Otsu, 1979). The two-dimensional (2-D) DWT expresses the decomposition of approximation coefficients, cA_j , into approximation coefficients matrix, cA_{j+1} , and detailed coefficients matrices are cH (Horizontal), cV (Vertical), and cD (Diagonal), respectively. The prime elementary decomposition flow step process for 2-D frames/images is shown in Figure 2.

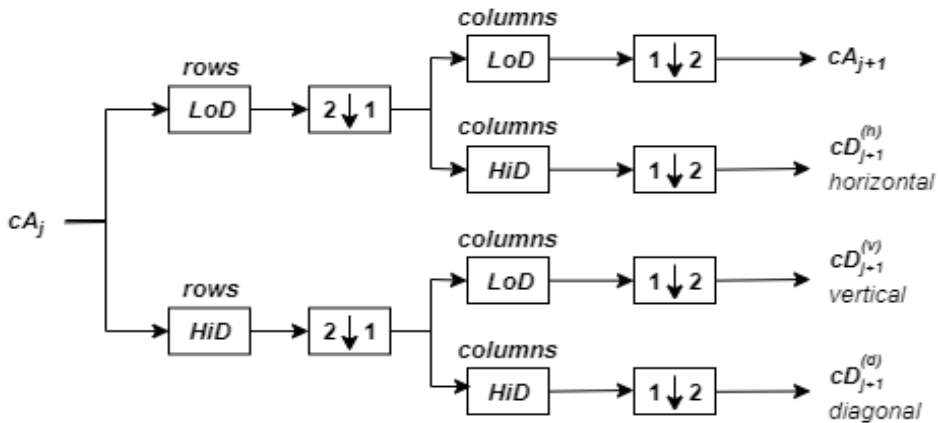


Figure 2. Decomposition Steps for 2-D using DWT

Initially, decomposition is done by setting the approximation coefficients equal to the image $f(i,j)$ [$cA_0 = x(i,j)$] (Zeng et al., 2006).

In this proposed method, seven GLCM features were extracted to characterize the texture of the fire image.

The mathematical model of each feature by following expressions (Equations 3 to 9):

$$\text{Mean: } \mu = \frac{1}{PQ} \sum_{i=0}^P \sum_{j=0}^Q x(i, j) \tag{3}$$

$$\text{Standard Deviation: } \sigma_{ij} = \sqrt{\frac{1}{PQ} \sum_{i=0}^P \sum_{j=0}^Q (x(i, j) - \mu)^2} \tag{4}$$

$$\text{Skewness: } \mu_3 = \frac{1}{PQ} \sum_{i=0}^P \sum_{j=0}^Q (x(i, j) - \mu)^3 \tag{5}$$

$$\text{Kurtosis: } \mu_4 = \frac{1}{PQ} \sum_{i=0}^P \sum_{j=0}^Q (x(i, j) - \mu)^4 \tag{6}$$

$$\text{Entropy: } \alpha_{ET} = \sum_{i,j} x(i, j) \log_2 \left(\frac{1}{x(i,j)} \right) \tag{7}$$

$$\text{Smoothness: } SI = \frac{\mu}{1+\mu} \tag{8}$$

$$\text{Variance: } \sigma_{ij}^2 = \frac{1}{PQ} \sum_{i=0}^P \sum_{j=0}^Q (x(i, j) - \mu)^2 \tag{9}$$

Step 5:

This method uses the optimum SVM classifier model for effective classification with high-dimensional data.

The linear SVM function is as Equation 10:

$$F(x) = x\beta + a \tag{10}$$

Where: x is an observation

β is the coefficient that characterizes an orthogonal vector to the hyper-plane and a is the biased term.

The dual-formalizations for linear SVM are as Equation 11:

For classes of separable, minimize

$$0.5 \sum_{i=1}^n \sum_{j=1}^n a_i a_j y_i y_j x_i' x_j - \sum_{j=1}^n a_i$$

with respect to a_1, \dots, a_n , subject to, $\alpha_i \geq 0$ for all $i = 1, \dots, n$.

For classes inseparable, the objective is the same as for separable classes, except for the additional condition $0 \leq a_i \leq C$ for all $i = 1, \dots, n$.

The final valued function is as Equation 12:

$$\hat{f}(x) = \sum_{i=1}^n \hat{a}_i y_i x' x_i + \hat{b} \tag{12}$$

Where: \hat{b} is the bias estimate, and \hat{a}_i is the i th estimate of the vector \hat{b} , $i = 1, \dots, n$.

Step 6: Train SVM binary learners.

Step 7: Testing SVM binary learners.

Step 8: Load Trained features, labels, and features extraction.

Step 9: Extract Image Features from the testing and training dataset.

Step 10: Fit a multiclass SVM Classifier.

Step 11: Classify Test Images: Classify the test images using the trained SVM model and features extracted from the test images. Prediction by minimizing the expected misclassification cost (Equation 13):

$$\hat{y} = \underset{y=1, \dots, K}{\operatorname{arg\,min}} \sum_{i=1}^K \hat{P}\left(\frac{i}{x}\right) C\left(\frac{y}{i}\right) \quad (13)$$

Where:

- \hat{y} is the predicted classification.
- K is the number of classes.
- $\hat{P}(i/x)$ is the posterior probability of class i for observation x .
- $C(y/i)$ is the cost of classifying an observation as y when its true class is i .

RESULTS AND DISCUSSION

In this paper, the experimental system configuration is as follows:

Processor: Intel Pentium CPU @ 2.30GHz

RAM: 4.00 GB

OS: Windows 10,

Tools: MATLAB (R2020a)

The performance evaluation parameters are expressed in equations from Equations 14 to 18:

$$\text{Accuracy (A)} = \frac{TP+TN}{TP+FP+TN+FN} \quad (14)$$

$$\text{Precision(P)} = \frac{TP}{TP+FP} \quad (15)$$

$$\text{Sensitivity (True Positive Rate)} = \frac{TP}{TP+FN} \quad (16)$$

$$\text{Sensitivity (True Positive Rate)} = \frac{TP}{TP+FN} \quad (17)$$

$$F1 = \frac{TP}{TP + \frac{1}{2}(FP+FN)} \quad (18)$$

Where

TP (True Positive) is the number of fire detection samples is accurately recognized

FN (False Negative) is the number of fire detection samples deemed as non-fire

TN (True Negative) is the number of non-fire detection samples judged as non-fire,

and FP (False Positive) is the number of fire detection samples as non-fire.



(a) Original fired image-1



(b) Original non-fired image-2

Figure 3. Original fired and non-fired input image



(a) Resize image (256 x 256)

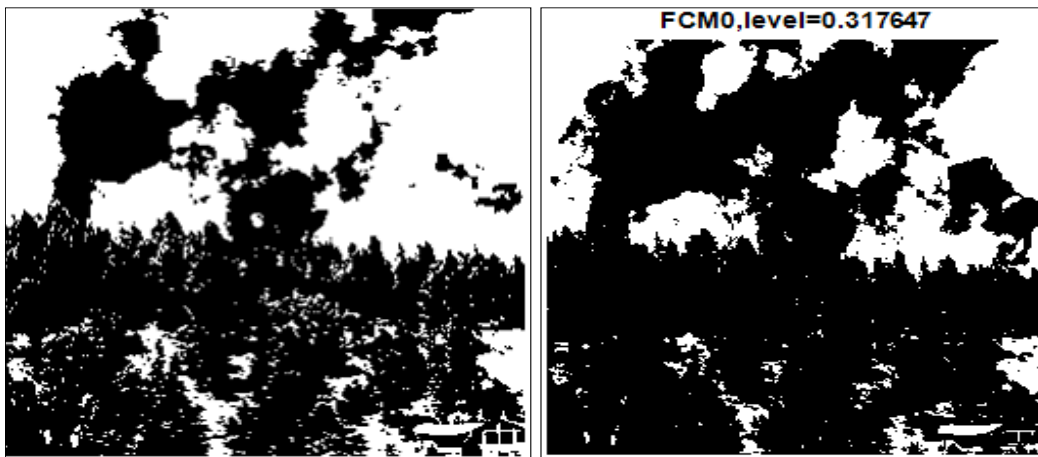


(b) Grayscale image



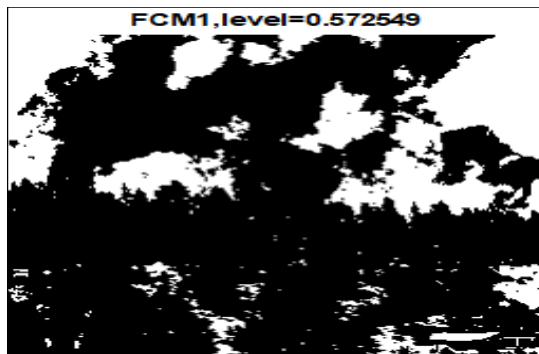
(c) Enhanced-image

Figure 4. Pre-processed images



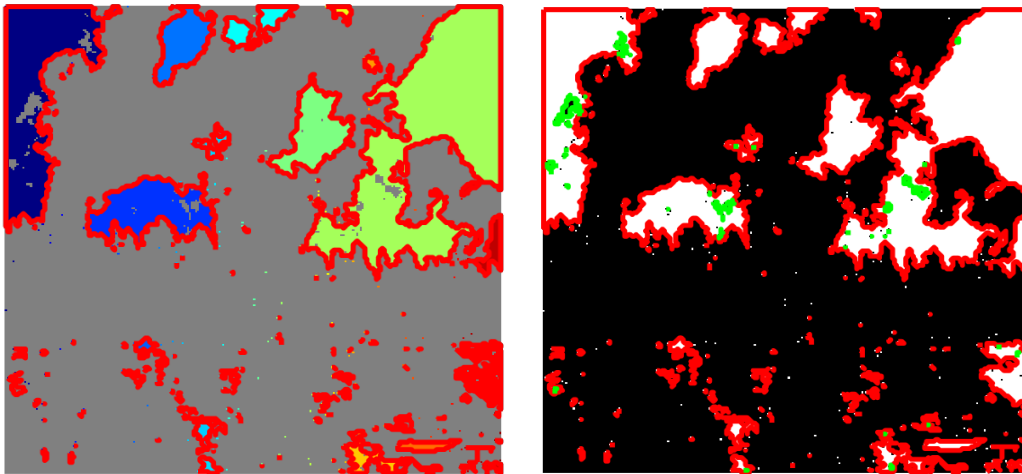
a) Binary version of enhanced original image-1

(b) FCM Level-0 segmented portion of image-1



(c) FCM Level-1 segmented portion of image-1

Figure 5. FCM segmentation images



(a) Overlay Region Boundaries of Segmented Image

(b) Object Boundaries and Hole Boundaries of Segmented Image

Figure 6. Boundaries of FCM segmentation images

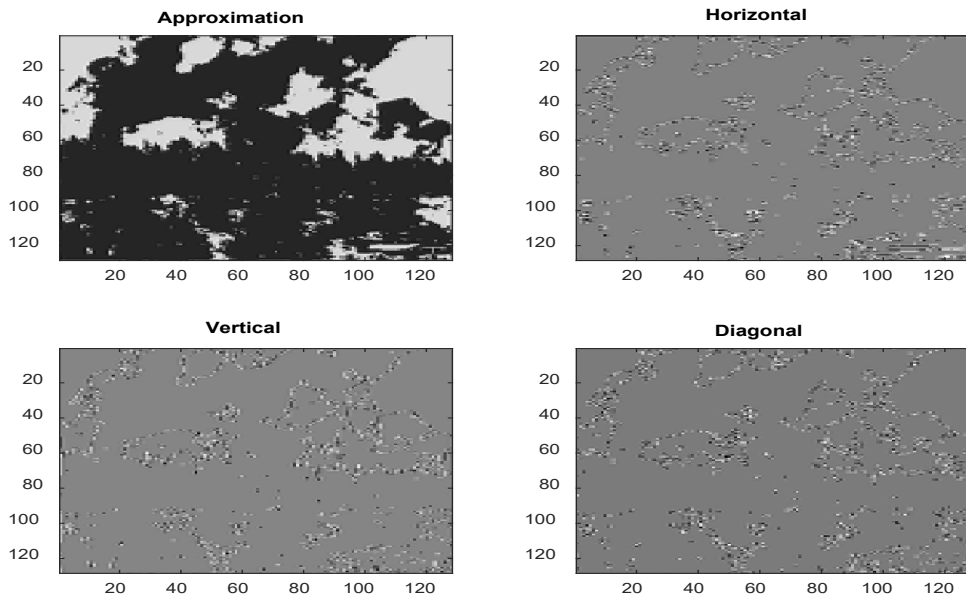
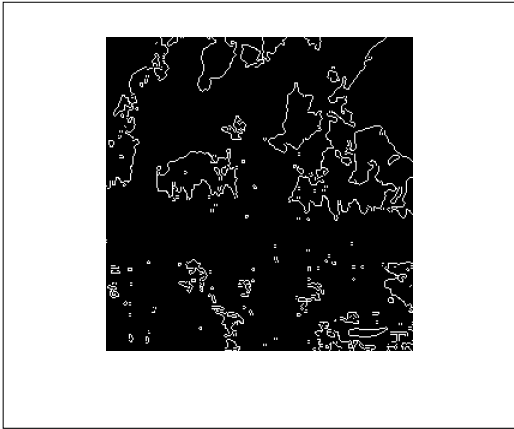
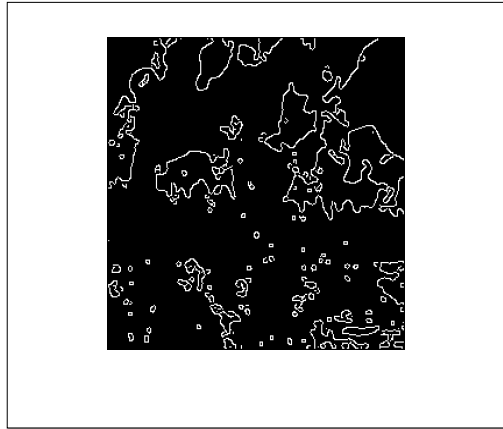


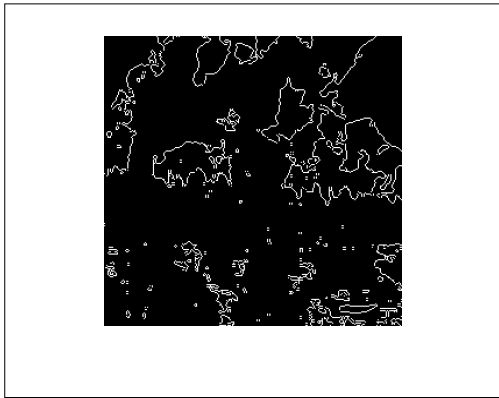
Figure 7. Approximation and Detail Coefficients (Horizontal, Vertical, and Diagonal) of FCM Segmentation Images



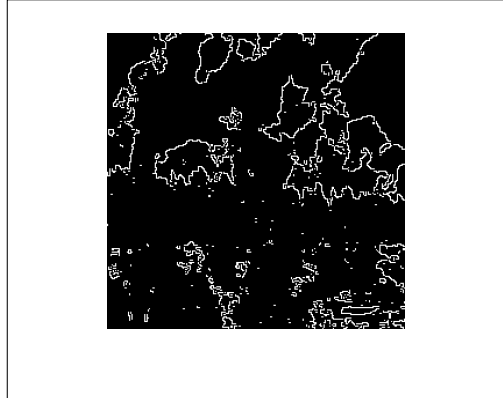
(a) Sobel-based Edge detected image



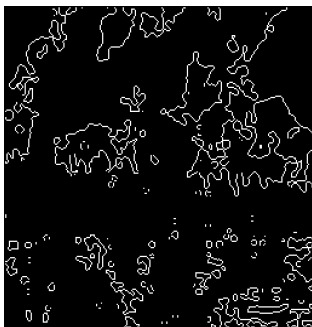
(b) Canny-based edge detected image



(c) Prewitt-based edge detected image



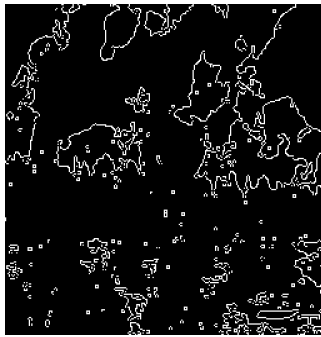
(d) Roberts-based edge detected image



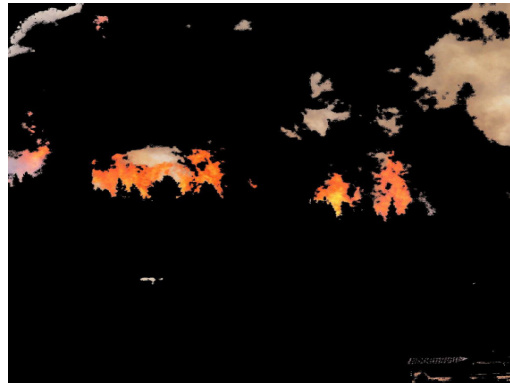
(e) Log-based edge detected image



(f) Zero-cross-based edge detected image

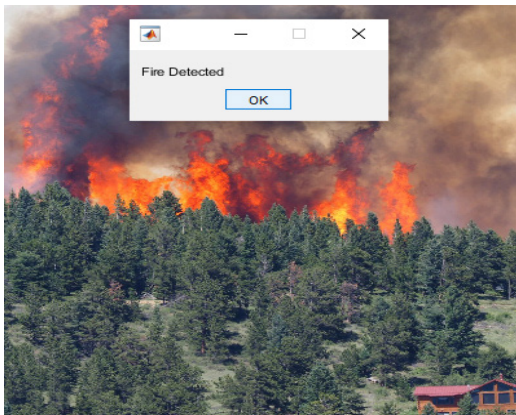


(g) Approx-canny based edge detected image

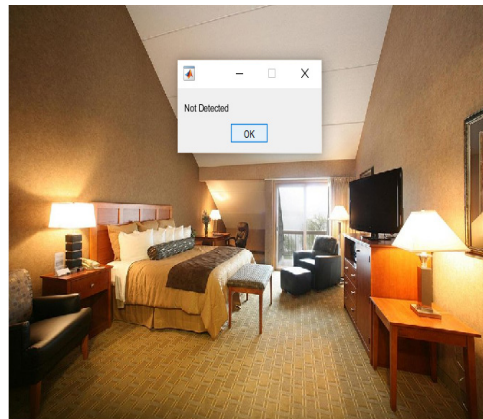


(g) Proposed fire detected image

Figure 8. Edge detection operators and proposed algorithm of fire detected image



(a) Fire detected image result



(a) Non-fire detected image result

Figure 9. Fire detected and non-fire detected images

Accuracy: 99.33%

Output Class	1	100.0% 43	0.9% 1
	1	0.0% 0	99.1% 106
		1	1
		Target Class	

Figure 10. Confusion matrix of proposed optimum classifier

Table 1

Performance parameters of proposed and existing methods

Performance Parameters/Methods	Muhammad et al. (2018)	Zhang et al. (2018)	Hou et al. (2019)	Huang et al. (2020)	Proposed Optimum Classifier
TP	100	101	102	104	106
TN	39	40	40	41	43
FP	6	5	4	3	1
FN	5	4	4	2	0
Accuracy(A)	92.67%	94.00%	94.67%	96.66	99.33%
Precision(P)	94.34%	95.28%	96.23%	97.19	99.06%
Sensitivity	95%	96%	96%	98.11	100%
Specificity	86.67%	88.89%	90.91%	93.18	97.72%
F1-Score	94.79%	95.73%	96.23%	97.65	99.53%
Training Accuracy					70.67%
Testing Accuracy					71.33%

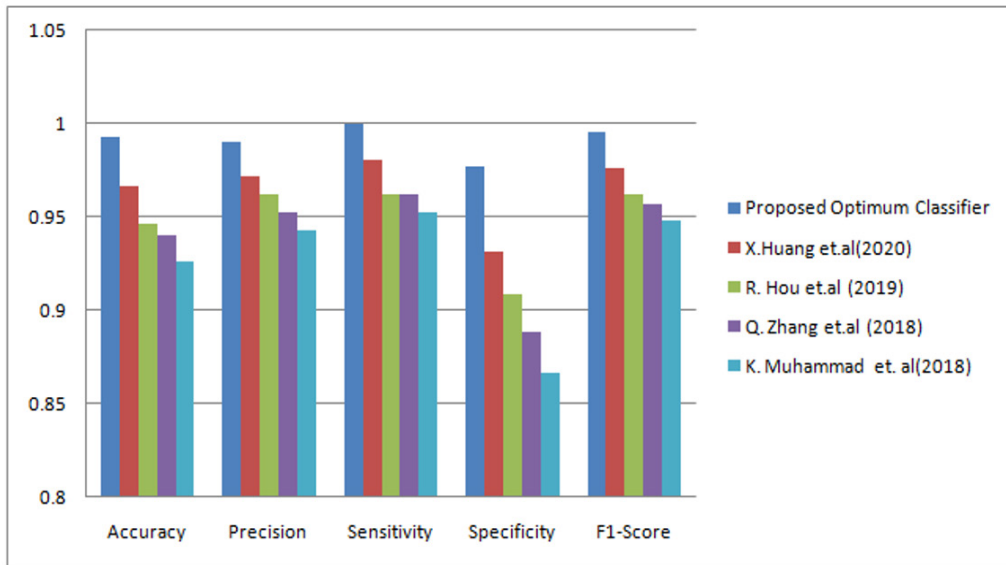


Figure 11. Comparison of Existing Methods Vs. Proposed Optimum Classifier

As shown in Figures 3 (a) and (b), original fired and non-fired images are used for testing the proposed method in the MATLAB simulation process (Sumathi & Panerselvam, 2010).

Figure 4 shows the simulation results of pre-processed images of the originally fired image-1 for the preliminary process in this proposed work. First, the originally fired image-1 is resized into (256 x 256) pixels as shown in Figure 4 (a), grayscale and enhanced images results of test images as shown in Figure 4 (b) and (c), respectively.

Figure 5 (a) shows the binary version of the original enhanced fired image-1. The binary versions of the originally fired image-1 are segmented into two threshold levels using Fc-M clustering, and the results are shown in Figure 5 (b) and (c), respectively.

The overlay region of boundaries of Fc-M segmented image-1 is shown in Figure 6 (a). In Figure 6 (b), the red color represents the object boundaries, and the green color characterizes the hole boundaries of segmented fired image-1. The approximation and detailed coefficients (horizontal, vertical, and diagonal) are extracted from the Fc-M segmented test image-1, and the results are shown in Figure 7. The experimental fire detection images results of Sobel, Canny, Prewitt, Roberts, log, zero-cross, approx-canny edge detections and proposed fire detection as shown in Figure 8 (a), (b), (c), (d), (e), (f) and (g), respectively. The experimental results show that the proposed algorithm can detect fires effectively. The comparison results with seven classical edge detection operators show that the proposed algorithm performs superior to other edge detection operators. The MATLAB simulation proposed method results of fire-detected image-1 and non-fire-detected image-2 as shown in Figure 9 (a) and (b), respectively.

The performance values of the proposed method are evaluated using confusion matrix values, shown in Figure 10. In the proposed confusion matrix, TP is 106, TN is 43, FP is 1, and FN is 0. The performance parameters resulted from Muhammad et al. (2018), Zhang et al. (2018), Hou et al. (2019), and Huang et al. (2020), and proposed optimum classifiers are tabulated in Table 1. The proposed classifier accuracy value is 99.33%, precision value is 99.06%, sensitivity value is 100%, specificity value is 97.72%, F1-score value is 99.53%, training accuracy value is 70.67%, and testing accuracy value is 71.33 % (Table 1). Furthermore, the proposed method's performance values are higher than the other methods. The values of the proposed method and other methods from Table 1 are graphically depicted in Figure 11. The proposed graph optimum classifier shows significant improvement in all metric values compared to other methods.

CONCLUSION

In this study, the optimum SVM-based classifier of fire image recognition has been implemented for active fire detection. The classification is achieved effectively by using DWT and GLCM feature extraction. The results for fire detection were quantitatively

and qualitatively evaluated. The experimental visual results show that the proposed fire recognition approach yields excellent robustness. This method's training and testing accuracies are 70.67% and 71.33%, respectively. The performance evaluation parameters of the proposed optimum classifier model significantly improved classification accuracy compared to other state-art algorithms. Future work will use satellite images with other feature extraction values for fast and higher-accuracy detection.

ACKNOWLEDGEMENTS

The authors wish to acknowledge support from the Advanced Integrated Circuits Lab, Department of Electronics and Communication Engineering, Vemu Institute of Technology, Pakala, Chittoor, Andhra Pradesh, India, under AICTE MODROB Scheme (Ref. No. 84-14/203/RIFD/MODOROB/Policy-1/2019-20) for the assistance given during the simulation work and also writing this article.

REFERENCES

- Ansari, M. D., & Ghreera, S. P. (2017). Copy-move image forgery detection using ring projection and modified fast discrete haar wavelet transform. *International Journal on Electrical Engineering and Informatics*, 9(3), 542-552. <https://doi.org/10.15676/ijeei.2017.9.3.9>
- Ansari, M. D., & Ghreera, S. P. (2018). Intuitionistic fuzzy local binary pattern for features extraction. *International Journal of Information and Communication Technology*, 13(1), 83-98. <https://doi.org/10.1504/IJICT.2018.090435>
- Ansari, M. D., Mishra, A. R., & Ansari, F. T. (2018). New divergence and entropy measures for intuitionistic fuzzy sets on edge detection. *International Journal of Fuzzy Systems*, 20, 474-487. <https://doi.org/10.1007/s40815-017-0348-4>
- Ansari, M. D., Mishra, A. R., Ansari, F. T., & Chawla, M. (2016). On edge detection based on new intuitionistic fuzzy divergence and entropy measures. In *2016 Fourth International Conference on Parallel, Distributed and Grid Computing (PDGC)* (pp. 689-693). IEEE Publishing. <https://doi.org/10.1109/PDGC.2016.7913210>
- Chen, S., Du, H., Wu, L., Jin, J., & Qiu, B. (2017). Compressed sensing MRI via fast linearized preconditioned alternating direction method of multipliers. *Biomedical Engineering Online*, 16, Article 53. <https://doi.org/10.1186/s12938-017-0343-x>
- Cohen, A. (1994). Ten lectures on wavelets, CBMS-NSF regional conference series in applied mathematics. *Journal of Approximation Theory*, 78(3), 460-461. <https://doi.org/10.1006/jath.1994.1093>
- Coppo, P. (2015). Simulation of fire detection by infrared imagers from geostationary satellites. *Remote Sensing of Environment*, 162, 84-98. <https://doi.org/10.1016/j.rse.2015.02.016>
- Cristianini, N., & Shawe-Taylor, J. (2000). *An Introduction to Support Vector Machines and other Kernel-Based Learning Methods*. Cambridge University Press.

- Dunnings, A. J., & Breckon, T. P. (2018). Experimentally defined convolutional neural network architecture variants for non-temporal real-time fire detection. In *2018 25th IEEE International Conference on Image Processing (ICIP)* (pp. 1558-1562). IEEE Publishing. <https://doi.org/10.1109/ICIP.2018.8451657>
- Elaiyaraja, G., & Kumaratharan, N. (2015). Enhancing medical images by new fuzzy membership function median based noise detection and filtering technique. *Journal of Electrical Engineering and Technology*, *10*(5), 2197-2204. <https://doi.org/10.5370/JEET.2015.10.5.2197>
- Elaiyaraja, G., Kumaratharan, N., & Rao, T. C. S. (2022). Fast and efficient filter using wavelet threshold for removal of Gaussian noise from MRI/CT scanned medical images/color video sequence. *IETE Journal of Research*, *68*(1), 10-22. <https://doi.org/10.1080/03772063.2019.1579679>
- Escalera, S., Pujol, O., & Radeva, P. (2009). Separability of ternary codes for sparse designs of error-correcting output codes. *Pattern Recognition Letters*, *30*(3), 285-297. <https://doi.org/10.1016/j.patrec.2008.10.002>
- Esfahlani, S. S. (2019). Mixed reality and remote sensing application of unmanned aerial vehicle in fire and smoke detection. *Journal of Industrial Information Integration*, *15*(9), 42-49. <https://doi.org/10.1016/j.jii.2019.04.006>
- Fan, R. E., Chen, P. H., Lin, C. J., & Joachims, T. (2005). Working set selection using second order information for training support vector machines. *Journal of Machine Learning Research*, *6*(12), 1889-1918.
- Filizzola, C., Corrado, R., Marchese, F., Mazzeo, G., Paciello, R., Pergola, N., & Tramutoli, V. (2016). RST-FIRES, an exportable algorithm for early-fire detection and monitoring: Description, implementation, and field validation in the case of the MSG-SEVIRI sensor. *Remote Sensing of Environment*, *186*, 196-216. <https://doi.org/10.1016/j.rse.2016.08.008>
- Fürnkranz, J. (2002). Round robin classification. *The Journal of Machine Learning Research*, *2*, 721-747.
- Garcia-Jimenez, S., Jurio, A., Pagola, M., De Miguel, L., Barrenechea, E., & Bustince, H. (2017). Forest fire detection: A fuzzy system approach based on overlap indices. *Applied Soft Computing*, *52*, 834-842. <https://doi.org/10.1016/j.asoc.2016.09.041>
- Genovese, A., Labati, R. D., Piuri, V., & Scotti, F. (2011). Virtual environment for synthetic smoke clouds generation. In *2011 IEEE International Conference on Virtual Environments, Human-Computer Interfaces and Measurement Systems Proceedings* (pp. 1-6). IEEE Publishing. <https://doi.org/10.1109/VECIMS.2011.6053841>
- Gottuk, D. T., Lynch, J. A., Rose-Pehrsson, S. L., Owrutsky, J. C., & Williams, F. W. (2006). Video image fire detection for shipboard use. *Fire Safety Journal*, *41*(4), 321-326. <https://doi.org/10.1016/j.firesaf.2005.12.007>
- Hackner, A., Oberpriller, H., Ohnesorge, A., Hechtenberg, V., & Müller, G. (2016). Heterogeneous sensor arrays: Merging cameras and gas sensors into innovative fire detection systems. *Sensors and Actuators B: Chemical*, *231*(8), 497-505. <https://doi.org/10.1016/j.snb.2016.02.081>
- Hastie, T., Tibshirani, R., Friedman, J. H., & Friedman, J. H. (2009). *The Elements of Statistical Learning: Data Mining, Inference, and Prediction*. Springer.
- Hou, R., Pan, M., Zhao, Y., & Yang, Y. (2019). Image anomaly detection for IoT equipment based on deep learning. *Journal of Visual Communication and Image Representation*, *64*(10), 212-223. <https://doi.org/10.1016/j.jvcir.2019.102599>

- Huang, X., & Du, L. (2020). Fire detection and recognition optimization based on virtual reality video image. *IEEE Access*, 8, 77951-77961. <https://doi.org/10.1109/ACCESS.2020.2990224>
- Jia, Y., Yuan, J., Wang, J., Fang, J., Zhang, Q., & Zhang, Y. (2016). A saliency-based method for early smoke detection in video sequences. *Fire Technology*, 52, 1271-1292. <https://doi.org/10.1007/s10694-014-0453-y>
- Kapil, S., Chawla, M., & Ansari, M. D. (2016). On K-means data clustering algorithm with genetic algorithm. In *2016 Fourth International Conference on Parallel, Distributed and Grid Computing (PDGC)* (pp. 202-206). IEEE Publishing. <https://doi.org/10.1109/PDGC.2016.7913145>
- Kecman, V., Huang, T. M., & Vogt, M. (2005). Iterative single data algorithm for training kernel machines from huge data sets: Theory and performance. In L. Wang (Ed). *Support Vector Machines: Theory and Applications* (pp. 255-274). Springer. https://doi.org/10.1007/10984697_12
- Koltunov, A., Ustin, S. L., Quayle, B., Schwind, B., Ambrosia, V. G., & Li, W. (2016). The development and first validation of the GOES early fire detection (GOES-EFD) algorithm. *Remote Sensing of Environment*, 184, 436-453. <https://doi.org/10.1016/j.rse.2016.07.021>
- Li, P., & Zhao, W. (2020). Image fire detection algorithms based on convolutional neural networks. *Case Studies in Thermal Engineering*, 19, Article 100625. <https://doi.org/10.1016/j.csite.2020.100625>
- Li, T. S. (2009). Applying wavelets transform and support vector machine for copper clad laminate defects classification. *Computers and Industrial Engineering*, 56(3), 1154-1168. <https://doi.org/10.1016/j.cie.2008.09.018>
- Lin, Z., Chen, F., Niu, Z., Li, B., Yu, B., Jia, H., & Zhang, M. (2018). An active fire detection algorithm based on multi-temporal FengYun-3C VIRR data. *Remote Sensing of Environment*, 211, 376-387. <https://doi.org/10.1016/j.rse.2018.04.027>
- López-García, D., Peñalver, J. M., Górriz, J. M., & Ruz, M. (2022). MVPAlab: A machine learning decoding toolbox for multidimensional electroencephalography data. *Computer Methods and Programs in Biomedicine*, 214, Article 106549. <https://doi.org/10.1016/j.cmpb.2021.106549>
- Mallat, S.G (1989). A theory for multi-resolution signal decomposition: The wavelet representation. *IEEE Transactions on Pattern Analysis and Machine Intelligence*, 11(7), 674-93. <https://doi.org/10.1109/34.192463>
- Meyer, Y. (1995). *Wavelets and Operators*. Cambridge University Press.
- Muhammad, K., Ahmad, J., & Baik, S. W. (2018). Early fire detection using convolutional neural networks during surveillance for effective disaster management. *Neurocomputing*, 288, 30-42. <https://doi.org/10.1016/j.neucom.2017.04.083>
- Otsu, N. (1979). A threshold selection method from gray-level histograms. *IEEE Transactions on Systems, Man, and Cybernetics*, 9(1), 62-66.
- Peng, Y., & Wang, Y. (2019). Real-time forest smoke detection using hand-designed features and deep learning. *Computers and Electronics in Agriculture*, 167, Article 105029. <https://doi.org/10.1016/j.compag.2019.105029>
- Scholkopf, B., & Smola, A. J. (2018). *Learning with Kernels: Support Vector Machines, Regularization, Optimization, and Beyond*. MIT Press.

- Schölkopf, B., Platt, J. C., Shawe-Taylor, J., Smola, A. J., & Williamson, R. C. (2001). Estimating the support of a high-dimensional distribution. *Neural Computation*, 13(7), 1443-1471. <https://doi.org/10.1162/089976601750264965>
- Seydi, S. T., Saeidi, V., Kalantar, B., Ueda, N., & Halin, A. A. (2022). Fire-Net: A deep learning framework for active forest fire detection. *Journal of Sensors*, 2022, Article 8044390.
- Sharma, A., Ansari, M. D., & Kumar, R. (2017). A comparative study of edge detectors in digital image processing. In *2017 4th International Conference on Signal Processing, Computing and Control (ISPCC)* (pp. 246-250). IEEE Publishing. <https://doi.org/10.1109/ISPCC.2017.8269683>
- Singh, C., Walia, E., & Kaur, K. P. (2018). Enhancing color image retrieval performance with feature fusion and non-linear support vector machine classifier. *Optik*, 158(3), 127-141. <https://doi.org/10.1016/j.ijleo.2017.11.202>
- Sumathi, S., & Paneerselvam, S. (2010). *Computational Intelligence Paradigms: Theory & Applications using MATLAB*. CRC Press. <https://doi.org/10.1201/9781439809037>
- Xiong, G. (2021). *Fuzzy c-means thresholding*. MATLAB central file exchange. <https://www.mathworks.com/matlabcentral/fileexchange/8351-fuzzy-c-means-thresholding>
- Zeng, Y., Zhou, Z., Chen, J., & Liu, W. (2006). An Improved UWB transmitted reference system based on wavelet decomposition. In *IEEE Vehicular Technology Conference* (pp. 1-5). IEEE Publishing. <https://doi.org/10.1109/VTCF.2006.203>
- Zhang, Q. X., Lin, G. H., Zhang, Y. M., Xu, G., & Wang, J. J. (2018). Wildland forest fire smoke detection based on faster R-CNN using synthetic smoke images. *Procedia Engineering*, 211(1), 441-446. <https://doi.org/10.1016/j.proeng.2017.12.034>



Conceptual Design of a Combined Brake-Accelerator Pedal for Limbs Disabled Driver Using a Hybrid Approach

Salami Bahariah Suliano*, Siti Azfanizam Ahmad, Azizan As'arry and Faieza Abdul Aziz

Department of Mechanical and Manufacturing Engineering, Faculty of Engineering, Universiti Putra Malaysia, 43400 UPM, Serdang, Selangor, Malaysia

ABSTRACT

This paper presents the conceptual design of a combined brake-accelerator pedal for limbs disabled drivers using a hybrid approach. A hybrid in which it consists of a combination of TRIZ for design generation, a Morphological Chart for design composition, and a Pugh Matrix for design selection. The aim is to generate and select the best concept design for a combined brake-accelerator pedal with special attention based on the needs of the disabled's ergonomics. In this paper, the function analysis, cause, and effects analysis, TRIZ contradiction matrix, and 40 Inventive principles were applied in the solution generation stage. The outcomes of solutions proposed in TRIZ were then refined using a Morphological chart to deliberate the design composition of the combined brake-accelerator pedal. As a result, three innovative design concepts of combined brake-accelerator pedals were produced. Pugh Matrix was finally utilized to perform multi-criteria scoring based on the baseline to select the best ergonomics concept for combined brake-accelerator pedals for disabled drivers.

Keywords: Combined brake-accelerator pedal, conceptual design, morphological chart, Pugh Matrix, TRIZ

ARTICLE INFO

Article history:

Received: 06 March 2022

Accepted: 31 May 2022

Published: 06 March 2023

DOI: <https://doi.org/10.47836/pjst.31.2.12>

E-mail addresses:

salami.suliano@gmail.com (Salami Bahariah Suliano)

s_azfanizam@upm.edu.my (Siti Azfanizam Ahmad)

zizan@upm.edu.my (Azizan As'arry)

faieza@upm.edu.my (Faieza Abdul Aziz)

*Corresponding author

INTRODUCTION

Ordinary or standard cars in the market are equipped with ordinary control; steering, accelerator, and pedal are designed to provide feedback to drivers (Peters & Ostlund, 2005). For example, steering and pedal are designed for a rotational control distribution towards drivers' hands and feet. However, certain points or types of disabilities limit the driver from driving a

conventional controlled car (Peters & Ostlund, 2005). Therefore, modifying or adaptive equipment is a proven step in maintaining on-the-road freedom for the disabled (NHTSA, 2015).

Being disabled gives a particular person the inner strength to stand on their own two feet, and achieving mobility is an important step towards this (Murata & Yoshida, 2013). Either disabled with or without a wheelchair, both need to drive their vehicle to attain greater self-sufficiency in their daily life (Monacelli et al., 2009). Likewise, driving is considered a complex task for the disabled, requiring physical attention, the ability to make decisions, quick responses, and accurate perception (MyHealth, 2017). It is the reason behind steps taken by the Ministry of Health, Malaysia, in introducing the Occupational Therapist role in Pre-Driving Screening and assessments on the car for disabled drivers. It includes a full check of both on and off-road functional ability and cognitive awareness (Frye, 2013).

Moreover, suggested modifications to Malaysian vehicles for the person with the disabled car are available online, in which the modifications can be made at a registered vehicle repair shop registered with the Road Transport Department (RTD, 2020). Car modification guidelines for a person with disabilities by RTD highlight the effects of driving for the disabled based on their disability and suggested aids for disabled driver assistance. Besides guidelines introduced by the Ministry of Health, a few other guidelines are available online, such as a self-evaluation outline for the driver to ensure the adaptation or modification is appropriate (MyHealth, 2017). An example is an outline from Driver Fitness Medical Guidelines produced by the Association of Motor Vehicle Administrators, National Highway Traffic Safety Administration (NHTSA) that shares tips on cost savings, licensing requirements, needs evaluations, qualified mobility dealers, vehicle selections, training, and vehicle maintenance (NHTSA, 2009).

Few countries worldwide, including Malaysia, Australia, America, and India, only allowed the disabled to drive an automatic transmission car modified with adaptable devices restricted to certain rules and guidelines. It is a good safety precaution to protect the disabled from road accidents. Other than safety, four other aspects of ergonomics are included: comfort, ease of use, productivity and performance, and aesthetics. These are important aspects in considering adaptation and modification for a disabled car to maintain its physical and physiological health.

Cars have been equipped with the same conventional foot pedals since a century ago. Automatic transmissions are equipped with separate brake and accelerator pedals that shall be pressed using the right foot. This design ensures that the throttle is released as soon as the driver applies the brakes. Hence, feet are mostly placed at the accelerator pedal instead of the brake pedal. Changing the accelerator pedal to the brake pedal will then add reaction time. It has been reported that braking in an emergency with separate brake and accelerator pedals takes a longer reaction time (Arora, 2016; Nilsson, 1989, 2002). The

foot may be placed on the brake incorrectly, resulting in poor braking performance, or even miss the brake and wrongly press the accelerator. Various combinations of brake pedals have been designed to overcome the disadvantages of conventional pedals. It is proven by the availability of modifications introduced in several studies, as illustrated in Table 1.

Table 1

Comparison of literature survey

Authors (Years)	Modification Type	Remarks Strength (S) / Recommendation (R)
Jones et al. (2010)	Flip Accelerator Pedal	S: Restore independence for disabled left limbs R: Dual advantage consideration. Those with right-sided pathology are disadvantaged in this respect
Nilsson (2002)	Brake- Accelerator Pedal (Improved)	S: Eliminate the operator's risk of pressing the wrong pedal as well as reduce the reaction time in braking R: Safety feature installation. It might cause the unintended or mixed function of the brake or accelerator
Nilsson (1989)	Combined Accelerator- Brake	S: Eliminate the operator's risk of pressing the wrong pedal as well as reduce the reaction time in braking R: Safety feature installation
Arora (2016)	Combined Accelerator- Brake	S: Improve confusion issues

MATERIALS AND METHODS

A hybrid approach that involving the Theory of Inventive Problem Solving (TRIZ) has been widely used by researchers across many industries, including Mansor et al. (2014), Sapuan et al. (2009), Mastura et al. (2017), and many more. The hybrid thoroughly defines problem, idea generation, concept design, and proper design selections and scorings. This section proposes the hybrid approach to fill gaps and improve the combined brake-accelerator pedal invented in previous studies. The proposed approach will combine three strong methods to systematically cater to conceptual design elements in producing improved products. Figure 1 shows that the conceptual design framework begins with problem definition in general. It then flows to three stages of conceptual design before it ends. Stage 1 consists of conceptual design generation made of TRIZ.

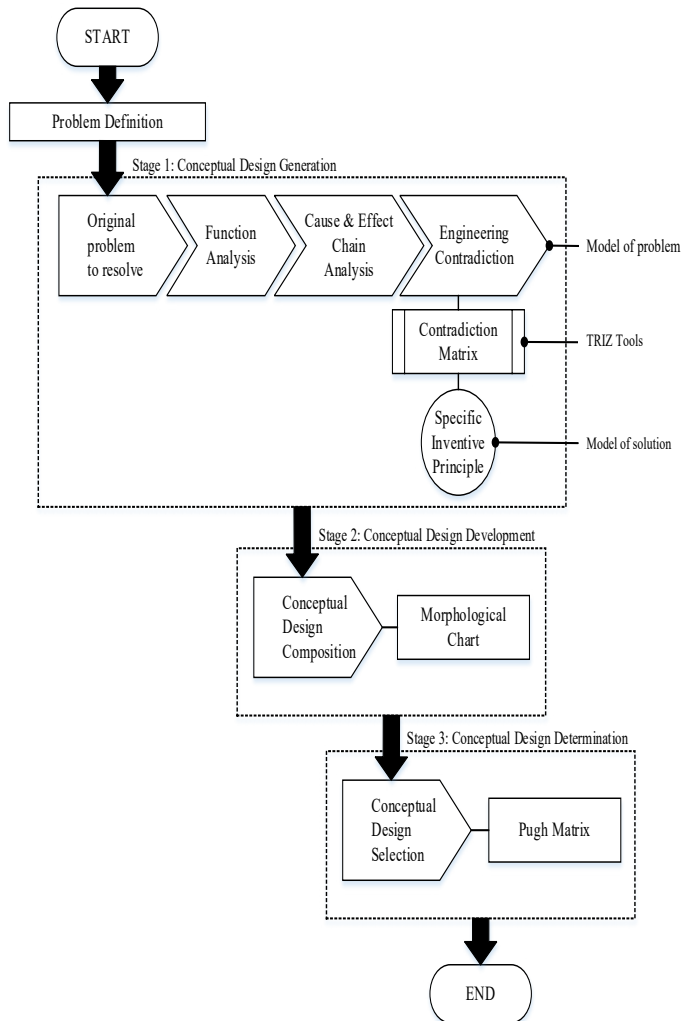


Figure 1. Framework of the hybrid approach

TRIZ theory emphasizes the existing differences in design needs and targets to promote efficiency in design work (Liu et al., 2016) as well as universal ways to solve problems and the ability of engineers to diverse the innovation to solve the problem (Yang & Chen, 2011). Besides, this is an inventive instrument necessary to invent the right thing and integrate it into products and processes with the right measure at the right time (Navas, 2013). With the ability to resolve contradictions related to engineering problems within different interests, TRIZ has been rapidly and widely adopted in an academic and industrial domain (Ferrer et al., 2012). Previous studies generally acclimatize TRIZ in industries as well as specific adaptations in the car design of automobile industries, including redesigning cars to solve parking issues (Manohar & Kalla, 2012) and modeling solar cars (Chang et al., 2016).

In TRIZ, an inventive solution comes after inventive problems. Technically, an inventive situation results from an inability of a technical system to fulfill current functional requirements. For the formulation of inventive problems, it should be sufficient to combine the description of the situation, effects, and goal to be achieved (Guin et al., 2015). In this study, the researcher uses Engineering Contradiction to build an inventive problem to proceed.

As illustrated in Figure 1, the researcher has undergone basic flow guided by TRIZ, namely function analysis, cause and effects analysis, engineering contradiction, and inventive principles to complete conceptual design generation in stage 1. Function analysis is a key aspect for engineers to understand, especially in a complex system design (Auriscchio et al., 2012), as it provides a systematic method for technical problem-solving (Pahl et al., 2006). It has the potential to improve product knowledge, highlight design key points, and identify useful, harmful, and useless functions (Auriscchio et al., 2012). Next, cause and effect analysis takes place to reveal the trivial that may entail significant consequences perfectly. It plays an important role before generating solutions or concepts (GEN3, 2006). Wrong identification of the root cause probably will not generate a working solution (Zare et al., 2016). Thus, spending time in cause-and-effect analysis helps in reducing ineffective solutions. The process of generating cause and effect analysis is similar to the 5-why-brainstorming method in which they correlate. This reference situation provides methodologically important conclusions. Next, Engineering Contradiction was used to devise a proper inventive problem. A contradiction matrix was applied with engineering contradiction statements, and an inventive principle was extracted.

In stage 2, conceptual design development needs morphological charts to come out with conceptual design composition respecting the inventive principle's model of solutions. Generally, the morphological chart provides design features to generate ideas together with sub-solution identification of each sub-function visually (Mansor et al., 2014). Since this project had a TRIZ solution method for problem-solving, the morphological chart works as a refiner (decision-making) of each part listed. This combination of TRIZ solution and morphological chart is a quick translation of a general problem (which is found by TRIZ) to a specific problem (which is visualized by the morphological chart).

Stage 3 works as a final stage to determine and select the best design via the scoring of the Pugh Matrix. Pugh Matrix helps to narrow down the option based on the concepts best gratifying the stated criteria, not to find the better design (Haris et al., 2016). Moreover, the Pugh matrix commonly has a clear loser rather than a winner to help designers remove the losing option (Madke & D. Jayabhaye, 2016) before selecting the best option among all available alternatives (Joshi et al., 2019). Therefore, the Pugh matrix was chosen due to its wide acceptance, simplicity (Cun et al., 2020), ease to use (Madke & D. Jayabhaye, 2016), user-friendly (Lonmo & Muller, 2014), and better efficiency (Karnjanasomwong & Thawesaengskulthai, 2016; Muller, 2011; Thakker et al., 2009). For the same reason,

the Pugh matrix has been applied to this project to analyze available choices of concept design composition.

RESULTS AND DISCUSSION

In this section, the conceptual design of ergonomics combined brake-accelerator pedal hybrid using TRIZ-morphological chart Pugh matrix approach is performed according to the initially proposed framework.

A combined brake-accelerator pedal has been through a few studies, as in Table 3. It starts with a flip accelerator pedal, and it is then combined to cater to a person with certain limb disabilities. These efforts are believed to help improve reaction time and reduce unwanted incidents, such as wrong pedals and late emergencies brake that might cause a crash. However, two problems are highlighted in this research: first is taking into consideration that a combined brake-accelerator pedal is used, and second is normal conventional pedal usage. Both carry pros and cons, so this case study shall resolve both issues with another improved design. Table 2 list the pro and cons of both applications.

Conceptual Design Generation (Stage 1)

As shown in Figure 1, Stage 1, concept generation begins with the original problem to resolve (problem listed in Table 2). The problem is clear, but it has no direction on where it starts and what is the root cause of the problem. Hence, the functional components and interactions are carefully identified to determine the real problem.

Initially, the pedals system as a product as a subject (rectangle) and interaction body parts as an object (oval) with function interactions and other outside components that influence the performance of the system as supersystem components (hexagon) shall be identified. Each function is represented as an arrow: useful, insufficient, excessive, and harmful. Equitable to the naming, a normal useful function does not cause any damage or undesired effect on the object, whereas insufficient and excessive useful function may create some amount of damage or undesired effect on the object, and a harmful function certainly causes harm to the object (Yeoh et al., 2015)

Table 2
Conventional pedals versus combined pedals

Type of pedal	Conventional pedals	Combined brake-accelerator pedals
PROS	<ul style="list-style-type: none"> The method of operation has been well-known since the early days. 	<ul style="list-style-type: none"> A new method of operation Quick response Effortless (minimize limbs movements as legs can stay on the pedals for both brake and accelerator functions)

Table 1 (Continue)

Type of pedal	Conventional pedals	Combined brake-accelerator pedals
PROS	<ul style="list-style-type: none"> The method of operation has been well-known since the early days. Long reaction time to change pedals Fatigue of long press on one pedal. 	<ul style="list-style-type: none"> A new method of operation Quick response Effortless (minimize limbs movements as legs can stay on the pedals for both brake and accelerator functions)
CONS	<ul style="list-style-type: none"> As it is fixed, certain disabled have a problem reaching. 	<ul style="list-style-type: none"> It can confuse a new user as it is newly introduced.

Figure 2 shows the Function analysis for this case study. The function analysis shows that one harmful effect in the foot and pedal pad interaction needs to be solved. Therefore, the next step will focus on this interaction to find the root cause of the problems.

Function analysis and cause and effects analysis are interrelated in that cause and effects analysis should highlight the most crucial interaction of function analysis and flow correspondingly with highlighted elements of functional analysis. In other words, within the same storyline, function analysis shows functions and interactions; meanwhile, cause and effects analysis answer why each cause questions until the potential root cause has been identified. For example, Figure 3 indicates the cause and effects analysis that starts with the cause (fatigue and discomforts while driving) as the utmost box and ends with two possible root causes; explicitly, one is a fixed bracket, and another one is the location of the pedals at the end of the analysis.

Subsequently, an inventive problem statement has to be determined to proceed with the concept design generations. The general problem statement then undergoes engineering contradiction to build up the statement, as shown in Table 3. Thus, the improving and worsening factors are extracted from the engineering contradiction equations. Finally, the inventive principle is reduced by referring to the contradiction matrix table, and the suggested inventive principle and realistic solution are listed in Table 4.

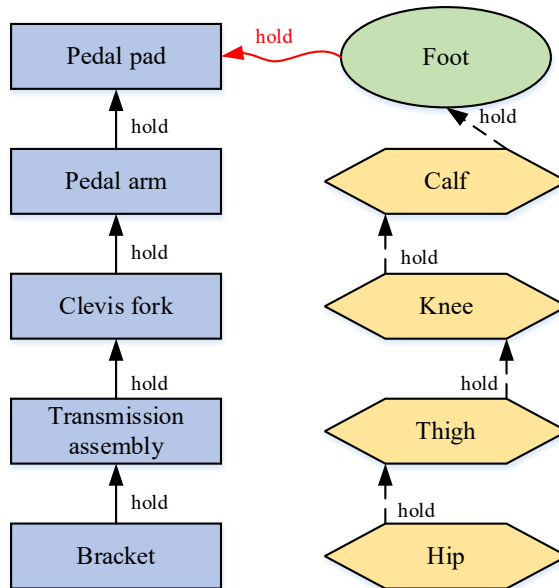


Figure 2. Function analysis for pedals

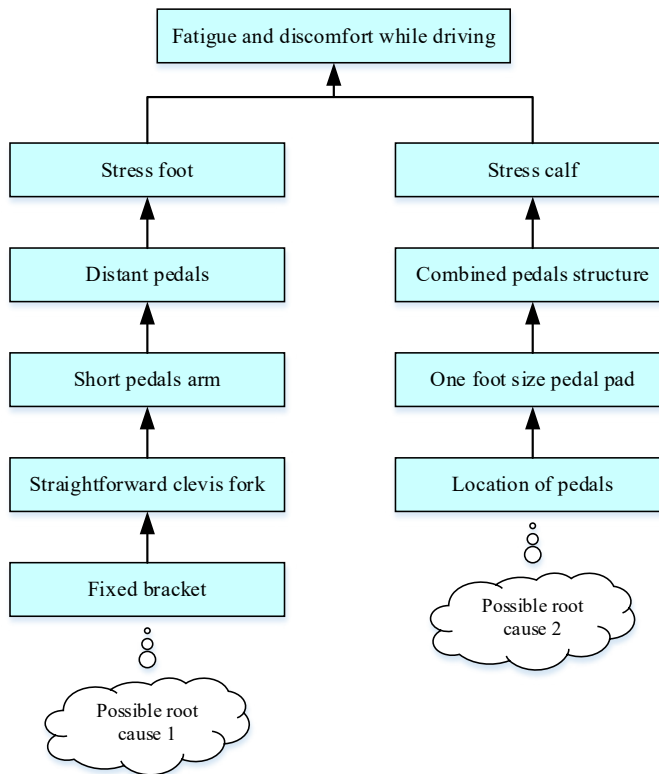


Figure 3. Cause and effect analysis for pedals

Table 3

General problem statements versus inventive problem statements

No.	General Problem Statements	Inventive Problem Statements (Engineering Contradiction)
1.	Operating pedals caused pain and discomfort towards limbs disabled drivers.	IF the accelerator and brake pedals are combined, THEN it improves pain and reduces rotation movements of the legs BUT it can cause confusion
2.	With various disabilities and sizes of disabled drivers, standard pedals cause a problem of reach.	IF it is in a fixed position THEN standardization in product production BUT the problem with disabled reaching and operating.

Table 4

Improving and worsening factors versus inventive principles



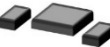
Improving factor	Worsening factor	Inventive Principle	Realistic solution
#35 Adaptability and versatility	#30 Object-generated harmful factors	#35 Parameter change #11 Beforehand cushioning #32 Color change #31 Porous material	Combine the brake pedal and accelerator pedal to the same cross-section pedal plates.
#35 Adaptability and versatility	#36 Device complexity	#29 Pneumatic & hydraulic #15 Dynamization #28 Mechanics substitution #37 Thermal expansion	To dynamize the plate of the pedal from static to movable to fit limbs' disabled needs.

Conceptual Design Development (Stage 2)

Based on the foregoing stage's evaluation of all design factors, it is time to merge all the concepts to generate new conceptual designs for the component. Numerous conceptual designs will result from combining all the ideas from all of the component's parts. There can be many concepts that possibly be generated from a combination of the morphological charts. However, only three are chosen in this case study. The three combinations come after the integration of the morphological chart and TRIZ. Since TRIZ is very abstract, a morphological chart helps visualize the ideas related to proposed solutions by TRIZ, as mapped in Table 5. The morphological chart used recommended inventive principles for two problems defined as the design strategy to inspire the design features. Three combinations named PD1, PD2, and PD3 as concept design composition developed, and the selection of

the most recommended design happens in the next stage. Table 5 has three main columns: TRIZ solution principles and design strategy, design features, and solution. The design feature's column lists all attributes that are manipulative. Meanwhile, the solution's column comprises another three sub-columns (A, B, and C) filled with elements to choose from. Another row in the same table is an outcome of combinations of attributes in design features and solutions under concept design composition.

Table 5
Morphological chart for pedals

TRIZ Solution principles and design strategy	Design features	Solution		
		A	B	C
#35: Parameter change Change the parameter	1. Cross section of the pedal plate	Square	Squirecle	Foot shaped
#5: Dynamization Moveable rest	2. Cross-section of a resting area	Square	Squirecle	Foot shaped
#5: Dynamization Moveable plate	3. Transmission	Manual	Auto (Button)	-
	4. Button location	at door	at dash	nearby gear
	5. Manual operation	shaft	lifter	-
Concept design composition		1. B1 - B2 - B3 - C4 = PD1		
		2. C1 - C2 - A3 - B5 = PD2		
		3. A1 - A2 - B3 - A4 = PD3		




The similarity of the three selected combinations is the dynamization of the rest and pedal plate. Therefore, it is very important to cater to variable sizes of disabled drivers. Meanwhile, the significant difference between all proposed concepts is the transmission assembly to hold the pedal arm and pedal plates, the shapes of the pedal, the location of the button (if it exists), and the manual operation part (if it exists). Nevertheless, the automatic transmissions, button locations, and shapes give value added to the concept with a slight addition of cost in contras.

Conceptual Design Selection (Stage 3)

In Stage 3, the final conceptual design for the combined brake pedal will be selected after the development of the composition in the previous stage. At this time, the Pugh matrix

took place. There are four main columns in the Pugh matrix analysis table, Table 6: Criteria, Baseline, Alternatives, and Totals (Burge, 2009). The criteria column was further devised into two sub-columns. The left column comprises five main ergonomics elements, as shared in the previous section, while the right column is a sub-criterion of each element. These criteria came from each element's definition, literature, and elaboration.

Table 6
Pugh matrix for pedals

Criteria	Weightage	Baseline	Alternatives			Totals
			 PD1	 PD2	 PD3	
Safety	3	0	+	+	+	9
Comfort	6	0	+	-	0	18
Ease of use	4	0	+	+	+	8
Productivity and performance	4	0	+	+	+	-8
Aesthetic	6	0	+	+	+	18
Others	6	0	+	-	0	18
		Totals	33	5	17	
		Rank	1 ✓	3	2	

The baseline indicates a number corresponding to the current design, which is '0', '+' indicating an improvement of design compared to the current design, and '-' indicates the deterioration of design compared to the current design or a negative impact on the design. The alternatives column is split into three sub-columns specifying design selections from the concept design composition of the morphological chart in the previous subsection.

The total column is the sum of marks according to the row. Another total at the end of the table indicates the total row that will be the final numbers for the column of each alternative, and the final row shows the ranking of the alternatives.

Table 6 shows that concept PD1 is leading in the first rank with 33 scores over the other two concepts, PD3 (17 scores) and PD2 (5 scores). It is because concept PD1 carries a few important criteria such as squircle pedal shape, squircle rest plate shape, automatic movable, and an automatic control located nearby gear drivers that can easily reach it. Henceforth, movable pedals and pedals rest with the control button to refine the reach of users.

The chosen concept design mechanism was prepared on the CATIA V5 R20, as shown in Figure 1. The middle pedal works as a combined brake-accelerator while the right and

left pedals rest. All three pedals are movable, but the resting paddle is non-pressable, and it serves the disabled driver with a left or right limb for resting. The working paddle accelerates upon pressing upwards, similar to a normal accelerator; meanwhile, pressing downwards is a braking mechanism. The initial position of the pedal is neither accelerating nor braking to avoid any confusion of action. This natural pedal function also can improve the driver from fatigue. Furthermore, since disabled driver varies in size of their legs and the capabilities of legs, right or left, movable pedals and resting improve the foot's reach.

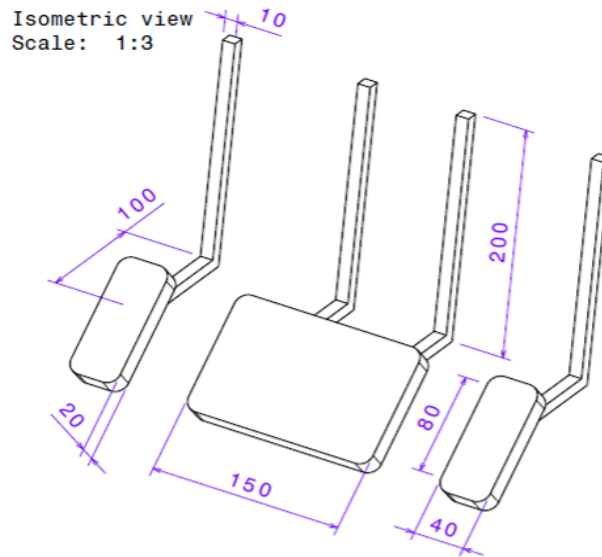


Figure 4. An ergonomics combined brake-accelerator pedal

CONCLUSION

In conclusion, the development of these improved ergonomics combined brake-accelerator pedals avoids braking and accelerating interference. It is advantageous over conventional pedals and previously combined pedals. A TRIZ, morphological chart, and Pugh matrix hybrid introduce systematic generation, development, and selection of the concept design. Also, making the pedal movable brings together better reach dimensions for the disabled to venture, as shown in Table 8. It is an ongoing project. There will be a verification step in the future to test further the redesign made to the combined-brake pedal development.

Table 8

Movable reach comparison

Part	Dimension/ Direction	Current Design (mm)	Redesigned (mm)	Improved	Same	Worsen
Pedals	X	n/a	160.00 (right/left)			
	Y	n/a	160.00 (front/back)			
	Z	n/a	350.00 (up/down)			

ACKNOWLEDGEMENT

The authors would like to acknowledge Road Transport Department Malaysia, Social Welfare Department, and FARESH MOTOR Sdn. Bhd., and Industrial Training and Rehabilitation Centre (PLPP), who provided insight, expertise, and documentation that greatly guided the research.

REFERENCES

- Arora, S. (2016). A combined pedal for brake and accelerator. *International Journal of Research in Aeronautical and Mechanical Engineering*, 4(1), 131-138.
- Auricchio, M., Bracewell, R., & Armstrong, G. (2012). The function analysis diagram. *Proceedings of the ASME Design Engineering Technical Conference*, 7(2015), 849-861. <https://doi.org/10.1115/DETC2012-70944>
- Burge, S. (2009). *The System Engineering Tool Box. The Innovator's Toolkit*. John Wiley & Sons, Inc. <https://doi.org/10.1002/9781118258316.ch36>
- Chang, Y. S., Chien, Y. H., Yu, K. C., Chu, Y. H., & Chen, M. Y. C. (2016). Effect of TRIZ on the creativity of engineering students. *Thinking Skills and Creativity*, 19, 112-122.
- Cun, L., Jun, H., Hengeveld, B., & Hummels, C. (2020). A framework designing for story sharing of the elderly: From design opportunities to concept selection. In T. Ahram, W. Karwowski, A. Vergnano, F. Leali & R. Taiar (Eds.), *Advances in Intelligent Systems and Computing* (Vol. 111, pp. 810-815). Springer International Publishing. https://doi.org/10.1007/978-3-030-39512-4_123
- Ferrer, J. B., Negny, S., Robles, G. C., & Le Lann, J. M. (2012). Eco-innovative design method for process engineering. *Computers & Chemical Engineering*, 45, 137-151. <https://doi.org/10.1016/j.compchemeng.2012.06.020>
- Frye, A. (2013). *Disabled and older persons and sustainable urban mobility*. Global Report on Human Settlements. https://unhabitat.org/sites/default/files/2013/06/GRHS.2013.Thematic.Disabled.and_Older_Persons.pdf
- GEN3. (2006). *TRIZ Group Training Manual (Level 1 Practitioner)*. <http://mytriz.com.my/>

- Guin, A. A., Kudryavtsev, A. V., Boubentsov, V. Y., & Seredinsky, A. (2015). *Level 1 Study Guide: Theory of Inventive Problem Solving* (7th ed.). First Fruit Sdn. Bhd.
- Haris, A., Motato, E., Mohammadpour, M., Theodossiades, S., Rahnejat, H., Kelly, P., O'Mahony, M. & Struve, B. (2016, September 7-9). Concept selection for clutch nonlinear absorber using PUGH matrix. In *3rd Biennial International Conference on Powertrain Modelling and Control: Testing, Mapping and Calibration*. Loughborough University, United Kingdom.
- Jones, C., Abbassian, A., Trompeter, A., & Solan, M. (2010). Driving a modified car: A simple but unexploited adjunct in the management of patients with chronic right sided foot and ankle pain. *Foot and Ankle Surgery*, 16(4), 170-173. <https://doi.org/10.1016/j.fas.2009.10.007>
- Joshi, A. K., Dandekar, I. A., Gaikwad, M. V., & Harge, C. G. (2019). Pugh Matrix and Kano Model - The significant techniques for customer's survey. *International Journal of Emerging Technology and Advanced Engineering*, 9, 53-55.
- Karnjanasomwong, J., & Thawesaengskulthai, N. (2016). TRIZ-PUGH model, new Approach for creative problem solving and decision making. In *IEEE International Conference on Industrial Engineering and Engineering Management, (IEEM)*, (pp. 1757-1761). IEEE Publishing. <https://doi.org/10.1109/IEEM.2015.7385949>
- Liu, W., Cao, G., & Tan, R. (2016). Research on optimization of TRIZ application driven by design needs and targets. *Procedia CIRP*, 39, 33-38. <https://doi.org/10.1016/j.procir.2016.01.162>
- Lonmo, L., & Muller, G. (2014). Concept selection - Applying Pugh Matrices in the subsea processing domain. *INCOSE International Symposium*, 24(1), 583-598. <https://doi.org/10.1002/j.2334-5837.2014.tb03169.x>
- Madke, P., & D. Jayabhaye, M. (2016). Application of pugh selection matrix and tospis method for fuel level sensing technology selection. *International Journal of Engineering Research*, 5(Special 2), 368-370. <https://doi.org/10.16962/elkapj/si.arimpie-2016.6>
- Manohar, N., & Kalla, P. (2012). Innovative conceptual design on car using TRIZ method for optimum parking space. *IOSR Journal of Engineering (IOSRJEN)*, 2(8), 52-57.
- Mansor, M. R., Sapuan, S. M., Zainudin, E. S., Nuraini, A. A., & Hambali, A. (2014). Conceptual design of kenaf fiber polymer composite automotive parking brake lever using integrated TRIZ-morphological chart-analytic hierarchy process method. *Materials and Design*, 54, 473-482. <https://doi.org/10.1016/j.matdes.2013.08.064>
- Mastura, M. T., Sapuan, S. M., Mansor, M. R., & Nuraini, A. A. (2017). Conceptual design of a natural fibre-reinforced composite automotive anti-roll bar using a hybrid approach. *International Journal of Advanced Manufacturing Technology*, 91(5-8), 2031-2048. <https://doi.org/10.1007/s00170-016-9882-8>
- Monacelli, E., Dupin, F., Dumas, C., & Wagstaff, P. (2009). A review of the current situation and some future developments to aid disabled and senior drivers in France. *IRBM*, 30(5-6), 234-239. <https://doi.org/10.1016/j.irbm.2009.09.004>
- Muller, G. (2011). Researching the application of Pugh Matrix in the sub-sea equipment industry. *Conference on Systems Engineering Research, 2011*, 1-11.

- Murata, Y., & Yoshida, K. (2013). Automobile driving interface using gesture operations for disabled people. *International Journal on Advance in Intelligent Systems*, 6(3 & 4), 329-341.
- MyHealth. (2017). *Pre-driving assessment for people with disabilities*. Kementerian Kesihatan Malaysia. <http://www.myhealth.gov.my/en/pre-driving-assessment-people-disabilities/>
- Navas, H. V. G. (2013). TRIZ: design problem solving with systematic innovation. In D. Coelho (Ed.), *Advances in Industrial Design Engineering* (pp. 75-98). InTech.
- NHTSA. (2009). *Driver fitness medical guidelines (September)*. National Highway Traffic Safety Administration, United States Department of Transportation. <https://www.nhtsa.gov/document/driver-fitness-medical-guidelines>
- NHTSA. (2015). *Adapting motor vehicles for people with disabilities*. National Highway Traffic Safety Administration, U.S. Department of Transportation. https://www.nhtsa.gov/sites/nhtsa.gov/files/documents/adapting_motor_vehicles_brochure_810733.pdf
- Nilsson, R. (1989). 10 Evaluation of a combined accelerator-brake pedal. *A New Approach to Traffic Planning and Street Design in Sweden*, 10, 99-100.
- Nilsson, R. (2002). Evaluation of a combined brake-accelerator pedal. *Accident; Analysis and Prevention*, 34(2), 175-183. [https://doi.org/10.1016/S0001-4575\(01\)00011-2](https://doi.org/10.1016/S0001-4575(01)00011-2)
- Pahl, G., Beitz, W., Feldhusen, J., & Grote, K. H. (2006). *Engineering design: A systematic approach* (3rd ed.). Springer.
- Peters, B., & Ostlund, J. (2005). *Joystick controlled driving for drivers with disabilities* (Part 2). Statens väg- och transportforskningsinstitut
- RTD. (2020). *Guidelines vehicle modification for disable (O.K.U)*. Jabatan Pengangkutan Jalan Malaysia. https://www.jpj.gov.my/en/web/main-site/teknikal-kenderaan-en/-/knowledge_base/technical/guidelines-vehicle-modification-for-disable-o-k-u-
- Sapuan, S. M., Ham, K. W., Ng, K. M., Woo, C. K., Ariffin, M. K. A., Baharudin, B. T. H. T., Faieza, A. A., Supeni, E. E., & Jalil, N. A. A. (2009). Design of composite racing car body for student based competition. *Scientific Research and Essays*, 4(11), 1151-1162.
- Thakker, A., Jarvis, J., Buggy, M., & Sahed, A. (2009). 3DCAD conceptual design of the next-generation impulse turbine using the Pugh decision-matrix. *Materials and Design*, 30(7), 2676-2684. <https://doi.org/10.1016/j.matdes.2008.10.011>
- Yang, C. J., & Chen, J. L. (2011). Accelerating preliminary eco-innovation design for products that integrates case-based reasoning and TRIZ method. *Journal of Cleaner Production*, 19(9-10), 998-1006. <https://doi.org/10.1016/j.jclepro.2011.01.014>
- Yeoh, T. S. (ed.), Yeoh, T. J., & Song, C. L. (2015). *TRIZ: Systematic Innovation in Manufacturing* (10th Print). First Fruit Sdn. Bhd.
- Zare, M., Croq, M., Hossein-Arabi, F., Brunet, R., & Roquelaure, Y. (2016). Does ergonomics improve product quality and reduce costs? A Review article. *Human Factors and Ergonomics in Manufacturing*, 26(2), 205-223. <https://doi.org/10.1002/hfm.20623>



The Photophysiology of Benthic Diatoms in the Intertidal Flats of Pulau Pinang (Malaysia)

Sazlina Salleh^{1,2*}, Elaine Ee Ling Cheng³, Md. Solaiman Hossain⁴, Shakila Samad³, Nur Ain Amani Abdul Mubin¹, Nur Aqilah Muhamad Darif², Michelle Glory G Jonik¹ and Mahadi Mohammad^{2,3}

¹Centre for Policy Research and International Studies, Universiti Sains Malaysia, 11800 USM, Minden, Pulau Pinang, Malaysia

²Centre for Marine and Coastal Studies, Universiti Sains Malaysia, 11800 USM, Minden, Pulau Pinang, Malaysia

³School of Biological Sciences, Universiti Sains Malaysia, 11800 USM, Minden, Pulau Pinang, Malaysia

⁴Department of Oceanography, Shahjalal University of Science and Technology, Sylhet 3114, Bangladesh

ABSTRACT

The *in-situ* photosynthetic activity in tropical intertidal benthic diatom in response to environmental variation was assessed in this study by measuring chlorophyll fluorescence. The investigation was carried out during the lowest tide in January (non-rainy day) and February 2013 (post-rainy day) at two sampling sites (A and B) from each selected location (Pantai Jerejak, Teluk Bahang and Tanjung Bungah, Pulau Pinang, Malaysia). Samples of surface sediment (top 0.5 cm) were collected, and chlorophyll *a* extracted as biomass estimation. Assessments of the photosynthetic activity of benthic diatoms were made using a pulse-amplitude modulated (PAM) fluorometer. Fifty-three species were identified, representing 27 genera from the three studied locations. Both locations showed similarities in species diversity and abundance. Two-way ANOVA showed no significant

differences ($p = 0.430$) in species richness (Margalef Index) among sampling locations, with an average value of 6.33 ± 0.247 . Both intertidal flats were dominated by *Cocconeis*, *Navicula*, *Actinopterychus*, and *Diploneis*. The community has low maximum quantum yields, F_v/F_m (ranging from 0.170 to 0.340) and is often light-limited (Photoacclimation Index, E_k , ranging from 67.96 to 236.71 $\mu\text{mol photons m}^{-2} \text{s}^{-1}$). The relative electron transport rate ($rETR_{\text{max}}$) was low, with

ARTICLE INFO

Article history:

Received: 06 March 2022

Accepted: 31 May 2022

Published: 06 March 2023

DOI: <https://doi.org/10.47836/pjst.31.2.13>

E-mail addresses:

sazlina@usm.my; sazlinsalleh@gmail.com (Sazlina Salleh)

elaimecheng888@gmail.com (Elaine Ee Ling Cheng)

solaiman-ocg@sust.edu (Md. Solaiman Hossain)

ila_samad@hotmail.com (Shakila Samad)

ainamanie08@gmail.com (Nur Ain Amani Abdul Mubin)

aqilahdarif@usm.my (Nur Aqilah Muhamad Darif)

michelleglory93@gmail.com (Michelle Glory G Jonik)

mahadi@usm.my (Mahadi Mohammad)

*Corresponding author

values ranging from 3.45 to 35.51 across three sampling locations. Fluctuation in salinity has caused a decrease in photosynthetic activity. This study suggests that the low values indicated a poorly adapted benthic microalgal community that is constantly light-limited. However, time-series data is needed to determine the ability of these communities to adapt to the changing environment.

Keywords: Chlorophyll *a*, fluoresces, intertidal, microalgae, microphytobenthos, PAM

INTRODUCTION

Benthic diatoms play an essential role in marine benthic environments by providing an adequate food supply for invertebrate grazers and stabilising the sediment substrate. The function of intertidal benthic diatom and species composition shows a strong relationship with environmental factors, mainly sediment grain size composition, tidal exposure, salinity, light availability, temperature, and nutrients (Dalu et al., 2016; Du et al., 2016). Among these factors, sediment characteristics are commonly used to explain variations in abundance and composition in tropical intertidal flats. It is noted that diatoms tend to dominate muddy sediments, while sandy sediments are overwhelmed by the mixed composition of cyanobacteria, diatoms, and euglenids (Ribeiro et al., 2013). In contrast, sediment with high silt content is known to favour high species diversity and larger diatoms (Grinham et al., 2011). Benthic diatoms are divided into two groups according to their colonisation substratum, epipelton, and epipsammon (Round et al., 1990). The epipelton consists of free-living diatoms that can move through muddy sediments. In contrast, the epipsammon comprises smaller, non-motile diatoms attached to the particles of sandy sediments.

In addition to sediment type, light and temperature are among the factors influencing diatom biomass and photosynthetic capacity in shallow coastal environments (Mitbavkar & Anil, 2002). For instance, differences in sediment size can influence light quality. Whereby, in muddy sediment, light is fully attenuated at a depth of a fraction of a millimetre, and in sediment or larger grain size, it can penetrate deeper (Cartaxana et al., 2011; Vieira et al., 2013). In tropical intertidal flats, the light intensity on the sediment surface varies from less than 50 $\mu\text{mol m}^{-2}\text{s}^{-1}$ at high tide to more than 1800 $\mu\text{mol m}^{-2}\text{s}^{-1}$ at low tide, and the exposure time can be as long as 6–7 hours depending on the tidal cycle (Salleh & McMinn, 2021). Besides, during low tide exposure, sediment temperature could vary from 25 to 40°C. In addition to light and temperature, environmental cues can rapidly vary to an extreme in intertidal environments when changes in salinity occur due to desiccation and heavy rainfall. Such rapid changes in these intense environmental factors can drive the benthic diatom to develop many acclimation mechanisms to reduce the stress of highly variable light intensity. Severe light stress could impair the Photosystem II (PSII) of diatom and cause a reduction in the quantum yield. However, many can migrate vertically, hence positioning

themselves within the sediment at a depth that provides shading from excess irradiance and provides an optimal light environment for their photosynthetic activities (Cartaxana et al., 2011; Perkins et al., 2010b), hence avoiding severe photoinhibition and maintaining their presence in the intertidal habitat. In addition, diatoms can activate their photoprotective mechanism (activation of the xanthophyll cycle) when exposed to saturating irradiance. A decrease in the maximum quantum yield (F_v/F_m) in benthic diatoms is commonly observed at low tide but increased at high tide. Their ability to subsequently recover during high tide suggests that down-regulation of photosynthesis and up-regulation of photoprotection occurs, preventing PSII damage (Salleh & McMinn, 2021). Fluctuations in light intensity and temperature are often considered the two major forcings of the photosynthetic activities in diatoms (Béchet et al., 2017).

Since most chlorophyll fluorescence originates from PSII, and PSII is the most sensitive component of photosynthesis, chlorophyll fluorescence is an ideal tool to measure the short-term response of photosynthetic efficiency to changes in environmental stressors. The introduction of Pulse Amplitude Modulated (PAM) fluorometer has allowed researchers to study the activity of PSII, based on the direct determination of variable chlorophyll *a* fluorescence index (Consalvey et al., 2005; Perkins et al., 2002; Serôdio et al., 2012). This method is rapid and non-destructive and allows in-situ assessment of photoacclimation by providing rapid collection of a suite of photophysiological parameters which can be used to assess the physiological status or as a measure of stress (Consalvey et al., 2005; Perkins et al., 2010a). Furthermore, the Rapid Light Curves (RLCs) (see Ralph, & Gademann, 2005) can be constructed to understand the current photosynthetic capacity and also responses over a broad range of ambient light conditions (Consalvey et al., 2005).

Pulau Pinang is in the Northern Straits of Malacca and is Malaysia's well-developed state. The coast of Pulau Pinang has changed in the last decade due to vast developments and land reclamation. The coastal area's water quality has significantly deteriorated due to excessive organic release from industrial, residential, mariculture activities and active coastal developments. Albeit this situation, the coastal intertidal flats of Pulau Pinang pose as one of the significant benthic habitats for marine communities and fishing grounds for coastal fisheries for nearby fishing communities. Here, using a PAM fluorometer, we examined the response of MPB to salinity change in the intertidal flats of Pulau Pinang post-rainfall at low tide. We aim to determine the physiological response of MPB to salinity change, testing the hypothesis that salinity change due to rainfall inhibits photosynthesis. In addition, limited data have been available on benthic diatom communities in Malaysia, especially Pulau Pinang. Thus, this paper focuses on the photosynthetic health, species composition, and photosynthetic characteristics of benthic diatom from three intertidal flats, which are Pantai Jerejak (industrial and residential), Tanjung Bungah (residential and tourism), and Teluk Bahang (fishing and aquaculture).

MATERIALS AND METHODS

Site Description and Sampling Procedure

Pulau Pinang is in the Northern Straits of Malacca (NSoM) (Figure 1). The area has a humid, tropical climate with daily temperatures between 23–32°C (Darif et al., 2016). Sampling was conducted at intertidal flats of Pantai Jerejak, PJ (5°20'35.6" N 100°18'43.9" E), Teluk Bahang, TB (5°27'46.05" N, 100°12'11.48" E), and Tanjung Bungah, TJB (5°28'3.94"N, 100°16'42.53"E) at low tide when most of the sediment was exposed during tidal emersion. To better understand the surrounding environment at each sampling location, two random sites were sampled at least 100 m apart (labelled as Site A and B). The sampling period was established to coincide with a spring tide to maximise tidal exposure; hence porewater was collected for analysis (nutrients, pH and salinity). The sampling was conducted once in January and February, whereby heavy rainfall was observed before sampling in February, thus allowing us to determine the impact of salinity change on the photosynthetic activities of MPB.

Pantai Jerejak (PJ) is located on the east coast of Pulau Pinang. The coast of Pantai Jerejak is currently undergoing rapid developments and land reclamation along its coast. Besides, it is surrounded by residential areas, industrial zones, and the aquaculture industry from Peninsular Malaysia and Pulau Pinang. A Free Industrial Zone (FIZ) of Bayan Lepas was established in 1976. It is consisted of four stages to accommodate various light and massive factories and is located close to the study area. Discharges from factories are drained into canals, the Keluang River, and the surrounding coastal area.

Tanjung Bungah (TJB), situated in the Northwest of Pulau Pinang and is also a moderately exposed sandy beach. The sandy beach of Tanjung Bungah is known to the locals for water sports activities. Tanjung Bungah is more of a residential area than Pantai Jerejak, where houses and resorts are built to accommodate the increase in the human population in that area. The sampling site is located within the proximity of a fishing village. This coastal area houses at least 50 small-scale fishing boats (<40GRT), which operates by traditional fishers within the coast (0–5 nautical miles, Zone A) of Tanjung Bungah and adjacent areas.

Teluk Bahang (TB) is in the north of Pulau Pinang. In addition, it is surrounded by the Penang National Park and is famous for its fishing landing area for various fishing vessels and the aquaculture industry with at least ten fish cages. Apart from being the largest fishing village in Pulau Pinang, the coastal area of Teluk Bahang has undergone minimal development without any reclamation by comparison to Pantai Jerejak and Tanjung Bungah.

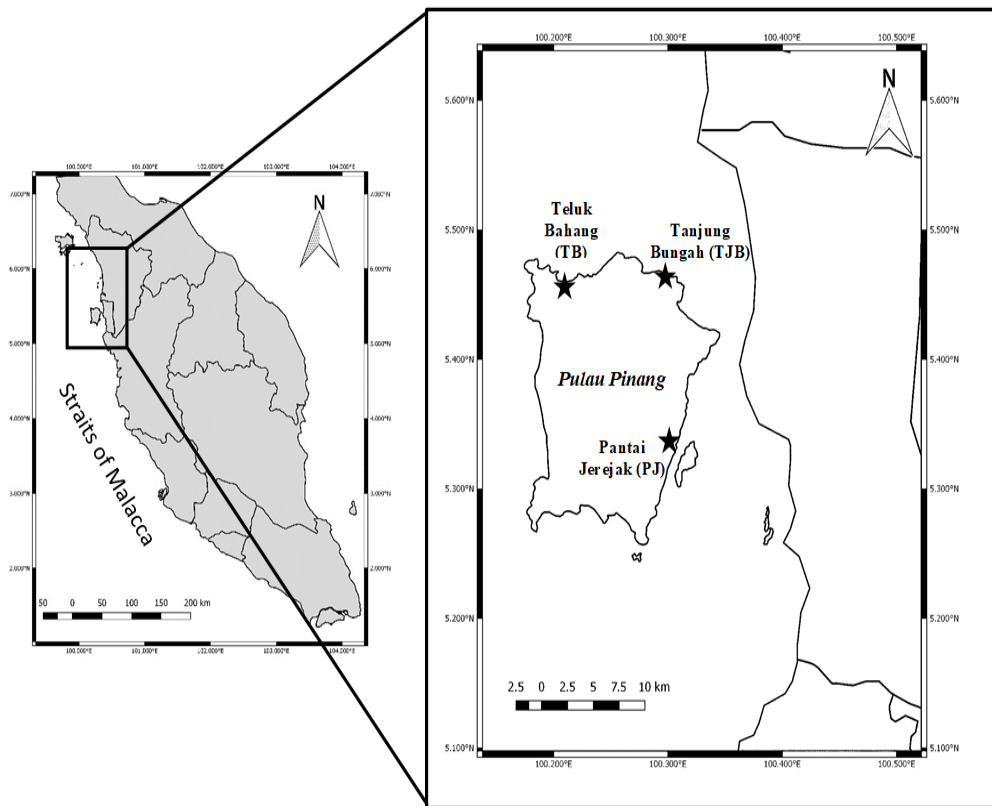


Figure 1. Sampling sites (★) on the coast of Pulau Pinang, Malaysia

Benthic Diatom Sampling and Processing

For species composition, benthic diatom samples were collected from the top 0.5 cm of sediment using a 15 mm diameter hand-pushed mini corer from the intertidal zone at each site (Jordan et al., 2010). The collected samples were stored in a polyethylene container and preserved using Lugol's iodine solution until the sample analysis (Dalu et al., 2016). The sample digestion was done using 10% hydrogen peroxide solution following Cunningham et al., (2003) and was identified and counted using the phase-contrast light microscope (Olympus BX41) at $\times 1000$ under oil immersion. Slides containing between 200 and 400 frustules were used to identify and count diatoms (in percentage relative abundance) (Dalu et al., 2016). Due to limited taxonomic information on tropical benthic diatoms, identification was mainly based on appropriate references from the temperate areas (Round et al., 1990; Stidolph, 1980; Witkowski, 2000).

Benthic Chlorophyll *a* Biomass

Benthic chlorophyll *a* was measured as a proxy for algal biomass. The chlorophyll biomass was determined following Jordan et al. (2010). For chlorophyll *a* biomass, a 30 mm diameter clear polycarbonate cores were manually pushed into the sediment and were stopped using a rubber bung and immediately returned to the temporarily established working place. The sediment for chlorophyll *a* analysis was placed in an ice-filled, light-proof container and immediately transferred to the laboratory. The top 0.5 cm of sediment was re-suspended in 10 ml methanol, thoroughly mixed, and then stored in the dark for 12 hours at 4°C. After the sediment had settled, the solvent was decanted to measure the chlorophyll *a* content using the acidification method (Holm-Hansen & Lorenzen, 1965). A spectrophotometer (UVmini-1240, Shimadzu, JAPAN) with 90% methanol as the blank was used to measure chlorophyll *a* Biomass (Strickland And Parsons 1968; Hing et al. 2012).

Environmental Parameters and Pore Water Nutrients

To determine the environmental and nutrient status at all sampling sites, environmental parameters and nutrients were recorded at low tide during each sampling event. Sediment temperature (°C) was, measured using a digital direct probe thermometer (Hanna Instrument, USA) and porewater pH was measured using a pH meter (Starter 300, OHAUS, USA). Porewater salinity and sediment surface irradiance ($\mu\text{mol photons m}^{-2} \text{s}^{-1}$) were measured using a digital refractometer (Hanna instrument, USA) and a LI-COR Biosciences LI-205A (USA) light meter, respectively. Determinations of nutrient concentrations such as nitrite ($\text{NO}_2^- - \text{N/L}$), nitrate ($\text{mg NO}_3^- - \text{N/L}$), ammonia ($\text{mg NH}_3 - \text{N/L}$), and ortho-phosphate ($\text{mg PO}_4^{3-} - \text{N/L}$) were analysed from 500 mL of pore water ($n=3$) using standard titration method (Hing et al., 2012; Strickland and Parsons, 1968). At every sampling event, three replicates of sediment cores (5 cm diameter; 1 cm depth) were also collected for sediment grain size determination (Abdullah et al., 2011). Samples for the analysis were wet sieved at 63 μm and 2000 μm mesh size that differentiated them into three different categories (mud, sand and gravel) using standard sieving methods (Folk, 1954).

PAM Chlorophyll Fluorescence Measurements

Using a Pocket Pulse Amplitude Modulation (PAM), we measured the variable fluorescence to determine the benthic diatom community's photosynthetic health. The PAM methodology followed McMinn et al. (2005). This study uses a Pocket-PAM, which might not be like other operating PAMs; care was taken when interpreting the photosynthetic output. Figueroa et al., (2013) noted that the Water-PAM has a lower detection limit ($0.025 \mu\text{g chl } a \text{ L}^{-1}$) by comparison to the Pocket-PAM ($500 \mu\text{g chl } a \text{ L}^{-1}$). Hence, the Water-PAM has higher sensitivity than the Pocket-PAM.

Three 30 mm diameter hand-pushed sediment cores were taken for photosynthetic parameter analysis on each sampling occasion. The collected sediment sample was then diluted with filtered seawater, and 10 ml of supernatant was then placed on the Pocket-PAM optical head for measurements. Photomultiplier gain (PM-Gain) settings were set to 2 before each measurement to keep the measures consistent between samples. The minimum (F_o) and maximum (F_m) fluorescence signals were determined on dark-adapted samples. To calculate the maximum quantum yield (F_v/F_m), samples were dark-adapted for 20 minutes by wrapping the containers in foil and placing them in the dark (Consalvey et al., 2005). The F_v/F_m was calculated according to (Schreiber, 2004). $F_v/F_m = (F_m - F_o)/F_m$, where F_v is the difference between F_o and F_m . F_v/F_m values are often used as a sensitive indicator of photosynthetic stress or health status for microalgae (Perkins et al., 2006).

Rapid light curves (RLCs) were taken under software control (Wincontrol, Walz) with 10 s interval duration to eight incremental irradiances at 90, 125, 190, 285, 420, 625, 820, and 1150 $\mu\text{mol photons m}^{-2} \text{s}^{-1}$ to obtain values for maximum quantum yield (F_v/F_m), relative electron transfer rate (rETR), photosynthetic efficiency (α) and photoacclimation index (E_k) (Ralph & Gademann, 2005). The rETR was calculated by multiplying the irradiance by the quantum yield measured at the end of that interval. PAR versus rETR curves was described using the non-linear regression curve fitting protocols on SPSS software (SPSS Inc. Version 21.0, IL, USA). RLCs provide an insight into an algae's physiological potential and its ability to adapt its photosynthetic apparatus to rapid changes in light intensities (Ralph & Gademann, 2005).

Data Analysis

Differences in environmental variables, abundance, biomass (benthic chlorophyll-*a* concentration), photosynthetic parameters and community indices of the sampling months and sites were tested through Two-way analysis of variance (ANOVA) followed by post hoc Tukey tests using SPSS V 21.0. Principal component analysis (PCA) was used to explore the major variation patterns in the environmental data set. The non-metric multidimensional scaling (nMDS) was used to classify the samples based on the species composition. Species data were square-root transformed to reduce the effects of dominant taxa, and the Bray-Curtis resemblance measure was applied using the PRIMER 7 software package (Clarke & Gorley, 2015). For each sample, the Shannon diversity index (H'), Species Evenness (Pielou Index), and Species Richness (Margalef Index) were calculated to characterise the species diversity in a community across locations.

RESULTS

Grain Size Composition

The grain size composition at the sampling locations and sites are shown in Figure 2. Sediment grain size was not significantly different ($p > 0.05$) across the sampling locations. The grain size composition was composed of a mixture of mud, sand, and gravel with high sand percentage at all sampling locations. However, In Tanjung Bungah (TJB), sediment composition changed significantly in February after the heavy rainfall. A higher percentage of gravel (84%) was observed in site A compared to January (13%), while the mud percentage increased in site B from 4 to 30% in February.

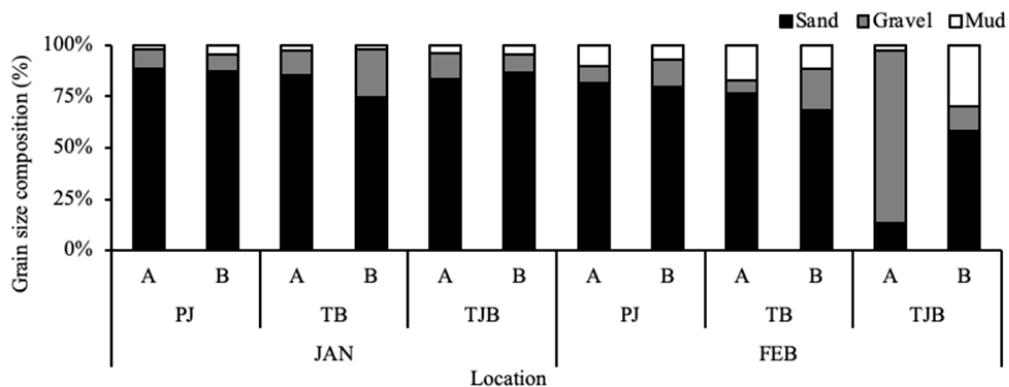


Figure 2. Grain size composition in the studied locations and sites. Grain size fractions were expressed in percentages and consisted of sand, gravel, and mud.

Environmental Parameters and Nutrients

Environmental parameters (porewater salinity and temperature) and nutrients varied significantly ($p < 0.001$) among the sampling locations across the three sampling locations and sites. As sample collection was conducted between 0730 to 0900 hrs in conjunction with low tide, cooler sediment temperature was recorded across all sampling locations by comparison to average tropical weather. Environmental parameters for the sampling sites in January and February are summarised in Table 1. A PCA of environmental data shows most locations as distinct groups (Figure 3). For instance, samples in Pantai Jerejak were spread on the upper right corner, and samples in Tanjung Bungah were located on the upper left-hand side. The first two axes accounted for 65.8% of the total variance. Pantai Jerejak was mainly characterized with positive correlation by salinity and ammonia, while Teluk Bahang by phosphate, nitrite, and nitrate.

Similarly, light availability was also low due to the sun angle, ranging from 156.08 ± 2.88 to $266.98 \pm 36.07 \mu\text{mol photons m}^{-2} \text{ s}^{-1}$ across sampling locations. Pantai Jerejak recorded the highest porewater salinity for both months (Average of site A and B, January: ~ 31.79 and February: ~ 31.00) and varied significantly ($p < 0.001$) between Teluk Bahang and Tanjung Bungah. The post-rainy condition caused a significant decrease in porewater salinity in February at all locations, with the lowest value recorded in Tanjung Bungah Site B (20.67 ± 1.15). A small stream in Tanjung Bungah and Teluk Bahang had caused a significant difference in salinity between sites A and B in both locations. Porewater pH ranged from 7.43 to 8.10 for all sampling sites. In January, the low temperature and salinity did not impact the pH, as no significant changes ($p = 0.907$) were observed during both months.

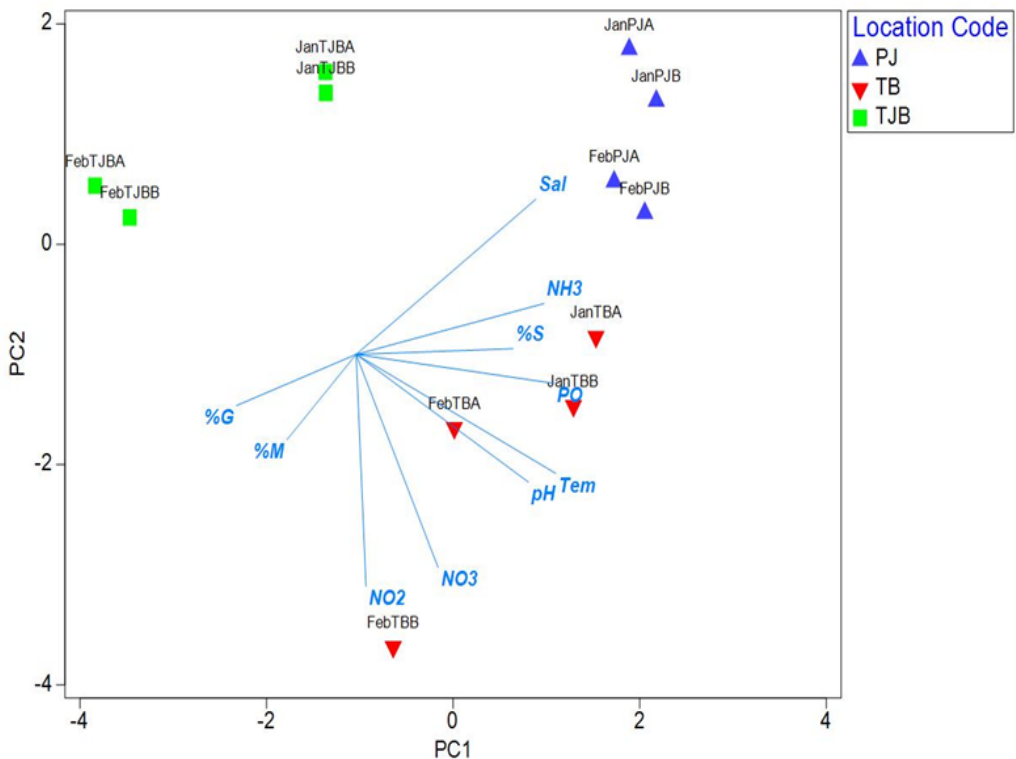


Figure 3. Principal Components Ordination (PCA) of environmental variables. Vector plots indicate the direction and size of the correlation between PC axes and variables. (*Sal*: Salinity, *NO2*: Nitrite, *NO3*: Nitrate, *PO*: Phosphate, *NH3*: Ammonia, *Tem*: Temperature, *%S*: Sand, *%G*: Gravel and *%M*: Mud)

Table 1

Environmental parameters of the sampling sites on the Pulau Pinang coastal area (Malaysia)

Location	Variables			
	ST	Light	PWS	PWpH
PJ A	29.10 ± 0.40 ^a	214.10 ± 0.00 ^a	31.57 ± 0.49 ^a	7.76 ± 0.05 ^{a,b}
PJ B	29.87 ± 0.06 ^a	214.87 ± 1.29 ^b	32.00 ± 0.00 ^a	8.01 ± 0.01 ^{b,c}
TB A	29.00 ± 0.53 ^a	166.80 ± 19.79 ^c	25.00 ± 0.00 ^a	7.70 ± 0.13 ^a
TB B	29.53 ± 0.12 ^a	156.08 ± 2.88 ^c	24.77 ± 0.68 ^a	8.09 ± 0.10 ^c
TJB A	29.00 ± 0.01 ^a	230.08 ± 22.34 ^d	25.00 ± 0.00 ^b	7.27 ± 0.06 ^a
TJB B	29.00 ± 0.01 ^a	266.98 ± 36.07 ^d	24.67 ± 0.58 ^b	7.43 ± 0.01 ^c
PJ A	29.07 ± 0.64 ^a	253.68 ± 7.24 ^a	31.00 ± 1.00 ^{a,b}	7.72 ± 0.14 ^{a,b}
PJ B	29.77 ± 0.06 ^a	266.19 ± 12.47 ^a	31.00 ± 0.00 ^a	8.10 ± 0.10 ^b
TB A	29.07 ± 0.64 ^b	659.52 ± 29.23 ^b	23.03 ± 2.00 ^b	7.81 ± 0.18 ^c
TB B	29.77 ± 0.06 ^b	637.55 ± 3.86 ^b	20.93 ± 1.01 ^b	8.03 ± 0.34 ^{a,c}
TJB A	29.20 ± 0.26 ^b	543.75 ± 192.20 ^a	22.93 ± 2.06 ^{a,b}	7.48 ± 0.02 ^{a,c}
TJB B	29.90 ± 0.10 ^b	681.73 ± 29.54 ^a	20.67 ± 1.15 ^a	7.59 ± 0.02 ^c

Note: ST indicates sediment temperature; light expressed as μmol photosynthetic photon flux density (PPFD) $\text{m}^{-2} \text{s}^{-1}$; PWS indicates porewater salinity, and PWpH indicates porewater pH. Values are reported as mean \pm SD. Same letter denotes no significant differences between different sites or months, and different letter denotes significant difference by $p < 0.05$ as determined by ANOVA and subsequent Tukey's post hoc test.

Nutrient concentrations differ significantly (ANOVA, $p < 0.001$) between all sites (Figure 4). A progressive improvement in water quality was noticeable in the locations that were further from rapid developments and mariculture activities. Teluk Bahang which is located near the mariculture facilities had the highest orthophosphate (0.385 mg/L) and nitrate (0.310 mg/L) concentrations in January. However, in February, post-rainy conditions have caused a decrease in nitrate and ortho-phosphate concentrations across all stations. Ammonia concentrations, however, were not impacted and remained low at all locations. Pantai Jerejak, located near the industrial and residential areas, recorded high ammonia concentrations (average: 0.070 mg/L).

Taxonomic Composition and Abundance of Benthic Diatom

Light microscopy examination revealed a total of 53 species of diatoms representing 27 genera across the sampling locations. Diatom dominated the benthic microalgae at all locations, though other groups (Dinoflagellate) were present at lower densities. Thus, in this study, only diatoms were observed. The genera containing the highest number of species (number given in parentheses) were *Amphora* C.G Ehrenberg ex Kützing (5), *Cocconeis*

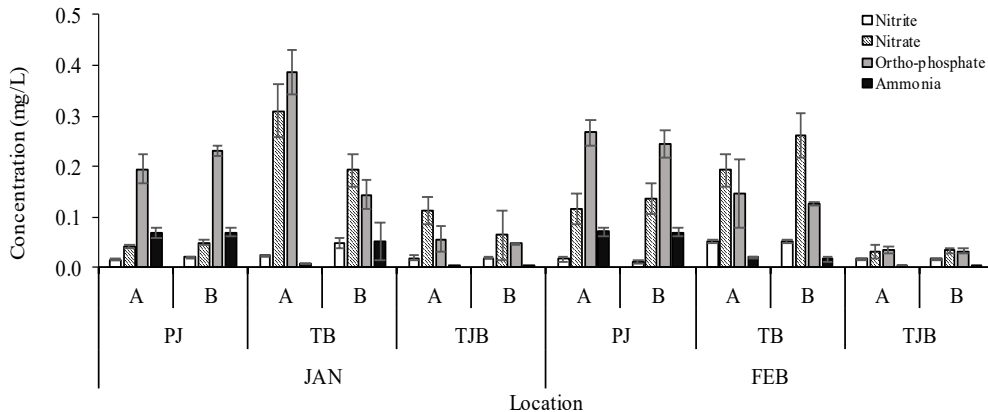


Figure 4. Porewater nutrients concentrations (mg/L) at the sampling sites on the Pulau Pinang coastal area

Ehrenberg, 1836 (6), and *Thalassionema* Grunow ex Mereschkowsky (5). Overall, the Genus *Cocconeis* was found to be the dominant genus for all locations and sites, whereby Pantai Jerejak (19.94%), Teluk Bahang (15.50%), and Tanjung Bungah (30.94%) (Figure 5). In terms of species dominance, Pantai Jerejak and Tanjung Bungah were dominated by *Cocconeis peltoides* and Teluk Bahang by *Navicula peregrina*.

The total abundance was significantly different ($p < 0.001$) among locations. Tanjung Bungah and Teluk Bahang have higher cell density by comparison to Pantai Jerejak. However, the total number of species and genera were relatively similar among locations (Table 2). The three diversity indices, species diversity (Shannon Index), evenness (Pielou Index), and richness (Margalef Index), used to differentiate both months and locations, are shown in Table 2. Due to the similarity in species composition, there were no significant differences ($p > 0.05$) between locations, sites, and sampling months. Shannon Index ranged between 2.93 to 3.12, Pielou Index was between 0.49–0.61 dan 6.72 to 5.95 for Margalef Index.

The n-MDS performed (two-dimension, stress = 0.1) on the relative abundance of 53 species collected at all locations and sites (12 samples) pointed out an apparent similarity among diatom communities of coastal intertidal areas of Pulau Pinang (Figure 6). Pantai Jerejak groups were easily distinguished from Tanjung Bungah and Teluk Bahang. The average dissimilarity between Pantai Jerejak and Teluk Bahang is 30.41%, Pantai Jerejak, and Tanjung Bungah 30.79%, Teluk Bahang and Tanjung Bungah 28.95% (SIMPER analysis).

Table 2

Species number, diversity, evenness, richness, abundance, and chlorophyll a biomass at three sampling locations during the study period

Sampling Location (Site)	Variables					
	Species Diversity (Shannon Index)	Species Evenness (Pielou Index)	Species Richness (Margalef Index)	Total Genera	Total Species	Abundance (cell x 10 ³ cm ⁻²)
PJ A	3.09 ± 0.13	0.61 ± 0.08	5.95 ± 0.13	23	39	361.04 ± 65.61
PJ B	3.02 ± 0.07	0.58 ± 0.08	6.24 ± 0.23	24	42	491.95 ± 66.92
TB A	3.00 ± 0.15	0.52 ± 0.08	6.26 ± 0.46	20	44	395.56 ± 35.83
TB B	3.08 ± 0.15	0.54 ± 0.05	6.30 ± 0.42	26	49	553.26 ± 32.33
TJB A	3.00 ± 0.17	0.52 ± 0.08	6.02 ± 0.61	24	46	524.59 ± 32.35
TJB B	3.09 ± 0.16	0.56 ± 0.10	6.22 ± 0.12	25	47	481.01 ± 111.95
PJ A	2.93 ± 0.10	0.49 ± 0.05	6.19 ± 0.51	22	41	416.31 ± 66.57
PJ B	3.20 ± 0.09	0.59 ± 0.00	6.72 ± 0.52	25	49	429.33 ± 54.47
TB A	3.16 ± 0.10	0.55 ± 0.02	6.66 ± 0.54	25	47	552.69 ± 60.82
TB B	3.25 ± 0.04	0.60 ± 0.04	6.60 ± 0.09	26	48	554.96 ± 59.38
TJB A	2.94 ± 0.13	0.47 ± 0.04	6.24 ± 0.42	24	47	549.68 ± 56.38
TJB B	3.08 ± 0.21	0.52 ± 0.11	6.54 ± 0.20	24	45	593.25 ± 116.71

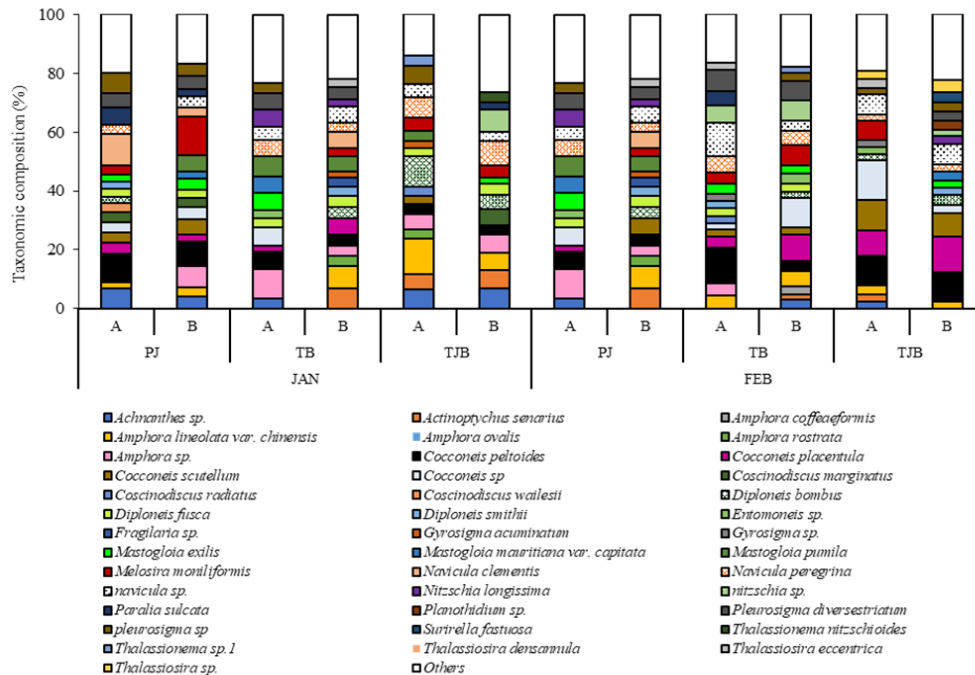


Figure 5. Taxonomic composition of benthic diatom communities of individual samples collected from three sampling locations. (The species with relative abundance above 2% are presented, with the remaining species grouped as “others”. The relative abundance is presented as the percentage of the total cells counted)

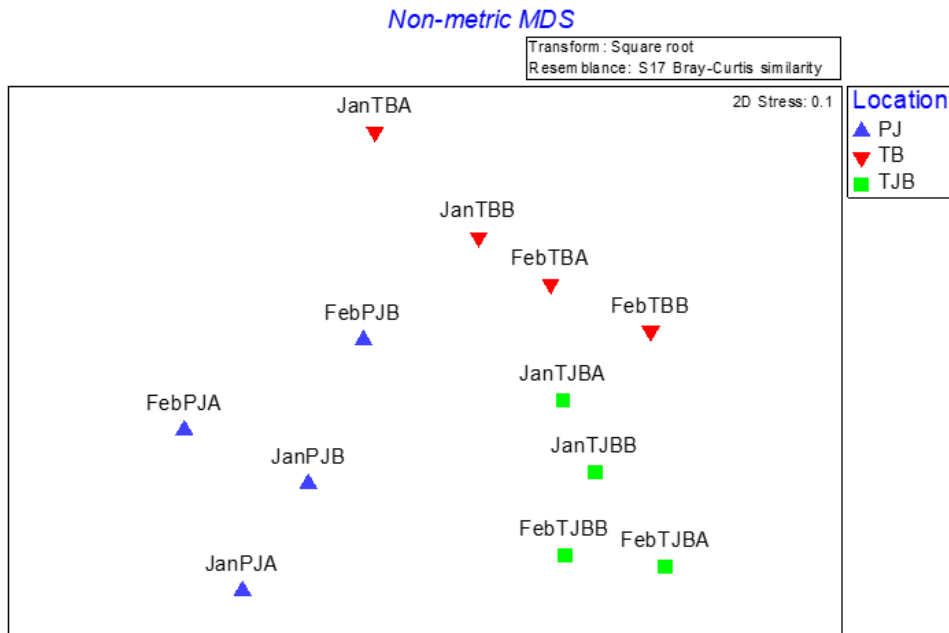


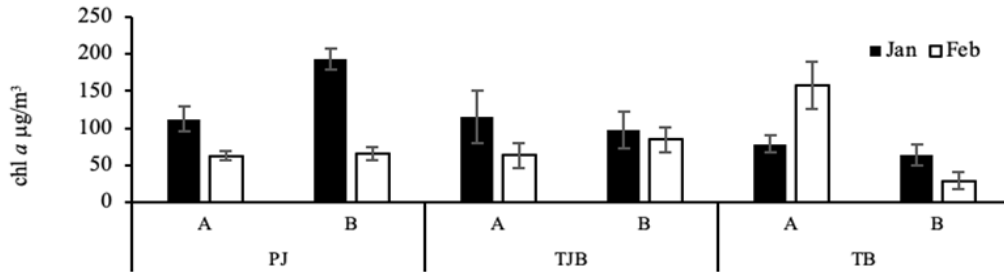
Figure 6. Classification of samples based on species composition by non-metric multidimensional scaling (nMDS)

Benthic Chlorophyll *a* Biomass and Photophysiological Parameters

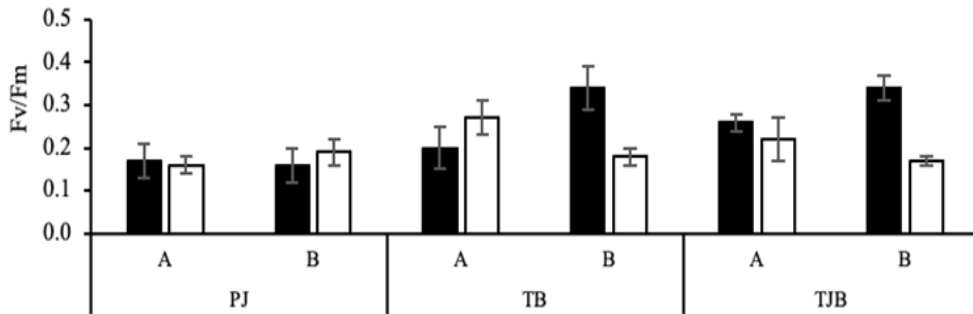
There was no significant difference ($p = 0.476$) between all sampling locations in benthic chlorophyll *a* concentration. However, significant differences ($p < 0.05$) were observed within the sampling site at each location. The highest value of $193.23 \pm 14.36 \mu\text{g}/\text{m}^3$ was recorded at Pantai Jerejak, Site A (Jan) and the lowest value at Teluk Bahang, Site B (Feb) (Figure 7a). However, the post rainy condition and the sediment composition changes have caused a significant decrease ($p < 0.05$) in chlorophyll *a* biomass, mainly in Teluk Bahang (Figure 7a).

The maximum quantum yield recorded at all locations ranged from 0.170 to 0.340, which is relatively low (Figure 7b). In general, higher values were recorded in January ($p > 0.05$) compared to February. The highest F_v/F_m values were measured in Tanjung Bungah (0.34 ± 0.03) and Teluk Bahang (0.340 ± 0.05). In contrast, the lowest F_v/F_m values ($\sim 0.16 - 0.19$) were measured at Site A (Pantai Jerejak) for both months were the highest in Tanjung Bunga (Site A (Jan): 35.51 ± 6.48 and B (Jan): 20.32 ± 5.26) but the value decreased to almost 80% in February. The $rETR_{\text{max}}$ values ranged from 3.45 to 35.51 for all locations (Figure 7c). Similar patterns were observed for the photosynthetic efficiency values with significant differences between sampling time ($p = 0.035$) and locations ($p = 0.001$). The α values were the highest in Teluk Bahang and lowest in Pantai Jerejak, with significant differences between all sampling sites ($p < 0.05$) (Figure 7d). The mean E_k (light

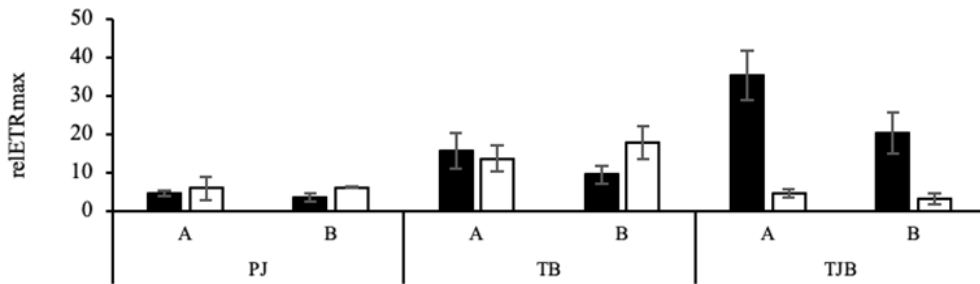
acclimation) parameter ranged between 67.96 ± 20.94 to $236.71 \pm 50.39 \mu\text{mol photons m}^{-2} \text{ s}^{-1}$, with low values recorded in Teluk Bahang (Figure 7e).



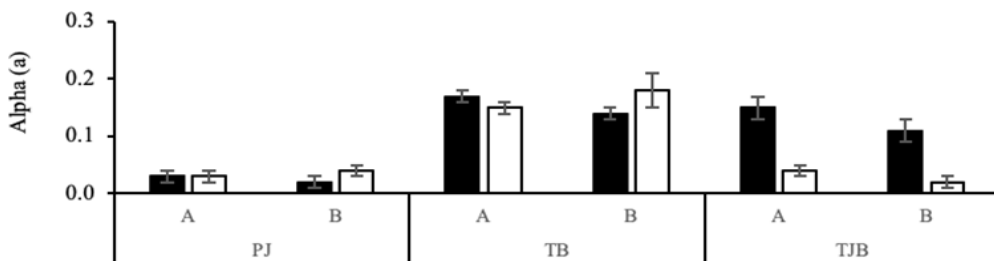
(a)



(b)



(c)



(d)

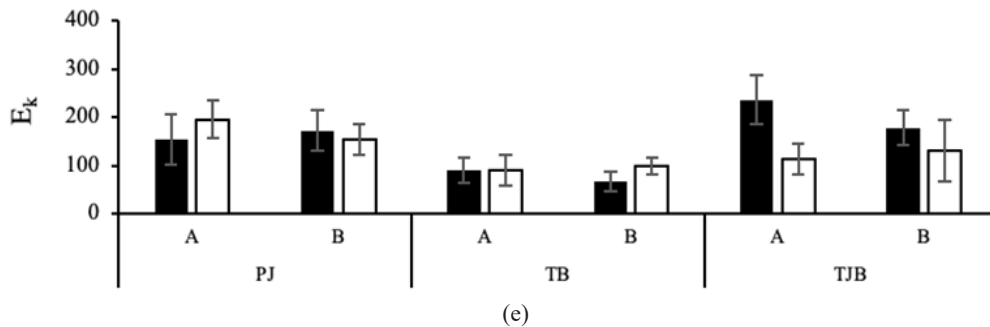


Figure 7. The measurement of a. Chl *a* biomass ($\mu\text{g}/\text{m}^3$) and photosynthetic parameters: b. Maximum quantum yield (F_v/F_m), c. relative electron transport rate (rETRmax), d. photosynthetic efficiency (α : $\mu\text{mol photons m}^{-2} \text{s}^{-1}$) and e. Photoacclimation Index (E_k : $\mu\text{mol photons m}^{-2} \text{s}^{-1}$) in the three sampling sites

DISCUSSION

Diatom Assemblages and Their Environmental Significance

Diatom is the dominant group of the intertidal microphytobenthos composition and has been noted as one of the most crucial elements in aquatic ecosystems. Despite their ecological role, very little is known about the distribution and ecology in tropical coastal intertidal flats, especially in Malaysia. The qualitative distribution of benthic diatom is one of the fundamental characteristics of intertidal flats. Like many other benthic diatom assemblages (Dalu et al., 2016), the composition and structure of benthic diatom inhabiting Pulau Pinang intertidal flats have resulted from a complex interaction of environmental variables, mainly nutrients, salinity, and temperature.

The genus *Amphora*, *Cocconeis*, and *Navicula* were noted as the dominant genus in this study, which is also prevalent in many intertidal flats, both in tropical and temperate (Du et al., 2009; Jordan et al., 2010; Salleh & McMinn, 2021). The benthic diatom inhabiting the Pulau Pinang coastal areas were distributed irregularly, and their species diversity is relatively low compared to other studies in the tropics (Chen et al., 2020). Similar low diversity was noted by McMinn et al. (2005) in the coastal areas of Pulau Pinang. Although having a similar number of species at all locations, the dominant genus/species varied between sites and months. The differences in the dominant genus/species at the stations each month can be explained by the differences in sediment nutrients, salinity, and *in-situ* temperature at each site. *Cocconeis peltoides* and *Navicula peregrina* were dominant in this study in most sampling sites. It is noted that diatom from both genera is dominant in many marine sediment surface (Mitbavkar & Anil, 2006). Genus *Cocconeis* was predominantly dominant in Tanjung Bungah, and *Navicula* was relatively evenly distributed in all locations.

The concentration of Chl *a* is generally used as an index of productivity (MacIntyre & Cullen, 1996). One of the main factors governing benthic diatom assemblages is substratum type (Cahoon et al., 1999) and is considered an essential variable in influencing benthic microalgae biomass and composition. For example, Jesus et al. (2009) noted higher diatom biomass in sandier substrates, while others contradict this finding and reported higher diatom biomass associated with muddier sediment (Du et al., 2009). Sandier substrates dominated sediment in Pantai Jerejak, and Tanjung Bungah noted higher chl *a* biomass than Teluk Bahang. Although studies have recorded correlations between chl *a* biomass and pore water nutrients (Magni & Montani, 2006). Du et al. (2009), noted that this is due to large oscillations of nutrient concentration in intertidal flats. However, in our study, chl *a* biomass was mainly influenced by salinity. Pantai Jerejak, with the highest chl *a* biomass, also recorded the most elevated salinity. The runoff from a small stream in Tanjung Bungah and Teluk Bahang has a significant influence on the diatom composition. Salinity is also one of the main parameters attributed to the diatom diversity and acts as a limiting factor influencing the community's distribution (Häusler et al., 2014).

Similarly, Darif et al. (2016) noted a considerable variation in salinity within the spatial scale (min value: 15.0 and max value 30.3) in Tanjung Bungah, which has impacted the presence of the macrobenthos. Generally, changes in the salinity of the intertidal habitats are due to the influx of freshwater from land runoff; caused by monsoon or tidal variations. Various studies have highlighted the importance of salinity (De Troch et al., 2012) gradients in marine ecosystems contributing to the spatial variability in these systems' biology (Thornton et al., 2002). Salinity and temperature were the most strongly related variables to assemblages' composition in intertidal areas. Thus, it is an essential factor in controlling diatom distribution within the coastal ecosystem in Pulau Pinang. Regardless of the many studies on the relationship between environmental variables and diatom assemblages, determining the primary regulating variables at most coastal sites is still complicated. Main environmental variables are usually interrelated with other organism distribution in coastal areas. Therefore, further studies and frequent monitoring are needed to highlight the critical relationship between biofilm taxonomic composition and water chemistry to identify species' ecological preferences.

***In-situ* Photophysiological Responses During Low Tide Exposure**

Maximum quantum yield (F_v/F_m) values can be used as a sensitive indicator of photosynthetic stress (Vieira et al., 2016). The F_v/F_m values recorded during low tide at all sites were relatively low compared to values of 0.650 for healthy microalgae (Schreiber, 2004). Although exposed to lower light intensity, F_v/F_m values in Pantai Jerejak were always low. F_v/F_m values indicated that benthic diatom in Teluk Bahang and Tanjung Bungah were relatively healthier or less impacted by environmental stressors (e.g., nutrient

limitation, harsh temperature, or high dissolved oxygen concentration) (Li et al., 2021). Also, F_v/F_m was also observed in samples with high mud content. Further analysis and prolong monitoring is needed to determine whether this is caused by grain size (shading) as vertical migration activities might be less possible as 10 s intervals in RLCs were used here, thus minimising the confounding effects of vertical cell migration (Perkins et al., 2010b; Serôdio et al., 2006).

RLCs characterised the *in-situ* physiological response to temperature and salinity changes during low tide exposure. The parameters generally declined, corroborating those changes in temperature and salinity resulted in a decrease in photosynthetic activity. However, there is no evidence of photoinhibition, possibly due to the downward migration or the presence of photoprotective pigments (Jesus et al., 2006). $rETR_{max}$ is a function of the enzymatic processes that depend on temperature, nutrient availability, light history, biochemical composition, and species composition, among other factors (e.g: Domingues et al. 2012; Laviale et al. 2015; Li et al. 2021). In this study, $rETR_{max}$ was relatively lower than other tropical areas. Similarly, low values were also recorded by McMinn et al. (2005) during their study in the coastal area of Pulau Pinang. Adding to this, as we used the Pocket-PAM, this could explain the variations. Thus, the values reported in this study are only relative.

Lower E_k values were noted for muddier sediment in Tanjung Bungah, supporting prior studies that diatom communities inhabiting muddier sediment exhibit lower light acclimation than sandier sediments (Cartaxana et al., 2016). It is noted that a well-acclimated community would be expected to have an E_k value similar to the *in-situ* PAR as they can adjust their metabolism to maximise their response to light (Serôdio et al., 2005). The photosynthetic efficiency (α) was relatively low in Pantai Jerejak, whereby *in-situ* PAR was always low in both sampling months. It is expected that low light acclimated communities would have a high α value as they are more effective at rapidly utilising light at low irradiances (Ralph & Gademann, 2005) as observed in Tanjung Bungah. Hence, this indicates that benthic diatom communities in Pantai Jerejak were severely adapted to the ambient PAR and light limitations. However, a more extended monitoring period would be needed to determine these communities' ability to adapt to their light environment. The highly variable environmental conditions in the intertidal flat are likely to cause damage to the photosynthetic apparatus, mainly through reactive oxygen accumulation (Goss & Lepetit, 2015).

CONCLUSION

In summary, this study represents a snapshot of benthic diatom communities in three coastal intertidal areas in Pulau Pinang, whereby 53 taxa were observed. The obtained results represent the photosynthetic adaptation of benthic diatom to the changes in environmental

factors, mainly salinity and temperature, while the constant low light did not significantly impact benthic diatom. The decrease in salinity resulted in lower photosynthetic capacity but did not induce photoinhibition. Our study lacks adequate long-term data to indicate specific environmental variables that significantly affect intertidal distributions of diatoms and their photosynthetic responses. However, the findings from this study provide baseline knowledge of diatom composition, photosynthetic health, and the relationship between their abundance and variations of environmental variables in the intertidal flats.

ACKNOWLEDGMENTS

This study was supported in part by a grant provided by Universiti Sains Malaysia Research Grant (1001/PBIOLOGI/8011062, 304/CDASAR/6311108 and 1001/CDASAR/8011046).

REFERENCES

- Abdullah, A. L., Yasin, Z., Shutes, B. R., & Fitzsimons, M. (2011). Sediment fallout rates in Tanjung Rhu coral reefs. *Kajian Malaysia*, 29(2), 1-30.
- Béchet, Q., Laviale, M., Arsapin, N., Bonnefond, H., & Bernard, O. (2017). Modeling the impact of high temperatures on microalgal viability and photosynthetic activity. *Biotechnology for Biofuels*, 10, Article 136. <https://doi.org/10.1186/s13068-017-0823-z>
- Cahoon, L. B., Nearhoof, J. E., & Tilton, C. L. (1999). Sediment grain size effect on benthic microalgal biomass in shallow aquatic ecosystems. *Estuaries*, 22, 735-741. <https://doi.org/10.2307/1353106>
- Cartaxana, P., Ribeiro, L., Goessling, J. W., Cruz, S., & Kühl, M. (2016). Light and O₂ microenvironments in two contrasting diatom-dominated coastal sediments. *Marine Ecology Progress Series*, 545, 35-47. <https://doi.org/10.3354/meps11630>
- Cartaxana, P., Ruivo, M., Hubas, C., Davidson, I., Seródio, J., & Jesus, B. (2011). Physiological versus behavioral photoprotection in intertidal epipelagic and epipsammic benthic diatom communities. *Journal of Experimental Marine Biology and Ecology*, 405(1-2), 120-127. <https://doi.org/10.1016/j.jembe.2011.05.027>
- Chen, M., Qi, H., Intasen, W., Kanchanapant, A., Wang, C., & Zhang, A. (2020). Distributions of diatoms in surface sediments from the Chanthaburi coast, Gulf of Thailand, and correlations with environmental factors. *Regional Studies in Marine Science*, 34, Article 100991. <https://doi.org/10.1016/j.rsma.2019.100991>
- Clarke, K. R., & Gorley, R. N. (2015). *User Manual/Tutorial*. Primer-E Ltd. http://updates.primer-e.com/primer7/manuals/User_manual_v7a.pdf
- Consalvey, M., Perkins, R. G., Paterson, D. M., & Underwood, G. J. C. (2005). PAM fluorescence: A beginners guide for benthic diatomists. *Diatom Research*, 20(1), 1-22. <https://doi.org/10.1080/0269249X.2005.9705619>
- Cunningham, L., Stark, J. J. S., Snape, I., McMinn, A., & Riddle, M. J. (2003). Effects of metal and petroleum hydrocarbon contamination on benthic diatom communities near Casey Station, Antarctica: An experimental approach. *Journal of Phycology*, 39(3), 490-503. <https://doi.org/10.1046/j.1529-8817.2003.01251.x>

- Dalu, T., Richoux, N. B., & Froneman, P. W. (2016). Distribution of benthic diatom communities in a permanently open temperate estuary in relation to physico-chemical variables. *South African Journal of Botany*, *107*, 31-38. <https://doi.org/10.1016/j.sajb.2015.06.004>
- Darif, N. A. N. A. M., Samad, N. S. N. S. A., Salleh, S., Mohammad, M., Nordin, N. A. N. A. A., Javeed, A. M. A. M. M., Jonik, M. G. G. M. G. G., & Zainudin, M. H. M. (2016). The abundance and spatial distribution of soft sediment communities in Tanjung Bungah, Malaysia: A preliminary study. *Tropical Life Sciences Research*, *27*, 71-77. <https://doi.org/10.21315/tlsr2016.27.3.10>
- De Troch, M., Vergaerde, I., Cnudde, C., Vanormelingen, P., Vyverman, W., & Vincx, M. (2012). The taste of diatoms: The role of diatom growth phase characteristics and associated bacteria for benthic copepod grazing. *Aquatic Microbial Ecology*, *67*(1), 47-58. <https://doi.org/10.3354/ame01587>
- Domingues, N., Matos, A. R., da Silva, J. M., & Cartaxana, P. (2012). Response of the diatom phaeodactylum tricorutum to photooxidative stress resulting from high light exposure. *PLoS ONE*, *7*(6), Article e38162. <https://doi.org/10.1371/journal.pone.0038162>
- Du, G., Chung, I. kyo, & Xu, H. (2016). Insights into community-based bioassessment of environmental quality status using microphytobenthos in estuarine intertidal ecosystems. *Acta Oceanologica Sinica*, *35*, 112-120. <https://doi.org/10.1007/s13131-016-0874-1>
- Du, G., Son, M., Yun, M., An, S., & Chung, I. K. (2009). Microphytobenthic biomass and species composition in intertidal flats of the Nakdong River estuary, Korea. *Estuarine, Coastal and Shelf Science*, *82*(4), 663-672. <https://doi.org/10.1016/j.ecss.2009.03.004>
- Figuerola, F. L., Jerez, C. G., & Korbee, N. (2013). Use of in vivo chlorophyll fluorescence to estimate photosynthetic activity and biomass productivity in microalgae grown in different culture systems. *Latin American Journal of Aquatic Research*, *41*(5), 801-819.
- Folk, R. (1954). The distinction between grain size and mineral composition in sedimentary-rock nomenclature. *The Journal of Geology*, *62*(4), 344-359.
- Goss, R., & Lepetit, B. (2015). Biodiversity of NPQ. *Journal of Plant Physiology*, *172*, 13-32. <https://doi.org/10.1016/j.jplph.2014.03.004>
- Grinham, A., Gale, D., & Udy, J. (2011). Impact of sediment type, light and nutrient availability on benthic diatom communities of a large estuarine bay: Moreton Bay, Australia. *Journal of Paleolimnology*, *46*, 511-523. <https://doi.org/10.1007/s10933-010-9407-7>
- Häusler, S., Weber, M., de Beer, D., & Ionescu, D. (2014). Spatial distribution of diatom and cyanobacterial mats in the Dead Sea is determined by response to rapid salinity fluctuations. *Extremophiles*, *18*, 1085-1094. <https://doi.org/10.1007/s00792-014-0686-1>
- Hing, L. S., Hii, Y. S., Yong, J. C., & Shazili, N. A. M. (2012). *A Handbook for Basic Water Quality Analysis*. Penerbit Universiti Malaysia Terengganu.
- Holm-Hansen, O., & Lorenzen, C. (1965). Fluorometric determination of chlorophyll. *ICES Journal of Marine Science*, *30*(1), 3-15. <https://doi.org/10.1093/icesjms/30.1.3>
- Jesus, B., Brotas, V., Ribeiro, L., Mendes, C. R., Cartaxana, P., & Paterson, D. M. (2009). Adaptations of microphytobenthos assemblages to sediment type and tidal position. *Continental Shelf Research*, *29*(13), 1624-1634. <https://doi.org/10.1016/j.csr.2009.05.006>

- Jesus, B., Perkins, R. G., Mendes, C. R., Brotas, V., & Paterson, D. M. (2006). Chlorophyll fluorescence as a proxy for microphytobenthic biomass: Alternatives to the current methodology. *Marine Biology*, *150*, 17-28. <https://doi.org/10.1007/s00227-006-0324-2>
- Jordan, L., McMinn, A., & Thompson, P. (2010). Diurnal changes of photoadaptive pigments in microphytobenthos. *Journal of the Marine Biological Association of the United Kingdom*, *90*(5), 1025-1032. <https://doi.org/10.1017/S0025315409990816>
- Laviale, M., Barnett, A., Ezequiel, J., Lepetit, B., Frankenbach, S., Méléder, V., Serôdio, J., & Lavaud, J. (2015). Response of intertidal benthic microalgal biofilms to a coupled light-temperature stress: evidence for latitudinal adaptation along the Atlantic coast of Southern Europe. *Environmental Microbiology*, *17*(10), 3662-3677. <https://doi.org/10.1111/1462-2920.12728>
- Li, Z., Li, W., Zhang, Y., Hu, Y., Sheward, R., Irwin, A. J., & Finkel, Z. V. (2021). Dynamic photophysiological stress response of a model diatom to ten environmental stresses. *Journal of Phycology*, *57*(2), 484-495. <https://doi.org/10.1111/jpy.13072>
- MacIntyre, H., & Cullen, J. (1996). Primary production by suspended and benthic microalgae in a turbid estuary: time-scales of variability in San Antonio Bay, Texas. *Marine Ecology Progress Series*, *145*, 245-268. <https://doi.org/10.3354/meps145245>
- Magni, P., & Montani, S. (2006). Seasonal patterns of pore-water nutrients, benthic chlorophyll a and sedimentary AVS in a macrobenthos-rich tidal flat. *Hydrobiologia*, *571*, 297-311. <https://doi.org/10.1007/s10750-006-0242-9>
- McMinn, Sellah, S., Llah, W. A. W. A., Mohammad, M., Merican, F. M. S., Omar, W. M. W., Samad, F., Cheah, W., Idris, I., Sim, Y. K., Wong, W. S., Tan, S. H., & Yasin, Z. (2005). Quantum yield of the marine benthic microflora of near-shore coastal Penang, Malaysia. *Marine and Freshwater Research*, *56*(7), 1047-1053. <https://doi.org/10.1071/MF05007>
- Mitbavkar, S., & Anil, A. (2006). Diatoms of the microphytobenthic community in a tropical intertidal sand flat influenced by monsoons: Spatial and temporal variations. *Marine Biology*, *148*, 693-709. <https://doi.org/10.1007/s00227-005-0112-4>
- Mitbavkar, S., & Anil, A. C. (2002). Diatoms of the microphytobenthic community: Population structure in a tropical intertidal sand flat. *Marine Biology*, *140*, 41-57. <https://doi.org/10.1007/s002270100686>
- Perkins, R. G., Lavaud, J., & Serôdio, J. (2010b). Vertical cell movement is a primary response of intertidal benthic biofilms to increasing light dose. *Marine Ecology Progress Series*, *416*, 93-103. <https://hal.archives-ouvertes.fr/hal-01095756/>
- Perkins, R. G., Oxborough, K., Hanlon, A., Underwood, G., & Baker, N. (2002). Can chlorophyll fluorescence be used to estimate the rate of photosynthetic electron transport within microphytobenthic biofilms? *Marine Ecology Progress Series*, *228*, 47-56. <https://doi.org/10.3354/meps228047>
- Perkins, R. G., Kromkamp, J. C., Serôdio, J., & Lavaud, J. (2010a). The application of variable chlorophyll fluorescence to microphytobenthic biofilms. In D. Suggett, O. Prášil & M. Borowitzka (Eds.), *Chlorophyll a Fluorescence in Aquatic Sciences: Methods and Applications* (Vol 4, pp. 237-275). Springer. https://doi.org/10.1007/978-90-481-9268-7_12
- Perkins, R. G., Mouget, J. L., Lefebvre, S., & Lavaud, J. (2006). Light response curve methodology and possible implications in the application of chlorophyll fluorescence to benthic diatoms. *Marine Biology*, *149*, 703-712. <https://doi.org/10.1007/s00227-005-0222-z>

- Ralph, P. J., & Gademann, R. (2005). Rapid light curves: A powerful tool for the assessment of photosynthetic activity. *Aquatic Botany*, 82(3), 222-237 <https://doi.org/10.1016/j.aquabot.2005.02.006>
- Ribeiro, L., Brotas, V., Rincé, Y., & Jesus, B. (2013). Structure and diversity of intertidal benthic diatom assemblages in contrasting shores: A case study from the Tagus Estuary. *Journal of Phycology*, 49(2), 258-270. <https://doi.org/10.1111/jpy.12031>
- Round, F., Crawford, R., & Mann, D. (1990). *Diatoms: Biology and Morphology of the Genera*. Cambridge University Press.
- Salleh, S., & McMinn, A. (2021). Response of tropical marine benthic diatoms exposed to elevated irradiance and temperature. *Biogeosciences*, 2021, 1-25. <https://doi.org/10.5194/bg-2021-18>
- Schreiber, U. (2004). *Pulse-Amplitude Modulation (PAM) fluorometry and saturation pulse method: An overview*. In G. C. Papageorgiou & Govindjee (Eds.), *Chlorophyll a Fluorescence: A Signature Photosynthesis Advances in Photosynthesis and Respiration* (Vol. 19, pp. 279-319). Springer.
- Serôdio, J., Cruz, S., Vieira, S., & Brotas, V. (2005). Non-photochemical quenching of chlorophyll fluorescence and operation of the xanthophyll cycle in estuarine microphytobenthos. *Journal of Experimental Marine Biology and Ecology*, 326(2), 157-169. <https://doi.org/10.1016/j.jembe.2005.05.011>
- Serôdio, J., Ezequiel, J., Barnett, A., Mouget, J., Méléder, V., Laviale, M., & Lavaud, J. (2012). Efficiency of photoprotection in microphytobenthos: role of vertical migration and the xanthophyll cycle against photoinhibition. *Aquatic Microbial Ecology*, 67(2), 161-175. <https://doi.org/10.3354/ame01591>
- Serôdio, J., Vieira, S., Cruz, S., & Coelho, H. (2006). Rapid light-response curves of chlorophyll fluorescence in microalgae: Relationship to steady-state light curves and non-photochemical quenching in benthic diatom-dominated assemblages. *Photosynthesis Research*, 90, 29-43. <https://doi.org/10.1007/s11120-006-9105-5>
- Stidolph, S. (1980). A record of some coastal marine diatoms from Porirua Harbour, North Island, New Zealand. *New Zealand Journal of Botany*, 18(3), 376-403. <https://doi.org/10.1080/0028825X.1980.10427255>
- Strickland, J. D. H., & Parsons, T. R. (1968). A practical handbook of seawater analysis. Pigment analysis. *Bulletin of Fisheries Research Board of Canada*, 167, 185-206.
- Thornton, D., Dong, L., Underwood, G., & Nedwell, D. (2002). Factors affecting microphytobenthic biomass, species composition and production in the Colne Estuary (UK). *Aquatic Microbial Ecology*, 27, 285-300. <https://doi.org/10.3354/ame027285>
- Vieira, S., Cartaxana, P., Máguas, C., & Da Silva, J. M. (2016). Photosynthesis in estuarine intertidal microphytobenthos is limited by inorganic carbon availability. *Photosynthesis Research*, 128, 85-92. <https://doi.org/10.1007/s11120-015-0203-0>
- Vieira, S., Ribeiro, L., Marques da Silva, J., & Cartaxana, P. (2013). Effects of short-term changes in sediment temperature on the photosynthesis of two intertidal microphytobenthos communities. *Estuarine, Coastal and Shelf Science*, 119, 112-118. <https://doi.org/10.1016/j.ecss.2013.01.001>
- Witkowski, A. (2000). Diatom flora of marine coasts I. *Iconographia Diatomologica*, 7, 1-925. <http://ci.nii.ac.jp/naid/10020542308/>



Review Article

The Impact of Calcium Chloride in Cementation Solution on Microbial Induced Calcite Precipitation: A Systematic Review

Aljohani Waad Awdah Saad¹, Siti Norathirah Mohd Anas¹, Nor Safiqah Seminin¹, Putri Nur Suhaina Naim¹, Dardau Abdulaziz², Rusea Go¹, Nor Azwady Abdul Aziz¹, Mona Fatin Syazwane Mohmed Ghazali¹ and Muskhazli Mustafa^{1*}

¹Department of Biology, Faculty of Science, Universiti Putra Malaysia, 43400 UPM, Serdang, Selangor, Malaysia

²Department of Microbiology, Faculty of Science, Federal University of Lafia, Akunza 950101, Nasarawa State, Nigeria

ABSTRACT

This review aims to quantify the impact of calcium chloride in cementation solutions on Microbial Induced Calcite Precipitation (MICP). Specific soil strength properties, such as the Unconfined Compressive Strength (UCS) test, permeability (k) and calcium carbonate content of the soil, form the basis of quantifying the test results. Relevant articles from various online databases such as Scopus, Science Direct, ProQuest Dissertations and Theses Global (PQDT), Mendeley and Google Scholar are obtained with search strings of suitable keywords. The Preferred Reporting Items for Systematic Reviews and Meta-Analyses (PRISMA) were used to screen and select related articles based on exclusion and inclusion characteristics. This review shows a positive correlation between calcium concentrations and soil strength properties, where higher concentrations of calcium solutions induce

stronger bonding between soil particles due to better calcite precipitation. However, we also note a reversed correlation when the concentration of calcium solutions is higher than 1 M. This review also verifies that the MICP process enhances soil strength using optimum calcium chloride concentration to avoid soil brittleness. This result benefits other fields, such as agricultural and soil engineering.

ARTICLE INFO

Article history:

Received: 16 March 2022

Accepted: 18 July 2022

Published: 06 March 2023

DOI: <https://doi.org/10.47836/pjst.31.2.14>

E-mail addresses:

waadalawda@hotmail.com (Aljohani Waad Awdah Saad)

sitiorathirahma99@gmail.com (Siti Norathirah Mohd Anas)

nursafiqah612@gmail.com (Nor Safiqah Seminin)

suhaina.naim@gmail.com (Putri Nur Suhaina Naim)

aliyuabdulaziz23@gmail.com (Dardau Abdulaziz)

rusea@upm.edu.my (Rusea Go)

azwady@upm.edu.my (Nor Azwady Abd Aziz)

mfsyazwane_ghazali@yahoo.com (Mona Fatin Syazwane Mohmed Ghazali)

muskhazli@upm.edu.my (Muskhazli Mustafa)

*Corresponding author

Keywords: Calcite, calcium chloride, permeability, polymorph, unconfined compressive strength, vaterite

INTRODUCTION

Immense awareness about sustainability in most aspects of life in recent times has influenced the curiosity of researchers worldwide regarding microbial-induced calcite precipitation (MICP) and the bio-cementation process (Chuo et al., 2020). Microbial activity induces and regulates chemical reactions in loose granular soil, solidifying its structure with incorporated tensile strength and a greater density (Duo et al., 2018). The crucial components for MICP application are bacteria, urea and calcium chloride. The bacteria present in the soil secrete specific enzymes for reactions, such as carbonic anhydrase and urease (Wei et al., 2015), to convert specific chemical substances into carbonate ions for MICP. Al Qabany et al. (2012) report that passive precipitation is the most preferred type of MICP technique used in research, where the pH value of the soil system is regularly changed as the hydrolysis of urea is influenced by bacterial activity.

According to Chahal et al. (2011), calcium chloride (CaCl_2) acts as a calcium source for the growth of respective bacteria, which are added to the media for calcium carbonate (CaCO_3) precipitation. The existence of calcium ions in the soil system induces the formation of CaCO_3 , which is established by the presence of CaCl_2 in the media (Golovkina et al., 2020; Lapierre et al., 2020). However, the use of commercial CaCl_2 in MICP applications can have disadvantages as (i) it is not cost-efficient, (ii) it can lead to a decrement in chemical efficiency, and (iii) it showcases corrosive characteristics (DeJong et al., 2006; Khadim & Zheng, 2017). Chemical efficiency in MICP is defined as the amount of precipitated calcite compared to the amount of pure chemical substances like urea and CaCl_2 percolated into the soil. However, Al Qabany et al. (2012) report that the best input rate of chemical efficiency with the use of pure urea and analytical grade CaCl_2 in creating MICP condition can reach up to 0:084 mol/L/h. However, it can drop to half the rate even within similar conditions. These findings indicate that there is no guarantee of high efficiencies of MICP even with commercial CaCl_2 .

There are still questions with inconclusive answers in MICP research studies, specifically on the impact of calcium chloride in the cementation solution in MICP. This systematic review thus intends to answer related questions by searching for alternative calcium sources such as mollusc shells, limestone powder, seawater and eggshells. This systematic literature review aims to explore more sustainable methods for MICP to be used in the future by setting the objectives to compare the impact of CaCl_2 on two properties of MICP, namely, (i) permeability values test and (ii) the Unconfined Compressive Strength (UCS).

MATERIALS AND METHODS

Literature Search Strategy

This study is focused on research on MICP processes that induce soil strength properties. The primary literature search was done using Scopus, Science Direct, Mendeley, Google Scholar, ProQuest Dissertations and Theses Global (PQDT) online databases. Search strings for terms in the title, keywords, or abstract were employed using the Boolean operators “AND” or “OR,” as shown in Table 1. The most effective search strategy that minimises irrelevant article results was found to be limiting search results to titles and abstracts. Publications published between 2011 and early 2021 were found using this search strategy, which also maintained data accuracy.

Table 1

Search strategy and search string terms used in PRISM

Num.	Subject	Search string
1.	Microbial Induced Calcite Precipitation (MICP)	‘Microbial induced calcite precipitation’ ‘Microbial induced calcium carbonate precipitation’ ‘Biocementation’ ‘Biom mineralization’
2.	Calcium	‘Calcium’ ‘Calcium chloride influence’ ‘Calcium chloride factor’ ‘Calcium shell’ ‘Calcium powder’
3.	Soil Strength Properties	‘Soil strength properties’ ‘Mechanical properties’ ‘Hydraulic properties’ ‘Unconfined Compressive Strength (UCS)’ ‘Permeability’

Screening Process

Inclusion criteria were used to finalise the research articles to fulfil the objectives of this study. Hence, published studies that did not meet the criteria from previous studies and review papers were excluded. A total of 300 published studies were screened by title, abstract and full-text evaluation. Briefly, 98 % of the screened English-language articles were rejected in the screening phase, and only six were included in the final screening stage. The search results were filtered based on the inclusion criteria throughout the screening process. The published articles were included if they (i) used the MICP

mechanism, (ii) used different calcium concentrations, (iii) used alternative calcium sources, (iv) reported Unconfined Compressive Strength (UCS) test data, (v) reported permeability test data, (vi) reported CaCO₃ content data, and (vii) reported polymorph produced. The PRISMA is shown in Figure 1, where all summaries of steps and exclusion explanations used to limit the search results further are included.

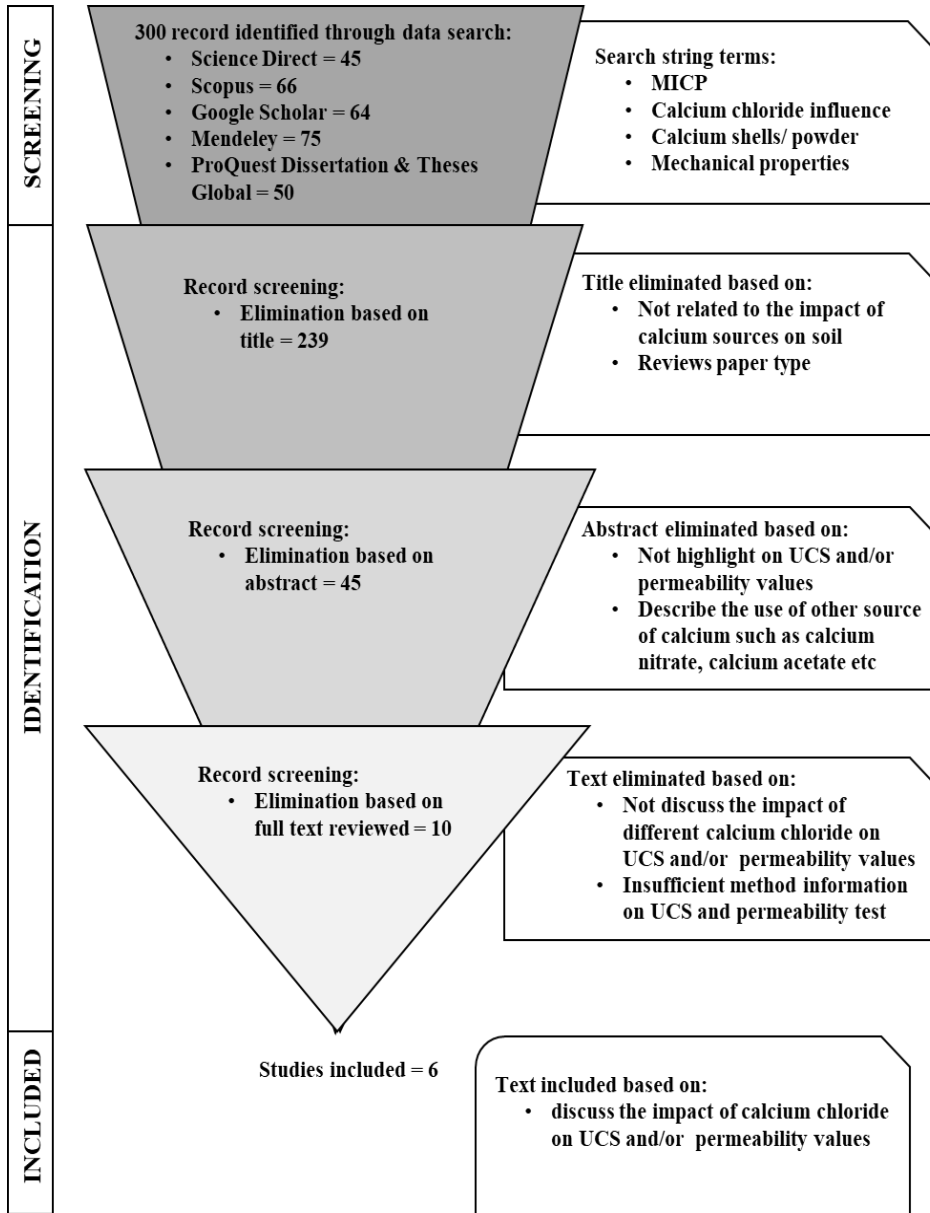


Figure 1. Preferred Reporting Items for Systematic Reviews and Meta-Analyses (PRISMA) for review on the impact of calcium chloride on MICP in soil

Data Extraction

A total of 6 publications that met the requirements were published in the last decade. All of these were used to evaluate CaCl₂'s impact on soil permeability, and the rest were further used to assess the impact of CaCl₂ on the Unconfined Compressive Strength. As a result, these articles have qualitative and quantitative data that may be used for further evaluation.

RESULTS AND DISCUSSION

A total of 300 articles were found using primary search string terms in five online databases. The screening process was based on titles, abstracts, and full text. In this process, 239 articles were rejected upon title screening, 45 were rejected upon abstract screening, and ten were rejected upon full-text screening, resulting in only six studies being included in this review. The oldest research article in this study was published in 2013, while the newest one was published in 2019. Four out of the final six articles used *Sporosarcina pasteurii* in their MICP studies, except for Soon et al. (2014) and Cheng et al. (2014), which used *Bacillus megaterium* and *Bacillus* sp., respectively (Table 2). Most of the included studies produced the most stable polymorph of CaCO₃, known as calcite, and only two articles reported the production of another polymorph of CaCO₃, vaterite, by *Sporosarcina pasteurii* (Liang et al., 2020; Al Qabany & Soga, 2013).

CaCl₂ Impact on Soil Permeability

Different concentrations of CaCl₂ influence soil particles in MICP treatment differently in terms of soil strength properties. This review extracted and analysed data on specific soil strength properties based on the UCS and permeability tests. Table 2 summarises the permeability test data extracted from selected studies.

Table 2

Types of calcifying bacteria, CaCl₂ polymorph, permeability and Unconfined Compressive Strength test values produced in MICP in the soil samples treated with different concentrations of calcium chloride

Studies	Bacteria	CaCO ₃ Polymorph	Calcium Chloride Concentration (M)	Permeability (m/s)	Unconfined Compressive Strength (kPa)
Soon et al. (2014)	<i>Bacillus megaterium</i>	Calcite	1	5.1 x 10 ⁻⁸	78
			0.5	0.5 x 10 ⁻⁸	130
			0.25	1.4 x 10 ⁻⁸	120
Liang et al. (2020)	<i>Sporosarcina pasteurii</i>	Vaterite	0.4	1.12 x 10 ⁻⁴	1454
				1.7 x 10 ⁻⁴	852
				1.5 x 10 ⁻⁴	984

Table 2 (Continue)

Studies	Bacteria	CaCO ₃ Polymorph	Calcium Chloride Concentration (M)	Permeability (m/s)	Unconfined Compressive Strength (kPa)
Al Qabany and Soga (2013)	<i>Sporosarcina pasteurii</i>	Vaterite	1	1.7 x 10 ⁻⁵	822
			0.5	5.7 x 10 ⁻⁶	1659
			0.25	1.9 x 10 ⁻⁶	1413
Choi et al. (2017)	<i>Sporosarcina pasteurii</i>	Calcite	0.3	6.0 × 10 ⁻⁶	1110
Cheng et al. (2014)	<i>Bacillus</i> sp.	Calcite	0.01 M	5.7 × 10 ⁻⁵	227
Shahrokhi-Shahraki et al. (2014)	<i>Sporosarcina pasteurii</i>	Calcite	1	2.6 x 10 ⁻⁵	240
			0.5	1.7 x 10 ⁻⁴	80
			0.25	1.8 x 10 ⁻⁴	75
			0.1	2.1 x 10 ⁻⁴	50

Generally, the main factors contributing to the permeability coefficient are the soil type, porosity, density, and soil composition (Koestel et al., 2018). The permeability test is one of the most important assessments used to determine the ability of MICP treatment to bind soil particles together. Despite the fact that each paper reported on a different experimental setup and type of sand, all data show that permeability is inversely proportional to CaCl₂ concentration up to 0.5 M (Table 2). The lowest measured permeability test value at 0.5 M CaCl₂ is 0.5 x 10⁻⁸ m/s (Soon et al., 2014), and the highest measured permeability test value at 0.5 M CaCl₂ is 5.7.1 x 10⁻⁴ m/s (Al Qabany & Soga, 2013). Nevertheless, it depends on the type of bacteria, concentration of CaCl₂ and type of CaCO₃ polymorph. The gap between adjacent soil structures is reduced at higher concentrations of cementation solution (1.5–2.5 mol/L) based on the CaCO₃ that bonds to the exterior of soil particles and clogged pores. More CaCO₃ is involved in the consolidating and interconnecting processes, which improves the structural rigidity of the soil system (Duo et al., 2018).

The reduction in permeability value is attributed to CaCO₃ polymorph distribution, particularly calcite precipitations at particle-particle interactions, which cause the opening of pores that inhibit water flow (DeJong et al., 2010; Duo et al., 2018). Even though there are no changes in the specimens' extrinsic appearance when MICP is used, the calcite precipitation distribution pattern at the pore level can produce significant permeability values compared to vaterite (Al Qabany & Soga, 2013). Because calcite and vaterite are different solid-state phases of CaCO₃, the impact of MICP on permeability varies. Calcite is a thermodynamically stable CaCO₃ polymorph that can withstand soil grain pressure

(Ganendra et al., 2014), while vaterite is a minor, metastable, and in a transitional phase to form a much stable polymorph, the calcite (Hua et al., 2007).

Soon et al. (2014) and Al Qabany and Soga (2013) report that the permeability data trend is violated when it reaches a threshold of CaCl₂ concentration, specifically at 1 M, and report permeability values of $5.1 \times 10^{-8} \text{ ms}^{-1}$ and $1.7 \times 10^{-5} \text{ ms}^{-1}$, respectively. The permeability data increased as the calcium concentration increased from this threshold value of 1 M of CaCl₂. These two articles prove the concept of an optimum cementation solution concentration in enhancing the strength of MICP-treated soil specimens, with the ideal cementation solution concentration ranging between 0.5–1 M of CaCl₂. A higher CaCl₂ concentration solution led to less homogenous precipitation at both the micro and macro scales (Soon et al., 2014). Although the reported samples were not entirely cemented, the early decline pattern seen in the observed permeability data of the 1 M samples is associated with localised clogging rather than an overall loss in permeability (Al Qabany & Soga, 2013). The use of a greater concentration of cementation solution did not only lead to denser calcite structures but also resulted in a rapid reduction of bacterial activity. The reduction in bacterial activity is explained by the urea compound becoming less abundant in the encapsulated bacteria to catalyse hydrolysis (Al Qabany et al., 2012).

A similar negative impact of calcium concentration beyond the optimum range on bacterial growth was also reported by Chunxiang et al. (2009); whereas calcium ions surround the cell membrane, bacterial enzyme digestion and the consequent changes in the properties of the CaCO₃ layer are inhibited with restriction of urea passage. The same trend was reported by Nemati et al. (2005), where an increase in the concentration of CaCl₂ led to greater conversion to CaCO₃, with the highest conversion of 99 % observed in cultures containing 25 and 30 g/L CaCl₂. A concentration of 40 g/L CaCl₂ resulted in a lag phase in CaCO₃ synthesis with a decreased conversion rate of 80 %. It demonstrates that concentrations of CaCl₂ higher than the threshold have an impeding effect on bacterial activity. High quantities of urea hinder bacterial growth, suggesting the vitality of an optimum CaCl₂ concentration, as aforementioned in the MICP technique, to improve soil structure (Nemati et al., 2005).

To overcome this problem, Chunxiang et al. (2009) suggested that both cementation solution and bacterial solution be introduced simultaneously since the bacterial cell wall is composed of numerous negative charges (Dardau et al., 2021) and thus, if positively charged ions are introduced first without urea, Ca²⁺ ions spontaneously adhere to the bacterial surface (even in the presence of urea), severely influencing and delaying bacterial activity. Thus, enzyme degradation is hindered no matter when urea is added, as bacterial surfaces would be coated with Ca²⁺, which impairs urea passage. In summary, the efficiency of the MICP process can be enhanced by using a low concentration of CaCl₂ and injecting both CaCl₂ and urea solutions at once in the soil sample. On the other hand, Chuo et al. (2020)

recommend higher concentrations of bio-cementation solution or longer treatment cycles to be used in MICP experiments to improve soil liquefaction susceptibility. The same pattern was also seen in the study by Duo et al. (2018), where the permeability coefficient of sand samples treated with 0.5, 1.0, 1.5, 2.0, and 2.5 M cementation solution dropped by 42.6, 71.3, 97.5, 98.6, and 99.1 %, respectively, as compared to traditional aeolian sand through eight treatment cycles.

The Impact of CaCl₂ on the Unconfined Compressive Strength

The effectiveness of MICP treatment to bind soil particles together is also evaluated using the UCS test. The highest UCS test value (1659 kPa) was attained when 0.5 M CaCl₂ was used in the cementation solution (Al Qabany & Soga, 2013). As with permeability, all experiments from selected articles were conducted in different configurations with various types of sand. However, similar patterns of increasing strength were discovered to be obtained. The combined data from four studies, Choi et al., 2017, Cheng et al., 2014; Liang et al., 2020 and Al Qabany & Soga, 2013, suggest the direct impact of incremental CaCl₂ concentrations on the UCS values (Table 2). In a study by Duo et al. (2018), the same trend was reported where the soil samples were treated with 0.5, 1.0, 1.5, 2.0, and 2.5 M solidification solutions for the UCS test with observed values of 1.71, 4.93, 6.64, and 3.69 MPa, respectively.

Although the UCS value reported in selected studies and previous studies varies depending on the type of test soil and CaCl₂ concentration, the MICP-treated sand shows an improvement in shear strength compared to the control. Soon et al. (2017) reported a 25–100 % improvement in a blend of coarse and fine grains sand, whereas Lu et al. (2010) published studies on fine sands that improved by 25–120 %. It was proposed that in any type or condition of sand, as long as pores exist between coarse grains, it will create a favourable environment for forming calcite bonds at particle-particle contacts, thereby improving the soil's shear strength (Ng et al., 2013). Most of the carbonate ions produced by urea hydrolysis combine with calcium ions to form CaCO₃ polymorphs in the intergranular spaces of soil columns (Okwadha & Li, 2010), leading to an improvement of the shear strength properties. Calcite particles (one of the polymorphs) that cover soil grains and deteriorated calcite crystal fines formed by shearing cause an increase in overall particle roughness, significantly impacting the UCS values (Feng & Montoya, 2016).

They also report that relatively high cementation solution concentrations result in increased calcite precipitation, manifested as large crystal formation on soil particles and localised deposition. Shahrokhi-Shahraki et al. (2015) state that more brittle responses are caused by stiffer, higher solution concentrations where the maximum UCS test value of 240 kPa was achieved in this report with a 1 M CaCl₂ concentration in soil capillary pores. The shear strength of samples treated with 0.25 M cementation reagent improved by

26–57 %, while the UCS of specimens treated with 0.5 M reagent improved by 25–69 %. Good correlations with UCS improvement were observed between 1.0 and 2.5 % calcite content ($R^2 = 0.87$), with the maximum enhancement in the UCS achieved at about 2.5 % calcite content (Soon et al., 2014).

Solutions with higher concentrations of calcium and urea are hypothesized to promote the binding between soil particles due to higher levels of calcite precipitation (Cui et al., 2021). The strength of bio-cemented calcareous soil also appeared to rise as the cementation level increased (Al Qabany et al., 2012). The MICP treatment may significantly improve the rigidity of calcareous soil (Cui et al., 2021) due to calcium carbonate cementation. However, Soon et al. (2014) and Al Qabany and Soga (2013) report that any increment of CaCl₂ beyond 0.5 M will reduce the UCS value to 40 % and 50 %, respectively. Studies by Al Qabany and Soga (2013) and Soon et al. (2014) showed a decrement in UCS test values when a 1 M calcium chloride solution was used in their experiments. When a high-concentration treatment (1 M) was employed, they observed a less homogenous calcite deposition pattern with bigger crystal sizes.

This proposed pattern was supported by Velpuri et al. (2016), as the calcite precipitation rate is affected by calcium concentration. Calcite precipitation occurs with increasing calcium ion concentration and remains relatively unchanged under specified urea and bacterial conditions. Nevertheless, with increasing calcium ion concentration levels, injection blockage became more severe, which made it harder to achieve uniformly cemented soil samples. Sheikh and Atmapoojya (2022) also indicated that crystal growth grows in size as the concentration of the cementation solution increases, yet inhibiting a homogeneous precipitation process. Al Qabany and Soga (2013) reported that the increased sample strength observed while using a low-concentration solution is linked to a better distribution or bigger proportion of deposition at particle interactions, resulting in more uniform cementation in the samples. Whiffin et al. (2007) created cemented samples with a 1 M solution, and when compared to the 0.25 M data (Al-Qabany et al., 2012), the strength values of the 1 M samples are lower. It is worth noting that Whiffin et al. (2007) work on the cemented core samples, as compared to Al-Qabany et al. (2012) studies on non-cemented samples. It is because the homogenous distribution of precipitated calcium carbonate all a uniform layer surrounding the soil particles, which leads to a higher UCS value (DeJong et al., 2010; Gebru et al., 2021).

It is also reported that inconsistently sized CaCO₃ distribution patterns with bigger crystal sizes are formed when the cementation solutions with higher CaCl₂ concentrations are used (Soon et al., 2014). It could support the promising results (better soil strength properties) obtained with MICP processes that used alternative calcium sources at low calcium concentrations compared to the commercial CaCl₂ (1 M). Figure 2 illustrates different sizes of CaCO₃ deposition in soil structures at various chemical concentrations.

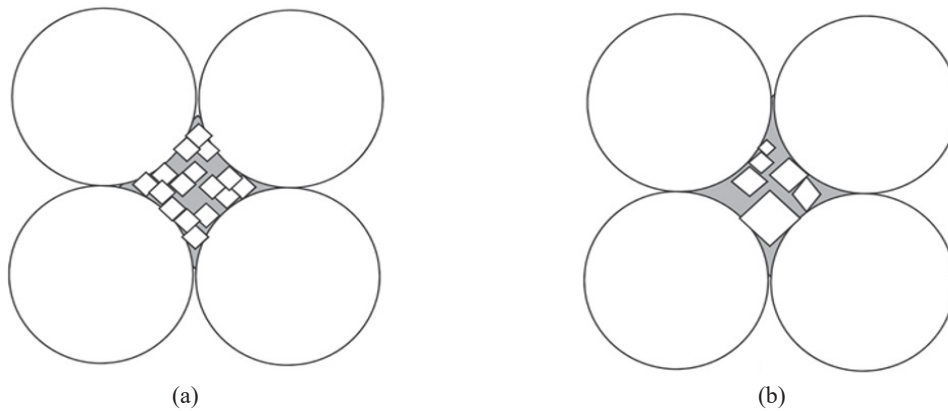


Figure 2. Pore blockage as an outcome of MICP utilising (a) a lower chemical concentration and (b) a higher chemical concentration is depicted in a conceptual illustration (Al Qabany & Soga, 2013)

The unfavourable effect of the 1 M cementation solutions on soil properties was also reported by Soon et al. (2014), where no discernible difference in shear strength or hydraulic conductivity was recorded post-treatment. Additionally, measurements of ammonium concentration and pH values indicated no observable urease activity. This claim is also supported by Whiffin (2004) during the first 8 hours of the cementation process in the experiment, when a two-fold rise in calcium concentration reduced urease activity by 10 %, with no impact beyond that. Al Qabany and Soga (2013) also noticed that the precipitation patterns indicated that greater amounts of cementation solution not only lead to thicker calcite structures but may also result in a rapid reduction of bacterial activity as urea becomes less accessible to the enclosed bacterial cells to catalyse hydrolysis. Therefore, it was proposed to use a minimal cementation solution that can be applied with uniform CaCO_3 deposition and many nucleation spots to gradually raise the consolidation solution to minimise the number of injections. Although this strategy may sound theoretically relevant, a further experimental study is required to demonstrate its efficacy.

In contrast, a controversial strategy has been proposed for applying CaCl_2 and urea to enhance the MICP process based on supersaturation. Bosak and Newman (2005) proposed that smaller deposits of CaCO_3 can be achieved through rapid nucleation by using higher cementation solutions and bacterial concentrations. Al-Thawadi et al. (2012) tested this concept and reported that ureolytic bacteria help precipitate calcite crystals as nanocrystalline clusters (specifically smaller particles) when exposed to high urea and calcium ions. These particles will enhance the solidification of soil structures by constructing bridge points between soil grains. Smaller CaCO_3 particles are thus formed due to the rise in supersaturation index (SI) in the soil system, leading to smaller calcite crystal formations (De Muynck et al., 2010; Mujah et al., 2019).

CONCLUSION

The CaCl₂ concentrations observed are directly proportional to soil strength properties. Greater concentrations of CaCl₂ lead to a rapid loss in permeability and elevate the UCS values. However, an optimum range of CaCl₂ concentrations in cementation solutions needs to be observed, as higher CaCl₂ concentration above a threshold will lead to localised clogging and inhibition of bacterial activity. Consequently, the heterogeneity of the calcite distribution in the soil will be disturbed with a reduction in the soil strength.

ACKNOWLEDGEMENT

Universiti Putra Malaysia supported this work with financial support through Geran Universiti Putra Malaysia (Grant No: GP-IPS/2020/9691000). The authors express their immense gratitude to the unwavering support of Universiti Putra Malaysia, all research assistants, and laboratory science officers of the Department of Biology, Faculty of Science, Universiti Putra Malaysia, for providing all the necessary assistance required.

REFERENCES

- Al Qabany, A., & Soga, K. (2013). Effect of chemical treatment used in MICP on engineering properties of cemented soils. *Geotechnique*, 63(4), 331-339. <https://doi.org/10.1680/geot.SIP13.P.022>
- Al Qabany, A., Soga, K., & Santamarina, C. (2012). Factors affecting efficiency of microbially induced calcite precipitation. *Journal of Geotechnical and Geoenvironmental Engineering*, 138(8), 992-1001. [https://doi.org/10.1061/\(ASCE\)GT.1943-5606.0000666](https://doi.org/10.1061/(ASCE)GT.1943-5606.0000666)
- Al-Thawadi, S., Cord-Ruwisch, R., & Bououdina, M. (2012). Consolidation of sand particles by nanoparticles of calcite after concentrating ureolytic bacteria *in situ*. *International Journal of Green Nanotechnology: Biomedicine*, 4(1), 28-36. <http://dx.doi.org/10.1080/19430892.2012.654741>
- Bosak, T., & Newman, D. K. (2005). Microbial kinetic controls on calcite morphology in supersaturated solutions. *Journal of Sedimentary Research*, 75(2), 190-199. <http://dx.doi.org/10.2110/jsr.2005.015>
- Chahal, N., Rajor, A., & Siddique, R. (2011). Calcium carbonate precipitation by different bacterial strains. *African Journal of Biotechnology*, 10(42), 8359-8372. <https://doi.org/10.5897/AJB11.345>
- Cheng, L., Shahin, M. A., & Cord-Ruwisch, R. (2014). Bio-cementation of sandy soil using microbially induced carbonate precipitation for marine environments. *Geotechnique*, 64(12), 1010-1013. <https://doi.org/10.1680/geot.14.T.025>
- Choi, S. G., Chu, J., Brown, R. C., Wang, K., & Wen, Z. (2017). Sustainable biocement production via microbially induced calcium carbonate precipitation: use of limestone and acetic acid derived from pyrolysis of lignocellulosic biomass. *ACS Sustainable Chemical and Engineering*, 5, 5183-5190. <https://doi.org/10.1021/acssuschemeng.7b00521>
- Chunxiang, Q., Jianyun, W., Ruixing, W., & Liang, C. (2009). Corrosion protection of cement-based building materials by surface deposition of CaCO₃ by *Bacillus pasteurii*. *Materials Science and Engineering C*, 29(4), 1273-1280. <https://doi.org/10.1016/j.msec.2008.10.025>

- Chuo, S. C., Mohamed, S. F., Setapar, S. H. M., Ahmad, A., Jawaid, M., Wani, W. A., & Ibrahim, M. N. M. (2020). Insights into the current trends in the utilization of bacteria for microbially induced calcium carbonate precipitation. *Materials*, *13*(21), 1-28. <https://doi.org/10.3390/ma13214993>
- Cui, M. J., Zheng, J. J., Chu, J., Wu, C. C., & Lai, H. J. (2021). Bio-mediated calcium carbonate precipitation and its effect on the shear behaviour of calcareous sand. *Acta Geotechnica*, *16*, 1377-1389. <https://doi.org/10.1007/s11440-020-01099-0>
- Dardau, A. A., Mustafa, M., & Aziz, N. A. A. (2021). Microbial-induced calcite precipitation: A milestone towards soil improvement. *Malaysian Applied Biology*, *50*(1), 11-27. <https://doi.org/10.55230/mabjournal.v50i1.9>
- De Muynck, W., Verbeken, K., De Belie, N., & Verstraete, W. (2010). Influence of urea and calcium dosage on the effectiveness of bacterially induced carbonate precipitation on limestone. *American Society for Microbiology*, *36*(2), 99-111. <https://doi.org/10.1016/j.ecoleng.2009.03.025>
- DeJong, J. T., Fritzges, M. B., & Nüsslein, K. (2006). Microbially induced cementation to control sand response to undrained shear. *Journal of Geotechnical and Geoenvironmental Engineering*, *132*(11), 1381-1392. [https://doi.org/10.1061/\(ASCE\)1090-0241\(2006\)132:11\(1381\)](https://doi.org/10.1061/(ASCE)1090-0241(2006)132:11(1381))
- DeJong, J. T., Mortensen, B. M., Martinez, B. C., & Nelson, D. C. (2010). Bio-mediated soil improvement. *Ecological Engineering*, *36*(2), 197-210. <https://doi.org/10.1016/j.ecoleng.2008.12.029>
- Duo, L., Kan-liang, T., Hui-li, Z., Yu-yao, W., Kang-yi, N., & Shi-can, Z. (2018). Experimental investigation of solidifying desert aeolian sand using microbially induced calcite precipitation. *Construction and Building Materials*, *172*, 251-262. <https://doi.org/10.1016/j.conbuildmat.2018.03.255>
- Feng, K., & Montoya, B. M. (2016). Influence of confinement and cementation level on the behavior of microbial-induced calcite precipitated sands under monotonic drained loading. *Journal of Geotechnical and Geoenvironmental Engineering*, *142*(1), 1-9. [https://doi.org/10.1061/\(ASCE\)GT.1943-5606.0001379](https://doi.org/10.1061/(ASCE)GT.1943-5606.0001379)
- Ganendra, G., De Muynck, W., Ho, A., Arvaniti, E. C., Hosseinkhani, B., Ramos, J. A., Rahier, H., & Boon, N. (2014). Formate oxidation-driven calcium carbonate precipitation by *Methylocystis parvus* OBBP. *Applied and Environmental Microbiology*, *80*, 4659-4667. <https://doi.org/10.1128/AEM.01349-14>
- Gebbru, K. A., Kidanemariam, T. G., & Gebretinsae, H. K. (2021). Bio-cement production using microbially induced calcite precipitation (MICP) method: A review. *Chemical Engineering Science*, *238*, Article 116610. <https://doi.org/10.1016/j.ces.2021.116610>
- Golovkina, D. A., Zhurishkina, E. V., Ivanova, L. A., Baranchikov, A. E., Sokolov, A. Y., Bobrov, K. S., Masharsky, A. E., Tsvigun, N. V., Kopitsa, G. P., & Kulminskaya, A. A. (2020). Calcifying bacteria flexibility in induction of CaCO₃ mineralization. *Life*, *10*(12), Article 317. <https://doi.org/10.3390/life10120317>
- Hua B., D & ng B., Thornton E. C., Yang J., & Amonette J.E. (2007). Incorporation of chromate into calcium carbonate structure during coprecipitation. *Water Air and Soil Pollution*, *179*, 381-390. <https://doi.org/10.1007/s11270-006-9242-7>
- Kadhim, F. J., & Zheng, J. (2017). Influences of calcium sources and type of sand on microbial carbonate precipitation. *International Journal of Advances in Engineering & Technology*, *10*(1), 20-29.

- Koestel, J., Dathe, A., Skaggs, T. H., Klakegg, O., Ahmad, M. A., Babko, M., Gimenez, D., Farkas, C., Nemes, A., & Jarvis, N. (2018). Estimating the permeability of naturally structured soil from percolation theory and pore space characteristics imaged by Xray. *Water Resources Research*, *54*(11), 9255-9263. <https://doi.org/10.1029/2018WR023609>
- Lapierre, F. M., Schmid, J., Ederer, B., Ihling, N., Büchs, J., & Huber, R. (2020). Revealing nutritional requirements of MICP-relevant *Sporosarcina pasteurii* DSM33 for growth improvement in chemically defined and complex media. *Scientific Reports*, *10*, Article 22448. <https://doi.org/10.1038/s41598-020-79904-9>
- Liang, S., Chen, J., Niu, J., Gong, X., & Feng, D. (2020). Using recycled calcium sources to solidify sandy soil through microbial induced carbonate precipitation. *Marine Georesources & Geotechnology*, *38*(4), 393-399. <https://doi.org/10.1080/1064119X.2019.1575939>
- Lu, W., Qian, C., & Wang, R. (2010). Study on soil solidification based on microbiological precipitation of CaCO₃. *Science China Technological Sciences*, *53*, 2372-2377. <https://doi.org/10.1007/s11431-010-4060-y>
- Mujah, D., Liang, C., & Shahin, M. A. (2019). Microstructural and geomechanical study on biocemented sand for optimization of MICP process. *Journal of Materials in Civil Engineering*, *31*(4), 1-10. [https://doi.org/10.1061/\(ASCE\)MT.1943-5533.0002660](https://doi.org/10.1061/(ASCE)MT.1943-5533.0002660)
- Nemati, M., Greene, E. A., & Voordouw, G. (2005). Permeability profile modification using bacterially formed calcium carbonate: Comparison with enzymic option. *Process Biochemistry*, *40*(2), 925-933. <https://doi.org/10.1016/j.procbio.2004.02.019>
- Ng, W. S., Lee, M. L., Tan, C. K., & Hii, S. L. (2013). Improvements in engineering properties of soils through microbial-induced calcite precipitation. *KSCE Journal of Civil Engineering*, *17*, 718-728. <https://doi.org/10.1007/s12205-013-0149-8>
- Okwadha, G. D. O., & Li, J. (2010). Optimum conditions for microbial carbonate precipitation. *Chemosphere*, *81*(9), 1143-1148. <https://doi.org/10.1016/j.chemosphere.2010.09.066>
- Shahroki-Shahraki, R., Zomorodian, S. M. A., Niazi, A., & O'Kelly, B. C. (2014). Improving sand with microbial-induced carbonate precipitation. *Proceedings of the Institution of Civil Engineers-Ground Improvement*, *168*(3), 217-230. <https://doi.org/10.1680/grim.14.00001>
- Sheikh, S. A., & Atmapoojya, S. L. (2022). Experimental study on factors affecting the efficiency of microbially induced carbonate precipitation in soil. *Materials Today: Proceedings*, *60*(Part 1), 275-280. <https://doi.org/10.1016/j.matpr.2021.12.530>
- Soon, N. W., Lee, L. M., Khun, T. C., & Ling, H. S. (2014). Factors affecting improvement in engineering properties of residual soil through microbial-induced calcite precipitation. *Journal of Geotechnical and Geoenvironmental Engineering*, *140*(5), 1-11. [https://doi.org/10.1061/\(ASCE\)GT.1943-5606.0001089](https://doi.org/10.1061/(ASCE)GT.1943-5606.0001089)
- Velpuri, N. V. P., Yu, X., Lee, H., & Chang, W. (2016). Influence factors for microbial-induced calcite precipitation in sands. In W. C. Cheng & J. Y. Wu (Eds.), *Geo-China 2016: Innovative and Sustainable use of Geomaterials and Geosystems* (pp. 44-52). ASCE Library. <https://doi.org/10.1061/9780784480069.006>
- Wei, S., Cui, H., Jiang, Z., Liu, H., He, H., & Fang, N. (2015). Biomineralization processes of calcite induced by bacteria isolated from marine sediments. *Brazilian Journal of Microbiology*, *46*(2), 455-464. <https://doi.org/10.1590/S1517-838246220140533>

Aljohani Waad Awdah Saad, Siti Norathirah Mohd Anas, Nor Safiqah Seminin, Putri Nur Suhaina Naim,
Dardau Abdulaziz, Rusea Go, Nor Azwady Abdul Aziz, Mona Fatin Syazwane Mohamed Ghazali and Muskhazli Mustafa

Whiffin, V. S. (2004). Microbial CaCO₃ precipitation for the production of biocement (Doctoral dissertation).
Murdoch University, Australia. <https://researchrepository.murdoch.edu.au/id/eprint/399/2/02Whole.pdf>.

Whiffin, V. S., van Paassen, L. A., & Harkes, M. P. (2007). Microbial carbonate precipitation as a soil improvement
technique. *Geomicrobiology Journal*, 24(5), 417-423. <https://doi.org/10.1080/01490450701436505>

Lung Function Analysis of Marble Home Industry Workers in Tulungagung Regency

Noeroel Widajati^{1*}, Tri Martiana¹, Tri Niswati Utami², Juliana Jalaludin³ and Titi Rahmawati Hamedon^{3,4}

¹Department of Occupational Safety and Health, Faculty of Public Health, Universitas Airlangga, 60115 Surabaya Jawa Timur, Indonesia

²Department of Occupational Safety and Health, Faculty of Public Health, Universitas Islam Negeri Sumatera Utara, 20371 Deli Serdang, Sumatera Utara, Indonesia

³Department of Environmental and Occupational Health, Faculty of Medicine and Health Sciences, Universiti Putra Malaysia, 43400 UPM, Serdang, Selangor, Malaysia

⁴Department of Community Health, Faculty of Medicine and Health Sciences, Universiti Putra Malaysia, 43400 UPM, Serdang, Selangor, Malaysia

ABSTRACT

This study analyzes the effect of dust exposure and worker characteristics on lung function. This type of research was observational with a cross-sectional design. The population was 20 marble home industry workers in Tulungagung. The total population technique determined the sample. Data analysis was carried out using Smart PLS software. The study results found that sociodemography, including age, nutritional status, and years of service, affected lung function with a t-statistic of 2.604. Dust exposure, which includes respirable dust content and duration of exposure, impacted lung function with a t-statistic of 2.522. Marble artisans in Tulungagung with the age of ≥ 35 years and a long working period of >5 years with a level of exposure to silica dust >3 mg/m³ and supported by a long working

period of >7 hours had great potential for lung function. The recommendation was for home industry entrepreneurs to provide masks according to standards. The role of public health center officers was to monitor the work environment and regularly check home industry workers' health.

Keywords: Long exposure, lung function, nutritional status, respiratory complaints, silica dust

ARTICLE INFO

Article history:

Received: 21 March 2022

Accepted: 28 July 2022

Published: 06 March 2023

DOI: <https://doi.org/10.47836/pjst.31.2.15>

E-mail addresses:

noeroel.widajati@fkm.unair.ac.id (Noeroel Widajati)

tri.martiana@fkm.unair.ac.id (Tri Martiana)

triniswatiutami@uinsu.ac.id (Tri Niswati Utami)

juliana@upm.edu.my (Juliana Jalaludin)

rahmawati@upm.edu.my (Titi Rahmawati Hamedon)

*Corresponding author

INTRODUCTION

Marble is one industry that contributes to high foreign exchange for the country. The largest marble-producing area in Indonesia is found in the Besole sub-district, Tulungagung Regency, East Java Province. Marble-making materials contain chemicals such as CaCO_3 , silica, iron, aluminum oxalate, MgCO_3 , and others (Kurniawati & Titisari, 2019). Making marble uses water and produces liquid waste containing lime and other chemicals (Videsia et al., 2017). Not only is liquid waste generated from the manufacture of marble but making marble that contains chemicals can also be a health threat that is dangerous for workers.

A previous study explained that marble home industry workers in Tulungagung mostly used Personal Protective Equipment from used cloth to substitute for masks. The cloth used as masks was not washed. The work time was more than 7 hours per day, but if the number of orders for marble increased, the working time was more than 9 hours. The working period was more than five years (Dewanti, 2019).

A preliminary survey conducted by interviewing six workers obtained data that workers had never had a regular pulmonary function test. The type of work was informal home industry (self-help). Moreover, if the workers bear the cost of this pulmonary physiology test, it will not be easy to implement. No Personal Protective Equipment or masks were available according to standards for occupational risks of exposure to marble dust. There were also respiratory problems and eye irritation (red eyes). Silica dust was exposed in mining, industry, construction, and granite workers using raw materials containing silica, causing health problems for workers (Roney et al., 2019). The total silica average of 0.61% to the research result (Kurniawati & Titisari, 2019).

One dust that causes occupational diseases is silica dust from marble because it contains SiO_2 , around 28.35-45% (Murat & Malak, 2012). Marble is a metamorphic rock or a change from the original rock, namely the limestone tab. This dust is fibrogenic and can cause restrictive lung disorders. The primary reaction to dust exposure in the lungs is fibrosis (Susanto, 2011). Based on the Minister of Manpower Regulation Number No. 5/MEN/2018, the Indonesian government regulates the threshold value of silica dust in the work environment at 3 mg/m^3 (Kemenaker, 2018). Previous researchers stated lung function and respiratory symptoms were found due to exposure to dust and chemicals inhaled through inhalation in 85 iron foundry workers in Sweden (Andersson et al., 2019).

The research result (Sahri et al., 2019) showed that 42.6% of respondents have an unsafe risk level of exposure to c-silica dust and potential health problems due to c-silica dust. Based on the estimated calculation of chronic exposure risk, the risk level tends to increase over the next 20 years. Silicosis is still present in workers who die exposed to silica dust between $0.05\text{--}0.1 \text{ mg/m}^3$. The result of the measurement of c-silica dust in the working environment by using a personal sampler on each respondent got a result that exceeds the limit value based on Indonesia regulation (Ministry of Manpower and Transmigration No.

PER.13/MEN/X/2011) amounted to 55.3%. The value of concentration is very influential on the value of intake in workers; the higher the concentration of dust c-silica in the work environment, the higher the intake value, so the risk value will also increase.

Silicosis is a pulmonary fibrosis disease caused by silica crystals' inhalation, retention, and lung reaction. Silica particles are deposited in the lungs, digested by alveolar macrophages, and activate proinflammatory cytokines and fibrogenic factors that cause lung damage and decrease lung function. Fibrosis is a Th2-mediated disease, and IL-13 is one of its components. Many studies report an increase in IL-13 rates of pulmonary fibrosis. Symptoms of silicosis develop 5 to 30 years after exposure (Jasminarti & Winaniarni, 2019).

Fibrosis is a Th2-mediated disease, and Th2, IL-4, IL-13, and IL-5 cytokines are essential in regulating tissue remodeling and fibrosis. In fibroblast subtypes, receptors for IL-4 and IL-13 were found, and in vitro studies showed that extracellular matrix protein synthesis and myofibroblast differentiation were induced by IL-4 or IL-13 stimulation (Esmail et al., 2014).

By seeing the magnitude of health problems due to exposure to ceramic makers' dust, it is necessary to carry out a strategy to prevent, control, reduce, and eliminate occupational risks due to occupational hazards on an ongoing basis. It is done considering the costs incurred due to health problems and work accidents caused by the work environment are significant with the harm it causes (ILO, 2008). The exposure can also develop into autoimmune disorders, chronic kidney disease, and others (Baron et al., 2002; De Maria et al., 2020). Studies in China showed that 10 million workers contracted silicosis, with 5000 reported deaths (Natural Stone Institute, 2018). Widajati's research (Armaeni & Widajati, 2017) revealed that ceramic makers in East Java, from 30 respondents studied, found a measurement of the level of health risk of 13.3% $RQ > 1$ (risk quotient), which means workers have an unsafe risk of exposure to dust in a safe work environment causing risk for health problems. Exposure to silica dust causes occupational disease silicosis.

In Indonesia, similar research on the impact of silica dust levels on marble artisans has not been widely carried out; therefore, it is necessary to investigate the presence of respiratory disorders through lung function tests and biomarkers of inflammatory and fibrogenic responses in the body, such as Interleukin-13. Similar researchers on exposure to silica dust in the workplace cause pulmonary tuberculosis. The work environment produces silica dust, namely construction, mining, and sand digging (Kootbodien, 2019).

This research refers to the concept by Kootbodien et al. (2019) and Tavakol et al. (2017). Tuberculosis is influenced by gold dust exposure, smoking, body mass index, and disease history. Furthermore, Tavakol et al. (2017) explain that respiratory function status is influenced by silica exposure, measured by vital lung capacity (FEV1/FVC). The most significant exposure to construction workers. In contrast, this study assessed pulmonary function disorders using indicators of respiratory complaints and lung function as measured

using an autspirometry due to exposure to dust, interleukin-13, and worker characteristics. The characteristics of the nutritional status of workers are assumed to have an effect on lung function and have not been carried out by previous researchers.

Therefore, it is essential to conduct this study to assess and analyze the effect of dust exposure and worker characteristics on the lung function of marble home industry workers in the Tulungagung Regency. The research hypotheses were determined as follows: (1) characteristics affect lung function, (2) dust exposure affects IL-13, (3) dust exposure affects lung function, and (4) IL-13 affects lung function. Proving the research hypothesis helps prevent the prevalence of respiratory disorders in-home industry workers and recommends improving the work environment.

MATERIALS AND METHODS

Research Design

This type of observational research used a cross-sectional design. The study was conducted on three marble home industry workers in Tulungagung Regency. Data collection was carried out at 3 locations/work units: (1) packing and finishing, (2) lathe and scrub polishing, and (3) cutting and craft operators. The population is 20 workers. The total population technique determined the sample.

Measurement

Characteristics data were collected using a questionnaire: age, years of work, duration of exposure to dust, and nutritional status measured by anthropometry (height and weight). Serum interleukin-13 data was measured using a sample of the respondent's blood serum, as much as 1 ml of blood serum. The level of IL-13 was measured using the ELISA (Enzyme-Linked Immunosorbent Assay) test technique. Measurements were taken using the personal dust sampler installed near the worker's breathing and during the worker's activities during working hours. The lung function test was measured using autspirometry. Furthermore, the condition of lung ventilation was assessed using FVC (Forced Vital Capacity) and FEV1 (forced expiratory volume in one second) parameters. Normal if FVC > 80%; FEV1 > 70%, restriction if FVC < 80%; FEV1 > 70%, Obstruction if FVC > 80%, FEV1 < 70%. Respiratory complaints data was measured using a questionnaire containing respiratory complaints felt by workers.

Data Analysis

Analysis of the data used is path analysis. The advantage of this analysis is that the relationship patterns of 4 variables (characteristics of marble craftsmen, levels of respirable dust, IL (interleukin) 13, and lung function) were studied directly or indirectly. The

hypothesis was tested based on the significance level of 0.05 and t-statistics of >1.96 ; the hypothesis was accepted.

RESULTS

The results of the data analysis on the characteristics of research respondents, including age, nutritional status, and length of employment, are shown in the frequency distribution in Table 1.

Table 1
Characteristics of research respondents

Characteristics	Total	Percentage (%)
Age		
< 35	4	20
≥ 35	16	80
Length of Employment		
< 5 years	6	30
≥ 5 years	14	70
Nutritional Status (BMI)		
Normal	12	60
Excess weight	4	20
Obesity	4	20

Source. primary data, 2019

Table 1 shows that most research respondents aged > 35 years were 16 people (80%), based on most working years five years as many as 14 people (70%). The term of service category was more than five years. Nutritional Status (BMI) was dominated by normal in 12 (60%) respondents, based on Body Mass Index in the overweight category in 4 (20%) respondents, and obesity in 4 (20%) workers.

Table 2
IL-13 levels in the workers

IL-13 Levels	Frequency	Percentage (%)
Normal (≤ 3 pg/mL)	17	85
Not normal (> 3 pg/mL)	3	15
Total	20	100

Source. primary data, 2019

Table 2 shows that as many as 17 workers (85%) had IL-13 levels within normal limits, and three (15%) had abnormal IL-13 levels. IL levels in 13 abnormal categories were found in workers over 35 years. Table 3 describes the distribution of respirable dust measurements during work.

Table 3
Frequency distribution of respiratory dust exposure by work unit

Measurement Results of Respiratory Dust Exposure	Frequency	Percentage (%)
Location 1: Packing and Finishing 1.683 mg/m ³	4	30
Location 2: Lathe and Polish scrub 1.101 mg/m ³	3	15
Location 3: Cutting and crafting operators 5.160 mg/m ³	13	65
Total	20	100

Source. primary data, 2019

The highest exposure to respirable dust is in the cutting work unit and craft operators, which is 5.160 mg/m³, and there are 13 workers at that location (Table 3). The work unit with the lowest exposure to dust was the lathe and polishing location, which was 1.101 mg/m³, and there were three workers in the work unit. On the other hand, workers at packing and finishing locations were exposed to the dust of 1.683 mg/m³; there were four workers. Based on the results of measurements of respiratory dust exposure that had been carried out on marble home industry workers, there were 13 workers (65%) exposed to dust above the Threshold Value (TV) and seven workers (35%) exposed to dust below the TV level, the TV standard is determined in a Ministerial Regulation Manpower and Transmigration Number 5 of 2018.

Table 4
Frequency distribution of lung function based on autspirometry test and marble workers

Lung Function	Frequency	Percentage (%)
Lung function		
Not normal	5	25
Normal	15	75
Respiratory complaints		
Yes	10	50
None	10	50

Source. primary data, 2019

Table 4 shows the results of the pulmonary function test using autspirometry. There were five categories of abnormal lung function (25%), and it was found that ten people had respiratory complaints (50%).

Figure 1 describes the pulmonary function analysis model for marble workers in Tulungagung using pathway analysis.

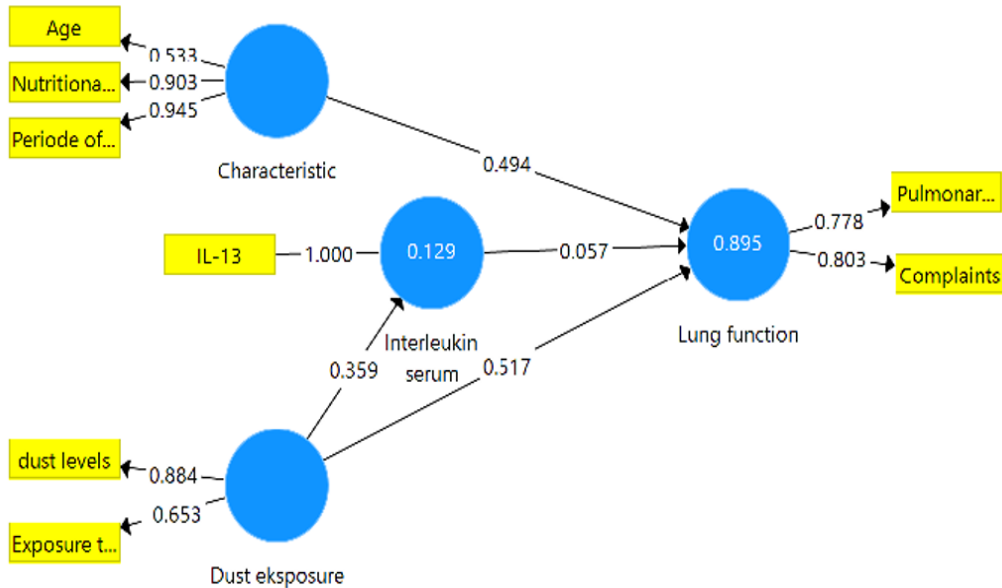


Figure 1. Lung function pathway analysis marble workers in Tulungagung

Pathway analysis model on the outer model variable characteristics, exposure to dust, interleukins, and lung function showed a loading factor greater than 0.50. Therefore, it was concluded that all research variables indicators were suitable for use as research instruments. The subsequent analysis is the inner model, as shown in Table 5.

Table 5
Hypothesis test

Variables	Original sample	Sample mean	Standard deviation	t-statistic	p-value
Characteristics → Lung function	0.494	0.445	0.190	2.604	0.009*
IL-13 → Pulmonary function	0.057	0.130	0.244	0.232	0.817
Dust exposure → IL-13	0.359	0.469	0.255	1.412	0.158
Exposure to dust → Lung function	0.517	0.448	0.205	2.522	0.012*

Source. Primary data, 2019. (*sig, p-value < 0.05)

Table 5 shows two variables that affect lung function: the worker's characteristic variable significantly affects lung function of the t-statistic value (2.604) and the p-value (0.009). Dust exposure significantly affected lung function t-statistical values (2.522) and p-value (0.012). Two variables had no effect: the IL-13 and the p-value (0.817) did not affect lung function. In addition, the dust exposure variable did not affect the IL-13 p-value (0.157).

DISCUSSION

Most of the characteristics of marble artisans are more than 35 years old. Most have more than five years of service and primarily normal nutritional status. The working period significantly contributes to lung function ($p = 0.000$), and 15.749% of lung function disorders are influenced by years of service, and other factors influence the rest. The longer the working period of marble artisans, the greater the risk for pulmonary function disorders. Workers with a working period of >5 years will be more likely to experience impaired lung function because dust particles are inhaled and have settled in the alveoli (Jonsson et al., 2019). Hochgatterer (Graff et al., 2020) explained that the duration of exposure to quartz dust had a significant effect ($p=0.000$) on the decline in workers' lung function. The risk of sarcoidosis increases in workers aged 20–65 due to dust exposure.

Characteristics of age, nutritional status, and years of service based on the external model show loading factors that meet the feasibility value of the characteristic variable indicator. The novelty of this study is that previous researchers did not use nutritional status as an indicator. Nutritional status affects a person's resistance to disease, so workers need to maintain nutritional status in normal conditions. Nutritional status based on anthropometry is directly related to disease (Thamaria, 2017). It was contrary to previous researchers who stated that nutritional status did not affect the lung function of wood industry workers (Rismandha et al., 2017).

Exposure to silica dust in the work environment, especially workers in the mineral mining industry, glassmakers, stone cutting, ceramics, and sand, must be aware of the risk of lung cancer. Silica dust is a carcinogenic and hazardous material that can cause lung cancer. Observations on 22 ceramic and glass-making industries in Egypt found that thousands of workers were exposed to silica dust exceeding the threshold value (Mohamed et al., 2018). The prevalence of silicosis is high in industrial mining countries. Respiratory damage, especially lung tissue for stone and sand mining workers due to the deposition of silica particles, reduces the quality of life and threatens death (Konečný et al., 2019).

Kozłowska et al. (2008) research results regarding age and lung function showed a significant relationship, maximum muscle strength at 20–40 years. They will decrease by 20% after 40 years, and the need for energy substances increases until it finally decreases after 40 years. The reduced need for energy is due to decreased physical strength. According

to Setiana et al. (2014), as a person's age increases, the ability of the body's organs will naturally decrease, which is no exception for impaired lung function. The condition of workers' lung function will worsen with dusty environmental conditions and other factors such as smoking habits, unavailability of masks, length of exposure, and history of the disease.

Based on the autspirometry test of Tulungagung marble home industry workers, of the 20 respondents, 25% of workers experienced pulmonary function disorders in the form of mild restrictions in 2 people and moderate restrictions in 3 people. Pulmonary restriction disorders are usually characterized by reduced lung volume caused by allergenic substances such as fungi, spores, and dust. In addition, the restriction is associated with limited lung expansion. It can occur due to changes in the chest wall, pleura, and neuromuscular apparatus (Kalamillah, 2018). Silica dust is the most common cause of lung disease in modern industrial countries such as Australia, Israel, and Turkey (Barnes et al., 2019).

In general, humans aged 30–40 years will experience a decrease in lung function, whereas, with increasing age, the disorders that occur are also increasing. Suyono (2001) also stated that the older a person ages, the greater the possibility of decreased lung function. In the elderly, several structural and functional changes occur in the thorax and lungs. At that age, it was found that the alveoli became less elastic and more fibrous and contained minor functioning capillaries; so, the utilization capacity decreased because the diffusion capacity of the lungs for oxygen could not meet the body's demands (Maryam, 2008). According to Fathmaulida (2013), a person's energy needs are related to the development and physiology of the body, especially the respiratory system so that it affects the work of the respiratory muscle strength in pumping O₂ throughout the body, controlling the respiratory rate and the formation of the body's immunological mechanism for the prevention of lung disease.

The results showed that the nutritional status of the respondents was primarily normal. Nutritional status is related to disease susceptibility in workers. IL-13 levels from the ELISA test showed that only three respondents (15%) had abnormal IL-13 above 3 pg/mL. It is supported by the statistical analysis results where IL-13 does not affect the lung function of Tulungagung marble artisans. Good nutritional status affects food intake in the body, which will be used as an energy source, where the primary energy source in the body is energy intake and carbohydrates, protein, and fat. If food intake is good, the digestive system will be good and affect the circulatory system throughout the body (Agustina et al., 2018). Exposure to silica dust can cause pulmonary fibrosis takes 5 to 30 years. It is also strongly influenced by the health status of the artisans, lifestyle, diet, PPE (masks) following the exposure used by artisans, and many factors that influence it (10). IL-13 is a pleiotropic cytokine produced by the chromosome 5 gene at q 31, produced significantly by Th2. Various evidence indicates that IL-13 is a mediator in the pathogenesis of asthma, airway hyperresponsiveness, mucus production, and airway subepithelial fibrosis. Fibrosis of the

lungs, liver, and kidneys is associated with the synthesis of IL-13 by T lymphocyte cells. IL-13 can trigger collagen synthesis independently of TGF β and cause the proliferation and contraction of smooth muscle cells, leading to fibrosis formation. Overexpression of IL-13 in the lung triggers subepithelial airway fibrosis in mice without other inflammatory stimuli. IL-13 levels increase in pulmonary fibrosis (Jasminarti & Winaniarni, 2019; Kalahasthi et al., 2010).

This study showed that the dominance of workers exposed to dust produced by marble stone processing was seen in the >7 hours/day category, which was as much as 90%. The Tulungagung marble home industry had working hours from 08.00 to 16.00 with six working days in one week, so the total working hours at the Tulungagung marble home industry was 48 hours in one week. Working hours that exceed 7 hours/day or 40 hours/week as applied by the Tulungagung marble home industry were not following the Law of the Republic of Indonesia Number 13 of 2003 concerning Manpower Article 77, which states that the working time for six working days is 7 hours/day or 40 hours/week.

According to Suma'mur (2009) and Wulandari et al. (2015), a person can usually work well for 40–50 hours a week. If it is more than that, the possibility of various health problems for workers will be even greater. Many home industries have closed, and only a few are still running with a small number of workers, on average, under 20 workers. The duration of exposure and the intensity of dust exposure also determines dust exposure in the workplace. In this research, the measured dust is respirable dust with a TV (threshold value) of less than 3 mg/m³ according to the Regulation of the Minister of Manpower of the Republic of Indonesia No. 5 of 2018. The results of the measurement of respirable dust showed that as many as 13 people from 20 craftsmen (65%) had a respiratory dust value exceeding 3 mg/m³, and only seven people (35%) were still below 3 mg/m³. The highest respiratory dust exposure measured in Tulungagung marble home industry workers was found in the cutting section and craft operators at 5,160 mg/m³. The packing section's lowest respiratory dust exposure value was 1,101 mg/m³. The statistical analysis showed that dust exposure to lung function was very significant ($p=0.012$).

The pulmonary function test results showed that five workers (25%) experienced mild and moderate restrictions. It is also supported by a relatively long employment length of more than five years, the age of the workers was more than 35 years, the working time mainly was more than 7 hours of work outside of resting hours (1 hour), special PPE (masks) according to the type of exposure does not provide, artisans only used a used cloth that was rarely washed. In addition, there had never been an HRA (health risk assessment) by the local Health Center Occupational Health Effort staff because the officers could not yet assess the hazards of the work environment and their impact on workers' health. It is also closely related to the lung function test of marble artisans who had never been carried out periodically at least once a year to protect workers' health and increase work productivity (BPK RI, 2003).

CONCLUSION

Sociodemographics of marble artisans, including age, nutritional status, and years of service, have a significant effect on lung function disorders. In addition, nutritional status is related to disease susceptibility in workers. Dust levels, including respirable dust levels and duration of exposure in the workplace, also significantly affect lung function disorders of marble artisans. However, IL-13 did not affect lung function, and dust exposure did not affect IL (interleukin)-13. It is hoped that the Health Center will establish an occupational health post in its working area to monitor the health of home industry workers in the informal work sector and support the country's foreign exchange.

ACKNOWLEDGEMENTS

The author would like to thank the Marble industrial homeowner, CV. Adhi Jembatan Batoe, Tulungagung, East Java, Indonesia.

REFERENCES

- Agustina, T., Indarto, D., & Sugiarto. (2018). Hubungan asupan protein dan kadar interleukin-6 dengan kadar hemoglobin pada remaja putri status gizi lebih [The correlation between protein intake and interleukin-6 levels and hemoglobin levels in female adolescents with overweight status]. *Biomedika*, *10*(2), 107-114.
- Andersson, L., Bryngelsson, I. L., Hedbrant, A., Persson, A., Johansson, A., Ericsson, A., Lindell, I., Stockfelt, L., Särndahl, E., & Westberg, H. (2019). Respiratory health and inflammatory markers - Exposure to respirable dust and quartz and chemical binders in Swedish iron foundries. *PLoS ONE*, *14*(11), 1-19. <https://doi.org/10.1371/journal.pone.0224668>
- Armaeni, E. D., & Widajati, N. (2017). Hubungan paparan debu kapur dengan status faal paru pada pekerja gamping [Correlation between exposure to lime dust and pulmonary function status in limestone workers]. *The Indonesian Journal of Occupational Safety and Health*, *5*(1), 61-70. <https://doi.org/10.20473/ijosh.v5i1.2016.61-70>
- Barnes, H., Goh, N. S. L., Leong, T. L., & Hoy, R. (2019). Silica-associated lung disease: An old-world exposure in modern industries. *Respirology*, *24*(12), 1165-1175. <https://doi.org/10.1111/resp.13695>
- Baron, P. A., Rice, F. L., Key-Schwartz, R., Bartley, D., & Schlecht, P. (2002). *Health effects of occupational exposure to respirable crystalline silica*. Center for Disease Control and Prevention. https://stacks.cdc.gov/gsearch?ref=docDetails&related_series=NIOSH%20hazard%20review
- BPK RI. (2003). Undang (UU) tentang ketenagakerjaan nomor 13 [Labour law number 13]. Database Peraturan. <https://peraturan.bpk.go.id/>
- De Maria, L., Caputi, A., Luisi, V., Delfino, M. C., Cavone, D., Acquafredda, P., Pallara, M., Lovreglio, P., & Vemercati, L. (2020). Silicosis in a paint-production worker study of a lung histological specimen.pdf. *Clinica Case Report*, *9*(1), 67-71. <https://doi.org/DOI: 10.1002/ccr3.3419>
- Dewanti, F. (2019). Hubungan paparan debu respirable dan penggunaan APD Masker dengan gangguan faal paru pada pekerja home industry marmer TULUNGAGUNG [Correlation between Exposure to respirable

- dust and the usage of PPE masks with reduced lung function in Tulungagung marble house industry workers] (Doctoral dissertation). Universitas Airlangga, Indonesia. <https://repository.unair.ac.id/87027/>
- Esmacil, N., Gharagozlo, M., Rezaei, A., & Grunig, G. (2014). Dust events, pulmonary diseases and immune system. *American Journal Clinical and Experimental Immunology*, 3(1), 20-29.
- Fathmaulida, A. (2013). *Faktor-faktor yang berhubungan dengan Gangguan Fungsi Paru pada Pekerja Pengolahan Batu Kapur di Desa Tamansari Kabupaten Karawang tahun 2013* [Factors Associated with Impaired Lung Function among Limestone Processing Employees in Tamansari Village, Karawang Region, in 2013] (Doctoral dissertation). Universitas Airlangga Universitas Islam Negeri Syarif Hidayatullah, Jakarta. <https://repository.uinjkt.ac.id/dspace/bitstream/123456789/25886/1/ANNISA%20FATHMAULIDA-fkik.pdf>
- Graff, P., Larsson, J., Bryngelsson, I. L., Wiebert, P., & Vihlborg, P. (2020). Sarcoidosis and silica dust exposure among men in Sweden: A case-control study. *BMJ Open*, 10(9), 1-6. <https://doi.org/10.1136/bmjopen-2020-038926>
- ILO. (2008). *Fundamental Principles of Occupational Health and Safety* (2nd ed.) International Labour Office.
- Jasminarti, A., & Winaniarni. (2019). Paparan kumulatif debu batu terhadap kadar IL(Interleukin)-13 serum dan faal paru pekerja pemecah batu [Cumulative exposure of dust stone serum levels to Interleukin-13 and lung function of breaking stones workers]. *Jurnal Respirologi Indonesia*, 5(2), 251-266.
- Jonsson, E., Järholm, B., & Andersson, M. (2019). Silica dust and sarcoidosis in Swedish construction workers. *Occupational Medicine*, 69(7), 482-486. <https://doi.org/10.1093/occmed/kqz118>
- Kalahasthi, R., Pradyuonna, A., Nerandran, P., & Rao, R. H. R. (2010). Evaluation of the relationship between pro-inflammatory cyto-kines and health hazard in workers involved in hazardous waste sites at Karnataka, India. *Journal of Research in Health Science*, 10(1), 7-14.
- Kalamillah, H. (2018). *Hubungan kadar debu total, ventilasi, dan karakteristik individu dengan kondisi faal paru pada pekerja bagian bubut di CV X Yogyakarta* [Correlation between total dust content, ventilation, and individual characteristics with pulmonary function in turning workers at CV X Yogyakarta] (Doctoral dissertation). Universitas Airlangga, Indonesia. <https://repository.unair.ac.id/70617/>
- Kemnaker. (2018). Peraturan Menteri Ketenagakerjaan tentang keselamatan dan kesehatan kerja lingkungan kerja *Permenaker Nomor 5 Tahun. Keselamatan dan Kesehatan di Lingkungan kerja*. [Regulation of the Minister of Manpower concerning occupational safety and health in the work environment of the Minister of Manpower Regulation Number 5. Safety and Health in the work environment.] Kementerian Tenaga Kerja Republik Indonesia. <https://peraturanpedia.id/peraturan-menteri-ketenagakerjaan-nomor-5-tahun-2018/>
- Konečný, P., Ehrlich, R., Gulumian, M., & Jacobs, M. (2019). Immunity to the dual threat of silica exposure and mycobacterium tuberculosis. *Frontiers in Immunology*, 10, 1-11. <https://doi.org/10.3389/fimmu.2018.03069>
- Kootbodien, T., Iyaloo, S., Wilson, K., Naicker, N., Kgalamono, S., Haman, T., Mathee, A., & Rees, D. (2019). Environmental silica dust exposure and pulmonary tuberculosis in Johannesburg, South Africa. *International Journal of Environmental Research and Public Health*, 16(10), Article 1867. <https://doi.org/10.3390/ijerph16101867>

- Kozłowska, W. J., Bush, A., Wade, A., Aurora, P., Carr, B. S., Castle, R. A., Hoo, A. F., Lum, S., Price, J., Ranganathan, S., Saunders, C., Stanojevic, S., Stroobant, J., Wallis, C., & Stocks, J. (2008). Lung function from infancy to the preschool years after clinical diagnosis of cystic fibrosis. *American Journal of Respiratory and Critical Care Medicine*, 178(1), 42-49. <https://doi.org/10.1164/rccm.200710-1599OC>
- Kurniawati, S., & Titisari, A. D. (2019). Rekomendasi pemanfaatan marmer Daerah Besole, Kecamatan Besuki, Kabupaten Tulungagung, Provinsi Jawa Timur berdasarkan karakteristiknya [Recommendations for using marble in the Besole Region, Besuki District, Tulungagung Regency, East Java Province based on its characteristics]. *Jurnal Pengabdian Kepada Masyarakat (Indonesian Journal of Community Engagement)*, 5(2), 251-266. <https://doi.org/10.22146/jpkm.35963>
- Maryam, S. (2008). *Mengenal Lanjut Usia dan Perawatannya* [Understanding Older People and Their Care]. Salemba Medica.
- Mohamed, S. H., El-Ansary, A. L., & El-Aziz, E. M. A. (2018). Determination of crystalline silica in respirable dust upon occupational exposure for Egyptian workers. *Industrial Health*, 56(3), 255-263. <https://doi.org/10.2486/indhealth.2016-0192>
- Murat, D., & Malak, A. (2012). Effect of SiO₂ in Turkish natural stones on cancer development. *Asian Pacific Journal Cancer Prevention*, 13(10), 4883-4888.
- Natural Stone Institute. (2018). *Silicosis: An industry guide to awareness and prevention*. Natural Stone Institute. <chrome-extension://efaidnbmnnnnibpcajpcglefindmkaj/https://pubs.naturalstoneinstitute.org/pub/8C001ED7-1866-DAAC-99FB-B0830F3121B1>
- Rismandha, R., Disrinima, A. M., & Dewi, T. U. (2017). Analisis pengaruh faktor-faktor risiko gangguan fungsi paru pada pekerja area produksi industri kayu [Analyse of the effect of risk factors for reduced pulmonary function in wood industry workers]. *Seminar Nasional K3 PPNS 2017*, 1(1), 199-204.
- Roney, N., Faroon, O., Williams, M., Jones, D. G., Klotzbach, J. M., Kawa, M., & Zaccaria, K. (2019). *Toxicological Profile for Silica*. U.S. Department of Health and Human Services, Agency for Toxic Substances and Disease Registry. <https://www.ncbi.nlm.nih.gov/books/NBK158872/>
- Sahri, M., Tualeka, A. R., & Widajati, N. (2019). Quantitative risk assesment of crystalline silica exposure in ceramics industry. *Indian Journal of Public Health Research and Development*, 10(2), 626-629.
- Setiana, T., Purnomo, L. B., & Budiono, E. (2014). Perbedaan fungsi paru pada penderita sindroma metabolik dan tanpa sindroma [Differences in lung function between patients with and without metabolic syndrome]. *Indonesian Journal of CHEST*, 1(2), 51-55.
- Suma'mur. (2009). *Higiene perusahaan dan keselamatan kerja (HIPERKES)* [Hygiene and safety in the workplace (HIPERKES)]. Sagung Seto.
- Susanto, A. (2011). Pneumokoniosis [Pneumoconiosis]. *Journal Indonesia Medical Association*, 61(12), 503-510.
- Suyono, J. (2001). *Deteksi Dini Penyakit Akibat kerja* [Early Detection of Occupational Diseases]. EGC. <https://r2kn.litbang.kemkes.go.id/handle/123456789/76294?show=full>

- Tavakol, E., Azari, M., Zendehtel, R., Salehpour, S., Khodakrim, S., Nikoo, S., & Saranjam, B. (2017). Risk evaluation of construction workers' exposure to silica dust and the possible lung function impairments. *Tanaffos*, 16(4), 295-303.
- Thamaria, N. (2017). *Bahan ajar gizi: Penilaian status gizi* [Nutritional teaching materials: Evaluation of nutritional status] (pp. 1-137). Pusat Pendidikan Sumber daya Manusia Kesehatan.
- Videsia, V., Pujiati, R. S., & Moelyaningrum, A. D. (2017). *Produksi marmer dan pengolahan limbah di sentra industri marmer Kabupaten Tulungagung* [Marble production and waste treatment at the Marble Industry Center in Tulungagung Regency]. Repository Universitas Jember.
- Wulandari, R., Setiani, O., & Dewanti, N. (2015). Hubungan masa kerja terhadap gangguan fungsi paru pada petugas penyapu jalan di Protokol 3, 4 dan 6 Kota Semarang [The correlation between work period and pulmonary function disorder in street sweepers in Semarang Protocols 3, 4, and 6]. *Jurnal Kesehatan Masyarakat (e-Journal)*, 3(3), 797-806.

Heat Stress and Noise Exposure Levels in a Manufacturing Plant

Qi Jie Kwong^{1*}, Nursyifaasahirah Terbizil¹, Normaisarah Nordin¹, Emma Marinie Ahmad Zawawi¹, Azli Abd Razak² and Jamalunlaili Abdullah¹

¹Faculty of Architecture, Planning and Surveying, Universiti Teknologi MARA, 40450 Shah Alam, Selangor Darul Ehsan, Malaysia

²School of Mechanical Engineering, College of Engineering, Universiti Teknologi MARA, 40450 Shah Alam, Selangor Darul Ehsan, Malaysia

ABSTRACT

This paper analyses skilled workers' heat stress and noise exposure levels at a pressure vessel manufacturing plant. Measurements were conducted at three partially enclosed workspaces of the plant where hot work and metal fabrications were conducted using a multi-function thermal environment data logger and a sound level recorder. A survey was developed to obtain the field workers' perceptions of their immediate heat and noise environments. The findings suggested that the heat and noise conditions were generally acceptable. The calculated mean Wet-bulb Globe Temperature (WBGT) indicated that there was only minimal risk of heat stress for the workers. It was also identified that the noise intensities in the sections studied were within the permissible exposure limit for an 8-hour duration specified in the Department of Occupational Safety and Health (DOSH) guideline. Besides, questionnaire survey results showed that the thermal and noise conditions at the workplace were acceptable. The workers perceived their work environment as warm with sensible air movement, moderately humid, free from heat and noise-related injuries, and able to have clear conversations with their co-workers while working.

ARTICLE INFO

Article history:

Received: 24 March 2022

Accepted: 10 June 2022

Published: 06 March 2023

DOI: <https://doi.org/10.47836/pjst.31.2.16>

E-mail addresses:

kwong.qjie@gmail.com (Qi Jie Kwong)

nursyifaa.9612@gmail.com (Nursyifaasahirah Terbizil)

normaisarahnordin@gmail.com (Normaisarah Nordin)

emmamarinie@uitm.edu.my (Emma Marinie Ahmad Zawawi)

azlirazak@uitm.edu.my (Azli Abd Razak)

jamal858@uitm.edu.my (Jamalunlaili Abdullah)

*Corresponding author

Keywords: Heat stress, manufacturing plant, noise exposure, Wet-bulb Globe Temperature (WBGT), workplace

INTRODUCTION

A safe, comfortable, and healthy workplace environment plays an important role in ensuring the good productivity of the employees. The impacts of undesirable workplace conditions, which led to poor work performance, have been documented (Srinivasan et al., 2016; Edem et al., 2017). Since workers are the most valuable assets of an organisation, improving their workplace's physical comfort is essential to ensure a satisfactory productivity level (Andrew, 2011). Besides, the need for the workers to understand the occupational safety and health (OSH) requirements and their participation in formulating preventive measures to create a safer working environment have been highlighted (Gravel et al., 2011). Heat stress is defined in the guideline as the overall heat exposed to a worker from the combination of metabolic heat and thermal parameters - air temperature, air velocity, humidity, radiant heat from machinery or building materials, and clothes worn by the workers. Therefore, these factors are considered in heat stress evaluations at workplaces. The Wet Bulb Globe Temperature (WBGT) index is widely used in heat stress analysis. This index considers the main thermal parameters such as dry bulb, natural wet bulb, and globe temperature. In Malaysia, a workplace heat stress management guideline was introduced in 2016, and important information such as environmental factors, assessment requirements, and preventive measures for heat stress are presented (DOSH, 2016). Heat stress is assessed using the WBGT index, and the values obtained are compared with the action limit, and threshold value limit reference values stated in the American Conference of Governmental Industrial Hygienists guideline (ACGIH, 2015 as cited in DOSH 2016). The international standard ISO 7243 prescribes a specific duration of rest time for employees, depending on the work intensity and the WBGT level, to prevent the core body temperature from exceeding 38°C (Parsons, 2006).

Heat-related illnesses could happen if the human body fails to control its temperature, and the symptoms include heat cramps, heat exhaustion, heat syncope, and a more life-threatening heatstroke (Parsons, 2014). It was evident that workers exposed to excessive heat and conducting manual labour in extremely hot environments may be at risk of heat stress and other occupational injuries (Xiang et al., 2014; Yang et al., 2017). It usually happens in industries with high-temperature equipment use and the associated processes, such as manufacturing, construction, mining, utility, agriculture, and others (Andrew, 2011). According to Rabei (2019), heat disorders were experienced by several bakery workers, and appropriate control measures were suggested. It was reported by the Bureau of Labour (2017) that exposure to environmental heat had resulted in 37 work-related mortalities and 2830 cases of non-life-threatening heat-related injuries and diseases in 2015 alone. A study of occupational heat stress in workplaces found that 60% of the workforce had experienced a loss in work productivity due to the air temperature level. Approximately 20% were also more vulnerable to heat illness during the hotter month (Venugopal et al.,

2015). Climate change was found as a factor that intensified heat stress, where a study conducted in an automotive parts manufacturing plant revealed that a high percentage of the workers were not satisfied with the temperature of the workplace where headache and exhaustion were among the occupational illnesses reported (Pogačar et al., 2018). Berry et al. (2010) summarised the effects of climate change on mental health. They concluded that heat exposure at work might cause psychological distress among workers due to the loss of work capacity, income and disruption in social activity.

A heat stress assessment of a metal workshop found that the heat stress condition was aggravated by the protective clothing worn during work (Bernard, 1999). Therefore, personalised monitoring using sensor technology was proposed to evaluate heat stress as this method was less invasive and could record workers' effort intensity (Pancardo et al., 2015). Furthermore, to reduce such thermal stress, introducing a liquid cooling garment was useful in lowering the temperature and relative humidity under the workers' clothing (Bartkowiak et al., 2014). In the tropics, Tawatsupa et al. (2013) analysed the environmental heat exposure of Thai workers. The findings showed that 18% of the survey respondents were exposed to uncomfortable high temperatures while working, and men were more likely to experience heat stress than women. Besides, some workers in the hot-humid region expressed dissatisfaction with the workplace thermal environment, drinking water and sanitation facilities provided but were compelled to tolerate such harsh working conditions because of economic vulnerability (Dutta et al., 2015).

Besides the thermal conditions, undesirable noise level (NL) has been recognised as an occupational hazard for various industries in developing and modern countries (Edelson et al., 2009; Mohammed & Rabeea, 2021). Noise annoyance and related issues in buildings were found to affect the emotions and productivity of the occupants (Lusk et al., 2009; Aalto et al., 2017). According to Manivasagam (2019), Malaysia's occupational noise-related hearing disorders cases have increased significantly in the past decades and contributed to more than 60% of the total occupational diseases recorded. More than 80% of the incidents were reported from the manufacturing sector. To assist businesses in Malaysia in complying with the Occupational Safety and Health (Noise Exposure) Regulations 2019 (DOSH, 2019b), the industry code of practice to manage occupational noise exposure and hearing conservation has been introduced by DOSH (2019a). This code of practice specifies the practical procedures to analyse and control the noise level in workplaces. For instance, noise dose (ND) and noise exposure level (NEL) is required for noise risk assessment in all workplaces, and research should be conducted to reduce emission whenever necessary.

Building acoustic studies have been conducted worldwide. The outcome of an online survey showed that a large proportion of the respondents stated that their workplaces' noise level had negatively affected their workability (Oseland & Hodsman, 2018). Nelson et al. (2005) concluded that workplace noise is responsible for 16% of adults' disabling hearing

loss, which is more apparent in developing nations. The noise level of two commonly used machines in a factory was studied by Tomozei et al. (2012), and the noise transmission reduction trend from the noise sources to the outdoors was documented. A noise exposure study in a Danish factory found that the sound level was higher than the permissible level, and negative perceptions were recorded due to machinery use (Berry et al., 2010). This finding echoed Sriopas et al. (2017), where the NEL in a tropical factory exceeded 86 dBA, contributing to the high prevalence of auditory problems. Similarly, the noise level in an Indian manufactory was higher than the permitted noise limits, mainly because of the machines' sound (Krishnamurthy et al., 2017). The importance of the management's role in creating a healthy occupational surrounding was highlighted by Bockstael et al. (2013). Bell et al. (2015) compared the noise control performance in different manufacturing companies. They highlighted that corporations categorised as "high performers" had better knowledge of noise-related issues, were more aware of the newest engineering or administrative methods in noise reduction, and the management was more supportive of noise control initiatives.

Some studies analysed both heat stress and noise exposure simultaneously. For example, Meegahapola and Prabodanie (2018) studied a rubber compound factory's temperature, noise, and lighting conditions. The findings demonstrated that the two former parameters significantly influenced workers' productivity. This study has also recommended using the WBGT index to predict the heat stress condition instead of merely considering the air temperature. The noise level, thermal exposure and workplace safety practices of casting and forging units were assessed using calibrated meters by Singh et al. (2010). The study outcomes showed that WBGT and NL were high compared to the limits specified in the guidelines. In another study, ND was the main factor in causing noise-induced temporary threshold shift (TTS), and such hearing fatigue was enhanced with the heavy workload and heat stress (Chen et al., 2007).

Since the concurrent studies of heat and noise conditions in factories in hot and humid climates have yet to be extensively conducted, more work is needed. Hence, this case study aims to analyse a manufacturing plant's heat stress and noise conditions in an equatorial country. The main objectives are to measure the air temperature, relative humidity, air velocity and globe temperature to calculate WBGT and the noise level for ND and NEL analysis. First, a field survey consisting of physical measurements and questionnaire surveys was conducted at the plant's fan-assisted and naturally aired working areas. The results were then compared to the previous studies and the acceptable ranges recommended in relevant standards and guidelines.

Case Study Location

The research team selected a plant that manufactures pressure vessels for heat stress and noise exposure analysis because hot works like welding, brazing, grinding and fabrication of steel materials were conducted within the premises. The production area was estimated to house around 30 field staff. This particular workspace was divided into three main sections - Section A was assigned as the mechanical fitting place where different pressure vessel parts were assembled, and Section B was allocated for cutting and welding jobs. At the same time, the drilling, grinding and fabrication works were mostly carried out in Section C. As this area was partially enclosed where outdoor air was used as the means for ventilation, portable industrial fans were used to enhance air movement within the work sections.

METHODS

A pilot walkthrough survey was conducted about a month before the actual assessment to identify the locations where data collection was to be held. Upon obtaining the factory management's consent, a field study covering physical condition measurement and subjective evaluation was conducted from 0900 to 1700 h at the plant's three work sections. The research team measured heat and noise parameters concurrently, and care was taken not to interrupt the employees' work.

Heat Stress and Noise Level Measurements

A digital climate measuring instrument was used to measure the heat stress parameters. The device is connected with three sensor probes, measuring air temperature, relative humidity, and air velocity levels. These thermal parameter readings were then used to calculate the WBGT index. Following the DOSH guideline (2016), the instrument was positioned at about 1.1m above floor level, as the workers mostly stood while performing their duties. The noise level inside the factory was recorded using a sound level meter, which complied with the IEC61672-1 Class 2 standard and met the noise measuring equipment requirement of DOSH (2019a) for the sound level meter. The meter was placed near the locations where mechanical work was conducted to ensure accuracy. Both meters provide real-time data for the ease of environmental monitoring and come with data logging functions that allow continuous measurements. The heat and noise data were collected at 1-minute intervals throughout the survey.

Calculation of WBGT, ND and NEL

This work calculated the WBGT values of all three locations studied using the measured heat stress data. As the workplace was only partially enclosed and the influence of solar radiation was considered, Equation 1 was used for the calculation of WBGT:

$$\text{WBGT} = 0.7 T_{\text{wb}} + 0.2 T_{\text{g}} + 0.1 T_{\text{db}} \text{ } ^\circ\text{C} \quad (1)$$

where T_{wb} = wet-bulb temperature, T_{g} = globe temperature and T_{db} = dry-bulb temperature

The workers' exposure to work-related noise was analysed using the daily noise exposure level (NEL) method (DOSH, 2019a). The ND of the workers was calculated using Equation 2:

$$\text{ND} = 100 \times (T_e/8) \times 10^{(L-85)/10} \% \quad (2)$$

where T_e = effective duration of work and L = measured noise level.

The NEL of the workers was estimated using Equation 3:

$$\text{NEL} = \text{NL}_{\text{eq}} + 10 \text{Log}_{10} (T_e / T_o) \text{ dBA} \quad (3)$$

where NL_{eq} = 8-hour A-weighted equivalent continuous noise level, T_e = effective duration of work and T_o = 8 hour.

Workers' Perception Survey

The questionnaire survey aimed to identify the workers' perceptions of their thermal and noise environments. The questionnaire covered perceptions on heat and noise exposures, clothing acclimatisation, symptoms of potential health impacts, possible productivity losses due to extreme conditions and employee acceptance. The survey form has four sections, as shown in Table 1. All the questions posed in the survey form were developed by referring to the sample checklists and questionnaires published in the Heat Stress Management at Workplace (DOSH, 2016) and the Industry Code of Practice for Management of Occupational Noise Exposure and Hearing Conservation 2019 (DOSH, 2019a). Some questions were modified to suit the factory environment. Part C of the survey form used the DOSH subjective scores to acquire the descriptions of the workers' immediate thermal and noise environments.

Table 1

Contents of the questionnaire

Questionnaire Part	Content	Question type
Part A	Employee personal details	Multiple choice
Part B	Identification of potential hazards in the workplace	Dichotomous and multiple choice
Part C	Heat stress and noise level perceptions of the staff using DOSH subjective scores and checklists	Likert scale and Dichotomous
Part D	Employee's acceptability of the current workplace environment	Dichotomous and open-ended

RESULTS

Heat Stress and Thermal-Related Parameters

Fan-assisted natural ventilation was the main mode for thermal comfort and fresh air provisions in the manufacturing sections. As presented in Table 2, the air temperature measured at all three workplaces ranged from 26.9 to 35.7°C. The relative humidity (RH) levels ranged from 44.3–83.6%, while the air velocity was recorded from 0.01–2.45 m/s. The globe temperature influenced by solar radiation was measured to be within the range of 27.4–36.9°C. Therefore, the WBGT index was calculated using the measured heat stress parameters to be within 25.2 to 29.8°C with a total mean value of 27.7°C, and the highest mean WBGT value was obtained in Section A. Since the clothing types were standard work clothes, no clothing-adjustment factor was added to the WBGT index (DOSH, 2016).

Table 2

Locations under study and heat stress parameters

Heat stress parameters/location		Section A	Section B	Section C
Air temperature (°C)	Range	26.9–35.7	28.6–33.9	31.7–33.8
	Mean	32.1	31.7	32.6
Air velocity (m/s)	Range	0.02–1.40	0.01–2.45	0.03–1.44
	Mean	0.24	0.27	0.37
Relative humidity (%)	Range	44.3–83.6	52.9–71.0	49.5–57.2
	Mean	60.3	62.1	53.5
Globe temperature (°C)	Range	27.4–36.9	29.3–34.3	32.6–34.5
	Mean	33.1	32.3	33.3
WBGT(°C)	Range	25.2–29.8	26.2–28.3	27.1–28.5
	Mean	27.8	27.3	27.7

Noise Level

The plant's noise level ranged from 40.4 to 111.4 dBA during working hours (Table 3). The background noise was below 45 dBA. As mechanical fitting works requiring hammering and joining heavy materials were conducted in Section A, the average noise level in this area was the highest among all work sections. Unlike the thermal environment, the noise level in such workplaces was more challenging to predict as it depended mainly on the duration and intensity of work. From the results obtained, the NL was below the 85 dBA threshold limit specified by DOSH (2019a) for more than 80% of the work time and the maximum dBA was only recorded for a brief period. This finding shows that the workplace was acoustically safe for the workers. Based on an 8-hour exposure period to the mean noise level, the mean NEL was calculated as 74.1 dBA, while the ND of the workers was within 6.3 to 9.3%.

Table 3
Noise level at different work sections

Location	Minimum noise level (dBA) (background)	Maximum noise level (dBA)	ND (%)	NEL
Section A	41.5	100.2	9.3	74.7
Section B	40.4	100.4	6.3	73.0
Section C	43.0	111.4	7.9	74.0
Mean				74.1

Questionnaire and Observation Findings

Twenty-five skilled workers responded to the questionnaire survey. All the survey participants were male and were full-time employees of the company. The participants were mostly physically fit and free from acute diseases during the survey, and their metabolic rate was estimated at 180 W because the work intensity was light. For safety and practical reasons, 16 employees (64%) engaged in hot work, such as welders and steel cutters, were seen wearing a cotton coverall with a safety jacket and other personal protective equipment (PPE). The rest of the field staff wore lighter clothes and company uniforms to safely and comfortably perform their tasks. More than 65% of the survey respondents found the workplace air temperature acceptable during working hours. Besides, 80% of them opined that the plant area's humidity level was comfortable. Although most were satisfied with the thermal environment, the workers' perception skewed towards the warmer side of the scale as 76% and 24% of the welders termed their working environment "warm" and "hot," respectively. No vote was placed on the cooler side (-1 to 1) and the extreme "very hot" categories of the heat sensation scale. The same goes for the staff with lighter clothing levels, of which 34% felt "hot" while working. However, the perception of radiant heat

was mostly placed on the central categories (1 to 3), where 84% of the workers felt a heat source, but there was no risk of contact burns.

Higher airflow rates are recommended for non-air-conditioned spaces in hot and humid regions to increase the neutral temperature (Toe & Kubota, 2013). Ventilation fans can increase airflow rates to maintain the core body temperature (Ravanelli et al., 2015). 56% of workers with cotton coveralls and jackets rated the air velocity as “still air at the warm environment,” while the rest of them voted for “warm air at low speed” (19%) and “still air in a hot environment” (25%). Similar outcomes were obtained from their lighter-clothed co-workers, where 75% of them found low air movement in their workplace. The air humidity condition was identified to be “very humid and very dry” by 92% of the test subjects. This result agreed well with the physical measurement outcomes, where the relative humidity was between 44.3 and 88.3%. It should be noted that the time and locations where the plant’s staff were invited to participate could have influenced their perceptions. The mean scores for each heat stress question using scale points are presented in Table 4. It can be observed that the workers generally considered their workspace as warm with sensible air movement, moderately humid and safe from contracting heat-related injuries.

The noise level perceptions among the staff were acquired during the field survey. For brevity, only the important data are presented in this paper. About 70% of the workers voted that their hearing ability was not affected by the noise level in their workplace, and they did not experience any dizziness due to noise. Furthermore, most of them had not experienced loud enough noise to make their hearing “muffled” for a moment. As for the question about using industrial equipment for work, less than 30% of the respondents stated that they used powered tools or machinery for more than half an hour each day. The survey results also demonstrated that more than 80% of the workers wore hearing protective equipment, such as earplugs and earmuffs provided by the company when using these tools. Besides, 75% opined that there was no need to raise their voice while communicating with their work colleagues.

Table 4
Mean scores for heat stress survey questions

Questions	Scale points/ Option	Mean Score/ Percentage
How do you feel about your workplace’s air temperature?	-1 (cool) to 4 (very hot)	2.24
How is the air movement at your workplace?	-3 (cool air at high speed) to 5 (very hot air at high speed)	1.76

Table 4 (Continue)

Questions	Scale points/ Option	Mean Score/ Percentage
How do you perceive the radiant heat condition?	-1 (cold object) to 6 (workers are not permitted to work without PPE)	1.60
How would you describe the humidity level?	0 (Air is dry) to 6 (Air is too humid)	2.04

DISCUSSION

Heat stress and elevated noise exposure at workplaces pose a significant challenge to occupational safety and health, impair the workers' general comfort, and lower their productivity (Meegahapola & Prabodanie, 2018). The heat stress measurements showed that the mean air velocity and relative humidity levels were within the acceptable ranges recommended in DOSH (2016). The plant's owner implemented a good workplace management system where all workers had periodic rest breaks besides mealtime to ensure they got enough rest during work. Referring to the DOSH's screening action limit (AL) and threshold limit value (TLV), the workers' risk of excessive exposure to heat stress was minimal. These findings contradicted the work of Singh et al. (2010), where high heat stress and noise levels in casting and forging units were found. It has indirectly suggested that the work sections in the plant were well-planned and organised.

The survey results showed that most employees found their thermal environment acceptable. As for air movement perception, one of the possible factors that made the respondents felt low air movement in the factory was their clothing type. The working locations that were equipment and material intensive may have contributed to this perception. As stationary pedestal fans were used to induce airflow, the workers' sensation of air movement would be affected if they moved around their work area without first adjusting the pedestal fans' blow direction. There were instances where the welders had to move to the other end of the work section, where airflow was slightly restricted to complete their welding task.

Since the studied workplace was partially enclosed and naturally ventilated, the Threshold Limit Value (TLV) for WBGT set by ISO 7243 is 28°C. Based on the results obtained from field measurement, the highest WBGT readings (29.8°C, 28.3°C and 28.5°C) at the work sections were mostly calculated during lunch break (1300 to 1400 h) when the ambient air temperature was high. The mean WBGTs were lower than the stipulated TLV value. Therefore, it has been suggested that the workforce was not exposed to high temperatures that may lead to heat stress while performing their tasks. In comparison, the WBGT values for this work were much lower than that of the earlier studies, where a heat

stress analysis in a steel factory found that the WBGT was more than 35°C owing to the influence of radiation heat (Krishnamurthy et al., 2017). It was evident in Section B where most questionnaire participants claimed that the surrounding temperature was warm but found their surrounding temperature level acceptable. Among the reasons for this was that workers working for an extended period in a warm environment are usually acclimatised to the thermal environment and may tolerate the workplace temperature (Joubert & Bates, 2008). Considering this, it can be assumed that the respondents of this study were already fully acclimatised to the workplace environment as they had been long-term employees of the company. It should be noted that this study did not consider personalised evaluations of heat stress levels, and the field data were analysed based on each selected location and the calculated mean scores for heat stress survey questions.

The measured sound intensities showed that the NEL did not exceed the permissible level of 85 dBA for an 8-hour exposure period stipulated in the Noise Exposure Regulation 2019. The daily ND was also far below the prescribed limit of 100%. The main reason for this was that the activities which generated high noise levels were only carried out for a brief moment during the time when this study was conducted. The highest NL was recorded when hammering work and the use of heavy machinery were carried out simultaneously, and this only occurred for a very short period of time. It was further identified that although machines and tools were used, the effect on background NL was not as high as expected, possibly because of the large openings at the plant's perimeter that dissipated the noise generated from work. It is in line with the workers' power tools and machinery use durations, where most did not use these industrial devices for more than half an hour a day. From the questionnaire survey, most respondents did not experience any noise or hearing impairment while working. It can be attributed to the low mean noise level in the plant and the use of personal auditory protectors when engaging with work that produced loud noise.

CONCLUSION

This study systematically measured and analysed a manufacturing plant's heat stress and noise levels. The field-measured data showed that the heat stress and noise exposure levels were generally below the stipulated limits of the guidelines, which suggested that the locations under study were safe and comfortable for the workers. It is in good agreement with the questionnaire survey outcomes. In future studies, other occupational safety and health requirements, such as light level and air quality, can be considered to make the research findings more comprehensive. Furthermore, since this study only focused on the heat and noise conditions of a hot and humid country's manufacturing plant, the workers' heat and noise exposure may differ from that of other places or industries that warrant further research in these areas.

ACKNOWLEDGEMENT

This study was funded by the Lestari SDGTriangle@UiTM 2.0 grant scheme (File No. 600-RMC/LESTARI SDG-T 5/3 (005/2021)) of Universiti Teknologi MARA. In addition, the authors would like to thank the approval and information given by the plant's owner, the manager and his co-workers throughout the field survey.

REFERENCES

- Aalto, L., Lappalainen, S., Salonen, H., & Reijula, K. (2017). Usability evaluation (IEQ survey) in hospital buildings. *International Journal of Workplace Health Management*, 10(3), 265-282. <https://doi.org/10.1108/IJWHM-03-2016-0014>
- Andrew, P. H. (2011). *Heat strain, hydration status and symptom of heat illness in surface mine workers* (Doctoral dissertation). Queensland University of Technology, Australia. https://eprints.qut.edu.au/44039/1/Andrew_Hunt_Thesis.pdf
- Bartkowiak, G., Dąbrowska, A., & Marszałek, A. (2014). Assessment of the human responses to the influence of personal liquid cooling system in the hot environment. *International Journal of Clothing Science and Technology*, 26(2), 145-163. <https://doi.org/10.1108/IJCST-03-2013-0024>
- Bell, N., Lunt, J., Webster, J., & Ward, T. (2015). Comparing high and low performers for noise control. *International Journal of Workplace Health Management*, 8(1), 46-60. <https://doi.org/10.1108/IJWHM-03-2014-0007>
- Bernard, T. E. (1999). Heat stress and protective clothing: and emerging approach from the United States. *The Annals of Occupational Hygiene*, 43(5), 321-327. <https://doi.org/10.1093/annhyg/43.5.321>
- Berry, H. L., Bowen, K., & Kjellstrom, T. (2010). Climate change and mental health: A causal pathways framework. *International Journal of Public Health*, 55, 123-132. <https://doi.org/10.1007/s00038-009-0112-0>
- Bockstael, A., De Bruyne, L., Vinck, B., & Botteldooren, D. (2013). Hearing protection in industry: Companies' policy and workers' perception. *International Journal of Industrial Ergonomics*, 43(6), 512-517. <https://doi.org/10.1016/j.ergon.2012.08.009>
- Bureau of Labor Statistics (2017). *The economics daily, work injuries in the heat in 2015*. U.S. Department of Labour. <https://www.bls.gov/opub/ted/2017/work-injuries-in-the-heat-in-2015.htm>
- Chen, C., Dai, Y., Sun, Y., Lin, Y., & Juang, Y. (2007). Evaluation of auditory fatigue in combined noise, heat and workload exposure. *Industrial Health*, 45(4), 527-534. <https://doi.org/10.2486/indhealth.45.527>
- DOSH. (2016). *Guideline of heat stress management at work place*. Ministry of Human Resources Malaysia. <https://www.dosh.gov.my/index.php/legislation/guidelines/industrial-hygiene-1/2017-guidelines-heat-stress-management-at-workplace/file>
- DOSH. (2019a). *Industry code of practice for management of occupational noise exposure and hearing conservation 2019*. Ministry of Human Resources Malaysia. <https://www.dosh.gov.my/index.php/competent-person-form/occupational-health/regulation/codes-of-practice/industrial-hygiene/3286-industry-code-of-practice-for-management-of-occupational-noise-exposure-and-hearing-conservation-2019/file>

- DOSH. (2019b). *Occupational safety and health (Noise Exposure) Regulations 2019*. Ministry of Human Resources Malaysia. <https://www.dosh.gov.my/index.php/ms/competent-person-form/occupational-health/regulation/regulations/regulations-under-occupational-safety-and-health-act-1994-act-514/3174-00-occupational-safety-and-health-noise-exposure-2019/file>
- Dutta, P., Rajiva, A., Andhare, D., Azhar, G. S., Tiwari, A., & Sheffield, P. (2015). Perceived heat stress and health effects on construction workers. *Indian Journal of Occupational and Environmental Medicine*, 19(3), 151-158. <https://doi.org/10.4103/0019-5278.174002>
- Edelson, J., Neitzal, R., Meischke, H., Danielle, W., Shepperd, L., Stover, B., & Seixas, N. (2009). Predictors of hearing protection use in construction workers. *The Annals of Occupational Hygiene*, 53(6), 605-615. <https://doi.org/10.1093/annhyg/mep039>
- Edem, M. J., Akpan, E. U., & Pepple, N. M. (2017). Impact of workplace environment on health workers. *Occupational Medicine and Health Affairs*, 5(2), Article 1000261. <https://doi.org/10.4172/2329-6879.1000261>
- Gravel, S., Rhéaume, J., & Legendre, G. (2011). Strategies to develop and maintain occupational health and safety measures in small businesses employing immigrant workers in metropolitan Montreal. *International Journal of Workplace Health Management*, 4(2), 164-178. <https://doi.org/10.1108/17538351111143321>
- Joubert, D., & Bates, G. (2008). Occupational heat exposure Part 1: The physiological consequences of heat exposure in the occupational environment. *Occupational Health Southern Africa*, 2008, 1-5.
- Lusk, S. L., Hong, O. S., Ronis, D. L., Eakin, B. L., Kerr, M. J., & Early, M. R. (1999). Effectiveness of an intervention to increase construction workers' use of hearing protection, *The Journal of Human Factors and Ergonomics Society*, 41(3), 487-494. <https://doi.org/10.1518/001872099779610969>
- Krishnamurthy, M., Ramalingam, P., & Perumal, K. (2017). Occupational heat stress impacts on health and productivity in a steel industry in southern India. *Safety and Health at Work*, 8(1), 99-104. <https://doi.org/10.1016/j.shaw.2016.08.005>
- Manivasagam, D. (2019). Empowering occupational health doctors through the occupational safety & health (noise exposure) regulations 2019. *Journal of Occupational Safety and Health*, 16(3), 1-7.
- Meegahapola, P. A., & Ranga Prabodanie, R. A. (2018). Impact of environmental conditions on workers' productivity and health. *International Journal of Workplace Health Management*, 11(2), 74-84. <https://doi.org/10.1108/IJWHM-10-2017-0082>
- Mohammed, M. I., & Rabeea, M. A. (2021). Effects of noise pollution from electric backup generators on the operators' health. *Pertanika Journal of Science and Technology*, 29(4), 2675-2687. <https://doi.org/10.47836/pjst.29.4.24>
- Nelson, D. I., Nelson, R. Y., Concha-Barrientos, M., & Fingerhut, M. (2005). The global burden of occupational noise-induced hearing loss. *American Journal of Industrial Medicine*, 48(6), 446-458. <https://doi.org/10.1002/ajim.20223>
- Oseland, N., & Hodsmann, P. (2018). A psychoacoustical approach to resolving office noise distraction. *Journal of Corporate Real Estate*, 20(4), 260-280. <https://doi.org/10.1108/JCRE-08-2017-0021>

- Pancardo, P., Acosta, F. D., Hernández-Nolasco, J. A., Wister, M. A., & López-de-Ipiña, D. (2015). Real-Time personalized monitoring to estimate occupational heat stress in ambient assisted working. *Sensors (Basel, Switzerland)*, *15*(7), 16956-16980. <https://doi.org/10.3390/s150716956>
- Parsons, K. (2006). Heat stress standard ISO 7243 and its global application. *Industrial Health*, *44*(3), 368-379. <https://doi.org/10.2486/indhealth.44.368>
- Parsons, K. (2014). *Human Thermal Environments: The Effects of Hot, Moderate, and Cold Environments on Human Health, Comfort, and Performance* (3rd ed.). CRC Press.
- Pogačar, T., Casanueva, A., Kozjek, K., Ciuha, U., Mekjavić, I. B., Bogataj, L. K., & Črepinšek, Z. (2018). The effect of hot days on occupational heat stress in the manufacturing industry: implications for workers' well-being and productivity. *International Journal of Biometeorology*, *62*, 1251-1264. <https://doi.org/10.1007/s00484-018-1530-6>
- Rabeiy, R. E. (2019). Evaluation of indoor heat stress on workers of bakeries at Assiut City, Egypt. *International Journal of Environmental Science and Technology*, *16*, 2637-2642. <https://doi.org/10.1007/s13762-018-1839-z>
- Ravanelli, N. M., Hodder, S. G., Havenith, G., & Jay, O. (2015). Heart rate and body temperature responses to extreme heat and humidity with and without electric fans. *JAMA*, *313*(7), 724-725. <https://doi.org/10.1001/jama.2015.153>
- Singh, L. P., Bhardwaj, A., & Deepak, K. K. (2010). Occupational exposure in small and medium scale industry with specific reference to heat and noise. *Noise Health*, *12*(46), 37-48. <https://doi.org/10.4103/1463-1741.59998>
- Srinivasan, K., Maruthy, K. N., Venugopal, V., & Ramaswamy, P. (2016). Research in occupational heat stress in India: Challenges and opportunities. *Indian Journal of Occupational and Environmental Medicine*, *20*(2), 73-78. <https://doi.org/10.4103/0019-5278.197522>
- Sriopas, A., Chapman, R. S., Sutammasa, S., & Siriwong, W. (2017). Occupational noise-induced hearing loss in auto part factory workers in welding units in Thailand. *Journal of Occupational Health*, *59*(1), 55-62. <https://doi.org/10.1539/joh.15-0291-OA>
- Tawatsupa, E., Yiengprugsawan, V., Kjellstrom, T., Berecki-Gisolf, J., Seubsman, A., & Sleigh, A. (2013). Association between heat stress and occupational injury among Thai workers: Findings of the Thai cohort study. *Industrial Health*, *51*(1), 34-46. <https://doi.org/10.2486/indhealth.2012-0138>
- Toe, D. H. C., & Kubota T. (2013). Development of an adaptive thermal comfort equation for naturally ventilated buildings in hot-humid climates using ASHRAE RP-884 database. *Frontiers of Architectural Research*, *2*(3), 278-291. <http://dx.doi.org/10.1016/j.foar.2013.06.003>
- Tomozei, C., Astolfi, A., Nedeff, V., & Lazar, G. (2012). Noise sources characterisation inside and outside a factory. *Environmental Engineering and Management Journal*, *11*(3), 701-708. <https://doi.org/10.30638/eeenj.2012.089>
- Venugopal, V., Chinnadurai, J. S., Lucas, R. A., & Kjellstrom, T. (2015). Occupational heat stress profiles in selected workplaces in India. *International Journal of Environmental Research and Public Health*, *13*(1), Article 89. <https://doi.org/10.3390/ijerph13010089>

- Xiang, J., Bi, P., Pisaniello, D., & Hansen, A. (2014). Health impacts of workplace heat exposure: An epidemiological review. *Industrial Health*, 52(2), 91-101. <https://doi.org/10.2486/indhealth.2012-0145>
- Yang, X., Li, B., Li, Y., Wang, Y., & Zheng, C. (2017). A research on characteristics of human heat stress in dynamic hot environment. *Procedia Engineering*, 205, 2749-2754. <https://doi.org/10.1016/j.proeng.2017.09.870>



TOPSIS for Analyzing the Risk Factors of Suicidal Ideation Among University Students in Malaysia

Sin Yin Chan* and Chee Keong Ch'ng

Department of Decision Science, School of Quantitative Sciences, Universiti Utara Malaysia, 06010 Sintok, Kedah, Malaysia

ABSTRACT

Globally, suicide is a major public health issue. Suicide is the first or second reason for death among college and university students. The suicide rate among university students is relatively high in Malaysia. Numerous risk factors exacerbate suicidal ideation. Therefore, it is critical to gain as much insight as possible into the risk factors for suicidal ideation among university students and prioritize them based on the importance level. Therefore, students with a high risk for suicide can be identified, and earlier precautions can be taken to assist the students. In this paper, 18 determinants of suicidal ideation were discovered through the systematic literature review, and these factors were then ranked according to the seriousness using the TOPSIS method. The results showed that *previous suicide attempts*, *mental disorders*, and *negative life events* were the most influential factors leading to suicide. In contrast, *gender* and the *residential area* had the least impact. The result enables the government, relevant stakeholders, and policymakers to develop comprehensive multisectoral strategies that can prevent suicide effectively.

Keywords: Risk factors, suicide, suicidal ideation, TOPSIS, university students

ARTICLE INFO

Article history:

Received: 26 March 2022

Accepted: 28 July 2022

Published: 06 March 2023

DOI: <https://doi.org/10.47836/pjst.31.2.17>

E-mail addresses:

chansinyin97@gmail.com (Sin Yin Chan)

chee@uum.edu.my (Chee Keong Ch'ng)

*Corresponding author

INTRODUCTION

Suicide is a serious public health issue worldwide. Globally, more than 700 000 people die owing to suicide every year (World Health Organization, 2021). Suicide has been identified as one of the critical mental health problems that occur among university students in the world (World Health Organization, 2019). Apart from that,

studies stated that suicide is categorized as the first or second key reason for death among college and university students (Abdu et al., 2020).

In Malaysia, suicide rates increased steadily in recent years. Polis Diraja Malaysia (PDRM) (2021) reported that the number of suicide cases in Malaysia rose from 609 cases in 2019 to 613 cases in 2020, and there were 468 cases in the first five months of the year 2021. Based on the statistics, females were more likely to be involved in suicide cases. Besides, people aged between 15 to 18 had a high possibility of committing suicide compared to other populations.

In Malaysia, the suicide rate among university students is relatively high. News concerning university students committing suicide has been widely reported and published. For example, two university students from Selangor committed suicide within a week (NST, 2019). Besides that, a female university student from Melaka was found suicide by jumping from an apartment (Mamat, 2021). Apart from that, a Chinese female university student from Sarawak was also found suicide by hanging in her bedroom due to academic pressure (Chang, 2021).

Numerous risk factors exacerbate suicide ideation. Some studies claim that suicide is closely related to *mental disorders*. Most of the people who commit suicide have suffered from mental disorder problems such as depression, eating disorders, and sleeping disorders, among others (Bilsen, 2018; Pillay, 2021; Shafiee & Mutalib, 2020). Not only that, but *hopelessness* also contributes to suicidal ideation. Losing passion for life will make a person tend to have suicidal thoughts (Primananda & Keliat, 2019).

Most university students feel *stress* when dealing with academic pressure, relationship problems, financial problems, and many other things (Pillay, 2021). Undeniably, these stressors are the main causes of mental health problems that result in suicidal thoughts (Jusnani et al., 2020; Pillay, 2021). *Society pressure* from peers, lecturers, social media, family, and roommates in university is also a critical reason for students to have suicidal thoughts (Jusnani et al., 2020). According to Bilsen (2018), *negative life events* such as relationship problems, sexual abuse, cyberbullying, and the death of the close one bring a huge impact on youth, and it may derive suicidal intention.

Poor social support is also an important factor that leads to suicidal ideation. Research stated that people who lack social assistance are more likely to have suicidal intentions than others (Abdu et al., 2020). Similarly, *interpersonal conflicts* may also bring suicidal ideation because they think that they are a burden to others (Jusnani et al., 2020).

Other than that, *family factors* such as child abuse, divorced parent, parents with alcohol and drugs addiction, and cold relationships among family members are closely linked to suicidal ideation (Bilsen, 2018; Costa et al., 2019; Abdu et al., 2020; Junior et al., 2020; Jusnani et al., 2020).

There are 25 to 33% of suicide cases occur in individuals who had a previous history of self-harming (Bilsen, 2018). Hence, it can be said that people who have *prior suicide attempts* are more probably to commit suicide again in the future (Olfson, 2018).

People with high self-esteem tend to accept themselves and always be satisfied with their life (Primananda & Keliat, 2019). In contrast, people with *low self-esteem* will always feel depressed and are more likely to have suicidal ideation in difficult times (Jusnani et al., 2020; Owusu-ansah et al., 2020).

Personality characteristic is also one of the reasons that lead to suicidal ideation. Personality characteristics such as a lack of ability to control emotions well and a lack of problem-solving skills are more likely to cause insecurity, low self-esteem, emotional issues, and even worse, suicide (Bilsen, 2018 & Wasserman et al., 2021).

People tend to *imitate* someone who has a similar background to them. Due to this, there are many suicide clusters formed from the news about suicide cases published frequently on social media (Bilsen, 2018). Durkee et al. (2011) also agreed that the internet and social media are the main medium for promoting suicidal behaviors.

Gender is one of the risk factors for suicidal ideation. Some studies stated that females have a higher possibility of suicidal intentions during the transition from school to university (Arafat et al., 2018; Shafiee & Mutalib, 2020). However, some researchers declared that male is more likely to have suicidal thoughts because they seldom seek help from others (Amini et al., 2016; Park et al., 2020; Wasserman et al., 2021; Pillay, 2021).

Another important risk factor that leads to suicidal ideation is *health problems* (Lyu & Zhang, 2019). The research claimed that people with severe disabilities and serious physical health problems tend to end their life (Yu et al., 2021; Pillay, 2021). Besides, suicidal ideation is more likely to appear in people with *the financial problem* (Shafiee & Mutalib, 2020; Berkelmans et al., 2021). Lack of money to pay university fees and living costs puts the student at high risk for suicide (Jusnani et al., 2020).

Suicidal ideation is found more vulnerable to people who are involved in *substance abuse*. Smoking addiction and lifetime alcohol and drug use are the important reasons for suicidal thoughts (Costa et al., 2019; Abdu et al., 2020; Junior et al., 2020).

Religion is also among the risk factors for suicidal thoughts. Participating in religious activities can help people get rid of stress and anxiety; the most important thing is that it can help reduce the tendency to have suicidal intentions (Abdu et al., 2020). It is because suicide is highly prohibited in almost all religions (Gearing & Alonzo, 2018; Nguyen et al., 2020).

Finally, *the residential area* is found to be related to suicidal thoughts. The research illustrated that suicide case in rural areas was higher than in urban areas because of the lower accessibility of medical help as well as the violence and substance abuse issues in rural areas that may result in mental health issues and suicidal crisis (Junior et al., 2020; Yu et al., 2021).

LITERATURE REVIEW

Several studies have been done previously. For example, through a comprehensive literature review strategy, several studies discovered the risk factors for suicide in the general population, adolescents, higher education students, and severe suicide attempters (Bilsen, 2018; Lyu & Zhang, 2019; Junior et al., 2020; Shafiee & Mutalib, 2020; Pillay, 2021). Furthermore, Jusnani et al. (2020) also discovered some factors that lead to suicide through semi-structured interviews. Based on the articles, mental disorders, depression, and poor social support were among the key leading causes of suicidal ideation. Apart from that, the relationship between some risk factors and suicide has been studied in previous studies by using data mining techniques like a decision tree and logistic regression (Amini et al., 2016; Cho et al., 2021; Ishaq et al., 2021).

Despite the fact that some research has been done on the issue of suicide to find the major factors that may lead to suicide among adolescents, studies that explicitly focus on university students are still rare. However, due to suicide thoughts being fairly common among university students, it is vital to investigate further by prioritizing risk variables according to their level of risk. (Prihadi et al., 2020).

The main function of MCDM is to rank several alternatives or variables. Some MCDM methods have been used in the field of psychiatry. For instance, Analytic Hierarchy Process (AHP) method was utilized to prioritize the stress factors of police officers (Öneren et al., 2016). Besides, Benfares et al. (2019) used the AHP method to predict depression among cancer patients. In addition, the Technique for Order Preference by Similarity to Ideal Solution (TOPSIS) was also used previously in this related aspect. Chauhan et al. (2021) implemented the TOPSIS approach in prioritizing the mental stress factors of farmers. Besides that, Pal et al. (2019) utilized the TOPSIS method to diagnose vector-borne diseases. The TOPSIS method was also used to assess the stress level in an urban area during the COVID-19 outbreak Gupta et al. (2021). Generally, both methods were the common methods employed in the psychiatry area. However, the TOPSIS method was chosen in this study due to its simplicity, ease of understanding, efficient computation, and the ability to measure the relative performance of each alternative (Rahim et al., 2018). Other than that, a pairwise comparison that is required in the AHP method is avoided in TOPSIS. Hence, this method is suitable for cases with numerous alternatives. Plus, TOPSIS can include an unlimited range of alternatives and has the fewest rank reversals compared with other MCDM techniques (Mukherjee, 2014).

MATERIALS AND METHOD

The formulation of this research involved five design thinking phases (Table 1).

Table 1

Design thinking process of the research

Phases	Process
Empathize	Discover that the suicide rate among university students in Malaysia has been getting higher in recent years.
Define	Determine the risk factors associated with suicide.
Ideate	Critically review the literature and determine the research gaps. Several MCDM methods have been determined to prioritize suicidal ideation.
Prototype	Select and implement the TOPSIS method to prioritize the risk factors for suicidal ideation.
Test	Run the analysis, and the order of each factor is recorded.

Data Collection Process

In this study, primary data was collected through a questionnaire. The questionnaire was distributed to the respondents randomly through social media, including WhatsApp and Facebook, using online Google Forms. The study sample only included university students in public universities in Malaysia. In order to ensure that there is no bias issue, the respondents were selected randomly from 13 states of Malaysia. The respondents were required to compare the importance of the risk factor over other risk factors.

The questionnaire consisted of 18 risk factors for suicide attempts which were *hopelessness, mental disorder, substance abuse, stress, previous suicide attempts, family factor, poor social support, negative life events, personality characteristic, health problem, low self-esteem, residential area, gender, imitation, society pressure, financial problem, religion, and interpersonal conflicts* that were discussed in the introduction section.

Sixty students received the questionnaire. However, 15 did not respond, while ten respondents were unsuitable for this study. This study only included university students under 26 who are experiencing pressure in life and are willing to participate in this survey. In order to ensure that they were suitable for the study, the respondents were required to answer some questions in the first section of the questionnaire, such as “Do you feel stress in your daily life?” “Are you facing financial pressure,” “Do you feel dissatisfied with your current life?” “Do you think you need to meet counselors?” and “Do you intend to suicide before?” Only the students who answered more than two “yes” from the five questions will be taken as samples. The willingness to answer the questionnaire was also asked. In the end, a total of 35 samples were received. According to Saaty (1980) and Kusnadi & Kurniawan (2017), there are no general rules for the sample size; however, it should be greater than five samples to run a valid analysis. Melillo and Pecchia (2016) indicated that at least 19 samples are considered appropriate and sufficient to run the analysis.

Table 2 illustrates the socio-demographics of the participants.

Table 2
Socio-demographics of the respondents

Category	Frequency	Percentage
Gender		
Male	17	48.57%
Female	18	51.43%
State		
Perlis	2	5.71%
Kedah	2	5.71%
Pulau Pinang	5	14.29%
Perak	2	5.71%
Selangor	5	14.29%
Negeri Sembilan	2	5.71%
Melaka	2	5.71%
Johor	5	14.29%
Pahang	2	5.71%
Terengganu	2	5.71%
Kelantan	2	5.71%
Sabah	2	5.71%
Sarawak	2	5.71%
Feeling stress in their life		
Yes	30	85.71%
No	5	14.29%
Facing financial pressure		
Yes	25	71.43%
No	10	28.57%
Dissatisfied with life		
Yes	20	57.14%
No	15	42.86%
Need to meet a counselor		
Yes	25	71.43%
No	10	28.57%
Intent to suicide before		
Yes	19	54.29%
No	16	45.71%

The measurement scale utilized in the questionnaire was the Likert scale, which ranges from 1 to 5 (Shirouyehzad & Dabestani, 2011). In order to compare the importance of the risk factors for suicidal ideation, respondents were asked to rate on a five-point Likert scale varying from “equally important” (1), “moderately important” (2), “strongly important” (3), “very strongly important” (4) to “extremely important” (5). Below are the samples of scales of the factors.

Compare Hopelessness with following factors *									
	H5	H4	H3	H2	1	2	3	4	5
Mental disorder (eg: depression, eating disorders, etc.)	<input type="radio"/>	<input type="radio"/>	<input type="radio"/>	<input type="radio"/>	<input checked="" type="radio"/>	<input type="radio"/>	<input type="radio"/>	<input type="radio"/>	<input type="radio"/>

Figure 1. Sample of scale

Figure 1 illustrates that hopelessness and mental disorder are equally important.

Compare Hopelessness with following factors *									
	H5	H4	H3	H2	1	2	3	4	5
Mental disorder (eg: depression, eating disorders, etc.)	<input type="radio"/>	<input type="radio"/>	<input checked="" type="radio"/>	<input type="radio"/>	<input type="radio"/>	<input type="radio"/>	<input type="radio"/>	<input type="radio"/>	<input type="radio"/>

Figure 2. Sample of Scale

Figure 2 shows that hopelessness is strongly important compared to mental disorders.

Process of Development of TOPSIS Method

Technique for Order Preference by Similarity to Ideal Solution (TOPSIS) is one of the multiple criteria decision-making approaches introduced by Hwang and Yoon in 1981 (Hwang & Yoon 1981). The principle of the method is to rank the alternatives by comparing them with the best and farthest solutions (Balioti et al., 2018). The best solution has the shortest distance from the positive ideal solution and the farthest from the negative ideal solution from the geometrical point. TOPSIS method was selected for this study because it is simple, easily understood, and can measure the relative performance of the alternatives. (Rahim et al., 2018). Moreover, the TOPSIS method has not been used in the suicide topic.

Figure 3 below illustrates the process flow of the TOPSIS method:

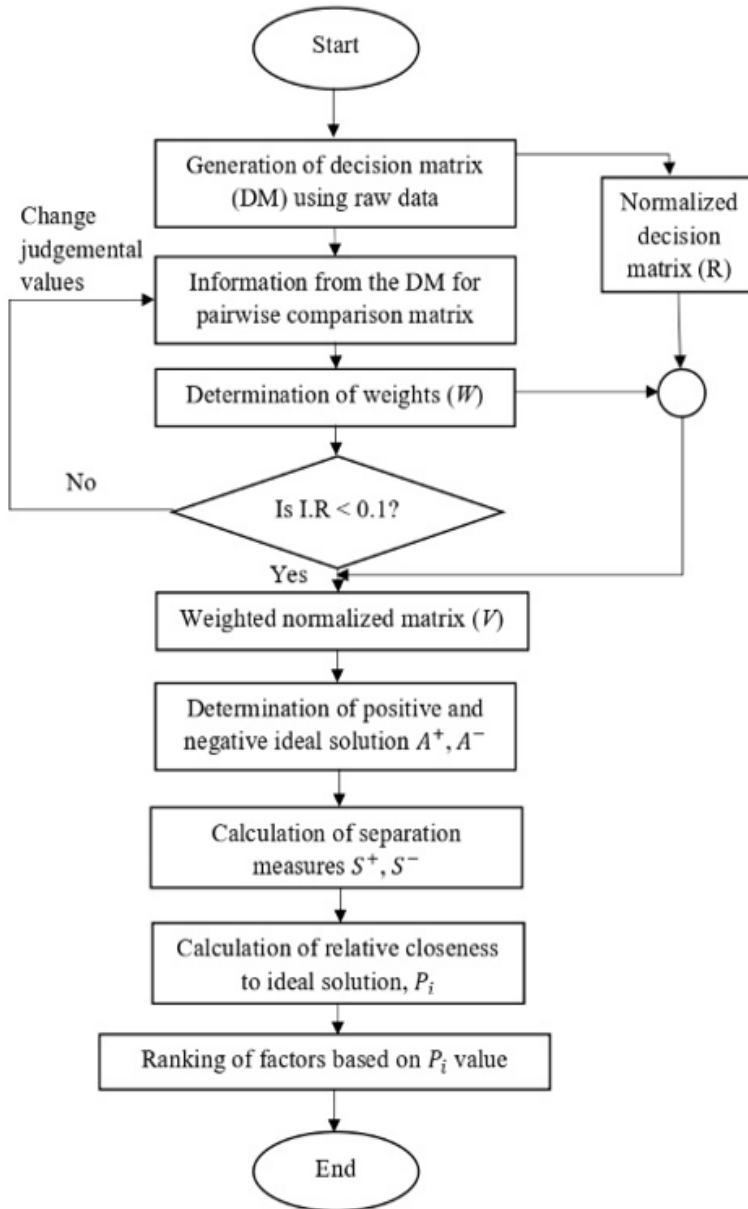


Figure 3. Process flow diagram

The steps for the TOPSIS method are as follows:

Construct the normalized decision matrix (Equation 1):

$$r_{ij} = \frac{X_{ij}}{\sqrt{\sum_{i=1}^m X_{ij}^2}} \quad (1)$$

Construct the weighted normalized decision matrix (Equation 2):

$$V_{ij} = w_j * r_{ij}, \quad j = 1, 2, 3, \dots, n \quad (2)$$

Determine the positive and negative ideal solutions (Equation 3):

$$\begin{aligned} A^+ &= \{(max v_{ij} | j \in J), (min v_{ij} | j \in J'), i = 1, 2, 3, \dots, m\} \\ &= \{V_1^+, V_2^+, V_3^+, \dots, V_n^+\} \end{aligned} \quad (3)$$

$$\begin{aligned} A^- &= \{(min v_{ij} | j \in J), (max v_{ij} | j \in J'), i = 1, 2, 3, \dots, m\} \\ &= \{V_1^-, V_2^-, V_3^-, \dots, V_n^-\} \end{aligned}$$

Calculate the separation measure (Equations 4 and 5):

Positive ideal separation, S^+

$$S_i^+ = \sqrt{\sum_{j=1}^n (A_{ij} - A_j^+)^2} \quad (4)$$

Negative ideal separation, S^-

$$S_i^- = \sqrt{\sum_{j=1}^n (A_{ij} - A_j^-)^2} \quad (5)$$

Where $i = 1, 2, 3, \dots, m$

Calculate the positive ideal solution (Equation 6):

$$P_i^+ = \frac{S_i^-}{\sqrt{(S_i^- + S_i^+)}} \quad (6)$$

Rank the alternatives

Sorted the alternatives C^+ from the largest to the smallest value. Alternative with the largest value of C^+ the best solution.

RESULTS

This section presents the ranking results of the 18 factors, including *hopelessness, mental disorder, substance abuse, stress, previous suicide attempts, family factor, poor social support, negative life events, personality characteristic, health problem, low self-esteem,*

residential area, gender, imitation, society pressure, financial problem, religion, and interpersonal conflicts using TOPSIS method. These significant factors were discovered from reviewing past research.

Table 3 shows the normalized decision matrix of the data.

Table 3

Normalized decision matrix

Factors	Hopelessness	MD	Stress	SA	FF	Religion	PSS	PSA
Hopelessness	0.2199	0.2707	0.3098	0.1829	0.2712	0.1563	0.2232	0.2095
MD	0.2252	0.2772	0.3052	0.3006	0.2407	0.2353	0.3002	0.3007
Stress	0.1778	0.2275	0.2504	0.3263	0.3015	0.2838	0.2378	0.2502
SA	0.2838	0.2176	0.1811	0.2360	0.2176	0.2848	0.2407	0.2692
FF	0.2056	0.2921	0.2107	0.2752	0.2536	0.2618	0.3338	0.2538
Religion	0.2669	0.2235	0.1675	0.1572	0.1838	0.1898	0.1979	0.2114
PSS	0.2094	0.1962	0.2238	0.2084	0.1615	0.2038	0.2125	0.2902
PSA	0.3420	0.3003	0.3261	0.2856	0.3255	0.2924	0.2386	0.3258
PC	0.2482	0.1850	0.2327	0.1903	0.2628	0.2463	0.2203	0.1859
NLE	0.2642	0.2852	0.2939	0.3142	0.2589	0.2696	0.3065	0.1890
Imitation	0.1789	0.2248	0.1714	0.1503	0.1854	0.1532	0.1513	0.2166
HP	0.2671	0.2326	0.2290	0.2226	0.2532	0.2446	0.2516	0.2284
IC	0.2556	0.2078	0.2465	0.2184	0.2275	0.2688	0.1998	0.1795
SP	0.2425	0.2761	0.2357	0.2483	0.1804	0.2281	0.2353	0.2073
FP	0.2646	0.2391	0.2476	0.3125	0.2899	0.2618	0.2930	0.2589
LSE	0.2024	0.2066	0.2012	0.2098	0.2303	0.2613	0.2227	0.2558
Gender	0.1511	0.1538	0.1473	0.1150	0.1547	0.1619	0.1299	0.1632
RA	0.1477	0.1541	0.1560	0.1313	0.1424	0.1516	0.1288	0.1659

Factors	PC	NLE	Imitation	HP	IC	SP	FP	LSE	Gender	RA
Hopelessness	0.2019	0.2153	0.2212	0.1993	0.1837	0.2115	0.2165	0.2478	0.2148	0.2159
MD	0.3414	0.2514	0.2219	0.2884	0.2849	0.2341	0.3021	0.3060	0.2660	0.2607
Stress	0.2452	0.2204	0.2629	0.2647	0.2169	0.2479	0.2635	0.2839	0.2508	0.2327
SA	0.2825	0.1943	0.2826	0.2566	0.2308	0.2217	0.1967	0.2566	0.3027	0.2607
FF	0.2199	0.2535	0.2461	0.2425	0.2380	0.3280	0.2279	0.2512	0.2418	0.2582
Religion	0.1756	0.1821	0.2229	0.1878	0.1507	0.1941	0.1888	0.1656	0.1729	0.1815
PSS	0.2198	0.1794	0.2527	0.2045	0.2271	0.2107	0.1889	0.2177	0.2413	0.2392
PSA	0.3992	0.4459	0.2706	0.3452	0.3874	0.3666	0.3278	0.2905	0.2946	0.2847
PC	0.2278	0.2358	0.2855	0.2461	0.2373	0.2583	0.2504	0.2463	0.2135	0.2291
NLE	0.2499	0.2587	0.2771	0.2947	0.2328	0.2441	0.2959	0.2161	0.3062	0.2615
Imitation	0.1436	0.1680	0.1799	0.2037	0.1930	0.1554	0.1832	0.1814	0.1868	0.1857
HP	0.2240	0.2124	0.2138	0.2420	0.3201	0.2484	0.2683	0.2194	0.2667	0.2242
IC	0.2050	0.2372	0.1991	0.1614	0.2135	0.1903	0.2135	0.2517	0.2355	0.2428
SP	0.2057	0.2472	0.2700	0.2273	0.2617	0.2332	0.2082	0.2497	0.2380	0.3143
FP	0.2371	0.2277	0.2559	0.2350	0.2605	0.2919	0.2605	0.2679	0.2101	0.2270
LSE	0.2110	0.2730	0.2262	0.2516	0.1935	0.2130	0.2218	0.2281	0.2275	0.2583
Gender	0.1575	0.1247	0.1421	0.1339	0.1338	0.1446	0.1830	0.1480	0.1476	0.1509
RA	0.1442	0.1434	0.1405	0.1566	0.1275	0.1076	0.1664	0.1280	0.1417	0.1450

Table 4

The weighted normalized decision matrix

Factors	Hopelessness	MD	Stress	SA	FF	Religion	PSS	PSA	PC
Hopelessness	0.0117	0.0180	0.0189	0.0108	0.0167	0.0072	0.0117	0.0165	0.0114
MD	0.0120	0.0184	0.0186	0.0178	0.0149	0.0108	0.0157	0.0236	0.0193
Stress	0.0095	0.0151	0.0153	0.0194	0.0186	0.0130	0.0124	0.0197	0.0138
SA	0.0151	0.0145	0.0111	0.0140	0.0134	0.0131	0.0126	0.0212	0.0159
FF	0.0110	0.0194	0.0129	0.0163	0.0157	0.0120	0.0174	0.0200	0.0124
Religion	0.0142	0.0148	0.0102	0.0093	0.0113	0.0087	0.0103	0.0166	0.0099
PSS	0.0112	0.0130	0.0137	0.0124	0.0100	0.0094	0.0111	0.0228	0.0124
PSA	0.0182	0.0199	0.0199	0.0169	0.0201	0.0134	0.0125	0.0256	0.0225
PC	0.0132	0.0123	0.0142	0.0113	0.0162	0.0113	0.0115	0.0146	0.0129
NLE	0.0141	0.0189	0.0179	0.0186	0.0160	0.0124	0.0160	0.0149	0.0141
Imitation	0.0095	0.0149	0.0105	0.0089	0.0114	0.0070	0.0079	0.0170	0.0081
HP	0.0142	0.0154	0.0140	0.0132	0.0156	0.0112	0.0131	0.0180	0.0126
IC	0.0136	0.0138	0.0150	0.0129	0.0140	0.0123	0.0104	0.0141	0.0116
SP	0.0129	0.0183	0.0144	0.0147	0.0111	0.0105	0.0123	0.0163	0.0116
FP	0.0141	0.0159	0.0151	0.0185	0.0179	0.0120	0.0153	0.0204	0.0134
LSE	0.0108	0.0137	0.0123	0.0124	0.0142	0.0120	0.0116	0.0201	0.0119
Gender	0.0081	0.0102	0.0090	0.0068	0.0096	0.0074	0.0068	0.0128	0.0089
RA	0.0079	0.0102	0.0095	0.0078	0.0088	0.0070	0.0067	0.0130	0.0081

Factors	NLE	Imitation	HP	IC	SP	FP	LSE	Gender	RA
Hopelessness	0.0139	0.0095	0.0117	0.0098	0.0122	0.0135	0.0136	0.0076	0.0075
MD	0.0163	0.0096	0.0169	0.0151	0.0136	0.0188	0.0168	0.0094	0.0090
Stress	0.0143	0.0113	0.0155	0.0115	0.0143	0.0164	0.0156	0.0089	0.0081
SA	0.0126	0.0122	0.0151	0.0123	0.0128	0.0123	0.0141	0.0107	0.0090
FF	0.0164	0.0106	0.0142	0.0126	0.0190	0.0142	0.0138	0.0086	0.0089
Religion	0.0118	0.0096	0.0110	0.0080	0.0112	0.0118	0.0091	0.0061	0.0063
PSS	0.0116	0.0109	0.0120	0.0121	0.0122	0.0118	0.0120	0.0086	0.0083
PSA	0.0289	0.0117	0.0203	0.0206	0.0212	0.0204	0.0160	0.0105	0.0099
PC	0.0153	0.0123	0.0144	0.0126	0.0150	0.0156	0.0135	0.0076	0.0079
NLE	0.0167	0.0120	0.0173	0.0124	0.0141	0.0185	0.0119	0.0109	0.0091
Imitation	0.0109	0.0078	0.0120	0.0102	0.0090	0.0114	0.0100	0.0066	0.0064
HP	0.0138	0.0092	0.0142	0.0170	0.0144	0.0167	0.0121	0.0095	0.0078
IC	0.0154	0.0086	0.0095	0.0113	0.0110	0.0133	0.0138	0.0084	0.0084
SP	0.0160	0.0116	0.0133	0.0139	0.0135	0.0130	0.0137	0.0084	0.0109
FP	0.0147	0.0110	0.0138	0.0138	0.0169	0.0162	0.0147	0.0075	0.0079
LSE	0.0177	0.0098	0.0148	0.0103	0.0123	0.0138	0.0125	0.0081	0.0089
Gender	0.0081	0.0061	0.0079	0.0071	0.0084	0.0114	0.0081	0.0052	0.0052
RA	0.0093	0.0061	0.0092	0.0068	0.0062	0.0104	0.0070	0.0050	0.0050

Table 5
Positive ideal solution (A+) and negative ideal solution (A-)

	Hopelessness	MD	Stress	SA	FF	Religion	PSS	PSA	PC	NLE	Imitation	HP	IC	SP	FP	LSE	Gender	RA
A+	0.0182	0.0199	0.0199	0.0194	0.0201	0.0134	0.0174	0.0256	0.0225	0.0289	0.0123	0.0203	0.0206	0.0212	0.0204	0.0168	0.0109	0.0109
A-	0.0079	0.0102	0.0090	0.0068	0.0088	0.0070	0.0067	0.0128	0.0081	0.0081	0.0061	0.0079	0.0068	0.0062	0.0104	0.0070	0.0050	0.0050

Table 6
Positive ideal separation (Si+) and negative ideal separation (Si-)

Factors	Si+	Si-
Hopelessness	0.0315	0.0218
MD	0.0192	0.0341
Stress	0.0256	0.0286
SA	0.0281	0.0252
FF	0.0242	0.0295
Religion	0.0380	0.0135
PSS	0.0330	0.0195
PSA	0.0057	0.0476
PC	0.0287	0.0231
NLE	0.0231	0.0312
Imitation	0.0403	0.0109
HP	0.0263	0.0252
IC	0.0322	0.0197
SP	0.0282	0.0241
FP	0.0230	0.0298
LSE	0.0289	0.0219
Gender	0.0477	0.0029
RA	0.0481	0.0021

Table 7

Positive ideal solution (Pi) and ranking of the factors

Factors	Pi	Ranking
PSA	0.8924	1
MD	0.6389	2
NLE	0.5743	3
FP	0.5642	4
FF	0.5493	5
Stress	0.5276	6
HP	0.4890	7
SA	0.4734	8
SP	0.4613	9
PC	0.4453	10
LSE	0.4312	11
Hopelessness	0.4086	12
IC	0.3793	13
PSS	0.3721	14
Religion	0.2619	15
Imitation	0.2132	16
Gender	0.0576	17
RA	0.0422	18

After that, the positive ideal solution (Pi) value for the factors is found. Finally, the factors were sorted according to the Pi value from the highest to the lowest.

Notation:

MD = Mental disorder

SA = Substance abuse

FF = Family factor

HP = Health problem

FP = Financial problem

NLE = Negative life events

PSS = Poor social support

LSE = Low self-esteem

PSA = Poor social attempts

IC = International conflicts

SP = Society pressure

RA = Residential area

DISCUSSION

Generally, the 18 risk factors for suicidal ideation were sorted based on the preferences using the TOPSIS method in this study. Table 5 shows that the most important reason for suicidal thoughts is *previous suicide attempts*, with a Pi value of 0.8924. It is followed

by *mental disorders* (0.6389), *negative life events* (0.5743), *financial problems* (0.5642), *family factors* (0.5493), and *stress* (0.5276), among others (Bilsen, 2018). In contrast, *gender* and *residential area* are the least important factors, with a value of less than 0.1.

Based on the result, it can be concluded that *prior suicide attempts* are the most significant factor for suicidal ideation (Bilsen, 2018; Junior et al., 2020). It is because a person with a history of self-injury is more likely to do the same actions again if they do not get help on their first attempt. Hence, people with previous suicide attempts have a high risk of suicidal crises.

Besides that, a *mental disorder* is also considered one of the important risk factors for suicidal ideation (Bilsen, 2018; Pillay, 2021). Most suicide cases are related to mental disorders such as depression, anxiety, and stress. University students are the population group that is more vulnerable to these mental disorder problems owing to various stressors in university life, including academic problems, financial problems, relationship problems, and many others.

Negative life events are also a key contributor that might lead to suicidal ideation (Bilsen, 2018; Pillay, 2021). It is because some mental disorders and problems like stress and depression may stem from negative life events. Negative life events such as the death of someone near the people, financial problems, and health problems will greatly impact the people. It will make people more likely to have serious suicidal thoughts.

Nevertheless, *gender* and *residential area* are the least important factors for suicidal ideation from the result (Abdu et al., 2020). Hence, gender and residential area are not crucial in leading to suicidal intentions among university students.

In a nutshell, the government, parents, and any related authorities should pay more attention to suspicious students with the characteristics of persons who tend to be involved in the suicide crisis. It can help them discover the particular students earlier and take proper actions immediately to help them.

CONCLUSION

The goal of the study is to rank the risk variables for suicide cases according to their seriousness. TOPSIS may be used to compare the many risk variables for suicidal ideation among university students. Although it is difficult to prevent suicide completely, knowing risk factors based on their relevant degree allows the government or society to be aware of the university students at high risk for suicide. The warning signs of the students can be detected earlier. Several rapid and effective solutions, such as suicide prevention programs and medical therapy, can be implemented specifically for the high-risk population to lessen the suicidal crises. Government should organize more suicide prevention events such as World Suicide Prevention Day, held on 10 September annually, and The Malaysian Suicide Prevention Awareness Campaign, among others, especially for targeting high-risk groups

for suicide to minimize the suicide rates. Other than that, mental health treatment or healthy ways to cope with stress can be provided for the students that are identified as a high-risk group individually.

There are some limitations in this study. One of them is that this study only involves public university students. Therefore, the outcome may not represent the condition of all the universities in Malaysia. Furthermore, this study only comprises undergraduate students; the situation of postgraduate students is uncertain.

ACKNOWLEDGEMENTS

The authors want to express deep gratitude to the School of Quantitative Sciences, Universiti Utara Malaysia (UUM), for providing the facilities and their consistent encouragement and assistance.

REFERENCES

- Abdu, Z., Hajure, M., & Desalegn, D. (2020). Suicidal behavior and associated factors among students in Mettu University, South West Ethiopia, 2019: An institutional based cross-sectional study. *Psychology Research and Behavior Management*, *13*, 233-243. <https://doi.org/10.2147/PRBM.S240827>
- Amini, P., Ahmadiania, H., Poorolajal, J., & Amiri, M. M. (2016). Evaluating the high risk groups for suicide: A comparison of logistic regression, support vector machine, decision tree and artificial neural network. *Iranian Journal of Public Health*, *45*(9), 1179-1187.
- Arafat, S. M. Y., Mali, B., & Akter, H. (2018). Demography and risk factors of suicidal behavior in Bangladesh: A retrospective online news content analysis. *Asian Journal of Psychiatry*, *36*, 96-99. <https://doi.org/10.1016/j.ajp.2018.07.008>
- Balioti, V., Tzimopoulos, C., & Evangelides, C. (2018). Multi-criteria decision making using TOPSIS method under fuzzy environment. Application in spillway selection. *Multidisciplinary Digital Publishing Institute Proceedings*, *2*(11), Article 637. <https://doi.org/10.3390/proceedings2110637>
- Benfares, C., El Idrissi, Y. E. B., & Hamid, K. (2019, March). Intelligent decision making for depression prevention and detection based on AHP. *Proceedings of the 2nd International Conference on Networking, Information Systems & Security* (pp. 1-7). ACM Publishing. <https://doi.org/10.1145/3320326.3320366>
- Berkelmans, G., Van der Mei, R., Bhulai, S., & Gilissen, R. (2021). Identifying socio-demographic risk factors for suicide using data on an individual level. *BMC Public Health*, *21*(1), Article 1702. <https://doi.org/10.1186/s12889-021-11743-3>
- Bilsen, J. (2018). Suicide and youth: Risk factors. *Frontiers in Psychiatry*, *9*, Article 540. <https://doi.org/10.3389/fpsy.2018.00540>
- Chang, C. (2021, January 10). *Uni student in Sarawak allegedly commits suicide due to stress from studies*. World of Buzz. <https://worldofbuzz.com/uni-student-in-sarawak-allegedly-commits-suicide-due-to-stress-from-studies/>
- Chauhan, H., Satapathy, S., & Sahoo, A. K. (2021). A QFD approach based on fuzzy TOPSIS to reduce the mental stress of farmers: A case study of Odisha. *International Journal of Service Science, Management, Engineering, and Technology (IJSSMET)*, *12*(5), 148-166. <https://doi.org/10.4018/ijssmet.2021090110>

- Costa, A. C. B., Mariusso, L. M., Canassa, T. C., Previdelli, I. T. S., & Porcu, M. (2019). Risk factors for suicidal behavior in a university population in Brazil: A retrospective study. *Psychiatry Research*, 278, 129-134. <https://doi.org/10.1016/j.psychres.2019.05.039>
- Durkee, T., Hadlaczky, G., Westerlund, M., & Carli, V. (2011). Internet pathways in suicidality: A review of the evidence. *International Journal of Environmental Research and Public Health*, 8(10), 3938-3952. <https://doi.org/10.3390/ijerph8103938>
- Gearing, R. E., & Alonzo, D. (2018). Religion and suicide: New findings. *Journal of Religion Health*, 57, 2478-2499. <https://doi.org/10.1007/s10943-018-0629-8>
- Gebre, S. L., Cattrysse, D., Alemayehu, E., & Orshoven, J. V. (2021). Multi-criteria decision making methods to address rural land allocation problems: A systematic review. *International Soil and Water Conservation Research*, 9(4), 490-501. <https://doi.org/10.1016/j.iswcr.2021.04.005>
- Gupta, S., Vijayvargy, L., & Gupta, K. (2021). Assessment of stress level in urban area's during COVID-19 outbreak using critic and TOPSIS: A case of Indian cities. *Journal of Statistics and Management Systems*, 24(2), 411-433. <https://doi.org/10.1080/09720510.2021.1879470>
- Hwang, C. L., & Yoon, K. (1981). *Multiple Attribute Decision Making: Methods and Applications*. Springer.
- Ishaq, A., Sadiq, S., Umer, M., Ullah, S., Mirjalili, S., Rupapara, V., & Nappi, M. (2021). Improving the prediction of heart failure patients' survival using SMOTE and effective data mining techniques. *IEEE Access*, 9, 39707-39716. <https://doi.org/10.1109/ACCESS.2021.3064084>
- Júnior, A. R., Fletes, J., Lemos, T., Teixeira, E., & Souza, M. (2020). Risk factors for suicide: Systematic review. *Saudi Journal for Health Sciences*, 9(3), 183-193. https://doi.org/10.4103/sjhs.sjhs_83_20
- Jusnani, E., Salmah, M. Y., & Razali, M. O. (2020). Exploration on perceptions of suicidal ideation among students of higher education. *Journal of Cognitive Sciences and Human Development*, 6(2), 31-51. <https://doi.org/10.33736/jcshd.1939.2020>
- Kusnadi, A., & Kurniawan, E. (2017). Implementation of TOPSIS method in web based system recommendations for students laptop selection (Case study: Bhinneka. com). *IJNMT International Journal of New Media Technology*, 4(1), 42-45. <https://doi.org/10.31937/ijnmt.v4i1.537>
- Lyu, J., & Zhang, J. (2019). BP neural network prediction model for suicide attempt among Chinese rural residents. *Journal of Affective Disorders*, 246, 465-473. <https://doi.org/10.1016/j.jad.2018.12.111>
- Mamat, A. (2021, January 10). Melaka university student commits suicide over boyfriend's alleged affair. *New Straits Times*. <https://www.nst.com.my/news/nation/2021/01/656110/melaka-university-student-commits-suicide-over-boyfriends-alleged-affair>
- Melillo, P., & Pecchia, L. (2016, August 4-7). *What is the appropriate sample size to run analytic hierarchy process in a survey-based research?* [Paper presentation]. International Symposium on the Analytic Hierarchy Process, London, UK. <https://doi.org/10.13033/isa hp.y2016.130>
- Mukherjee, K. (2014). Analytic hierarchy process and technique for order preference by similarity to ideal solution: A bibliometric analysis from past, present and future of AHP and TOPSIS. *International Journal of Intelligent Engineering Informatics*, 2(2-3), 96-117. <https://doi.org/10.1504/IJIEI.2014.066210>

- Nguyen, M., Cabral, M. D., & Patel, D. R. (2020). Suicide in adolescents: Exploring the role of religion. *International Journal of Child Health and Human Development*, 13(4), 379-382.
- NST. (2019, May 15). Private university reels from two student suicides in space of a week. *New Straits Times*. <https://www.nst.com.my/news/nation/2019/05/488510/private-university-reels-two-student-suicides-space-week>
- Olfson, M., Wall, M., Wang, S., Crystal, S., Bridge, J. A., Liu, S. M., & Blanco, C. (2018). Suicide after deliberate self-harm in adolescents and young adults. *Pediatrics*, 141(4), Article e20173517. <https://doi.org/10.1542/peds.2017-3517>
- Öneren, M., Arar, T., & Celebioglu, E. S. (2016). Determining the overall stress factors for policemen by AHP method. *International Journal of the Analytic Hierarchy Process*, 8(3). <http://dx.doi.org/10.13033/ijahp.v8i3.384>
- Owusu-Ansah, F. E., Addae, A. A., Peasah, B. O., Asante, K. O., & Osafo, J. (2020). Suicide among university students: Prevalence, risks and protective factors. *Health Psychology and Behavioral Medicine*, 8(1), 220-233. <https://doi.org/10.1080/21642850.2020.1766978>
- Pal, K., Kumar, V., Arora, H. D., & Kumar, S. (2019). Application of TOPSIS in the diagnosis of vector borne diseases. *International Journal of Engineering and Advanced Technology (IJEAT)*, 8(6), 5217-5223. <https://doi.org/10.35940/ijeat.F8585.088619>
- Park, C. H. K., Lee, J. W., Lee, S. Y., Moon, J., Jeon, D. W., Shim, S. H., Cho, S. J., Kim, S. G., Lee, J., Paik, J. W., Kim, M. H., You, S., Jeon, H. J., Rhee, S. J., Kim, M. J., Kim, J., & Ahn, Y. M. (2020). Suicide risk factors across suicidal ideators, single suicide attempters, and multiple suicide attempters. *Journal of Psychiatric Research*, 131, 1-8. <https://doi.org/10.1016/j.jpsychires.2020.08.018>
- Pillay, J. (2021). Suicidal behaviour among university students: A systematic review. *South African Journal of Psychology*, 51(1), 54-66. <https://doi.org/10.1177/0081246321992177>
- Polis Diraja Malaysia. (2021). *Statistic kes bunuh diri di Malaysia* [Statistics of suicide cases in Malaysia]. Polis Diraja Malaysia.
- Primananda, M., & Keliat, B. A. (2019). Risk and protective factors of suicidal ideation in adolescents. *Comprehensive Child and Adolescent Nursing*, 42(sup1), 179-188. <https://doi.org/10.1080/24694193.2019.1578439>
- Rahim, R., Supiyandi, S., Siahaan, A. P. U., Listyorini, T., Utomo, A. P., Triyanto, W. A., Irawan, Y., Aisyah, S., Khairani, M., Sundari, S., & Khairunnisa, K. (2018). TOPSIS method application for decision support system in internal control for selecting best employees. In *Journal of Physics: Conference Series* (Vol. 1028, No. 1, pp. 012052). IOP Publishing. <https://doi.org/10.1088/1742-6596/1028/1/012052>
- Saaty, T. L. (1980). *The Analytic Hierarchy Process*. McGraw-Hill.
- Shafiee, S. M., & Mutalib, S. (2020). Prediction of mental health problems among higher education student using machine learning. *International Journal of Education and Management Engineering (IJEME)*, 10(6), 1-9. <https://doi.org/10.5815/ijeme.2020.06.01>
- Shirouyehzad, H., & Dabestani, R. (2011). Evaluating projects based on safety criteria: Using TOPSIS. In *2011 2nd International Conference on Construction and Project Management IPEDR* (Vol. 15, pp. 69-73). LACSIT Press.

- Wasserman, D., Carli, V., Iosue, M., Javed, A., & Herrman, H. (2021). Suicide prevention in childhood and adolescence: A narrative review of current knowledge on risk and protective factors and effectiveness of interventions. *Asia-Pacific Psychiatry, 13*(3), Article e12452. <https://doi.org/10.1111/appy.12452>
- World Health Organization. (2019). *Adolescent mental health*. World Health Organization. <https://www.who.int/news-room/fact-sheets/detail/adolescent-mental-health>
- World Health Organization. (2021). *Suicide*. World Health Organization. <https://www.who.int/news-room/fact-sheets/detail/suicide>
- Yu, R., Chen, Y., Li, L., Chen, J., Guo, Y., Bian, Z., Lv, J., Yu, C., Xie, X., Huang, D., Chen, Z., & Fazel, S. (2021). Factors associated with suicide risk among Chinese adults: A prospective cohort study of 0.5 million individuals. *PLoS Medicine, 18*(3), Article e1003545. <https://doi.org/10.1371/journal.pmed.1003545>

Influencing Physical Characteristics of Landslides in Kuala Lumpur, Malaysia

Syaidatul Azwani Zulkaffli, Nuriah Abd Majid*, Sharifah Zarina Syed Zakaria, Muhammad Rizal Razman and Minhaz Farid Ahmed

Institute for Environment and Development (LESTARI), Universiti Kebangsaan Malaysia, 43600 UKM Bangi, Selangor Darul Ehsan, Malaysia

ABSTRACT

Landslide is one of the natural disasters that commonly occurs in terrestrial environments with slopes throughout the world. Located among countries with tropical climates, the hot and humid conditions expose Kuala Lumpur, Malaysia, to the risk of landslides. This paper aims to delineate the influencing physical characteristics of landslide occurrences in Kuala Lumpur. In this study, a 100 landslides historical data set and eight landslide factors were obtained from proper field validation and maps provided by those concerned in the government, such as distance to roads, distance to streams, elevation, slope angle, curvature, slope aspect, land use, and lithology. These factors were processed using GIS as geospatial analysis provides a useful tool for planning, disaster management, and hazard mitigation. By using ArcMap 10.8.2, a GIS software, different spatial analyses in which maps for each physical factor were layered with landslide events distribution. The weights for each factor were determined using the ANN approach resulting in the slope angle having the highest relative importance with a 100.0% value. In comparison, 8.3% represents the slope aspect

as the most insignificant factor out of the eight selected characteristics for this study area. Therefore, a proper perspective and a thorough understanding of the certain slope condition have to be established for future mitigation action to support the agenda of SDG 15.

ARTICLE INFO

Article history:

Received: 01 April 2022

Accepted: 16 August 2022

Published: 06 March 2023

DOI: <https://doi.org/10.47836/pjst.31.2.18>

E-mail addresses:

syaidatulzulkaffli@gmail.com (Syaidatul Azwani Zulkaffli)

nuriah@ukm.edu.my (Nuriah Abd Majid)

szarina@ukm.edu.my (Sharifah Zarina Syed Zakaria)

mrizal@ukm.edu.my (Muhammad Rizal Razman)

minhaz@ukm.edu.my (Minhaz Farid Ahmed)

*Corresponding author

Keywords: ANN, GIS, geospatial, Kuala Lumpur, landslide

INTRODUCTION

Landslide is one of the natural disasters that commonly occur worldwide, mainly in terrestrial environments with slopes. This disaster has had a devastating toll on lives and the economy. More than 8,935 landslide incidents were recorded worldwide, with approximately 1,120 landslides scattered in Southeast Asia until 2019 (NASA, 2020). Although landslides caused a lower death toll than other disasters, the destructive effects of the latter consequences on the economy are rather devastating because landslides have affected nearly 130 billion USD worth of assets across the world (Ritchie & Roser, 2014). These examples of bad economic outcomes of landslides demonstrate that having a good disaster preparedness program in a particular region is vital to reducing the chances of a disaster and its impacts.

For a record, the US National Aeronautics Space Administration (NASA) affirmed that Malaysia had 171 landslides between 2007 to 2016, making it the 10th country with the highest frequency of landslides (Sim et al., 2018). A total of 262 landslide cases were discovered in recent circumstances across the country, with which Kuala Lumpur and Selangor contributed to most landslide occurrences in Malaysia (The Star, 2022). On the other hand, numerous landslide history data have been accumulated near Kuala Lumpur, indicating that several more landslide occurrences have occurred since the first event (excluding the non-reported cases). Due to the high frequency of landslides, Kuala Lumpur is selected as the area of interest for this study.

Figure 1 clearly shows that Kuala Lumpur is an urban area with the highest population density of 7,188 people per square kilometer, where multiple conversions have been ongoing for decades (Department of Statistics Malaysia, 2022). As a developed region, Kuala Lumpur is often planted with shallow-rooted greenery for aesthetics with fewer infiltration capabilities that would loosen soil particles, specifically during uncertain intense precipitation, leading to slope movements (Huang et al., 2012). Overgrowing urbanization has also become one of the major contributors to landslides for years. The latest statistics for 2019, recorded by the Department of Statistics, found that urbanization covered 76.2% of Malaysia (Department of Statistics Malaysia, 2020). In short, unsustainable land expansion may soar illegal logging activities, which later cause erosion of the covered soil masses, posing a serious threat to slope stability (Pradhan & Lee, 2009).

Landslides can be triggered by many factors and occasionally correspond to one another. Apart from the most common landslide-triggering factor, rainfall, the rising events of landslides are also closely linked to the instability of slopes due to soil gestures failures. This high-risk catastrophe has encouraged the experts and scientific community to construct several landslide research in the past few years to provide proper information to planners, geotechnical consultants, and governments. With the introduction of GIS, multiple physical characteristics of landslides can be analyzed. Many researchers have continuously

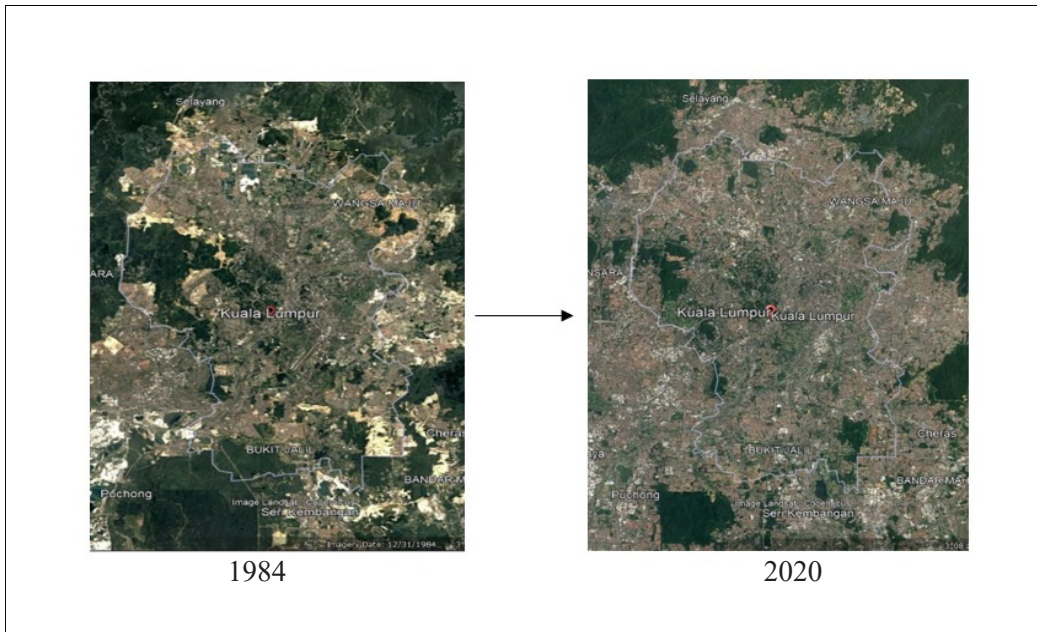


Figure 1. Land use conversion of Kuala Lumpur from 1984 to 2020
 Source. Google Earth Pro 1984 and 2020

constructed different types of landslide analyses, for instance, landslide susceptibility and assessments (Shahabi & Hashim, 2015; Majid et al., 2017; Majid et al., 2018; Mersha & Meten, 2020; Majid & Rainis, 2019; Naseer et al., 2021). However, the scope of this study will be narrowed down to the selected physical factors initiation to landslides in a growing city, Kuala Lumpur, as it requires greater precise spatial analysis to be done down to the local level. This study will also encourage the efficiency of landslide prevention and mitigations, as well as enhance the conservation of the physical environment and human safety (Kyriou et al., 2021).

Advanced computing performance and the development of accessible geographical information system (GIS) platforms have further contributed to the extensive use of such reliable landslide forecasting targeted to the regional scale (Song et al., 2020). GIS is also often used as a tool to predict the occurrence of slope failures by warning of potential slope failures in the future (Majid & Ibrahim, 2015). In addition, GIS provides information and tools to quantitatively analyze multiple variables' functional relationships (Psomiadis et al., 2020; Simon et al., 2017). Therefore, spatial analysis using GIS software, namely ArcMap 10.8.2, is efficient for landslide studies as it always delivers high credibility of methods and results. By means, GIS will indirectly decrease the inaccuracy of landslide studies that could lead to major faults in analyzing and predicting landslide occurrences in Kuala Lumpur.

MATERIALS AND METHODS

Study Area

The Federal Territory of Kuala Lumpur was selected as the study area, which covers approximately 243.6 sq km within Selangor (Figure 2). Located at latitude $03^{\circ} 2' N$ to $03^{\circ} 12' N$ and longitude $101^{\circ} 38' E$ to $101^{\circ} 46' E$, Kuala Lumpur is a part of Klang Valley with a population of 1.7 million as of 2015 (Alnaimat et al., 2017). Situated on the west coast of Peninsular Malaysia, Kuala Lumpur territory receives a higher rainfall during the southwest monsoon from April to November annually (Saadatkhah et al., 2014). The temperature in Kuala Lumpur remains at a fairly constant $22\text{--}33^{\circ}C$ all year round, with average annual precipitation of around 2,800 mm (Department of Irrigation and Drainage, 2018). With an average population growth of 2% per year, increasing housing and facilities demand have made developments in hilly areas around Kuala Lumpur. However, slope, drainage, and vegetation are disrupted during these developments, exposing the neighborhood to potential landslide risk (Mahmud et al., 2013). Apart from human factors, the lithology structure of Kuala Lumpur and its surroundings comprised of the pre-existence of a variety of weak zones in granite and ski rocks has led to slope movement (Yusoff et al., 2016).

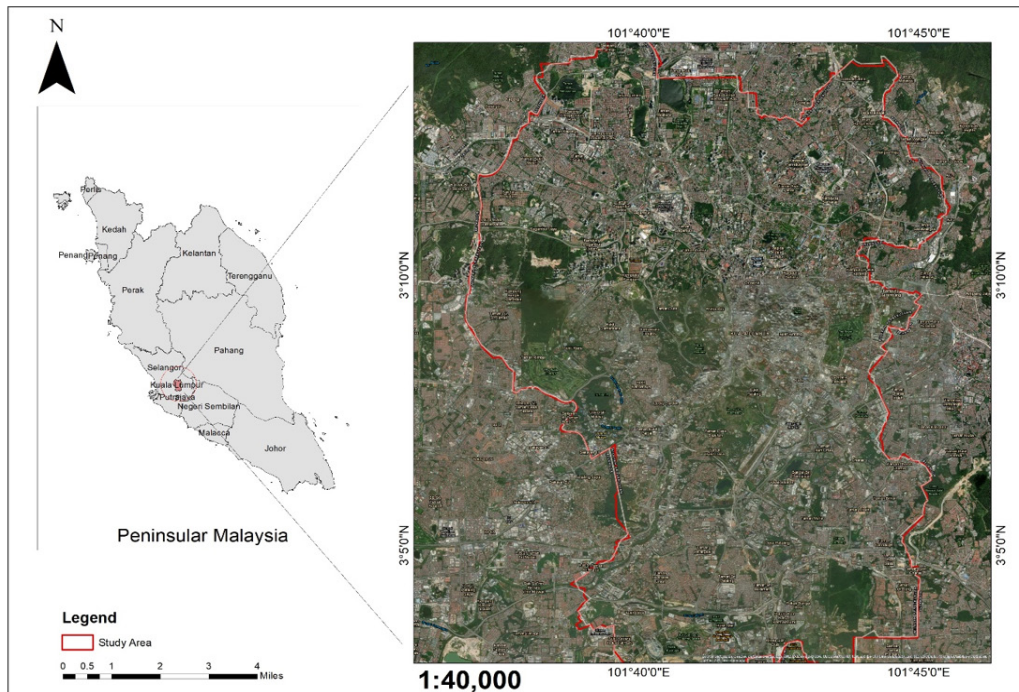


Figure 2. Federal Territory of Kuala Lumpur, Malaysia

Data Acquisition

In many landslide studies, preparing landslide inventory maps is crucial to understanding their previous occurrences and causes in predicting future landslide-susceptible zone. Therefore, a landslide inventory map was constructed with 100 landslide locations identified using the combined findings of previous studies, the interpretation of Google Earth images, and fieldwork validation. According to Zhang et al. (2022), there are no specific rules for choosing landslide characteristics. Thus, based on analysis of the landslide inventory map and the underlying geomorphometric conditions, eight physical characteristics, including roads and highways, stream network, DEM, slope angle, slope aspect, curvature, land use, and lithology were selected as landslide physical factors (Table 1). These physical characteristics were considered based on observation of past landslides and their possible contribution to inducing instability to the slopes in the area (Mahmud et al., 2013; Alnaimat et al., 2017; Ismail & Yaacob, 2018; Rahman et al., 2020). Considering this study's aim and the scale of available data, the landslide incidents were depicted as points in GIS shapefile format and later used to overlap as maps for each physical factor.

Table 1
Dataset based on GIS

Data	Type	Format
Landslides	Points	Vector
Road network	Polyline	Vector
Stream network	Polyline	Vector
Digital elevation model (DEM)	Grid	Raster
Slope angle	Grid	Raster
Curvature	Grid	Raster
Slope aspect	Grid	Raster
Land use	Polygon	Raster
Lithology	Polygon	Raster

Data Processing

Spatial Analysis Using GIS. For the data analysis, most layers in this study were projected in the Kertau RSO coordinate system. A layer of roads and highways in Kuala Lumpur obtained in polyline stretching throughout this territory was processed to produce a physical map with the landslide incidents layer on top. A multiple ring buffer analysis with 125 meters is appointed as the interval distance based on the nearest and farthest landslide locality from the road and equally classified into five equal classes. Furthermore, multiple

analyses on different buffer distances were carried out, and 125 meters were deemed the buffer distance for this study. Meanwhile, the same buffer analysis is conducted towards stream characteristics at 500-meter intervals with five equal classes. On the other hand, the stream data layer represents the branches of the stream network and water bodies across Kuala Lumpur. The river network layer was combined with the same landslide distribution layer to generate the physical map in GIS.

A contour map acquired was used to derive a 10-meter DEM resolution using the 3D Analyst extension of ArcMap. DEM is further classified using a natural break of five classes and the slope layer is extracted from DEM from the spatial analyst tool. In 2002, the Department of Minerals and Geoscience Malaysia (JMG) constructed official guidelines on hillside development where slopes are classified into four categories (Class I, II, III, and IV) (Gue & Wong, 2009). Since then, the guidelines have been used in most landslide studies in Malaysia. Class I is determined as the least severe slope angle and ranges below 15° meanwhile Class II is reserved between 15° to 25° . Slopes between 25° to 35° are for Class III and any slope angle greater than 35° is classified as Class IV. Aside from the slope, the curvature values represent the topography's morphology (Rasyid et al., 2016). Curvature is categorized as negative or concave, indicating valleys, zero or flat surfaces, and positive or convex indicating peaks. It is generally related to a surface that can hold more water and retains water from heavy rainfall for a longer period (Lee & Thalib, 2005). The slope aspect is the orientation of a slope between 0° and 360° from the northern direction (Erener & Duzgun, 2010). The slope aspect map is derived from DEM with 1 additional class for flat ground and 9 directional classes: flat (-1°), north (337.5° – 360° , 0° – 22.5°), northeast (22.5° – 67.5°), east (67.5° – 112.5°), southeast (112.5° – 157.5°), south (157.5° – 202.5°), southwest (202.5° – 247.5°), west (247.5° – 292.5°), and northwest (292.5° – 337.5°) and north (337.5° – 360°) (Rahmati et al., 2016).

As Kuala Lumpur is a highly developing region, it is essential to observe the land use type in this area and its relation to landslide incidents spatially. Thus, the land use data obtained from Plan Malaysia were analyzed and reclassified into five differentiations: (1) water bodies, (2) forest, (3) built-up, and (4) bare land. Furthermore, based on the provided geological map by the Department of Mineral and Geoscience Malaysia (JMG), lithology is classified into five different types of soil: (1) acid intrusive (undifferentiated), (2) limestone/marble, (3) mainly sandstone with subordinate shale, mudstone, siltstone, conglomerate, and volcanic, (4) schist and gneiss, and (5) vein quartz. This classification determines the factors and types of soil compositions involved in landslides.

Artificial Neural Network (ANN). ANN can learn and generalize from experience (Mandal & Mondal, 2019). The purpose of ANN is to build a model of the data-generating process so that the network can generalize and predict outputs from inputs that it has not previously seen (Pradhan & Lee, 2009). However, for this study, the ANN method was

used to determine the weight of each selected physical characteristic involving a set of training data. In order to determine the weight of the characteristic, another 100 points were generated from ArcMap. This generation is taken into consideration to represent non-landslide events to avoid overfitting issues (Selamat et al., 2022). Hence, a total of 200 points were used in this analysis, randomly separated into 70% training set and 30% for testing.

RESULTS AND DISCUSSIONS

Frequent landslide incidents in Kuala Lumpur can be observed distributed particularly along the west of this city, also known as the Damansara Penchala zone, and in the northwest or the Sentul Menjalara zone according to Kuala Lumpur City Hall Government Agency (Figure 3).

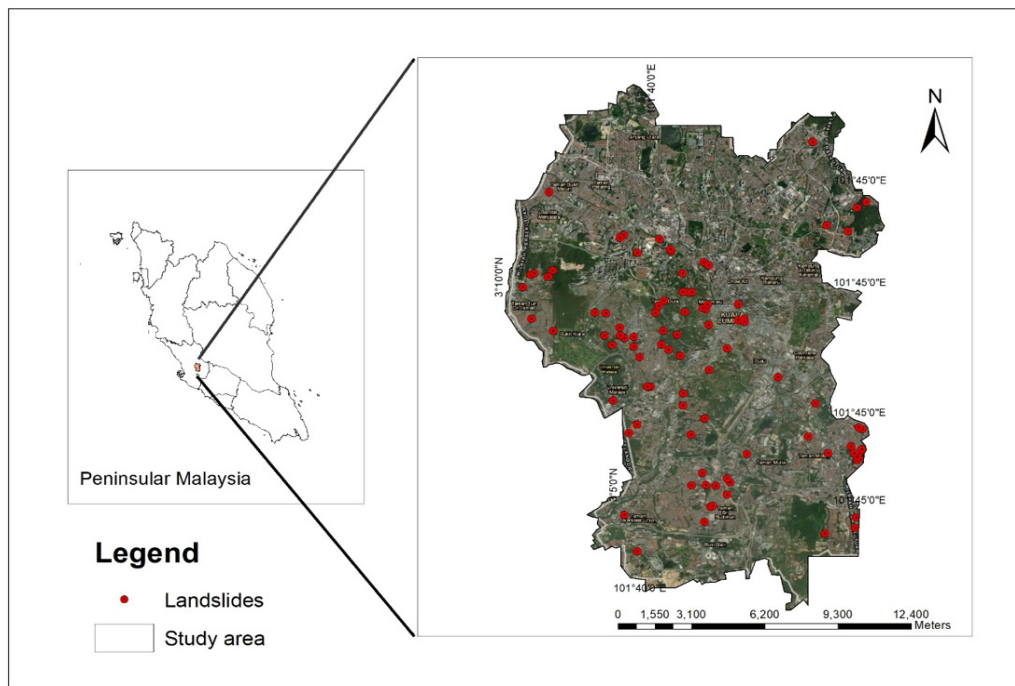


Figure 3. Landslide distribution map

New infrastructure, for instance, highways, road networks, and dams have a significant relationship to landslides in Kuala Lumpur (Department of Irrigation and Drainage, 2018; Hong & Hong, 2016). Therefore, rampant soil reclamation and slope deforestation for urban development can cause unprecedented devastation to ecological sustainability, especially during road construction. In addition, the proximity to the road network is often related to

an increase in landslide occurrences, so disturbance zones were created around the road network of the study area (Skilodimou et al., 2018).

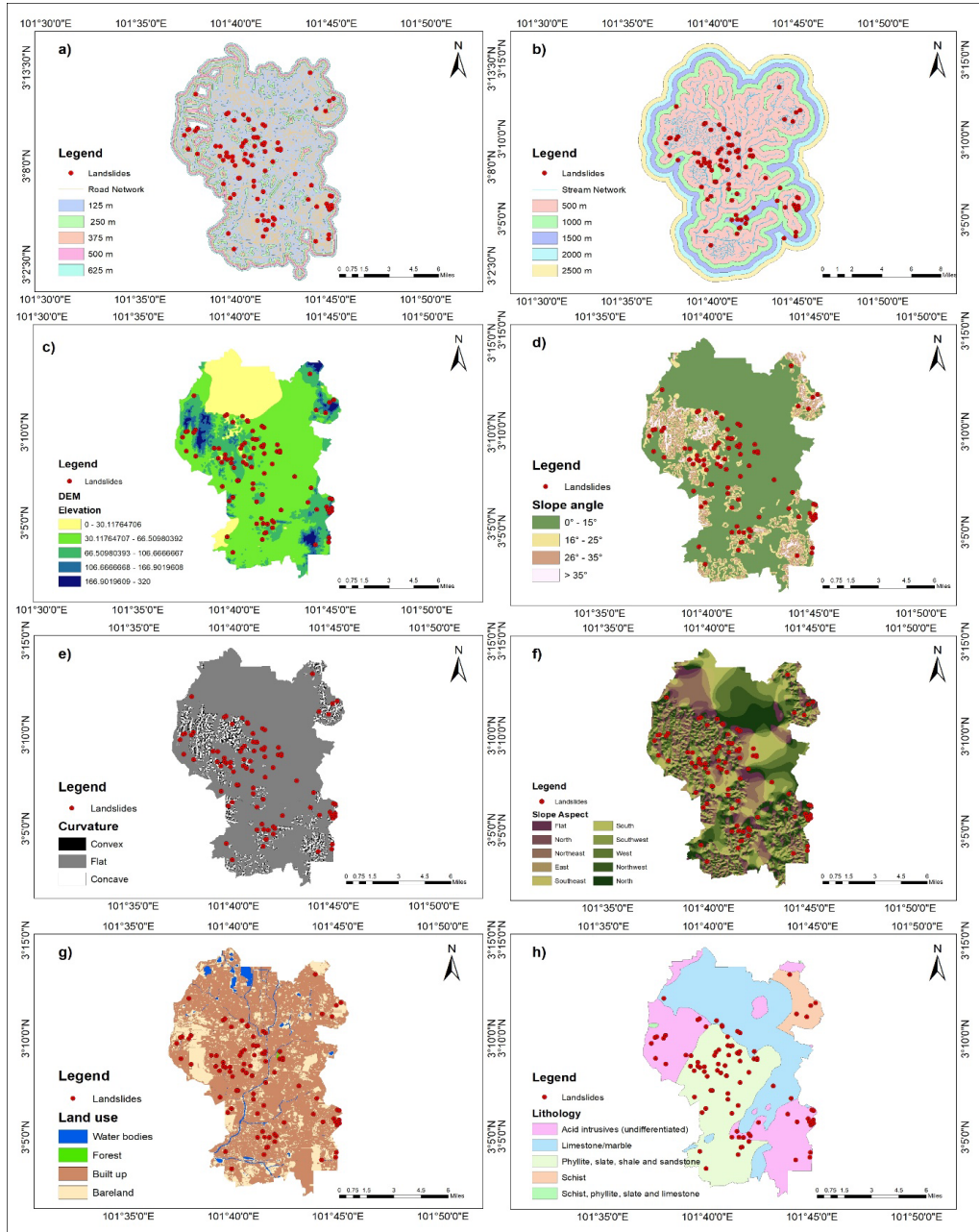


Figure 4. Landslide distribution on physical characteristics: a) distance to road, b) distance to stream, c) DEM, d) slope angle, e) curvature, f) slope aspect, g) land use, h) lithology

Kuala Lumpur is well-known for its complex roads and highways for faster accessibility within the territory. Figure 4(a) shows that most landslides have occurred at road embankments and highways compared to off-roads with a 0 to 250 meters range. These constructions inadvertently cause slope instability and disturb the natural topology. In addition, highways can have the highest percentage of losses during landslides, located in highly hazardous areas. For example, highways in Damansara Penchala zones on the north and west part of Kuala Lumpur with over 10 km experienced frequent landslide occurrences as most highways pass through the high-risk area landslide-prone in that zone (Althuwaynee & Pradhan, 2017). It has demonstrated that unsustainable slope cutting for road constructions influences the changes in gradient flow, leading to slope inclining.

About 120 kilometers long river network flow covering the whole territory, which originated from Besar Range, almost half of the Klang River Basin. It is observed that the Klang River is the mainstream in this city, forking its branch into smaller streams known as the Kerayong river towards the east, the Batu River towards the northwest, the Jinjang river towards the north, and the Gombak River towards the southeast of Kuala Lumpur. Landslide incidents were observed around the Klang River, Kerayong river, and the smaller streams of the Batu River. Figure 4(b) shows that most landslides occurred from the streams' 0–500 meters range. It supports that the distance to the stream is significantly related to landslides as water flow density naturally creates different types of erosion thus, increasing the vulnerability of slope angle (Mahmud et al., 2013).

Furthermore, Kuala Lumpur is surrounded by mountainous topography with the highest peak elevates at more than 300 meters and is often associated with high-rise buildings due to their luxurious viewpoint. Figure 4(c) shows that most landslide incidents took place at 0–106 meters in height. Landslide occurrences in this area were also concentrated in developed areas where human activities have significantly disturbed and altered most slopes. For instance, in 2021, one of the hilly developments known as the Sri Duta 1 residence building experienced a slope failure affecting four blocks and 34 residential units. Damaged columns, surface tension fractures, and floor cracks are all signs of soil movement that surfaced before the landslide event and further quickly declared that the residence is unsafe (Palansamy, 2021). This situation proves that hilly developments will always be at risk of landslides.

However, a slope is considered to have a greater influence on landslides than elevation. Therefore, slope angle has always been recognized as one of the crucial landslide factors by many studies. Generally, the slope indicates the surface's degree of inclination and shows the elevation change rate (Paudel et al., 2016). A slope with a steeper degree of inclination is more susceptible to instability than a gentle slope. In this study, however, most landslides occurred at slope gradients of 0° to 15° (Figure 4(d)) as former mining sites mostly cover this region. This situation explains the rationale for landslide occurrences on

flat surfaces in Kuala Lumpur over the past decades (Sanusi et al., 2017). Furthermore, the Kuala Lumpur area is also covered with 92% of slopes ranging between 0° to 15° while the steep slopes only represent 8% area showing landslides that occurred in this area are shallows. In addition, Kuala Lumpur has recorded a notable rise in population growth; thus, development has expanded in the hilly regions. Slope alteration and heavy materials on top of undercutting slopes have also significantly affected slope stability, inducing landslides.

Figure 4(e) shows a landslide distribution map of the curvature layer. The curvature also plays a significant role in landslide occurrences. In this study, it is found that a concave surface that represents negative values is favorable for landslides in Kuala Lumpur. Meanwhile, the convex surface recorded the least number of landslide occurrences. As the slope with a concave surface is in the upward direction, it tends to hold rainfall and infiltrate more water into the slopes, contrasting the convex surface (Lee et al., 2003). On top of that, infiltration forces a slope under a complex stress state as it will be fully saturated with water. It supports that if the negative value increases, the probability of landslide occurrences will increase too. In addition, there is no clear agreement exists in the context of aspects as one of the contributing factors, however, it acts as a geomorphological factor that indirectly triggers landslides occurrences indicating that the slope aspect is an important factor in landslide studies (Erener & Duzgun, 2010; Pawluszek & Borkowski, 2016; Silalahi et al., 2019). Figure 4(f) shows that landslides are concentrated on the Northwest-facing slopes. Following this, landslides are mostly spread from the Northeast-facing to the Northwest-facing slopes. It shows that exposure to sunlight and drying winds could control soil moisture concentration and, in the end, lead to landslide occurrences (Sharir et al., 2017). It indirectly influences the flow of landslide incidents as the direction of the slope face depends on exposure to sunlight, rainfall, evaporation, and vegetation distribution on slopes (Jaafari et al., 2014; Jebur et al., 2014; Wen & Jiang, 2016).

Land use elements in the northwest stretching towards the northeast of Kuala Lumpur are the safest compared with those in the western and southern parts (Figure 4(g)). The highest percentages of affected elements due to landslides were found in urban areas with high populations including residential areas, commercial buildings, industrial buildings, and utility areas (Althuwaynee & Pradhan, 2017). The development of residential buildings on hilltops has expanded dramatically as a result of the depletion of flat land (Gue & Tan, 2003). In the future, this will cause changes in water flow from the highland to the ground. It is also found that landslides are greatly influenced by the lithological properties of the land surface (Dhianaufal et al., 2018).

Moving on to Figure 4(h), which represents lithology appears that landslide events in Kuala Lumpur are scattered mainly on sandstone with subordinate shale, mudstone, siltstone, conglomerate, and volcanic. The weathering of the shale and sandstone from sedimentary rocks of the Kenny Hill formation have metamorphosed into metasediments of

schist, quartzite, and phyllite (Sanusi et al., 2017). Lithology profiles of the acid intrusive region, also known as the Kuala Lumpur granite, were observed to have separated largely from the northwest to the southeast. Some parts are surrounded by limestone lithology southwest of this study area. It is also discovered that the same lithology profile can be found in patches in the upper northwest and southeast, and some part of it is surrounded by limestone in the southwest. Landslide incidents on schist and gneiss are the least distributed in southeast Kuala Lumpur. Another large part of the lithology type with landslide incidents reported on it is the area with a limestone profile, locally known as the Kuala Lumpur Limestone. This limestone is characterized by a thin layer of topsoil for vegetation and is comprised of the alluvial soil beneath this region which contained heavy mineral and tin-bearing soil. Frequent quarries on slopes and cliffs in the past few decades to acquire limestone as the main source of construction materials have threatened the stability of its soil layers (Althuwaynee & Pradhan, 2017).

The weight of each landslide is calculated using the ANN approach. A higher-weight factor indicates a higher contribution to landslide occurrences (Ibrahim et al., 2022). Among these landslide physical characteristics, slope angle plays the most significant role in influencing the landslides with a 100% normalized importance value. In contrast, the slope aspect represents the least significant landslide factor (Table 2). According to the expert, gravity is the prime cause of landslides when it overcomes the internal resistance of the rock, soil, or sediment and friction. Hence, a steeper slope combined with other contributing factors is always susceptible to landslides. In addition, rapid developments in hilly areas also significantly induce slope instability (Rahim et al., 2022).

Table 2

The weight of each landslide factor

Independent Variable Importance	
Factors	Weight of Landslide Factors
Distance to road	43.30%
Distance to stream	16.00%
DEM	25.90%
Slope aspect	8.30%
Slope angle	100.00%
Curvature	32.40%
Land use	28.70%
Lithology	31.70%

Meanwhile, distance to the road shows the second highest value with 43.3%. Considering that the artificial and natural parts of the slopes around a road network are more sensitive to landslide manifestations, making both slope angle and road network associated strongly with one another. In the meantime, road constructions often cause slope instability as the process often creates cut slopes and inadvertently disturbs the natural topology exposing prone areas to possible landslides.

From this weightage calculation, it is also found that the slope aspect has the least value of significance to landslide. In many studies, the slope aspect is also insignificant to most landslide occurrences as its role in landslide contribution remains unclear (Capitani et al., 2013; Yuri & Andri, 2021). The slope aspect only influenced landslides if they were superficial and in clayey deposits (Capitani et al., 2013). However, the slope aspect can still be used as one of the conditioning factors in landslide studies to understand the role or influence of the slope aspect on landslide occurrences. By implication, it shows the accuracy of the factor weightage results for this study.

CONCLUSION

Landslide occurrences in an urbanized region increase the risk of a high population. This study conducted physical characterizations of landslides in Kuala Lumpur. Landslide mitigation, especially in urban areas, requires critical planning and monitoring. This study found that 18.0% of landslides occurred along the Northwest of Kuala Lumpur, where most of these areas are surrounded by altered slopes. It indicates that the authorities are responsible for constructing an advanced prevention and mitigation procedure as the landslide-prone areas require critical planning and monitoring. In the meantime, a higher slope inclination can contribute to a higher gravity force in pulling materials down the slope, thereby increasing the risk of landslides. Therefore, a proper perspective and a thorough understanding of the certain slope condition have to be established to avoid more landslide occurrences in the future to ensure the conservation, restoration, and sustainable use of terrestrial and inland freshwater ecosystems as stated in the 15th SDG.

ACKNOWLEDGEMENT

This study was funded by a grant number (FRGS/1/2019/SS07/UKM/02/1) research project of the Ministry of Higher Education. We want to thank the party concerned for the data provided by this grant.

REFERENCES

- Alnaimat, A., Choy, L. K., & Jaafar, M. (2017). An assessment of current practices on landslides risk management: A Case of Kuala Lumpur Territory. *Geografia*, 13(2), 1-12.
- Althuwaynee, O. F., & Pradhan, B. (2017). Semi-quantitative landslide risk assessment using GIS-based exposure analysis in Kuala Lumpur City. *Geomatics, Natural Hazards and Risk*, 8(2), 706-732. <https://doi.org/10.1080/19475705.2016.1255670>
- Capitani, M., Ribolini, A., & Bini, M. (2013). The slope aspect: A predisposing factor for landsliding? *Comptes Rendus Geoscience*, 345(11-12), 427-438. <https://doi.org/10.1016/j.crte.2013.11.002>
- Department of Irrigation and Drainage. (2018). *Laporan banjir tahunan 2017/2018* [Annual flood report 2017/2018]. Ministry of Natural Resources, Environment and Climate Change. http://h2o.water.gov.my/man_hp1/LBT2017-2018.pdf
- Department of Statistics Malaysia. (2020). *Latest statistics 2019*. Prime Minister's Department. <https://www.mycensus.gov.my/>
- Department of Statistics Malaysia. (2022). *Malaysia current population estimates, 2021*. Prime Minister's Department. [https://www.dosm.gov.my/v1/index.php?r=column/cthemByCat&cat=155&bul_id=ZjJOSnpJR21sQWVUcUp6ODRudm5JZz09&menu_id=L0pheU43NWJwRWVVSZklWdzQ4TlhUUT09#:~:text=Kuala%20Lumpur%20had%20the%20highest,1%2C691%20people\)%20per%20square%20kilometre.](https://www.dosm.gov.my/v1/index.php?r=column/cthemByCat&cat=155&bul_id=ZjJOSnpJR21sQWVUcUp6ODRudm5JZz09&menu_id=L0pheU43NWJwRWVVSZklWdzQ4TlhUUT09#:~:text=Kuala%20Lumpur%20had%20the%20highest,1%2C691%20people)%20per%20square%20kilometre.)
- Dhianaufal, D., Kristyanto, T. H. W., Indra, T. L., & Syahputra, R. (2018). Fuzzy logic method for landslide susceptibility mapping in volcanic sediment area in Western Bogor. *AIP Conference Proceedings 2023*, Article 020190. <https://doi.org/10.1063/1.5064187>
- Erener, A., & Duzgun, H. S. B. (2010). Improvement of statistical landslide susceptibility mapping by using spatial and global regression methods in the case of More and Romsdal (Norway). *Landslides*, 7, 55-68. <https://doi.org/10.1007/s10346-009-0188-x>
- Gue, S. S., & Tan, Y. C. (2003, August 19-20). *The engineering aspects of hill-site development*. [Paper presentation]. Hillside Development—Issues and challenges, Kuala Lumpur, Malaysia.
- Gue, S. S., & Wong, S. Y. (2009, August 26-27). *Slope engineering design and construction practice in Malaysia*. [Paper presentation]. CIE-IEM Joint Seminar on Geotechnical Engineering, Yilan, Taiwan.
- Hong, L. J., & Hong, K. A. (2016). Flood forecasting for Klang River at Kuala Lumpur using artificial neural networks. *International Journal of Hybrid Information Technology*, 9(3), 39-60. <https://doi.org/10.14257/ijhit.2016.9.3.05>
- Huang, H. F., Yi, W., Yi, Q. L., & Zhang, G. D. (2012). Analysis of landslide surface deformation using geographically weighted regression. *Advanced Materials Research*, 594-597, 2406-2409. <https://doi.org/10.4028/www.scientific.net/amr.594-597.2406>
- Ibrahim, M. B., Mustaffa, Z., Balogun, A. L., & Sati, H. H. I. (2022). Landslide risk analysis using machine learning principles: A case study of Bukit Antarabangsa landslide incidence. *Journal of Hunan University Natural Sciences*, 49(5), 112-126. <https://doi.org/10.55463/issn.1674-2974.49.5.13>

- Ismail, N. I., & Yaacob, W. Z. W. (2018). An investigation of landslides in Bukit Aman and Puncak Setiawangsa, Kuala Lumpur, Malaysia. *AIP Conference Proceedings, 1940*, Article 020031. <https://doi.org/10.1063/1.5027946>
- Jaafari, A., Najafi, A., Pourghasemi, H. R., Rezaeian, J., & Sattarian, A. (2014). GIS-based frequency ratio and index of entropy models for landslide susceptibility assessment in the Caspian Forest, Northern Iran. *International Journal of Environment Science and Technology, 11*, 909-926. <https://doi.org/10.1007/s13762-013-0464-0>
- Jebur, M. N., Pradhan, B., & Tehrany, M. S. (2014). Optimization of landslide conditioning factors using very high-resolution airborne laser scanning (LiDAR) data at catchment scale. *Remote Sensing Environment, 152*, 150-165. <https://doi.org/10.1016/j.rse.2014.05.013>
- Kyriou, A., Nikolakopoulos, K., Koukouvelas, I., & Lampropoulou, P. (2021). Repeated UAV campaigns, GNSS measurements, GIS, and petrographic analyses for landslide mapping and monitoring. *Minerals, 11*(3), Article 300. <https://doi.org/10.3390/min11030300>
- Lee, S., RyuRyu, J. H., Min, K., & WonWon, J. S. (2003). Landslide susceptibility analysis using GIS and artificial neural network. *Earth Surface Processes and Landforms, 28*, 1361-1376. <https://doi.org/10.1002/esp.593>
- Lee, S., & Thalib, J. A. (2005). Probabilistic landslide susceptibility and factor effect analysis. *Environmental Geology, 47*, 982-990. <https://doi.org/10.1007/s00254-005-1228-z>
- Mahmud, A. R., Awad, A., & Billa, R. (2013). Landslide susceptibility mapping using averaged weightage score and GIS: A case study at Kuala. *Pertanika Journal of Science and Technology, 21*(2), 473-486.
- Majid, N. A., & Ibrahim, W. M. M. W. (2015, August 19-20). *GIS in studying slope failure in Penang: Challenges and potential* [Paper presentation]. Proceedings of International Conference on Development and Socio Spatial Inequalities, Penang, Malaysia.
- Majid, N. A., Rainis, R., & Ibrahim, W. M. M. W. (2017). Pemodelan ruangan pelbagai jenis kegagalan cerun di Pulau Pinang menggunakan kaedah nisbah kekerapan [Spatial modeling of various slope failures in Pulau Pinang using frequency ratio method]. *Geografi, 5*(2), 13-26.
- Majid, N. A., Rainis, R., & Ibrahim, W. M. M. W. (2018). Pemodelan ruangan pelbagai jenis kegagalan cerun menggunakan rangkaian saraf buatan (ANN) di Pulau Pinang, Malaysia [Spatial modeling various types of slope failure using artificial neural network (ANN) in Pulau Pinang, Malaysia]. *Jurnal Teknologi, 80*(4), 135-146.
- Majid, N. A., & Rainis, R. (2019). Application of geographical information systems (GIS) and discriminant analysis in modelling slope failure incidence in Pulau Pinang, Malaysia. *Sains Malaysiana, 48*(7), 1367-1381. <http://dx.doi.org/10.17576/jsm-2019-4807-06>
- Mandal, S., & Mondal, S. (2019). Artificial neural network (ANN) model and landslide susceptibility. In *Statistical Approaches for Landslide Susceptibility Assessment and Prediction 4* (pp. 123-133). Springer. https://doi.org/10.1007/978-3-319-93897-4_5-
- Mersha, T., & Meten, M. (2020). GIS-based landslide susceptibility mapping and assessment using bivariate statistical methods in Simada area, northwestern Ethiopia. *Geoenvironmental Disasters, 7*, Article 20. <https://doi.org/10.1186/s40677-020-00155-x>

- NASA. (2020). *Global landslide catalog: Rainfall-triggered landslide events around the world*. Data World. <https://data.world/nasa/global-landslide-catalog>
- Naseer, S., Haq, T. U., Khan, A., Tanoli, J. I., Khan, N. G., Qaiser, F. R., & Shah, S. T. H. (2021). GIS-based spatial landslide distribution analysis of district Neelum, AJ&K, Pakistan. *Nat Hazards*, *106*, 965-989. <https://doi.org/10.1007/s11069-021-04502-5>
- Palansamy, Y. (2021). DBKL: Seri Duta 1 condo unsafe after partial landslide, situation being monitored. *Malay Mail*. <https://www.malaymail.com/news/malaysia/2021/12/27/dbkl-seri-duta-1-condo-unsafe-after-partial-landslide-situation-being-monit/2031312>
- Paudel, U., Oguchi, T., & Hayakawa, Y. (2016). Multi-resolution landslide susceptibility analysis using a DEM and random forest. *International Journal of Geosciences*, *7*(5), 1-18. <https://doi.org/10.4236/ijg.2016.75056>
- Pawluszek, K., & Borkowski, A. (2017). Impact of DEM-derived factors and analytical hierarchy process on landslide susceptibility mapping in the region of Rożnów Lake, Poland. *Natural Hazards*, *86*, 919-952. <https://doi.org/10.1007/s11069-016-2725-y>
- Pradhan, B., & Lee, S. (2009). Landslide risk analysis using artificial neural network model focussing on different training sites. *International Journal of Physical Sciences*, *4*(1), 001-015.
- Psomiadis, E., Papazachariou, A., Soulis, K. X., Alexiou, D. S., & Charalampopoulos, I. (2020). Landslide mapping and susceptibility assessment using geospatial analysis and earth observation data. *Land*, *9*(5), Article 133. <https://doi.org/10.3390/LAND9050133>
- Rahim, A. F. A., Rafek, A. G. M., Serasa, A. S., Abdullah, R. A., Rahim, A., Sami, W. H. W., Foong, S. W., Abdurrahman, M., Lee, K. E., Nguyen, X. H., Tran, V. X., & Goh, T. L. (2022). Application of a comprehensive rock slope stability assessment approach for selected Malaysian granitic rock slopes. *Sains Malaysiana*, *51*(2), 421-436. <http://doi.org/10.17576/jsm-2022-5102-08>
- Rahman, A. A. A., Majid, N. A., & Selamat, S. N. (2020). A comprehensive deriving the factors of landslide happened in Malaysia. *International Journal on Emerging Technologies*, *11*(5), 310-314.
- Rahmati, O., Haghizadeh, A., Pourghasemi, H. R., & Noormohamadi, F. (2016). Gully erosion susceptibility mapping: The role of GIS-based bivariate statistical models and their comparison. *Natural Hazards*, *82*, 1231-1258. <https://doi.org/10.1007/s11069-016-2239-7>
- Rasyid, A. R., Bhandary, N. P., & Yatabe, R. (2016). Performance of frequency ratio and logistic regression model in creating GIS-based landslides susceptibility map at Lompobattang Mountain, Indonesia. *Geoenvironmental Disasters*, *3*(19), 1-16. <https://doi.org/10.1186/s40677-016-0053-x>
- Ritchie, H., Rosado, P., & Roser, M. 2014. *Natural disasters*. Our World in Data. <https://ourworldindata.org/natural-disasters>
- Saadatkah, N., Kassim, A., & Lee, M. L. (2014). Spatial patterns of precipitation, altitude and monsoon directions in Hulu Kelang area, Malaysia. *Electronic Journal of Geotechnical Engineering*, *19*(C), 521-534.
- Sanusi, M. S. M., Ramli, A. T., Hassan, W. M. S. W., Lee, M. H., Izham, A., Said, M. N., Wagiran, H., & Heryanshah, A. (2017). Assessment of impact of urbanisation on background radiation exposure and human health risk estimation in Kuala Lumpur, Malaysia. *Environment International*, *104*, 91-101. <https://doi.org/10.1016/j.envint.2017.01.009>

- Selamat, S. N., Majid, N. A., Taha, M. R., & Osman, A. (2022). Landslide susceptibility model using artificial neural network (ANN) approach in Langat River Basin, Selangor, Malaysia. *Land*, 11(6), Article 833. <https://doi.org/10.3390/land11060833>
- Shahabi, H., & Hashim, M. (2015). Landslide susceptibility mapping using GIS-based statistical models and Remote sensing data in tropical environment. *Scientific Reports*, 5, Article 9899. <https://doi.org/10.1038/srep09899>
- Sharir, K., Roslee, R., Lee, K. E., & Simon, N. (2017). Landslide factors and susceptibility mapping on natural and artificial slopes in Kundasang, Sabah. *Sains Malaysiana*, 46(9), 1531-1540. <http://dx.doi.org/10.17576/jsm-2017-4609-23>
- Silalahi, F. E. S., Pamela, Arifianti, Y., & Hidayat, F. (2019). Landslide susceptibility assessment using frequency ratio model in Bogor, West Java, Indonesia. *Geoscience Letters*, 6(10), 1-17. <https://doi.org/10.1186/s40562-019-0140-4>
- Sim, L. L., Adrian C., & Trisha N. (2018, December 4). Malaysia among countries especially prone to landslides. *The Star*. [https://www.thestar.com.my/news/nation/2018/12/04/msia-ranks-highly-for-landslides-country-experienced-185-occurrences-annually-in-past-10-years#:~:text=Based%20on%20Nasa's%20GLC%20website,%20and%20Selangor%20\(eight\)](https://www.thestar.com.my/news/nation/2018/12/04/msia-ranks-highly-for-landslides-country-experienced-185-occurrences-annually-in-past-10-years#:~:text=Based%20on%20Nasa's%20GLC%20website,%20and%20Selangor%20(eight)).
- Simon, N., De Roiste, M., Crozier, M., & Rafek, A. G. (2017). Representing landslides as polygon (areal) or points? How different data types influence the accuracy of landslide susceptibility maps. *Sains Malaysiana*, 46(1), 27-34. <https://doi.org/10.17576/jsm-2017-4601-04>
- Skilodimou, H. D., Bathrellos, G. D., Koskeridou, E., Soukis, K., & Rozos, D. (2018). Physical and anthropogenic factors related to landslide activity in the Northern Peloponnese, Greece. *Land*, 7(3), Article 85. <https://doi.org/10.3390/land7030085>
- Song, Z. C., Li, X., Lizárraga, J. J., Zhao, L., & Buscarnera, G. (2020). Spatially distributed landslide triggering analyses accounting for coupled infiltration and volume change. *Landslides*, 17, 2811-2824. <https://doi.org/10.1007/s10346-020-01451-1>
- The Start. (2022, January 6). 12 more landslide incidents reported, says NADMA. *The Star*. <https://www.thestar.com.my/news/nation/2022/01/06/12-more-landslide-incidents-reported-says-nadma>
- Wen, B. P., & Jiang, X. Z. (2016). Effect of gravel content on creep behavior of clayey soil at residual state: Implication for its role in slow-moving landslides. *Landslides*, 14, 559-576. <https://doi.org/10.1007/s10346-016-0709-3>
- Yuri, G., & Andrii, V. (2021). Implications of slope aspect for landslide risk assessment: A case study of Hurricane Maria in Puerto Rico in 2017. *Geomorphology*, 391, Article 107874. <https://doi.org/10.1016/j.geomorph.2021.107874>
- Yusoff, Z. M., Raju, G., & Nahazanan, H. (2016). Static and dynamic behaviour of Kuala Lumpur limestone. *Malaysian Journal of Civil Engineering*, 28(1), 18-25.
- Zhang, S., Bai, L., Li, Y., Li, W. L., & Xie, M. (2022). Learning models in landslide susceptibility mapping: A case study in Wenchuan County. *Frontier in Environment Science*, 10, Article 886841. <https://doi.org/10.3389/fenvs.2022.886841>

Review Article

Subcritical Water Pretreatment for Anaerobic Digestion Enhancement: A Review

Adila Fazliyana Aili Hamzah¹, Muhammad Hazwan Hamzah^{1,2*}, Hasfalina Che Man^{1,2}, Nur Syakina Jamali³, Shamsul Izhar Siajam³ and Pau Loke Show^{4,5,6,7}

¹Department of Biological and Agricultural Engineering, Faculty of Engineering, Universiti Putra Malaysia, 43400 UPM, Serdang, Selangor, Malaysia

²Smart Farming Technology Research Centre, Faculty of Engineering, Universiti Putra Malaysia, 43400 UPM, Serdang, Selangor, Malaysia

³Department of Chemical and Environmental Engineering, Faculty of Engineering, Universiti Putra Malaysia, 43400 UPM, Serdang, Selangor, Malaysia

⁴Department of Chemical Engineering, Khalifa University, P.O. Box 127788, Abu Dhabi, United Arab Emirates

⁵Zhejiang Provincial Key Laboratory for Subtropical Water Environment and Marine Biological Resources Protection, Wenzhou University, Wenzhou 325035, China

⁶Department of Chemical and Environmental Engineering, Faculty of Science and Engineering, University of Nottingham Malaysia, Jalan Broga, 43500 Semenyih, Selangor Darul Ehsan, Malaysia

⁷Department of Sustainable Engineering, Saveetha School of Engineering, SIMATS, Chennai 602105, India

ABSTRACT

This work reviews hydrothermal subcritical water pretreatment to enhance biogas production through anaerobic digestion. The complexity of the lignocellulosic structure has been the main limitation contributing to unsatisfactory biogas production throughout the anaerobic digestion. The high resistance of the structure to biological hydrolysis has increased the interest in applying pretreatment prior to anaerobic digestion to facilitate hydrolysis. Hydrothermal subcritical water technology, an environmentally friendly

pretreatment that uses water as the main medium, is gaining prominence in biogas enhancement. However, the subcritical water pretreatment influence on structural properties, biogas production, and the production of anaerobic process inhibitors signifies a knowledge gap and needs an evaluation. This review presents the need for pretreatment reaction and properties in the subcritical water region, biogas production from subcritical water pre-treated waste, production of inhibitors, and its challenges

ARTICLE INFO

Article history:

Received: 11 April 2022

Accepted: 12 July 2022

Published: 06 March 2023

DOI: <https://doi.org/10.47836/pjst.31.2.19>

E-mail addresses:

adilafazliyana28@gmail.com (Adila Fazliyana Aili Hamzah)

hazwanhamzah@upm.edu.my (Muhammad Hazwan Hamzah)

hasfalina@upm.edu.my (Hasfalina Che Man)

syakina@upm.edu.my (Nur Syakina Jamali)

shamizhar@upm.edu.my (Shamsul Izhar Siajam)

PauLoke.Show@ku.ac.ae; PauLoke.Show@nottingham.edu.my;

showpauloke@gmail.com (Pau Loke Show)

*Corresponding author

are discussed. This pretreatment could be a promising option and further enhance biogas production throughout the anaerobic digestion process.

Keywords: Anaerobic digestion, biogas, hydrothermal, lignocellulosic pretreatment, subcritical water

INTRODUCTION

In recent years, researchers have focused on using agricultural and food waste to value goods on the ground of the waste-to-wealth idea to lower the downsides of inappropriate waste management practices (Hamzah et al., 2016; Rico et al., 2020). The derivation of energy from agricultural and food waste can be seen as a sustainable approach in line with the 12th Malaysia Plan 2021–2025 (RMK12) and Sustainable Development Goals (SDG) (RMK12, 2021). By focusing on implementing a circular economy and accelerating the adoption of integrated resources management, this plan encourages the public and private sectors to implement and integrate the SDGs values in their decision-making in pursuing sustainability. Apart from ensuring supply safety, the circular economy will reduce dependency on non-renewable energy, waste production, pollution, and greenhouse gas emissions. Replacement of non-renewable energy sources through bioenergies such as biofuels and biogas could be one possible way toward sustainability plans (Lemaire & Limbourg, 2019). Biogas is produced through anaerobic digestion by degrading substrates assisted by microbes throughout some biochemical phases (Aili et al., 2021).

The anaerobic digestion process has four major phases: hydrolysis, acidogenesis, acetogenesis, and methanogenesis. The process is carried out by several mixed-culture microbial communities working through syntrophy (Morales-Polo et al., 2018). The hydrolysis phase is the rate-determining step, while methanogenesis restricts the digestion rate of more easily degradable substrates (Paudel et al., 2017). Improving the hydrolysis and biogas production during anaerobic digestion generates improvement opportunities and challenges for anaerobic digestion since the lignocellulosic substrates have different characteristics, indicating different kinds and levels of boundaries to accomplish the ideal anaerobic digestion process (Carlsson et al., 2012). Therefore, pretreatment for biodegradability improvement is a prerequisite for the amendment of lignocellulosic biomass for anaerobic digestion. The primary purpose of the pretreatment for lignocellulose feedstock is to disrupt lignin structure; consequently, cellulose and hemicellulose become accessible for microbial attack. In addition, the crystallinity of cellulose decreased, and the porosity of the substrate increased with pretreatment. (Brodeur et al., 2011; Carrere et al., 2016). Therefore, the problem mentioned above can be eliminated by pretreatment. Over the years, pretreatment has been commonly practiced before anaerobic digestion, and various pretreatment technologies have been conducted, including thermal, chemical, biological, and combined pretreatment or its combination (Chen et al., 2020; Dahunsi, 2019; Pečar et al., 2020; Sun et al., 2016).

Biogas production using the acai pre-treated by subcritical water (SCW) pretreatment presented a noteworthy performance compared to the untreated acai processing waste, resulting in 30% more methane in the biogas and 100 times higher yield (Maciel-Silva et al., 2019). According to Edwiges et al. (2019), when compared to untreated garden waste, alkaline pretreatment followed by solid/liquid phase separation at 5% NaOH concentration at 20°C for 12 hours produced the best results, increasing methane yield by 70%. However, despite high methane yield, the final effluent with high soluble chemical oxygen demand (COD) was produced from the digestion. Dilute acid pretreatment by 0.2M acetic acid yielded the highest sugar recovery of 95% and improved the crystallinity index to 56% after disrupting complex lignocellulosic during pretreatment (Saha et al., 2018). In addition, substrate hydrolysis of agricultural waste was improved through intermediate ozonation (Almomani et al., 2017). As a result, utilization of the substrates by the microbes is quicker, and the ozonation reduces the hydrolysis period while increasing the microbial activity in the digester.

Combined biological and chemical pretreatment of maize straw using 1% NaOH and enzyme transformed cellulose and hemicellulose into reducing sugars and monomers, making them ready to use by microbes in the anaerobic digestion process, improving 20.24% of the biogas (Zhao et al., 2018). Chen et al. (2020) reported using acid and alkali pretreatments for wheat straws. The study reported that biogas production increased by 7% with the addition of 0.01 mol/L NaOH pre-treated wheat straw. In contrast, 0.1 mol/L NaOH negatively affected biogas yield due to the inhibition of propionic acid into acetic acid in the systems (Chen et al., 2020). All these studies concluded that the available pretreatment technology of lignocellulosic wastes is vital, especially for complex substrates feedstocks, to improve biogas and methane yield, better hydrolysis, and higher lignin, cellulose, and hemicellulose removal, as well as a few more parameters. Thus, before anaerobic digestion, pretreatment application should fully utilize the substrate potential.

Hydrothermal pretreatment at SCW temperature has been broadly accepted as an eco-friendly green technology due to its excellent performance for bioenergy generation from lignocellulosic wastes. The pretreatment promotes structure-breaking and substrate availability after pretreatment (Wang et al., 2018a). Hydrothermal pretreatment is also commonly identified as SCW pretreatment, autohydrolysis, liquid hot water, hydrothermal carbonization, aquasolv, hydro thermolysis, or hot-compressed water pretreatment (Ahmad et al., 2018; Saha et al., 2013; Shitu et al., 2015; Toor et al., 2011). SCW pretreatment promotes structure-breaking and substrate availability after pretreatment (Wang et al., 2018a). SCW pretreatment technology is gaining prominence in biogas production enhancement. SCW pretreatment involves using very sustainable and environmentally friendly water since it does not require acid recycling and is non-corrosive, non-toxic, and inflammable (Antwi et al., 2019; Saha et al., 2013). Water penetrates the lignocellulosic structure to hydrate cellulose, solubilize hemicellulose and partially remove lignin (Ahmad

et al., 2018). The practicality of the SCW depends on the process parameters such as temperature, reaction time, and water-to-solid ratio. These parameters are the aspects of dominant importance concerning pretreatment efficiency and anaerobic digestion.

This review aims to present basic knowledge, and recent states of hydrothermal SCW pretreatment applied to the anaerobic of various lignocellulosic wastes. This review also discussed the major recalcitrance components in lignocellulosic wastes that hinder the anaerobic digestion of lignocellulosic waste. Recent studies discuss fundamental information on the reaction and properties of the pretreatment at the subcritical region. The recent study on the enhancement of biogas production from hydrothermal SCW pretreatment as the effective pretreatment method is reviewed. The inhibitory potential of this pretreatment as the main challenge of pretreatment during the process was also provided.

Pretreatment

The addition of pretreatment can enhance the performance of anaerobic digestion. Owing to the irregularity of lignocellulosic compounds, an ideal pretreatment process and conditions rely on its compositions (Zheng et al., 2014). The structure and compositions of lignocellulosic wastes were found to have influences on lignocellulosic biodegradability. The purpose of pretreatment is to modify the lignocellulosic structure, especially lignin, to improve and assist the enzymes and microbial attack (Ahmad et al., 2018; Carrere et al., 2016). Through pretreatment strong structure of the lignocellulose parts becomes easily disintegrated, lignin and hemicellulose are degraded, and the hydrolysis of cellulose occurs more efficiently, thus converting them to the soluble fraction. The expected outcome of pretreatment on lignocellulosic wastes is shown schematically in Figure 1. Several pretreatment approaches have been developed to improve the utilization of carbohydrates as the primary source of biogas. Pretreatment enhances microbial hydrolysis, evades the degradation of sugars, minimizes the formation of inhibitors, recovers lignin, and is cost-effective by operating in an anaerobic digester by reducing heat and power requirements (Brodeur et al., 2011).

The optimal pretreatment method and conditions depend on the types of lignocellulose present (Neshat et al., 2017). It is essential to analyze its characteristics since different lignocellulosic waste is divergent according to their types. It is also vital to ensure the microbial stability and balance of the nutrient for an effective process. Lignin supports the cell structure, covering cellulose and hemicellulose and resisting hydrolysis for microbial attack (Atelge et al., 2020). The structure's resistance to hydrolysis is correlated with crystalline cellulose, recalcitrant lignin, and its linkage (Paudel et al., 2017). Figure 2 shows the close association of cellulose, hemicellulose, and lignin. Pretreatment has commonly been subjected before being applied to anaerobic digestion to eliminate the problem associated with the lignocellulosic compound, as mentioned above.

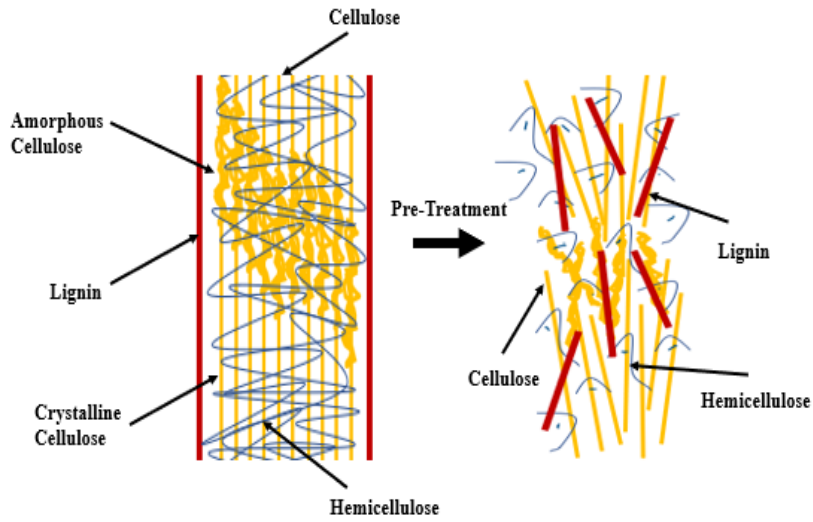


Figure 1. The schematic effect of pretreatment on the lignocellulosic waste (adapted and modified from Ahmed et al. (2019))

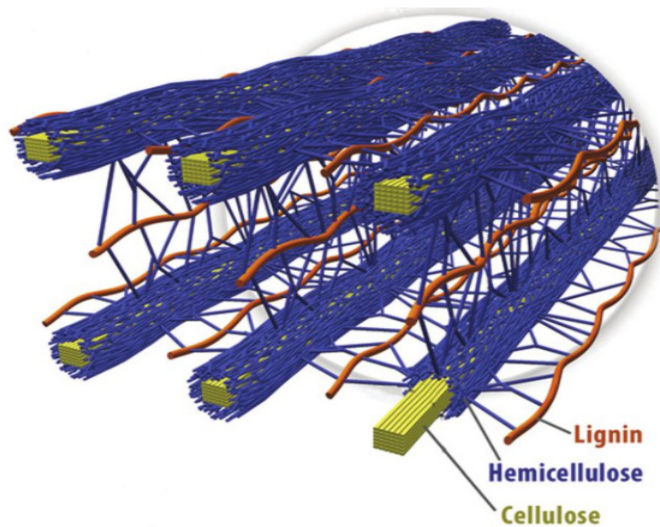


Figure 2. Cellulose strands surrounded by hemicellulose and lignin (Brandt et al., 2013)

Composition of Lignocellulosic Waste

The main difficulty hindering the efficiency of biogas generation from lignocellulosic waste feedstocks is overcoming the slow hydrolysis due to the recalcitrance of these wastes towards microbial degradation. Lignocellulose wastes have complex structures that restrict microbial attack due to combinations of interactions between lignocellulosic

fractions (Atelge et al., 2020). Lignocellulosic wastes are mainly made up of a skeleton surrounded by three types of polymers: cellulose (30–70%), hemicellulose (15–30%), and lignin (10–25%), with extractives, and a number of inorganic materials (Ahmad et al., 2018; Brodeur et al., 2011). Table 1 shows the composition of some lignocellulosic waste reported by researchers. After hydrolysis, carbohydrates release fermentable sugar, making it an appropriate source for biogas production. Though, very complex structures make it resistant to hydrolysis by microorganisms (Zheng et al., 2014).

Table 1
Composition of lignocellulosic waste

Lignocellulosic waste	Lignin (%)	Cellulose (%)	Hemicellulose (%)	References
Rice straw	23–24	29–32	16–17	Wang et al. (2018a); Xiang et al. (2021)
Wheat straw	11.9	38.7	23	Tian et al. (2020)
Cocoa pods	21.29	26.10	4.82	Antwi et al. (2019)
Napier grass	4–23	36–42	20–27	Jomnonkhaow et al. (2022); Suaisom et al. (2019)
Paper tube	23	NS	NS	Teghammar et al. (2010)
Acai	24.56	43.81	25.89	Maciel-Silva et al. (2019)
OFMSW	48.93	85.28	54.81	Dasgupta and Chandel (2019)

Note. NS: Not Stated, OFMSW: organic fraction of municipal solid waste

Cellulose

Cellulose is the key component of lignocellulose cell walls and the most abundant linear polysaccharide of cellobiose, making a molecular chain between 100 and 14,000 units (Paudel et al., 2017; Zheng et al., 2014). Cellulose is strongly linked by β ,1–4 glycosidic linkages (Ahmad et al., 2018; Paudel et al., 2017). The cellulose units contain organized crystalline structures with poorly organized amorphous structures and form the so-called cellulose fibrils or cellulose bundles (Carrere et al., 2016). Cellulose chains are intertwined by hydrogen bonds and van der Waals forces (Zheng et al., 2014). The intramolecular hydrogen bonds made microfibrils with high tensile strength and hydrophilic, but they are not highly soluble in water due to their large size. The bonds support cellulose by creating a crystalline and amorphous structure (Paudel et al., 2017). Cellulose chains have numerous angles of amorphous regions intertwined with crystalline cellulose, which determine their crystallinity level (Ahmad et al., 2018). The bond of hydrogens between

glucan units influences its crystallinity, characterized by the crystallinity index. They consist of two regions: amorphous (low crystallinity) and crystalline (high crystallinity) regions (Zheng et al., 2014). At a high crystallinity index, the degradation of cellulose turns out to be more complex. The cellulose chains also are packed into microfibrils and stabilized by hydrogen bonds. Hemicelluloses connect these fibrils, amorphous polymers, and other polymers, such as pectin, and are protected by lignin (Brodeur et al., 2011). It makes cellulose complicated and resistant to biological and chemical attacks. While the chain length is contrarywise relative to hydrolysis effectiveness, they are insoluble in water and are most prone to microbial degradation (Ahmad et al., 2018).

Hemicellulose

Hemicelluloses are more amorphous than cellulose and are made of linear, highly-branched heteropolymers of pentoses, hexoses, and acids (Ahmad et al., 2018). Hemicellulose is not attached to the cellulose by a covalent bond and builds an amorphous region in the lignocellulosic structure (Brandt et al., 2013). Hemicellulose has amorphous structures and is more readily hydrolyzed than cellulose (Carrere et al., 2016). They are also firm due to the short and branched chains that assist in forming a structure with cellulose fibrils and interact with lignin. Due to these properties, hemicelluloses are highly susceptible to hydrolysis (Zheng et al., 2014). Cellulose has a higher molecular weight than hemicellulose, a low polymerization degree (70 to 200°C), and less crystal with arbitrary amorphous composition, making hemicellulose more sensitive to hydrolysis (Ahmad et al., 2018; Brodeur et al., 2011). Hemicellulose is not as robust, and mostly amongst others, it performs a weighty part in firming the lignocellulosic complex in covering cellulose fibrils (Paudel et al., 2017).

Lignin

Lignin is the second most abundant natural polymer after cellulose and is a combination of aromatic complexes and consists of aquaphobic heteropolymers alcohols linked through ether bonds. Also include hydroxyl, methoxyl, and carbonyl functional groups, the C-C bonds, or a linkage of C-C and ether (Ahmad et al., 2018; Carrere et al., 2016; Zhao et al., 2018). Coniferyl alcohol is the main monomer in softwood lignin and is the foundation for lignin, especially hardwood. Other than that, aromatic monomers are also integrated into the lignin structure that protects the cellulose and hemicellulose as a hydrophobic layer (Ahmad et al., 2018). Lignin is an amorphous polymer cross-linked between the hemicellulose and cellulose to a rigid three-dimensional structure of the lignocellulosic matrix. The fibrils present in the lignocellulosic structure are often associated with packs or macro fibrils cellulose (Brodeur et al., 2011). The fibrils are mainly crystalline, hindering microbial attack, and are the primary physical block between polymers (Brodeur et al.,

2011; Paudel et al., 2017). Moreover, lignin commonly forms a covalent bond, mainly with hemicellulose. The rigidity of lignin makes them resistant to biological degradation (Carrere et al., 2016). Lignin is also hydrophobic and optically inert and only dissolve at high temperature ($> 180^{\circ}\text{C}$). Therefore, lignin is the main obstacle to biodegradation; the higher the percentage of lignin, the resistance to microbial degradation are greater, and softwood lignin is the most recalcitrant to pretreatment and bioconversion (Talaiekhazani & Rezania, 2020; Zheng et al., 2014).

Subcritical Water (SCW) Technology

The SCW, known as hydrothermal pretreatment has been broadly accepted due to its excellent performance in improving bioenergy generation (Lee et al., 2019; Shitu et al., 2015; Toor et al., 2011). This pretreatment destroys the crystallographic structure of cellulose and promotes lignocellulosic structure-breaking and substrate availability after pretreatment (Wang et al., 2018a). The SCW pretreatment occurs when substrates are subjected to water at a higher temperature (100 to 374°C) in a liquid state at a selected reaction time and pressure (Dasgupta & Chandel, 2019). The water in the subcritical region is still in a liquid state (Figure 3), and in these environments, water has a range of exotic properties (Möller et al., 2011; Shitu et al., 2015). Match up to conventional pretreatments such as acid and alkali; after SCW pretreatment, the solid filtrate contains high cellulose and lignin. At the same time, most hemicellulose solubilizes in the liquid portion (Figure 4), thus showing the possibility of improving lignocellulosic hydrolysis and biogas yield and promoting changes in lignocellulosic structure.

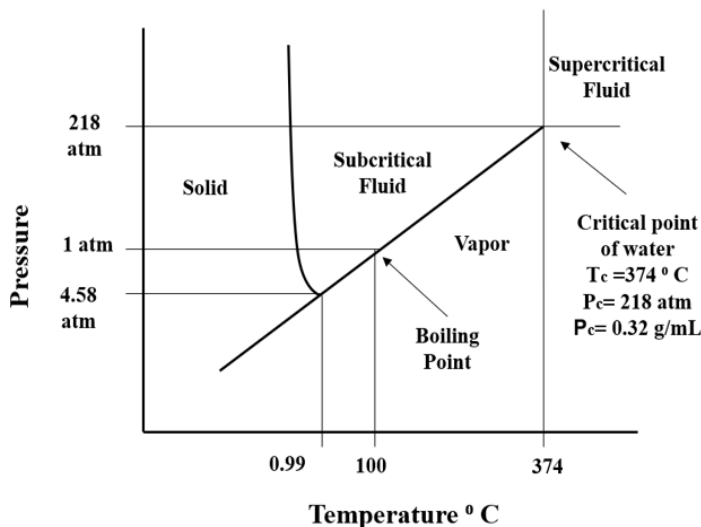


Figure 3. Water phase diagram as a function of pressure and temperature (Shitu et al., 2015)

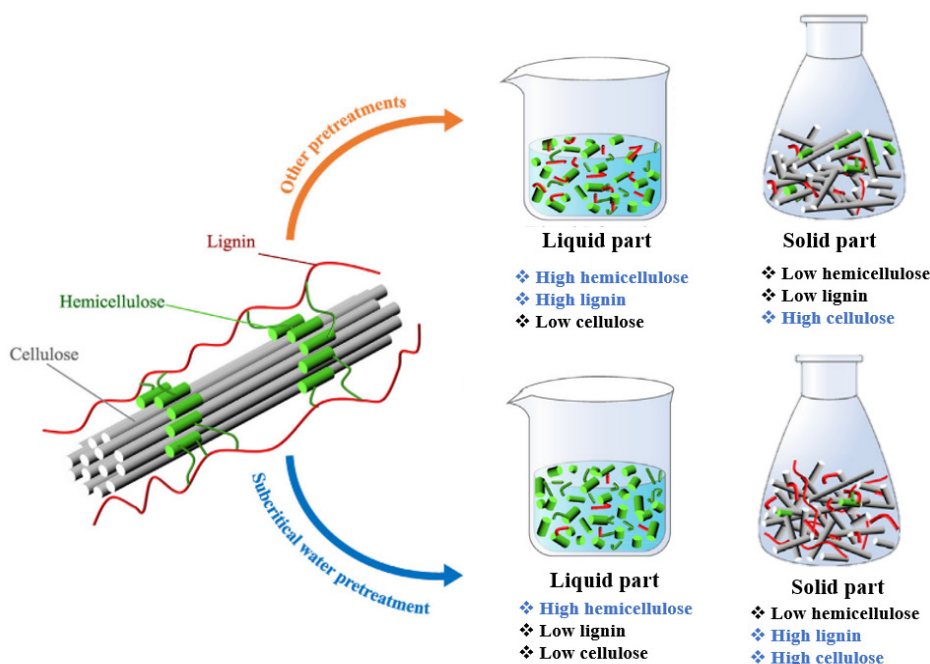


Figure 4. Changes in lignocellulosic content between SCW pretreatment and other pretreatments (adapted and modified from Chen et al., 2021)

Reaction and Properties at Subcritical Water Condition

During SCW pretreatment, lignocellulosic waste undertakes high temperatures in water at high pressure at a specific reaction time and solid-to-water ratio (Lachos-Perez et al., 2017; Lee et al., 2019). SCW promotes structural modification to the lignocellulosic waste by enlarging the available surface area of cellulose, improving cellulose degradation, and generating low inhibitors concentration in pre-hydrolysates, compared with low pH pretreatment methods (Chen et al., 2021; Maciel-Silva et al., 2019; Suaisom et al., 2019). Water in SCW regions possesses some unique characteristics, it stays in liquid states and does not require any chemical as a medium, and is considered an environmentally friendly technique for lignocellulosic pretreatment. SCW has a low dielectric constant and high ionic product, indicating water polarity and solubility. Water behaves as an acid catalyst due to autoionization at high temperatures.

The water autoionization release acid hydronium ion (H_3O^+) that catalyze the polysaccharides (mainly hemicellulose) hydrolysis to form sugars (pentoses and hexoses) (Jomnonkhaow et al., 2022). The increase in reaction temperature increased the ionic constant of water and created a low pH medium for subsequent hydrolysis. The affinity of water performing as reaction media indicates the dielectric constant. Water in the SCW region has the same polarity as an organic solvent because the dielectric constant is reduced

and contributes to the organic compound's solubilization. Reduction of the dielectric constant reduced the polarity of water while increasing hydrocarbon solubility. Water reduced the quantity of organic solvent required during hydrolysis since the increase in temperature increases the mid-polar compound solubilization.

High kinetic energy at high temperatures increases the polymerization reactions rate for the rupture of cell wall structure while enhancing diffusivity and decreasing viscosity are beneficial to enhance the mass transfer and pretreatment effectiveness. (Abdelmoez et al., 2014; Ahmad et al., 2018; Chen et al., 2021; Lachos-Perez et al., 2017; Maciel-Silva et al., 2019; Shitu et al., 2015). Thus, in general, SCW penetrates the structure to hydrate cellulose, solubilize a substantial part of hemicellulose and partially remove lignin. Increases in the polymerization rate help breakdown down the cell wall and cellulose swelling. It increases cellulose accessibility by expanding the surface area following enzymatic reaction. Also, subcritical water assists in acetyl and uronic acid groups' cleavage yielding acetic acid and other organic acids and boosting the solubilization of oligosaccharides (Ahmad et al., 2018). Thus, the subcritical water allows the depolymerization of the lignocellulosic biomass by cleavage, dehydration, swelling, and recombination of reactive fragments (Toor et al., 2011).

Subcritical Water Pretreatment Process Parameters

The SCW pretreatment parameters, temperature, reaction time, and solid-to-water ratio are the aspects of dominant importance concerning pretreatment efficiency and, subsequently, anaerobic digestion (Ahmad et al., 2018; Toor et al., 2011). Therefore, the effect of those parameters is discussed further in the following subsection.

Temperature. The extent of the SCW pretreatment at the SCW temperature region's effect on the lignocellulosic composition modification is influenced mainly by the reaction temperature. The pretreatment disrupts the cellulose microfibrils bundles, improving surface porosity, fractures, and drains on the deformed surface, increasing the surface area depending on pretreatment severity (Ahmad et al., 2018; Maciel-Silva et al., 2019). The sugar production increased with temperature, and the highest sugar produced from SCW pre-treated spent Java citronella was obtained at 160°C (Timung & Goud, 2018). Higher pretreatment temperatures over 200°C caused the formation of furfural and 5-hydroxymethylfurfural (HMF), one of the methanogenesis inhibitors (Phuttaro et al., 2019). Tian et al. (2020) observed a reduction in methane yield after pre-treated wheat straw at 175°C. At 90°C and 180°C, Wang et al. (2018a) reported that biogas produced from pre-treated rice straw improved compared to untreated rice straw. Temperature 210°C presented a 30% reduction with a more extended lag period. Antwi et al. (2019) observed that optimum biogas yield was obtained at 150°C with low severity of 2.65. The SCW on cocoa pod waste observed that temperature influences the lignin solubilization compared to

reaction time (Antwi et al., 2019). Higher SCW temperature has resulted in more significant degradation, and soluble sugars produced from hemicellulose solubilization have been stated at 160 and 200°C (Dasgupta & Chandel, 2019).

The cellulose microfibrils are linked by hemicellulose and amorphous polymers and protected by lignin (Brodeur et al., 2011). Cellulose is crystalline and has a high level of polymerization (Ahmad et al., 2018; Toor et al., 2011), and disruption of the structure through the SCW pretreatment can modify the bond between cellulose and make cellulose more accessible to microbial attack. According to Ahmed et al. (2019), the decomposition of cellulose begins at a temperature of 230°C. The cellulose hydrolysis rate and conversion increase from temperature 240 to 270°C (Ahmed et al., 2019; Lachos-Perez et al., 2017; Toor et al., 2011). Hemicelluloses are amorphous and easily hydrolyzed compared to cellulose, and solubilization occurs above 150°C and 180°C (Ahmed et al., 2019; Carrere et al., 2016). Lignin is also hydrophobic and optically inert and only dissolve at high temperature (> 180°C). Lignin is a major barrier to microbial attack; the higher the percentage of lignin, the higher the resistance to microbial degradation, and it is the most recalcitrant to pretreatment and bioconversion (Zheng et al., 2014). Furans (furfural and HMF) are inhibitory compounds formed through the degradation of hemicellulose to its monomeric sugars and depending upon pretreatment conditions, they might inhibit the anaerobic digestion process (Dasgupta & Chandel, 2019).

Reaction Time. Reaction time is also a parameter that affects the SCW pretreatment performance. Though, the temperature has a better impact on the digestibility of cellulose than reaction time (Ahmad et al., 2018; Carrere et al., 2016). Previous studies stated that a longer reaction time is not an ideal approach since it contributes to excessive cellulose breakdown, formation of solid residue, and severity of the pretreatment (González et al., 2014; Toor et al., 2011). However, lignin in the solid fraction increases as time increases due to reordering between lignin and holocellulose (Ahmad et al., 2018). Furthermore, Chandra et al. (2012b) stated that energy could be saved by less reaction time than by higher reaction time. Besides, higher residency time causes pyrolysis, causing charring together with greater energy requirements. According to Dasgupta and Chandel (2019), at the SCW temperature region, the VS of municipal solid wastes increases as the reaction time increases to 120 minutes. Increasing the reaction time decreased the TS and VS by 6.4% and 11%, respectively.

The SCW on cocoa pod waste observed that reaction time does not influence the lignin solubilization compared to temperature (Antwi et al., 2019). However, maximum biogas production is produced at a shorter reaction time, and the optimal reaction time observed by the authors is 15 minutes. Therefore, lower severity of SCW pretreatment contributes to better biogas production. At high temperatures (>175°C), a shorter reaction

time should be considered since high temperatures and longer reaction times risk the furans to aldehydes degradation and organic acids that will increase the accumulation of volatile fatty acid (VFA) inside the digester (González et al., 2014). Therefore, a longer reaction time seems beneficial for temperatures lower than 150°C. The pretreatment reaction time of 15 minutes was applied to rice straw (Wang et al., 2018a), empty fruit bunch (O-Thong et al., 2012), Napier grass (Phuttaro et al., 2019), and cocoa pods (Antwi et al., 2019). At the same time, a reaction time of 10 minutes was used to pre-treat rice straw (Chandra et al., 2012b) and wheat straw (Chandra et al., 2012b). A longer pretreatment reaction time of 30 minutes was conducted on municipal solid waste (Dasgupta & Chandel, 2019) and waste-activated sludge (Kim et al., 2015).

Solid to Water Ratio. The ratio of solid to water during the SCW pretreatment is one more significant parameter that influences the SCW pretreatment process and is generally expressed as the ratio of the solid (g) weight to the volume of water (mL). Water remains an alternate solvent in the sub-critical state to dissolve substrates due to its low viscosity, and high diffusivity allows the water to permeate the complex structure (Chen et al., 2021; Timung & Goud, 2018). According to the mass transfer theory, a high concentration gradient increases the diffusion rate due to a high solid-solvent ratio. It thereby facilitates the extraction by the solvent of solids (Shitu et al., 2015). Previously, optimization of SCW hydrothermal pretreatment of Napier grass for biogas production reported that the optimal Napier grass-to-water ratio of 1:6 gives optimal conditions for methane production. Similarly, Manorach et al. (2015) observed a significant effect of bagasse to water ratio for the sugarcane bagasse hydrolysis. The hydrolysis of sugarcane bagasse increased after applying SCW pretreatment at a 1:1.69 solid-to-water ratio. About 87.52% cellulose conversion rate was obtained by SCW pretreatment of wheat straw at a 1 to 5 solid-to-water ratio (5%).

Anaerobic Digestion

Biogas is produced through anaerobic digestion by degrading substrates facilitated by a group of microbes through several biochemical reactions (Hamzah et al., 2022). The anaerobic digestion process has four major phases: hydrolysis, acidogenesis, acetogenesis, and methanogenesis. The anaerobic digestion process is carried out by several mixed-culture microbial communities working through syntrophy (Morales-Polo et al., 2018). The microbes work synergistically to decompose recalcitrant waste structures into their simplest form (Sawatdeenarunat et al., 2015). The hydrolysis process turns organic macromolecules into smaller compounds that acidogenic bacteria can use. While acidogenesis is the fastest reaction in which acidogens convert soluble molecules from the previous phase to acetic acid and other longer VFAs, alcohols, and carbon dioxide (Caruso et al., 2019). Then the

VFAs are then converted into acetate, carbon dioxide, and hydrogen via acetogenesis. At the last phase of anaerobic digestion, methane and carbon dioxide are produced by two groups of methanogens; acetoclastic and hydrogen-utilizing methanogens (Hagos et al., 2017).

Methane-rich biogas is produced from various feedstocks, consisting of primarily 50–75% methane, 19–34% carbon dioxide, and less than 1% hydrogen through the anaerobic digestion process (Hamzah et al., 2020; Elhenawy et al., 2021). Anaerobic digestion is a very complex method to produce biogas from different types of waste. The important process parameters should be learned to achieve the maximum potential of the anaerobic digestion process. Temperature, pH, carbon-to-nitrogen ratio, organic loading, mixing, and concentration of VFAs and ammonia nitrogen are among the most important parameters that affect the performance of an anaerobic digestion system. Mono digestion often observes lower biogas yield, and even with anaerobic co-digestion, the biogas yield is not satisfying due to the complexity of the structure. High resistance of lignocellulose to biological hydrolysis is associated with the presence of refractory lignin, its linkage to the strong bond between cellulose and hemicelluloses, and the presence of crystalline cellulose (Paudel et al., 2017). The primary purpose of the pretreatment for lignocellulose feedstock is to disrupt lignin structure; consequently, cellulose and hemicellulose become accessible for microbial attack. SCW pretreatment promotes structure-breaking and substrate availability after pretreatment (Wang et al., 2018a).

Biogas Production Using SCW Pretreatment

SCW pretreatment for biogas production has been broadly conducted to enhance methane yield from lignocellulosic wastes, including Napier grass (Phuttaro et al., 2019), acai residue (Maciel-Silva et al., 2019), rice straw (Wang et al., 2018a), cocoa pods waste (Antwi et al., 2019), and wheat straw (Chandra et al., 2012a). Table 2 shows some studies on SCW pretreatment using lignocellulosic waste to improve methane yield. According to Chen et al. (2021), SCW pretreatment of wheat straw destroyed the microstructure of the straw and increased the cellulose crystallinity. The SCW also reduced the hemicellulose by 18.37%, while most of the cellulose preserved in the solid part of lignin and cellulose increased by 8.81% and 25.92%, respectively. SCW pretreatment for spent citronella biomass increases the fermentable sugar production during the hydrolysis and increases the crystallinity index to 52.68% (Timung & Goud, 2018). Likewise, this pretreatment also boosts the pre-hydrolysis of straw, and the lag phase throughout the fermentation is correspondingly reduced (Tian et al., 2020). Enhancement of methane production from sewage sludge was reported at optimal pretreatment conditions of 186°C using response surface methodology (Park et al., 2021).

It is also reported that the hydrothermal SCW pretreatment was useful in enhancing the hydrolysis of the lignocellulosic complex and subsequently improving methane

production (Dasgupta & Chandel, 2019). Earlier, hydrothermal SCW pretreatment sped up the pre-hydrolysis of rice straw resulting in biogas and methane enhancement in anaerobic digestion. The pre-treated rice straw improved by 225.6% and 222% of biogas and methane, respectively (Chandra et al., 2012b). Similar pretreatment applied to wheat straw reported that pre-treated wheat straw had an increase of 9.2% in their production of biogas, while methane production increased by 20.0% (Chandra et al., 2012a). Hydrothermal SCW pretreatment for empty fruit bunch and palm oil mill effluent by co-digestion at 230°C for 15 minutes improved the biodegradability to 64% (O-Thong et al., 2012).

However, adding NaOH in the pretreatment improved the biodegradability to 91%. Pretreatment of Napier grass at 190°C improves methane production (Jomnonkhaow et al., 2022). However, during the breakdown of the lignin, the two-step reaction occurs, which leads to a reduction in methane yield due to the two-step reaction. During the pretreatment, solubilization of lignin and subsequent lignin depolymerization occurs, causing insoluble condensation. Table 3 shows lignin, cellulose, and hemicellulose changes after SCW pretreatment. Pre-treated common reed at 120°C for 2 hours increased the methane yield by 28.8% and improved the volatile solid content by 15% (Vakalis et al., 2022). Also, the performance of biogas yield in a two-stage anaerobic digester improved with the application of pretreatment at 140°C for 2 minutes (Wei et al., 2022). The pretreatment at 140°C enriched Acetolactic methanogens during the methanogenic bacteria responsible for enhancing methane content.

Table 2

The SCW pretreatment using lignocellulosic waste to improve methane yield

Substrates	Temperature (°C)	Time (min)	Solid-to-water ratio	Improvement	Yield	References
Municipal solid waste	140	30	NS	Increase by 32% in biogas production	200 mL/gVS	Dasgupta and Chandel (2019)
Napier grass	175	15	1:10	Increase by 35% in biogas production	248.2 NmL/gVS	Phuttaro et al. (2019)
Wheat straw	175	60	1:20	Increase by 52% in biogas production	225.7 mL/gVS	Tian et al. (2020)
Acai residue	200	20	1:80	Increase of 30% in methane production	791.81 L/KgTVS	Maciel-Silva et al. (2019)

Table 2 (Continue)

Substrates	Temperature (°C)	Time (min)	Solid-to-water ratio	Improvement	Yield	References
Rice straw	180	15	1:10	Increase of 3% in methane yield	306.6 mL/g TS	Wang et al. (2018a)
Cocoa pods	150	15	1:5	Increase 1.70% methane yield	357 LN/gVS	Antwi et al. (2019)
Waste activated sludge	180	30	1:1	Increase methane content to 63.4% and VS removal to 60%	130.2 mL/gVS	Kim et al. (2015)

Notes. NS-not stated

Rice straw pre-treated at 110 to 120°C helps methane production rather than 180°C (Xiang et al., 2021). The release of the soluble portion from pretreatment helps the methanogenesis that is responsible for biogas enhancement. Antwi et al. (2019) reported optimal biogas production of pre-treated cocoa pods at 150°C for 15 min. The authors suggested that pretreatment at low severity enhances the biogas production, and a severity of more than three resulted in low biogas yield. Wang et al. (2018a) reported that pre-treated rice straw at 180°C improved the biogas yield by 3%, and increasing the SCW temperature to 210°C lowered the biogas production by 30%. López González et al. (2014) stated that the pretreatment increases 63% the methane yield of pre-treated sugar cane press mud at 150°C for 20 minutes. As the temperature increases over >200°C, methane production decrease with temperature due to the formation of a recalcitrant product (furfural) responsible for methanogenesis inhibition.

The effectiveness of SCW pretreatment is different for various types of lignocellulosic wastes, according to the chemical and structural characteristics and the ideal pretreatment conditions. Thus, it is essential to find the optimal set of pretreatment parameters to ensure the highest substrate utilization can be achieved. The most recent studies evaluating the performance of SCW pretreatment for biogas production observed that pre-treated common reed at 120°C increased the methane potential by 28.8%, while temperature over 200°C had an adverse effect on methane production (Vakalis et al., 2022). Similarly, pre-treated wheat straw at 120°C obtained the highest methane yield, which was 32% higher than that of untreated wheat straw (He et al., 2022). While highest methane production, with an increase of 19% compared to untreated wheat straw, was observed at 160°C for 45 minutes (Zerback et al., 2022). According to the authors, increasing the pretreatment intensity reduces the methane conversion potential.

Table 3

Changes in lignin, cellulose, and hemicellulose after hydrothermal SCW pretreatment

Lignocellulosic Waste	Lignin (%)	Cellulose (%)	Hemicellulose (%)	References
Rice straw	12	12	-16	Wang et al. (2018a)
Rice straw	29.4	46.4	NS	Xiang et al. (2021)
Wheat straw	7	10	14	Tian et al. (2020)
Cocoa pods	8	10	-0.38	Antwi et al. (2019)
OFMSW	17.9	NS	-43.5	Dasgupta and Chandel (2019)

Note. NS: Not Stated, OFMSW: organic fraction of municipal solid waste: reduction in the content, Changes extracted based on the optimal parameter set that gives the highest biogas production.

Potential Inhibitors

Depending upon SCW pretreatment conditions, the inhibitory compound may be formed from the hydrolysis of lignocellulosic biomass during the pretreatment. The formation of refractory inhibitors could inhibit methanogenesis and contribute to low biogas production. In addition, pretreatment could change the properties of the substrates through esterification, caramelization, or Maillard reaction, which causes nutrient loss and formation of toxic melanoidins and inhibitors, thus affecting the substrate's biodegradability and anaerobic digestion process (Carrere et al., 2016; Meegoda et al., 2018; Wenjing et al., 2019). Via Maillard reaction, sugars and amino acids are concurrently generated through hydrolysis and produce compounds such as pyrroles, pyridines, and other compounds containing nitrogen cyclic organic components. These compounds also act as free radical chain reaction inhibitors and scavengers often associated with biogas production at SCW (Toor et al., 2011).

It was also reported that at the higher reaction temperature, the Maillard reaction occurs with the generation of Maillard products, and the SCW pre-treated biomass changed from dark brown to black coloration due to this reaction (Dasgupta and Chandel, 2019; Tampio, 2016; González et al., 2014). Park et al. (2017) reported that the brown color of the pre-treated samples proved the presence of anaerobic digestion inhibitory compounds such as Amadori and melanoidins at temperatures of 200°C and 220°C. Furans (furfural and HMF) are refractory inhibitors during anaerobic digestion formed during the degradation of hemicellulose to monosaccharides, oligosaccharides, and monomers (Dasgupta & Chandel, 2019). Depending on the availability and concentration levels throughout the anaerobic digestion process, compounds such as phenols, organic acids, and furans can potentially be process inhibitors (Prado et al., 2014; Wang et al., 2018a).

Table 4 shows the concentration of inhibitory compounds from hydrothermal SCW pretreatment from various substrates. The inhibitory levels of HMF and phenolic acid were reported to be at 3 g/L and 10 g/L, respectively, according to López González et al. (2014). Furfural is more lethal than 5-HMF due to its low molecular weight, which assists in easy access to the microbial cell membrane (Ahmad et al., 2018). In an anaerobic environment, HMF and furfural are mostly transformed to furan dimethanol, and furfuryl alcohol, respectively, while respiratory metabolism produced furonic acid from furfural. The concentration of furfural and 5-HMF in SCW pre-treated slurry increased with temperature (Tian et al., 2020). The inhibition of both compounds is often significant at a temperature higher than 160°C (Timung & Goud, 2018). Phuttaro et al. (2019) reported the formation of 5-HMF and furfural when pre-treated the substrates at 200°C, significantly inhibiting methanogenesis.

Table 4

The inhibitory compound from hydrothermal SCW pretreatment from various substrates

Substrates	Pretreatment Temperature (°C)	Furfural (g/L)	5-HMF (g/L)	Maillard Reaction	References
Wheat straw	175	4.1	2.9	NS	Tian et al. (2020)
Rice Straw	210	ND	2.3	NS	Wang et al. (2018a)
Press Mud	210	2.3	0.3	Yes	González et al. (2014)
Sugarcane bagasse	290	10	1.37	NS	Prado et al. (2014)
Sugarcane bagasse	213	2.84	0.47	NS	Prado et al. (2014)
Rice Straw	180	0.13	0.04	NS	Xiang et al. (2021)

Note. NS: Not Stated

Challenges

The SCW pretreatment for lignocellulosic biomass appears with challenges. The production and generation of methanogenic inhibitors such as furfurals and HMFs are the most common challenges related to SCW pretreatment. Various studies reported HMF and furfural inhibition when dealing with elevated temperatures. Common inhibitors such as furan aldehydes, weak acids, and phenolic compounds are the most common fermentation and enzyme inhibitors (Ahmed et al., 2019). The reduction of the concentration and detoxification of these compounds is crucial before being subjected to anaerobic digestion.

Numerous physical, chemical, and biological methods, combined with those pretreatments, have been suggested to eliminate the inhibitors. The removal and detoxification approaches including extracting, evaporating, over-liming, pH adjustment, adsorption, and ion exchange of those compounds are some of the approaches conducted by former studies to remove these inhibitors (Malav et al., 2017; Wang et al., 2018b).

Removal of inhibitory compounds and giving a higher yield of available convertible sugar can be achieved by various chemical detoxification processes, however, these methods may contribute to high industrial costs, waste production, and wastage of fermentable sugars (Ahmed et al., 2019). Over 90% of the inhibitors, including weak acid, HMF, and furfural, were removed using ozonation (Rosen et al., 2022). Removal of inhibitors using nanofiber hybrid hydrogel beads provides an effective and practical method for removing inhibitors from lignocellulosic hydrolysates (Sun et al., 2022). According to the authors, this detoxification strategy removes the inhibitors and can also retain glucose and xylose. The loss of monosaccharides often occurs when dealing with inhibitory compound removals. Thus, this strategy might be useful to be extended since, according to the study, only 6.3% and 8.2% of glucose and xylose loss during the process, respectively. A comparison between nanofiltration and reverse osmosis for removing the inhibitory compound revealed that reverse osmosis membranes are better than nanofiltration membranes, especially for retaining monosaccharides (Wang et al., 2018b). Thus, extensive research should be conducted to remove the inhibitory compound formed during the SCW pretreatment process. The removal and detoxification method should be carefully selected to avoid wasting fermentable sugars and monosaccharides from the lignocellulosic biomass.

CONCLUSION

Based on a review regarding SCW pretreatment for agricultural wastes for anaerobic digestion, the SCW pretreatment efficiency is reliant on the characteristic of feedstocks—predominantly its composition, including lignin, cellulose, and also hemicellulose. SCW pretreatment is considered environmentally friendly on account of water usage as a pretreatment solvent. They promote structural breaking to help facilitate hydrolysis and can apply to a broad range of lignocellulosic waste. However, high lignocellulosic content needs a severer pretreatment, and these methods can give an impact on anaerobic digestion if not properly implemented. Thus, more extensive research should be conducted to test the efficacy of this SCW on a wide range of lignocellulosic waste for biogas enhancement.

ACKNOWLEDGMENTS

The authors are grateful for the research project under the Fundamental Research Grant Scheme (Ref. No: FRGS/1/2021/TK0/UPM/02/28) awarded by the Ministry of Higher Education Malaysia. In addition, the authors wish to acknowledge the support and technical

facilities from the Faculty of Engineering Universiti Putra Malaysia and the Faculty of Science and Engineering, University of Nottingham Malaysia.

REFERENCES

- Abdelmoez, W., Nage, S. M., Bastawess, A., Ihab, A., & Yoshida, H. (2014). Subcritical water technology for wheat straw hydrolysis to produce value added products. *Journal of Cleaner Production*, *70*, 68-77. <https://doi.org/10.1016/j.jclepro.2014.02.011>
- Ahmad, F., Silva, E. L., & Varesche, M. B. A. (2018). Hydrothermal processing of biomass for anaerobic digestion - A review. *Renewable and Sustainable Energy Reviews*, *98*, 108-124. <https://doi.org/10.1016/j.rser.2018.09.008>
- Ahmed, B., Aboudi, K., Tyagi, V. K., Álvarez-Gallego, C. J., Fernández-Güelfo, L. A., Romero-García, L. I., & Kazmi, A. A. (2019). Improvement of anaerobic digestion of lignocellulosic biomass by hydrothermal pretreatment. *Applied Sciences*, *9*(18), Article 3852. <https://doi.org/10.3390/app9183853>
- Almomani, F., Shawaqfah, M., Bhosale, R. R., Kumar, A., & Khraisheh, M. A. M. (2017). Intermediate ozonation to enhance biogas production in batch and continuous systems using animal dung and agricultural waste. *International Biodeterioration & Biodegradation*, *119*, 176-187. <https://doi.org/10.1016/j.ibiod.2016.11.008>
- Antwi, E., Engler, N., Nelles, M., & Schüch, A. (2019). Anaerobic digestion and the effect of hydrothermal pretreatment on the biogas yield of cocoa pods residues. *Waste Management*, *88*, 131-140. <https://doi.org/10.1016/j.wasman.2019.03.034>
- Atelge, M. R., Atabani, A. E., Banu, J. R., Krisa, D., Kaya, M., Eskicioglu, C., Kumar, G., Lee, C., Yildiz, Y. Ş., Unalan, S., Mohanasundaram, R., & Duman, F. (2020). A critical review of pretreatment technologies to enhance anaerobic digestion and energy recovery. *Fuel*, *270*, Article 117494. <https://doi.org/10.1016/j.fuel.2020.117494>
- Brandt, A., Gräsvik, J., Hallett, J. P., & Welton, T. (2013). Deconstruction of lignocellulosic biomass with ionic liquids. *Green Chemistry*, *15*(3), 550-583. <https://doi.org/10.1039/c2gc36364j>
- Brodeur, G., Yau, E., Badal, K., Collier, J., Ramachandran, K. B., & Ramakrishnan, S. (2011). Chemical and physicochemical pretreatment of lignocellulosic biomass: A review. *Enzyme Research*, *2011*, Article 787532. <https://doi.org/10.4061/2011/787532>
- Carlsson, M., Lagerkvist, A., & Morgan-Sagastume, F. (2012). The effects of substrate pretreatment on anaerobic digestion systems: A review. *Waste Management*, *32*(9), 1634-1650. <https://doi.org/10.1016/j.wasman.2012.04.016>
- Carrere, H., Antonopoulou, G., Affes, R., Passos, F., Battimelli, A., Lyberatos, G., & Ferrer, I. (2016). Review of feedstock pretreatment strategies for improved anaerobic digestion: From lab-scale research to full-scale application. *Bioresource Technology*, *199*, 386-397. <https://doi.org/10.1016/j.biortech.2015.09.007>
- Caruso, M. C., Braghieri, A., Capece, A., Napolitano, F., Romano, P., Galgano, F., Altieri, G., & Genovese, F. (2019). Recent updates on the use of agro-food waste for biogas production. *Applied Sciences*, *9*(6), Article 1217. <https://doi.org/10.3390/app9061217>

- Chandra, R., Takeuchi, H., & Hasegawa, T. (2012a). Hydrothermal pretreatment of rice straw biomass: A potential and promising method for enhanced methane production. *Applied Energy*, *94*, 129-140. <https://doi.org/10.1016/j.apenergy.2012.01.027>
- Chandra, R., Takeuchi, H., Hasegawa, T., & Kumar, R. (2012b). Improving biodegradability and biogas production of wheat straw substrates using sodium hydroxide and hydrothermal pretreatments. *Energy*, *43*(1), 273-282. <https://doi.org/10.1016/j.energy.2012.04.029>
- Chen, J., Wang, X., Zhang, B., Yang, Y., Song, Y., Zhang, F., Liu, B., Zhou, Y., Yi, Y., Shan, Y., & Lü, X. (2021). Integrating enzymatic hydrolysis into subcritical water pretreatment optimization for bioethanol production from wheat straw. *Science of The Total Environment*, *770*, Article 145321. <https://doi.org/10.1016/j.scitotenv.2021.145321>
- Chen, Y., Yang, H., Zou, H., Sun, T., Li, M., Zhai, J., He, Q., Gu, L., & Tang, W. Z. (2020). Effects of acid/alkali pretreatments on lignocellulosic biomass mono-digestion and its co-digestion with waste activated sludge. *Journal of Cleaner Production*, *277*, Article 123998. <https://doi.org/10.1016/j.jclepro.2020.123998>
- Dahunsi, S. O. (2019). Liquefaction of pineapple peel: Pretreatment and process optimization. *Energy*, *185*, 1017-1031. <https://doi.org/10.1016/j.energy.2019.07.123>
- Dasgupta, A., & Chandel, M. K. (2019). Enhancement of biogas production from organic fraction of municipal solid waste using hydrothermal pretreatment. *Bioresource Technology Reports*, *7*, Article 100281. <https://doi.org/10.1016/j.biteb.2019.100281>
- Edwiges, T., Bastos, J. A., Alino, J. H. L., D'Avila, L., Frare, L. M., & Somer, J. G. (2019). Comparison of various pretreatment techniques to enhance biodegradability of lignocellulosic biomass for methane production. *Journal of Environmental Chemical Engineering*, *7*(6), Article 103495. <https://doi.org/10.1016/j.jece.2019.103495>
- Elhenawy, Y., El-Kadi, S., Elsayy, K., Abdelmotalip, A., & AbdelrahmanIbrahim, I. (2021). Biogas production by anaerobic digestion of cow dung using floating type fermenter. *Journal of Environmental Treatment Techniques*, *9*(2), 446-451.
- Hagos, K., Zong, J., Li, D., Liu, C., & Lu, X. (2017). Anaerobic co-digestion process for biogas production: Progress, challenges and perspectives. *Renewable and Sustainable Energy Reviews*, *76*, 1485-1496. <https://doi.org/10.1016/j.rser.2016.11.184>
- Hamzah, A. F. A., Hamzah, M. H., Man, H. C., Jamali, N. S., Siajam, S. I., & Show, P. L. (2022). Biogas production through mono- and co-digestion of pineapple waste and cow dung at different substrate ratios. *BioEnergy Research*, *2022*, Article 254. <https://doi.org/10.1007/s12155-022-10478-2>
- Hamzah, A. F. A., Hamzah, M. H., Man, H. C., Jamali, N. S., Siajam, S. I., & Ismail, M. H. (2021). Recent updates on the conversion of pineapple waste (*Ananas comosus*) to value-added products, future perspectives and challenges. *Agronomy*, *11*(11), Article 2221. <https://doi.org/10.3390/agronomy11112221>
- Hamzah, A. F. A., Hamzah, M. H., Mazlan, F. N. A., Man, H. C., Jamali, N. S., & Siajam, S. I. (2020). Anaerobic co-digestion of pineapple wastes with cow dung: Effect of different total solid content on bio-methane yield. *Advances in Agricultural & Food Research Journal*, *1*(1), Article a0000109. <https://doi.org/10.36877/aaftrj.a0000109>

- Hamzah, M. H., Bowra, S., Simmons, M., & Cox, P. (2016, June 6-9). *The impact of process parameters on the purity and chemical properties of lignin extracted from miscanthus x giganteus using a modified organosolv method*. [Paper presentation]. 24th European Biomass Conference and Exhibition, Amsterdam, The Netherlands.
- He, C., Hu, J., Shen, F., Huang, M., Zhao, L., Zou, J., Tian, D., Jiang, Q., & Zeng, Y. (2022). Tuning hydrothermal pretreatment severity of wheat straw to match energy application scenarios. *Industrial Crops and Products*, 176, Article 114326. <https://doi.org/10.1016/J.INDCROP.2021.114326>
- Jomnonkhaow, U., Sittijunda, S., & Reungsang, A. (2022). Assessment of organosolv, hydrothermal, and combined organosolv and hydrothermal with enzymatic pretreatment to increase the production of biogas from Napier grass and Napier silage. *Renewable Energy*, 181, 1237-1249. <https://doi.org/10.1016/j.renene.2021.09.099>
- Kim, D., Lee, K., & Park, K. Y. (2015). Enhancement of biogas production from anaerobic digestion of waste activated sludge by hydrothermal pretreatment. *International Biodeterioration and Biodegradation*, 101, 42-46. <https://doi.org/10.1016/j.ibiod.2015.03.025>
- Lachos-Perez, D., Brown, A. B., Mudhoo, A., Timko, M. T., Rostagno, M. A., & Forster-Carneiro, T. (2017). Applications of subcritical and supercritical water conditions for extraction, hydrolysis, gasification, and carbonization of biomass: a critical review. *Biofuel Research Journal*, 4(2), 611-626. <https://doi.org/10.18331/BRJ2017.4.2.6>
- Lee, Z. S., Chin, S. Y., & Cheng, C. K. (2019). An evaluation of subcritical hydrothermal treatment of end-of-pipe palm oil mill effluent. *Heliyon*, 5(6), Article e01792. <https://doi.org/10.1016/j.heliyon.2019.e01792>
- Lemaire, A., & Limbourg, S. (2019). How can food loss and waste management achieve sustainable development goals? *Journal of Cleaner Production*, 234, 1221-1234. <https://doi.org/10.1016/j.jclepro.2019.06.226>
- López González, L. M., Reyes, I. P., Dewulf, J., Budde, J., Heiermann, M., & Vervaeren, H. (2014). Effect of liquid hot water pretreatment on sugarcane press mud methane yield. *Bioresource Technology*, 169, 284-290. <https://doi.org/10.1016/j.biortech.2014.06.107>
- Maciel-Silva, F. W., Mussatto, S. I., & Forster-Carneiro, T. (2019). Integration of subcritical water pretreatment and anaerobic digestion technologies for valorization of açai processing industries residues. *Journal of Cleaner Production*, 228, 1131-1142. <https://doi.org/10.1016/j.jclepro.2019.04.362>
- Malav, M. K., Prasad, S., Kharia S. K., Kumar, S., Sheetal, K. R., & Kannojiya, S. (2017). Furfural and 5-HMF: Potent fermentation inhibitors and their removal techniques. *International Journal of Current Microbiology and Applied Sciences*, 6(3), 2060-2066. <https://doi.org/10.20546/ijemas.2017.603.235>
- Manorach, K., Poonsrisawat, A., Viriya-empikul, N., & Laosiripojana, N. (2015). Optimization of sub-critical water pretreatment for enzymatic hydrolysis of sugarcane bagasse. *Energy Procedia*, 79, 937-942. <https://doi.org/10.1016/j.egypro.2015.11.590>
- Meegoda, J. N., Li, B., Patel, K., & Wang, L. B. (2018). A review of the processes, parameters, and optimization of anaerobic digestion. *International Journal of Environmental Research and Public Health*, 15(10), Article 2224. <https://doi.org/10.3390/ijerph15102224>

- Möller, M., Nilges, P., Harnisch, F., & Schröder, U. (2011). Subcritical water as reaction environment: Fundamentals of hydrothermal biomass transformation. *ChemSusChem*, 4(5), 566-579. <https://doi.org/10.1002/cssc.201000341>
- Morales-Polo, C., Cledera-Castro, M. D. M., & Soria, B. Y. M. (2018). Reviewing the anaerobic digestion of food waste: From waste generation and anaerobic process to its perspectives. *Applied Sciences*, 8(10), Article 1804. <https://doi.org/10.3390/app8101804>
- Neshat, S. A., Mohammadi, M., Najafpour, G. D., & Lahijani, P. (2017). Anaerobic co-digestion of animal manures and lignocellulosic residues as a potent approach for sustainable biogas production. *Renewable and Sustainable Energy Reviews*, 79, 308-322. <https://doi.org/10.1016/j.rser.2017.05.137>
- O-Thong, S., Boe, K., & Angelidaki, I. (2012). Thermophilic anaerobic co-digestion of oil palm empty fruit bunches with palm oil mill effluent for efficient biogas production. *Applied Energy*, 93, 648-654. <https://doi.org/10.1016/j.apenergy.2011.12.092>
- Park, M., Kim, N., Jung, S., Jeong, T. Y., & Park, D. (2021). Optimization and comparison of methane production and residual characteristics in mesophilic anaerobic digestion of sewage sludge by hydrothermal treatment. *Chemosphere*, 264, Article 128516. <https://doi.org/10.1016/j.chemosphere.2020.128516>
- Park, S., Yoon, Y. M., Han, S. K., Kim, D., & Kim, H. (2017). Effect of hydrothermal pre-treatment (HTP) on poultry slaughterhouse waste (PSW) sludge for the enhancement of the solubilization, physical properties, and biogas production through anaerobic digestion. *Waste Management*, 64, 327-332. <https://doi.org/10.1016/j.wasman.2017.03.004>
- Paudel, S. R., Banjara, S. P., Choi, O. K., Park, K. Y., Kim, Y. M., & Lee, J. W. (2017). Pretreatment of agricultural biomass for anaerobic digestion: Current state and challenges. *Bioresource Technology*, 245(Part A), 1194-1205. <https://doi.org/10.1016/j.biortech.2017.08.182>
- Pečar, D., Pohleven, F., & Goršek, A. (2020). Kinetics of methane production during anaerobic fermentation of chicken manure with sawdust and fungi pre-treated wheat straw. *Waste Management*, 102, 170-178. <https://doi.org/10.1016/j.wasman.2019.10.046>
- Phuttaro, C., Sawatdeenarunat, C., Surendra, K. C., Boonsawang, P., Chaiprapat, S., & Khanal, S. K. (2019). Anaerobic digestion of hydrothermally-pretreated lignocellulosic biomass: Influence of pretreatment temperatures, inhibitors and soluble organics on methane yield. *Bioresource Technology*, 284, 128-138. <https://doi.org/10.1016/j.biortech.2019.03.114>
- Prado, J. M., Follegatti-Romero, L. A., Forster-Carneiro, T., Rostagno, M. A., Filho, F. M., & Meireles, M. A. A. (2014). Hydrolysis of sugarcane bagasse in subcritical water. *The Journal of Supercritical Fluids*, 86, 15-22. <https://doi.org/10.1016/j.supflu.2013.11.018>
- Rico, X., Gullón, B., Alonso, J. L., & Yáñez, R. (2020). Recovery of high value-added compounds from pineapple, melon, watermelon and pumpkin processing by-products: An overview. *Food Research International*, 132, Article 109086. <https://doi.org/10.1016/j.foodres.2020.109086>
- RMK12. (2021). *Twelfth Malaysia plan, 2021-2025*. Economic Planning Unit. <https://rmk12.epu.gov.my>
- Rosen, Y., Maslennikov, A., Trabelcy, B., Gerchman, Y., & Mamane, H. (2022). Short ozonation for effective removal and detoxification of fermentation inhibitors resulting from thermal pretreatment. *Renewable Energy*, 189, 1407-1418. <https://doi.org/10.1016/j.renene.2022.03.065>

- Saha, B. C., Yoshida, T., Cotta, M. A., & Sonomoto, K. (2013). Hydrothermal pretreatment and enzymatic saccharification of corn stover for efficient ethanol production. *Industrial Crops and Products*, *44*, 367-372. <https://doi.org/10.1016/j.indcrop.2012.11.025>
- Saha, S., Jeon, B. H., Kurade, M. B., Jadhav, S. B., Chatterjee, P. K., Chang, S. W., Govindwar, S. P., & Kim, S. J. (2018). Optimization of dilute acetic acid pretreatment of mixed fruit waste for increased methane production. *Journal of Cleaner Production*, *190*, 411-421. <https://doi.org/10.1016/j.jclepro.2018.04.193>
- Sawatdeenarunat, C., Surendra, K. C., Takara, D., Oechsner, H., & Khanal, S. K. (2015). Anaerobic digestion of lignocellulosic biomass: Challenges and opportunities. *Bioresource Technology*, *178*, 178-186. <https://doi.org/10.1016/j.biortech.2014.09.103>
- Shitu, A., Izhar, S., & Tahir, T. M. (2015). Sub-critical water as a green solvent for production of valuable materials from agricultural waste biomass: A review of recent work. *Global Journal of Environmental Science and Management*, *1*(3), 255-264.
- Suaisom, P., Pholchan, P., Man, H. C., & Aggarangsi, P. (2019). Optimization of hydrothermal conditioning conditions for *Pennisetum purpureum* x *Pennisetum americanum* (napier pakchong1 grass) to produce the press fluid for biogas production. *Pertanika Journal Science and Technology*, *27*(S1), 109-122.
- Sun, H., Liu, L., Liu, W., Liu, Q., Zheng, Z., Fan, Y., & Ouyang, J. (2022). Removal of inhibitory furan aldehydes in lignocellulosic hydrolysates via chitosan-chitin nanofiber hybrid hydrogel beads. *Bioresource Technology*, *346*, Article 126563. <https://doi.org/10.1016/j.biortech.2021.126563>
- Sun, S. S., Sun, S. S., Cao, X., & Sun, R. (2016). The role of pretreatment in improving the enzymatic hydrolysis of lignocellulosic materials. *Bioresource Technology*, *199*, 49-58. <https://doi.org/10.1016/j.biortech.2015.08.061>
- Talaiekhosani, A., & Rezania, S. (2020). A critical review on the various pretreatment technologies of lignocellulosic materials. *Journal of Environmental Treatment Techniques*, *8*(3), 925-935.
- Tampio, E. (2016). *Utilization of Food Waste via Anaerobic Digestion: From Feedstock to Biogas and Fertilizers*. Tampere University of Technology.
- Teghammar, A., Yngvevsson, J., Lundin, M., Taherzadeh, M. J., & Horváth, I. S. (2010). Pretreatment of paper tube residuals for improved biogas production. *Bioresource Technology*, *101*(4), 1206-1212. <https://doi.org/10.1016/j.biortech.2009.09.029>
- Tian, W., Chen, Y., Shen, Y., Zhong, C., Gao, M., Shi, D., He, Q., & Gu, L. (2020). Effects of hydrothermal pretreatment on the mono- and co-digestion of waste activated sludge and wheat straw. *Science of The Total Environment*, *732*, Article 139312. <https://doi.org/10.1016/j.scitotenv.2020.139312>
- Timung, R., & Goud, V. V. (2018). Subcritical water hydrolysis of spent java citronella biomass for production of reducing sugar. *Materials Today: Proceedings*, *5*(11), 23128-23135. <https://doi.org/10.1016/j.matpr.2018.11.043>
- Toor, S. S., Rosendahl, L., & Rudolf, A. (2011). Hydrothermal liquefaction of biomass: A review of subcritical water technologies. *Energy*, *36*(5), 2328-2342. <https://doi.org/10.1016/j.energy.2011.03.013>
- Vakalis, S., Georgiou, A., Moustakas, K., & Fountoulakis, M. (2022). Assessing the effect of hydrothermal treatment on the volatile solids content and the biomethane potential of common reed (*Phragmites australis*). *Bioresource Technology Reports*, *17*, Article 1009231. <https://doi.org/10.1016/j.biteb.2021.1009231>

- Wang, D., Shen, F., Yang, G., Zhang, Y., Deng, S., Zhang, J., Zeng, Y., Luo, T., & Mei, Z. (2018a). Can hydrothermal pretreatment improve anaerobic digestion for biogas from lignocellulosic biomass? *Bioresource Technology*, *249*, 117-124. <https://doi.org/10.1016/j.biortech.2017.09.197>
- Wang, T., Meng, Y., Qin, Y., Feng, W., & Wang, C. (2018b). Removal of furfural and HMF from monosaccharides by nanofiltration and reverse osmosis membranes. *Journal of the Energy Institute*, *91*(3), 473-480. <https://doi.org/10.1016/j.joei.2017.01.005>
- Wei, Y., Gao, J., Shi, Z., Li, X., Ma, W., & Yuan, H. (2022). Effect of hydrothermal pretreatment on two-stage anaerobic digestion of food waste and Enteromorpha: Digestion performance, bioenergy efficiency, and microbial community dynamics. *Fuel*, *318*, Article 123639. <https://doi.org/10.1016/j.fuel.2022.123639>
- Wenjing, L., Chao, P., Lama, A., Xindi, F., Rong, Y., & Dhar, B. R. (2019). Effect of pretreatments on biological methane potential of dewatered sewage sludge under dry anaerobic digestion. *Ultrasonics Sonochemistry*, *52*, 224-231. <https://doi.org/10.1016/j.ultsonch.2018.11.022>
- Xiang, C., Tian, D., Hu, J., Huang, M., Shen, F., Zhang, Y., Yang, G., Zeng, Y., & Deng, S. (2021). Why can hydrothermally pretreating lignocellulose in low severities improve anaerobic digestion performances? *Science of The Total Environment*, *752*, Article 141929. <https://doi.org/10.1016/J.SCITOTENV.2020.141929>
- Zerback, T., Schumacher, B., Weinrich, S., Hülsemann, B., & Nelles, M. (2022). Hydrothermal pretreatment of wheat straw-evaluating the effect of substrate disintegration on the digestibility in anaerobic digestion. *Processes*, *10*(6), Article 1048. <https://doi.org/10.3390/pr10061048>
- Zhao, X., Luo, K., Zhang, Y., Zheng, Z., Cai, Y., Wen, B., Cui, Z., & Wang, X. (2018). Improving the methane yield of maize straw: Focus on the effects of pretreatment with fungi and their secreted enzymes combined with sodium hydroxide. *Bioresource Technology*, *250*, 204-213. <https://doi.org/10.1016/j.biortech.2017.09.160>
- Zheng, Y., Zhao, J., Xu, F., & Li, Y. (2014). Pretreatment of lignocellulosic biomass for enhanced biogas production. *Progress in Energy and Combustion Science*, *42*(1), 35-53. <https://doi.org/10.1016/j.pecs.2014.01.001>

Distribution of Six Urban Bird Species in Urban Agglomeration of Central Region of Peninsular Malaysia Using eBird Database

Aminah Madi, Fatihah Najihah Arazmi, Shukor Md. Nor and Mohammad Saiful Mansor*

Department of Biological Sciences and Biotechnology, Faculty of Science and Technology, Universiti Kebangsaan Malaysia, UKM Bangi, Selangor 43600, Malaysia

ABSTRACT

Developing countries are undergoing rapid urbanisation to fulfil the high demands of incremental population growth, construction, and development. Excessive development has negative impacts on biodiversity by altering or destroying habitats. However, each bird species may respond differently to habitat alteration. Therefore, this study was conducted to determine the distribution of urban bird species in metropolitan cities and nearby areas in Peninsular Malaysia. The main objective of this study was to determine the distribution patterns of six aesthetically valuable urban bird species (Black-naped Oriole [*Oriolus chinensis*], Yellow-vented Bulbul [*Pycnonotus goiavier*], White-throated Kingfisher [*Halcyon smyrnensis*], Pink-necked Green-Pigeon [*Treron vernans*], Coppersmith Barbet [*Psilopogon haemacephalus*] and Common Iora [*Aegithina tiphia*]) in Greater Kuala Lumpur (the Klang Valley region) using observations from a citizen science (eBird) database. We mapped species abundance throughout the focal area using ArcGIS and analysed the data using Minitab. Three urban bird species dominated, with the highest number of observations recorded: Yellow-vented Bulbul (46.59%), Pink-necked Green-Pigeon (19.25%), and Black-naped Oriole (13.00%). While, the Coppersmith Barbet had the lowest recorded observations (2.76%). Species abundance differed significantly across the study region ($F=5.12, p<0.05$), with the studied species' occurrence increasing

as green spaces increased. Such dynamic mapping is crucial for better understanding the mechanisms of the persistence of urban biodiversity. We suggest creating more green areas and planting roadside trees to provide green corridors within cities to help sustain urban biodiversity.

Keywords: Citizen science data, distribution, green space, Malaysia, metropolitan city, urban birds

ARTICLE INFO

Article history:

Received: 03 April 2022

Accepted: 10 June 2022

Published: 20 March 2023

DOI: <https://doi.org/10.47836/pjst.31.2.20>

E-mail addresses:

aminahbintimadi@gmail.com (Aminah Madi)

n.fatihahnajihah@gmail.com (Fatihah Najihah Arazmi)

shukor@ukm.edu.my (Shukor Md. Nor)

msaifulmansor@gmail.com (Mohammad Saiful Mansor)

*Corresponding author

INTRODUCTION

Urban populations in developing countries increased from 286 million in 1950 to 2,251 million in 2000 (Yaakob et al., 2010), and 79.7% of the world's population lives in developing countries in Southeast Asia, such as Malaysia (United Nations, 2019). Urbanisation is a multidimensional process that is influenced by rapid transformations in the human population in an area, where land-use changes and population transitions can cause a complex habitat mosaic and have significant impacts to varying degrees on the environment (Brush, 2016). For example, rapid forest exploitation during urbanisation transforms green areas into residential, commercial, and recreational areas.

Urbanisation and sub-urbanisation, which have become the latest universal trends in the rapid development phase, have negative impacts, either directly or indirectly, on the environment and the ecological dimension of sustainable development (Sandström et al., 2006). Increased levels of urbanisation can result in the decline in arthropods, amphibians, mammals, reptiles and birds due to habitat loss. On the other hand, the reduction in the quality of the remaining habitats due to the replacement of green areas by built-up areas exacerbates the effects of disturbance on animals (Marzluff & Ewing, 2001; McKinney, 2008). Approximately 60% of bird studies considering species richness generally show declining richness with increasing urbanisation (Chace & Walsh, 2006; Marzluff, 2001).

However, urbanisation can also benefit avian biodiversity due to the ability of certain species to adapt to cities. Not all species are potentially susceptible to urbanisation-induced fragmentation (Callaghan et al., 2019; Kark et al., 2007). In general, bird species may show different responses to urbanisation which can be influenced by both intrinsic and extrinsic landscape elements in the urban environment (Callaghan et al., 2018). In addition, some species may have special traits that allow them to adapt to uncertain environments, potentially resulting in ecological inheritance through trait distributions filtered by the environment (Odling-Smee et al., 2013; Webb et al., 2010).

Birds are the ideal subjects to study the effects of habitat fragmentation and landscape change as they are easily identified, clearly visible and sensitive to land-use changes (Hensley, 2018; Mansor et al., 2011; Nasruddin-Roshidi et al., 2021). Birds are also often clearly visible to the public in the city, and their presence is highly anticipated by most visitors to urban parks (Jasmani et al., 2017). Moreover, birds are ecologically highly diverse and show different responses to urbanisation according to the specific ecological traits of each species (Sol et al., 2013). Likewise, an avian group's life history and ecological characteristics are more competent than other vertebrate groups.

Urban birds tend to be common species, most of which are found near human settlements since they can tolerate human disturbance due to their ability to adapt and survive and reproduce (Idilfitri & Mohamad, 2012). Urban birds could find alternatives to nesting sites and search for food within human-occupied areas. Urbanisation favours common species of avian omnivores, insectivores, granivores and frugivores. Bird communities

can be categorised into three groups along an increasing urbanisation gradient: ‘urban avoiders’ living outside the city; ‘suburban adapters’ that live in areas with a moderate level of urbanisation; and ‘urban exploiters’ that live surrounded by buildings and roads in the most developed areas (Blair, 1996).

Citizen science data can be used to collect large amounts of bird occurrence data in a number of habitats and locations over the long term (Callaghan & Gawlik, 2015). In this study, we used citizen science data from the online database eBird (<https://ebird.org/home>) to examine the distribution of six aesthetically pleasing urban bird species: Pink-necked Green-Pigeon (*Treron vernans*), White-throated Kingfisher (*Halcyon smyrnensis*), Coppersmith Barbet (*Psilopogon haemacephalus*), Black-naped Oriole (*Oriolus chinensis*), Common Iora (*Aegithina tiphia*), and Yellow-vented Bulbul (*Pycnonotus goiavier*) in Greater Kuala Lumpur (Klang Valley). These six species are common colourful birds and have aesthetic value for urban biodiversity. The selected six bird species in the study are categorised as Least Concern in the IUCN Red List of Threatened Species and have conservation values toward urban ecosystems. We excluded abundant, feral, and introduced/invasive species such as the Eurasian Tree Sparrow (*Passer montanus*), Asian Glossy Starling (*Aplonis panayensis*), Rock Pigeon (*Columba livia*), House Crow (*Corvus splendens*), Peaceful Dove (*Geopelia striata*), Common Myna (*Acridotheres tristis*) and Javan Myna (*Acridotheres javanicus*), as well as swifts and swallows. Abundant, feral, and introduced/invasive species were excluded to reduce the bias in citizen science datasets because these factors can lead to an increase in the number of records by casual observers.

MATERIALS AND METHODS

Study Area

Malaysia consists of two regions, Peninsular Malaysia and Malaysian Borneo. Peninsular Malaysia comprises 11 of the 13 states of the country, including two of the three federal territories (Federal Territory of Kuala Lumpur and Federal Territory of Putrajaya). This study focused on the Central Region of Peninsular Malaysia (the Klang Valley region) comprising Kuala Lumpur, Putrajaya, and all Selangor districts except Kuala Langat, Kuala Selangor, Sabak Bernam and Hulu Selangor. Selangor is a metropolitan state that surrounds the two federal territories with a 6.56 million population (Figure 1). Kuala Lumpur is Malaysia’s capital and largest metropolitan city, with a population of 1.808 million. Putrajaya is a planned city and the federal administrative centre of Malaysia with 91,900 population. Greater Kuala Lumpur has experienced rapid population growth and urbanisation, which has led to drastic changes in the landscape, with green space replaced by concrete infrastructure and high-rise developments. However, in Putrajaya, a large proportion of the land has been designated as a green space, with some artificial landscapes that consist of wetland parks, parks, roads, and green connectors.

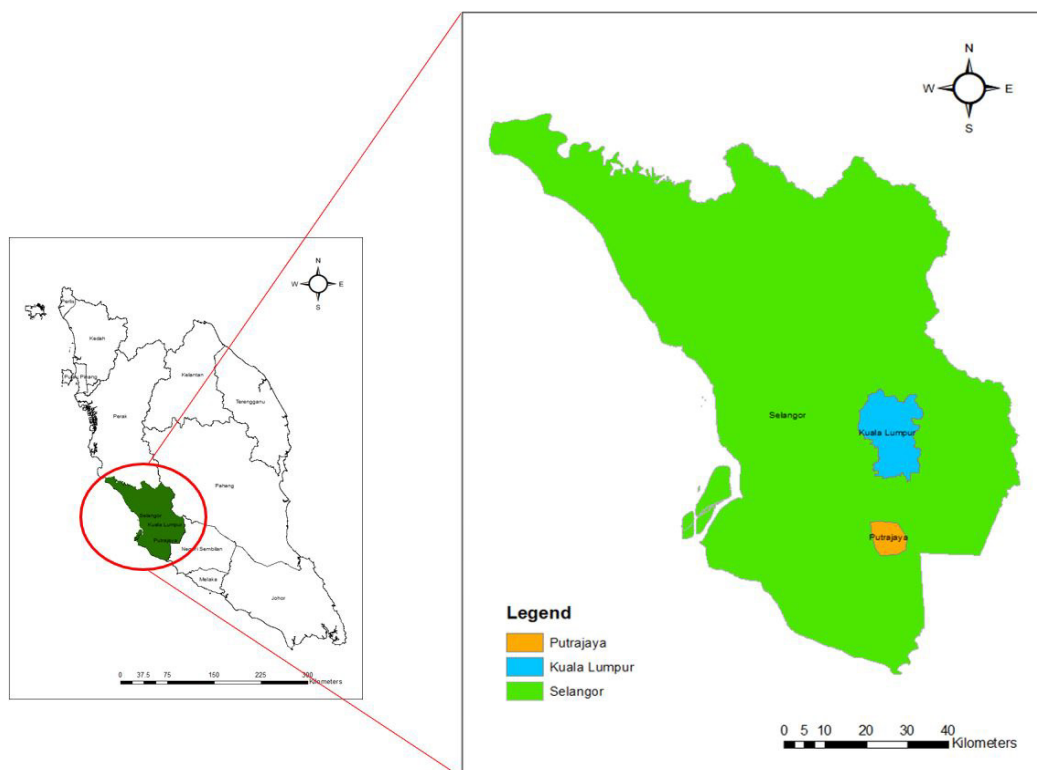


Figure 1. Map of Peninsular Malaysia (left) and the three areas selected for study—Selangor, Federal Territory of Kuala Lumpur, and Federal Territory of Putrajaya.

eBird Data

We used the online citizen science database eBird (<https://ebird.org/home>) easily accessible and used by researchers worldwide. eBird provides over 180,000 locations across the globe in a format that is accessible at any time. Observations data of the study bird species were downloaded to examine their distribution patterns in the metropolitan–urban–suburban region, particularly in Kuala Lumpur, Selangor, and Putrajaya. The dataset obtained from eBird provided all validated observations that consisted of observation dates, observer’s id, specific locations, coordinates, and observation counts. The downloaded data were filtered to obtain only ‘complete’ checklists for inclusion in the study. The checklist of species was defined as ‘complete’ if ‘stationary,’ ‘travelling,’ or ‘exhaustive’ protocols were followed (Sullivan et al., 2014). We analysed the abundance and populations of the six bird species in the selected regions to identify differences in distribution patterns between urban and suburban areas.

Data Analysis

In order to address estimated position error, all distribution data for the year 2020 were analysed using ArcGIS 10.8 to ensure that the occurrences were within 100 m of the border of the study region. Distributions outside the study area were omitted. The Kernel Density tool was used to determine the density and distribution pattern of the urban bird species studied across Greater Kuala Lumpur. Kernels were analysed with a UTM Zone 48N projection at 1 km resolution. The Arc Toolbox was used to generate kernel estimators through Point Density in the Spatial Analyst Tools, and the data were processed in the same layer as the study area map. Kernel output was stretched using a histogram equaliser and resampled with the bilinear interpolation technique to enhance the appearance and smoothness of the raster data. The data were normally distributed (determined by inspection with quantile–quantile plots and the Shapiro–Wilk test). Species abundance was analysed with ANOVA in Minitab 19 software.

RESULTS AND DISCUSSION

A total of 5,538 occurrences of the urban bird species considered in this study were recorded across Greater Kuala Lumpur in 2020 in eBird (Table 1). Observations in 2020 suggest that three urban bird species, with the highest number of observations, were dominant in Greater Kuala Lumpur: the Yellow-vented Bulbul with 2,580 observations (46.59% of the total number of observations); Pink-necked Green-Pigeon with 1,066 observations (19.25%); and Black-naped Oriole with 720 observations (13.00%). In contrast, the Coppersmith Barbet had the lowest observations, with only 153 (2.76%).

Table 1
Occurrence of six urban bird species in 2020

Bird species	Occurrence	Percentage (%)
Yellow-vented Bulbul	2580	46.59
Pink-necked Green-Pigeon	1066	19.25
Black-naped Oriole	720	13.00
White-throated Kingfisher	552	9.97
Common Iora	467	8.43
Coppersmith Barbet	153	2.76

All six species were concentrated in the west and southeast, outside the Kuala Lumpur region (Figure 2), with each species' distribution varying across Greater Kuala Lumpur (Figure 3). Species abundance significantly differed across regions ($F = 5.12, p < 0.05$).

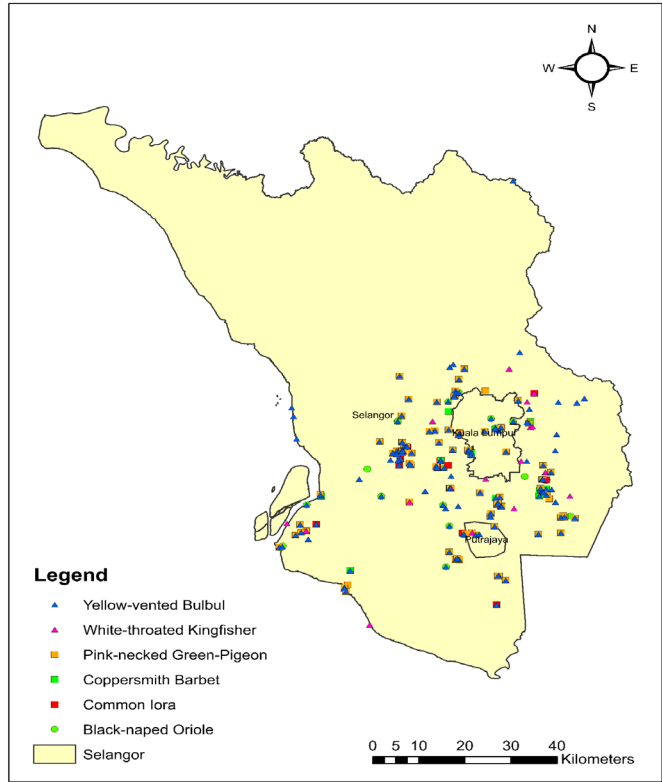


Figure 2. Distribution of the six urban bird species in Greater Kuala Lumpur in 2020

This study shows that the occurrence of the bird species studied increased with increasing distance from the Kuala Lumpur metropolitan centre. Urban birds are commonly found in open areas, residential areas and urban parks (Yusop et al., 2021). The green landscapes of Selangor include urban parks and street trees, which provide bird nesting and foraging opportunities (Mansor & Ramli, 2017; Zhou et al., 2012). Many new townships and developments in Selangor have allocated green areas that provide bird habitats (Puan et al., 2019). Urban birds make nests in trees and high-development areas (Seress & Liker, 2015). They show less intraspecific competition for food and habitats due to their high resistance to environmental tolerance and ability to develop niches in green areas since they have a broader geographic range size (Mohd-Taib et al., 2014; Palacio, 2020). The shape and size of the urban park also play an important role in supporting biodiversity and ecological functions (Jasmani et al., 2017). Medium- and small-sized green areas show higher rates of biotic relaxation than large-sized gardens, which have a high potential to provide nesting sites (Chaiyarat et al., 2019), indicating that habitats surrounding parks and street trees are crucial. The extent to which parks provide nesting sites is also determined by physical factors and anthropogenic disturbance (Aziz & Rasidi, 2013). The more

Distribution of Six Urban Bird Species in Kuala Lumpur

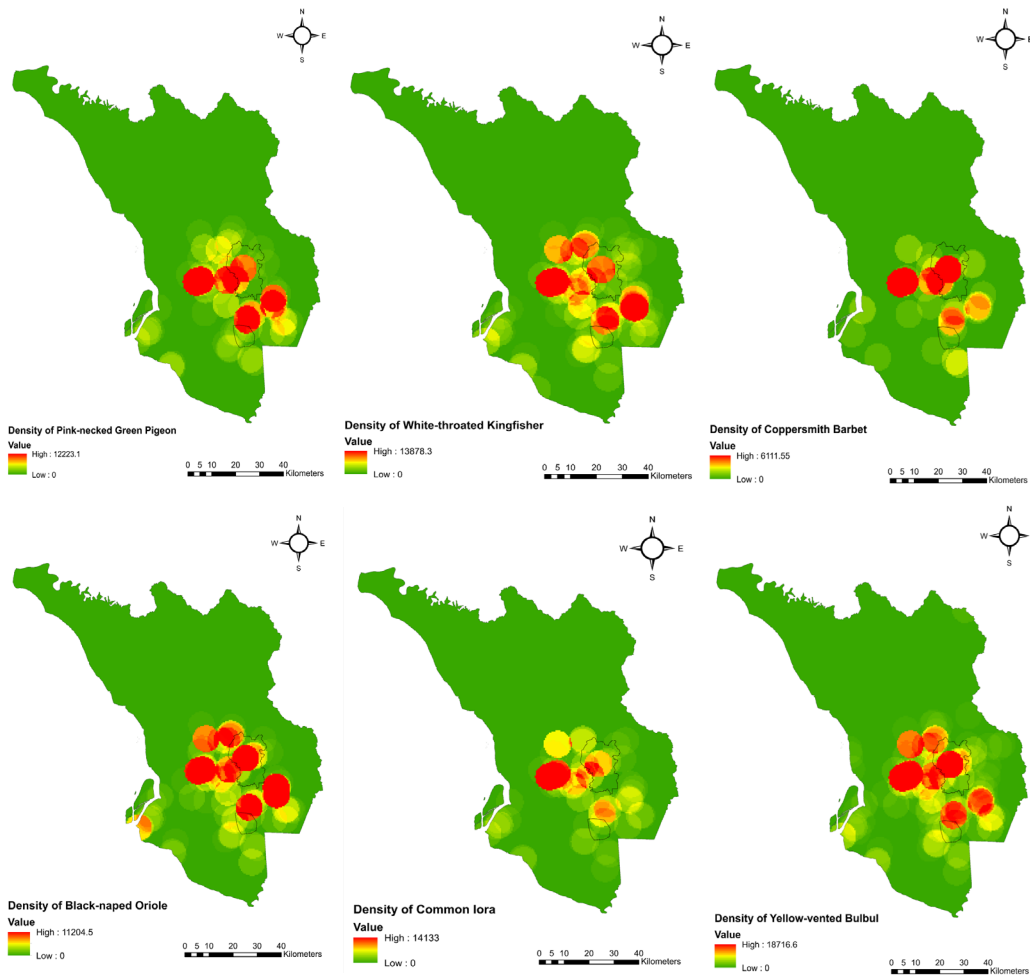


Figure 3. The density of the six urban bird species in Greater Kuala Lumpur in 2020: a) Pink-necked Green-Pigeon; b) White-throated Kingfisher; c) Coppersmith Barbet; d) Black-naped Oriole; e) Common Iora; and f) Yellow-vented Bulbul.

complex and heterogenous the vegetation, the higher the diversity of faunal species is in a given location (Mohd-Taib et al., 2014). Abundant green space in urban areas and sites connected by waterbodies and street trees enhances animal diversity (Puan et al., 2019). Therefore, including green areas in the city is crucial to maintaining urban bird diversity.

Kuala Lumpur has undergone drastic development over the past three decades to become one of the top 20 cities in the world by 2020 (Puan et al., 2019) estimated 2, 436 ha covered by the area of greenspace (Akmar et al., 2011), coupled with the lack of green spaces, has contributed to the low occurrence of urban birds in the city. The scarcity of green spaces and a high level of human activities in the metropolitan city limit the availability

of nesting sites and foraging opportunities, leading to a higher likelihood of urban birds preferring the outskirts. The increased size of city parks creates greater niche space for birds, resulting in higher habitat diversity and greater resource availability (Jasmani et al., 2017; Mansor et al., 2015). Other factors such as tree abundance, cleanliness, noise, human presence and traffic also affect urban biodiversity (Wilson et al., 2015). These factors impact the abundance and distribution of bird species in a given area depending on the current level of adaptation and niches that determine species survival.

The Yellow-vented Bulbul was the most abundant urban bird species in Greater Kuala Lumpur. However, it was highly different in number between Selangor (n=2503) and Kuala Lumpur (n = 169), indicating that population density may decline in metropolitan cities. Wells (2007) reported a decline in the population density of this bulbul species in Greater Kuala Lumpur. Without considering highly abundant or introduced species (e.g. the Eurasian Tree Sparrow, Peaceful Dove, Common Myna, Javan Myna and House Crow), the Yellow-vented Bulbul is considered among the most abundant urban bird species (Aida et al., 2016; Jasmani et al., 2017; Karuppappan et al., 2014; Puan et al., 2019). This bulbul is a widespread species found in almost all habitats except deep forests, ranging from mangrove forests to secondary forests, from farmland to plantations, and from the suburbs to the city. Urban areas consisting of open spaces, gardens, wetlands and vegetation are advantageous to urban birds that can adapt and find high levels of food (Idilfitri et al., 2014). Therefore, introducing a green corridor linking forested areas, street trees, gardens, and parks are important to ensure the survival of urban birds, such as recreational areas, cultural spaces and sports facilities for essential urban walking. A wide range of diets, including insects, carcasses, flowers, nectar, and fruits, guarantees their adaptation and population success.

Other abundant aesthetically valuable urban bird species in this study were the Pink-necked Green-Pigeon and Black-naped Oriole, probably due wide range of diets. Yellow-vented Bulbul and Black-naped Oriole are omnivores that eat insects and fruits due to the presence of figs (e.g. *Ficus benjamina*). Meanwhile, the Pink-necked Green Pigeon is a frugivore that seeks to eat fruit trees, shrubs and fruits from the palm trees (e.g. the Macarthur palm [*Ptychosperma macarthurii*]), which provide food and nesting places in the city along roadsides and parks (Malaysia Biodiversity Information System, 2021; Idilfitri et al., 2014; Jasmani et al., 2017). The wide range of diets for birds can influence the richness of urban bird species. Furthermore, these bird species are important in urban ecosystems because they are seed dispersers.

The important criteria of urban bird species are their ability to adapt to high-risk areas and proximity to human habitation when searching for food and alternative nesting sites (Daud et al., 2022; Idilfitri & Nik, 2012). According to (Moller, 2009), urban bird species have higher breeding rates than rural species due to their capacity to adapt to various conditions and use different sources of nutrition as needed. For example, the Pink-necked

Green Pigeon has successfully adapted to all types of urban and rural habitats, green areas in cities and urban parks (Malaysia Biodiversity Information System, 2021); it also favours swamps, mangroves and in-shore islet habitats (Wells, 2009). Aida et al. (2016) reported that most rural bird species have also adapted to the urban environment due to the suitability of urban centres that provide shelter similar to that found in rural areas resulting in the presence of similar trees and immensity of the green areas covered in those areas.

Among the six species studied, the Coppersmith Barbet has the lowest number of records in e-Bird. Its behaviour of foraging alone, in small groups or pairs, foraging in tree canopies for fruits and insects such as termites in cities may contribute to this result. Furthermore, the size of the bird may also contribute to the small number of records. Smaller birds and forage high in the canopy are more likely to be neglected by the public and birdwatchers compared to larger birds and lower-canopy foragers. The Yellow-vented Bulbul, Pink-necked Green-Pigeon and Black-naped Oriole have a larger body size of 20–32 cm compared to the Coppersmith Barbet, which is 16–17 cm in size. However, despite these factors, the great difference in the number of abundant species, coupled with the presence of invasive species such as crows and mynas, may lead to the instability of rare species and, consequently, reduce the likelihood of their survival in the future (Arazmi et al., 2022). Additionally, the predator-prey relationship, fertility, and territorial behaviour of this species may cause naturally occur in lesser numbers of species abundance.

CONCLUSION

Detailed analysis based on citizen science data, such as those recorded in eBird, can provide useful results and a reference to multiple stakeholders, such as town planners, developers, sociologists, economists, and conservationists, for effective urban planning and urban biodiversity management. City spaces and green areas are important in providing habitats for urban birds and are a central component of the urban ecosystem. In order to sustain urban biodiversity, parks in metropolitan cities should be improved by planting suitable trees and shrubs, green areas, such as gardens and parks, and roadside trees should be maintained to serve as a green corridor.

ACKNOWLEDGEMENTS

This study was funded by the Fundamental Research Grant Scheme (FRGS), Ministry of Higher Education Malaysia (MOHE), under grant FRGS/1/2020/STG03/UKM/02/5. We thank the numerous contributors to eBird, including observers, the project team, and data reviewers.

REFERENCES

- Akmar, A. N., Konijnendijk, C. C., Sreetheran, M., & Nilsson, K. (2011). Greenspace planning and management in Klang valley, Peninsular Malaysia. *Arboriculture and Urban Forestry*, 37(3), 99-107.
- Aida, N., Sasidhran, S., Kamarudin, N., Aziz, N., Puan, C. L., & Azhar, B. (2016). Woody trees, green space and park size improve avian biodiversity in urban landscapes of Peninsular Malaysia. *Ecological Indicators*, 69, 176-183. <https://doi.org/10.1016/j.ecolind.2016.04.025>
- Arazmi, F. N., Ismail, N. A., Daud, U. N. S., Abidin, K. Z., Nor, S. M., & Mansor, M. S. (2022). Spread of the invasive Javan myna along an urban-suburban gradient in Peninsular Malaysia. *Urban Ecosystems*, 25, 1007-1014. <https://doi.org/10.1007/s11252-022-01216-9>
- Aziz, H. A., & Rasidi, M. H. (2013). Study of habitat indicator: Openness and complexity level in the parks of Putrajaya. *Procedia-Social and Behavioral Sciences*, 85, 332-344. <https://doi.org/10.1016/j.sbspro.2013.08.363>
- Blair, R. B. (1996). Land use and avian species diversity along an urban gradient. *Ecological Applications*, 6(2), 506-519. <https://doi.org/10.2307/2269387>
- Brush, J. S. (2016). *Avian communities in an urbanizing region: Abundance patterns and effects of local habitat features*. University of Texas Rio Grande Valley.
- Callaghan, C. T., Major, R. E., Lyons, M. B., Martin, J. M., & Kingsford, R. T. (2018). The effects of local and landscape habitat attributes on bird diversity in urban greenspaces. *Ecosphere*, 9(7), Article e02347. <https://doi.org/10.1002/ecs2.2347>
- Callaghan, C. T., & Gawlik, D. E. (2015). Efficacy of eBird data as an aid in conservation planning and monitoring. *Journal of Field Ornithology*, 86(4), 298-304. <https://doi.org/10.1111/jof.12121>
- Callaghan, C. T., Major, R. E., Wilshire, J. H., Martin, J. M., Kingsford, R. T., & Cornwell, W. K. (2019). Generalists are the most urban-tolerant of birds: A phylogenetically controlled analysis of ecological and life history traits using a novel continuous measure of bird responses to urbanization. *Oikos*, 128(6), 845-858. <https://doi.org/10.1111/oik.06158>
- Chace, J., & Walsh, J. J. (2006). Urban effects on native avifauna: A review. *Landscape and Urban Planning*, 74(1), 46-69. <https://doi.org/10.1016/j.landurbplan.2004.08.007>
- Chaiyarat, R., Wutthithai, O., Punwong, P., & Taksintam, W. (2019). Relationships between urban parks and bird diversity in the Bangkok metropolitan area, Thailand. *Urban Ecosystems*, 22, 201-212.
- Daud, U. N. S., Ismail, N. A., Nor, S. M., & Mansor, M. S. (2022). Biparental incubation behavior in the domestic house-farmed swiftlets (*Aerodramus* sp.) in central Peninsular Malaysia. *Animal Biology*, 1(aop), 1-11.
- Hensley, C. B. (2018). *Effects of Urbanization on Bird Assemblages in Three Southwestern U.S. Cities* (Thesis dissertation). California State University, US. <https://www.proquest.com/dissertations-theses/effects-urbanization-on-bird-assemblages-three/docview/2073727538/se-2>
- Idilfitri, S., & Mohamad, H. N. N. (2012). Role of Ornamental Vegetation for Birds' Habitats in Urban Parks: Case Study FRIM, Malaysia. *Procedia - Social and Behavioral Sciences*, 68, 894-909. <https://doi.org/10.1016/j.sbspro.2012.12.275>
- Idilfitri, S., Sulaiman, S., & Salleh, N. S. (2014). Role of ornamental plants for bird community'habitats in urban parks. *Procedia-Social and Behavioral Sciences*, 153, 666-677. <https://doi.org/10.1016/j.sbspro.2014.10.098>

- Jasmani, Z., Ravn, H. P., & van den Bosch, C. C. K. (2017). The influence of small urban parks characteristics on bird diversity: A case study of Petaling Jaya, Malaysia. *Urban Ecosystems*, *20*, 227-243. <https://doi.org/10.1007/s11252-016-0584-7>
- Kark, S., Iwaniuk, A., Schalimtzek, A., & Banker, E. (2007). Living in the city: Can anyone become an 'urban exploiter'? *Journal of Biogeography*, *34*(4), 638-651. <https://doi.org/10.1111/j.1365-2699.2006.01638.x>
- Karuppanan, S., Baharuddin, Z. M., Sivam, A., & Daniels, C. B. (2014). Urban green space and urban biodiversity: Kuala Lumpur, Malaysia. *Journal of Sustainable Development*, *7*(1), 1-16.
- Malaysia Biodiversity Information System. (2021). *Treron Vernans*. <https://www.mybis.gov.my/sp/22659>
- Mansor, M. S., & Ramli, R. (2017). Niche separation in flycatcher-like species in the lowland rainforests of Malaysia. *Behavioural Processes*, *140*, 121-126. <https://doi.org/10.1016/j.beproc.2017.04.010>
- Mansor, M. S., Ramli, R., & Sah, S. A. M. (2015). The foraging tactics of Chestnut-winged Babbler (*Stachyris erythroptera*) and Abbott's Babbler (*Malacocincla abbotti*) in a lowland rainforest, Malaysia. *Sains Malaysiana*, *44*(5), 687-692.
- Mansor, M. S., Sah, S. A. M., Lim, C. K., & Rahman, M. A. (2011). Bird species diversity in the Padawan limestone area, Sarawak. *Tropical Life Sciences Research*, *22*(2), 65-85.
- Marzluff, J. M. (2001). Worldwide urbanization and its effects on birds. In J. Marzluff, R. Bowman, & R. Donnelly (Eds.), *Avian Ecology in an Urbanizing World* (pp. 19-47). Springer. https://doi.org/10.1007/978-1-4615-1531-9_2
- Marzluff, J. M., & Ewing, K. (2001). Restoration of fragmented landscapes for the conservation of birds: A general framework and specific recommendations for urbanizing landscapes. In J. M. Marzluff, E. Shulenberg, W. Endlicher, M. Alberti, G. Bradley, C. Ryan, U. Simon, & C. ZumBrunnen (Eds.), *Urban Ecology*, (pp. 739-755). Springer. https://doi.org/10.1007/978-0-387-73412-5_48
- McKinney, M. L. (2008). Effects of urbanization on species richness: A review of plants and animals. *Urban Ecosystems*, *11*, 161-176. <https://doi.org/10.1007/s11252-007-0045-4>
- Mohd-Taib, F., Rabiatal-Adawiyah, S., & Md-Nor, S. (2014). Birds communities of fragmented forest within highly urbanized landscape in Kuala Lumpur, Malaysia. *AIP Conference Proceedings*, *1614*, Article 651. <https://doi.org/10.1063/1.4895279>
- Moller, A. P. (2009). Successful city dwellers: A comparative study of the ecological characteristics of urban birds in the Western Palearctic. *Oecologia*, *159*, 849-858. <https://doi.org/10.1007/s00442-008-1259-8>
- Nasruddin-Roshidi, A., Mansor, M. S., Ismail, N. A., Ngadi, E., Izzat-Husna, M., Husin, S. M., Mohd-Taib, F. S., Illias, R., & Nor, S. M. (2021). Recovery of bird communities following the construction of a large-scale hydroelectric dam. *Ecological Processes*, *10*, Article 30. <https://doi.org/10.1186/s13717-021-00298-1>
- Odling-Smee, J., Erwin, D. H., Palkovacs, E. P., Feldman, M. W., Laland, K. N., & Thomson, J. (2013). Niche construction theory: A practical guide for ecologists. *The Quarterly Review Biology*, *88*(1), 4-28. <https://doi.org/10.1086/669266>
- Palacio, F. X. (2020). Urban exploiters have broader dietary niches than urban avoiders. *Ibis*, *162*(1), 42-49. <https://doi.org/10.1111/ibi.12732>

- Puan, C. L., Yeong, K. L., Ong, K. W., Fauzi, M. I. A., Yahya, M. S., & Khoo, S. S. (2019). Influence of landscape matrix on urban bird abundance: evidence from Malaysian citizen science data. *Journal of Asia-Pacific Biodiversity*, 12(3), 369-375. <https://doi.org/10.1016/j.japb.2019.03.008>
- Sandström, U. G., Angelstam, P., & Mikusiński, G. (2006). Ecological diversity of birds in relation to the structure of urban green space. *Landscape and Urban Planning*, 77(1-2), 39-53. <https://doi.org/10.1016/j.landurbplan.2005.01.004>
- Seress, G., & Liker, A. (2015). Habitat urbanization and its effects on birds. *Acta Zoologica Academiae Scientiarum Hungaricae*, 61(4), 373-408. <https://dx.doi.org/10.17109/AZH.61.4.373.2015>
- Sol, D., González-Lagos, C., Moreira, D., & Maspons, J. (2013). Measuring tolerance to urbanization for comparative analyses. *Ardeola*, 60(1), 3-13. <https://doi.org/10.13157/arla.60.1.2012.3>
- Sullivan, B. L., Aycrigg, J. L., Barry, J. H., Bonney, R. E., Bruns, N., Cooper, C. B., Damoulas, T., Dhondt, A. A., Dietterich, T., Farnsworth, A., Fink, D., Fitzpatrick, J. W., Fredericks, T., Gerbracht, J., Gomes, C., Hochachka, W. M., Iliff, M. J., Lagoze, C., La Sorte, F. A., ... & Kelling, S. (2014). The eBird enterprise: An integrated approach to development and application of citizen science. *Biological Conservation*, 169, 31-40. <https://doi.org/10.1016/j.biocon.2013.11.003>
- United Nations. (2019). *World urbanization prospects. The 2018 revision*. Department of Economic and Social Affairs, United Nations. <https://population.un.org/wup/publications/Files/WUP2018-Report.pdf>
- Webb, C. T., Hoeting, J. A., Ames, G. M., Pyne, M. I., & LeRoy Poff, N. (2010). A structured and dynamic framework to advance traits-based theory and prediction in ecology. *Ecology Letters*, 13(3), 267-283. <https://doi.org/10.1111/j.1461-0248.2010.01444.x>
- Wells, D. R. (2007). *Birds of the Thai-Malay Peninsula: Non-passerines* (Vol. 1). Bloomsbury Publishing Plc.
- Wells, D. R. (2009). *The Birds of the Thai-Malay Peninsula: Passerines* (Vol. 2). Christopher Helm Publishers Ltd.
- Wilson, R. F., Sarim, D., & Rahman, S. (2015). Factors influencing the distribution of the invasive house crow (*Corvus splendens*) in rural and urban landscapes. *Urban Ecosystems*, 18(4), 1389-1400. <https://doi.org/10.1007/s11252-015-0448-6>
- Yaakob, U., Masron, T., & Masami, F. (2010). Ninety years of urbanization in Malaysia: A geographical investigation of its trends and characteristics. *Journal of Ritsumeikan Social Sciences and Humanities*, 4(3), 79-101.
- Yusop, M. Y. M., Ibrahim, Z., Hamzah, M. H., Mamat, I., Isa, J. M., Salikan, S., & Hussein, S. Z. (2021). A survey of birds in an urban tropical rainforest park: Kuala Lumpur Eco-Forest Park, Bukit Nanas. *The Malaysian Forester*, 84(1), 114-119.
- Zhou, D., Fung, T., & Chu, L. (2012). Avian community structure of urban parks in developed and new growth areas: A landscape-scale study in Southeast Asia. *Landscape and Urban Planning*, 108(2-4), 91-102. <https://doi.org/10.1016/j.landurbplan.2012.08.004>

A Single Objective Crow Search for Modelling of Horizontal Flexible Plate Structure

Aida Nur Syafiqah Shaari, Muhamad Sukri Hadi* and Abdul Malek Abdul Wahab

School of Mechanical Engineering, College of Engineering, Universiti Teknologi MARA, 40450 UiTM, Selangor, Malaysia

ABSTRACT

The magnificent features of flexible plate structure, including lightweight and high-speed response, resulted in additional market demand, especially in the automotive and manufacturing industries. Nevertheless, the structure may incur structural damage and performance degradation when the system encounters excessive vibration. Therefore, a system identification approach utilising a metaheuristic algorithm via crow search to develop a horizontal flexible plate (HFP) model for vibration control is introduced in this paper. Crow search (CS) is a modern algorithm inspired by a crow's intellectual operation to store additional food and memorise the food storage location. In this study, CS is employed to optimise the objective function, which is the mean squared error for accomplishing a precise predicted model in replicating the dynamic response of the actual structure. Hence, the preliminary action for modelling using this approach is designing and fabricating an HFP rig for experimentally gathering the real input-output vibration data. After that, the mathematical modelling utilising the CS algorithm was implemented using a parametric model structure. Finally, the best-fit model is chosen for the representation of the HFP based on the lowest mean squared error, correlation test within a 95% confidence

level and stability in a pole-zero plot. The simulation result reveals that the CS algorithm with a second-order estimated model accomplished a minimum MSE of 1.1168×10^{-5} , an unbiased correlation test and excellent stability for the HFP structure.

ARTICLE INFO

Article history:

Received: 09 March 2022

Accepted: 28 June 2022

Published: 20 March 2023

DOI: <https://doi.org/10.47836/pjst.31.2.21>

E-mail addresses:

aida.fieqa@gmail.com (Aida Nur Syafiqah Shaari)

msukrihadi@uitm.edu.my (Muhamad Sukri Hadi)

abdmalek@uitm.edu.my (Abdul Malek Abdul Wahab)

*Corresponding author

Keywords: Active vibration control, crow search, flexible structure, metaheuristic, modelling, swarm intelligence algorithm, system identification

INTRODUCTION

The effectiveness of a system is always a major concern in an industry, especially when a precise and ample output is needed. Since the 1760s, structures like plates, beams, manipulators and shells have been extensively used to build machinery and other facilities for manufacturing goods. Many human safety and health issues have been recorded in this era as a result of the exploitation of people and animals to perform economic activities for nearly 16 hours per day (Mohajan, 2019). Furthermore, their lives have been put in jeopardy as a result of the massive equipment and rigid structures that they handle.

To date, the government website also has several incidents involving heavy equipment. For instance, on the official website of Malaysia's Department of Occupational Safety and Health (DOSH), two cases resulting in death because of being hit by heavy equipment were registered in February 2019 (Ministry of Human Resources, 2021). In addition, site cleanliness has become a top priority, as large machinery requires a huge amount of lubricant to keep it cool and minimise friction between collided metal pieces, increasing the machine's operating hours. Moreover, according to Mamuda and Mukhtar (2017), fossil fuel-based lubricants influence the climate.

The use of fossil fuel lubricant dates to the first industrial revolution and continues to this day. However, because of its widespread usage in various industries, including transportation, the source of the lubricant is gradually diminishing (Nagendramma & Kaul, 2012). The rise in fatal cases concerning rigid structures and the reduction of non-renewable sources has prompted the growth of facilities and industries employing renewable energy and flexible structure.

Flexible structure, also known as a thin and light structure, has received prominent interest from researchers owing to its numerous advantages (Yatim et al., 2013; Hou, 2018). Nevertheless, the continuous vibration exerted on flexible structures such as plates, manipulators and shells is a crucial issue in the industry. The system efficiency would deteriorate, ultimately leading to total failure, especially when the resonance occurs (Mohammed et al., 2019). This issue has gotten considerable attention in the research sector, particularly in the control and system department.

Most researchers did not want to abandon the structure mentioned above because it has been proven to contribute to economic growth and meets social demands in the future (Agarwal & Agarwal, 2017). As a result, various control techniques for vibration suppression in the system have been identified. However, PID controller is the most prominent industry because of their mobility, less energy usage and require small actuator (Pedro & Tshabalala, 2015). For instance, the implementation of PID controllers has been introduced in autonomous joint dental and flexible systems by Matin et al. (2016) and Tavakolpour et al. (2011).

Although PID controllers have been extensively used in a research area, their effectiveness is often criticised by industry, especially for the non-linear system, due to the uncertainty aspect that the system influences, such as excessive payloads and changes in the operating environment (Visioli, 2012; Nayak & Singh, 2015). Besides that, Rao et al. (2016) stated that the nonlinearities of a system are mainly caused by the failure to obtain an exact model, consequently affecting the controller's accuracy. Therefore, most researchers concentrate on modelling methods before the development of the controller.

Nowadays, scholars have recently focused their study on system identification via swarm intelligence algorithm (SIA) to model a system and solve optimisation problems, including sparse signal reconstruction, sensor characteristics, and seismic response output (Erkoc & Karaboga, 2021; Jiang et al., 2021; Tsipianitis & Tsompanakis, 2021). SIA was motivated by a group of animal and biological interactions allowing them to survive by securing food and hunting prey. Harmony search (HS), genetic algorithm (GA), particle swarm optimisation (PSO), and sheep flock optimisation (SFO) are some examples of SIA employed in the research sector (Gheisarnejad, 2018; Kivi & Majidnezhad, 2021; Khairuddin et al., 2014).

The remarkable benefits of this optimisation approach have also stimulated the interest of researchers in modelling a flexible structure. Hadi et al. (2013) applied PSO in modelling a horizontal flexible plate system. They successfully attenuated the first mode of vibration by 34.37 dB. In addition, Hadi and his coworkers employed an artificial bee colony (ABC) to determine the real characteristic of the flexible plate (Hadi et al., 2014). Furthermore, Eek et al. (2016) and Yatim et al. (2013) have chosen PSO and ABC to develop flexible beam and manipulator structures, respectively. The results indicate a substantial reduction in vibration after the transfer function from the developed model is deployed in the PID controller.

Many topics leveraging various SIA techniques have been published, all of which have yielded outstanding performances, as outlined above. However, one of the disadvantages of an optimisation algorithm is that a lot of parameter setting will lead to time-consuming (Majhi et al., 2020). According to Majhi and his co-investigator, PSO and ABC required 4 tuning parameters, whereas GA needed 6 (Majhi et al., 2020). A new approach based on nature-inspired, namely crow search (CS), has been proposed by Askarzadeh (2016). CS own the same benefit as other global algorithms capable of solving the optimisation problem. Unlike PSO, ABC and GA, which require 4 to 6 tuning parameters, CS, on the other hand, is only dependent on two variables, flight length and awareness probability (Hussien et al., 2020). These two parameters are used to find the optimal solution.

The purpose of this work is to utilise the CS technique to identify a horizontal flexible plate structure. Prior to that, a simulation environment that characterises non-linear characteristics of the horizontal flexible plate structure is developed using a system

identification strategy. Initially, input-output vibration datasets are collected experimentally. The dataset acquired is then employed to develop CS-based identification. The responses were extracted in both time and frequency domains. The effectiveness of the developed model also will be validated using correlation tests, pole-zero maps and mean squared error. In addition, this research contributed to modelling a flexible plate structure using a metaheuristic approach via the crow search algorithm.

MATERIALS AND METHODS

Experimental Setup

The input-output vibration datasets of horizontal flexible plate structures are collected using the experimental setup conducted by the previous researcher, as illustrated in Figure 1 (Hadi et al., 2014). The boundary condition of the horizontal flexible plate structure has been modelled with all clamped edges. In this experiment, the flexible structure was mounted in the horizontal plane to let it vibrate vertically. The vibration responses were acquired using the NI data acquisition (DAQ) system through a completed experimental rig with sensors and actuators mounted on a square, flat and thin aluminium plate with dimensions of $0.7\text{ m} \times 0.7\text{ m} \times 0.001\text{ m}$. Table 1 outlines the detailed specifications of the flexible plate employed in this study.

The information flow in DAQ is divided into a few steps. Initially, an actuation force was generated at the excitation point on the test structure by a magnetic shaker positioned 1 cm parallel to a circular shape permanent magnet. Next, the excitation on the plate was done by a generation of sine wave force produced using a magnetic shaker linked with a function generator and power amplifier. Then, the acceleration signal is sensed using two pieces of a piezo-beam type accelerometer to represent the vibration of the flexible plate. Next, the accelerometers were installed at two separate locations: detection and observation points. After that, the accelerometers were directly attached to the data acquisition system, which was embedded inside the computer. Finally, utilising specialised software, the collected input-output vibration data were processed, analysed, stored and displayed.

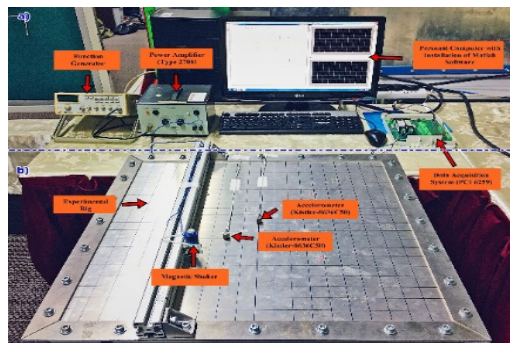


Figure 1. Horizontal flexible plate rig employed in the experiment a) signal conversion using data acquisition system, b) bottom view of the plate (Hadi et al., 2014)

Table 1

The detailed specifications of the flexible plate employed in this study (Hadi et al., 2014)

Parameters	Value
Length, L	0.7 m
Width, w	0.7 m
Thickness, t	0.001 m
Poison ratio, ν	0.3
Density, ρ	$2.17 \times 10^3 \text{ kgm}^{-3}$
Modulus of elasticity, E	$7.11 \times 10^{10} \text{ Nm}^{-2}$
Moment of inertia, I	$5.1924 \times 10^{-11} \text{ kgm}^2$

System Identification

Parametric identification was conducted in this research using a linear ARX model structure. In addition, the crow search algorithm (CSA) was utilised as an optimisation technique.

Model Structure. The development of a satisfactory model of the structure can be obtained through a relationship between the input and output of the system. Therefore, it is crucial to obtain an adequate order and parameters for the model that closely fits the input-output data acquired from the experiment to meet this purpose. The Equation 1 of this relationship for the ARX model in zero-order hold can be expressed as:

$$y(t) = \frac{B(z^{-1})}{A(z^{-1})}u(t) \tag{1}$$

while $A(z^{-1})$ and $B(z^{-1})$ denoted as

$$A(z^{-1}) = 1 + a_1z^{-1} + \dots + a_nz^{-n}$$

$$B(z^{-1}) = b_1z^{-1} + \dots + b_nz^{-n}$$

where $y(t)$ and $u(t)$ depicted the signal input and computed output, respectively with $t = 1, 2, 3, \dots, N$. The z^{-1} is indicated as the backshift operator, $a_1 \dots a_n$ and $b_1 \dots b_n$ are the model parameters, and n is an order of the model. The system parameters that need to be predicted are given by polynomials $A(z^{-1})$ and $B(z^{-1})$.

The optimisation is based on the mean squared error (MSE) of the difference between real and approximate output, which is described in Equation 2:

$$\text{MSE} = \frac{1}{S} \sum_{i=1}^S (|y(i) - \hat{y}(i)|)^2 \tag{2}$$

$y(i)$ and $\hat{y}(i)$ are measured and estimated outputs, respectively, and S is the sample size. The important aim of system identification is to predict the optimum model parameters that meet the objective function, which in this research is MSE minimisation. Hence, the model development of a horizontal flexible plate structure was obtained by utilising CSA as an optimisation strategy.

Crow Search. The crow search algorithm is a global optimisation approach inspired by crow behaviour, which can be used to find the minimum value of mean squared error. Crows are among the most sophisticated birds, with the largest brain-to-body ratio. They have distinct characteristics, such as self-awareness and the ability to create tools. They employ tools to recognise their hidden food location for a period. Each crow pursues the hidden food supply of another crow and steals it while the owner is away. As a result, every crow takes precautionary measures to secure its food in the best possible location.

Askarzadeh recommended the comprehensive approach following the four basic principles outlined below (Askarzadeh, 2016);

- Crows gather in a cluster, and the population size is defined as flock size, N .
- Crows remember the location of their hiding spot and store it as memory, m .
- Crows choose and follow one of the other crows in the swarm to steal their food.
- Crows protect their food from being stolen by probability.

Implementation of CS Algorithm to Develop an HFP

The utilisation of the CS algorithm for model development of the horizontal flexible plate structure is discussed as follows (Askarzadeh, 2016).

Stage 1: Problem initialisation and setting parameters. Initially, the optimisation problem and decision variable are defined. The decision variable in this study refers to the number of parameters needed in the ARX structure, where the number is twice the value of the model order. For instance, if the model order is fixed to 2, the problem dimension is 4. The problem dimension consists of parameters that can be addressed as a_1, a_2, b_1 and b_2 . These values will then be expressed in a transfer function, reflecting the real characteristics of the horizontal flexible plate structure. After that, the adjustable CSA parameters, including flock size (N), awareness probability (AP), flight length (fl), lower (LB) and upper boundaries (UB) and a maximum number of iterations ($iter_{max}$), are valued. The crows' exploration range in obtaining the possible solution is lower and upper boundaries. For example, if the $[LB, UB] \in [-4, 4]$, hence, the crows will explore from the lower bound, $LB = -4$ and $UB = 4$.

Stage 2: Initialisation of crows' position and memory. The location of the crows is specified randomly within the stated range. The values were obtained randomly by using Equation 3:

$$x_{ij} = UB - (UB - LB) \cdot rand_{ij} \tag{3}$$

where x_{ij} is a number of flocks representing the possible solution within the lower and upper boundary at a random value between 0 and 1, denoted as $rand$ in the equation. Each crow embodies a possible solution to the problem. Equation 4 denotes the matrix structure of each crow position in a dimensional search space resulting from the calculated value using Equation 3 (Askarzadeh, 2016).

$$\text{Crows, } \mathbf{x} = \begin{bmatrix} x_1^1 & x_2^1 & \dots & x_d^1 \\ x_1^2 & x_2^2 & \dots & x_d^2 \\ \vdots & \vdots & \vdots & \vdots \\ x_1^N & x_2^N & \dots & x_d^N \end{bmatrix} \tag{4}$$

After that, a memory of the crow is initialised. The initial values of the memory are the same as the current position as they have no prior experiences. Equation 5 shows the matrix form of memory in a dimensional search space (Askarzadeh, 2016).

$$\text{Memory, } \mathbf{m} = \begin{bmatrix} m_1^1 & m_2^1 & \dots & m_d^1 \\ m_1^2 & m_2^2 & \dots & m_d^2 \\ \vdots & \vdots & \vdots & \vdots \\ m_1^N & m_2^N & \dots & m_d^N \end{bmatrix} \tag{5}$$

The numerical examples in this stage can be illustrated as follows:

Number of maximum iterations, $iter_{max} = 10$,

Flock size, $N = 5$,

Awareness probability, $AP = 0.1$,

Flight length, $fl = 2$,

Lower boundary, $LB = -4$,

Upper boundary, $UB = 4$,

Model order, $mo = 3$,

Number of parameters in ARX structure, $para = 6$ ($a_1, a_2, a_3, b_1, b_2,$ and b_3) – Decision variables

In this situation, each parameter consists of the same lower and upper bounds, which are -4 and 4, respectively. Therefore, if $a_1 = a_2 = a_3 = b_1 = b_2 = b_3 = [-4, 4]$, and let $rand_{11}(0,1) = 0.3124$, $rand_{12}(0,1) = 0.7124$, $rand_{13}(0,1) = 0.1323$, $rand_{14}(0,1) = 0.5512$, $rand_{15}(0,1) = 0.8931$ and $rand_{16}(0,1) = 0.9111$, then each individual representing the initial position are calculated using Equation 3 as:

$$\begin{aligned}
 \text{For } a_1 \in [-4, 4] \quad & x_{11} = 4 - (4 - (-4)) \cdot 0.3124 \\
 & x_{11} = 1.5008 = a_1 \\
 \text{For } a_2 \in [-4, 4] \quad & x_{12} = 4 - (4 - (-4)) \cdot 0.7124 \\
 & x_{12} = -1.6992 = a_2 \\
 \text{For } a_3 \in [-4, 4] \quad & x_{13} = 4 - (4 - (-4)) \cdot 0.1323 \\
 & x_{13} = 2.9416 = a_3 \\
 \text{For } b_1 \in [-4, 4] \quad & x_{14} = 4 - (4 - (-4)) \cdot 0.5512 \\
 & x_{14} = -0.4096 = b_1 \\
 \text{For } b_2 \in [-4, 4] \quad & x_{15} = 4 - (4 - (-4)) \cdot 0.8931 \\
 & x_{15} = -3.1448 = b_2 \\
 \text{For } b_3 \in [-4, 4] \quad & x_{16} = 4 - (4 - (-4)) \cdot 0.9111 \\
 & x_{16} = -3.2888 = b_3
 \end{aligned}$$

The calculation above only reflects the first flock and is repeated with subsequent flocks (in this example, the calculation is repeated 5 times with different random numbers). These values can be presented in the matrix structure as denoted in Equation 4. For the numerical example, the values for the first flock are displayed in the first column of the matrix. In addition, since the memory at the initial phase is the same as the position of the crows' value, therefore,

$$\begin{aligned}
 \text{Crows, } x = \text{Memory, } m = \\
 \begin{bmatrix}
 1.508 & 3.1234 & -2.1134 & 0.1108 & 3.9123 & 2.1141 \\
 -1.6992 & 0.1451 & -1.1412 & -2.0796 & 1.4231 & -3.9991 \\
 2.9416 & -3.814 & 0.1415 & 3.0081 & -1.982 & -2.132 \\
 -0.4096 & 2.9824 & 1.1421 & 2.4071 & -1.932 & 0.3142 \\
 -3.1448 & 2.1312 & 1.2411 & -0.2007 & 2.1238 & -1.7282 \\
 -3.2888 & -1.9782 & 3.1231 & -1.1091 & 3.8912 & 1.3249
 \end{bmatrix}
 \end{aligned}$$

Stage 3: Evaluation of fitness function. The reliability of each crow's location is calculated by integrating the decision variable values into the objective function. In this study, the objective function is to find the minimum values of MSE. As a result, by inserting the values into Equation 2, the fitness function for each flock is calculated and compared. The flock with the lowest values among the 5 flocks is selected as *fmin*. For example, if each fitness function is obtained for a crow shown in Table 2, the current best solution is found at flock 1 with *fmin* = 0.0013 since it has the lowest fitness value.

Table 2

Examples of choosing the initial best solution

	Individual solution (Flock size)				
	1	2	3	4	5
Fitness	0.0013	0.0123	0.0094	0.0841	0.0014

Stage 4: Generation of a new position. The next stage is the generation of the crows' new position. At this stage, by assuming a crow j visits its hiding spot, $m^{j,iter}$ on an iteration, $iter$, and another crow (for instance, crow i) secretly follow the crow j to that spot. There are two possible conditions for this situation which are (Askarzadeh, 2016):

1. Crow j is unaware of the attendance of crow i at its place, $m^{j,iter}$, resulting in crow i entering crow j hiding spot. In this case, the current location of crow i is computed as Equation 6 (Askarzadeh, 2016):

$$x^{i,iter+1} = x^{i,iter} + r_i \cdot fl^{i,iter} \cdot (m^{j,iter} - x^{i,iter}) \quad [6]$$

where $fl^{i,iter}$ and r_i represent the crow i flight length at $iter$ and random number within 0 and 1 with uniform distribution. The value set for fl is important as it affects the search capability. According to Azkarzadeh, a small and large value of fl results in a local and global search. The effect values of fl on search capability in its current state were thoroughly clarified and demonstrated by Askarzadeh (2016).

2. Crow j is aware that it is being followed by crow i . Hence, it deceives crow i by travelling to a different position in the search space, ensuring its hiding spot remains secure.

Conditions 1 and 2 can be described as Equation 7:

$$x^{i,iter+1} = \begin{cases} x^{i,iter} + r_i \cdot fl^{i,iter} \cdot (m^{j,iter} - x^{i,iter}), & r_j \geq AP^{j,iter} \\ a \text{ random position} & \text{otherwise} \end{cases} \quad [7]$$

where $AP^{j,iter}$ and r_j depict the awareness probability of crow j at iteration and random number within 0 and 1 with uniform distribution, respectively. The role of AP in the CS algorithm is to provide a good balance between diversification and intensification in exploring the search space. The decreases in AP value would prompt the CSA to explore a local region where a potentially feasible solution can be discovered. As a result, the intensification will be increased. On the other hand, the increases in AP value will reduce the possibility of the current discovery (local region) in finding a good solution, and CSA will attempt to expand the search space on a global level by randomisation (Askarzadeh, 2016).

The following calculation is performed to show the process in stage 4. Assuming the crow j hidden location is shown in Table 3 (Askarzadeh, 2016).

Table 3

Random position of crow j followed by crow i

	Crow j current position at each flock, $m^{j,iter}$				
	1	2	3	4	5
a_1	3.9012	2.9384	2.2417	-2.3113	-2.1234
a_2	0.1293	-2.3181	-1.4156	2.3114	2.1293
a_3	-3.1921	-1.3911	-3.1201	-3.1234	1.2930
b_1	-4.000	1.0292	1.3901	2.3141	-3.1234
b_2	0.7182	-0.9821	1.9241	-3.9182	-1.3914
b_3	-2.1313	-2.4121	1.9020	-1.3481	2.3411

Next, a random number between 0 and 1 was placed in each flock, and a comparison was made with the AP value. After that, for any random number greater than the AP value, the crow will update its memory using Equation 6. Otherwise, the crow's new position is placed randomly. For example, let $AP = 0.1$, and the random number of all flocks are tabulated as in Table 4 (Askarzadeh, 2016).

Table 4

The random number for the crow i the new position using random distribution

	Random number, r_i				
	1	2	3	4	5
a_1	0.431	0.006	0.912	0.009	0.014
a_2	0.134	0.003	0.120	0.014	0.009
a_3	0.001	0.914	0.100	0.566	0.001
b_1	0.032	0.009	0.039	0.003	0.014
b_2	0.340	0.521	0.020	0.102	0.011
b_3	0.002	0.011	0.410	0.001	0.912

The current memory of crow j , which satisfies condition 1, will be updated by substituting the required values in Equation 6. Therefore, the new position of crow j at $x_{36}^2 = -3.2680$. While the position of crow x_{16}^2 , which satisfies condition 2, is placed randomly using Equation 3. The calculation is performed for each flock.

$$\begin{aligned} \text{For } b_3 \text{ at flock 3} \quad & x_{36}^2 = -3.2888 + (0.002)(2)(1.9020 - (-3.2888)) \\ (r > AP) \quad & x_{36}^2 = -3.2680 \end{aligned}$$

$$\begin{aligned} \text{For } b_3 \text{ at flock 1} \quad & x_{16}^2 = 4 - (4 - (-4)) \cdot 0.3131 \\ (r < AP) \quad & x_{16}^2 = 1.4952 \end{aligned}$$

Stage 5: Feasibility check of the new position. The generation of the new position is checked. If the solution is feasible, replace the crow position with a new one. Otherwise, the position is not updated.

Stage 6: Evaluation of fitness function at new positions. The new position of each crow is evaluated by measuring its fitness function using Equation 2. For example, the new fitness function is presented in Table 5. Hence the best new solution is found at flock 4 with $f_{min} = 0.03 \times 10^{-5}$ since it has the lowest fitness value.

Table 5
Examples of choosing the best new solution

	Individual solution (Flock size)				
	1	2	3	4	5
New Fitness ($\times 10^{-5}$)	1.82	3.21	0.91	0.03	4.12

Stage 7: Update memory. The crows update their memory as Equation 7 (Askarzadeh, 2016):

$$m^{i,iter+1} = \begin{cases} x^{i,iter}, & f(x^{i,iter+1}) \text{ is better than } f(m^{i,iter}) \\ m^{i,iter}, & \text{otherwise} \end{cases} \quad [7]$$

where $f(.)$ indicates the measured objective function value. Hence, $f(x^{i,iter+1})$ denotes the objective function value for the new position at the current iteration, while represents the objective function of the crow’s previous memory location. This stage involves comparing the fitness function of a crow’s current and memorised positions. If the fitness function of the new position is better than the memorised position’s, the crow will replace its memory with a new position.

Now, by comparing the fitness value in Tables 2 and 5, the memory of the crow will update according to the rules (Table 6).

Table 6
Comparison of fitness value between the initial and new position

	Individual solution (Flock size)				
	1	2	3	4	5
Fitness	0.0013	0.0123	0.0094	0.0841	0.0014
New Fitness ($\times 10^{-5}$)	1.82	3.21	0.91	0.03	4.12

Since all new positions achieved better fitness value than memorised positions, all crows will update their memory with a new position as calculated at stage 4 (Table 7).

Table 7
Updated position of a crow after evaluation

	Updated position of crow i at each flock, $x^{i,iter+1}$				
	1	2	3	4	5
a_1	3.9121	3.0121	3.9123	-2.8172	-3.9121
a_2	0.2033	-4.000	-2.8192	3.9817	1.0928
a_3	-1.234	-2.421	-4.000	-3.7167	3.0912
b_1	-3.8122	1.4214	2.6172	2.9182	-1.9821
b_2	1.2314	-2.9125	2.8123	-1.8264	-2.0918
b_3	1.4952	-3.9128	-3.2913	2.0918	3.6710

Stage 8: Check termination criterion. The stages from 4 until 7 are performed until $iter_{max}$ is achieved. The optimisation task is completed after the termination condition is satisfied. Finally, the global minimum fitness value is obtained, which refers to the optimal parameter for the ARX structure.

From a numerical example, let $iter_{max} = 10$ and model order = 3. After the generation of new positions of all crows is done 10 times, the optimisation task will stop from finding the solution. Hence, the final result for 10 iterations can be seen in Table 8. After completing the 10th generation, best fitness = 0.08×10^{-5} . The value of the best solution converged at the 7th iteration as the value remained unchanged until the last iteration.

Table 8
Generation of new position until ten iterations

Generation	1	2	3	4	5
a_1	0.312	0.141	0.981	1.921	0.012
a_2	0.051	0.248	1.891	0.012	1.002
a_3	1.001	1.002	0.910	0.021	0.041
b_1	1.321	0.023	1.902	0.231	0.007
b_2	0.012	1.023	0.101	0.009	0.001
b_3	1.001	0.031	1.451	1.021	1.023
Fitness ($\times 10^{-5}$)	1.901	1.589	1.209	0.101	0.102

The best solution is kept and substituted in the transfer function Equation 8 to represent the horizontal flexible plate structure.

$$\frac{y(t)}{u(t)} = \frac{a_1 z^{-1} + a_2 z^{-2} + a_3 z^{-3}}{1 + b_1 z^{-1} + b_2 z^{-2} + b_3 z^{-3}} \quad [8]$$

The pseudocode and flowchart of the optimisation task using CS are illustrated in Figures 2 and 3 (Askarzadeh, 2016).

Crow Search Algorithm

Initialize a random number of crow position in flock, N in the dimensional search space

Initialize the maximum number of iterations, $iter_{max}$

Evaluate the crows' position

Initialize each crow memory

while $iter < iter_{max}$

for $i: N$ (all N crows (crow i) of the flock

$Crow_i$ randomly follow one of the other crows (for instance j)

Define an awareness probability, AP

if $r_j \geq AP^{i,iter}$

$x^{i,iter+1} = x^{i,iter} + r_i \cdot fl^{i,iter} \cdot (m^{j,iter} - x^{i,iter})$

else

$x^{i,iter+1} = a \text{ random position}$

end if

end for

Check the quality of crow new positions

Evaluate the new position of the crows using Equation [2]

Update the crow memory

end while

Figure 2. Pseudo code for the CSA optimisation (Askarzadeh, 2016)

RESULTS AND DISCUSSIONS

In this study, the dynamic model of a horizontal flexible plate was developed using a system identification technique via swam intelligent algorithm known as crow search (CS) by utilising ARX structure. The parameters of the developed model were determined using MATLAB software. These parameters were given in the form of a transfer function, representing the real characteristics of the horizontal flexible plate structure. Initially,

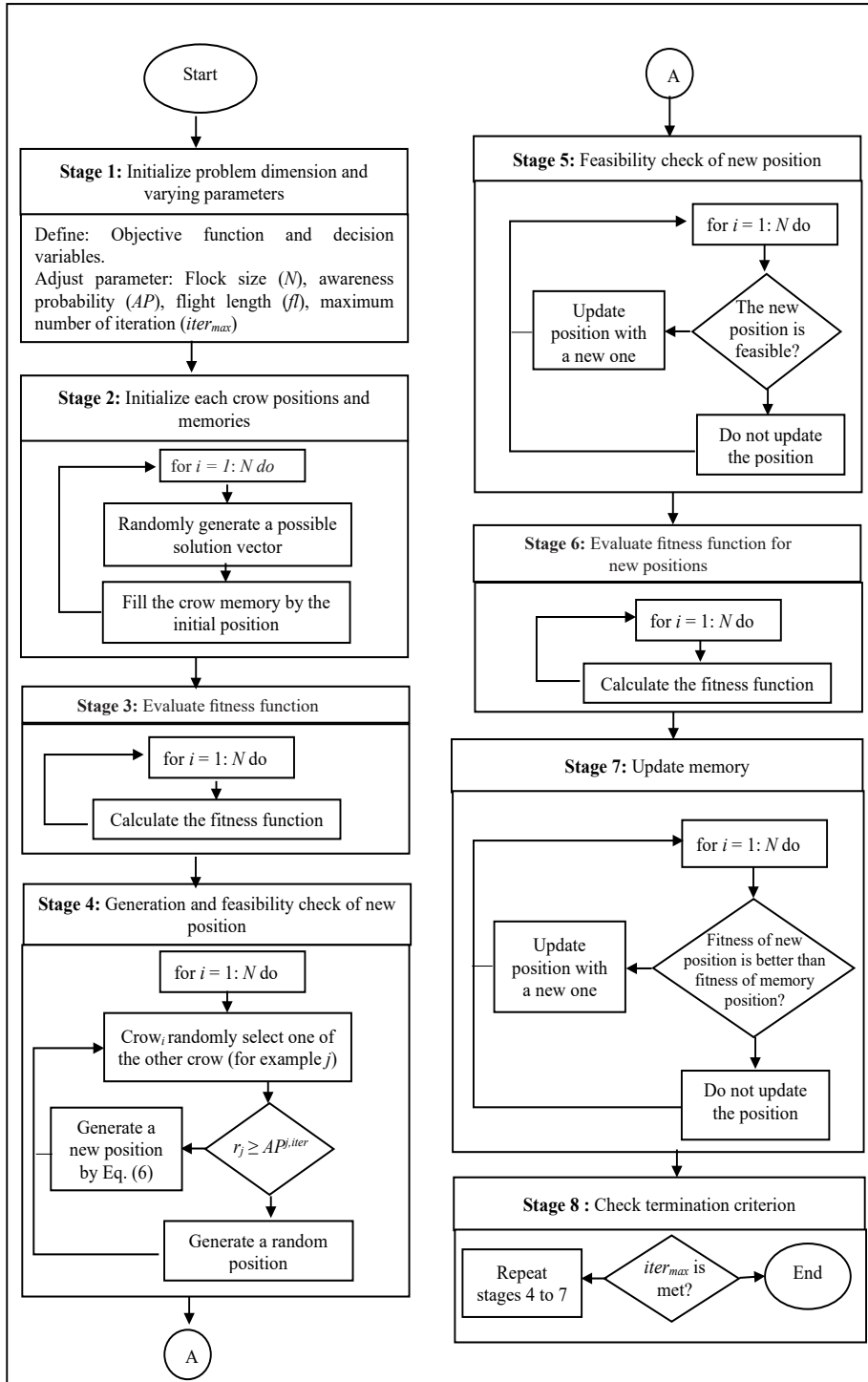


Figure 3. Flowchart of CSA (Askarzadeh, 2016)

5000 input-output vibration datasets extracted through experiments are split into two sections. The first 2500 data points were employed for training, and the remaining 2500 were employed for testing. The effectiveness of the developed model was evaluated using three robustness approaches: pole-zero maps, correlation analysis, and mean squared error (MSE). A high-quality model was selected based on the lowest MSE, unbiased in correlation tests and stable result in a pole-zero map. Furthermore, a heuristic approach was used to obtain the best model order for the proposed structure because there is no prior information regarding the right model order for the model above. This approach was executed by tuning one parameter per variable while leaving the other parameter unchanged.

Six parameters were tuned heuristically in the CS tuning process, including several iterations, model order, population size, lower and upper boundaries, awareness probability and flight length. Although most research papers claimed that CS consists of only two parameters, in this study, all parameters were tuned to validate the statements. Based on the literature review, some implementations use different values for population size, awareness probability and flight length (Souza et al., 2018; Islam et al., 2020). On the other hand, Adhi et al. (2018) and Majhi et al. (2020) tuned the lower and upper boundaries for their applications. Due to the inconsistencies of the parameter setting in the previous works, all parameters were considered and observed in this analysis.

The tuning phase began by varying the population size while the remaining parameters stayed unchanged. In this research, the population size was tuned from 5 to 45 because previous analyses discovered these values offered superior results for most optimisation problems (Islam et al., 2020; Askarzadeh, 2016). Once the best population size value was determined, the value was set, and the next parameter was adjusted. Next, the awareness probability was set from 0.05 until 0.45 with an increment of 0.05. Following that, the range of flight lengths and boundary limits were adjusted from 0.5 to 2.5 and 1 to 10, respectively. Next, the number of iterations was adjusted based on the previous researchers' recommendations, which ranged from 100 to 500 with an increment of 100 (Souza et al., 2018; Majhi et al., 2020). The iteration was terminated at 500 because the outcomes were consistent, which helped reduce the computational time. Finally, the model order was tuned from 1 to 10.

The second order was the best model order, achieved with the parameters outlined (Table 9). The second order is considered the optimal and most preferable in control design. The controller analysis can be simplified by using fewer parameters in the transfer function (Okuy et al., 2015; Aly, 2013). In addition, the graph of convergences for the CS algorithm against iteration was plotted in Figure 4. The graph depicts the accelerated convergence rate for CS to explore the search space to find the best solution. According to previous studies, the CS algorithm converged faster than other algorithms like GA and ABC (Hadi et al., 2012). Furthermore, Figures 5 and 6 indicate the measured and predicted outputs of the horizontal flexible plate structure in the time and frequency domains. The developed CS model managed to imitate the real structure because they overlapped (Figures 5 and 6).

In order to assure the reliability of the developed model, three validations were conducted: pole-zero diagram, correlation analysis, and mean squared error. The MSE for the developed model using CS are 1.6205×10^{-5} and 1.1168×10^{-5} for training and testing results, respectively. This finding was compared to previous studies that used GA to model a flexible plate using the same experimental data set (Hadi et al., 2012). The developed model using CS outperformed the GA model in terms of MSE and the number of orders in the transfer function. Additionally, the error between the real and CS outputs is illustrated in Figure 7. Figures 8 and 9 display the correlation analysis and pole-zero map results. The correlation analysis is comprised of two tests, cross and autocorrelations. Only cross-correlation was observed to be unbiased from this correlation analysis since the response was within the 95% correlation test. The pole-zero diagram reveals that all the poles are located in the unit circle, resulting in a stable outcome. Finally, Equation 9 describes the transfer function representing the best horizontal flexible plate structure model.

$$\frac{y(t)}{u(t)} = \frac{0.384z^{-1} - 0.002184z^{-2}}{1 - 1.414z^{-1} + 0.9931z^{-2}} \quad [9]$$

Table 9

The best value of parameters achieved in developing the CS model

Parameters	Values
Number of flocks	15
Awareness probability	0.1
Flight length	2
Lower and upper boundary	[-10,10]
Model order	2
Iteration	200

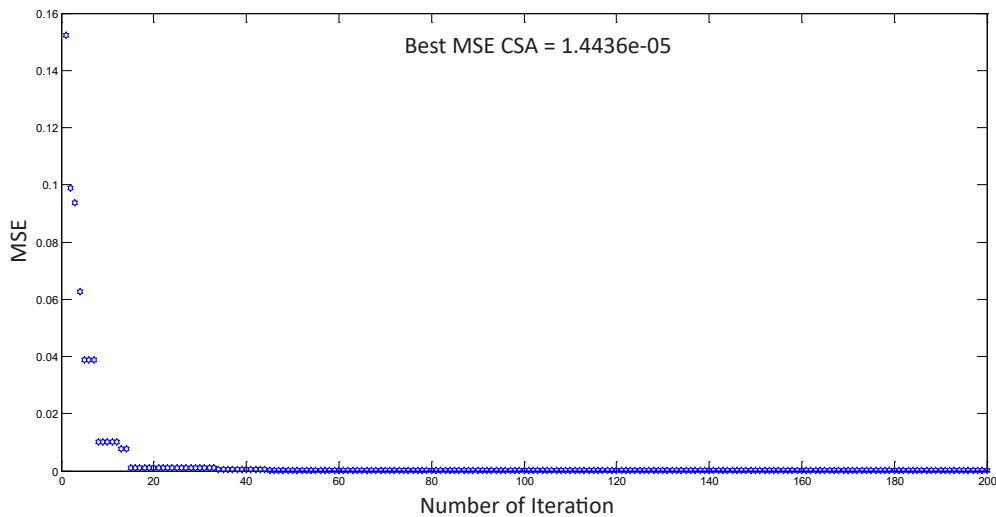


Figure 4. Convergence graph of the estimated model using CSA

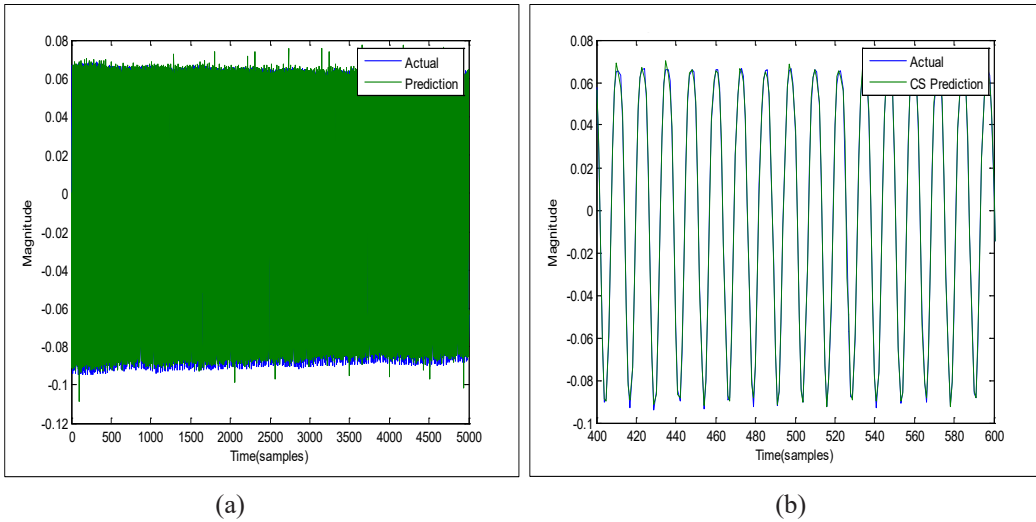


Figure 5. Experimental and CS model in the time domain for flexible plate structure (a) for 5000 data; (b) an extended view of the data from 400 to 600

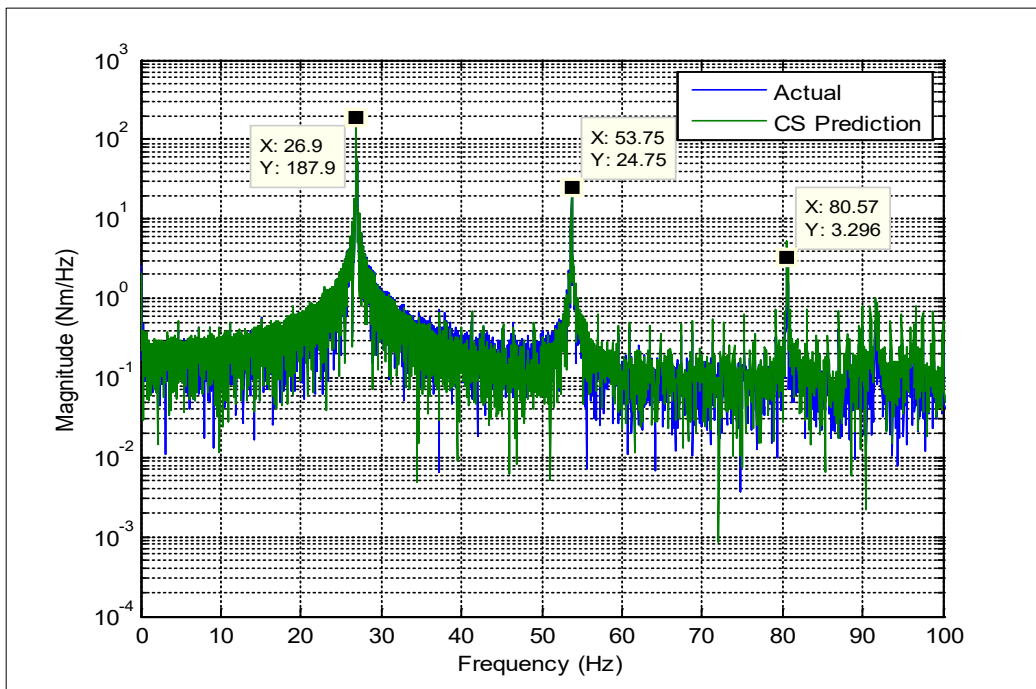


Figure 6. Experimental and CS model in the frequency domain for flexible plate structure

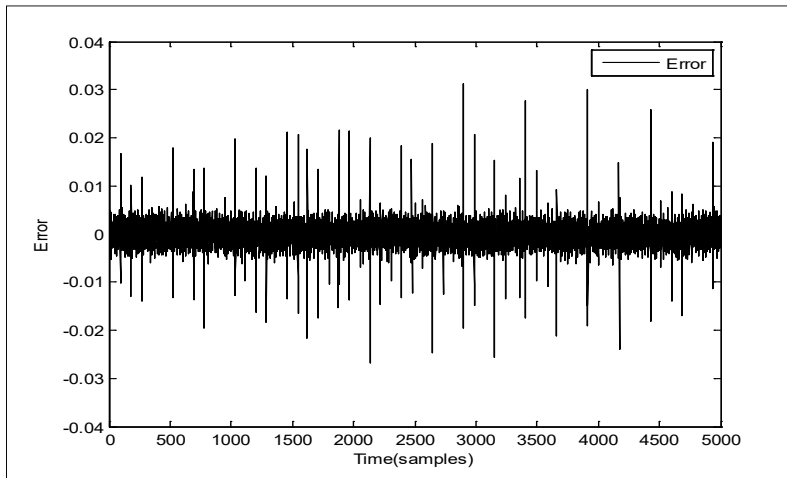


Figure 7. Calculated MSE between the experimental and CS model for flexible plate structure

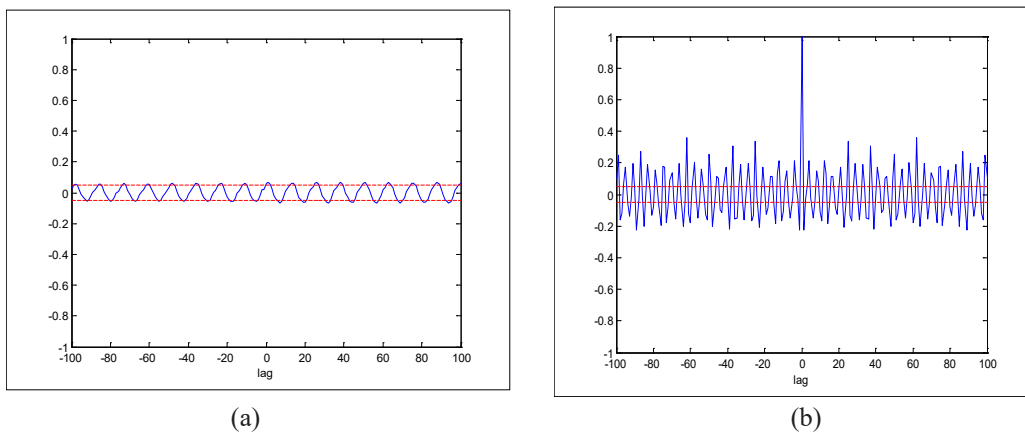


Figure 8. Correlation of the error for CS algorithm in (a) cross-correlation; (b) auto-correlation

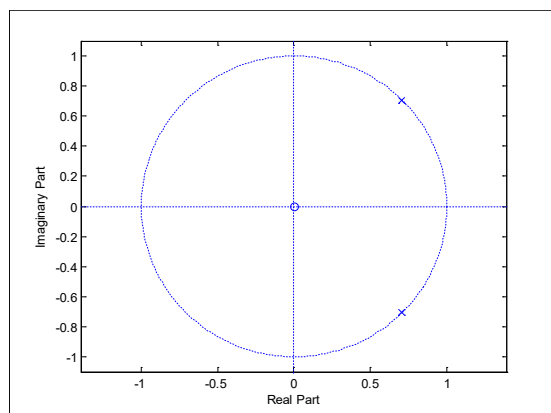


Figure 9. Pole-zero diagram

CONCLUSION

This paper presented an optimisation approach using a swarm intelligence algorithm via crow search for model development of horizontal flexible plate structure. The CS flow is described in detail to obtain an accurate system model. The developed model was validated using correlation analysis, mean squared error and pole-zero map. It is worth noting that the developed model utilising CS has performed well in predicting the system characteristics because it fulfilled all the validation requirements. Furthermore, the developed model achieved the lowest MSE, unbiased in the correlation test and stable in the pole-zero map. In addition, a comparison with previous studies shows that the CS algorithm is superior in modelling a horizontal flexible plate structure. Hence, the aim of this study to utilise the CS technique for the identification of a horizontal flexible plate structure is accomplished. The results achieved can be used to develop a robust and effective controller.

ACKNOWLEDGEMENTS

The authors want to express their gratitude to Universiti Teknologi MARA (UiTM), Universiti Teknologi Malaysia (UTM) and the Ministry of Higher Education (MOHE Malaysia) for funding the research and providing facilities to conduct this research. FRGS-RACER Grant with the sponsor file number (RACER/1/2019/TK03/UITM//1).

REFERENCES

- Adhi, A., Santosa, B., & Siswanto, N. (2018). A meta-heuristic method for solving scheduling problem: Crow search algorithm. In *Materials Science and Engineering* (pp. 1-6). IOP Publishing. <https://doi.org/10.1088/1757-899X/337/1/012003>
- Agarwal, H., & Agarwal, R. (2017). First industrial revolution and second industrial revolution: Technological differences and the differences in banking and financing of the firms. *Saudi Journal of Humanities and Social Sciences*, 5(4), 1062-1066.
- Aly, W. M. (2013). Evaluation of cuckoo search usage for model parameters estimation. *International Journal of Computer Applications*, 78(11), 1-6.
- Askarzadeh, A. (2016). A novel metaheuristic method for solving constrained engineering optimization problems: Crow search algorithm. *Computers and Structures*, 169, 1-12. <https://doi.org/10.1016/j.compstruc.2016.03.001>
- Eek, R. T. P., Darus, I. Z. M., Sahlan, S., Samin, P. M., & Shaharuddin, N. M. (2016). Implementation of swarm algorithm in modeling a flexible beam structure. *Journal of Vibroengineering*, 18(8), 4914-4934. <https://doi.org/10.21595/jve.2015.15182>
- Erkoc, M. E., & Karaboga, N. (2021). Sparse signal reconstruction by swarm intelligence algorithms. *Engineering Science and Technology-An International Journal-JESTECH*, 24(2), 319-330. <https://doi.org/10.1016/j.jestech.2020.09.006>

- Gheisarnejad, M. (2018). An effective hybrid harmony search and cuckoo optimization algorithm based fuzzy PID controller for load frequency control. *Applied Soft Computing*, 24(3), 121-138. <https://doi.org/10.1016/j.asoc.2018.01.007>
- Hadi, M. S., Darus, I. Z. M., & Yatim, H. M. (2013). Modeling flexible plate structure system with free-free-clamped-clamped (FFCC) edges using particle swarm optimization. In *2013 IEEE Symposium on Computers & Informatics* (pp. 39-44). IEEE Publishing. <https://doi.org/10.1109/ISCI.2013.6612372>
- Hadi, M. S., Darus, I. Z. M., Eck R. T. P., & Yatim, H. M. (2014). Swarm intelligence for modeling a flexible plate structure system with clamped-clamped-free-free boundary condition edges. In *2014 IEEE Symposium on Industrial Electronics & Applications (ISIEA)* (pp. 119-124). IEEE Publishing. <https://doi.org/10.1109/ISIEA.2014.8049883>
- Hadi, M. S., Hashim, M. H., & Darus, I. Z. M. (2012). Genetic modeling of a rectangular flexible plate system with free-free-clamped-clamped (FFCC) edges. In *2012 IEEE Conference on Control, Systems and Industrial Informatics (CCSII)* (pp. 173-179). IEEE Publishing. <https://doi.org/10.1109/CCSII.2012.6470496>
- Hou, X. (2018). A variable structural control for a flexible plate. *American Review of Mathematics and Statistics*, 6(2), 1-8. <https://doi.org/10.15640/arms.v6n2a1>
- Hussien, A. G., Amin, M., Wang, M., Liang, G., Alsanad, A., Gumaei, A., & Chen, H. (2020). Crow search algorithm: Theory, recent advances, and applications. *IEEE Access*, 8, 173548-173565. <https://doi.org/10.1109/ACCESS.2020.3024108>
- Islam, J., Vasant, P., Negash, B. M., Gupta, A., Watada, J., & Banik, A. (2020). Well placement of optimization using firefly algorithm and crow search algorithm. *Journal of Advanced Engineering and Computation*, 4(3), 181-195. <http://dx.doi.org/10.25073/jaec.202043.287>
- Jiang, H., Liu, T., He, P. H., Ding, Y. H., & Chen, Q. S. (2021). Rapid measurement of fatty acid content during flour storage using a color-sensitive gas sensor array: Comparing the effects of swarm intelligence optimization algorithms on sensor features. *Food Chemistry*, 338, Article 127828. <https://doi.org/10.1016/j.foodchem.2020.127828>
- Khairuddin, I. M., Dahalan, A. S., Abidin, A. F. Z., Lai, Y. Y., Nordin, N. A., Sulaiman, S. F., & Amer, N. H. (2014). Modeling and simulation of swarm intelligence algorithms for parameters tuning of PID controller in industrial couple tank system. *Advanced Materials Research*, 903, 321-326. <https://doi.org/10.4028/www.scientific.net/AMR.903.321>
- Kivi, M. E., & Majidnezhad, V. (2021). A novel swarm intelligence algorithm inspired by the grazing of sheep. *Journal of Ambient Intelligence and Humanized Computing*, 13, 1201-1213. <https://doi.org/10.1007/s12652-020-02809-y>
- Majhi, S. K., Sahoo, M., & Pradhan, R. (2020). A space transformational crow search algorithm for optimization problems. *Evolutionary Intelligence*, 13(3), 345-364.
- Mamuda, M., & Mukhtar, M. (2017). Formulation of renewable energy lubricants using antimony dialkyl dithio-carbonate and zinc dialkyl dithio-phosphate additives. *Nigerian Journal of Renewable Energy*, 17(1&2), 55-64.

- Matin, F., Cheraghi, H., Sobhani, N., Piltan, F., & Rahmani, M. (2016). Research on PID-based minimum rule base fuzzy controller in active joint dental automation. *International Journal of Grid and Distributed Computing*, 9(6), 315-338. <http://dx.doi.org/10.14257/ijgdc.2016.9.6.29>
- Ministry of Human Resource. (2021). *Fatal accident case*. Department of Occupational Safety and Health. <https://www.dosh.gov.my/index.php/fatal-accident-case>
- Mohajan, H. K. (2019). The first industrial revolution: Creation of a new global human era. *Journal of Social Sciences and Humanities*, 5(4), 377-387.
- Mohammed, M. J., Ahmed, M. K., & Abbas, B. A. (2019). Modeling and control of horizontal flexible plate using PID-CS controller. *Journal of Mechanical Engineering Research and Developments (JMERC)*, 24(4), 138-142. <http://dx.doi.org/10.26480/jmerd.04.2019.138.142>
- Nagendramma, P., & Kaul, S. (2012). Development of ecofriendly/biodegradable lubricants: An overview. *Renewable and Sustainable Energy Reviews*, 16(1), 764-774. <https://doi.org/10.1016/j.rser.2011.09.002>
- Nayak, A., & Singh, M. (2015). Study of tuning of PID controller by using particle swarm optimization. *International Journal of Advanced Engineering Research and Studies*, 2015, 346-350.
- Okiy, S., Okeye, C. C. N., & Igboanugo, A. C. (2015). Transfer function modelling: A literature survey. *Research Journal of Applied Sciences, Engineering and Technology*, 11(11), 1265-1279.
- Pedro J. O., & Tshabalala T. (2015). Hybrid NNMPD/PID control of a two-link flexible manipulator with actuator dynamics. In *10th Asian Control Conference (ASCC)* (pp. 1-6). IEEE Publishing. <https://doi.org/10.1109/ascc.2015.7244737>
- Rao, V. S., George, V. I., Kamath, S., & Shreesha, C. (2016). Performance evaluation of reliable H infinity observer controller with robust PID controller designed for TRMS with sensor, actuator failure. *Far East Journal of Electronics and Communications*, 16(2), 355-380. <http://dx.doi.org/10.17654/EC016020355>
- Souza, R. C., Coelho, L. D., Macedo, C. A., & Pierezan, J. (2018). A v-shaped binary crow search algorithm for feature selection. In *2018 IEEE Congress on Evolutionary Computation (CEC)* (pp. 1-8). IEEE Publishing. <https://doi.org/10.1109/CEC.2018.8477975>
- Tavakolpour, A., Mailah, M., & Darus, I. Z. M. (2011). Modeling and simulation of a novel active vibration control system for flexible structures. *WSEAS Transactions on Systems and Control*, 5(6), 184-195.
- Tsipianitis, A., & Tsompanakis, Y. (2021). Optimizing the seismic response of base-isolated liquid storage tanks using swarm intelligence algorithms. *Computers & Structures*, 243, Article 106407. <https://doi.org/10.1016/j.compstruc.2020.106407>
- Visioli, A. (2012). Research trends for PID controller. *ACTA Polytechnica*, 52(5), 144-150.
- Yatim, H. M., Darus, I. Z. M., & Hadi, M. S. (2013). Particle swarm optimization for identification of a flexible manipulator system. In *IEEE Symposium on Computers & Informatics* (pp. 112-117). IEEE Publishing. <https://doi.org/10.1109/ISCI.2013.6612386>



Physical and Electrical Breakdown Characteristics of Oil-Impregnated Kenaf Paper with the Introduction of External PVA for Transformer Application

Muhammad Umair¹, Norhafiz Azis^{1,2*}, Rasmina Halis³ and Jasronita Jasni¹

¹Advanced Lightning, Power and Energy Research Centre (ALPER), Faculty of Engineering, Universiti Putra Malaysia, 43400 UPM, Serdang, Selangor, Malaysia

²Institute of Nanoscience and Nanotechnology (ION2), Universiti Putra Malaysia, 43400 UPM, Serdang, Selangor, Malaysia

³Department of Natural Resource Industry, Faculty of Forestry and Environment, Universiti Putra Malaysia, 43400 UPM, Serdang, Selangor, Malaysia

ABSTRACT

This work examines the physical and electrical breakdown characteristics of kenaf paper coated with Polyvinyl Alcohol (PVA) for application in power transformers. The paper was made from kenaf bast fibers using the soda pulping method, whereby the pulps were subjected to 12,000 beating revolutions. PVA with weight percentage concentration up to 6% was introduced to the beaten kenaf through a spin coating approach. The structure of the kenaf paper was examined through Scanning Electron Microscopy (SEM). The physical properties examined were apparent density, Tensile Index (TI), Burst Index (BI), and Tear Index (TeI), while AC breakdown voltage and strength were analyzed for the electrical property. It is found that the beating and external PVA improve the kenaf paper's apparent density, TI, BI, and AC breakdown strength while the TeI decreases.

Keywords: Kenaf paper, physical and electrical properties, PVA coating

ARTICLE INFO

Article history:

Received: 15 April 2022

Accepted: 05 July 2022

Published: 20 March 2023

DOI: <https://doi.org/10.47836/pjst.31.2.22>

E-mail addresses:

umair9926@gmail.com (Muhammad Umair)

norhafiz@upm.edu.my (Norhafiz Azis)

jas@upm.edu.my (Jasronita Jasni)

rasmina@upm.edu.my (Rasmina Halis)

* Corresponding author

INTRODUCTION

Kraft paper has been used as electrical insulation material in power transformers for years due to its high mechanical and electrical strengths (Mathes, 1991). Kraft paper is made from wood fibers, which produce strong paper. Due to recent environmental concerns about extensive deforestation, alternative resources such as

non-wood fibers are utilized for paper production (Hammett et al., 2001; Kamoga et al., 2013). Fibers such as cotton, manila, hemp, and flax are also utilized to produce papers for electrical insulation (Krause, 2012; Schaible, 1987). Currently, the application of kenaf fibers for electrical insulation is still limited.

Kenaf bast has long fibers that can produce high-strength papers and can be used as electrical insulation in transformers (Umair et al., 2019). Among kraft paper's important characteristics is its ability to retain its strength properties after oil impregnation (Lundgaard et al., 2008). Tensile, burst, and AC breakdown strength characterize kraft paper's mechanical and electrical strengths (Feng et al., 2020; Li et al., 2016). The beating process or chemical treatment can improve a paper's mechanical and electrical properties (Brännvall, 2009; Song et al., 2009). For example, the beating process on pulps improves a paper's mechanical and electrical strengths through fibrillation. On the other hand, chemical treatment can also enhance mechanical and electrical properties by introducing additives (Edeerozey et al., 2007; Wistara & Young, 1999). The most common chemical additives that can enhance a paper's strength are oxidized/natural starches, cationic starches, soluble cellulose derivatives, and synthetic/natural polymers (Auhorn, 2006). Polyvinyl Alcohol (PVA) is a synthetic polymer soluble in water, and it can be used for the chemical treatment of paper. It is biodegradable, non-toxic, and chemically stable. It has high mechanical strength and adhesive properties, which lead to its suitability for a wide range of applications.

The combination of cellulose and PVA can improve the intermolecular and intramolecular hydrogen bonds due to the high concentration of hydroxyl groups, thereby increasing paper strength (Abdulkhali et al., 2013; Moore et al., 2012; Shokrieh et al., 2015; Finch, 2002; Zhang et al., 2019). In addition, the hydrogen bonds can increase the paper's mechanical and electrical strengths (Bao et al., 2011; Medhekar et al., 2010). PVA can be introduced into cellulose internally before the formation of paper or externally after the paper has been produced. The introduction of PVA internally increases paper's mechanical strength by enhancing the hydrogen bonding among fibers. External application of PVA increases the mechanical strength through an extra thin layer of barrier on the surface of a paper. The external PVA can be applied by using the PVA coating process.

PVA coating is the process of external PVA application on the surface of the paper to improve the paper's properties (Schuman et al., 2004). PVA is applied on the paper surface to cement the fibers together and deposit a continuous thin film layer. Electrostatic or non-electrostatic interaction bonds the thin film to the cellulose substrate, which improves a paper's mechanical and electrical properties (Hubbe, 2006). Spin coating is one of the several methods to perform PVA coating. It is a process of depositing coating solution to a horizontal spinning disc through centrifugal force, which results in the removal and evaporation of the solvent and the emergence of a uniform solid film on the surface of the

paper (Norrman et al., 2005). PVA can improve the barrier properties of paper, improving the mechanical strength (Schuman et al., 2003, 2004). The PVA coating process is normally used for writing, printing, food, and paper packaging (Schuman et al., 2003). In addition, it can also improve moisture and heat resistance as a result of barrier properties improvement (Edeerozey et al., 2007). The addition of a 10% weight percentage concentration of PVA to cellulose can increase the thermal resistance of paper up to 5% (Nuruddin et al., 2015; Yenidoğan, 2019). Currently, using a polymer such as PVA to improve the mechanical and electrical strengths of kenaf bast fiber-based paper for electrical insulation purposes is still not widely examined.

In this paper, the kenaf paper is developed using the soda pulping technique with 12,000 beating revolutions. The external PVA is applied externally to the kenaf paper through the spin coating approach. The kenaf paper with external PVA weight percentage concentrations of 2%, 4%, and 6% are examined for Tensile Index (TI), Burst Index (BI), and Tear Index (TeI). The oil-impregnated kenaf paper is also prepared to determine AC breakdown voltage and strength.

MATERIALS AND METHODS

Development of Kenaf Paper

The development process of kenaf's paper with the introduction of external PVA is shown in Figure 1. First, kenaf bast fibers were sourced locally, whereby the fiber threads were thoroughly cleaned and screened to remove dust and grime before being cut into 10 cm. In total, 1 kg of raw fibers was prepared through Oven Dry (OD) method. Then, soda pulping was performed whereby the concentration of Sodium Hydroxide (NaOH) was set

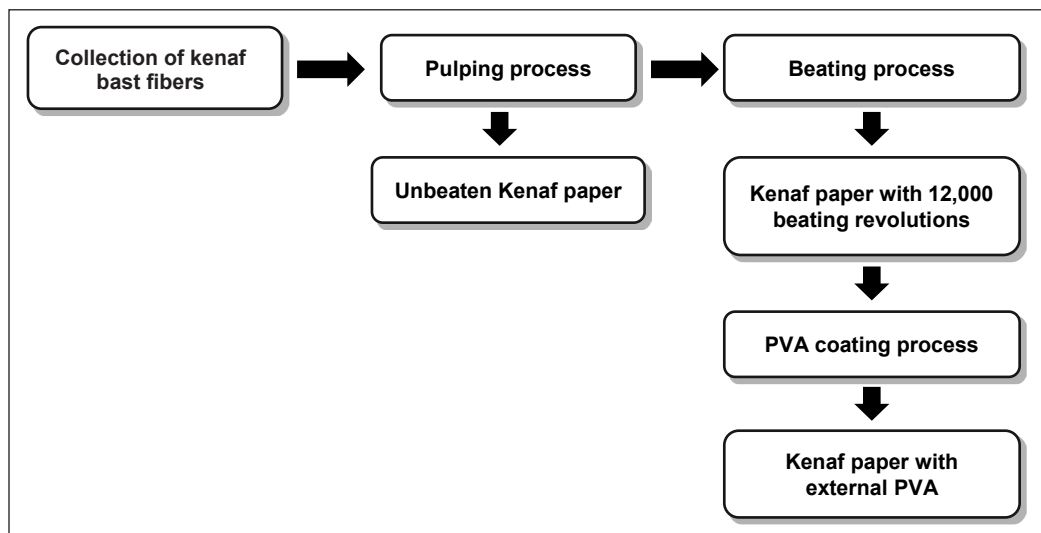


Figure 1. The process to develop Kenaf paper with external PVA

to 14% with the liquor: wood ratio set to 7:1. The liquor is a mixture of NaOH and water. Finally, the raw fibers were cooked in the rotary digester for the soda pulping process. First, the temperature of the rotary digester was set to 35°C with a pressure of 140 psi. The temperature required 90 minutes to reach the maximum set point of 170°C, and it was maintained for 30 minutes during the soda pulping process.

The pulp and paper without the beating process were defined as unbeaten kenaf's pulp and paper. The pulp was subjected to the beating process of up to 12,000 beating revolutions according to the Technical Association of the Pulp and Paper Industry (TAPPI) standard T248. The freeness of the pulp was measured as per TAPPI standard T227. After the beating process, the kenaf paper was formed on the paper machine according to the TAPPI standard T205. The grammage of kenaf paper after the process was 52 g/m². Next, the PVA coating was applied on the kenaf paper with 12,000 beating revolutions.

Preparation of PVA Solution

The PVA solution was prepared before the coating process, with weight percentage concentrations set to 2%, 4%, and 6% using Equation 1. The solution was prepared using Fisher Scientific Isotemp heated magnetic stirrer. First, the PVA powder was added to 100 ml of distilled water at a temperature of 90°C using the magnetic stirrer for 2 hours to produce a uniform PVA solution, as seen in Figure 2. Next, the solution was left to cool for 2 hours in a cleanroom at the temperature of 25°C ± 2°C and relative humidity of 25% ± 2%. Next, the PVA solution was applied to the kenaf paper with 12,000 beating revolutions.

$$PVA\ concentration\ (\%) = \frac{Weight\ of\ PVA\ (g)}{Volume\ of\ water\ (ml)} \times 100 \quad (1)$$

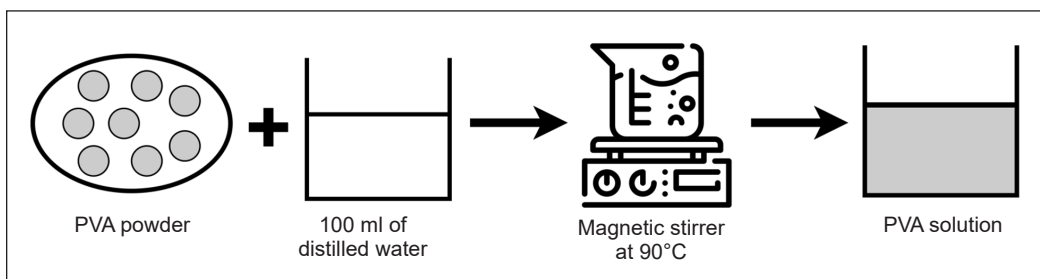


Figure 2. Preparation of PVA solution

PVA Coating Procedure

The spin coating on the kenaf paper was performed by spin coater POLOS SPIN150i as shown in Figure 3. The spin coater consists of a single-phase oil-less piston vacuum pump MAJP-140V(L) with maximum vacuum and power of 60 torrs and 0.41 kW, respectively.

The vacuum pump was used to hold the substrate before the spin coating was performed. The test was performed in a cleanroom at a temperature of $25^{\circ}\text{C} \pm 2^{\circ}\text{C}$ and relative humidity of $25\% \pm 2\%$. The spin coater's rotation speed and time were set to 2,000 rpm and 60 seconds, respectively. A total of 3 ml of PVA solution was dropped at the center of kenaf paper using a syringe while the spin coater was in operation under the influence of centrifugal forces. The procedure was repeated for all weight percentage concentrations of PVA.

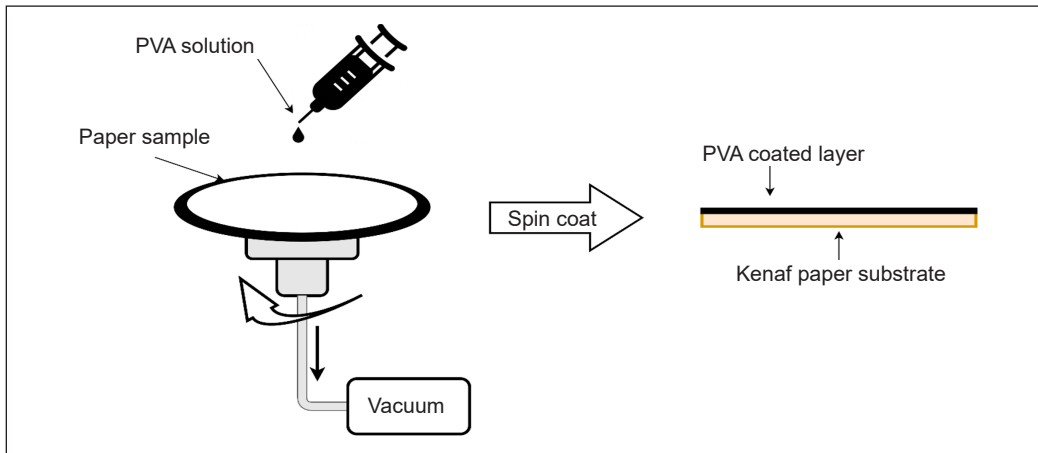


Figure 3. PVA coating process

EXPERIMENTAL SETUP

Physical and Morphological Properties of Paper

The papers were cut into $10\text{ cm} \times 10\text{ cm}$ squares to determine the grammage of the paper. Equation 2 was used to determine the grammage of the paper based on the mass and area of the paper. The mass of the paper was determined using an OHAUS analytical balance with a sensitivity of $\pm 0.0001\text{g}$. Equation 3 was used to determine the apparent density of the paper. An L&W micrometer was used to measure the thickness of the paper as per TAPPI standard T411. The coating weight was determined based on differences in grammage between coated and uncoated kenaf papers (Afra et al., 2016; Ni et al., 2021).

$$\text{Grammage (g/m}^2\text{)} = \frac{\text{Mass (g)}}{\text{Area (m}^2\text{)}} \quad (2)$$

$$\text{Apparent density (g/cm}^3\text{)} = \frac{\text{Grammage (g/m}^2\text{)}}{\text{Thickness (\mu m)}} \quad (3)$$

The surface morphology of kenaf paper with beating revolutions and external PVA was observed using SEM imaging through COXEM EM-30ax. Oil-impregnated papers

were cleaned with acetone to remove oil and dried in the air-circulating oven for 24 hours at 105°C to negate the effect of moisture on the image quality. An ion coater, COXEM SPT-20, was used to prepare the paper to avoid the charging effect on the image.

Tensile, Burst, and Tear Indexes of Paper

The measurement of the tensile strength of kenaf paper was carried out using Buchel B.V horizontal tensile tester as per TAPPI standard T494. The gap between the 2 clamps was adjusted to 100 mm ± 1 mm. The length and width of the paper under test were 150 mm and 15 mm. The crosshead speed of 20 mm/s was used for the tensile strength measurement. The test was performed at a temperature of 23°C ± 1°C and relative humidity of 50% ± 2%. The TI was determined based on Equation 4.

$$TI (Nm/g) = \frac{\text{Tensile strength (N/m)}}{\text{Grammage (g/m}^2\text{)}} \quad (4)$$

The burst strength measurement of kenaf paper was carried out using a Frank burst machine as per TAPPI standard T403. The paper was cut into length and width of 62 mm × 62 mm. The test was performed at the same temperature and relative humidity conditions as tensile strength. The clamping pressure was set to less than 1,200 kPa. The pressure was subjected to the paper via a rubber diaphragm to a 30.5 mm circular area. The BI was calculated based on Equation 5.

$$BI (kPa.m^2/g) = \frac{\text{Burst strength (kPa)}}{\text{Grammage (g/m}^2\text{)}} \quad (5)$$

The tear strength refers to the amount of energy necessary to shred the paper. The tear strength measurement of kenaf paper was performed using an Elmendorf tearing tester based on TAPPI T414. The paper was cut into length and width of 63 mm × 50 mm. The test was performed at the same temperature and relative humidity conditions as tensile strength. Identical clamping pressures of 0.55 MPa were subjected to the clamps that held the paper. A small cut was made at the center of the paper before the tearing force was applied. The TeI was calculated based on Equation 6.

$$TeI (mN.m^2/g) = \frac{\text{Tear strength (mN)}}{\text{Grammage (g/m}^2\text{)}} \quad (6)$$

Preparation of the Oil-Impregnated Paper

The kenaf and kraft papers were impregnated in Mineral Oil (MO) to determine the AC breakdown voltage and strength based on the process, as shown in Figure 4. First, the

paper was vacuum drying for 48 hours at 105°C and 0.08 kPa. On the other hand, MO was subjected to air-circulating drying for 48 hours at 85°C. Next, the paper was impregnated with MO in a vacuum oven for 24 hours at 105°C and 0.08 kPa.

Measurement of AC Breakdown Strength of Paper

The measurement of AC breakdown voltage was carried out using BAUR DPA 75 C tester, according to International Electrotechnical Commission (IEC) 60156. The test was performed using spherical electrodes with both sides facing each other. The diameter of the spherical electrode was set to 12.5 mm. The walls of the test cell and electrodes were thoroughly rinsed 3 times using MO. In total, 400 ml of MO was gently filled into the test cell to avoid the formation of bubbles. The distance between electrodes inside the test cell was adjusted based on the thickness of the paper (Figure 5). Since the thickness of 1 layer of kenaf paper was low, the measurement could not be computed. Therefore, 2 and 3 layers of kenaf and kraft papers were used to measure the AC breakdown voltage. The voltage ramping rate was set to 2 kV/s. During the test, the paper was moved to a new position after each breakdown. An average of 20 AC breakdown voltages data was utilized for the study. The AC breakdown strength of the oil-impregnated kenaf paper was calculated based on Equation 7.

$$AC \text{ breakdown strength (kV/mm)} = \frac{AC \text{ breakdown voltage (kV)}}{\text{Thickness of paper (mm)}} \quad (7)$$

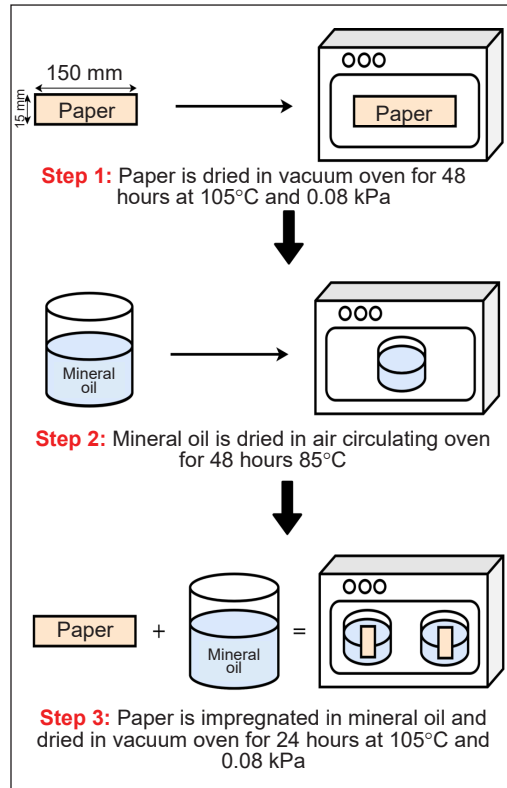


Figure 4. Preparation of oil-impregnated paper

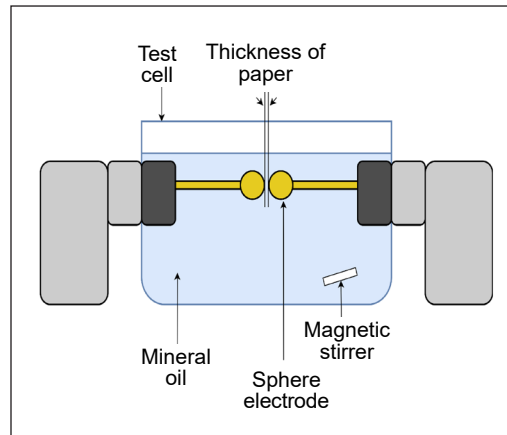


Figure 5. Configuration of AC breakdown measurement

EXPERIMENTAL RESULTS

Impact of External PVA on Kenaf Fiber

The SEM images of kenaf papers with and without beating revolutions and with external PVA are shown in Figure 6. The kenaf paper, without beating revolutions, shows a clear network of fibers joining together to create a strong bond with each other. The pores in unbeaten kenaf paper are visible, which can promote the flow of MO, as seen in Figure 6(a). There is no fibrillation to the kenaf fibers due to the absence of mechanical and chemical treatments. Fibrillation occurs once the beating to the pulp is applied, as shown in Figure 6(b). Several fibrils on the wall of fiber cells can stimulate bonding and increase the apparent density and mechanical strength. After applying PVA, the fibrillary bridges are improved, and new bonding with fibers and fibrils are formed, which can lead to the increment of the paper strength, as seen in Figure 6(c).

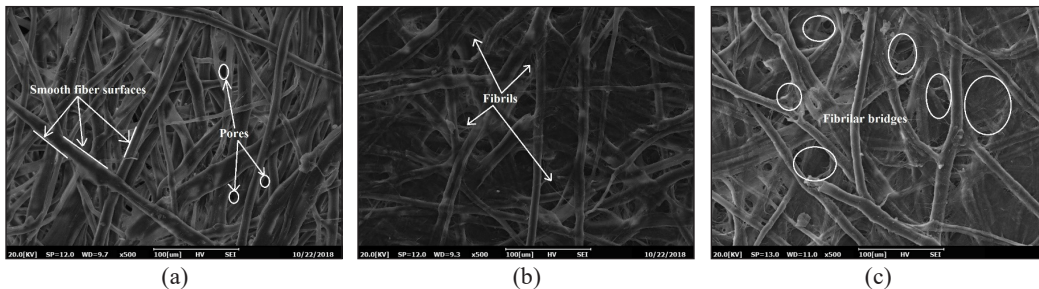


Figure 6. SEM images of Kenaf paper at a magnification of $\times 500$: (a) Unbeaten Kenaf paper; (b) With 12,000 beating revolutions; (c) With 12,000 beating revolutions and 6% weight percentage concentration of PVA

The Relationship of Coating Weight with PVA Weight Percentage Concentration

The apparent density of kenaf paper increases as the coating weight of PVA increases, as seen in Figure 7. Kenaf paper with 0% PVA weight percentage concentration is referred to as kenaf paper with 12,000 beating revolutions. The coating weight increases linearly at a rate of $0.68 \text{ g/m}^2 \pm 0.02 \text{ g/m}^2$. The grammage increases as the coating weight increases, which leads to the increment of the apparent density

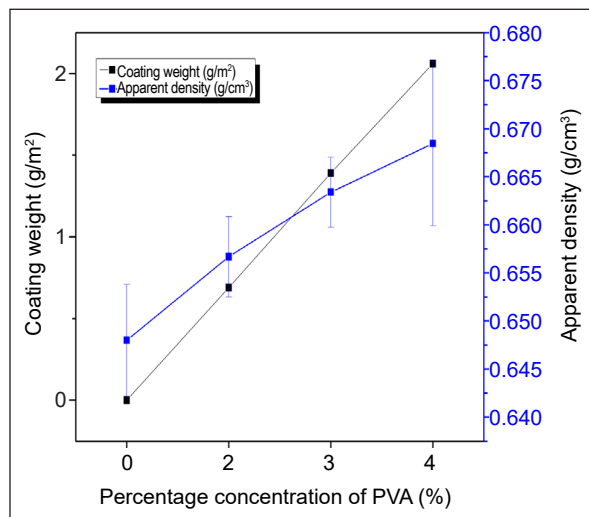


Figure 7. Coating weight and apparent density versus PVA weight percentage concentration

of kenaf paper (Huber et al., 2012). The apparent density of kenaf paper increases by 3% with the introduction of a 6% PVA weight percentage concentration.

Impact of External PVA on Tensile, Burst, and Tear Indexes

The TI of unbeaten kenaf paper is 27.41 Nm/g. It is observed that TI increases almost linearly as the PVA weight percentage concentration increases (Figure 8). The TI of kenaf paper improves by 6%, 8%, and 12% with 2%, 4%, and 6% PVA weight percentage concentrations. The TI of kenaf paper with 6% PVA weight percentage concentration is 81.36 Nm/g, which is 28% lower than the TI of kraft paper. The TI of kenaf paper increases due to the increment of inter-fiber bonding between fibers caused by the presence of the external PVA (Balan et al., 2015).

It is observed that the BI of unbeaten kenaf paper is 1.45 kPa, increasing to 4.59 kPa with 12,000 beating revolutions. The BI of kenaf paper increases as the PVA weight percentage concentration increases, as seen in Figure 9. The BI of kenaf paper increases by 39% with a 2% PVA weight percentage concentration. The increments for BI of kenaf paper with 4% and 6% PVA weight percentage concentrations are quite low. The highest increment for BI of kenaf paper is found at 6% PVA weight percentage concentration, which increases by 51%.

It is observed that the TeI of kenaf paper decreases as the external PVA increases, as shown in Figure 10. The TeI of kenaf paper decreases by 3%, 12%, and 21%, with 2%, 4%, and 6% PVA weight percentage concentration, respectively. Once the inter-fiber bonding exceeds a certain threshold, the TeI of paper normally decreases. It is because high inter-fiber bonding can lead to the brittleness of paper, which causes fracture in a narrow region. As a result, it does not consume high tearing energy, resulting in a lower TeI of paper

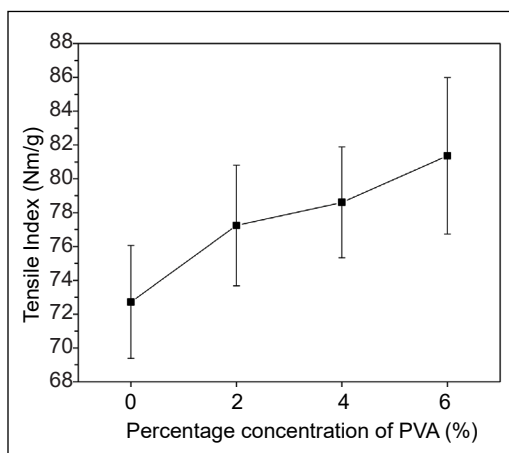


Figure 8. Tensile Index versus PVA weight percentage concentration

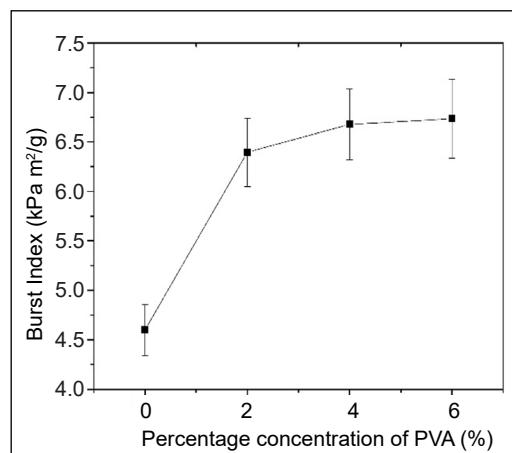


Figure 9. Burst Index versus PVA weight percentage concentration

(Karlsson, 2010). The phenomenon can also lead to the partial dissolution of cellulosic material and affects the TeI of kenaf paper.

Impact of External PVA on AC Breakdown Strength

The AC breakdown voltage of MO-impregnated kenaf paper in the presence of external PVA is shown in Figure 11. The unbeaten kenaf paper has a lower AC breakdown voltage than the kenaf paper, with 12,000 beating revolutions for 2 and 3 layers. It is found that the AC breakdown voltage of both types of paper increases as the layer number increases.

The pattern is expected since the gap distance increases with the increment of paper thickness, which results in the increment of AC breakdown voltage. The AC breakdown voltage for the 2 layers of kenaf paper remains constant with the increment of PVA weight percentage from 2% to 4%. However, it increases with the increment of the PVA weight percentage to 6%. For 3 layers of kenaf paper, the AC breakdown voltage steadily increases with the external PVA. The highest increment of kenaf paper AC breakdown voltage is observed at 6% PVA weight percentage concentration, which increases by 44% and 72% for 2 and 3 layers, respectively.

The AC breakdown strength of MO-impregnated kenaf paper in the presence of external PVA is shown in Figure 12. The AC breakdown strength is the lowest for unbeaten kenaf paper, and it increases as the external PVA increases. The highest increment of AC

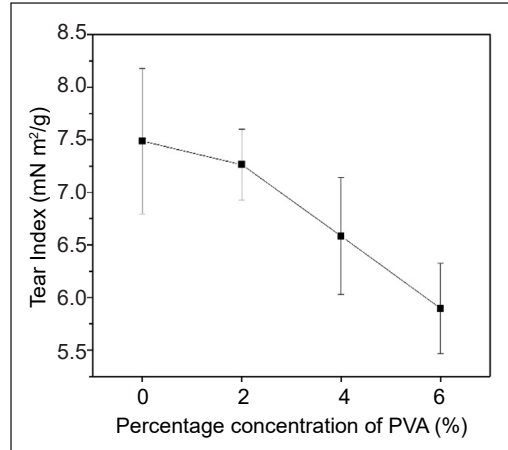


Figure 10. Tear Index versus PVA weight percentage concentration

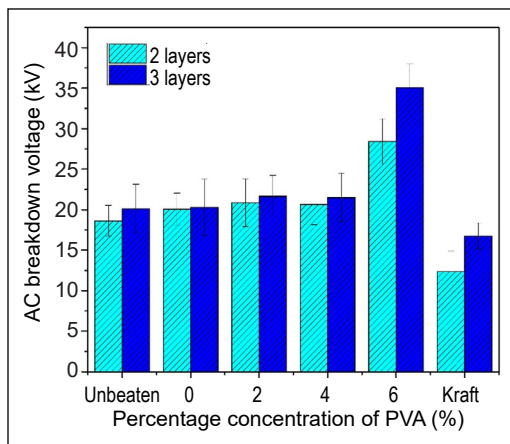


Figure 11. AC breakdown voltage of 2 and 3 layers of Kenaf paper with external PVA

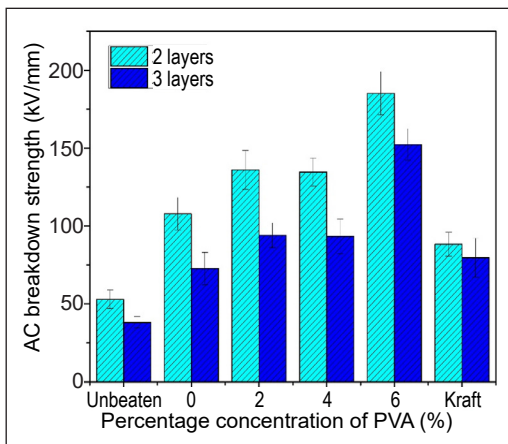


Figure 12. AC breakdown strength of 2 and 3 layers of Kenaf paper with external PVA

breakdown strength is observed at 6% PVA weight percentage concentration, with 74% and 108% increments for 2 and 3 layers of kenaf paper. The AC breakdown strength of kenaf paper in the presence of external PVA is higher than kraft paper.

Effect of Electrical Stress on Kenaf Fiber

The effect of electrical stress on the fiber networks of oil-impregnated kenaf and kraft paper after the AC breakdown voltages can be observed using SEM imaging, as shown in Figure 13. The clear hole is produced through the fiber networks after the AC breakdown test due to the vaporization of fibers under electrical stress.

The AC breakdown strength improves with the decrement of pore size inside the kenaf fiber network (Kamata et al., 1990; Liu et al., 2016). The diameters of the hole caused by electrical breakdown are less than 200 μm for both kenaf and kraft papers. The images obtained by SEM exhibit differences at the edges of the holes for kenaf and kraft papers. The edges of the holes are smooth in kraft paper, whereas it is uneven in kenaf paper with 12,000 beating revolutions and 6% PVA weight percentage concentration. The diameters of the hole after breakdowns in kenaf papers are between 151.1 μm and 155.7 μm , while the diameter of the hole in kraft paper is around 111 μm . There is no clear conclusion that can be carried out to compare the relationship between the diameter of the hole and the AC breakdown strength of kenaf and kraft papers.

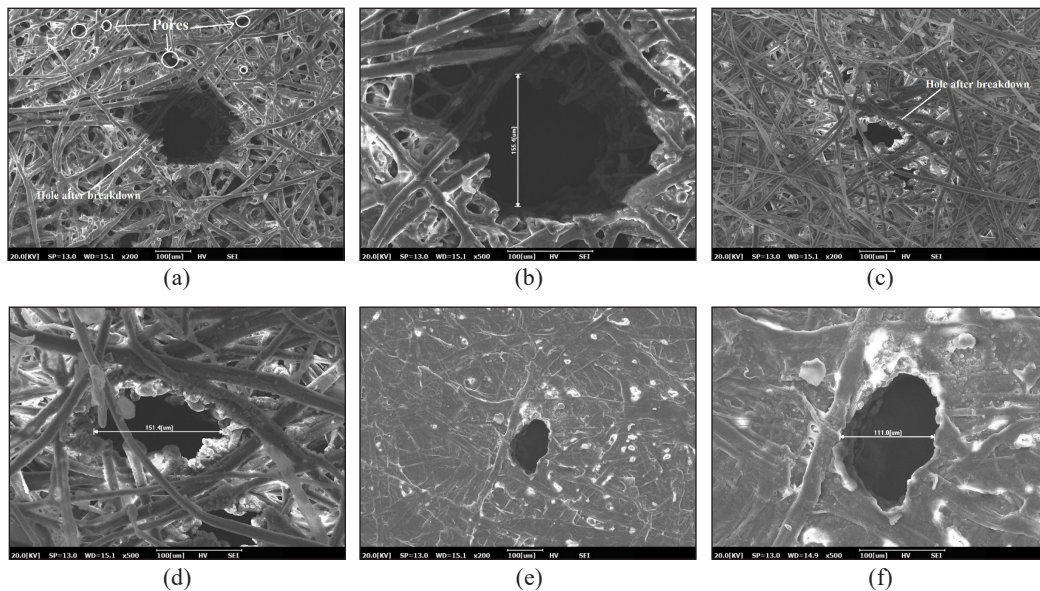


Figure 13. SEM image of oil-impregnated Kenaf paper after the AC breakdown strength measurement: (a) With 12,000 beating revolutions at a magnification of $\times 200$; (b) With 12,000 beating revolutions at a magnification of $\times 500$; (c) With 12,000 beating revolutions and 6% PVA weight percentage concentration at a magnification of $\times 200$; (d) With 12,000 beating revolutions and 6% PVA weight percentage concentration at a magnification of $\times 500$; (e) Kraft paper at a magnification of $\times 200$; (f) Kraft paper at a magnification of $\times 500$.

DISCUSSION

A paper is a dielectric material where an electric field may be maintained with either zero or near-zero power dissipation, whereby only a few electrons can move on the surface (McShane et al., 2003; Qu et al., 2020). AC breakdown strength of paper is an intrinsic property of dielectric material, independent of the electrode configuration where the electric stress is applied (Amin et al., 2018; Ramli et al., 2014; Zhou & Chen, 2017). The minimum voltage at which the dielectric material fails is known as AC breakdown voltage (Baur et al., 2017; Elanseralathan et al., 2000).

The beating process initiates the fibrillation process and decreases the number of pores. The application of external PVA further decreases pore number, as shown in Figure 6. The porosity and pore size distribution can affect the apparent density of a paper (Gao et al., 2015). It is found that the increment of PVA coating weight increases the apparent density of paper (Figure 7). The increment of apparent density could be due to the reduction of pores in the paper. The AC breakdown behavior is also affected by the fibers' properties and the paper's porous structure (Mo et al., 2019). It is found that the AC breakdown strength of kenaf paper has a positive correlation with fibrillation in fibers since the AC breakdown strength increases with beating and external PVA (Figure 12). The fibrillation process increases the fibrils on the surface of the fibers and reduces the pores in the paper (Wai et al., 1985). The dry-strength additive in the paper structure improves the strength properties through the improvement of the inter-fiber bonding (Balan et al., 2015). The improvement of TI due to external PVA could be caused to the migration of PVA into the internal structure of the paper (Balan et al., 2015). This phenomenon can reduce the number of pores and increase the AC breakdown strength of paper. The reduction of inter-fiber bonding caused by repeated wetting and drying during the coating process is one of the factors that affect the mechanical strength of paper (Balan et al., 2015). Therefore, it is important to control these parameters to further improve the strength properties of kenaf paper with external PVA.

The AC breakdown strength for 2 layers of kenaf paper increases by 74%, resulting in an increment of 12% in TI, as shown in Figure 14. The apparent density of kenaf paper is found to increase to 0.67 g/cm³ with a 6% PVA weight percentage concentration. The AC breakdown strength is 191.41 kV/mm for 2 layers of kenaf paper with a 6% PVA weight percentage concentration. The increment of apparent density also leads to

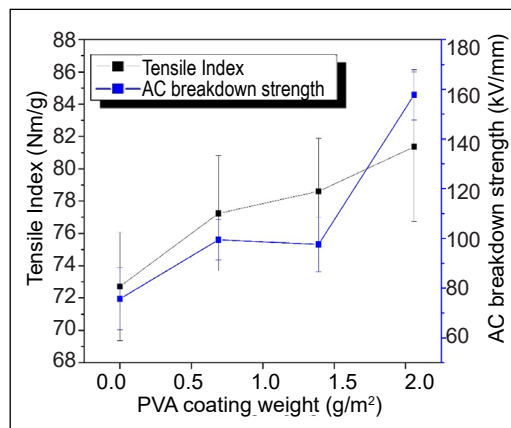


Figure 14. The relationship between AC breakdown strength and TI with PVA coating weight.

the increment of the BI of the kenaf paper (Umair et al., 2019). Since cellulose and PVA both contain hydroxyl groups, it increases hydrogen bonding, which leads to the increment of the BI of kenaf paper.

The physio-mechanical and electrical breakdown properties of kenaf paper with internal and external PVA are summarized in Table 1. External PVA has a better impact on the physio-mechanical properties of kenaf paper than internal PVA, even at low percentage concentrations. The apparent density of kenaf paper with 6% external PVA is 28% higher than the 12% internal PVA, but it is still 9% lower than kraft paper. On the other hand, the TI and BI of kenaf paper with external PVA are 10% and 31% higher than internal PVA. Kenaf paper's AC breakdown voltage and strength with external PVA is 50% higher than internal PVA.

Table 1

Comparison of physical and electrical breakdown characteristics of kenaf paper with internal and external PVA

Property	Kenaf paper				Kraft paper
	Unbeaten	With 12,000 beating revolutions	With 12% internal PVA (Umair et al., 2020)	With 6% external PVA	
Apparent density (g/cm ³)	0.35	0.648	0.522	0.67	0.74
Tensile Index (Nm/g)	27.41	72.72	74.1	81.36	113
Burst Index (kPa.m ² /g)	1.45	4.47	5.12	6.73	-
Tear Index (mN.m ² /g)	16.52	7.49	6.67	5.89	-
AC breakdown voltage (kV)	21.045	21.11	26.54	36.30	17.605
AC breakdown strength (kV/mm)	39.88	75.67	89.37	157.76	83.83

It is well known that adding enhancement materials can improve paper's mechanical and electrical strengths (Umair et al., 2020). In this study, PVA is one of the enhancement materials that can enhance kenaf paper's physiomechanical and electrical breakdown characteristics for application as electrical insulation in transformers. In comparison to internal PVA, external PVA has positive impacts on the apparent density, TI, BI, and AC breakdown strength of kenaf paper.

CONCLUSION

The external PVA increases kenaf paper's TI, BI, and AC breakdown strength. The TI and BI of kenaf paper increase by 165% and 208% with 12,000 beating revolutions, and these parameters further increase by 12% and 51% with 6% PVA weight percentage concentration. On the other hand, the TeI of kenaf paper decreases by 55% with 12,000 beating revolutions and decreases by 21% with a 6% PVA weight percentage concentration. Furthermore, the kenaf paper has 102% and 90% AC breakdown strengths increments with

12,000 beating revolutions for 2 and 3 layers of kenaf paper. Further increments of 74% and 108% are found with 6% PVA weight percentage concentration for the same number of layers. The external PVA improves kenaf paper's mechanical and AC breakdown strength properties, possibly due to the reduction of the number of pores and increment of the inter-fiber bonding among fibers.

ACKNOWLEDGMENTS

The authors express sincere gratitude to the Ministry of Higher Education for the funding provided for this study under the FRGS scheme of FRGS/1/2019/TK07/UPM/02/3 (03-01-19-2071FR).

REFERENCES

- Abdulkhani, A., Hojati Marvast, E., Ashori, A., Hamzeh, Y., & Karimi, A. N. (2013). Preparation of cellulose/polyvinyl alcohol biocomposite films using 1-n-butyl-3-methylimidazolium chloride. *International Journal of Biological Macromolecules*, 62, 379-386. <https://doi.org/10.1016/j.ijbiomac.2013.08.050>
- Afra, E., Mohammadnejad, S., & Saraeyan, A. (2016). Cellulose nanofibils as coating material and its effects on paper properties. *Progress in Organic Coatings*, 101, 455-460. <https://doi.org/10.1016/j.porgcoat.2016.09.018>
- Amin, N. A. M., Ishak, M. T., & Md Din, M. F. (2018). *AC breakdown voltage and partial discharge of palm oil as insulating liquid with the presence of cellulose particles*. [Paper presentation]. IEEE 7th International Conference on Power and Energy (PECon), Kuala Lumpur, Malaysia. <https://doi.org/10.1109/PECON.2018.8684062>
- Auhorn, W. J. (2006). Chemical additives. In H. Holik (Ed.), *Handbook of Paper and Board* (pp. 62-149). Wiley. <https://doi.org/10.1002/3527608257.ch3>
- Balan, T., Guezennec, C., Nicu, R., Ciolacu, F., & Bobu, E. (2015). Improving barrier and strength properties of paper by multi-layer coating with bio-based additives. *Cellulose Chemistry and Technology*, 49(8), 607-615.
- Bao, C., Guo, Y., Song, L., & Hu, Y. (2011). Poly (vinyl alcohol) nanocomposites based on graphene and graphite oxide: A comparative investigation of property and mechanism. *Journal of Materials Chemistry*, 21(36), 13942-13950. <https://doi.org/10.1039/c1jm11662b>
- Baur, M., Knauel, J., Calcara, L., & Pompili, M. (2017). *Insulating liquids breakdown voltage determination: Test method efficiency*. [Paper presentation]. 2017 IEEE 19th International Conference on Dielectric Liquids (ICDL), Manchester, United Kingdom. <https://doi.org/10.1109/ICDL.2017.8124657>
- Brännvall, E. (2009). Overview of pulp and paper processes. In M. Ek, G. Gellerstedt & G. Henriksson (Eds.), *Pulping Chemistry and Technology* (pp. 1-13). Walter de Gruyter. <https://doi.org/10.1515/9783110213423>
- Edeerozey, A. M. M., Akil, H. M., Azhar, A. B., & Ariffin, M. I. Z. (2007). Chemical modification of kenaf fibers. *Materials Letters*, 61(10), 2023-2025. <https://doi.org/10.1016/j.matlet.2006.08.006>

- Elanseralathan, K., Joy, T. M., & Nagabhushana, G. R. (2000). *Breakdown of solid insulating materials under high frequency high voltage stress*. [Paper presentation]. Proceedings of the IEEE International Conference on Properties and Applications of Dielectric Materials, Xi'an, China. <https://doi.org/10.1109/icpadm.2000.876399>
- Feng, D., Hao, J., Yang, L., Liao, R., Chen, X., & Li, J. (2020). Comparison of AC breakdown characteristics on insulation paper (pressboard) immersed by three-element mixed insulation oil and mineral oil. *High Voltage*, 5(3), 298-305. <https://doi.org/10.1049/hve.2019.0103>
- Finch, C. A. (Ed.). (1973). *Polyvinyl Alcohol; Properties and Applications*. John Wiley & Sons.
- Gao, W., Xiang, Z., Chen, K., Yang, R., & Yang, F. (2015). Effect of depth beating on the fiber properties and enzymatic saccharification efficiency of softwood kraft pulp. *Carbohydrate Polymers*, 127, 400-406. <https://doi.org/10.1016/j.carbpol.2015.04.005>
- Hammett, A. L., Youngs, R. L., Sun, X., & Chandra, M. (2001). Non-wood fiber as an alternative to wood fiber in China's pulp and paper industry. *Holzforschung*, 55(2), 219-224. <https://doi.org/10.1515/HF.2001.036>
- Hubbe, M. (2006). Bonding between cellulosic fibers in the absence and presence of dry-strength agents – A review. *BioResources*, 1(2), 281-318. <https://doi.org/10.15376/biores.1.2.281-318>
- Huber, P., Lyannaz, L., & Carré, B. (2012). Specks masking by the coating layer in coated paper made from deinked pulp. *Nordic Pulp and Paper Research Journal*, 27(2), 466-471. <https://doi.org/10.3183/NPPRJ-2012-27-02-p466-471>
- Kamata, Y., Endoh, K., Furukawa, S., Endoh, F., Nonomura, K., Iwata, Y., Horiuchi, S., & Takasu, N. (1990). Dielectric strength of oil-immersed transformer insulation with Superimposed ac and lightning impulse voltage. *IEEE Transactions on Electrical Insulation*, 25(4), 683-687. <https://doi.org/10.1109/14.57090>
- Kamoga, O. L. M., Byaruhanga, J. K., & Kirabira, J. B. (2013). A review on pulp manufacture from non wood plant materials. *International Journal of Chemical Engineering and Applications*, 4(3), 144-148. <https://doi.org/10.7763/ijcea.2013.v4.281>
- Karlsson, H. (2010). *Strength properties of paper produced from softwood kraft pulp – Pulp mixture, reinforcement and sheet stratification* (Doctoral dissertation). Karlstad University, Sweden. <http://www.diva-portal.org/smash/get/diva2:317178/FULLTEXT01.pdf>
- Krause, C. (2012). Power transformer insulation - History, technology and design. *IEEE Transactions on Dielectrics and Electrical Insulation*, 19(6), 1941-1947. <https://doi.org/10.1109/TDEI.2012.6396951>
- Li, X., Li, J., Xiang, C., Zhang, J., Bao, L., & Ran, H. (2016). *The influence of oil-impregnated insulation paper's thickness on electrical breakdown strength*. [Paper presentation]. IEEE Conference on Electrical Insulation and Dielectric Phenomena (CEIDP), Toronto, Canada. <https://doi.org/10.1109/CEIDP.2016.7785511>
- Liu, Z., Liu, Q., & Wang, Z. D. (2016). Effect of electric field configuration on streamer and partial discharge phenomena in a hydrocarbon insulating liquid under AC stress. *Journal of Physics D: Applied Physics*, 49(18), Article 185501. <https://doi.org/10.1088/0022-3727/49/18/185501>

- Lundgaard, L. E., Hansen, W., & Ingebrigtsen, S. (2008). Ageing of mineral oil impregnated cellulose by acid catalysis. *IEEE Transactions on Dielectrics and Electrical Insulation*, 15(2), 540-546. <https://doi.org/10.1109/TDEI.2008.4483475>
- Mathes, K. N. (1991). *A brief history of development in electrical insulation*. [Paper presentation]. Proceedings of the Electrical Electronics Insulation Conference, Boston, Massachusetts. <https://doi.org/10.1109/eic.1991.162590>
- McShane, C. P., Corkran, J. L., Rapp, K. J., & Luksich, J. (2003). *Aging of paper insulation retrofilled with natural ester dielectric fluid*. [Paper presentation]. Annual Report Conference on Electrical Insulation and Dielectric Phenomena, New Mexico, USA. <https://doi.org/10.1109/ceidp.2003.1254810>
- Medhekar, N. V., Ramasubramaniam, A., Ruoff, R. S., & Shenoy, V. B. (2010). Hydrogen bond networks in graphene oxide composite paper: Structure and mechanical properties. *ACS Nano*, 4(4), 2300-2306. <https://doi.org/10.1021/nn901934u>
- Mo, Y., Yang, L., Zou, T., Hou, W., & Liao, R. (2019). Preparation of composite insulating paper with decreased permittivity, good mechanical and thermal properties by kevlar/nano cellulose fibrils/softwood pulp hybrid. *IEEE Access*, 7, 104258-104268. <https://doi.org/10.1109/ACCESS.2019.2930981>
- Moore, S., Rapp, K., & Baldyga, R. (2012). *Transformer insulation dry out as a result of retrofilling with natural ester fluid*. [Paper presentation]. Proceedings of the IEEE Power Engineering Society Transmission and Distribution Conference, Florida, USA. <https://doi.org/10.1109/TDC.2012.6281441>
- Ni, S., Liu, N., Fu, Y., Bian, H., Zhang, Y., Chen, X., Gao, H., & Dai, H. (2021). Laccase-catalyzed chitosan-monophenol copolymer as a coating on paper enhances its hydrophobicity and strength. *Progress in Organic Coatings*, 151, Article 106026. <https://doi.org/10.1016/j.porgcoat.2020.106026>
- Norrman, K., Ghanbari-Siahkali, A., & Larsen, N. B. (2005). 6 Studies of spin-coated polymer films. *Annual Reports on the Progress of Chemistry - Section C*, 101, 174-201. <https://doi.org/10.1039/b408857n>
- Nuruddin, M., Gupta, R., Tcherbi-Narteh, A., Hosur, M., & Jeelani, S. (2015, June 10-12). *Thermal and mechanical properties of cellulose nanofibers reinforced polyvinyl alcohol composite films*. [Paper presentation]. The 69th FPS International Convention. Atlanta, Georgia.
- Qu, G., Cui, H., Zhu, Y., Yang, L., & Li, S. (2020). Substantial improvement of the dielectric strength of cellulose-liquid composites: Effects of traps at the nanoscale interface. *Journal of Physical Chemistry Letters*, 11(5), 1881-1889. <https://doi.org/10.1021/acs.jpcclett.0c00235>
- Ramli, M. R., Arief, Y. Z., Azli, S. A., Muhamad, N. A., Lau, K. Y., Farhan, M., Bashir, N., Mohd, N. K., Huey, L. W., & Kiat, Y. S. (2014). *Partial discharge characteristics of palm fatty acid ester (PFAE) as high voltage insulating material*. [Paper presentation]. The 2nd IEEE Conference on Power Engineering and Renewable Energy (ICPERE), Bali, Indonesia. <https://doi.org/10.1109/ICPERE.2014.7067217>
- Schaible, M. (1987). Electrical insulating papers - An overview. *IEEE Electrical Insulation Magazine*, 3(1), 8-12. <https://doi.org/10.1109/MEI.1987.290616>
- Schuman, T., Wikström, M., & Rigdahl, M. (2003). The effect of hot calendering of the substrate on the barrier properties of poly(vinyl alcohol)-coated papers. *Nordic Pulp and Paper Research Journal*, 18(1), 81-89. <https://doi.org/10.3183/npprj-2003-18-01-p081-089>

- Schuman, T., Wikström, M., & Rigdahl, M. (2004). Coating of surface-modified papers with poly(vinyl alcohol). *Surface and Coatings Technology*, 183(1), 96-105. <https://doi.org/10.1016/j.surfcoat.2003.09.059>
- Shokrieh, M. M., Mahmoudi, A., & Shadkam, H. R. (2015). Hybrid polyvinyl alcohol and cellulose fiber pulp instead of asbestos fibers in cement-based composites. *Mechanics of Composite Materials*, 51(2), 231-238. <https://doi.org/10.1007/s11029-015-9494-7>
- Song, R., Ino, H., & Kimura, T. (2009). Mechanical property of silk/bamboo composite paper for effective utilization of waste silk. *Journal of Textile Engineering*, 55(3), 85-90. <https://doi.org/10.4188/jte.55.85>
- Umair, M., Azis, N., Halis, R., & Jasni, J. (2019). *Investigation on the effect of beating on the physical and mechanical properties of untreated kenaf based insulation paper*. [Paper presentation]. IEEE 5th International Conference on Smart Instrumentation, Measurement and Application (ICSIMA), Songkhla, Thailand <https://doi.org/10.1109/ICSIMA.2018.8688758>
- Umair, M., Azis, N., Halis, R., & Jasni, J. (2020). Investigation of kenaf paper in the presence of pva for transformers application. *Materials*, 13(21), 1-23. <https://doi.org/10.3390/ma13215002>
- Wai, N. N., Nanko, H., & Murakami, K. (1985). A morphological study on the behavior of bamboo pulp fibers in the beating process. *Wood Science and Technology*, 19(3), 211-222. <https://doi.org/10.1007/BF00392050>
- Wistara, N., & Young, R. A. (1999). Properties and treatments of pulps from recycled paper. Part I. Physical and chemical properties of pulps. *Cellulose*, 6(4), 291-324. <https://doi.org/10.1023/A:1009221125962>
- Yenidoğan, S. (2019). Nanocrystalline cellulose and polyvinyl alcohol coating application to cardboard packaging papers and investigation of the effects on paper properties. *Medziagotyra*, 26(3), 317-322. <https://doi.org/10.5755/j01.ms.26.3.21499>
- Zhang, P., Wang, Q., Guo, R., Zhang, M., Wang, S., Lu, C., Xue, M., Fan, J., He, Z., & Rao, W. (2019). Self-assembled ultrathin film of CNC/PVA-liquid metal composite as a multifunctional Janus material. *Materials Horizons*, 6(8), 1643-1653. <https://doi.org/10.1039/c9mh00280d>
- Zhou, C., & Chen, G. (2017). Space charge and AC electrical breakdown strength in polyethylene. *IEEE Transactions on Dielectrics and Electrical Insulation*, 24(1), 559-566. <https://doi.org/10.1109/TDEI.2016.005811>



The Predictive Ability of Total Genotype Score and Serum Metabolite Markers in Power-Based Sports Performance Following Different Strength Training Intensities — A Pilot Study

Elin Elisa Khairul^{1,2}, Wan Atiyah Ab Wahab^{1,2}, Lay Kek Teh^{1,3}, Mohd Zaki Salleh¹, Mohd Salleh Rofiee^{1,4}, Raja Mohammed Firhad Raja Azidin² and Sarina Md. Yusof^{2*}

¹Integrative Pharmacogenomic Institute, Universiti Teknologi MARA Selangor Branch, Puncak Alam Campus, 42300 UiTM, Puncak Alam, Selangor, Malaysia

²Faculty of Sports Science and Recreation, Universiti Teknologi MARA, Shah Alam Campus, 40450 UiTM, Shah Alam, Selangor, Malaysia

³Faculty of Pharmacy, Universiti Teknologi MARA Selangor Branch, Puncak Alam Campus, 42300 UiTM, Puncak Alam, Selangor, Malaysia

⁴Faculty of Health Science, Universiti Teknologi MARA Selangor Branch, Puncak Alam Campus, 42300 UiTM, Puncak Alam, Selangor, Malaysia

ABSTRACT

Muscular power is one of the factors that contribute to an athlete's performance. This study aimed to explore the predictive ability of total genotype score (TGS) and serum metabolite markers in power-based sports performance following different strength training (ST) intensities. We recruited 15 novice male field hockey players (age = $16.27 \pm .12$ years old, body mass index = 22.57 ± 2.21 kg/m²) and allocated them to; high-intensity strength training (HIST, n=5), moderate intensity strength (MIST, n=5), and control group (C, n=5). Both training groups completed an eight-week ST intervention. Pre- and

post-training muscular power (vertical jump) was measured. The participants were genotyped for; *ACE* (rs1799752), *ACTN3* (rs1815739), *ADRB3* (rs4994), *AGT* (rs699), *BDKRB2* (rs1799722), *PPARA* (rs4253778), *PPARGC1A* (rs8192678), *TRHR* (rs7832552), and *VEGF* (rs1870377). TGS was calculated to annotate for strength-power (STP) and endurance (END) qualities. Subsequently, serum metabolomics analysis was conducted using Liquid chromatography-mass spectrometry

ARTICLE INFO

Article history:

Received: 17 April 2022

Accepted: 16 August 2022

Published: 20 March 2023

DOI: <https://doi.org/10.47836/pjst.31.2.23>

E-mail addresses:

elinelisa89@gmail.com (Elin Elisa Khairul)

atiyyahwahab@gmail.com (Wan Atiyah Ab Wahab)

tehlakek@uitm.edu.my (Lay Kek Teh)

zakisalleh@uitm.edu.my (Mohd Zaki Salleh)

sallehrofee@uitm.edu.my (Mohd Salleh Rofiee)

firhad@uitm.edu.my (Raja Mohammed Firhad Raja Azidin)

sarin864@uitm.edu.my (Sarina Md. Yusof)

* Corresponding author

Quadrupole-Time-of-Flight (LC-MS QTOF) to profile differentially expressed metabolite changes induced by training. Multiple regression analysis was conducted to explore the ability of TGS and differentially expressed metabolite markers to predict muscular power changes following the intervention. Multiple Regression revealed that only TGS STP might be a significant predictor of muscular power changes following MIST (adjusted $R^2=.906$, $p<.05$). Additionally, ST also resulted in significant muscular power improvement ($p<.05$) and perturbation of the sphingolipid metabolism pathway ($p<.05$). Therefore, selected gene variants may influence muscular power. Therefore, STP TGS might be able to predict muscular power changes following MIST.

Keywords: Genetics, metabolomics, single nucleotide polymorphism, strength training, training response

INTRODUCTION

Field hockey is a field-based team sport characterised as a high-intensity intermittent event that places greater demand on athletes' physiological and physical capacities (Lemos et al., 2017; Ibrahim Hassan, 2018). This sport requires the dynamic action of accelerating, decelerating, jumping, and changing direction (Pimenta et al., 2012). Relevant studies demonstrated that it is essential for athletes to have a significant level of muscular strength, power, and cardiorespiratory fitness to perform optimally (Lemos et al., 2017; Bishop et al., 2015; Lemmink & Visscher, 2006; Konarski et al., 2012).

Generally, strength training (ST) is widely used to enhance performance across various sports events (Kikuchi et al., 2019). ST is known to improve muscle energy status, resulting in the ability to maintain greater force output for a longer time (Laursen, 2010). A good design ST program involves the manipulation of training variables (e.g., intensity, volume, frequency, rest interval, exercise selection, and order) (Kikuchi et al., 2019; Mangine et al., 2015). Studies have demonstrated that both high-intensity (HI) and moderate-intensity (MI) ST improved several performance components in intermittent sport (Mangine et al., 2015; Assuncao et al., 2016; Astorino et al., 2004; Christou et al., 2006; Lesinski et al., 2016).

It has been shown that there were associations between gene variants and athletic performance (e.g., muscular strength, muscular power, endurance, and neuromuscular coordination) (Varillas-Delgado et al., 2022; Ahmetov et al., 2016). Gene variants that involve metabolism regulation, muscle fibre type, muscle contraction and circulatory homeostasis in at least two independent studies were selected (Jones et al., 2016; Ahmetov et al., 2016; Egorova et al., 2014). Athletic performance is highly polygenic as it involves complex multiple genes interactions that affect overall outcomes (de la Iglesia et al., 2020). The total genotype score (TGS) was used to quantify the combined influence of multiple gene interactions (Massida et al., 2019). Genes and environment (e.g., training, experience, and diet) are likely to play an important role, but further investigation is required to explore

the contribution of genetic factors toward performance (Kelly et al., 2020; Wishart, 2019; Sarzynski et al., 2016).

ST is an external challenge that leads to differentially expressed metabolites (Kelly et al., 2020). Different ST intensity imposes variable demands on the physiological and physical capacities, shown via changes in the metabolic pathways (Laursen, 2010). Therefore, exploring metabolite profile changes is useful for illustrating an individual's current state and responses to stimuli (Kelly et al., 2020; Wishart, 2019). Metabolic changes have been observed in response to acute ST, but less is known about the ST response following a longer intervention period (Morville et al., 2020). To improve the understanding of metabolite alteration following ST, the employment of the metabolomics approach is deemed essential. Therefore, this study aimed to explore the ability of TGS to predict changes in muscular power and the associated metabolic pathways following different ST intensities being prescribed.

METHOD

Participants and Study Design

A true experimental design was used in the present study. Purposive sampling was employed to recruit fifteen (N=15) male field hockey players who represented their district, aged between 16 to 17 years old. The study was conducted during the off-season and commenced in October 2018. The participants were randomly assigned to; high-intensity strength training (HIST, n=5), moderate-intensity strength training (MIST, n=5), and control group (C, n=5). Study inclusion criteria were that participants; were healthy and active field hockey players, who had participated in competitive tournaments, free from any injuries for the past six months, had not performed strength training at least six months prior to participation, and had not taken any supplementation prior to participation. Participants were informed about the study procedure and potential risks associated with the study, and informed consent was obtained before participation. In addition, participants completed the PAR-Q⁺ questionnaire as a pre-screening and Electrocardiogram (ECG) test (Tanisawa et al., 2020). The study was approved by Universiti Teknologi MARA Research Ethics Committee [ref no.:600-IRMI(5/1/6)]. A flow chart of the study design is presented in Figure 1.

Muscular Power Measurement

Pre- and post-test muscular power was measured by vertical jump (VJ) (Yingling et al., 2018). Participants were to perform the jump with a pause at >90° squat before jumping with the dominant hand reaching for the swivel vane on a vertec apparatus (Yingling et al., 2018). Three jump attempts were carried out with one minute of rest in between

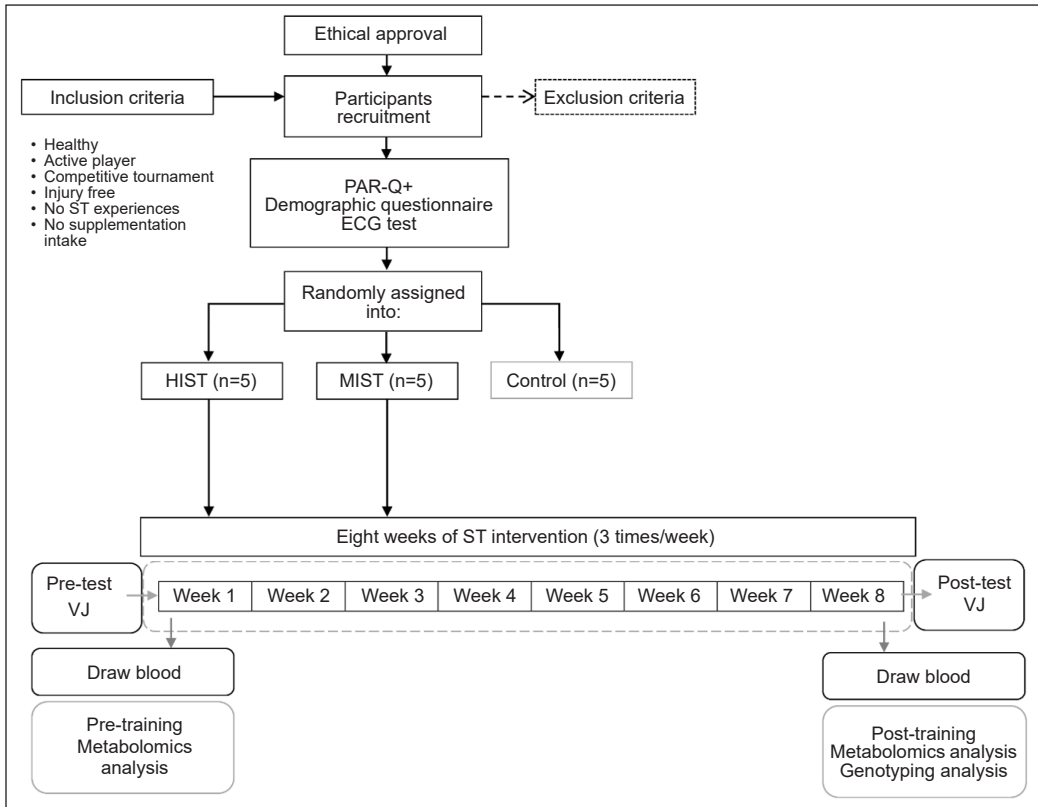


Figure 1. Study design flow chart

jumps. The best jump was equated to the equation (Sayers et al., 1999). The procedure was explained and demonstrated to the participants. Proper stretching, warm-up, and cooling-down sessions were conducted prior to the test. In addition, a familiarisation session was provided before the actual measurement.

Strength Training Intervention

The training was held three times per week for eight weeks. Training volume was pre-determined and equated (Klemp et al., 2016). Familiarisation was designed to ensure correct lifting techniques. The upper body (biceps curl, triceps extension, shoulder press) and lower body (leg press, hamstring curl, calf raise) exercises were prescribed to the participants. The HIST performed three sets of one to six repetitions at 80 to 90% 1-RM, while the MIST performed three sets of eight to 12 repetitions at 60 to 75% 1-RM. The warm-up was conducted using the peck deck machine (upper body) and leg press machine (lower body) at 50% of 1RM for 10 repetitions. Participants in the training groups were advised to refrain from additional ST sessions and maintain their habitual physical activity and dietary intake. In contrast, the control group maintained their usual activities without engaging in ST sessions.

Genotyping

Deoxyribonucleic Acid (DNA) Extraction. DNA was extracted using an in-house modified conventional DNA extraction method. Five (5 ml) of 1 × lysis buffer (0.64 M sucrose, 0.02 M Tris hydrochloric acid, 2% Triton X-100, autoclaved Mili-Q water) were added to 5 ml of blood sample and inverted (10 times). Later, another 5 ml of 0.5 × lysis buffer was added to the blood sample and inverted (10 times), left on ice (10 minutes), and later centrifuged (Eppendorf, model 5810R, Hamburg, Germany) at $2,700 \times g$, 20°C for 15 minutes. Next, the pellet was rinsed with 25 ml of Tris Ethylenediaminetetraacetic acid (EDTA) (pH 8.0) buffer followed by centrifugation at $2,700 \times g$, 20°C for 15 minutes. The supernatant was discarded while the pellet was kept. The steps above were repeated three times until a clear supernatant and pellet were formed. The pellet was re-suspended with 2 ml saline EDTA (pH 8.0) and incubated overnight in a water bath at 37°C with 100 µl of 20% Sodium Dodecyl Sulfate (SDS) and 10 µl proteinase-K solution (20 mg/ml). This step was taken to lyse the cell and nuclear membrane while maintaining DNA's integrity. Then, 100 µl of 2.0 M Potassium Chloride (KCl) was added, followed by 4 ml of cold 100% ethanol. The step was taken to precipitate the DNA. DNA became visible as a floating strand in the solution. Then, 700 µl of cold 70% ethanol was used to rinse the DNA by allowing excess KCl to dissolve. The DNA was left to dry. The DNA was reconstituted with Tris EDTA buffer and stored at -20°C. The DNA's concentration and purity were measured using NanoDrop 2000 Spectrophotometer (Thermo Scientific, Wilmington, USA).

Allele-Specific Polymerase Chain Reaction (ASPCR). In-house genotyping procedures were conducted using ASPCR assays. The primers were designed to target specific single nucleotide polymorphisms (SNPs). ASPCR was conducted using a thermal cycler (Takara Bio, CA, USA) with the final mixture volume of 20 µl, containing the participant's DNA (100 ng/µl), 0.5 U/µl of *taq* DNA polymerase (NEB, MA, USA), various concentrations of primers (0.1–2.0 µM), 0.16 mM deoxyribonucleotide triphosphate (dNTPs) and autoclaved Mili-Q water. A touchdown thermal cycle condition was composed of; pre-denaturation at 95°C (2 minutes), denaturation at 95°C (30 seconds), and extension at 68°C (30 seconds). In the initial 10 cycles of annealing, the temperature was gradually decreased (-1°C) from 65°C to 55°C (30 seconds). In the latter half (30 cycles), the temperature was maintained at 55°C (30 seconds). Finally, post-extension was set at 68°C (5 minutes). PCR products were electrophoresed at 200 V for 60 minutes and examined on 3.5% agarose gel stained with Ethidium Bromide (EtBr). The gel was visualised under ultraviolet light to detect the specific band sizes that indicate the alleles.

Total Genotype Score (TGS) Calculation. The TGS was calculated using an algorithm that incorporated all genotype scoring (GS) in a simple additive model, $TGS = 100 / (9 \div$

2) $\times GS_1 + GS_2 + \dots + GS_9$ (Ruiz et al., 2009; Ruiz et al., 2010). Next, the homozygous, intermediate ‘heterozygous’ and ‘less optimal’ homozygous were assigned with the scoring of 2, 1, and 0, respectively. Finally, the total score was calculated and associated with strength-power (STP) and endurance (END) qualities (Table 1).

Metabolomics

Serum Sample Collection and Preparation.

Ten (10) ml of blood samples were drawn pre-and post-training. It was collected in a serum separator tube. Serum samples were prepared by centrifugation

(ALC, model PK 121R, Turin, Italy) at $4,600 \times g$, $4^\circ C$, 15 minutes, and stored at $-80^\circ C$ until analysis. Prior to the analysis, 150 μl of double distilled water (ddH₂O) was added to 150 μl of aliquoted serum. In order to precipitate the protein, 450 μl of cold Acetonitrile (Merck, Darmstadt, Germany) was added, followed by 30 seconds of vortex mixing and centrifuged (ALC, model PK 121R, Turin, Italy) at $10,600 \times g$, $4^\circ C$, 10 minutes. Then, 650 μl of supernatant was transferred to a new microcentrifuge tube. This step was repeated two times and dried in the vacuum concentrator (Eppendorf, model 5301, Hamburg, Germany). Quality control (QC) was prepared from pooled serum samples. Each QC sample was analysed independently with each batch of samples. The performance of QC was evaluated by the determination of relative standard deviation (RSD).

LC-MS Conditions and Analysis. The samples were analysed using LC/MS (Agilent Technologies, model 6250, CA, USA). The column used was the ZORBAX Eclipse Plus C18, 100 mm \times 2.10 mm \times 1.80 μm (Agilent Technologies, CA, USA) with electrospray ionisation (ESI) in positive mode. The drying gas temperature was set at $300^\circ C$ with a flow rate of 3.0 L/min. The nebuliser pressure was set at 15 psi, and the fragmentor voltage was set at 175 V. The temperature was maintained at $40^\circ C$ and the total run time was 48 minutes. The system was operated at a 0.25 ml/min flow rate with mobile phase A (ddH₂O with 0.1% Formic acid) and B (Acetonitrile with 0.1% Formic acid) over a gradient of 0 to 36 minutes with an increasing percentage of B from 5 to 95%. The dried sample was reconstituted with 30 μl of mobile phases (15 μl from mobile phase A and 15 μl from mobile phase B) followed by 30 seconds of vortex mixing and centrifuged at $16,400 \times g$, $4^\circ C$, 10 minutes. Four randomly selected samples, one QC and one blank, were analysed per

Table 1
Genotype scoring

Variables	Genotype scoring (GS)	Qualities
Genes		
ACE	DD=2, ID=1, II=0	STP
	DD=0, ID=1, II=2	END
ACTN3	CC=2, CT=1, TT=0	STP
	CC=0, CT=1, TT=2	END
PPARA	CC=2, CG=1, GG=0	STP
	GG=2, CG=1, CC=0	END
ADRB3	AA=2, AG=1, GG=0	END
BDKRB2	TT=2, TC=1, CC=0	END
VEGF	CC=2, CG=1, GG=0	END
PPARGC1A	GG=2, AG=1, AA=0	END
AGT	TT=2, TC=1, CC=0	STP
TRHR	CC=2, AC=1, AA=0	STP

Abbreviation: END=endurance, STP=strength-power

batch. Twenty (20) μl from each sample was transferred into inserts and injected into the LC-MS for further analysis. The analysis was performed in four replicates for each sample.

Untargeted Metabolomics Data Processing. The raw data (.d) from the LC-MS QTOF analysis were collected using the Agilent MassHunter Data Acquisition software version B.05.00 (Agilent Technologies, CA, USA) and processed in the Agilent MassHunter Qualitative Analysis software version B.05.00 (Agilent Technologies, CA, USA). Data was converted from (.d) to (.cef) using DA Reprocessor software (Agilent Technologies, CA, USA) and transferred into Agilent MassHunter Profiler Professional (MPP) software version B.12.01 (Agilent Technologies, CA, USA). MPP software was used to conduct differential analyses of the entities. Data were subjected to normalisation, filtration, and recursion analysis. MetaboAnalyst 5.0 (<https://dev.metaboanalyst.ca>) was used to conduct a multivariate analysis. The principal component analysis method (PCA) was used to visualise the clustering of metabolites following the intervention. Later, pathway analysis was conducted to identify the significant pathway involved following the intervention. Then, receiver operating characteristic (ROC) curve analysis was conducted on the identified significant metabolites. The metabolites with an area under the curve (AUC) value of $>.65$ and the Variable Influence on Projection (VIP) index (>1.00) were used to screen significant metabolites.

Statistical Analysis

Statistical analysis was performed using SPSS for Windows version 26.0. Statistical significance was set at ($p < .05$). Data are presented in mean \pm standard deviation ($M \pm S.D$) unless otherwise stated. Muscular power data were normally distributed (Shapiro-Wilk test, $p > .05$). Differences in TGS were analysed using the independent sample t-test, whilst muscular power changes following intervention were analysed using paired sample t-test. Multiple regression was conducted to assess the ability of TGS and serum metabolite markers to predict muscular power changes following ST intervention.

RESULTS

Demographic and TGS

The participants were homogenous at baseline. There were no significant differences between training groups: age (HIST = $16.00 \pm .00$, MIST = $16.40 \pm .55$, C = $16.40 \pm .55$ years old), height (HIST = $1.67 \pm .04$, MIST = $1.60 \pm .06$, C = $1.70 \pm .08$ m), body weight (HIST = $67.70 \pm .04$, MIST = 57.98 ± 8.65 , C = 61.24 ± 5.21 kg) and body mass index (HIST = 24.11 ± 1.96 , MIST = 22.48 ± 2.72 , C = $21.12 \pm .48$ kg/m^2). All participants completed the training program with no missing sessions. No injuries were reported in the study. There were no statistically significant muscular power differences between training groups. Most

participants presented with heterozygous genotypes except for *PPARA* GG = 100% and *ADRB3* AA = 100%, which were homozygous genotypes. There was a significant difference ($p < .05$) in the TGS STP across training groups, whereby MIST (M=22.24) is higher as compared to HIST (M=17.79) and C (M=13.34). There was no significant difference in TGS END across training groups. The TGS is presented in Table 2.

Table 2
TGS between training groups

Variables	HIST (M±S.D)	MIST (M±S.D)	C (M±S.D)	<i>p</i> -value
TGS				
STP	17.79 ± 4.65	22.24 ± 3.93	13.34 ± 4.97	.03*
END	50.04 ± 6.81	48.93 ± 4.65	54.49 ± 10.69	.51

*significant different ($p < .05$), Abbreviation: END=endurance, STP=strength-power

Muscular Power Changes Between Training Groups

There was a significant muscular power improvement ($p < .05$) in both training groups, HIST ($M_{diff} = .84$ kW) and MIST ($M_{diff} = .41$ kW), pre-and post-training. The muscular power changes are presented in Table 3.

Table 3
Muscular power changes between training groups

Variables	n	Pre-test (M±S.D)	Post-test (M±S.D)	M_{diff}	<i>p</i> -value
LB muscular power (kW)					
HIST	5	4.30 ± .61	5.14 ± .55	.84	.00*
MIST	5	3.65 ± 1.06	4.06 ± 1.09	.41	.00*
C	5	3.71 ± .46	3.56 ± .47	.15	.00*

*significant different ($p < .05$), Abbreviation: M_{diff} =mean difference

Serum Metabolite Analysis Between Training Groups

Data Acquisition and Processing of Metabolite Profile. Total ion chromatograms (TIC) for the analysis of the serum samples representing the HI, MI and control groups are shown in Figures 2, 3 and 4, respectively. Analytical reproducibility between batches was within the acceptable range of RSD (<20%), as shown in Table 4.

Serum Metabolomics Profile and Biomarker Identification. LC-MS analysis revealed that a total of 941 metabolites were detected, and about 224 differed significantly between training groups and post-tests. The PCA score plot between training groups demonstrated a clear separation between the training and control groups (Figure 5). The pathway analysis revealed about 35 pathways involved in differentiating the effect of strength training intensity. However, only the Sphingolipid metabolism pathway was significantly

Table 4
Relative standard deviation (RSD) values of selected mass in the pooled sample between batches

Compound	Mass different (ppm)			Retention time (mins)		
	Mean	S.D	RSD (%)	Mean	S.D	RSD (%)
2	199.15	28.53	14.32	.96	.01	.88
3	140.36	22.56	16.07	.98	.03	2.85
4	142.28	26.56	18.66	1.02	.04	3.90
9	161.64	23.20	14.35	1.57	.26	16.55
36	524.46	89.06	16.98	22.72	2.14	9.43
37	504.87	79.02	15.65	23.12	1.94	8.39
40	513.95	86.28	16.78	24.21	2.10	8.68

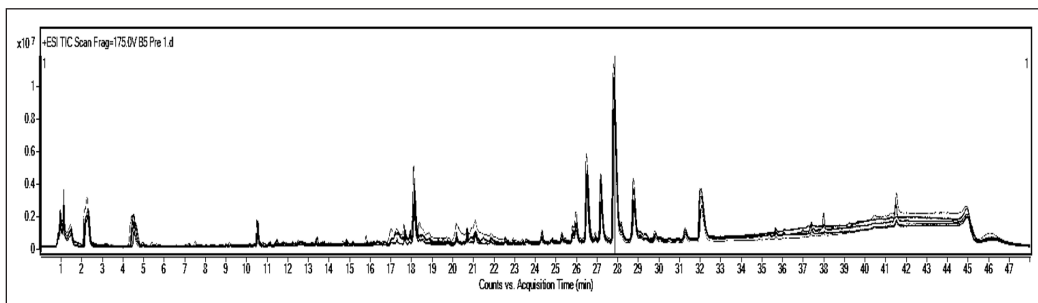


Figure 2. TIC in the HI ST group

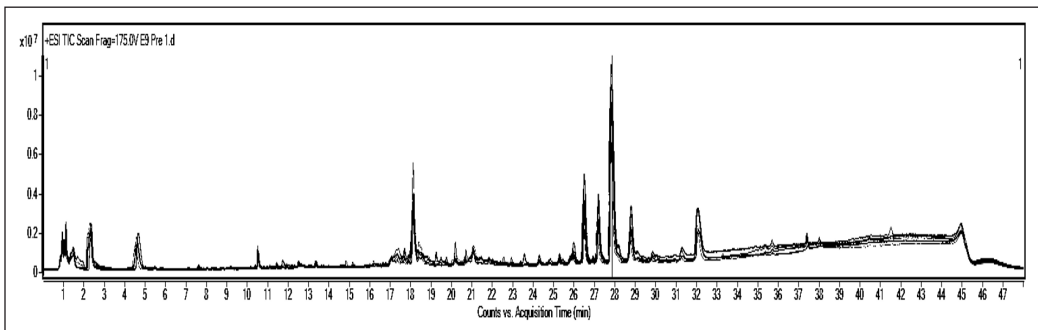


Figure 3. TIC in MI ST group

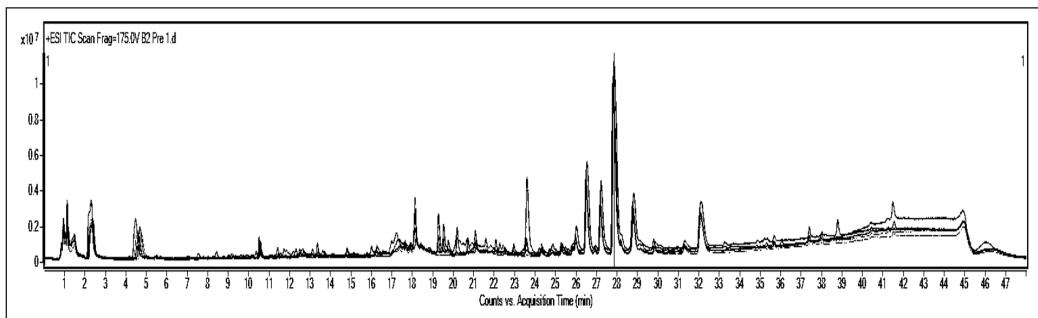


Figure 4. TIC in the control group

different ($p < .05$) across training groups. Presently, only three metabolites ($AUC > .65$, $VIP \geq 1.0$, $p < .05$) (Figures 6, 7, and 8) belong to the Sphingolipid pathway, which is the most perturbed pathway (Table 5). There is a pattern of differences in Sphingolipid metabolite between strength-trained participants and their healthy non-trained counterparts.

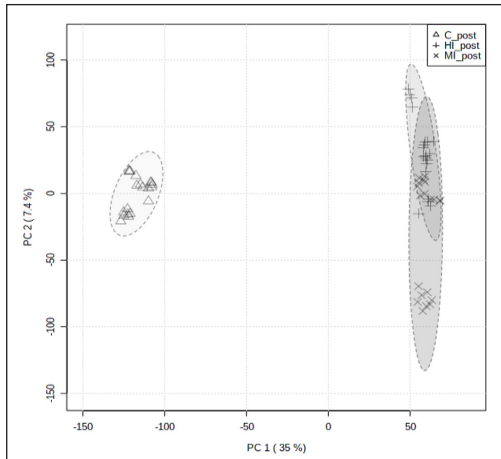


Figure 5. PCA score plot across training groups

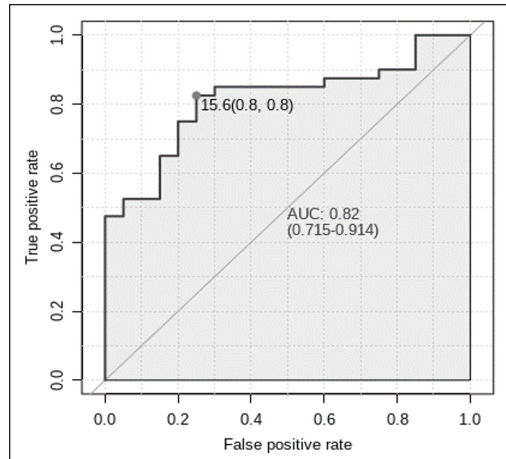


Figure 6. ROC curve of 3-O-Sulfogalactosylceramide

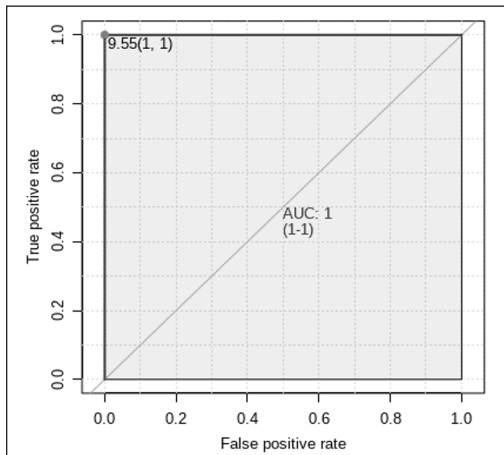


Figure 7. ROC curve of Sphingosine-1-phosphate

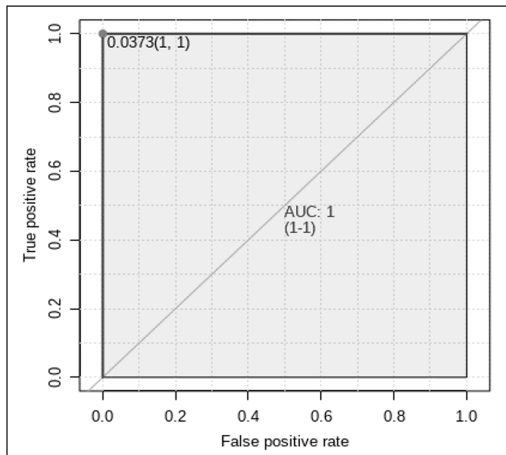


Figure 8. ROC curve of Sphinganine

Table 5
Potential serum metabolite markers between training groups

Variables	AUC	VIP	FC	p-value
Metabolites				
3-O-Sulfogalactosylceramide	.82	1.08	1.17	<.05*
Sphingosine-1-phosphate	1.00	1.90	-2.43	<.05*
Sphinganine	1.00	1.23	-9.28	<.05*

*significant different ($p < .05$)

Regression Analysis Between Predictors and Muscular Power Changes Between Training Groups

There is a significant regression (adjusted $R^2=.91$) of TGS STP with muscular power changes following MI ST, $F(2,2)=20.30$, $p<.05$. The predicted muscular power is equal to $.42-.01$ (TGS STP) + $.00$ (TGS END). Other predictors did not significantly predict muscular power changes. The regression coefficient is presented in Table 6.

Table 6
The regression coefficient of predictors on muscular power changes between training groups

Variables	B	S.E	t	p-value	95% CI
LB muscular power (kW)					
HI (n=5)					
TGS					
Constant	1.78	.39	4.51	.05	.08, 3.48
STP	-.00	.01	-.35	.76	-.04, .04
END	-.02	.01	-2.77	.11	-.05, .01
Biomarkers					
Constant	.85	.11	7.50	.08	-.59, 2.29
3-O-Sulfogalactosylceramide	.03	.07	.46	.72	-.85, .91
Sphingosine-1-phosphate	-.39	.93	-.42	.75	-12.23, 11.45
Sphinganine	.01	.01	.58	.67	-.17, .19
MI (n=5)					
TGS					
Constant	.42	.08	5.58	.03	.10, .74
STP	-.01	.00	-6.34	.02*	-.02, -.00
END	.01	.00	3.22	.09	-.00, .01
Biomarkers					
Constant	.45	.06	7.09	.09	-.35, 1.25
3-O-Sulfogalactosylceramide	-.00	.01	-.15	.91	-.08, .08
Sphingosine-1-phosphate	.12	.12	1.01	.50	-1.38, 1.62
Sphinganine	.01	.01	.71	.61	-.11, .12
C (n=5)					
TGS					
Constant	-.25	.58	-.43	.71	-2.77, 2.26
STP	.01	.02	.59	.62	-.06, .08
END	.00	.01	-.05	.97	-.02, .03
Biomarkers					
Constant	-.23	.02	-10.77	.01	-.33, -.14
3-O-Sulfogalactosylceramide	.01	.00	3.07	.09	-.00, .02
Sphinganine	.01	.00	3.62	.07	-.00, .03

*significant different ($p<.05$), Abbreviation: END=endurance, STP=strength-power

DISCUSSION

The study aimed to determine the predictive ability of TGS and serum metabolite marker power-based sports performance following different strength training (ST) intensities. Most of the participants harboured endurance-related genotypes, and Amato et al. (2018) demonstrated similar findings whereby their professional Italian soccer athletes were more

endurance-oriented (TGS=56.44%) as compared to strength (TGS=43.52%). However, the Russian professional soccer players presented with higher strength TGS (M=52.00) as compared to healthy control (M=41.30) (Egorova et al., 2014). The present study demonstrated that only TGS STP might significantly predict muscular power changes following MIST. Murtagh et al. (2020) also demonstrated similar findings among elite soccer players who were more strength-power oriented than control. Although the endurance component dominates energy delivery during the match, the strength-power component plays a greater role in determining success during events in intermittent sports (e.g., winning ball possession, scoring, conceding goals) (Egorova et al., 2014; Lemmink & Visscher, 2006).

Suraci et al. (2021) demonstrated that the mean percentage change for power performance in power TGS was higher compared to the endurance TGS following eight weeks of soccer-specific training compared to the small-sided game and a combination of both among adolescent soccer players. Pickering et al. (2019) demonstrated a greater endurance improvement in participants who presented with greater TGS endurance following aerobic training. The inter-individual variation in response to training must be considered, as some participants might experience greater improvement than others with the same intensity being prescribed (Pickering et al., 2019).

In addition, participants also demonstrated significant improvement in muscular power following HIST and MIST interventions. McKinlay et al. (2018) also demonstrated a similar finding whereby eight weeks of strength and plyometric training among novice adolescent soccer players significantly improved muscle strength and power performance. Earlier, Juarez et al. (2009) also demonstrated similar findings as their male habitually active collegiate athletes presented with power performance improvement (12.3%) following eight weeks of a conventional strength training program. Novice athletes typically possessed a significant reserve of potential improvement regardless of the training they were prescribed (Juarez et al., 2009). Wetmore et al. (2020) also agreed that untrained participants required lesser stimulus than previously trained participants.

Th three serum metabolite markers which were significant in this study could not predict muscular power changes following ST intervention. However, there was a significant alteration of sphingolipid metabolites following different ST interventions. Participants in HIST showed an increment in ceramides metabolites post-training. The sphingolipids are a family of lipid molecules that circulate in the serum and accumulate around the skeletal muscle (Bergman et al., 2015). Skeletal muscle is well-known for sphingolipid metabolism (Nikolova-Karakashian & Reid, 2011). Recently, Nikolova-Karakashian and Reid (2011) explained the 'sphingolipid rheostat' mechanism whereby sphingosine-1-phosphate slows fatigue, preserving force over time, ceramides, on the other hand, promote fatigue. The findings of Shepherd et al. (2014) and Sarin et al. (2019)

were contradictory to the present study as they demonstrated that ST led to a significant increment in intramuscular triglyceride (IMTG) storage, muscle strength, and body fat percentage reduction. Shepherd et al. (2014) assumed that greater IMTG storage might be created, leading to low availability of circulating ceramides following the ST.

It is well known that muscular strength and power are partly responsible for rapid movements such as sprinting and accelerating (Kobal et al., 2017). This study emphasises that effectively prescribing HIST and MIST developed muscular power, especially in novice field hockey players. Moreover, identifying an individual's TGS might be useful in predicting response to training. An individual with higher strength-power or endurance TGS could be given appropriate training to maximise training adaptation. The combination of a favourable genetic profile with appropriate training prescription is advantageous to novice field hockey players.

Although the current study yielded some useful findings, there is a limitation that should be taken into consideration. The sample size in this study is relatively small for a gene-metabolite study. Further larger studies should be conducted to obtain a sufficient sample size for a more accurate result. Despite the limitations, the results remain valid and applicable since the training intervention was standardised, and participants in each group were homogenous in terms of age, sex, training experience, training volume, and baseline muscular power.

CONCLUSION

This study improves the understanding of the predictive ability of TGS and serum metabolite markers in determining muscular power changes following ST among novice athletes. It is concluded that STP TGS may influence muscular power changes following MIST in novice field hockey players. Selected gene variants may potentially influence muscular power following strength training. Overall, the result of the current study could potentially represent the tentative steps toward understanding the application of genomic and metabolomic in a sport that improves overall sports performance.

ACKNOWLEDGMENT

MITRA Grant partially funded this study, Universiti Teknologi MARA [600-IRMI/MYRA5/3MITRA(005/2017)] and operation budget Integrative Pharmacogenomic Institute [ref no: 241810/2017/DDS/19], Malaysia. The authors thank all the participants and coaches who volunteered their time and effort to participate in the study.

REFERENCES

Ahmetov, I. I., Egorova, E. S., Gabdrakhmanova, L. J., & Fedotovskaya, O. N. (2016). Genes and athletic performance: An update. *Medicine and Sport Science*, 61, 41-54. <https://doi.org/10.1159/000445240>

- Amato, A., Messina, G., Contrò, V., Sacco, A., & Proia, P. (2018). Total genetic score: An instrument to improve the performance in the elite athletes. *Acta Medica Mediterranea*, 34(6), 1857-1862. https://doi.org/10.109193/0393-6384_2018_6_287
- Assuncao, A. R., Bottaro, M., Ferreira-Junior, J. B., Izquierdo, M., Cadore, E. L., & Gentil, P. (2016). The chronic effects of low- and high-intensity resistance training on muscular fitness in adolescents. *Public Library of Science*, 11(8), 4-7. <https://doi.org/10.1371/journal.pone.0160650>
- Astorino, T. A., Tam, P. A., Rietschel, J. C., Johnson, S. M., & Freedman, T. P. (2004). Changes in physical fitness parameters during a competitive field hockey season. *Journal of Strength and Conditioning Research*, 18(4), 850-854. <https://doi.org/10.1519/13723.1>
- Bergman, B. C., Brozinick, J. T., Strauss, A., Bacon, S., Kerege, A., Bui, H. H., Sanders, P., Siddall, P., Kuo, M. S., & Perreault, L. (2015). Serum sphingolipids: relationships to insulin sensitivity and changes with exercise in humans. *American Journal of Physiology-Endocrinology and Metabolism*, 309(4), E398-E408. <https://doi.org/10.1152/ajpendo.00134.2015>
- Bishop, C., Brazier, J., Cree, J., Turner, A. N., & Anthony, T. (2015). A needs analysis and testing battery for field hockey. *Professional Strength and Conditioning*, 36, 15-36.
- Christou, M., Smilios, I., Sotiropoulos, K., Volaklis, K., Piliandis, T., & Tokmakidis, S. P. (2006). Effects of resistance training on the physical capacities of adolescent soccer players. *Journal of Strength and Conditioning Research*, 20(4), 783-791. <https://doi.org/10.1519/R-17254.1>
- de la Iglesia, R., Espinosa-Salinas, I., Lopez-Silvarrey, F. J., Ramos-Alvarez, J. J., Segovia, J. C., Colmenarejo, G., Borregon-Rivilla, E., Marcos-Pasero, H., Aguilar-Aguilar, E., Loria-Kohen, V., Reglero, G., & Ramirez-de Molina, A. (2020). A potential endurance algorithm prediction in the field of sports performance. *Frontiers in Genetics*, 11, 1-11. <https://doi.org/10.3389/fgene.2020.00711>
- Egorova, E. S., Borisova, A. V., Mustafina, L. J., Arkhipova, A. A., Gabbasov, R. T., Druzhevskaya, A. M., Astratenkova, I. V., & Ahmetov, I. I. (2014). The polygenic profile of Russian football players. *Journal of Sports Sciences*, 32(13), 1286-1293. <https://doi.org/10.1080/02640414.2014.898853>
- Ibrahim Hassan. I., H. (2018). Relationship between strength, speed, and change direction performance in field hockey players. *MOJ Sports Medicine*, 2(1), 54-58. <https://doi.org/10.15406/mojsm.2018.03.00046>
- Jones, N., Kiely, J., Suraci, B., Collins, D. J., Lorenzo, D. D., Pickering, C., & Grimaldi, K. A. (2016). A genetic-based algorithm for personalized resistance training. *Biology of Sport*, 33(2), 117-126. <https://doi.org/10.5604/20831862.1198210>
- Juárez, D., González-Ravé, J. M., & Navarro, F. (2009). Effects of complex vs. non-complex training programs on lower body maximum strength and power. *Isokinetics and Exercise Science*, 17(4), 233-241. <https://doi.org/10.3233/IES-2009-0359>
- Kelly, R. S., Kelly, M. P., & Kelly, P. (2020). Metabolomics, physical activity, exercise and health: A review of the current evidence. *Biochimica et Biophysica Acta (BBA) - Molecular Basis of Disease*, 1866(12), 1-17. <https://doi.org/10.1016/j.bbadis.2020.165936>
- Kikuchi, N., Honma, H., & Nakazato, K. (2019). Effect of gene polymorphisms on sensitivity to resistance training. In D. Barh & I. Ahmetov (Eds.), *Sports, Exercise, and Nutritional Genomics: Current Status and Future Directions* (pp. 189-209). Elsevier Inc. <https://doi.org/10.1016/B978-0-12-816193-7.00009-9>

- Klemp, A., Dolan, C., Quiles, J. M., Blanco, R., Zoeller, R. F., Graves, B. S., & Zourdos, M. C. (2016). Volume-equated high- and low-repetition daily undulating programming strategies produce similar hypertrophy and strength adaptations. *Applied Physiology, Nutrition and Metabolism*, *41*(7), 699-705. <https://doi.org/10.1139/apnm-2015-0707>
- Kobal, R., Loturco, I., Barroso, R., Gil, S., Cuniyochi, R. R., Ugrinowitsch, C., Roschel, H., & Tricoli, V. (2017). Effects of different combinations of strength, power, and plyometric training on the physical performance of elite young soccer players. *Journal of Strength and Conditioning Research*, *31*(6), 1468-1476. <https://doi.org/10.1519/JSC.0000000000001609>
- Konarski, J., Krzykała, M., Podgórski, T., Pawlak, M., Strzelczyk, R., & Malina, R. M. (2012). Variations in functional and morphological characteristics of elite polish field hockey players in a complete macrocycle. *International Journal of Sports Science and Coaching*, *7*(3), 527-541. <https://doi.org/10.1260/1747-9541.7.3.527>
- Laursen, P. B. (2010). Training for intense exercise performance: High-intensity or high-volume training? *Scandinavian Journal of Medicine & Science in Sports*, *20*(Suppl. 2), 1-10. <https://doi.org/10.1111/j.1600-0838.2010.01184.x>
- Lemmink, K. A. P. M., & Visscher, S. H. (2006). Role of energy systems in two intermittent field tests in women field hockey players. *The Journal of Strength and Conditioning Research*, *20*(4), 682-688. <https://doi.org/10.1519/R-17124.1>
- Lemos, R. S., Paz, G. A., Freitas Maia, M. de, Baptista da Silva, J., Lima, V. P., Brandão Pinto de Castro, J., & Miranda, H. (2017). Anthropometric and physical fitness parameters versus specific performance tests in Brazilian field hockey athletes: A pilot study. *Biomedical Human Kinetics*, *9*(1), 57-63. <https://doi.org/10.1515/bhk-2017-0009>
- Lesinski, M., Prieske, O., & Granacher, U. (2016). Effects and dose-response relationships of resistance training on physical performance in youth athletes: A systematic review and meta-analysis. *British Journal of Sports Medicine*, *50*(13), 781-795. <https://doi.org/10.1136/bjsports-2015-095497>
- Mangine, G. T., Hoffman, J. R., Gonzalez, A. M., Townsend, J. R., Wells, A. J., Jajtner, A. R., Beyer, K. S., Boone, C. H., Miramonti, A. A., Wang, R., LaMonica, M. B., Fukuda, D. H., Ratamess, N. A., & Stout, J. R. (2015). The effect of training volume and intensity on improvements in muscular strength and size in resistance-trained men. *Physiological Reports*, *3*(8), 1-17. <https://doi.org/10.14814/phy2.12472>
- Massidda, M., Calò, C. M., Cięszczyk, P., Kikuchi, N., Ahmetov, I. I., & Williams, A. G. (2019). Genetics of team sports. In D. Barh & I. Ahmetov (Eds.) *Sports, Exercise, and Nutritional Genomics* (pp. 105-128). Elsevier Inc. <https://doi.org/10.1016/b978-0-12-816193-7.00005-1>
- McKinlay, B. J., Wallace, P., Dotan, R., Long, D., Tokuno, C., Gabriel, D. A., & Falk, B. (2018). Effects of plyometric and resistance training on muscle strength, explosiveness, and neuromuscular function in young adolescent soccer players. *Journal of Strength and Conditioning Research*, *32*(11), 3039-3050. <https://doi.org/10.1519/JSC.0000000000002428>
- Morville, T., Sahl, R. E., Moritz, T., Helge, J. W., & Clemmensen, C. (2020). Plasma metabolome profiling of resistance exercise and endurance exercise in humans. *Cell Reports*, *33*(13), Article 108554. <https://doi.org/10.1016/j.celrep.2020.108554>

- Murtagh, C. F., Brownlee, T. E., Rienzi, E., Roquero, S., Moreno, S., Huertas, G., Lugioratto, G., Baumert, P., Turner, D. C., Lee, D., Dickinson, P., Amber Lyon, K., Sheikhsharaf, B., Biyik, B., O'Boyle, A., Morgans, R., Massey, A., Drust, B., & Erskine, R. M. (2020). The genetic profile of elite youth soccer players and its association with power and speed depends on maturity status. *PLoS ONE*, *15*(6 June), 1-24. <https://doi.org/10.1371/journal.pone.0234458>
- Nikolova-Karakashian, M. N., & Reid, M. B. (2011). Sphingolipid metabolism, oxidant signaling, and contractile function of skeletal muscle. *Antioxidants and Redox Signaling*, *15*(9), 2501-2517. <https://doi.org/10.1089/ars.2011.3940>
- Pickering, C., Kiely, J., Grgic, J., Lucia, A., & Del Coso, J. (2019). Can genetic testing identify talent for sport? *Genes*, *12*(2), 1-15. <https://doi.org/10.3390/genes10120972>
- Pimenta, E. M., Coelho, D. B., Cruz, I. R., Morandi, R. F., Veneroso, C. E., De Azambuja Pussieldi, G., Carvalho, M. R. S., Silami-Garcia, E., & De Paz Fernández, J. A. (2012). The ACTN3 genotype in soccer players in response to acute eccentric training. *European Journal of Applied Physiology*, *112*(4), 1495-1503. <https://doi.org/10.1007/s00421-011-2109-7>
- Ruiz, J. R., Arteta, D., Buxens, A., Artieda, M., Gómez-Gallego, F., Santiago, C., Yvert, T., Moran, M., & Lucia, A. (2010). Can we identify a power-oriented polygenic profile? *Journal of Applied Physiology*, *108*(3), 561-566. <https://doi.org/10.1152/jappphysiol.01242.2009>
- Ruiz, J. R., Gómez-Gallego, F., Santiago, C., González-Freire, M., Verde, Z., Foster, C., & Lucia, A. (2009). Is there an optimum endurance polygenic profile? *Journal of Physiology*, *587*(7), 1527-1534. <https://doi.org/10.1113/jphysiol.2008.166645>
- Sarin, H. V., Ahtiainen, J. P., Hulmi, J. J., Ihalainen, J. K., Walker, S., Kääsmaa-Schildt, M., Perola, M., & Peltonen, H. (2019). Resistance training induces antiatherogenic effects on metabolomic pathways. *Medicine and Science in Sports and Exercise*, *51*(9), 1866-1875. <https://doi.org/10.1249/MSS.000000000000203>
- Sarzynski, M. A., Loos, R. J. F., Lucia, A., Pérusse, L., Roth, S. M., Wolfarth, B., Rankinen, T., & Bouchard, C. (2016). Advances in exercise, fitness, and performance genomics in 2015. *Medicine and Science in Sports and Exercise*, *48*(10), 1906-1916. <https://doi.org/10.1249/MSS.0000000000000982>
- Sayers, S. P., Harackiewicz, D. V., Harman, E. A., Frykman, P. N., & Rosenstein, M. T. (1999). Cross-validation of three jump power equations. *Medicine and Science in Sports and Exercise*, *31*(4), 572-577. <https://doi.org/10.1097/00005768-199904000-00013>
- Shepherd, S. O., Cocks, M., Tipton, K. D., Witard, O. C., Ranasinghe, A. M., Barker, T. A., Wagenmakers, A. J. M., & Shaw, C. S. (2014). Resistance training increases skeletal muscle oxidative capacity and net intramuscular triglyceride breakdown in type I and II fibres of sedentary males. *Experimental Physiology*, *99*(6), 894-908. <https://doi.org/10.1113/expphysiol.2014.078014>
- Suraci, B. R., Quigley, C., Thelwell, R. C., & Milligan, G. S. (2021). A comparison of training modality and total genotype scores to enhance sport-specific biomotor abilities in under 19 male soccer players. *Journal of Strength and Conditioning Research*, *35*(1), 154-161. <https://doi.org/10.1519/JSC.00000000000003299>
- Tanisawa, K., Wang, G., Seto, J., Verdouka, I., Twycross-Lewis, R., Karanikolou, A., Tanaka, M., Borjesson, M., Di Luigi, L., Dohi, M., Wolfarth, B., Swart, J., Bilzon, J. L. J., Badtieva, V., Papadopoulou, T., Casasco,

- M., Geistlinger, M., Bachl, N., Pigozzi, F., & Pitsiladis, Y. (2020). Sport and exercise genomics: The FIMS 2019 consensus statement update. *British Journal of Sports Medicine*, *54*(16), 969-975. <https://doi.org/10.1136/bjsports-2019-101532>
- Varillas-Delgado, D., Del Coso, J., Gutiérrez-Hellín, J., Aguilar-Navarro, M., Muñoz, A., Maestro, A., & Morencos, E. (2022). Genetics and sports performance: The present and future in the identification of talent for sports based on DNA testing. *European Journal of Applied Physiology*, *122*, 1811-1830. <https://doi.org/10.1007/s00421-022-04945-z>
- Wetmore, A. B., Moquin, P. A., Carroll, K. M., Fry, A. C., Hornsby, W. G., & Stone, M. H. (2020). The effect of training status on adaptations to 11 weeks of block periodization training. *Sports*, *8*(11), 1-12. [10.3390/sports8110145](https://doi.org/10.3390/sports8110145)
- Wishart, D. S. (2019). Metabolomics for investigating physiological and pathophysiological processes. *Physiological Reviews*, *99*(4), 1819-1875. <https://doi.org/10.1152/physrev.00035.2018>
- Yingling, V. R., Castro, D. A., Duong, J. T., Malpartida, F. J., Usher, J. R., & O, J. (2018). The reliability of vertical jump tests between the Vertec and My Jump phone application. *PeerJ*, *6*(4), 1-13. <https://doi.org/10.7717/peerj.4669>



Investigation of Acoustic and Vibrational Properties Using Laser Doppler Vibrometry (LDV) and Electronic Speckle Pattern Interferometry (ESPI) of the Kulintangan Instruments

Sinin Hamdan^{1*}, Ahmad Faudzi Musib², Khairul Anwar Mohamad Said¹,
Saiful Hairi Othman³ and Marini Sawawi¹

¹Faculty of Engineering, Universiti Malaysia Sarawak, 94300 UNIMAS, Kota Samarahan, Sarawak, Malaysia

²Faculty of Human Ecology, Universiti Putra Malaysia, 43400 UPM, Serdang, Selangor, Malaysia

³Institute of Creative Arts and Technology, Universiti Malaysia Sarawak, 94300 UNIMAS, Kota Samarahan, Sarawak, Malaysia

ABSTRACT

This study visualises the mode of the vibration of kulintangan using Electronic Speckle Pattern Interferometry (ESPI) to reveal the modes. It was found that the production of sound by the kulintangan was dominated by a particular mode which may be the (0,1), (1,1), (2,2), (3,2), and (4,2) of free edge circular gong. The spectrum distribution from the strike on the kulintangan showed it. The small gong A-H has an approximately harmonic spectrum with a fundamental frequency of 1240, 1055, 934, 792, 705, 624, 474, and 422 Hz. The gong does not display a similar occurrence of harmonics due to the ruggedness of the surface texture of the gong. This finding can be of great importance to facilitate a better understanding of the mechanisms involved in the sound production of musical instruments. Our research is visualising the sound sonically through PicoScope oscilloscopes and ESPI.

Keywords: Acoustic, Electronic Speckle Pattern Interferometry (ESPI), Laser Doppler Vibrometry (LDV), vibrations

ARTICLE INFO

Article history:

Received: 22 April 2022

Accepted: 16 August 2022

Published: 20 March 2023

DOI: <https://doi.org/10.47836/pjst.31.2.24>

E-mail addresses:

hsinin@unimas.my (Sinin Hamdan)

faudzimusib@upm.edu.my (Ahmad Faudzi Musib)

mksanwar@unimas.my (Khairul Anwar Mohamad Said)

hosaiful@unimas.my (Saiful Hairi Othman)

smarini@unimas.my (Marini Sawawi)

* Corresponding author

INTRODUCTION

Visualising structural vibrations is important to understand acoustics. Two hundred years ago, Ernst Chladni introduced a common technique by placing sand on a vibrating flat plate for imaging the vibrations. Over the last 50 years, inexpensive methods to help students visualise vibrational mode shapes are still not widely available. Scanning Laser

Doppler Vibrometry (LDV) is an effective method for visualising steady-state structural vibrations, which costs several hundred thousand dollars. Electronic speckle pattern interferometry (ESPI) is one method of visualising structural deflection shapes that are widely used for research and can be used in an educational setting.

A kulintangan is a traditional musical instrument from the general region of Sabah Malaysia. The backbone of the kulintangan consists of gongs of various sizes with a similar general form and made of iron. The kulintangan is central to the musical art of Sabah, which commands huge respect and reverence. Scanning Laser Doppler Vibrometry (LDV) and electronic speckle pattern interferometry (ESPI) are used together with acoustical measurements.

The data validity from tone measurements of idiophones (particularly gongs) was questionable by Schneider (2001). Normal modes of a small gamelan gong using ESPI and finite element methods were done by Perrin et al. (2014) and Herington et al. (2010). Finite element analysis and gong acoustics were done by McLachlan (1997). The spectral analysis of tones produced on such instruments does not show clear, obvious ‘fundamental,’ but an inharmonic spectrum that yields auditory uncertainty. The data generated by tone-measuring equipment produced erroneous results. Bronze is the favoured and most expensive material of construction for gongs. Bronze instruments produce a richer tone, i.e., more appealing than iron instruments. Iron instruments, especially iron gongs, are much easier to tune than bronze counterparts. Figure 1 shows the vibrational modes of circular plates (a) free edge and (b) clamped or simply supported edge (Fletcher & Rossing, 1999). From Figure 1, the symbol (m, n) is used where ‘ m ’ is the nodal diameter, whereas ‘ n ’ is the nodal circle of the node produced from the vibration. $(3,0)$ means 3 nodal diameters and 0 nodal circles. The sound from musical instruments is strongly related to their vibrational mode, and Raman (1934) first reported the viewing technique. The main objective of this study was to gain a better understanding of how kulintangan vibrates when it is struck. It can be achieved partially by first investigating the mode of its vibration.

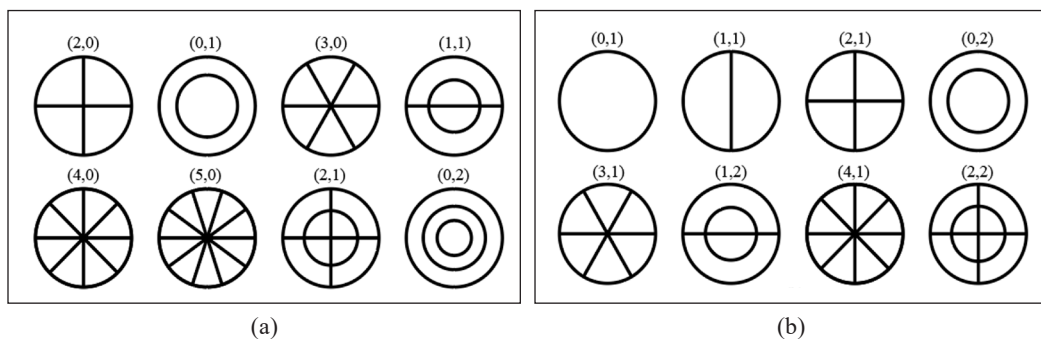


Figure 1. Vibrational modes of circular plates: (a) free edge and (b) clamped or simply supported edge [Fletcher and Rossing, 1999]

Kulintangan is a traditional musical instrument of the Kadazan Dusun, Bajau, Brunei Malay, and other ethnic groups in Sabah. A set of kulintangan consists of 8 to 12 small gongs (Alman, 1961) or 7 to 9 (Frame 1976). This work investigates 8 small steel gongs (label A to H) and a big steel gong. This work explored both the acoustical and vibrational aspects of the gongs. Previous measurements on the kulintangan frequency using the Fourier transform were done by Dusin (2001), whereas the physical characteristics, i.e., the correlation between the diameter and frequency, were done by Batahong and Dayou (2001). Dayou (2002) found that the sound from a good-quality kulintangan should consist of a single frequency for each gong.

The pitch of an iron gong can be increased or decreased by cold hammering (with little risk of permanent damage). Bronze gongs' pitch can be altered by hammering (which could result in cracking) or by scraping (permanently removes metal and reduces a tuner's options for future pitch adjustments). The approach to tuning an iron gong differs from that of a bronze gong. The pitch is lowered by cold hammering the flat surface around the knob of an iron gong from the top. The pitch can be raised by hammering the same surface inside the iron gong.

MATERIAL AND METHODS

A set of kulintangan consisting of 8 small iron gongs was used in this research. This work reports a typical small iron gong from Sabah with a diameter of <20cm. The dimension of the gong varies in the diameter where the rim and the thickness are consistent except for gongs A and H. The rim length for all gongs is 38mm except gong A and gong H, i.e., 34 and 43 mm, respectively. The diameter for the gongs increased gradually from A (17 cm), B (17.6 cm), C (17.8 cm), D (17.8 cm), E (18.2 cm), F (19 cm), G (20 cm) to H (18.6 cm). The thickness of the gongs ranges between 1.66 to 1.72 mm. This work reported gong G with a diameter of 20 cm. The resonance testing was conducted for all the gongs. Figure 2 shows one of the typical small iron gongs. The gongs were bought from the street market at Kundasang, Sabah, Malaysia. Most sound analyses and re-synthesis of the gong are investigating the tone systems. This work measured the fundamental frequency, harmonics, and sub-harmonics using Fourier transformation. The different intensities and harmonics or sub-harmonics (overtones) differentiate individual gong characters. Most importantly, this work showed the range of available frequencies at a specific time. Our study was conducted on a series of small iron gongs with a diameter of less



Figure 2. A typical small iron gong

than 20 cm. All the gongs sit on two pieces of stretch string and simulate the real situation when played.

Microphone Method

Figure 3 shows the experimental setup for the microphone method. An expert player struck the gong. The microphone was held above the top surface of the gong along the axis of symmetry at a distance of about 20 cm.

In this study, the audio signal derived from the striking by an expert player (an experienced gamelan ensemble player with a musical ear and knowledge of musical notation) is recorded. The audio signal is recorded in mono, at 24-bit resolution and 48 kHz sampling rate. The audio signal is recorded with a digital interface in a “.wav” format.

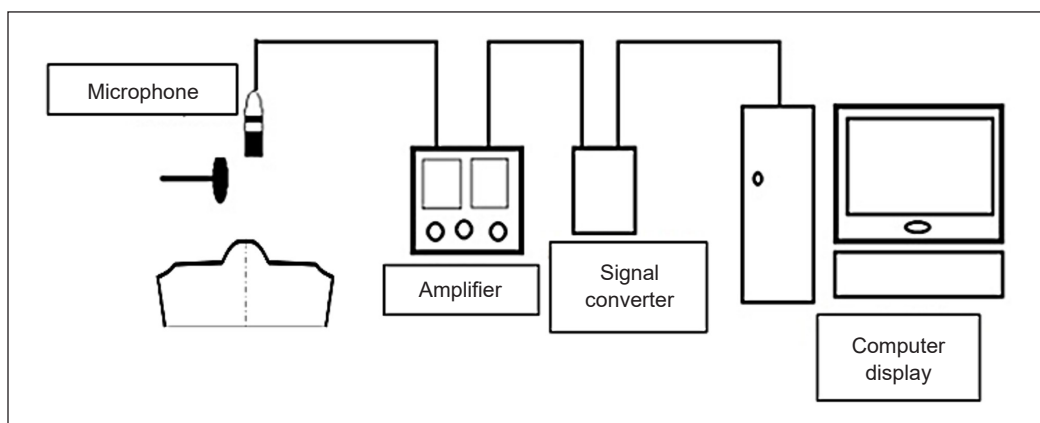


Figure 3. Schematic diagram of the experimental setups for the microphone method.

Audio signal calibration of the recording system is carried out to ensure the recorded audio signal is at the optimum level. A 1 kHz sine wave test tone calibrates the recording system. Here the ‘unity’ calibration level is at +4 dBu or -10 dBV and is read by the recording device at ‘0 VU’. In this regard, the European Broadcast Union (EBU) recommended that the digital equivalent of 0VU is that the test tone generated by the recording device of the experimentation is recorded at -18 dBFS (Digital) or +4 dBu (Analog), which is equivalent to 0VU. EBU defines the calibration standard for all manufactured professional audio recording devices and replay units. In this thorough calibration procedure, no devices unknowingly boost or attenuate its amplitude in the signal chain when the recording is carried out. The recording apparatus was the Steinberg UR22 mkII audio interface, Audio-Technica AT4050 microphone, XLR cable (balance), with microphone position on axis (<20 cm) and microphone setting with low cut (flat) 0 dB.

The PicoScope computer software (Pico Technology, 3000 series, Eaton Socon, UK) was used to view and analyse the time signals from PicoScope oscilloscopes (Pico

Technology, 3000 series, Eaton Socon, UK) and data loggers for real-time signal acquisition. PicoScope software enables analysis using Fast Fourier transform (FFT), a spectrum analyser, voltage-based triggers, and the ability to save/load waveforms to a disk. The amplifier (Behringer Powerplay Pro XL, Behringer, China) ensured the sound capture was loud enough to be detected by the signal converter.

Laser Doppler Vibrometer (LDV)

Having identified all the possible frequencies obtained through the microphone method, the Laser Doppler Vibrometer (LDV) was conducted to capture the vibration of the Eigen frequency from the gong and reconfirm all the resonance frequencies obtained from the microphone method. To investigate the motion at selected places on the surface of the gong, a Polytec Compact Laser Vibrometer was used to complement the ESPI measurements. The laser sampled an area of about 4 mm², considered as taking point measurements. The vibrometer output was recorded on a PC, and a Fourier transform was performed to determine the frequencies present. In the acoustic case, the vibration is excited by a hard rubber hammer, while in the LDV case, it is excited by the loudspeaker. The gongs were excited acoustically by means of a speaker driven by a signal generator and placed approximately a meter away from the gong. The distance was adjusted to yield the optimum vibrations on the gong to be captured by the LDV. The vibrations of the gong were recorded using the Pico oscilloscope, which can perform Fourier transform. A precautionary measure was taken with regard to the above measurements possibly being made on a nodal section of the gong. If the laser were normally pointed downwards onto a section of the gong's surface acting at a node, then no frequencies relevant to the gong's vibration would be found during the Fourier transform. Six locations were chosen on the surface of the gong, and LDV was undertaken at each point. The points were nominated as points 1-6, with point 1 being at the closest proximity to the knob and with increasing integer labels, the greater the distance from the knob.

Not all the resonance frequencies obtained from the microphone method are shown by the LDV, especially the high frequencies mode, although this is very clear through the microphone method. Since the microphone does not detect a frequency lower than 100 Hz, the LDV had the advantage of detecting the lower frequency by scanning through from 0 to 100 Hz. It appears to be consistent. The small gong was labelled considering its diameter, and the results of the resonance frequencies of each gong are shown as a series where the ordinate of the graph represents the frequency (Hz). At the same time, the abscissa counts a number of resonance frequencies. Figure 4 shows the experiment performed on the gong using non-contact sinusoidal excitation at a frequency close to one Eigen frequency of the gong.

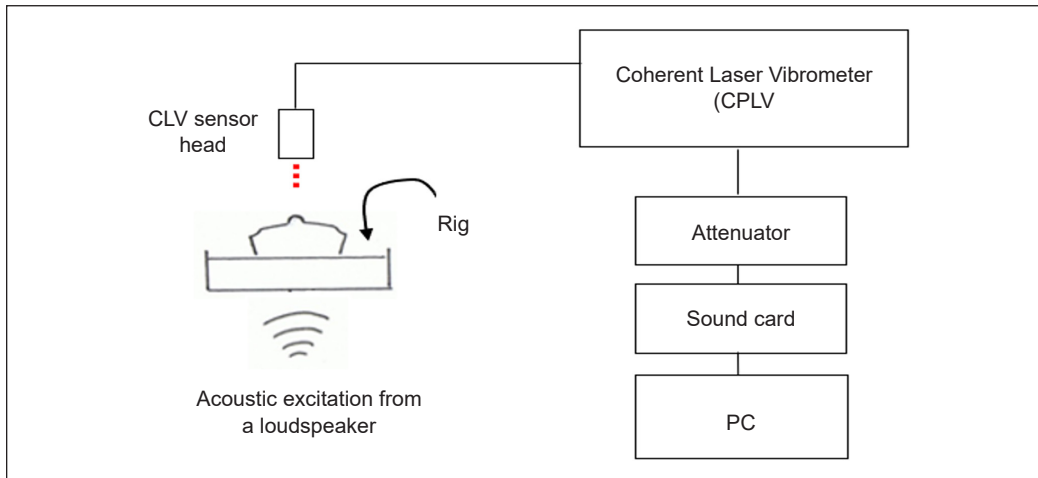


Figure 4. Apparatus setup for non-contact sinusoidal acoustic excitation and non-contact laser detector at specific Eigen frequency

Electronic Speckle Pattern Interferometry (ESPI)

Having done the microphone method and LDV, the electronic speckle pattern interferometry (ESPI) experiment was conducted on all the small gongs. ESPI is another non-contact technique that allows qualitative measurements of displacement to be made. The investigation analyses the linear modal analysis of the gongs. It makes several comparisons for the whole gongs. ESPI reported several mode patterns of resonance, similar among all the series of gongs. The gong was mounted on a vibration-isolated optical table inside an anechoic chamber driven by a speaker about 50 cm from it. A sinusoidal signal which drove the speaker was produced from a high-quality function generator (to avoid introducing harmonic and subharmonic signals). Unfortunately, the system did not permit the gong to be supported horizontally, as it would be during normal playing. Instead, it was hung vertically, clamped to a stand along a small section near the rim's centre. It would certainly have influenced some of the modes when interpreting the results.

The frequencies explored were in the range of 30 Hz-5 kHz. Images were observed on the computer screen, and when a pattern of deflections of the gong was observed, an image was saved for analysis. It is essential to have some information about the nodal patterns for as many cases as possible, i.e., m and n values, to identify split doublets, harmonics, and subharmonics. The results obtained by the CCD camera were shown on a computer monitor, and screenshots were taken. The frequency of the input signal supplied by the speaker was noted. The gong area placed under the test was perpendicular to the beam of the laser to increase the intensity of the results; the modes are analysed almost exclusively independently.

RESULTS AND DISCUSSION

Microphone Method

These investigations started with an experiment using a microphone method on the gongs subjected to a big strike on the dome. When struck by a soft hammer, the spectrum of the sound examined is notable that it evolves significantly over a time of about one second. The initial sound just decayed without any significant partials, as shown in Figures 5 and 6. The dimension of the small gong varies in diameter, where the rim and the thickness are consistent except for gongs A and H. The rim length for all gongs is 38 mm except gong A and gong H, i.e., 34 and 43 mm, respectively. The diameter for the gongs increased

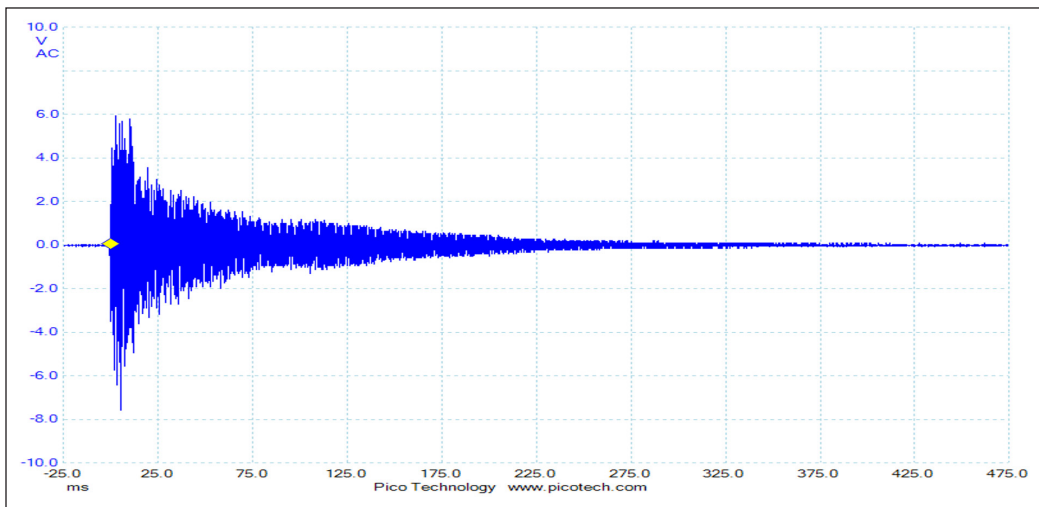


Figure 5: Acoustic signal of a small gong

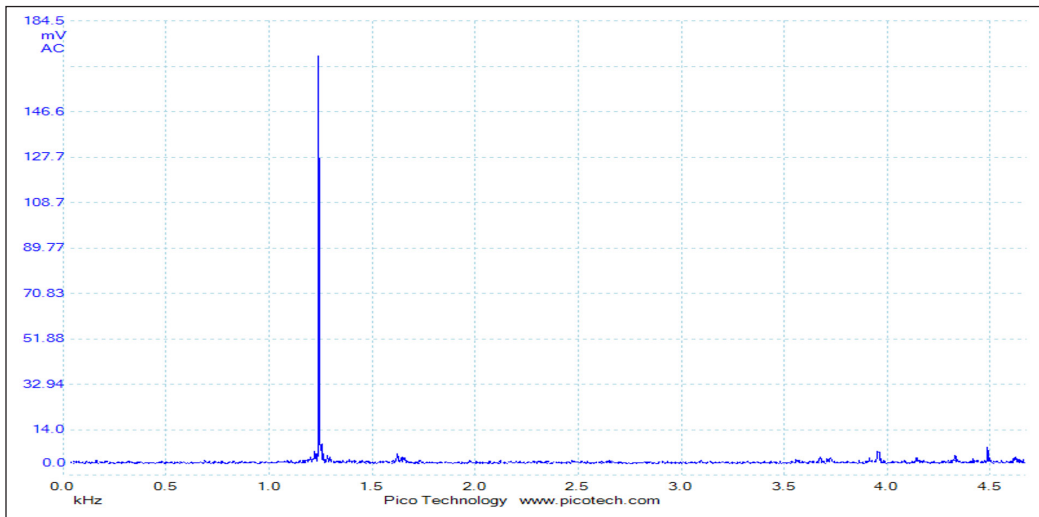
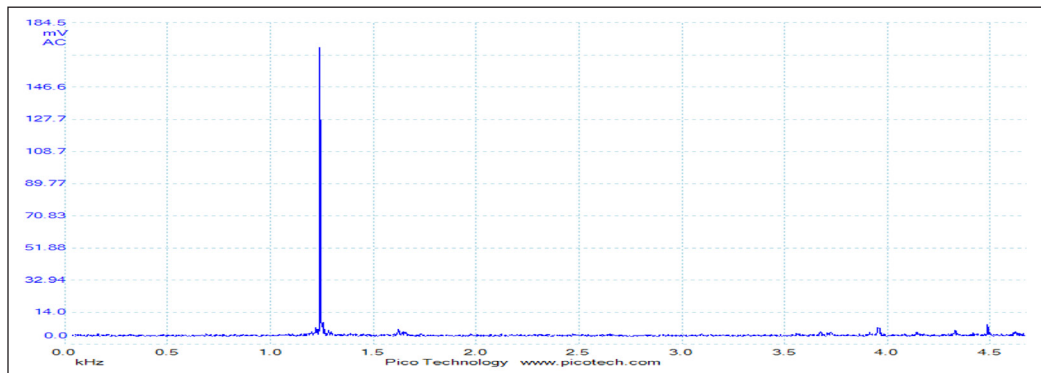


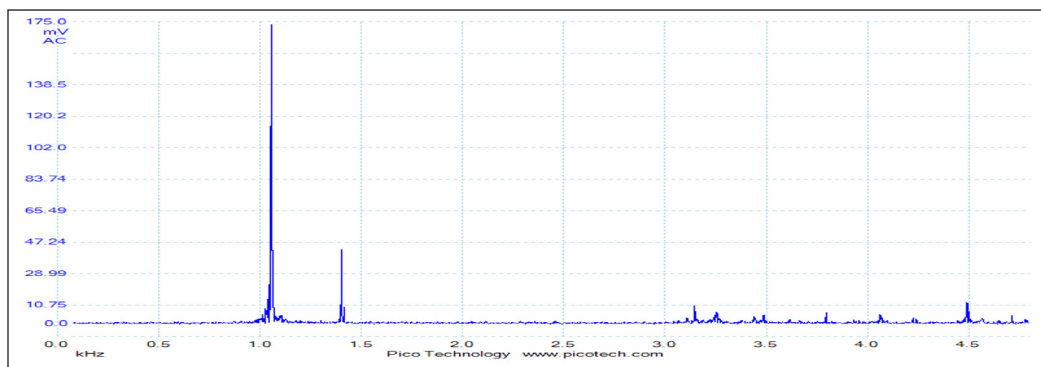
Figure 6. Sound pressure level spectra of a small gong

gradually from A (17 cm), B (17.6 cm), C (17.8 cm), D (17.8 cm), E (18.2 cm), F (19cm), G (20 cm) to H (18.6 cm). The thickness of the gongs ranges between 1.66 to 1.72 mm.

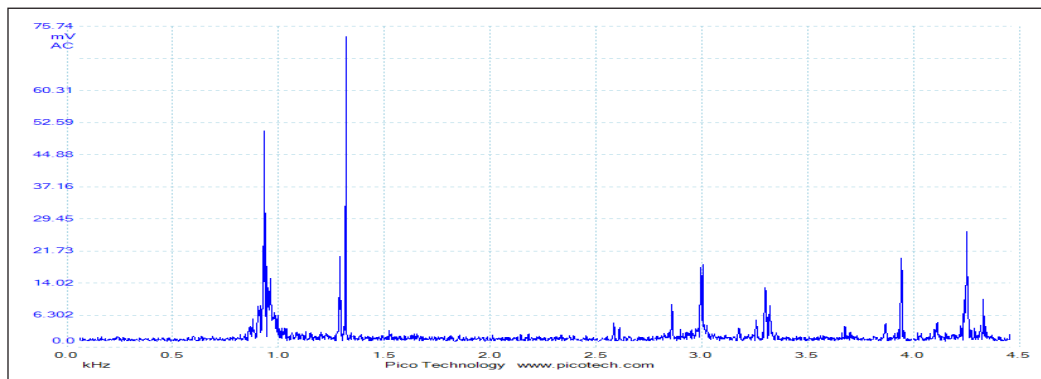
Figure 7 shows the acoustic spectra recorded about 500 milliseconds after excitation of 8 small iron gongs of less than 200 mm diameter. These acoustic spectra agree quite well with the non-contact sinusoidal excitation at a frequency close to one Eigen frequency



(a)



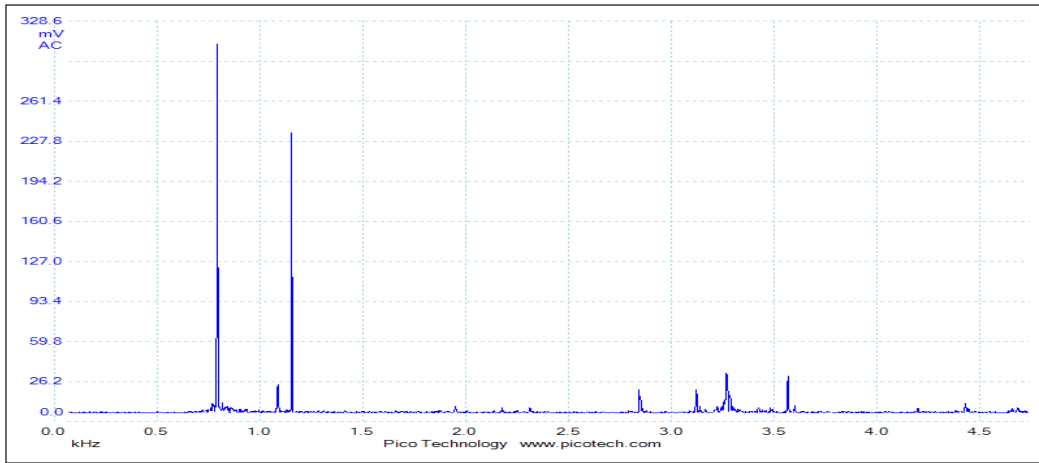
(b)



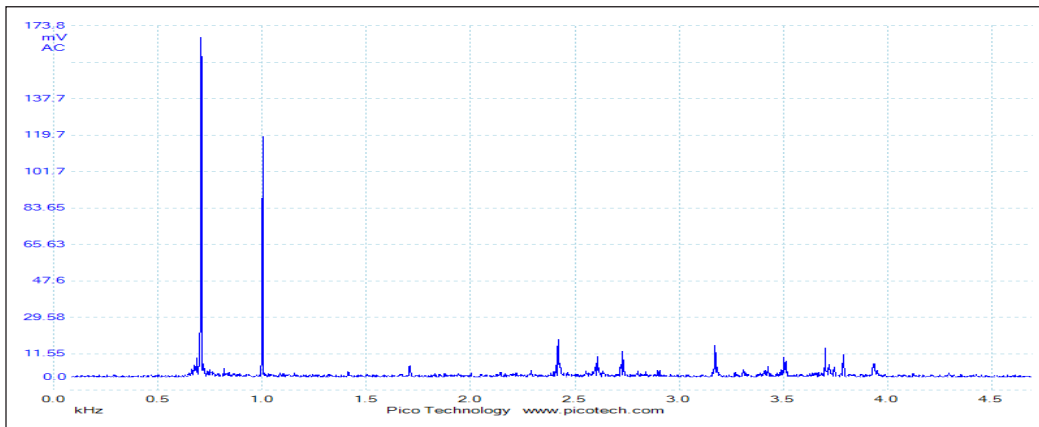
(c)

Figure 7. The acoustic spectra of 8 small gongs of less than 200 mm diameter (label A-H) were recorded about 500 milliseconds after excitation: (a) Gong A; (b) Gong B; and (c) Gong C

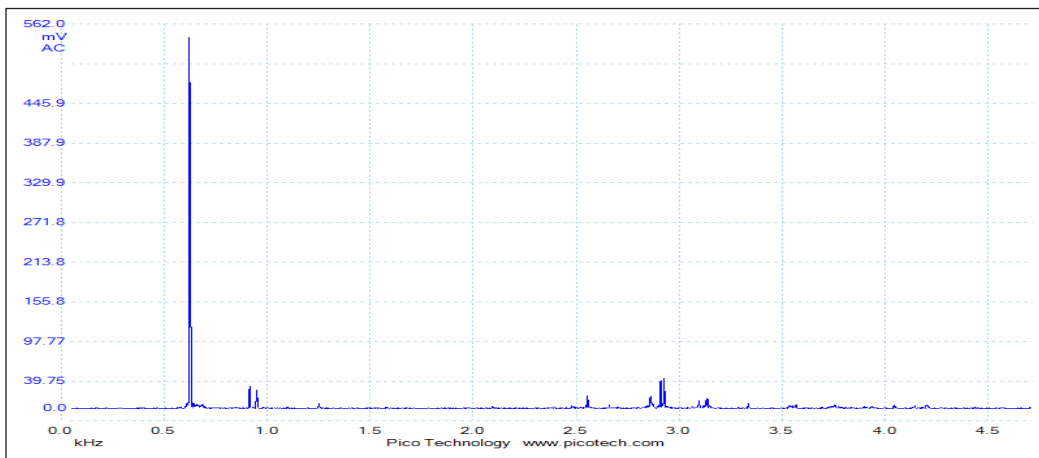
Acoustic and Vibrational Properties of the Kulintang



(d)

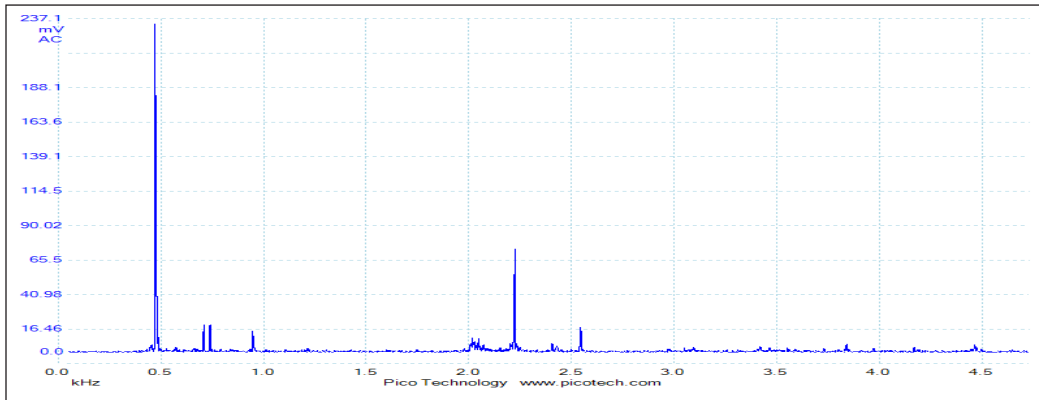


(e)

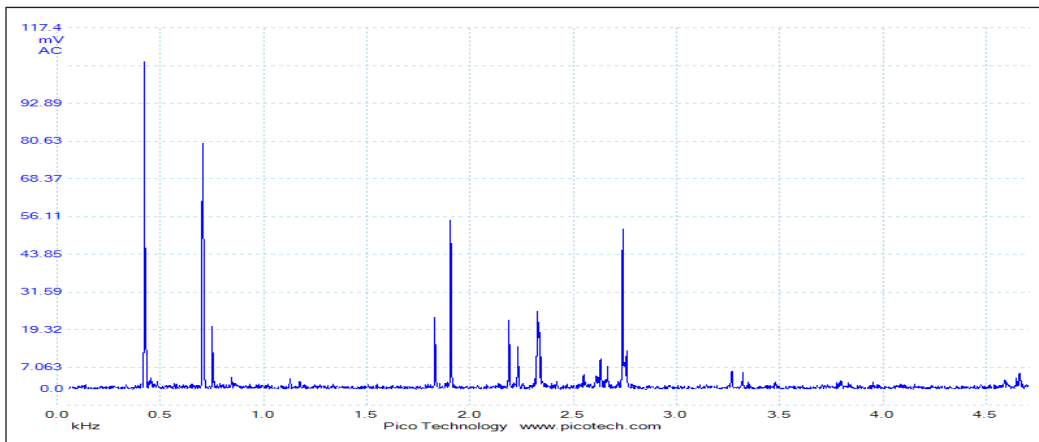


(f)

Figure 7 (continue). The acoustic spectra of 8 small gongs of less than 200 mm diameter (label A-H) were recorded about 500 milliseconds after excitation: (d) Gong D; (e) Gong E; and (f) Gong F



(g)



(h)

Figure 7 (continue). The acoustic spectra of 8 small gongs of less than 200 mm diameter (label A-H) were recorded about 500 milliseconds after excitation: (g) Gong G; and (h) Gong H

of the gong. In Figure 7, we show the gong's time-averaged acoustic power spectrum. It shows that the singlet (0,1) was the most important mode. The (1,1) and (2,2) modes were also significant. It is proven in Table 2 in the ESPI experiment. Only $n=1$ modes and some of their (non-linear) harmonics made worthwhile contributions. No evidence of a second important axisymmetric mode, as reported by Rossing using a different small gong, was found. Rossing may have observed a harmonic or a subharmonic of the (0,1). In the present ESPI experiments, a true (0,1) mode was found at 1055 Hz (gong B), 624 Hz (gong F), and 474 Hz (gong G).

Laser Doppler Vibrometer (LDV)

By identifying the resonance frequencies, the gong was subjected to harmonic excitation while keeping the excitation frequency constant and increasing the amplitude; a Laser

Doppler vibrometer (LDV) captured the vibration of the Eigen frequency from the gong. The spectra showed that all resonant peaks are extremely sharp. Some peaks did not correspond to any modes detected by ESPI. These enabled gaps in the overall mode data to be filled, although their nodal patterns had to be inferred.

The frequency obtained using LDV and ESPI measurements are shown in Tables 1 and 2, respectively. Data above 5 kHz had been excluded due to difficulty interpreting their ESPI forms. Such a deviation is caused by variations in the thickness of the gong during casting. Table 1 shows the Eigen frequency with the Eigen number for all series of gongs obtained from the LDV.

Table 1
Eigen number with Eigen frequency (Hz) for all series of gongs obtain from the LDV

Eigen number	1	2	3	4	5	6	7	8	9	10	11	12
A	1240	1621	3954	4484	-	-	-	-	-	-	-	-
B	1055	1400	3143	3253	3442	3795	4061	4224	4491	4642	-	-
C	934	1317	2584	2858	2994	3299	3675	3943	4251	-	-	-
D	792	1155	1949	2177	2311	2843	3119	3267	3564	-	-	-
E	705	1000	1708	2419	2607	2727	2897	3170	3503	3703	3786	4856
F	624	915	1251	2552	2911	3097	3334	3534	3753	4045	4197	4827
G	474	708	950	2018	2225	2406	2545	3050	3420	3466	3841	4168
H	422	704	1904	2188	2325	2632	2739	3264	4662	-	-	-

Figure 8 shows the typical progressive decay from the gong at a specific Eigen frequency using LDV. The Eigen frequency versus Eigen number for all series of gongs obtained from the LDV is shown in Figure 9.

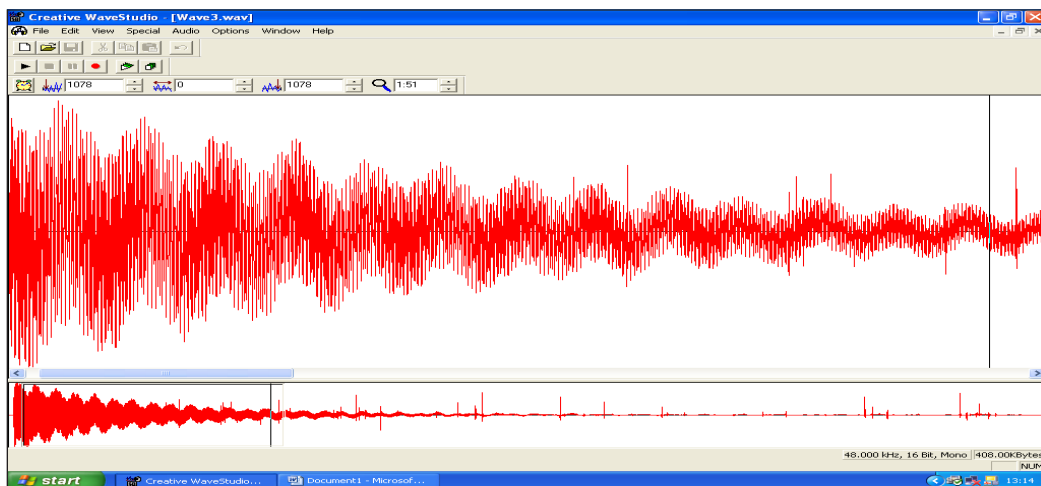


Figure 8. Decay signal from the gong at a specific Eigen frequency using LDV

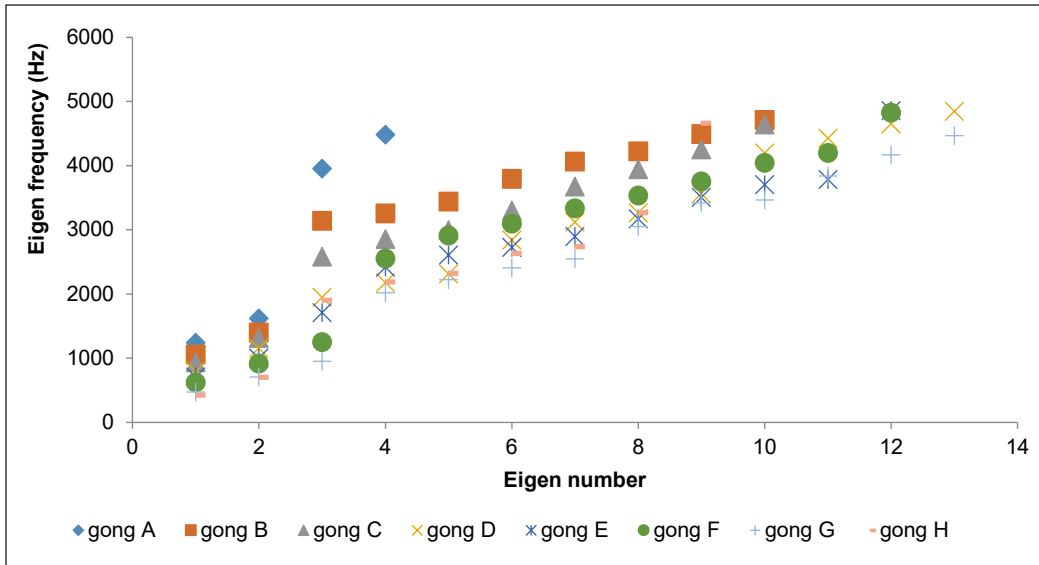


Figure 9. Eigen frequency versus Eigen number for all series of the gong from the LDV

Electronic Speckle Pattern Interferometry (ESPI)

The operational deflection shapes were studied using Electronic Speckle Pattern Interferometry ESPI. The patterns of the vibration from ESPI are shown in Figure 10. The frequencies and frequency ratio (bold number indicates near harmonic) of the modes (obtained from the ESPI) for all small gongs are given in Table 2.

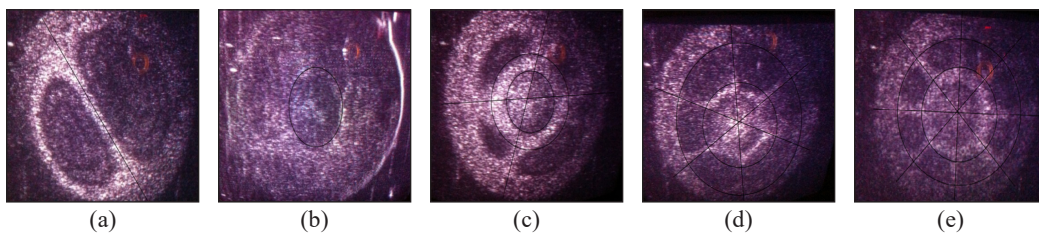


Figure 10. The patterns of the vibration from ESPI: (a) (1,1) from all gongs; (b) (0,1) from Gong B, (1055), F (624), and G (474) Hz; (c) (2, 2) from Gong B (3143), D (2311), E (2607), F (2544), and H (1904) Hz; (d) (3, 2) from Gong C (3299), D (3119), F (2911), G (2018), and H (2188) Hz; and (e) (4, 2) from Gong C (3675) and E (3170) Hz

The notation (m, n) represented a mode with ‘m’ nodal diameters and ‘n’ nodal circles. The approximate ESPI suggested that the fundamental peak at 1055 Hz (gong B), 624 Hz (gong F), and 474 Hz (gong G) is the (0, 1) mode. From Table 2, all gongs display the (1, 1) mode at 1621 Hz (A), 1400 Hz (B), 1317 Hz (C), 1155 Hz (D), 1000 Hz (E), 915 Hz (F), 788 Hz (G) and 701 Hz (H). The strong modes at 3143 Hz (harmonic ratio 3:1 for gong B) are the (2, 2) mode, at 3675 Hz (harmonic ratio 4:1 for gong C) is the (4, 2)

Table 2
Prominent partials in the sound measured acoustically obtained from LDV and (m, n) obtained from ESPI

Gong A (17 cm)	Freq (Hz)	1240	1621	3954	4484	---	---	---	---	---	---
	Freq ratio	1	1.30	3.19	3.62	---	---	---	---	---	---
	Mode(m,n)	---	(1,1)	---	---	---	---	---	---	---	---
Gong B (17.6 cm)	Freq (Hz)	1055	1400	3143	3253	3442	3795	4061	4224	---	---
	Freq ratio	1	1.33	2.98	3.08	3.26	3.6	3.85	4.00	---	---
	Mode(m,n)	(0,1)	(1,1)	(2,2)	---	---	---	---	---	---	---
Gong C (17.8 cm)	Freq (Hz)	934	1317	2548	2858	2994	3299	3675	3943	4251	4642
	Freq ratio	1	1.41	2.77	3.06	3.21	3.53	3.93	4.22	4.55	4.97
	Mode(m,n)	---	(1,1)	---	---	---	(3,2)	(4,2)	---	---	---
Gong D (17.8 cm)	Freq (Hz)	792	1155	1949	2177	2311	2843	3119	3267	3564	4197
	Freq ratio	1	1.46	2.46	2.74	2.91	3.59	3.94	4.13	4.5	5.30
	Mode(m,n)	---	(1,1)	---	---	(2,2)	(2,2)	(3,2)	---	---	---
Gong E (18.2 cm)	Freq (Hz)	705	1000	1708	2419	2607	2727	2897	3170	3503	3703
	Freq ratio	1	1.42	2.42	3.43	3.69	3.86	4.11	4.50	4.97	5.25
	Mode(m,n)	---	(1,1)	---	---	(2,2)	---	---	(4,2)	---	---
Gong F (19 cm)	Freq (Hz)	624	915	1251	2554	2911	3097	3334	3534	3753	4045
	Freq ratio	1	1.47	2.00	4.09	4.67	4.96	5.34	5.66	6.01	6.48
	Mode(m,n)	(0,1)	(1,1)	(1,2)	(2,2)	(3,2)	---	---	---	---	---
Gong G (20 cm)	Freq (Hz)	474	708	950	2018	2225	2406	2545	3050	3420	3466
	Freq ratio	1	1.49	2.00	4.26	4.69	5.08	5.37	6.43	7.22	7.31
	Mode(m,n)	(0,1)	(1,1)	---	(3,2)	---	---	---	---	---	---
Gong H (18.6 cm)	Freq (Hz)	422	704	1904	2188	2325	2632	2739	3264	4662	---
	Freq ratio	1	1.67	4.51	5.18	5.51	6.24	6.49	7.73	11.1	---
	Mode(m,n)	---	(1,1)	(2,2)	(3,2)	---	---	---	---	---	---

mode, at 2311 Hz and 3119Hz (harmonic ratio 3:1 and 4:1 for gong D) is the (2, 2) and (3, 2) mode, at 2607 Hz, and 3170 Hz (non-harmonic ratio 3.69 and 4.50 for gong E) is the (2, 2) and (4, 2) mode, at 1251 Hz, and 2554 Hz (harmonic ratio 2:1 and 4:1 for gong F) is the (1, 2) and (2, 2) mode, at 2018 Hz (non-harmonic ratio 4.26 for gong G) is the (3, 2) mode, at 1904 Hz and 2188 Hz (non-harmonic ratio 4.51 and 5.18 for gong H) is the (2, 2) and (3, 2) mode. The finding of this research shows that the mode of vibration for each gong may be the (1, 1) mode (Table 2). Mode (0, 1) appears for B, F, and G gongs. Mode (2, 2) appears for B, D, F, E, and H gongs. Mode (3, 2) appears for C, D, F, G, and H gongs. Mode (4, 2) appears for C and E gongs. Issues with the above images must be discussed before meaningful evaluation can begin. Noticeably, there appear to be repetitions of mode shapes, i.e., (2, 2) for gong D at 2311 and 2843 Hz. It is not simply the opposing member of a degenerate pair but repetitions of the mode shapes and nodal line locations. These modes (2, 2) appear and can therefore be denoted as sub-harmonics or harmonics,

respectively (at frequency ratios of 2.91 and 3.59). A prime example of this phenomenon is in Figure 10 is shown for gong D at 2311 Hz.

In Figure 10, harmonic relationships can be found for the (0, 1) modes for gong B at 1055 Hz, gong F at 624 Hz, and gong G at 474 Hz at a frequency ratio of 1 (octave). For gong B and C, harmonic relationships can also be found for the (2, 2) modes (at 3142 Hz at a frequency ratio of 2.98) and (4, 2) modes (at 3675 Hz at a frequency ratio of 3.93), respectively. Two harmonic relationships can also be found for the (2, 2) and (3, 2) modes for gong D (at 2311 and 3119 Hz, respectively, at frequencies ratio of 2.91 and 3.94, respectively). Harmonic relationships for gong F and H can also be found for the (2, 2) modes (at 2554 Hz at a frequency ratio of 4.09) and (3, 2) modes (at 2188 Hz at a frequency ratio of 5.18), respectively. This phenomenon can represent a difficulty in mode classification, as the modes are visible at more than one frequency ratio and could be different for different gongs where the mode for a harmonic relationship can be one only or two.

The frequencies observed in ESPI are real results forced through acoustic excitations. The Eigen frequencies in LDV are obtained from the resonance frequency through the microphone method. LDV, however, only simply showed the Eigen frequencies, but not the vibration mode of the gong. It is, therefore, not surprising that these two sets of frequencies, LDV and ESPI, do not complement each other. The modes from the ESPI images were much more difficult to identify. The gong has significant non-linear properties, as shown by both harmonics and subharmonics of many true modes and some mixed-symmetry types. With $n \geq 2$, some serious pattern distortions occur. $n=1$ was relatively easy to identify because their single nodal circle occurred at or near the inner edge of the shoulder.

In Figure 10, it is clearly visible that the modes are not perfectly formed. There is a large evanescent area to the top right of the gong in the lower-frequency images, and in the higher-frequency images, the nodes are not fully formed and of equal size. These imperfections in the nodal shapes could be caused due to an asymmetry in the gong or perhaps between the gong and the clamp used to hold the gong in place during experiments.

In the above mode shape, there are more partially formed modes than would be expected from a well-produced symmetric gong, and as such, the classification of the modes became arduous. The (4, 2) mode is a possible example of symmetry causing mode shapes to become uniform. A previously mentioned difficulty is the challenge of correctly denoting nodal patterns. The acoustical radiation is produced by motion normal to the surface. The modes are described in terms of the nodal patterns of their radial components.

Due to its axial symmetry, a perfect gong is subject to the same consequences for its normal modes as are other systems with the symmetry group C , such as bells, cymbals, and at circular plates. (m, n) can be used to specify a degenerate pair of modes of a particular physical type. However, there are always imperfections in both geometry and metallurgy

since the gongs are cast or formed. These imperfections caused the doublets to be split and the locations of their nodal diameters to be fixed. The gong deviated considerably from perfect axial symmetry causing significant distortions in some of the nodal patterns.

CONCLUSION

The small gong A-H has an approximately harmonic spectrum with a fundamental frequency of 1240, 1055, 934, 792, 705, 624, 474, and 422 Hz. Gong A with third harmonic (3.19) at 3954 Hz. Gong B with third harmonics (2.98 and 3.08) at 3143 and 3252 Hz and fourth harmonic (4.00) at 4224 Hz. Gong C with third (3.06), fourth (3.93), and fifth harmonics (4.97) at 2858, 3675, and 4642 Hz, respectively. Gong D with third (2.91) and fourth (3.94) harmonics at 2311 and 3119 Hz, respectively. Gong E with fifth harmonics (4.97) at 3503 Hz. Gong F with the second (2.00) and sixth (6.01) harmonics at 1251 and 3753 Hz, respectively. Gong G with the second (2.00) and fifth (5.08) harmonics at 950 and 2406 Hz, respectively. Gong H did not show any harmonics at all.

In this paper, a method to visualise the vibrational mode of kulintangan has been discussed. It is possible to view the type of the mode. It was found that kulintangan may be vibrated at (0, 1), (1, 1), (2, 2), (3, 2), and (4, 2) modes with free edge conditions. The pattern of the vibration can be seen from the ESPI. This finding can be a starting point for further research on the vibrational mode of kulintangan.

ACKNOWLEDGEMENTS

The authors are grateful to Universiti Malaysia Sarawak for the financial and technical support.

REFERENCES

- Alman, J. H. (1961). If you can sing, you can beat a Gong. *Sabah Society Journal*, 2, 29-41.
- Dayou J. (2002, July 15-18). *A method to determine the quality of sound from a Kulintangan Set*. [Paper presentation]. Borneo Research Council Seventh Biennial International Conference, Kota Kinabalu, Sabah.
- Batahong, R. Y. & Dayou, J. (2003, March 18-19). Visualizing the vibrational modes of Kulintangan. [Paper Presentation]. National Postgraduate Seminar, Kota Kinabalu, Sabah, Malaysia. https://www.researchgate.net/publication/339391008_VISUALIZING_THE_VIBRATIONAL_MODES_OF_KULINTANGAN
- Dusin, L. (2001). Pengukuran frekuensi bunyi Gong menggunakan kaedah transformasi fourier [Gong sound frequency measurement using Fourier transformation method] [Bachelor thesis]. Universiti Malaysia Sabah, Malaysia. https://books.google.com.my/books/about/Pengukuran_frekuensi_bunyi_gong_mengguna.html?id=i0LItQEACAAJ&redir_esc=y
- Fletcher, N. H., & Rossing, T. D. (1998). *The physics of musical instruments* (2nd ed.). Springer.

- Frame, E. M. (1976). Several major musical forms of Sabah, Malaysia. *Journal of the Malaysian Branch of the Royal Asiatic Society*, 49(230), 156-163.
- Herington, N., Elford, D. P., Swallowe, G. M., Chalmers, L., Perrin, R., & Moore, T. R. (2010, September 15-18). *Normal modes of a Gamelan Gong*. [Paper presentation]. 1st EAA EuroRegio: Congress on Sound and Vibration, Ljubljana, Slovenia.
- McLachlan, N. (1997). Finite element analysis and gong acoustics. *Acoustics Australia*, 25(3), 103-108.
- Perrin, R., Elford, D. P., Chalmers, L., Swallowe, G. M., Moore, T. R., Hamdan, S., & Halkon, B. J. (2014). Normal modes of a small gamelan gong. *The Journal of the Acoustical Society of America*, 136(4), 1942-1950. <https://doi.org/10.1121/1.4895683>.
- Raman, C.V. (1934). The Indian musical drums. *Proceedings of the Indian Academy of Sciences - Section A*, 1(3), 179-188. <https://doi.org/10.1007/BF03035705>.
- Schneider, A. (2001). Sound, pitch, and scale: From "tone measurements" to sonological analysis in ethnomusicology. *Ethnomusicology*, 45(3), 489-519. <https://doi.org/10.2307/852868>

The Breeding Ecology of the Painted Stork *Mycteria leucocephala* in Central Peninsular Malaysia

Mohd Amir Zakaria, Umami Nur Syafiqah Daud, Mohammad Saiful Mansor* and Shukor Md. Nor

Department of Biological Sciences and Biotechnology, Faculty of Science & Technology, Universiti Kebangsaan Malaysia, 43600 UKM Bangi, Selangor, Malaysia

ABSTRACT

The Painted Stork (*Mycteria leucocephala*) populations in Putrajaya and Shah Alam, Peninsular Malaysia, have increased by almost 10%–13% every year. If this trend continues, it is believed that habitat overlap may occur between this species and the Milky Stork (*Mycteria cinerea*), which is currently threatened with extinction. Habitat overlap could lead them to compete for food and other necessary resources, and consequently, one species would outcompete another. However, little is known about the breeding ecology of the Painted Stork in Peninsular Malaysia. Therefore, this study aimed to evaluate the breeding ecology of the Painted Stork and examine its nesting characteristics and their effects on breeding success. Direct observations were made of colonies in the Upper Bisa Putrajaya Wetland (UBPW) and Tasik Shah Alam (TSA) during the breeding season from March to September 2016 and 2017. The peak of the breeding season was in June, and no differences were found in nesting colony parameters between study sites, including the nest diameter and nest building period, except for nest height. The average height above the ground level of TSA nests was higher than in UBPW. Human activities near the nesting site in Shah Alam may have led to the birds constructing nests higher to prevent disturbance and predation. Nest diameter and nest building period were influenced by the number of

nestlings raised by parents. These findings provide new information that may be used in management programs to control Painted Stork populations and can be useful for conserving threatened species, particularly the Milky Stork.

ARTICLE INFO

Article history:

Received: 28 April 2022

Accepted: 13 July 2022

Published: 20 March 2023

DOI: <https://doi.org/10.47836/pjst.31.2.25>

E-mail addresses:

amirbiologikmns@gmail.com (Mohd Amir Zakaria)

ummisyafiqah96@gmail.com (Umami Nur Syafiqah Daud)

msaifulmansor@ukm.edu.my (Mohammad Saiful Mansor)

shukormn63@gmail.com (Shukor Md. Nor)

* Corresponding author

Keywords: Breeding ecology, conservation, *Mycteria leucocephala*, nesting waterbird, Painted Stork

INTRODUCTION

Painted Storks are exclusively piscivorous birds that occupy a high trophic level in aquatic food chains and are a prominent feature of wetlands (Kalam & Urfi, 2008). In addition to fish, their diet consists of crustaceans, molluscs and insects and is fed by tactolocation strategies (Prabhakar & Dudhmal, 2016). The Painted Stork, *Mycteria leucocephala*, uses wetlands as foraging and breeding grounds (Kaluthota et al., 2005). Wetlands provide not only ideal nesting conditions for the Painted Stork but also attract other waterbirds in the Family Ciconiidae, including the Milky Stork (*Mycteria cinerea*), Asian Openbill (*Anastomus oscitans*), Lesser Adjutant (*Leptoptilos javanicus*) and Storm's Stork (*Ciconia stormi*).

The Painted Stork's distributional range is in the Indian subcontinent (BirdLife International, 2020) and certain parts of Southeast Asia (Hancock et al., 2010). They are commonly seen in the Delhi area in north India (Kalam & Urfi, 2008). This species is listed as near threatened in the IUCN Red List (BirdLife International, 2020). In Malaysia, the Painted Stork was introduced from Sri Lanka to Zoo Negara for captive breeding in 1965, with an early population of four individuals. In 1985, Painted Storks were released from captivity in Zoo Negara and started nesting and roosting in the surrounding area, and since then, the population has continued to increase and is known to have reached 923 individuals in 2014 (Zakaria & Nor, 2019).

Painted Storks were first detected foraging far away from Zoo Negara in Putrajaya and Shah Alam in 2004. The Upper Bisa Putrajaya Wetland (UBPW) and Tasik Shah Alam (TSA) were identified as nesting locations of the Painted Stork in 2008. Besides Zoo Negara, TSA and UBPW, Saujana Golf and Bestari Jaya have also become preferred nesting sites of Painted Stork. These areas provide favourable nesting conditions for waterbirds. An uncontrolled increase in the Painted Stork population in certain areas is likely to cause this species to become a nuisance. Faeces and food left behind by waterbirds, especially in recreational areas, can attract unwanted pests that could affect human health, pollute the environment, and disturb people's daily activities (Murray & Hamilton, 2010). Therefore, wider distribution of the Painted Stork in Malaysia could cause problems due to increasing and uncontrollable populations. In addition to the environmental and human health problems caused by this species, it may threaten and interfere with the survival of local waterbirds. The spatial distributions of species are likely to overlap and cause competition for habitat, food, and other resources (Mansor & Ramli, 2017; Mansor et al., 2020). Apart from habitat loss and fragmentation, one of the most serious threats to the related endangered species, the Milky Stork, is hybridisation. A previous study has reported several incidents of the Painted Stork mating with the Milky Stork, an endangered species native to Southeast Asia (Yee et al., 2013; Baveja et al., 2019). Therefore, this study was conducted to examine the breeding ecology of the Painted Stork and to evaluate its nest

characteristics and their effects on its breeding success towards the management and conservation of Malaysian storks.

MATERIALS AND METHODS

Study Area

This study was conducted on two artificial islands in Upper Bisa, one of the five branches of the Putrajaya Wetland (UBPW) (Figure 1), and two sections of the island in Tasik Shah Alam (TSA). Islands in the UBPW that had been planted with tembusu tree (*Fagraea racemosa*) with a maximum height of 7 meters were classified as Island 1 (P1 UBPW), and islands planted with ara akar (*Ficus globosa*) with a maximum height of 9 meters were classified as Island 2 (P2 UBPW). TSA is an artificial recreational lake located in Selangor (Figure 1). The only island in this lake used as a nesting site by the Painted Stork was selected for this study; it consisted of ara akar, sealing wax palm (*Cyrtostachys renda*) and coconut (*Cocos nucifera*). The island was divided into two sections: Island 1 (P1 TSA) and Island 2 (P2 TSA), with a maximum plant height of 11.3 meters on both islands. Temperature and rainfall distributions for each month were obtained from the Malaysian Meteorological Department (MET) weather stations nearest the study area. Abiotic data were obtained from National Climate Centre stations, for the UBPW from the Serdang

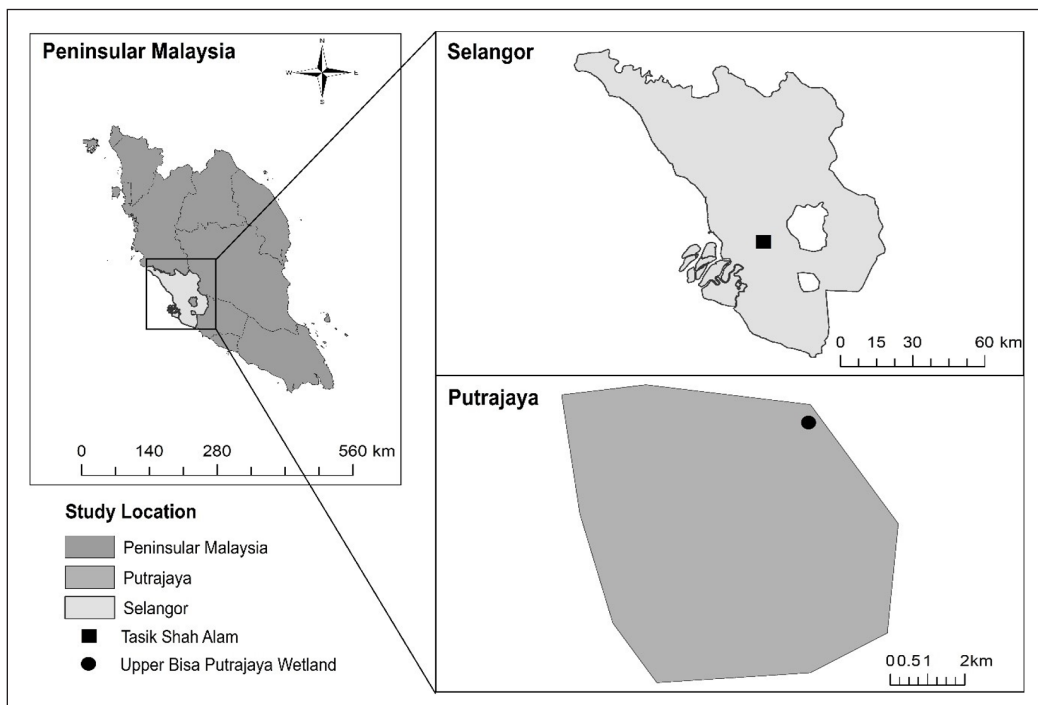


Figure 1. (Left) Map of Peninsular Malaysia, with an enlarged plan of Selangor State and Federal Territory of Putrajaya; the square (Tasik Shah Alam) and circle (Upper Bisa Putrajaya Wetland) indicate the study area

Agricultural Centre station (within a 3.52-km radius from the UBPW) and TSA from the Subang station (within an 8-km radius of TSA).

Data Collection

Data were collected during two breeding seasons of the Painted Stork, from March to September in 2016 and 2017. Direct observations of Painted Storks were made continuously from 0700 hours to 1900 hours using an HC-V380 video camera fitted with a 90× zoom lens (Panasonic, Kadoma, Japan) and a Nikon Coolpix P900 digital camera (Nikon Corporation, Tokyo, Japan). The distance between the observation point and the islands of the study area is between 33 m to 54 m. The nests were monitored for three days every week, from nest building initiation in March to all fledglings and their parents beginning to leave the nest in September. Each nest was identified and allocated a serial number to facilitate observation from the video recording. According to Meganathan and Urfi (2009), the percentage comparison method was employed, with the Painted Stork's beak length (approximately 24 cm) used as a scale to estimate tree and nest heights as the bird can be easily seen from observation points. Different aspects of breeding were recorded, such as nest building period, type of nesting tree, nest diameter and nest height above ground level. The number of nests and nestlings and nest fate at the end of the breeding season were also observed.

Nestling Development

Nestling success was classified based on the percentage of nestlings that successfully fledged from the nest. The development of each nestling was observed, and the following parameters were recorded: (1) the number of nestlings per nest, (2) the age at which the hatchling began to flap, (3) the age at which the nestling began to fly around the nest, and (4) the age at which the fledgling began to leave the nest. Each nestling was characterised based on its developmental stage: hatchling (1 to 30 days), semi-independent (31 to 85 days), and juvenile (after 85 days).

Data Analysis

Data were normally distributed (by inspection with quantile-quantile plots and Shapiro-Wilk tests). Pearson correlation was used to examine the relationship of each parameter of nest characteristics (duration of nest construction, nest diameter, nest height) to the number of nestlings per nest. The correlation was also used to test the relationship between abiotic parameters (temperature and rainfalls) and the number of nests and hatchlings. One-sample t-test was used to examine the differences between two breeding colonies between UBPW and TSA, and a two-sample t-test was used to examine the differences between colonies in 2016 and 2017. All tests were performed using SPSS Software.

RESULTS

Breeding Success

The incubation period of Painted Storks at UBPW and TSA was 29 days (range 26.5–32 days; Table 1). The number of nests in both study areas increased in 2017 compared to the previous year, with a total of 122 nests recorded in UBPW (2016 = 54; 2017 = 68) and 139 in TSA (2016 = 59; 2017 = 80). Nesting success, defined as the number of breeding

Table 1

The breeding ecology of the Painted Stork in the Upper Bisa Putrajaya Wetland (UBPW) and Tasik Shah Alam (TSA)

	Upper Bisa		Tasik	
	Putrajaya Wetland		Shah Alam	
	2016	2017	2016	2017
Total number of nests	54	68	59	80
Nesting success	47	61	53	69
Nesting failed	7	7	6	11
Average incubation period	29.3	29.4	29	29.2
Minimum	27	27.5	27	26.5
Maximum	32	31.5	32	31
Average nest diameter (cm):	68.63	65.38	69.13	65.14
No nestling	53	50	62.55	53.5
Single nestling	53.25	50.5	60.78	58.7
Two nestlings	71.5	65.5	67.55	71.55
Three nestlings	96.75	95.5	85.63	76.8
Average nest building duration (day)	5.6	5.8	5.7	5.8
No nestling	4.5	4.8	4.5	4.8
Single nestling	4.5	4.8	4.5	4.8
Two nestlings	6.3	6	6.3	6
Three nestlings	7.3	7.5	7.3	7.5
Average nest height (m)	6.8	6.87	7.44	7.59
Total number of nestlings (N)	100	110	98	108
Number of nestlings per nest	2.1	1.8	1.9	1.6
Number of fledglings	96	108	97	103
Nest fates at the end of the breeding season				
Abandoned	2	4	6	12
Destroyed	14	24	39	48
Nest used by other birds				
Purple Heron	26	25	0	0
Grey Heron	9	11	14	20
Black-crowned Night Heron	2	3	0	0
Cattle Egret	1	1	0	0

pairs that successfully hatched at least one egg in each nest, was high in both study areas (UBPW = 88.52%; TSA = 87.77%). A two-sample *t*-test showed no significant difference in the number of chicks per nest between UBPW and TSA, with 1.94 chicks and 1.69 chicks per nest, respectively ($t = 1.55, p = 0.18$). In addition, another paired *t*-test showed no significant difference in the number of nestlings per nest between 2016 and 2017 in

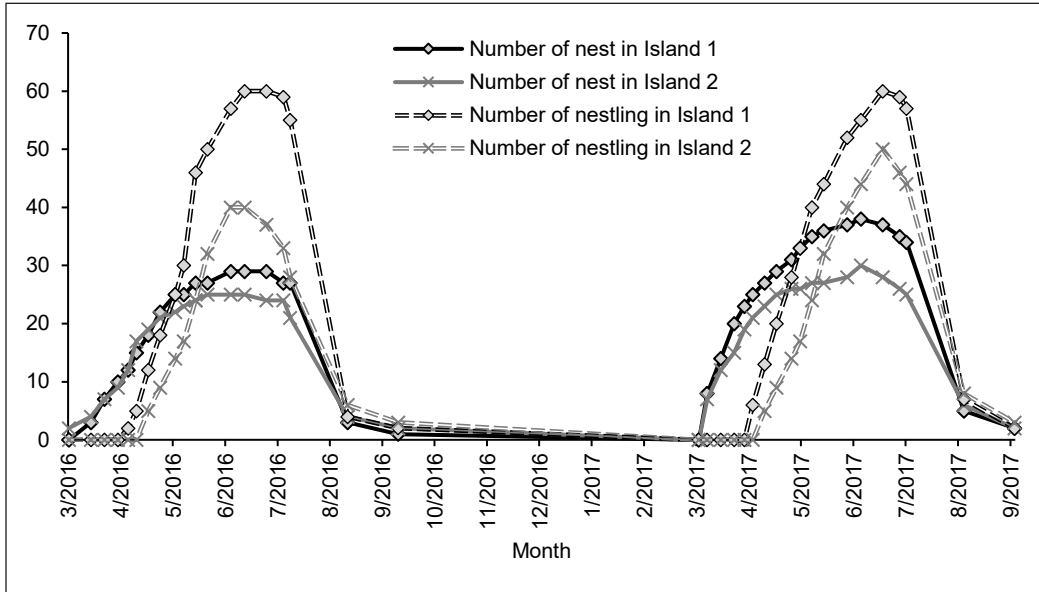


Figure 2. The number of nests and nestlings on Island 1 (Tembusu Island) and Island 2 (Ara Island) of Upper Bisa Putrajaya Wetland from 2016 to 2017

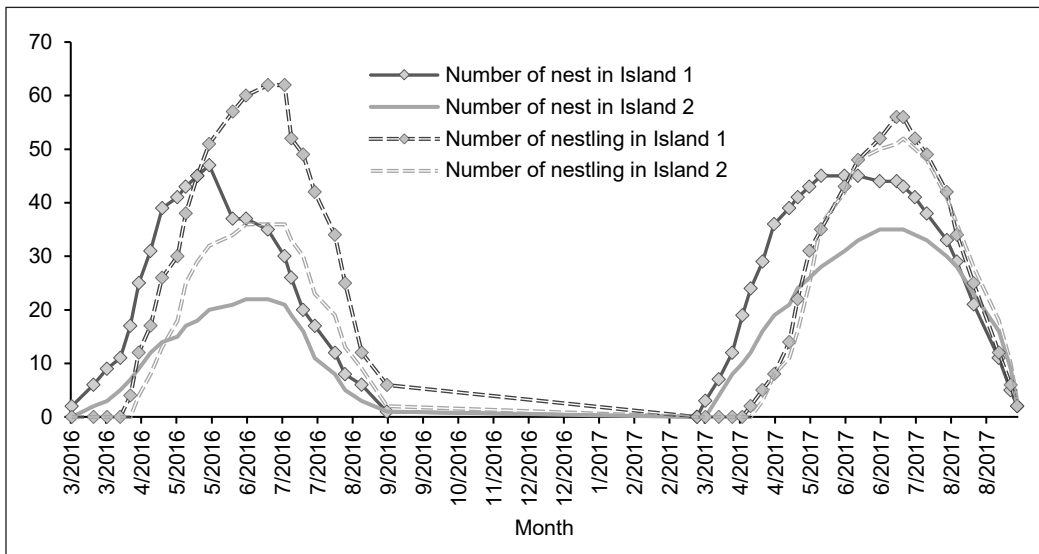


Figure 3. The number of nests and nestlings on Island 1 and Island 2 of Tasik Shah Alam from 2016 to 2017

UBPW, while TSA showed a significant difference in the number of nestlings per nest ($p > 0.05$; UBPW, $p = 0.3$; TSA, $p = 0.03$; Table 1). The number of nestlings per nest in UBPW was 2.13 ($n = 100$) in 2016 and 1.8 ($n = 110$) in 2017. In TSA, a total of 1.85 nestlings ($n = 98$) per nest were recorded in 2016 and 1.57 ($n = 108$) in 2017. Hatchling fatality was very low in both years, with a survival rate of 97.14% ($n = 204$), with four deaths in 2016 and two deaths in 2017 at UBPW, while the survival rate of nestlings at TSA was 97.19% ($n = 200$) with one death recorded in 2016 and five deaths in 2017. Correlation analysis showed a positive relationship between the number of nests on each island in 2016 and 2017 and the number of offspring per nest ($r = >0.5$), with the average number of nestlings peaking in June in UBPW (Figure 2) and TSA (Figure 3).

Nest Diameter and Duration of Nest Building Based on Clutch Size

Nest diameter did not differ between sites. Nest diameter in UBPW and TSA was directly proportional to the number of nestlings. The average diameter of the nest in UBPW was 67.0 cm, while in TSA, it was 67.14 cm, with an average nest-building period in UBPW of 5.7 days and 5.8 days in TSA (Table 1). The size of the Painted Stork nest was related to the number of nestlings produced by the breeding pair, with nest diameters ranging from 44 to 93.7 cm in UBPW and from 40 to 110 cm in TSA. Figure 4 shows that the diameter of nests with three nestlings was the largest, with an average of 88.67 cm (UBPW = 96.13 cm; TSA = 81.22 cm), compared to nests with two nestlings which averaged 69.03 cm (UBPW = 68.5 cm; TSA = 69.55 cm), while parents with only one successfully raised nestling had nests with the smallest size, with the average being 55.81 cm (UBPW = 51.88 cm; TSA = 59.74 cm).

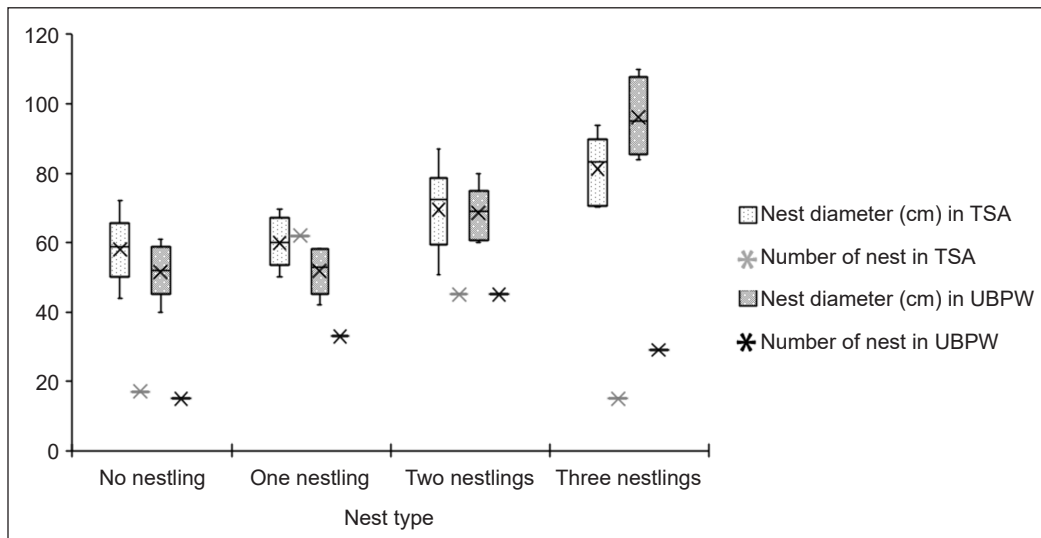


Figure 4. Number of nests by diameter and number of offspring

The nest-building duration of the Painted Stork was the same in both study areas, but it was based on the number of nestlings per nest (Table 1). Pairs raising three nestlings took longer to build their nest, on average, 7.4 days compared to 6.15 days for pairs with two nestlings and only 4.65 days for pairs with one nestling. In UBPW, 36.89% of the nests found during observations had two nestlings (n = 122), while in TSA, nests with only one nestling were more common (44.6%, n = 139).

Above-Ground Nest Site Selection

Our observations indicated that nest site selection by the Painted Stork was not random and that the type of tree and human presence influenced nest site preference in TSA. The average nest height above ground level in UBPW was lower than in TSA (Table 1). The average height was 6.84 m in UBPW and 7.56 m in TSA (Table 2). In the latter location, all nests were built above ground on trees at more than 49% of the tree height (Figure 7). Nests at less than 49% of tree height were found only in UBPW (Figure 6). Most nests (54 nests) found in UBPW were at 50%–74% of tree height, followed by 49 nests at 75%–100% of tree height, while most nests (78 nests) found in TSA were at 75%–100% of tree height (Figure 5).

Table 2
Maximum and minimum nest height above ground level at each study location

Location	Island	Minimum height (m)	Maximum height (m)
UBPW	P1	1.96	7.9
	P2	5.13	11.5
TSA	P1	11.3	7.25
	P2	10.2	7.93

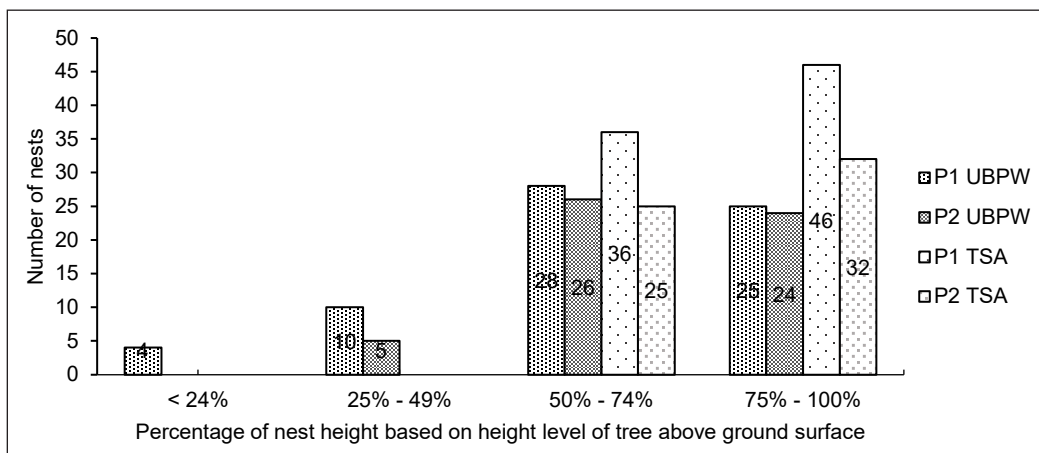


Figure 5. The number of nests above ground level based on nest position on the tree as a percentage of tree height



Figure 6. Position of Painted Stork nests as a percentage of tree height in Island 1 (top) and Island 2 (bottom) in UBWP

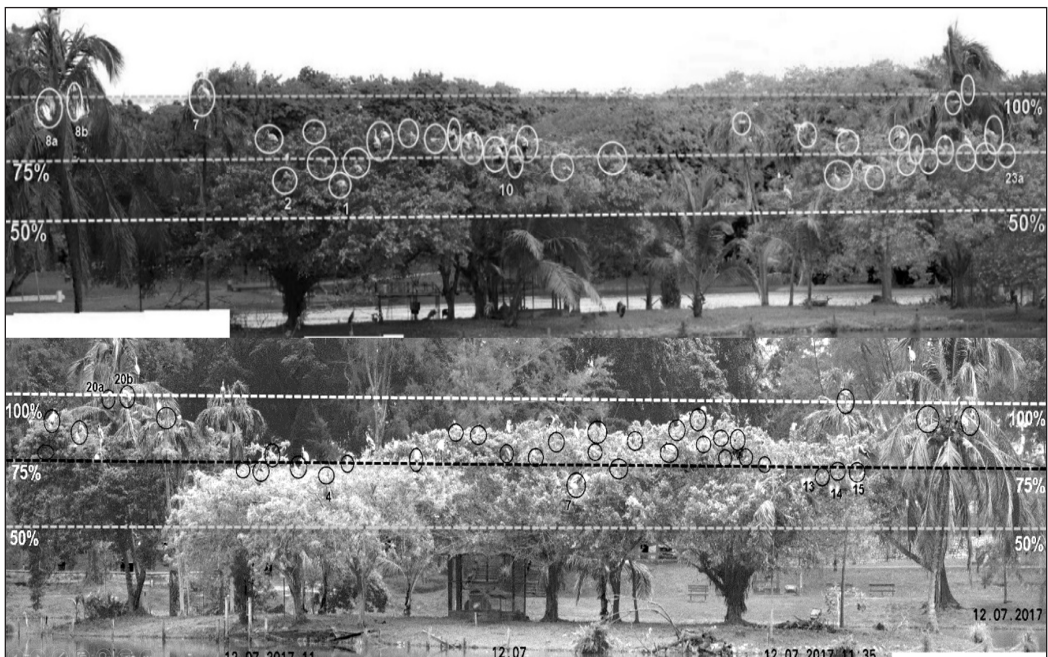


Figure 7. Position of Painted Stork nests as a percentage of tree height in Island 1 (top) and Island 2 (bottom) in Tasik Shah Alam

Nest Fate

Painted Stork was observed to have peak nesting season during both April and July in TSA and UBWP. At the end of the breeding season, while some Painted Stork nests in UBWP were destroyed or abandoned, others were observed to have been taken over by four other waterbird species, the Purple Heron (*Ardea purpurea*), Grey Heron (*Ardea cinerea*), Black-crowned Night Heron (*Nycticorax nycticorax*), and Cattle Egret (*Bubulcus ibis*). Nests in TSA also experienced the same fates, but only the Grey Heron was seen to take over some Painted Stork nests while the other nests were destroyed or abandoned by their owners.

Of the Painted Stork nests taken over by the four waterbird species in UBWP, 41.8% were occupied by the Purple Heron, 41% by the Black-crowned Night Heron, 16.4% by the Grey Heron, and 1.64% by the Cattle Egret, while 31.15% of the nests were destroyed and 4.92% were left empty (Figure 8). On the other hand, more than half (62.6%) of the Painted Stork nests in TSA were destroyed by their owners, while the Grey Heron took over 24% of the nests, and the rest (12.95%) were abandoned.

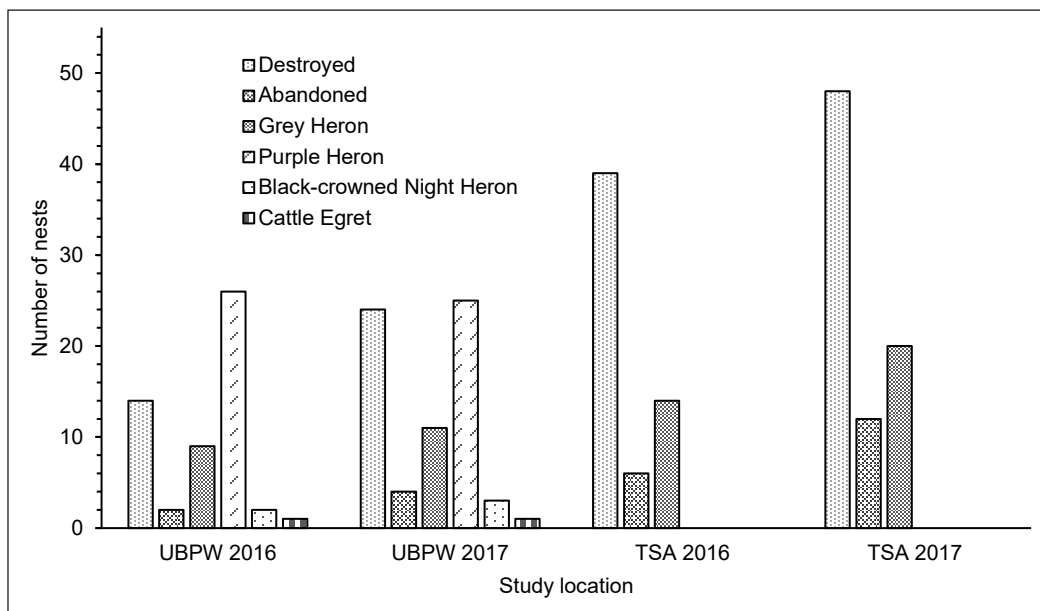


Figure 8. The fate of Painted Stork nests in the two study areas

Abiotic Conditions

Table 3 shows that June’s highest number of nests and nestlings occurred. There was a highly significant positive relationship between the number of nests and the highest average temperature (UBPW: $r = 0.815$; TSA: $r = 0.776$; $p < 0.01$), while there was a negative relationship between the number of nests and average rainfall distribution and between the number of juveniles and average rainfall distribution.

Table 3
Average temperature, rainfall, number of nests and number of nestlings by month in the UBPW and TSA in 2017

Month	Average highest temperature (°C)		Average lowest temperature (°C)		Average rainfall (mm)		Number of nests		Number of nestlings	
	UBPW	TSA	UBPW	TSA	UBPW	TSA	UBPW	TSA	UBPW	TSA
January	29	30	24	24	189	208	0	0	0	0
February	30	31	24	24	181	189	0	0	0	0
March	31	32	24	24	319	310	26	13	0	0
April	31	32	25	25	381	360	54	56	29	5
May	31	32	25	25	307	282	63	81	76	54
June	31	32	25	25	171	165	65	84	110	92
July	30	31	25	24	146	155	40	71	64	97
August	30	31	24	24	167	177	10	44	18	53
September	30	31	24	24	213	219	3	3	5	5
October	30	31	25	24	270	273	0	0	0	0
November	30	30	24	24	312	318	0	0	0	0
December	29	30	24	24	251	270	0	0	0	0

DISCUSSION

We found that the Painted Stork in Peninsular Malaysia began nesting in mid-March in Malaysia, after the monsoon season, which occurs between November and March (METMalaysia). This study also shows that the number of nests and nesting success is reduced when rainfall increases. This result is similar to Urfi's (2011a) findings for the nesting season of the Painted Stork in Sri Lanka, likely because Malaysia and Sri Lanka are located at similar latitudes. The monsoon season is unsuitable for nesting as heavy rains affect the incubation process, which requiring high temperatures for embryo development. Although the rainy season is not suitable for breeding birds, the water rises causes an increase in fish populations by the end of the monsoon season in February, thus sufficient as a food resource for the Painted Stork to start nesting and breeding (Urfi et al., 2007). Such strategies and adaptations could ensure their population's success (Mansor et al., 2015).

The Painted Stork nests were built on trees in UBPW, and TSA is mostly at 50%–100% of the tree's height, facilitating landing and avoiding threats from predators (Urfi, 2011b). Hatching failure is not influenced by nest height. This study provides observational evidence for this; some nests built at 75% of the tree's height were left empty by parents after incubating for almost a month and a half. Hatching success, nesting success, nest size, the number of nestlings per nest, and parental care are not affected by the height of the nest on the tree (Lambrechts et al., 2012), but they are influenced by biotic factors, including predation and egg viability and abiotic factors such as the weather and disturbance caused by humans (Urfi, 2010). Although nesting success is not guaranteed by nest site selection, it is influenced by interference by humans or other animals. In this study, the lowest nest

in TSA was 5.16 m from the ground, possibly due to human activities such as kayaking. In contrast, no human activities were observed in UBPW, and the lowest nest was 1.96 m from the ground, similar to the nest placements recorded by Urfi (2011b), who found nests as low as the water surface in the Delhi Zoo. It suggests that human presence influences nest height in breeding colonies of the Painted Stork. Anthropogenic activities force storks to change their foraging area and increase their energy requirement for flight and food searching (Prabhakar & Dudhmal, 2016).

This study showed that trees with a larger branch diameter were preferred as nesting sites by Painted Storks in both colonies. Painted Storks were observed to build their nests on islands planted with the tembusu tree (*Cyrtophyllum fragrans*), which has branches with a larger diameter than ara akar (*Ficus globosa*). Larger branches are believed to ensure the safety of nests and support the weight of the nest and nestlings (Urfi & Kalam, 2006). The most preferred tree was tembusu, followed by coconut and ara akar; the least preferred tree was sealing wax palm (*Crytostachy renda*). Both ara akar and sealing wax palm can support only one nest per branch, unlike tembusu and coconut tree, which can support more than one nest per branch.

The results of this study show that nest-building duration was related to the diameter of the nest and the number of nestlings per nest. The volume of the clutch, as well as the size of the incubating parent, determines the surface area and size of the nest for structural support of the parent and their nestlings (Heenan & Seymour, 2011). The positive relationship between nest size and clutch size shows that females alter the size of their nests to accommodate eggs and hatchlings based on the number of eggs they plan to lay (Slagsvold, 1989; Álvarez & Barba, 2008). The construction of a larger nest indicates the nest quality with high breeding success and may also be due to the need to prepare an extra space for storing prey as food supplies (Korpimäki, 1985; Vergara et al., 2010). Moreover, cooperation between partners in which the female builds the nest while the male looks for nest material and biparental incubation strategy contribute to nesting success (Daud et al., 2022).

The results showed that the number of nests in the Putrajaya and Shah Alam colonies was inversely proportional to the amount of rainfall. In June, the average rainfall decreased by 44.3% to 171 mm in the Putrajaya colony, but the number of nests continued to increase to 65, and a total of 110 Painted Storks had 155 successful hatchlings. The last breeding season occurred in September, when the average rainfall increased by 27.54%, from 172 mm in August to 216 mm in September. There were no more nesting Painted Storks in both study areas in October and after the monsoon season began in Peninsular Malaysia. Environmental factors, such as rainfall and temperature, play an important role in nest building and parent and nestling activity (Sparks & Tryjanowski, 2005; Daud et al., 2022) and can affect nesting success, nestling development and nesting density throughout the

breeding season, especially in the early stages of the breeding phase (Ismail & Rahman, 2013). The weather can also affect the hatching rate and nestling mortality at the end of the breeding season (Jovani & Tella, 2004; Novoa et al., 2008). At the end of the breeding season, Painted Stork nests were observed either destroyed, abandoned or have been taken over by other species. Due to its robust size, certain species, such as herons and egrets, may re-use the nest. While nest abandonment at the end of the breeding season is normal behaviour in most birds, why storks destroy their nest is still uncertain. It was observed that Milky Stork in Kuala Gula destroyed their nest after failing to hatch the eggs (Faiq, pers. comm.). Future studies should focus on the detailed breeding biology of storks, including Milky Storks, to help us to understand the potential of wetlands as conservation sites for storks and other waterbirds.

CONCLUSION

We found that the peak of the breeding season of Painted Stork was in June, and no differences were found in nesting colony parameters between study sites, including the nest diameter and nest building period, except for nest height. The selection of nesting location is the main successful nesting strategy of the Painted Stork. These findings provide information about the breeding activities of the Painted Stork in Peninsular Malaysia and highlight the importance of wetlands as nesting sites for waterbirds. These findings provide useful information that may be used in management strategies to control Painted Stork populations and can be useful for conserving related threatened species, the Milky Stork.

ACKNOWLEDGEMENTS

We are grateful to Universiti Kebangsaan Malaysia Research Fund [GUP-2021-048], which provides financial support for this study. We thank the Department of Wildlife and National Parks, Shah Alam City Council and Putrajaya Corporation, Malaysia for their permission to perform this research. We also thank all lab members for field assistance and data analysis.

REFERENCES

- Àlvarez, E., & Barba, E. (2008). Nest quality in relation to adult bird condition and its impact on reproduction in Great Tits *Parus major*. *Acta Ornithology*, 43(1), 3-9. <https://doi.org/10.3161/000164508x345275>
- Baveja, P., Tang, Q., Lee, J. G. H., & Rheindt, F. E. (2019). Impact of genomic leakage on the conservation of the endangered Milky Stork. *Biological Conservation*, 229, 59-66. <https://doi.org/10.1016/j.biocon.2018.11.009>
- BirdLife International. (2020). *Species factsheet: Mycteria leucocephala*. <http://www.birdlife.org>
- Daud, U. N. S., Ismail, N. A., Nor, S. M., & Mansor, M. S. (2022). Biparental incubation behavior in the domestic house-farmed swiftlets (*Aerodramus* sp.) in central Peninsular Malaysia. *Animal Biology*, 72(1), 39-49. <https://doi.org/10.1163/15707563-bja10066>

- Hancock, J., Kushlan, J. A., & Kahl, M. P. (2010). *Storks, ibises and spoonbills of the world*. A&C Black.
- Heenan, C. B., & Seymour, R. S. (2011). Structural support, not insulation, is the primary driver for avian cup-shaped nest design. *Proceedings of the Royal Society B: Biological Sciences*, 278(1720), 2924-2929. <https://doi.org/10.1098/rspb.2010.2798>
- Ismail, A., & Rahman, F. (2013). Does weather play an important role in the early nesting activity of colonial waterbirds? A case study in Putrajaya Wetlands, Malaysia. *Tropical Life Sciences Research*, 24(1), 1-7.
- Jovani, R., & Tella, J. L. (2004). Age-related environmental sensitivity and weather mediated nestling mortality in White Stork *Ciconia ciconia*. *Ecography*, 27(5), 611-618. <https://doi.org/10.1111/j.0906-7590.2004.03925.x>
- Kalam, A., & Urfi, A. J. (2008). Foraging behaviour and prey size of the Painted Stork. *Journal of Zoology*, 274(2), 198-204. <https://doi.org/10.1111/j.1469-7998.2007.00374.x>
- Kaluthota, C. D., Gamage, S. N., & Kaluthota, U. L. S. (2005, December 2-3). Breeding status of the Painted Stork (*Mycteria leucocephala*) in the Kumana villu of the Yala East National Park. In *Proceedings of International Forestry and Environment Symposium*. Kabool Lanka, Thulhiriya, Sri Lanka
- Korpimäki, E. (1985). Clutch size and breeding success in relation to nest-box size in Tengmalm's owl *Aegolius funereus*. *Ecography*, 8(3), 175-180. <https://doi.org/10.1111/J.1600-0587.1985.TB01168.X>
- Lambrechts, M. M., Aimé, C., Midamegbe, A., Galan, M. J., Perret, P., & Grégoire, A. (2012). Nest size and breeding success in first and replacement clutches: An experimental study in Blue Tits *Cyanistes caeruleus*. *Journal of Ornithology*, 153(1), 173-179. <https://doi.org/10.1007/s10336-011-0722-1>
- Mansor, M. S., & Ramli, R. (2017). Niche separation in flycatcher-like species in the lowland rainforests of Malaysia. *Behavioural Processes*, 140, 121-126. <https://doi.org/10.1016/j.beproc.2017.04.010>
- Mansor, M. S., Nor, S. M., & Ramli, R. (2020). Shifts in foraging behaviour of heterospecific flocking birds in a lowland Malaysian rainforest. *Behavioural Processes*, 180, Article 104229. <https://doi.org/10.1016/j.beproc.2020.104229>
- Mansor, M. S., Ramli, R., & Sah, S. A. M. (2015). The foraging tactics of Chestnut-winged babbler (*Stachyris erythroptera*) and Abbott's babbler (*Malacocincla abbotti*) in a lowland rainforest, Malaysia. *Sains Malaysiana*, 44(5), 687-692. <https://doi.org/10.17576/jsm-2015-4405-07>
- Meganathan, T., & Urfi, A. J. (2009). Inter-colony variations in nesting ecology of Painted Stork (*Mycteria leucocephala*) in the Delhi Zoo (North India). *Waterbird*, 32(2), 352-356. <https://doi.org/10.1675/063.032.0216>
- Murray, C. G., & Hamilton, A. J. (2010). Perspectives on wastewater treatment wetlands and waterbird conservation. *Journal of Applied Ecology*, 47, 976-985. <https://doi.org/10.1111/j.1365-2664.2010.01853.x>
- Novoa, C., Besnard, A., Brenot, J. F., & Ellison, L. N. (2008). Effect of weather on reproductive rate of Rock Ptarmigan *Lagopus muta* in the eastern Pyrenees. *Ibis*, 150(2), 270-278. <https://doi.org/10.1111/j.1474-919X.2007.00771.x>
- Prabhakar, C. S., & Dudhmal, D. (2016). Painted Stork (*Mycteria leucocephala*): Population status, shift in food and behavioral ecology from isolated ponds of Godavari River basin in Nanded district, India. *Science Research Reporter*, 6(1), 50-57.

- Slagsvold, T. (1989). On the evolution of clutch size and nest size in passerine birds. *Oecologia*, 79(3), 300-305. <https://doi.org/10.1007/BF00384308>.
- Sparks, T. H., & Tryjanowski, P. (2005). The detection of climate impacts: Some methodological considerations. *International Journal of Climatology*, 25(2), 271-277. <https://doi.org/10.1002/joc.1136>
- Urfi, A. J., Meganathan, T., & Kalam, A. (2007). Nesting ecology of Painted Stork (*Mycteria leucocephala*) at Sultanpur National Park (Haryana), India. *Forktail*, 23, 150-153.
- Urfi, A. J. (2010). Factors causing nest losses in the Painted Stork *Mycteria leucocephala*: A review of some Indian studies. *Journal of the Bombay Natural History Society*, 107, 55-58.
- Urfi, A. J. (2011a). Storks and humans. In A. J. Urfi (Ed.), *The Painted Stork* (pp. 121-130). Springer. https://doi.org/10.1007/978-1-4419-8468-5_7
- Urfi, A. J. (2011b). *The Painted Stork: Ecology and Conservation*. Springer.
- Urfi, A. J., & Kalam, A. (2006). Sexual size dimorphism and mating pattern in the Painted Stork (*Mycteria leucocephala*). *Waterbirds*, 29(4), 489-496. [https://10.1675/1524-4695\(2006\)29\[489:SSDAMP\]2.0.CO;2](https://10.1675/1524-4695(2006)29[489:SSDAMP]2.0.CO;2)
- Vergara, P., Gordo, O., & Aguirre, J. I. (2010). Nest size, nest building behaviour and breeding success in a species with nest reuse: The white stork *Ciconia ciconia*. *Annales Zoologici Fennici*, 47(3), 184-194. <https://doi.org/10.5735/086.047.0303>
- Yee, E. Y. S., Zainuddin, Z. Z., Ismail, A., Yap, C. K., & Tan, S. G. (2013). Identification of hybrids of Painted and Milky Storks using FTA card-collected blood, molecular markers, and morphologies. *Biochemical Genetics*, 51(9-10), 789-799. <https://doi.org/10.1007/s10528-013-9607-8>.
- Zakaria, M. A., & Nor, S. M. (2019). Population estimates of painted stork (*Mycteria leucocephala*) in three main breeding sites Peninsular Malaysia. *AIP Conference Proceedings*, 2111, 060005. <https://doi.org/10.1063/1.5111267>



REFEREES FOR THE PERTANIKA JOURNAL OF SCIENCE & TECHNOLOGY

Vol. 31 (2) Mar. 2023

The Editorial Board of the Pertanika Journal of Science and Technology wishes to thank the following:

Abdulrazak Yahya Saleh Al-Hababi (UNIMAS, Malaysia)	Lai Kee Huong (Sunway University, Malaysia)	Muhammed Nafis Osman Zahid (UMP, Malaysia)
Ahmad Ramli Mohd Yahya (USM, Malaysia)	Lam Man Kee (UTP, Malaysia)	Muzamir Isa (UNIMAP, Malaysia)
Akbulut Bilal (CFRI, Turkey)	Lee Loong Chuen (UKM, Malaysia)	Nor Atiqah Norazlimi (UTHM, Malaysia)
Amirreza Talaiekhazani (JIT, Iran)	Lee Min Lee (University of Nottingham, Malaysia)	Nor Azman Kasan (UMT, Malaysia)
Ana Sakura Zainal Abidin (UNIMAS, Malaysia)	Leong Siow Hoo (UiTM, Malaysia)	Nor Kamaliana Khamis (UKM, Malaysia)
Ayu Suzailiana Muhamad (USM, Malaysia)	Leow Soo Kar (Sunway University, Malaysia)	Noramalina Abdullah (USM, Malaysia)
Azhari Muhammad Syam (Malikussaleh University, Indonesia)	Luthffi Idzhar Ismail (UPM, Malaysia)	Norashikin Mohd Fauzi (UMK, Malaysia)
Chew Few Ne (UMP, Malaysia)	Mahirah Jahari (UPM, Malaysia)	Nurul Hashimah Ahamed Hassain Malim (USM, Malaysia)
Chua Han Bing (Curtin University, Malaysia)	Maria Justine Stephany (UiTM, Malaysia)	Phang Chang (UTHM, Malaysia)
Chuah Joon Huang (UM, Malaysia)	Marsyita Hanafi (UPM, Malaysia)	Puan Chong Leong (UPM, Malaysia)
Claudia Tomozei (University of Bacau, Romania)	Maziah Mohamad (UTM, Malaysia)	R. A. Ranga Prabodanie (Wayamba University, Sri Lanka)
Emienour Muzalina Mustafa (UMT, Malaysia)	Melody Kimi (UNIMAS, Malaysia)	Raja Kamarulzaman Raja Ibrahim (UTM, Malaysia)
Faizal Abdul Manaf (UPNM, Malaysia)	Milad Abbasi (KUMS, Iran)	Razi Ahmad (UNIMAP, Malaysia)
Gopinath Halder (NITDGP, India)	Mohamad Ikhsan Selamat (UiTM, Malaysia)	Robiah Ahmad (UTM, Malaysia)
Hasfalina Che Man (UPM, Malaysia)	Mohd Dilshad Ansari (CMRCET, India)	Rosli Ramli (UM, Malaysia)
Jasronita Jasni (UPM, Malaysia)	Mohd Husairi Fadzilah Suhaimi (UiTM, Malaysia)	Santy Paulla Dewi (Universitas Diponegoro, Indonesia)
Jayaraj Vijaya Kumaran (UMK, Malaysia)	Mohd Narizee Mohd Nasir (UKM, Malaysia)	Sapto Purnomo Putro (Diponegoro University, Indonesia)
K. Kannan (SASTRA University, India)	Mohd Shareduwan Mohd Kasihmuddin (USM, Malaysia)	Sara Yasina Yusuf (UNIMAP, Malaysia)

Sendilvelan Subramanian
(DRMGRDU, India)

Shahrul Anuar Mohd Sah
(USM, Malaysia)

Siti Nur Aliaa Roslan
(UPM, Malaysia)

Sitti Raehanah Muhamad Shaleh
(UMS, Malaysia)

Sivanesan Subramanian
(Anna University, India)

Suzanna Bono
(USM, Malaysia)

Syarifuddin Misbari
(UMP, Malaysia)

Vijay Kumar
(Manav Rachna International
University, India)

Wan Mohd Rauhan Wan Hussin
(UMT, Malaysia)

Zainab Ngaini
(UNIMAS, Malaysia)

CFRI - Central Fisheries Research Institute
CMRCET - CMR College of Engineering and Technology
DRMGRDU - Dr.M.G.R.Educational and Research Institute
JIT - Jami Institute of Technology
KUMS - Kermanshah University of Medical Sciences
NITDGP - National Institute of Technology Durgapur
UiTM - Universiti Teknologi MARA
UKM - Universiti Kebangsaan Malaysia
UM - Universiti Malaya
UMK - Universiti Malaysia Kelantan

UMP - Universiti Malaysia Pahang
UMS - Universiti Malaysia Sabah
UMT - Universiti Malaysia Terengganu
UNIMAP - Universiti Malaysia Perlis
UNIMAS - Universiti Malaysia Sarawak
UPM - Universiti Putra Malaysia
UPNM - Universiti Pertahanan Nasional Malaysia
USM - Universiti Sains Malaysia
UTHM - Universiti Tun Hussein Onn Malaysia
UTM - Universiti Teknologi Malaysia

While every effort has been made to include a complete list of referees for the period stated above, however if any name(s) have been omitted unintentionally or spelt incorrectly, please notify the Chief Executive Editor, *Pertanika* Journals at executive_editor.pertanika@upm.edu.my

Any inclusion or exclusion of name(s) on this page does not commit the *Pertanika* Editorial Office, nor the UPM Press or the university to provide any liability for whatsoever reason.

- Investigation of Acoustic and Vibrational Properties Using Laser Doppler Vibrometry (LDV) and Electronic Speckle Pattern Interferometry (ESPI) of the Kulintangan Instruments 1105
Sinin Hamdan, Ahmad Faudzi Musib, Khairul Anwar Mohamad Said, Saiful Hairi Othman and Marini Sawawi
- The Breeding Ecology of the Painted Stork *Mycteria leucocephala* in Central Peninsular Malaysia 1121
Mohd Amir Zakaria, Ummi Nur Syafiqah Daud, Mohammad Saiful Mansor and Shukor Md. Nor

Heat Stress and Noise Exposure Levels in a Manufacturing Plant <i>Qi Jie Kwong, Nursyifaasahirah Terbizi, Normaisarah Nordin, Emma Marinie Ahmad Zawawi, Azli Abd Razak and Jamalunlaili Abdullah</i>	961
TOPSIS for Analyzing the Risk Factors of Suicidal Ideation Among University Students in Malaysia <i>Sin Yin Chan and Chee Keong Ch'ng</i>	977
Influencing Physical Characteristics of Landslides in Kuala Lumpur, Malaysia <i>Syaidatul Azwani Zulkaflī, Nuriah Abd Majid, Sharifah Zarina Syed Zakaria, Muhammad Rizal Razman and Minhaz Farid Ahmed</i>	995
<i>Review Article</i>	
Subcritical Water Pretreatment for Anaerobic Digestion Enhancement: A Review <i>Adila Fazliyana Aili Hamzah, Muhammad Hazwan Hamzah, Hasfalina Che Man, Nur Syakina Jamali, Shamsul Izhar Siajam and Pau Loke Show</i>	1011
Distribution of Six Urban Bird Species in Urban Agglomeration of Central Region of Peninsular Malaysia Using Ebird Database <i>Aminah Madi, Fatihah Najihah Arazmi, Shukor Md. Nor and Mohammad Saiful Mansor</i>	1035
A Single Objective Crow Search for Modelling of Horizontal Flexible Plate Structure <i>Aida Nur Syafiqah Shaari, Muhamad Sukri Hadi and Abdul Malek Abdul Wahab</i>	1047
Physical and Electrical Breakdown Characteristics of Oil-Impregnated Kenaf Paper with the Introduction of External PVA for Transformer Application <i>Muhammad Umair, Norhafiz Azis, Rasmina Halis and Jasronita Jasni</i>	1069
The Predictive Ability of Total Genotype Score and Serum Metabolite Markers in Power-Based Sports Performance Following Different Strength Training Intensities — A Pilot Study <i>Elin Elisa Khairul, Wan Atiyyah Ab Wahab, Lay Kek Teh, Mohd Zaki Salleh, Mohd Salleh Rofiee, Raja Mohammed Firhad Raja Azidin and Sarina Md. Yusof</i>	1087

Potential of Fatty Acid Methyl Ester as Diesel Blends Produced from Free Fatty Acid in Waste Cooking Oil Catalyzed by Montmorillonite-Sulfonated Carbon	781
<i>Hasanudin Hasanudin, Wan Ryan Asri, Firda Rahmania Putri, Fahma Riyanti, Zainal Fanani, Addy Rachmat, Novia Novia and Tuty Emilia Agustina</i>	
Transfer Learning VGG16 Model for Classification of Tomato Plant Leaf Diseases: A Novel Approach for Multi-Level Dimensional Reduction	813
<i>Premkumar Borugadda, Ramasami Lakshmi and Satyasangram Sahoo</i>	
Efficient Frequency-Dependent Coefficients of Explicit Improved Two-Derivative Runge-Kutta Type Methods for Solving Third-Order IVPs	843
<i>Lee Khai Chien, Norazak Senu, Ali Ahmadian and Siti Nur Iqmal Ibrahim</i>	
An Optimum Classifier Model with Fuzzy C-Means for Fire Detection Technology	875
<i>Elaiyaraja Gandhi and Kumaratharan Narayanaswamy</i>	
Conceptual Design of a Combined Brake-Accelerator Pedal for Limbs Disabled Driver Using a Hybrid Approach	895
<i>Salami Bahariah Suliano, Siti Azfanizam Ahmad, Azizan As'arry and Faeza Abdul Aziz</i>	
The Photophysiology of Benthic Diatoms in the Intertidal Flats of Pulau Pinang (Malaysia)	911
<i>Sazlina Salleh, Elaine Ee Ling Cheng, Md. Solaiman Hossain, Shakila Samad, Nur Ain Amani Abdul Mubin, Nur Aqilah Muhamad Darif, Michelle Glory G Jonik and Mahadi Mohammad</i>	
<i>Review Article</i>	
The Impact of Calcium Chloride in Cementation Solution on Microbial Induced Calcite Precipitation: A Systematic Review	933
<i>Aljohani Waad Awdah Saad, Siti Norathirah Mohd Anas, Nor Safiqah Seminin, Putri Nur Suhaina Naim, Dardau Abdulaziz, Rusea Go, Nor Azwady Abdul Aziz, Mona Fatin Syazwaneer Mohamed Ghazali and Muskhazli Mustafa</i>	
Lung Function Analysis of Marble Home Industry Workers in Tulungagung Regency	947
<i>Noeroel Widajati, Tri Martiana, Tri Niswati Utami, Juliana Jalaludin and Titi Rahmawati Hamedon</i>	

Pertanika Journal of Science & Technology

Vol. 31 (2) Mar. 2023

Content

Foreword <i>Mohd Sapuan Salit</i>	i
<i>Review Article</i>	
The Impact of Integrating Multi-Microgrid System with FACTS Devices for Voltage Profile Enhancement and Real Power Loss Reduction in Power System: A Review <i>Ainna Nadirah Zubidi, Bazilah Ismail, Ibrahim Mohamed Ali Al Hamrounni, Nadia Hanis Abd Rahman and Mohd Helmy Hakimie Mohd Rozlan</i>	633
Modified K-Means Clustering for Demand-Weighted Locations: A Thailand's Convenience Store Franchise - Case Study <i>Chartchai Leenawong and Thanrada Chaikajonwat</i>	655
Visible-Near-Infrared Spectroscopy and Chemometrics for Authentication Detection of Organic Soybean Flour <i>Rudiati Evi Masithoh, Muhammad Fahri Reza Pahlawan, Devi Alicia Surya Saputri and Farid Rakhmat Abadi</i>	671
Optimum Temperature and Salinity Conditions for Growth, Lipid Contents, and Fatty Acids Composition of Centric Diatoms <i>Chaetoceros Calcitrans</i> and <i>Thalassiosira Weissflogii</i> <i>Ahmed Awadh Ahmed Sas, Aziz Arshad, Simon Kumar Das, Suriyanti Su Nyun Pau and Zaidi Che Cob</i>	689
Production of Biosurfactant Using <i>Bacillus subtilis</i> Natto Fermentation <i>Yew Seng Leow, Norhafizah Abdullah, Dayang Radiah Awang Biak, Nur Syakina Jamali, Rozita Rosli and Huey Fang Teh</i>	709
Aquaculture Wastewater Quality Improvement by Floating Raft of Native Aquatic Plants in An Giang Province, Vietnam <i>Khanh Tran Thien Nguyen, Chi Thi Dao Vo, An Thuy Ngo, Nghi Thanh Doan, Luyen Phuc Huynh and Dung Huynh Thuy Tran</i>	729
Characterising Colour Feature Descriptors for <i>Ficus carica</i> L. Ripeness Classification Based on Artificial Neural Network (ANN) <i>Ilyia Adhwa Mazni I, Samsul Setumin, Mohamed Syazwan Osman, Muhammad Khusairi Osman and Mohd Subri Tahir</i>	759



Pertanika Editorial Office, Journal Division,
Putra Science Park,
1st Floor, IDEA Tower II,
UPM-MTDC Center,
Universiti Putra Malaysia,
43400 UPM Serdang,
Selangor Darul Ehsan
Malaysia

<http://www.pertanika.upm.edu.my>
Email: executive_editor@upm.edu.my
Tel. No.: +603- 9769 1622

PENERBIT
UPM
UNIVERSITI PUTRA MALAYSIA
PRESS

<http://www.penerbit.upm.edu.my>
Email: penerbit@upm.edu.my
Tel. No.: +603- 9769 8851

